

# IIUM ENGINEERING JOURNAL

**Volume 21**

**Number 2**

**July 2020**



**IIUM  
Press**

**INTERNATIONAL ISLAMIC UNIVERSITY MALAYSIA**

**ISSN: 1511-788X E-ISSN: 2289-7860**

**<http://journals.iium.edu.my/ejournal>**



# IIUM ENGINEERING JOURNAL

---

## **CHIEF EDITOR**

Ahmad Faris Ismail, IIUM, Malaysia

## **EXECUTIVE EDITOR**

AHM Zahirul Alam, IIUM, Malaysia

## **ASSOCIATE EDITOR**

Nor Farahidah Za'bah, IIUM, Malaysia

## **LANGUAGE EDITOR**

Lynn Mason, Malaysia

## **COPY EDITOR**

Hamzah Mohd. Salleh, IIUM, Malaysia

## **EDITORIAL BOARD MEMBERS**

Abdullah Al-Mamun, IIUM, Malaysia  
Abdumalik Rakhimov, IIUM, Malaysia  
Ali Sophian, IIUM, Malaysia  
Erry Yulian Triblas Adesta, IIUM, Malaysia  
Erwin Sulaeman, IIUM, Malaysia  
Hanafy Omar, Saudi Arabia  
Hazleen Anuar, IIUM, Malaysia  
Konstantin Khanin, University of Toronto, Canada  
Ma'an Al-Khatib, IIUM, Malaysia  
Md Zahangir Alam, IIUM, Malaysia  
Meftah Hrairi, IIUM, Malaysia  
Mohamed B. Trabia, United States  
Mohammad S. Alam, Texas A&M University-Kingsville, United States  
Mustafizur Rahman, National University Singapore, Singapore  
Ossama Abdulkhalik, Michigan Technological University, United States  
Razi Nalim, IUPUI, Indianapolis, Indiana, United States  
Rosminazuin AB. Rahim, IIUM, Malaysia  
Waqar Asrar, IIUM, Malaysia

## **AIMS & SCOPE OF IIUMENGINEERING JOURNAL**

The **IIUM Engineering Journal**, published biannually (January and July), is a carefully refereed international publication of International Islamic University Malaysia (IIUM). Contributions of high technical merit within the span of engineering disciplines; covering the main areas of engineering: Electrical and Computer Engineering; Mechanical and Manufacturing Engineering; Automation and Mechatronics Engineering; Material and Chemical Engineering; Environmental and Civil Engineering; Biotechnology and Bioengineering; Engineering Mathematics and Physics; and Computer Science and Information Technology are considered for publication in this journal. Contributions from other areas of Engineering and Applied Science are also welcomed. The IIUM Engineering Journal publishes contributions under *Regular papers and Invited review papers*. It also welcomes contributions that address solutions to the specific challenges of the developing world, and address science and technology issues from an Islamic and multidisciplinary perspective.

## **REFEREES' NETWORK**

All papers submitted to IIUM Engineering Journal will be subjected to a rigorous reviewing process through a worldwide network of specialized and competent referees. Each accepted paper should have at least two positive referees' assessments.

## **SUBMISSION OF A MANUSCRIPT**

A manuscript should be submitted online to the IIUM-Engineering Journal website at <http://journals.iium.edu.my/ejournal>. Further correspondence on the status of the paper could be done through the journal website.

---

## INTERNATIONAL ADVISORY COMMITTEE

A. Anwar, United States  
Abdul Latif Bin Ahmad, Malaysia  
Farzad Ismail, USM, Pulau Pinang, Malaysia  
Hanafy Omar, Saudi Arabia  
Hany Ammar, United States  
Idris Mohammed Bugaje, Nigeria  
K.B. Ramachandran, India  
Kunzu Abdella, Canada  
Luis Le Moyne, ISAT, University of Burgundy, France  
M Mujtaba, United Kingdom  
Mohamed Al-Rubei, Ireland  
Mohamed B Trabia, United States  
Syed Kamrul Islam, United States  
Tibor Czigany, Budapest University of Technology and Economics, Hungary  
Yiu-Wing Mai, The University of Sydney, Australia.

Published by:

**IUM Press,**  
International Islamic University Malaysia  
Jalan Gombak, 53100 Kuala Lumpur, Malaysia  
Phone (+603) 6421-5014, Fax: (+603) 6421-6298

Whilst every effort is made by the publisher and editorial board to see that no inaccurate or misleading data, opinion or statement appears in this Journal, they wish to make it clear that the data and opinions appearing in the articles and advertisement herein are the responsibility of the contributor or advertiser concerned. Accordingly, the publisher and the editorial committee accept no liability whatsoever for the consequence of any such inaccurate or misleading data, opinion or statement.

ISSN 1511 - 788X



**IUM Engineering Journal**  
ISSN: 1511-788X E-ISSN: 2289-7860

**IUM ENGINEERING JOURNAL**  
Volume 21, Issue 2, July 2020  
<https://doi.org/10.31436/iiumej.v21i2>

**Table of Content**

---

<b>EDITORIAL</b> .....	i
<b>CHEMICAL AND BIOTECHNOLOGY ENGINEERING</b>	
1150: THE EFFECTS OF CERIUM PROMOTER ON THE PERFORMANCE OF COBALT-BASED CATALYSTS IN FISCHER TROPSCH SYNTHESIS FOR LIQUID FUEL PRODUCTION .....	1
<i>Firas Khaleel Al-zuhairi, Wafaa Abdul Kadhim , Ahmed Lateef Khalaf and Mohd Hasbi Ab Rahim</i>	
1203: EFFECTS OF PH, DOSAGE AND CONTACT TIME ON BORON REMOVAL FROM SYNTHETIC SALINE WATER USING MORINGA OLEIFERA SEEDS .....	12
<i>Mohammed Saedi Jami, Nur Syahirah Zakaria, Moussa Mahamed Ahmed, Nik Rashida Nik Abdul Ghani, Mohammed Ngabura and Mani Malam Ahmad</i>	
1207: NITROGEN AND PHOSPHORUS REMOVAL EFFICIENCY OF THREE HELOPHYTES IN CONSTRUCTED SURFACE FLOW WETLANDS FOR URBAN WASTEWATER TREATMENT .....	25
<i>Abdeslam Ennabili and Michel Radoux</i>	
1306: ANALYSIS AND CORRELATIONS OF DIMENSIONLESS NUMBERS RELEVANT TO ORIFICES' CAVITATING FLOW .....	41
<i>Abdul-Fattah Mohammed Ali and Mohanad Jasim Mohammed-Ridha</i>	
1320: BIODELIGNIFICATION OF LEMON PEELS USING ASPERGILLUS SP. TO IMPROVE YIELD AND COMPOSITION OF EXTRACTED LEMON OIL.....	55
<i>Muhammad Yusuf Abduh, Enjelina Nababan, Firdanta Ginting and Jenny Juliati, Husna Nugrahapraja</i>	
1351: STATISTICAL ANALYSIS OF GROWTH CONDITIONS OF NEWLY ISOLATE BACILLUS SP. PRODUCING L-ASPARAGINASE ...	67
<i>Dzun Noraini Jimat1, Intan Baizura Firda Mohamed, Azlin Suhaida Azmi1 and Azura Amid</i>	
<b>CIVIL AND ENVIRONMENTAL ENGINEERING</b>	
1245: A COMPARATIVE STUDY ON TREATMENT TECHNOLOGIES FOR SEWAGE RECLAMATION: A FOCUS ON THE DISINFECTION PROCESS .....	80
<i>Noorini Izzati Mohamad Mazuki, Teow Yeit Haan and Abdul Wahab Mohammad</i>	
1285: INFLUENCE OF PALM OIL BIOMASS CLINKER AND EMPTY FRUIT BUNCH FIBERS ON CONCRETE PROPERTIES .....	100
<i>Mohd Haziman Wan Ibrahim, Sajjad Ali mangi, Sharifah Salwa Mohd Zuki, Ramadhansyah Putra Jaya and Dadang Supriyatno</i>	
1293: THE CHARACTERISTICS OF REED LIGHTWEIGHT CLAY BRICKS AFTER DRYING PROCESS .....	111
<i>Ghazwan Abdulsamad Salman</i>	
1329: INFLUENCE OF WIND WAVES ON THE FLOW IN FLOWING RESERVOIRS .....	125
<i>Sobir Samatovich Eshev, Alisher Normurodovich Khazratov, Ashraf Rasul o`gli Rahimov and Shahboz Alisher o`gli Latipov</i>	
<b>ELECTRICAL, COMPUTER AND COMMUNICATIONS ENGINEERING</b>	
1273: IMPROVE THE EFFICIENCY OF THE POWER TRANSMISSION SYSTEM USING THE GENETIC ALGORITHM TO DETERMINE THE OPTIMUM LOCATION AND FACTS DEVICES .....	133
<i>Husam Hasan Mohammed, Hiba Zuhair Abdul Kareem and Wafaa Mohammed Ridha</i>	
1322: BORDER SURVEILLANCE USING FACE RECOGNITION, MOBILE OTP AND EMAIL .....	145
<i>Naresh Kumar, Deepali Gupta</i>	
1408: WORD SEGMENTATION OF OUTPUT RESPONSE FOR SIGN LANGUAGE DEVICES .....	153
<i>Nor Farahidah Za`bah, Ahmad Amierul Asyraf Muhammad Nazmi and Amelia Wong Azman</i>	
<b>MATERIALS AND MANUFACTURING ENGINEERING</b>	
1197: SPACE MAPPING OF HIP AND WRISTS MOTIONS FOR DIFFERENT TRANSFER DISTANCES IN MANUAL MATERIAL HANDLING TASK .....	164
<i>Radin Zaid Radin Umar, Fatin Ayuni Mohd Azli Lee, Muhammad Naqiuddin Khafiz, Nadiyah Ahmad and Nazreen Abdullasim</i>	
1227: CUTTING TOOL PERFORMANCE IN TURNING OF AL 7075-T651 ALUMINIUM ALLOY .....	177
<i>Nur Sofwati Daud @ Ab Aziz, Natasha A. Raof, Abdul Rahman A. Ghani, Aishah Najiah Dahne, Suhaily Mokhtar and Nor Khairusshima Muhamad Khairussaleh</i>	

1317: INVESTIGATION ON INFLUENCE OF ANIONIC SURFACTANT FOR HOMOGENISATION OF MWCNT IN ALUMINIUM 6065 MATRIX.....	186
<i>Savina Jaddinagadhe Puttaswamy and Raghavendra Bommanahalli Venkatagiriappa</i>	
1336: EFFECT OF SPINNING PARAMETERS ON PLA/PPC/CURCUMIN MICROFIBER DIAMETER: AN INVESTIGATION VIA RESPONSE SURFACE METHODOLOGY.....	197
<i>Sharifah Imihezri Syed Shahrudin, Amirul Akmal Fauzan, Mohamad Faris Izzudin Mohamad Jazi, Nur Atiqah Mohd. Akhir, Maizatunisa Othman, Nor Khairushima Muhamad Khairussaleh, Norhashimah Shaffiar and Zaimah Hasan</i>	
1354: DEVELOPMENT OF LOW-COST ADDITIVE MANUFACTURING SYSTEM THROUGH SELECTIVE INHIBITION SINTERING (SIS) PROCESS AND EVALUATION OF MECHANICAL CHARACTERISTICS OF FABRICATED PARTS.....	212
<i>Mesfin Sisay Mengesha, Balasubramanian Esakki, Arunkumar Ponnambalam, Silambarasan Mathiyazhagan and Rajamani Devaraj</i>	
1388: PREPARATION AND CHARACTERIZATIONS OF LATEX/FILLER NANOCOMPOSITES .....	230
<i>Mohamad Firdaus Omar, Nuriah Mohamad and Fathilah Binti Ali</i>	
1469: EFFECT OF CHITIN SOURCE AND CONTENT ON PROPERTIES OF CHITIN NANOWHISKERS FILLED POLYLACTIC ACID COMPOSITES .....	239
<i>Syazeven Effatin Azma Mohd Asri, Zainoha Zakaria, Azman Hassan and Mohamad Haafiz Mohamad Kassim</i>	

#### **ENGINEERING MATHEMATICS AND APPLIED SCIENCE**

1456: FORMALIZATION OF THE COTTON DRYING PROCESS BASED ON HEAT AND MASS TRANSFER EQUATIONS .....	256
<i>Yunusova Sayyora Toshkenboyevna, Halmatov Davron Abdalimovich, Atajonov Muhiddin Odiljonovich and Huzan azarov Ulugbek Olimovich</i>	

#### **MECHANICAL AND AEROSPACE ENGINEERING**

1454: CRACK INFLUENCE ON A PIPE WITH DOUBLE SLOPE UNDER INTERNAL PRESSURE: NUMERICAL SIMULATION WITH XFEM.....	266
<i>Salmi Houda, Hachim Abdelilah, EL bhilat Hanan and El Had Khalid</i>	

## THE EFFECTS OF CERIUM PROMOTER ON THE PERFORMANCE OF COBALT-BASED CATALYSTS IN FISCHER TROPSCH SYNTHESIS FOR LIQUID FUEL PRODUCTION

FIRAS KHALEEL AL-ZUHAIRI<sup>1</sup>, WAFAA ABDUL KADHIM<sup>2</sup>,  
AHMED LATEEF KHALAF<sup>3\*</sup> AND MOHD HASBI AB RAHIM<sup>4</sup>

<sup>1</sup>Petroleum Technology Department,

<sup>2</sup>Nanotechnology & Advanced Material Research Center (NAMRC),  
University of Technology, Baghdad, Iraq

<sup>3</sup>Department of Computer Engineering Techniques,  
Al-Ma'moon University College, Baghdad, Iraq

<sup>4</sup>Faculty of Industrial Sciences & Technology, Universiti Malaysia Pahang,  
Gambang, Pahang, Malaysia

\*Corresponding author: [ahmed.l.khalaf@almamonuc.edu.iq](mailto:ahmed.l.khalaf@almamonuc.edu.iq)

Received: 28<sup>th</sup> April 2019; Accepted: 13<sup>th</sup> March 2020; Published on-line: 4<sup>th</sup> July 2020)

**ABSTRACT:** An intensive work of Fischer-Tropsch synthesis (FTS) on a cobalt-based catalyst supported with cerium as a promoter was presented. The influence of space velocity and inlet gas feed ratio on FTS reaction performance was studied for the synthesized catalysts. Incipient wetness impregnation method was utilized to synthesis both unpromoted (25%Co/ $\gamma$ -Al<sub>2</sub>O<sub>3</sub>) and cerium promoted (1%Ce-25%Co/ $\gamma$ -Al<sub>2</sub>O<sub>3</sub>) catalysts. The proposed catalysts were examined by N<sub>2</sub> adsorption and temperature-programed reduction (TPR). The performance of Ce-promoted and unpromoted cobalt-based catalysts in FTS was assessed in terms of activity and selectivity to desired products (C<sub>5+</sub>). The obtained results revealed that the addition of cerium by impregnation notably favours the reducibility of cobalt oxides by reducing the reduction temperature. In addition, the promoted catalysts exhibited higher activity and selectivity toward desired products at low space velocity and high inlet gas feed ratio as compared with the unpromoted catalysts. In conclusion, a cerium based cobalt catalyst considered as a suitable candidate to be used in gas to the liquid conversion process.

**ABSTRAK:** Kajian intensif sintesis Fischer-Tropsch (FTS) adalah tentang pemangkin berasas kobalt bersama penggalak cerium. Pengaruh tindak balas FTS pada halaju ruang dan nisbah suapan gas masuk dikaji menggunakan pemangkin yang disintesis. Kaedah impregnasi insipien basah telah digunakan bagi mensintesis pemangkin bukan penggalak (25%Co/ $\gamma$ -Al<sub>2</sub>O<sub>3</sub>) dan penggalak cerium (1%Ce-25%Co/ $\gamma$ -Al<sub>2</sub>O<sub>3</sub>). Pemangkin ini diuji dengan penjerapan N<sub>2</sub> dan pengurangan suhu terprogram (TPR). Hasil tindak balas penggalak-Ce dan bukan penggalak berasas kobalt dalam FTS diperiksa dari segi aktiviti dan pemilihan hasil (C<sub>5+</sub>). Tindak balas menunjukkan dengan penambahan cerium melalui kaedah impregnasi dengan ketara mengurangkan kobalt oksida bersama pengurangan suhu. Di samping itu, pemangkin penggalak menunjukkan aktiviti dan pemilihan ke arah hasil pada halaju ruang dan nisbah suapan gas masuk yang tinggi berbanding dengan pemangkin bukan penggalak. Kesimpulan, pemangkin kobalt berasas cerium dianggap sesuai sebagai pemangkin sintesis bagi digunakan dalam proses penukaran gas ke cecair.

**KEYWORDS:** catalyst, cerium promoter, Fischer-Tropsch synthesis, GTL, syngas;

## 1. INTRODUCTION

Over the past few decades, natural gas has been considered a plentiful and cleanest natural fuel that should be altered to liquid form to prevent safety hazards and to reduce transportation costs [1]. Natural gas, methane (CH<sub>4</sub>) is commonly employed to produce synthesized gas (syngas) via different techniques, such as partial oxidation [2], steam reforming [3], and auto-thermal reforming [4].

Recently, the gas-to-liquid technique (GTL) has been considered one of the most efficient processes that is mainly used to convert natural gas into a syngas intermediate through a Fischer-Tropsch (FT) synthesis technology [5]. In general, the GTL process produces oil crudes that contain different fractions of useful hydrocarbons that can be amended and segregated to different types of necessary transportation sector fuels [6], in the presence of solid catalysts.

Because of their high C<sub>5+</sub> selectivity, excellent activity, and ability to work at low operating temperatures (between 200 and 250 °C), Co-based catalysts are in the limelight recently as an effective catalyst for attaining heavy hydrocarbons in FT synthesis [7, 8]. Thus, it is of a great necessity to improve the efficiency of Co-based catalysts. Many researches have demonstrated that adding different promoters and loadings to the catalyst assists in improving the selectivity and activity of the catalyst towards C<sub>5+</sub> contents. Guo et al. [9] reported that adding a small amounts of Lanthanum to the Co/ $\gamma$ -Al<sub>2</sub>O<sub>3</sub> catalyst could enhance the performance of the catalyst in terms of selectivity, activity, and Co reducibility to heavy hydrocarbons. Co reducibility was significantly increased by adding different loading of silver to the Co-based catalyst [10]. Furthermore, the addition of silver helps in decreasing the reduction temperatures by up to 100 °C and increasing the Co reduction, dispersion, and electronic properties.

Another study by Pedersen et al. [11] employed manganese (Mn) as a promoter for a Co-based catalyst supported by  $\gamma$ -Al<sub>2</sub>O<sub>3</sub>. They found that Mn enhanced the intrinsic Co catalyst activity, Co dispersion, and selectivity to C<sub>5+</sub> species due to its stable effect on the adsorption of CO, C, H, O, CHX, thereby decreasing the CO dissociation barrier. Rare earth elements were also utilized to improve the performance of the Co-based catalyst supported by Al<sub>2</sub>O<sub>3</sub>, SiO<sub>2</sub>, TiO<sub>2</sub>, ZrO<sub>2</sub>, and CNTs [12, 13].

Among all the discussed promoters, Co-based catalysts promoted with Cerium (Ce) attained excellent performance in FT synthesis technology due to its ability to facilitate the dissociation of CO, weaken the interaction between support and Co and improve the activity, C<sub>5+</sub> selectivity and the olefin/paraffin ratio of the Co-based catalyst [13-15]. Although many studies have been conducted on Ce as a promoter for Co-based catalysts, there are great opportunities in further investigating the influence of reaction conditions on the cerium- promoted cobalt-based catalyst in FTS reactions.

Herein, we thoroughly study and evaluate the effects of reaction conditions (space velocity and H<sub>2</sub>/CO ratio) on the cerium-promoted Co-based catalyst in terms of FTS activity and product selectivity. The developed catalyst shows excellent results as compared with those of the un-promoted cobalt-based catalyst.

## 2. MATERIALS AND METHODS

### 2.1 Catalysts Preparation

Incipient wetness impregnation method was employed to synthesize the Co-based catalysts supported by  $\gamma$ -Al<sub>2</sub>O<sub>3</sub> (Axens) according to the method reported by Trépanier et

al. [16]. Initially, the support ( $\gamma$ - $\text{Al}_2\text{O}_3$ ) was calcined in airflow at 500 °C for 4 h. After cooling down the temperature to room temperature (25 °C), sequential impregnation with continuous stirring in aqueous solutions of Cobalt (II) nitrate hexahydrate ( $\text{Co}(\text{NO}_3)_2 \cdot 6\text{H}_2\text{O}$ ) was performed at ambient temperature. Then, 25 % of Co by weight was laden to the mixture and left to dry for 12 h at 110 °C and then calcined at 400 °C for 6 h beneath airflow with a degree of temperature increase 2°C/min to attain 25 Co/ $\gamma$ - $\text{Al}_2\text{O}_3$  reduced catalyst.

To obtain the Ce promoted catalyst, 1wt. % of Ce promoter was added to 25 Co/ $\gamma$ - $\text{Al}_2\text{O}_3$  dried un-calcined catalyst by the co-impregnation in an aqueous solution of Cerium nitrate hexahydrate ( $\text{Ce}(\text{NO}_3)_2 \cdot 6\text{H}_2\text{O}$ ) and dried overnight for 12 h at 110 °C. Later, the catalyst was calcined at 400 °C for 6 h with a heating rate of 2 °C/min under airflow. The developed catalysts were labelled as  $\text{Co}_0$  and  $\text{Co}_1$  representing unpromoted and Ce promoted Co-based catalysts, respectively.

## 2.2 Catalyst Characterization

The calcined prepared catalysts were characterized by temperature-programed reduction (TPR) and  $\text{N}_2$  physisorption. The temperature-programed reductions were accomplished to decide the reducibility of metal oxides to metallic using a TP-5000 analyser fitted with a quartz tubular reactor and TCD. A 50 mg of each sample was exposed to a continuous argon gas flow at rate of 1.8 L/h containing 5 % of  $\text{H}_2$  with heating temperature ranging from 25 °C to 900 °C with increments of 10 °C per min.

$\text{N}_2$  physisorption isotherm analysis was done using the Micromeritics ASAP-2020 system, to estimate the BET surface area, pore-volume, and the average pore radius for the  $\gamma$ - $\text{Al}_2\text{O}_3$  and catalysts.

## 2.3 Fischer-Tropsch Reaction (FTR)

As aforementioned, the FTR process was utilized to convert synthesized gas to liquid fuel (high molecules weight hydrocarbons). The activity and selectivity of the developed catalysts were investigated in a fixed-bed flow reactor made from a stainless steel metal with internal diameter of 10 mm. Two grams of the promoted and unpromoted Co-based was loaded in the centre of the reactor and fixed between two quartz beads, then heated under argon gas to reduction temperature, the reduction was conducted by (5%  $\text{H}_2$ -95%Ar) gas mixture to convert the forms of metal from oxide to the metallic. After finishing the reduction, the reactant gases mixtures ( $\text{H}_2$  and CO) were introduced to the reactor with a desired flow rate using a mass flow controller (Brooks 5850) fitted with a PID controller.

The FT reactions were conducted at a temperature of 230 °C and pressure of 15 bar with different space velocity (SV) in the range of 2 - 8 L/h.g<sub>cat</sub>. (with increments of 2) and different feed gas ratio ( $\text{H}_2/\text{CO}$ ) of 1 to 2 (with increments of 0.5). The output stream from the reactor was lowered to atmospheric pressure by a control valve (BPR) and then went over two traps. The first one was at 100 °C and the other was 0 °C to condense the products. The compositions of products in a gas and liquid phase were analysed online and off-line using a gas chromatograph (GC-Shimadzu-2014) equipped with (TCD and FID) and Varian CP 3800 equipped with FID, respectively.

# 3. RESULTS AND DISCUSSION

## 3.1 Catalyst Characterization

The TPR profiles for the unpromoted (25%Co/ $\gamma$ - $\text{Al}_2\text{O}_3$ ) and promoted (1%Ce-25%Co/ $\gamma$ - $\text{Al}_2\text{O}_3$ ) calcined catalysts are illustrated in Fig. 1. Three reduction peaks are

clearly observed for the un-promoted Co-based catalyst. The reduction of  $\text{Co}_3\text{O}_4$  to  $\text{CoO}$  ( $\text{Co}^{3+} \rightarrow \text{Co}^{2+}$ ) and  $\text{CoO}$  to  $\text{Co}$  metal ( $\text{Co}^{2+} \rightarrow \text{Co}^0$ ) can be allocated at 350 °C and 577 °C, respectively [17]. While, the weak peak noticed around 702 °C can be attributed to the reduction of cobalt aluminate compounds [18]. On the other hand, the catalyst promoting with 1% Ce has robustly influenced the TPR profile, as revealed in Fig. 1, where the first and second peaks obviously shifted to lower temperature, at 252 °C and 527 °C, respectively, due to the significant easy reduction of  $\text{CoO}$  to  $\text{Co}$  metal along with the low interaction between  $\text{Co}$  ions and the  $\text{Al}_2\text{O}_3$  support [19, 20]. As a result, the third peak related to cobalt aluminate compounds observed in the un-promoted catalyst disappeared. In addition, the TPR outcomes confirmed that the selected reduction parameters (5%  $\text{H}_2$ -95%  $\text{Ar}$ ) mixture by rate of flow 1.8 L/h at 570 °C for 10 h) were appropriate for reducing the cobalt oxides into cobalt metal in- suite apparatus prior to the FT reaction.

Table 1 listed the results of single point pore volume, BET surface area (SA) and pore size for the calcined support ( $\gamma\text{-Al}_2\text{O}_3$ ),  $\text{Co}_0$ , and  $\text{Co}_1$  catalysts. From the table, it can be noticed that the SA of  $\gamma\text{-Al}_2\text{O}_3$ ,  $\text{Co}_0$ , and  $\text{Co}_1$  were found to be 145, 95.2 and 94.6  $\text{m}^2/\text{g}$ , respectively.

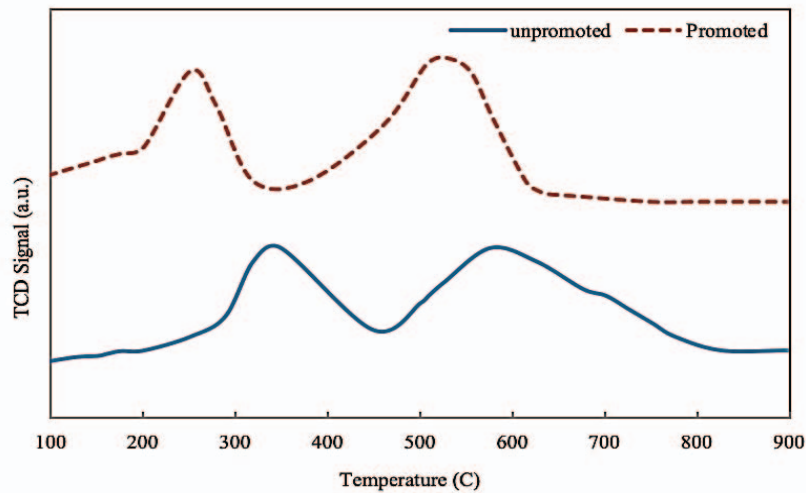


Fig. 1: TPR profiles for the un-promoted ( $25\%\text{Co}/\gamma\text{-Al}_2\text{O}_3$ ) and promoted ( $1\%\text{Ce-}25\%\text{Co}/\gamma\text{-Al}_2\text{O}_3$ ) calcined catalysts.

Table 1: BET surface area and pore volume for the developed catalysts

Catalyst	Symbol	BET ( $\text{m}^2/\text{g}$ )	SA pore volume ( $\text{cm}^3/\text{g}$ )	pore size (nm)
$\gamma\text{-Al}_2\text{O}_3$	-	145	0.542	6.8
$25\%\text{Co}/\gamma\text{-Al}_2\text{O}_3$	$\text{Co}_0$	95.2	0.276	4.9
$1\%\text{Ce-}25\%\text{Co}/\gamma\text{-Al}_2\text{O}_3$	$\text{Co}_1$	94.6	0.265	4.7

SA for the support was 145  $\text{m}^2/\text{g}$  which plunged to 95.2  $\text{m}^2/\text{g}$  for the un-promoted catalyst, the 25% of  $\text{Co}$  corresponds to 34%  $\text{Co}_3\text{O}_4$ . According to the obtained cobalt oxide percentage, the theoretical value of the BET surface area catalyst was approximately 95.6  $\text{m}^2/\text{g}$  for the un-promoted catalyst. The theoretical and experimental BET surface area values were more closed owing to the minimum pore plugged by cobalt species [21]. Adding the Ce promoter causes a small decrement in the surface area. In addition, the pore volume and pore size for the  $\gamma\text{-Al}_2\text{O}_3$  were 0.542  $\text{cm}^3/\text{g}$  and 6.8 nm, respectively, that

decreases to 0.276 cm<sup>3</sup>/g and 4.9 nm, accordingly, for Co<sub>0</sub>. Pore volume and pore size were slightly altered in Co<sub>1</sub>. These results are in good agreement with the results reported by Gnanamani et al. [22].

### 3.2 Fischer-Tropsch Synthesis

Production of liquid fuels by FT synthesis process is considered as one of the most important techniques used to tackle the problem of fuel shortage in the transport sector [23]. To investigate the influences of space velocity and inlet feed ratio (H<sub>2</sub>/CO) on the activity of unprompted and Ce promoted catalysts and their selectivity toward liquid fuels production, number of experiments of Fischer-Tropsch reaction were conducted at a temperature of 230 °C, pressure of 15 bar, and different space velocity and inlet feed ratios (H<sub>2</sub>/CO). After steady-state condition of about 8 to 9 h, the percentage of carbon monoxide conversion (%X<sub>CO</sub>) and product selectivity (%) were examined.

#### 3.2.1 Influence of Space Velocity on Catalyst Performance

Figure 2 shows that the CO conversion (%X<sub>CO</sub>) as a function of space velocities of the developed catalysts (Co<sub>0</sub> and Co<sub>1</sub>) ranges from 2 to 8 L/h. g<sub>cat.</sub> with different H<sub>2</sub>/CO ratios between 1 and 2 for each SV at operating temperature and applied pressure of 230 °C and 15 bar, respectively. The obtained results demonstrated that the CO conversion sharply decreased when SV increased thereby, the residence time of reaction decreased. Thus, CO conversion and chain growth decrease, which assures the rapid increase in the formation of low molecular weight hydrocarbons (CH<sub>4</sub> and C<sub>2</sub>-C<sub>4</sub>) and the decrease in production of high molecular weight hydrocarbons (C<sub>5+</sub>) [24].

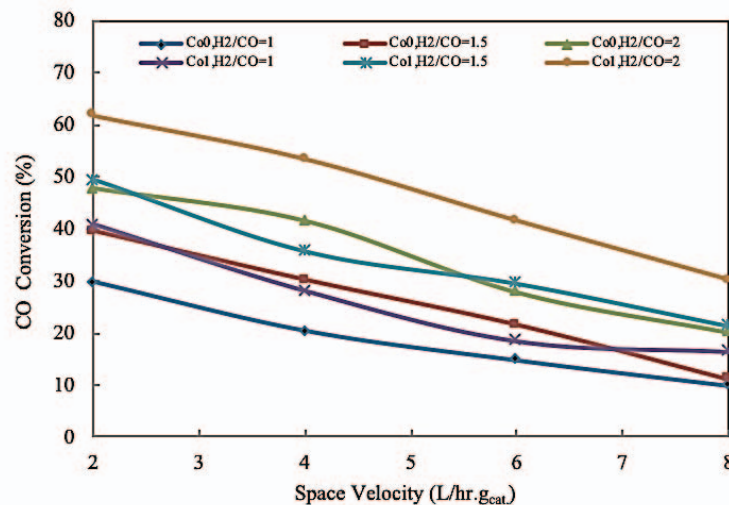


Fig. 2: Effect of space velocity on carbon monoxide conversion for the Ce-promoted and unprompted cobalt catalysts at P = 15 bar, T= 230 °C, and H<sub>2</sub>/CO= 1, 1.5, and 2.

The selectivity of the developed catalysts (Co<sub>0</sub> and Co<sub>1</sub>) toward CH<sub>4</sub>, C<sub>2</sub>-C<sub>4</sub> hydrocarbons, C<sub>5+</sub>, and CO<sub>2</sub> are demonstrated in Fig. 3(a-d). It is evident that the product selectivity of both catalysts against CH<sub>4</sub>, C<sub>2</sub>-C<sub>4</sub> hydrocarbons, and CO<sub>2</sub> increased proportionally with SV while the desired product (C<sub>5+</sub>) decreased. This is because an increase in SV leads to a significant decrease in the residence time of reaction, thereby decreasing the CO conversion, which is in agreement with the results reported in [24]. Figure 3a shows that the selectivity of Co<sub>0</sub> and Co<sub>1</sub> toward CO<sub>2</sub> were very small (< 3). This can be attributed to the little activity of water-gas shift mainly obtained by the Co

based catalyst [25, 26]. Furthermore, the promoted Co-based catalysts exhibited an excellent Co conversion and  $C_{5+}$  selectivity by decreasing the SV due to the presence of Ce promoter which aids in increasing the amount of chemisorbed hydrogen and weakening the strong bond of Co–H [27]. Table 2 summarized the obtained results.

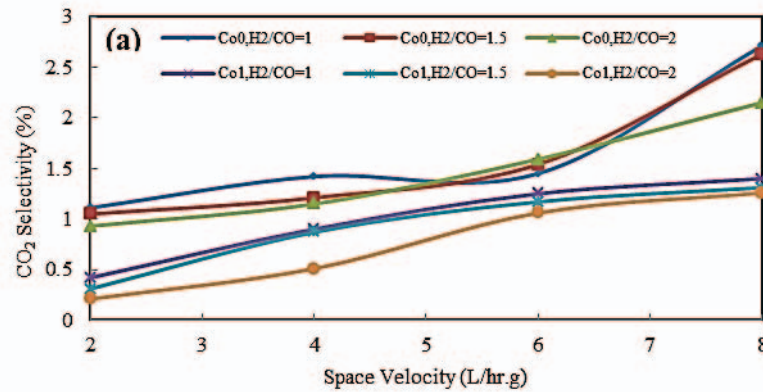


Fig. 3: (a) Effect of SV on CO<sub>2</sub> selectivity for the Ce-promoted and unpromoted cobalt catalysts at P = 15 bar, T= 230 °C and H<sub>2</sub>/CO ranging from 1 to 2.

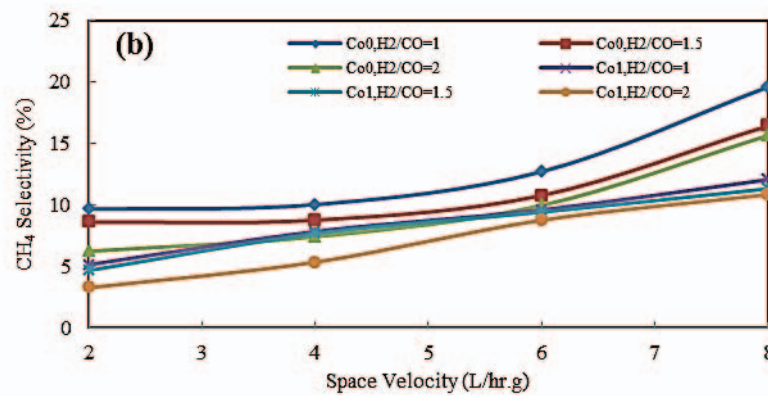


Fig. 3: (b) Effect of SV on CH<sub>4</sub> selectivity for the Ce-promoted and unpromoted cobalt catalysts at P = 15 bar, T= 230 °C and H<sub>2</sub>/CO ranging from 1 to 2.

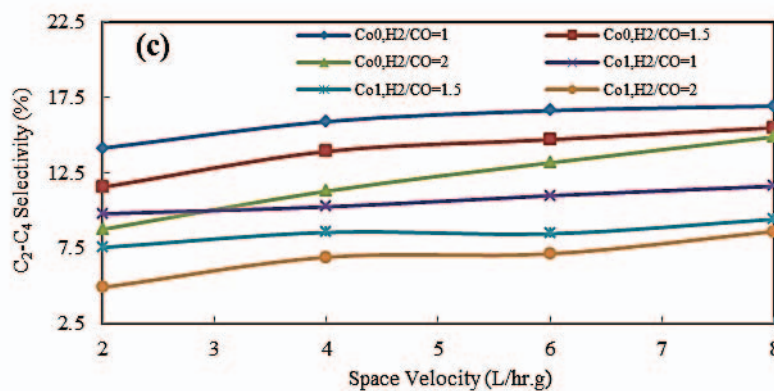


Fig. 3: (c) Effect of SV on C<sub>2</sub>-C<sub>4</sub> selectivity for the Ce-promoted and unpromoted cobalt catalysts at P = 15 bar, T= 230 °C and H<sub>2</sub>/CO ranging from 1 to 2.

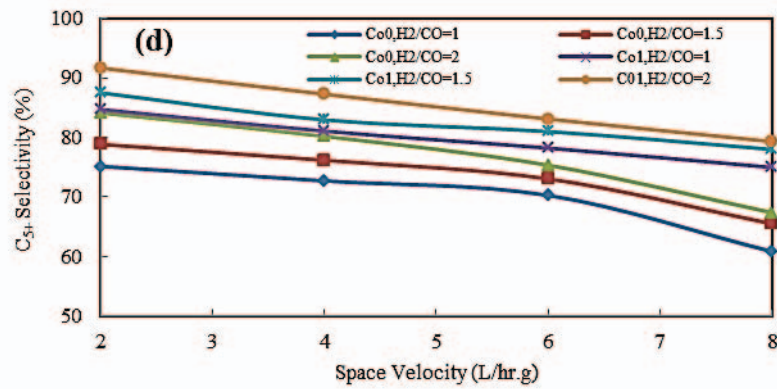


Fig. 3: (d) Effect of SV on C<sub>5</sub>+ selectivity for the Ce-promoted and unpromoted cobalt catalysts at P = 15 bar, T= 230 °C and H<sub>2</sub>/CO ranging from 1 to 2.

### 3.2.2 Influence of Inlet Feed Ratio (H<sub>2</sub>/CO) on Catalyst Performance

The effect of inlet feed ratio (H<sub>2</sub>/CO) on the developed catalysts (Co<sub>0</sub> and Co<sub>1</sub>) has been thoroughly investigated in terms of %XCO and selectivity at operating temperature of 230 °C and under a pressure of 15 bar with different SV, as shown in Fig. 4 and Fig. 5 and listed in Table 2.

Table 2: Catalytic performance of Co-based catalysts during CO hydrogenation

Catalyst	SV (L/hr. gcat.)	H <sub>2</sub> /CO ratio	%X <sub>CO</sub>	%Selectivity			
				CH <sub>4</sub>	C <sub>2</sub> -C <sub>4</sub>	C <sub>5</sub> +	CO <sub>2</sub>
25%Co/γ-Al <sub>2</sub> O <sub>3</sub> (Co <sub>0</sub> )	2	1	29.8	9.65	14.12	75.12	1.11
		1.5	39.5	8.6	11.53	78.82	1.05
		2	47.8	6.23	8.74	84.1	0.93
	4	1	20.4	10.02	15.88	72.68	1.42
		1.5	30.2	8.75	13.9	76.14	1.21
		2	41.5	7.41	11.27	80.17	1.15
	6	1	14.7	12.7	15.6	70.25	1.45
		1.5	21.6	10.76	14.68	73.02	1.54
		2	27.8	9.95	13.15	75.31	1.59
	8	1	9.8	19.58	16.9	60.81	2.71
		1.5	11.2	16.42	15.47	65.48	2.63
		2	20.1	15.64	14.86	67.35	2.15
1%Ce-25%Co/γ-Al <sub>2</sub> O <sub>3</sub> (Co <sub>1</sub> )	2	1	40.8	5.13	9.77	84.68	0.42
		1.5	49.4	4.67	7.54	87.48	0.31
		2	61.9	3.26	4.89	91.64	0.21
	4	1	28.1	7.84	10.23	81.03	0.9
		1.5	35.7	7.66	8.54	82.93	0.87
		2	53.5	5.34	6.9	87.25	0.51
	6	1	18.5	9.59	10.97	78.19	1.25
		1.5	29.5	9.41	8.45	80.97	1.17
		2	41.6	8.75	7.12	83.07	1.06
	8	1	16.5	12.05	11.6	74.95	1.4
		1.5	21.4	11.31	9.41	77.97	1.31
		2	30.2	10.84	8.61	79.29	1.26

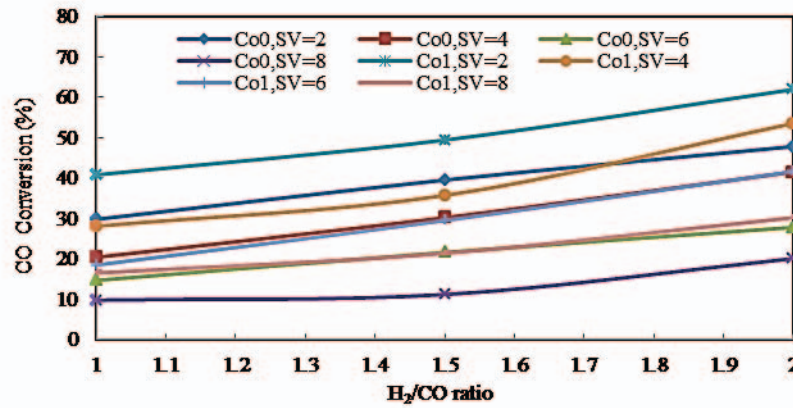


Fig. 4: Effect of H<sub>2</sub>/CO ratio on CO conversion for the Ce-promoted and unpromoted cobalt catalysts at P = 15 bar, T= 230 °C and SV= 2, 4, 6 and 8 L/h. g<sub>cat.</sub>.

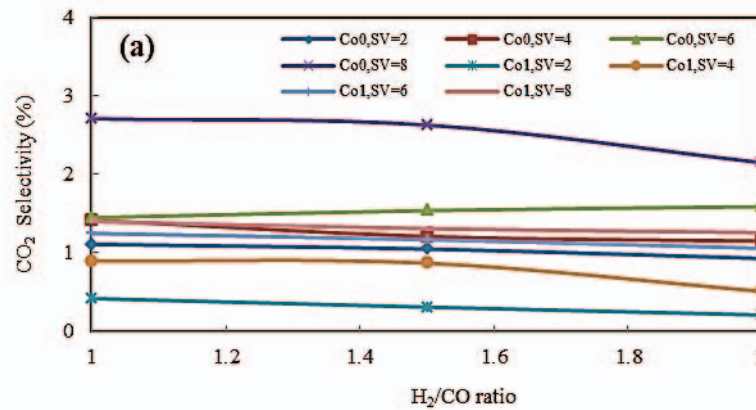


Fig. 5: (a) Effect of H<sub>2</sub>/CO ratio on CO<sub>2</sub> selectivity for the Ce-promoted and unpromoted cobalt catalysts at P = 15 bar, T= 230 °C and SV= 2, 4, 6 and 8 L/h. g<sub>cat.</sub>.

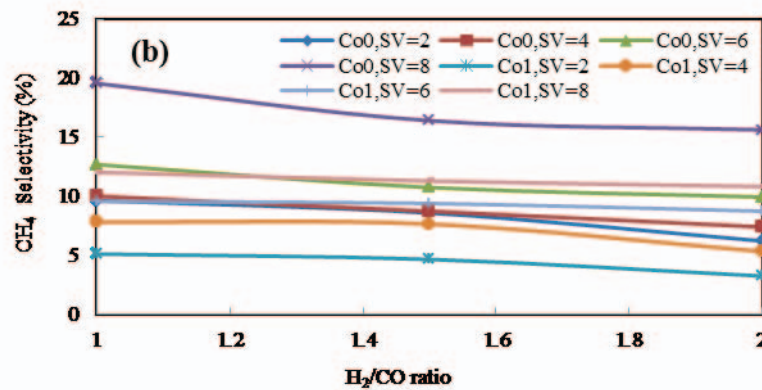


Fig. 5: (b) Effect of H<sub>2</sub>/CO ratio on CH<sub>4</sub> selectivity for the Ce-promoted and unpromoted cobalt catalysts at P = 15 bar, T= 230 °C and SV= 2, 4, 6 and 8 L/h. g<sub>cat.</sub>.

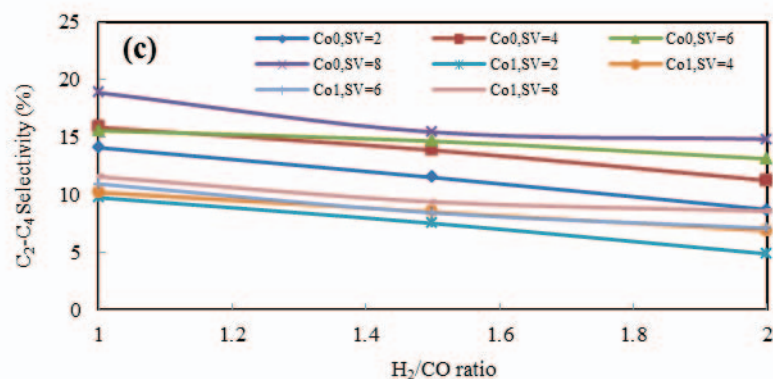


Fig. 5: (c) Effect of H<sub>2</sub>/CO ratio on C<sub>2</sub>-C<sub>4</sub> selectivity for the Ce-promoted and unpromoted cobalt catalysts at P = 15 bar, T= 230 °C and SV= 2, 4, 6 and 8 L/h. g<sub>cat.</sub>.

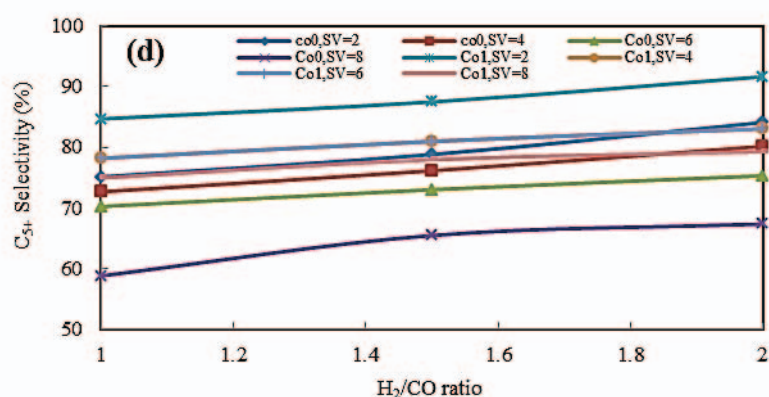


Fig. 5: (d) Effect of H<sub>2</sub>/CO ratio on C<sub>5</sub>+ selectivity for the Ce-promoted and unpromoted cobalt catalysts at P = 15 bar, T= 230 °C and SV= 2, 4, 6 and 8 L/h. g<sub>cat.</sub>.

#### 4. CONCLUSION

In conclusion, the performance of FT synthesis reaction for unpromoted and Ce-promoted cobalt-based catalysts was investigated based on space velocity and inlet gas feed ratio reaction conditions. The relevant results demonstrated that the addition of Ce promoter remarkably enhances the reducibility of cobalt oxides by decreasing the reduction temperature. In addition, Ce promoted Co-based catalysts show a significant C<sub>5</sub>+ selectivity and CO conversion ascribed to the high reducibility of Co that provides huge number of active sites for the reactant species. For both Co catalysts, the results exhibited that the reaction properties have strongly affected the catalysts' activity and products' selectivity, consequently, improved C<sub>5</sub>+ selectivity with low water-gas shift reaction activity were observed at high H<sub>2</sub>/CO ratio and low space velocity. Thus, Ce based Co catalyst is considered to be a suitable candidate for use in the gas to liquid conversion process.

#### REFERENCES

- [1] Hall KR. (2005) A new gas to liquids (GTL) or gas to ethylene (GTE) technology. *Catalysis Today*, 106(1-4): 243-246.
- [2] Singha RK, Shukla A, Yadav A, Konathala LNS, Bal R. (2017) Effect of metal-support interaction on activity and stability of Ni-CeO<sub>2</sub> catalyst for partial oxidation of methane. *Applied Catalysis B: Environmental*, 202: 473-488.

- [3] Kim H, Jang W, Yoo S, Shim J, Jeon K, Na H, Lee Y, Jeon B, Bae JW, Roh H.(2018) Low temperature steam reforming of methane using metal oxide promoted Ni-Ce<sub>0.8</sub>Zr<sub>0.2</sub>O<sub>2</sub> catalysts in a compact reformer. *International Journal of Hydrogen Energy*, 43(1): 262-270.
- [4] Shahhosseini HR, Saeidi S, Najari S, Gallucci F. (2017) Comparison of conventional and spherical reactor for the industrial auto-thermal reforming of methane to maximize synthesis gas and minimize CO<sub>2</sub>. *International Journal of Hydrogen Energy*, 42(31): 19798-19809.
- [5] Ma W, Jacobs G, Pendyala VRR, Sparks DE, Shafer WD, Thomas GA, MacLennan A, Hu Y, Davis BH. (2018) Fischer-Tropsch synthesis. Effect of KCl contaminant on the performance of iron and cobalt catalysts. *Catalysis Today*, 299: 28-36.
- [6] Bao B., El-Halwagi M. M., Elbashir N. O.(2010) Simulation, integration, and economic analysis of gas-to-liquid processes. *Fuel Processing Technology*, 91(7): 703-713.
- [7] Mousavi S, Zamaniyan A, Irani M, Rashidzadeh M.(2015) Generalized kinetic model for iron and cobalt based Fischer–Tropsch synthesis catalysts: review and model evaluation. *Applied Catalysis A: General*, 506: 57-66.
- [8] Zhu C, Bollas GM.(2018) Gasoline selective Fischer-Tropsch synthesis in structured bifunctional catalysts. *Applied Catalysis B: Environmental*, 235: 92-102.
- [9] Guo Q, Huang J, Qian W, Zhang H, Ma H, Ying W. (2018) Effect of Lanthanum on Zr–Co/γ- Al<sub>2</sub>O<sub>3</sub> Catalysts for Fischer–Tropsch Synthesis. *Catalysis Letters*, 148(9): 2789-2798.
- [10] Rahmati M, Huang B, Schofield LM, Fletcher TH, Woodfield BF, Hecker WC, Bartholomew CH, Argyle MD. (2018) Effects of Ag promotion and preparation method on cobalt Fischer-Tropsch catalysts supported on silica-modified alumina. *Journal of Catalysis*, 362: 118-128.
- [11] Pedersen EØ, Svenum I-H, Blekkan EA.(2018) Mn promoted Co catalysts for Fischer-Tropsch production of light olefins—An experimental and theoretical study. *Journal of Catalysis*, 361: 23-32.
- [12] Zeng S, Du Y, Su H, Zhang Y. (2011) Promotion effect of single or mixed rare earths on cobalt-based catalysts for Fischer–Tropsch synthesis. *Catalysis Communications*, 13(1): 6-9.
- [13] He L, Zhang Y, Fan M.(2015) Development of composited rare-earth promoted cobalt-based Fischer–Tropsch synthesis catalysts with high activity and selectivity. *Applied Catalysis A: General*, 505: 276-283.
- [14] Pardo TF., Cabrera S, Sanchez DM., Boutonnet M.(2017) Ce-promoted Co/Al<sub>2</sub>O<sub>3</sub> catalysts for Fischer–Tropsch synthesis. *International journal of hydrogen energy*, 42(15): 9754-9765.
- [15] de Lima AEP, de Oliveira DC. (2017) In situ XANES study of cobalt in Co-Ce-Al catalyst applied to steam reforming of ethanol reaction. *Catalysis Today*, 283:104-109.
- [16] Trepanier M, Tavasoli A, Dalai AK, Abatzoglou N.(2009) Co, Ru and K loadings effects on the activity and selectivity of carbon nanotubes supported cobalt catalyst in Fischer–Tropsch synthesis. *Applied Catalysis A: General*, 353(2): 193-202.
- [17] Jacobs G, Ji Y, Davis BH, Cronauer D, Kropf AJ, Marshall CL.(2007) Fischer–Tropsch synthesis: temperature programmed EXAFS/XANES investigation of the influence of support type, cobalt loading, and noble metal promoter addition to the reduction behavior of cobalt oxide particles. *Applied Catalysis A: General*, 333(2): 177-191.
- [18] Hilmen A, Schanke D, Holmen A. (1996) TPR study of the mechanism of rhenium promotion of alumina-supported cobalt Fischer-Tropsch catalysts. *Catalysis letters*, 38(3-4): 143-147.
- [19] Chu W, Chernavskii PA, Gengembre L, Pankina GA, Fongarland P, Khodakov AY. (2007) Cobalt species in promoted cobalt alumina-supported Fischer–Tropsch catalysts. *Journal of Catalysis*, 252(2): 215-230.
- [20] Osa AR, Lucas AD, Valverde JL, Romero A, Monteagudo I, Coca P, Sáncheza P.(2011) Influence of alkali promoters on synthetic diesel production over Co catalyst. *Catalysis today*, 167(1): 96-106.
- [21] Osa AR, Lucas AD, Romero A, Valverde JL, Sáncheza P. (2011) Fischer–Tropsch diesel production over calcium-promoted Co/alumina catalyst: Effect of reaction conditions. *Fuel Processing Technology*, 90(5): 1935-1945.

- [22] Gnanamani MK, Jacobs G, Graham UM, Pendyala VRR, Martinelli M, Lennan AM, Hu Y, Davis BH. (2017) Effect of sequence of P and Co addition over silica for Fischer-Tropsch synthesis. *Applied Catalysis A: General*, 538: 190-198.
- [23] Dry ME.(1999) Fischer-Tropsch reactions and the environment. *Applied Catalysis A: General*, 189(2): 185-190.
- [24] Zhang L, Chu H, Qu H, Zhang Q, Xu H, Cao J, Tang Z, Xuan J. (2018) An investigation of efficient microstructured reactor with monolith Co/anodic  $\gamma$ -Al<sub>2</sub>O<sub>3</sub>/Al catalyst in Fischer-Tropsch synthesis. *International Journal of Hydrogen Energy*, 43(6): 3077-3086.
- [25] Pendyala VRR, Jacobs G, Bertaux C, Khalid S, Davis BH.(2016) Fischer-Tropsch synthesis: Effect of ammonia on supported cobalt catalysts. *Journal of Catalysis*, 337: p. 80-90.
- [26] Tristantini D ,Lögdberg S, Gevert B, Borg Ø, Holmen A. (2007) The effect of synthesis gas composition on the Fischer-Tropsch synthesis over Co/ $\gamma$ -Al<sub>2</sub>O<sub>3</sub> and Co-Re/ $\gamma$ -Al<sub>2</sub>O<sub>3</sub> catalysts. *Fuel processing technology*, 88(7): 643-649.
- [27] Xu D, Li W, Duan H, Ge Q, Xu H. (2005) Reaction performance and characterization of Co/Al<sub>2</sub>O<sub>3</sub> Fischer-Tropsch catalysts promoted with Pt, Pd and Ru. *Catalysis Letters*, 102(3-4): 229-235.
- [28] Storsæter S, Tøtdal B, Walmsley JC, Tanem BS, Holmen A. (2005) Characterization of alumina-, silica-, and titania-supported cobalt Fischer-Tropsch catalysts. *Journal of catalysis*, 236(1): 139-152.
- [29] Visconti CG, Ballova Z, Lietti L, Tronconi E, Zennaro R, Forzatti P. (2010) *Advances in Fischer-Tropsch Synthesis*. Catalysts and Catalysis, CRC Press Taylor Francis Group, New York.

## EFFECTS OF pH, DOSAGE AND CONTACT TIME ON BORON REMOVAL FROM SYNTHETIC SALINE WATER USING *Moringa oleifera* SEEDS

MOHAMMED SAEDI JAMI<sup>1\*</sup>, NUR SYAHIRAH ZAKARIA<sup>1</sup>, MOUSSA MAHAMED AHMED<sup>1</sup>, NIK RASHIDA NIK ABDUL GHANI<sup>1</sup>, MOHAMMED NGABURA<sup>2</sup>, AND MANI MALAM AHMAD<sup>3</sup>

<sup>1</sup>Department of Biotechnology Engineering, Kulliyyah of Engineering, International Islamic University, Malaysia, Jalan Gombak, 53100 Kuala Lumpur, Malaysia

<sup>2</sup>Department of Chemical and Environmental Engineering, Faculty of Engineering, Universiti Putra Malaysia, 43400 UPM Serdang, Selangor, Malaysia

<sup>3</sup>Department of Biology, Faculty of Science, Kano University of Science and Technology, Wudil, 3244 Wudil-Gaya Road, Kano, Nigeria

\*Corresponding author: [saedi@iium.edu.my](mailto:saedi@iium.edu.my)

(Received: 18<sup>th</sup> July 2019; Accepted: 12<sup>th</sup> May 2020; Published on-line: 4<sup>th</sup> July 2020)

**ABSTRACT:** Boron is one of the key elements required in flora, fauna, as well as human beings. However, human life and eco-systems could be seriously affected when exposed to excessive levels of boron, especially in seawater and groundwater. In this work *Moringa oleifera* was selected as a precursor adsorbent owing to its eco-friendliness characteristics and favourable removal efficiency of adsorbates. Besides, *M. oleifera* does not significantly affect the conductivity of water and pH value after the treatment. The main aim of this work was to investigate the potentiality of *M. oleifera* in the treatment of boron from contaminated saline water. The effect of adsorption parameters such as pH (7 - 9), adsorbent dose of 4000 – 8000 mg/L of solution and contact time of 60 – 180 min was thoroughly investigated. Face-centred Central Composite Design (FCCCD) was applied to optimize these parameters. Consequently, the highest percentage of removal (65%) was achieved at the pH of 8, 120 min of contact time and 6000 mg/L of adsorbent dosage. The adsorption studies stated that the adsorption fitted well with the Freundlich isotherm. Therefore, the outcome of this work revealed that boron could be significantly treated using a prepared adsorbent from *M. oleifera*.

**ABSTRAK:** Boron merupakan salah satu elemen yang diperlukan oleh flora, fauna, juga manusia. Walau bagaimanapun, hidup manusia dan ekosistem pasti terkesan apabila di dedahkan secara berlebihan, terutama pada air di lautan dan daratan. Kajian ini menggunakan *Moringa oleifera* sebagai penjerap kerana ia mempunyai ciri-ciri mesra dan berkesan membuang bahan terjerap dengan berkesan. Selain itu, *M. oleifera* tidak langsung memberi kesan kepada konduktiviti air dan nilai pH selepas perawatan. Tujuan utama kajian ini adalah mengkaji potensi *M. oleifera* dalam larutan rawatan air garam boron yang tercemar. Kesan parameter penjerapan seperti pH (7-9), dos penjerapan 4000 – 8000 mg/L larutan dan masa interaksi 60 – 180 minit di kaji dengan teliti. Kaedah Komposisi Tumpuan Tengah Muka (FCCCD) digunakan bagi mengoptimumkan parameter-parameter ini. Hasilnya, peratus tertinggi penyingkiran adalah sebanyak (65%) pada pH 8, 120 min masa interaksi dan 6000 mg/L dos penjerapan. Kesimpulannya, kajian penjerapan ini menyokong kuat teori isoterma Freundlich. Oleh itu, hasil kajian ini menunjukkan boron dapat dirawat dengan menggunakan larutan penjerapan daripada *M. oleifera*.

**KEYWORDS:** optimization; boron; sea water; *Moringa oleifera* seeds

## 1. INTRODUCTION

Boron is a major constituent needed in plants, animals, and humans for metabolic and biosynthesis [1, 2]. It is an essential component for carbohydrate metabolism, sugar translocation, and other hormonal mechanisms in plants. It was reported that it is the basic marker for animal and human immune mechanism specifically in bone metabolism and central nervous systems [3]. Its deficiency in plants leads to retarded growth and enzymatic activities that could result in the death of the plants. In human and animals, deficiency may lead to low absorption capability for nutrient components and cause the deformity in embryo development for vertebrates as well as in cardiovascular coronary [4]. However, despite the importance of this chemical to plant and animal life, its redundancy (excess) may be toxic, leading to severe health and environmental damages. The toxicity in humans is manifested by nausea, vomiting, poor appetite, and weight loss [5, 6]. Moreover, its excess in soil and irrigation water could endanger plant life [7].

Numerous conventional techniques for boron removal from sea water are reported including reverse osmosis (RO), membrane distillation, and ion exchange methods [8-10]. However, these current techniques are identified with certain drawbacks such as high cost and high energy intensity [11]. Adsorption technique is an effective and recommended method to remove boron from water even at very low concentration. A wide range of sorbents have been used in the adsorption processes to remove boron such as activated carbon, clays, fly ash, biological materials, natural minerals, nanoparticles, layered double hydroxide, and other complexing membranes [12-14]. On the other hand, adsorption technique using agro-based materials was found to be cost effective, eco-friendly, easily accessible, easy to handle, and highly selective [15].

*Moringa oleifera* trees also known as a drumstick trees have a deciduous shrub characteristic in a rapidly growing small tree. The size of the tree is about 10-13 m tall and 35-45 cm in diameter with an umbrella-shaped open cap [16]. *Moringa oleifera* belongs to the Moringaceae family and is the most widely distributed species worldwide [17, 18]. The fruit changes to brown colour when mature and usually contains about 10 to 50 seeds inside it [16]. The *Moringa oleifera* seeds have demonstrated to be persuasive as primary coagulants for water treatment after being tested over the years and can be compared to conventional chemical coagulant (alum). Its high efficiency removal rate and its edible properties make the *M. oleifera* seeds adsorbent a standout potential candidate for Boron removal from sea water [19].

In the present study, the optimal values of pH, contact time and adsorbent dosage as the process parameters for effective boron removal were established using face-centred central composite design (FCCCD). In addition, the prediction ability of the established model was tested based on the Freundlich and Langmuir adsorption isotherms.

## 2. MATERIALS AND METHODS

### 2.1 Materials

The dry *Moringa oleifera* seeds were purchased from an accredited agent in Sabah, Malaysia. All reagents were commercial products of analytical grade.

## 2.2 Experimental Procedures

### 2.2.1 Sample Preparation

The seeds of *Moringa oleifera* were peeled manually and dried in the oven at a temperature of 105 °C for 24 hours to eliminate the moisture content according to the reported standard procedure [20]. Afterwards, the seeds were ground in a common processor and then sieved using standard sieve of 212 µm size mesh. Stock solution for synthetic sea water was prepared by measuring and suspending 5.719 g of boric acid into 1000 mL distilled water from which a working concentration of 5 mg/L was made through an appropriate dilution. For synthetic seawater preparation, stock solution of boron (1000 µg/mL) was prepared by dissolving 0.5636 g boric acid in water and diluting to 100 mL in a volumetric flask as described by Zarei et al. [21].

### 2.2.2 Spectrophotometric Assay

For the analysis of Boron depletion, samples were systematically withdrawn according to the methods described by Zarei et al. and Ahmad et al. [21, 22]. Standard methylene blue method by Zarei et al. [10] was applied and the analysis was done by observing the absorbance on spectrophotometer. One (1) mL of the boron solution was poured into 15 mL centrifuge tube then 0.5% of NaF (1 mL) was added followed by 1 mL of 1.5 mM methylene blue and 1 mL of 0.2 M sulfuric acid. Then, the contents were mixed well by vortex before diluted with 1 mL distilled water. Dichloromethane (100 µL) was prepared in 400 µL of acetonitrile solvent and added into the reaction solution. After a cloudy solution was formed, the solution was centrifuged for 2 minutes at 3800 rpm. The supernatant was discarded and the remaining pellet was dissolved with 400 µL acetonitrile. Then, the absorbance was measured at 657 nm. The standard curve (Fig. 1) from this assay was utilized to determine the final concentration of boron.

### 2.2.3 Batch Adsorption Experiments

A series of experiments was conducted batch wise in 500 mL Erlenmeyer flasks mounted on a hot plate with magnetic stirrer. The flask was covered with aluminium foil paper to prevent splash. The agitation was maintained at 200 rpm, while ambient temperature was adopted throughout the experiment. The removal efficiency of boron (%) was determined using the Eq. 1:

$$\text{Boron removal (\%)} = \frac{(C_i - C_f)}{C_i} \times 100 \quad (1)$$

where  $C_0$  and  $C_t$  are the initial and final concentrations of lead in the solution (mg/L), respectively.

### 2.2.4 Adsorption isotherm

Langmuir and Freundlich isotherms were investigated to explain the metal ion distribution between solid and liquid phases. The Langmuir model demonstrates there is no interaction between adsorbate molecules on adjacent sites and the adsorption occurs on a set of distinct localized adsorption sites within the natural material [23], whereas the Freundlich theory states that the uptake of metal ions occurs on a heterogeneous surface by monolayer sites adsorption. The adsorption capacity of the *M. oleifera* can be obtained from Eq. 2 below.

$$Q = \frac{(C_i - C_f)V}{m} \quad (2)$$

where  $C_i$  is the initial concentration (mg/L) and  $C_f$  is the final concentration (mg/L). The standard and linearized equations for Langmuir isotherm are given in Eq. 3 and Eq. 4:

$$q_e = \frac{\theta b C_e}{1 + b C_e} \quad (3)$$

$$\frac{C_e}{q_e} = \frac{1}{b q_m} + \frac{C_e}{q_m} \quad (4)$$

where,  $q_e$  is the quantity of adsorbate adsorbed in mg/g,  $C_e$  is the equilibrium concentration (mg/L),  $b$  is the constant of adsorption equilibrium (L/mg) which is related to the energy of adsorption, and  $q_m$  (mg/g) is the maximum adsorption capacity. The Langmuir isotherm experimental data were plotted as  $C_e/q_e$  against  $C_e$  graph. The model parameters can be obtained from the slope of the straight-line graph,  $1/q_m$  and the  $y$ -intercept,  $1/bq_m$   $1/b$  [24].

The Freundlich isotherm equations can be expressed as given in Eq. 5:

$$q_e = K C_e^{1/n} \quad (5)$$

Linearized form of Eq. 5 is given as:

$$q_e = K C_e^{1/n} \quad (6)$$

where  $K_F$  ( $\text{mol}^2/\text{KJ}^2$ ) is an indicator of adsorption capacity and  $1/n$  (mg/L) is a measure of intensity of adsorption. In Freundlich isotherm, the linearized graph of  $\log(q_e)$  against  $\log(C_e)$  gives a slope of  $1/n$  and an intercept of  $\log 10(K)$ .

### 2.3 Design of Experiment and Statistical Analysis

Three process parameters, namely, pH (7-9), contact time (60-180 min) and adsorbent dosage (0.4-0.8 g) were optimized using FCCCD with Design Expert software (Stat-Ease, Inc., Version 10.0.5.0 Minneapolis, USA) as reported by [24]. A total of 20 experiments with three-coded levels (1, 0 and +1) were conducted. Regression analysis was performed using second-order polynomial empirical model to correlate the influence of independent variables on boron removal (Eq. 7).

$$Y = \beta_0 + \sum_i \beta_i x_i + \sum_{ii} \beta_{ii} x_i^2 + \sum_{ij} \beta_{ij} x_i x_j \quad (7)$$

where  $Y$  is the predicted response,  $\beta_0$  is the offset term,  $\beta_i$  is the  $i^{\text{th}}$  linear coefficient,  $\beta_{ii}$  is the  $i^{\text{th}}$  quadratic coefficient, and  $\beta_{ij}$  is the  $ij^{\text{th}}$  interaction coefficient.

## 3. RESULTS AND DISCUSSION

### 3.1 Standard Curve of Boron

The standard curve used in finding the final concentration of boron illustrated in Fig. 1. The equation was  $y = 0.0054x + 0.0363$ , where  $R^2 = 0.9702$ . The standard curve is accepted as the value of  $R^2$  was more than 0.95. The final concentration of boron determined by inserting the measured value of absorbance at 657 nm of solution after the batch experiment was done as  $y$  value whereby the  $x$  value is the final concentration of boron.

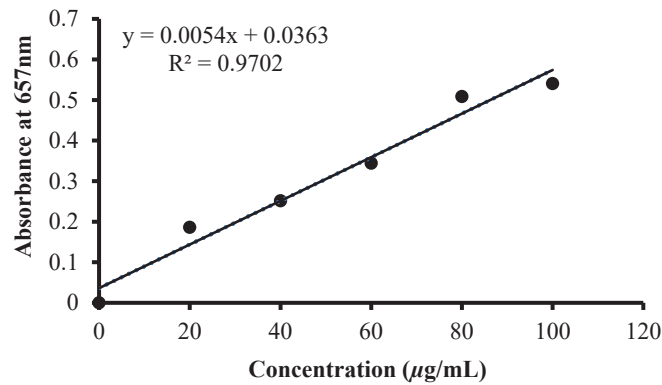


Fig. 1: Standard curve of boron.

### 3.2 Effect of Time

Figure 2 shows the effect of contact time for the adsorption of boron using *Moringa oleifera* seeds. The figure shows that the contact time has remarkable influence on the adsorption of boron. The highest boron removal by *M. oleifera* seeds can be observed at 120 minutes of contact time with 60% of removal.

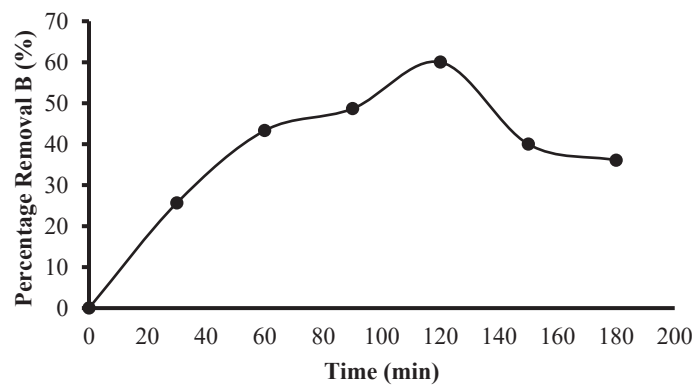


Fig. 2: Effect of time on boron removal at pH 8 and 6000 mg/L of adsorbent dosage.

Initially, the percentage removal of boron increased gradually until it reached the peak that is 120 minutes of contact time, afterwards, the rate starts decreasing until equilibrium was achieved. This trend could be due to the saturation on the available adsorption sites present on the *M. oleifera* seed. Initially the adsorption is fast but gradually decreased after it reached equilibrium due to the aggregation of *M. oleifera* seeds when it is increased. This phenomenon decreased the availability of adsorption surface area and increased the diffusion path length of boron. Besides, the unavailability of the surface area of adsorbent, the number of vacant sites and the interaction between the ions in the solution would lower the adsorption process [25,26].

### 3.3 Effect of pH

The percentage of boron removal was observed to be at its highest peak in the condition of 0.6 g adsorbent dosage within 120 minutes of contact time. The agitation speed was fixed at 200 rpm throughout the experiment. The adsorption capacity of the adsorbent with varying pH values was plotted in Fig. 3.

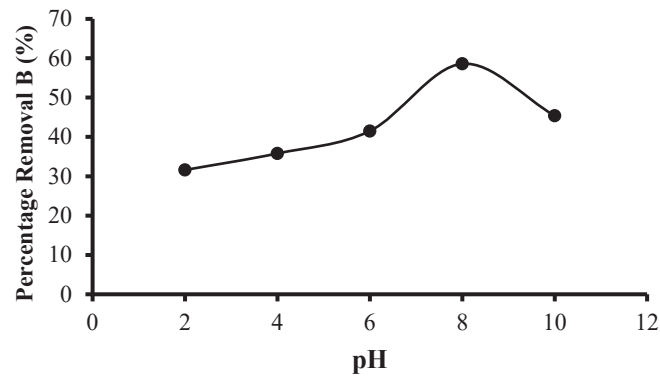


Fig. 3: Effect of pH on boron removal at 120 minutes of contact time and adsorbent dosage of 6000 mg/L.

The effect of pH on the adsorption of boron onto *Moringa oleifera* seed was studied in the range from pH 2 to pH 10. The result displayed that boron removal was at its highest peak at pH 8 with about 59% removal of boron. Initially, the percentage removal of boron increased with an increment of pH until it reached optimal pH value of 8. Further pH increment causes a dramatic decline in the adsorption percentage because of the electrostatic force of attraction become weak between the different charges of an adsorbate and adsorbent resulting in the lowering of adsorption. Simply at that pH, the protein of *M. oleifera* seeds have isoelectric point where over 90% of the amino acid molecules are in ionized state [21].

### 3.4 Effect of Adsorbent Dosage

The effect of adsorbent dosage on boron removal was investigated at varying adsorbent dosage from 2000-10000 mg/L of boron solution with 5 mg/L of boron concentration. The results are presented in Fig. 4.

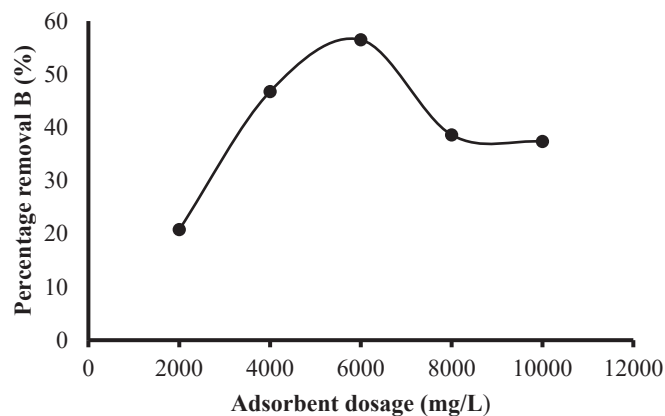


Fig. 4: Effect of adsorbent dosage on boron removal at 120 minutes of contact time with pH 8.

From Fig. 4 above, the graph displayed that the highest percentage removal of boron using *Moringa oleifera* seeds was at 6000 mg/ L of adsorbent dosage. The removal of boron increases rapidly from 2000 mg/L until it reached maximum peak at 6000 mg/L adsorbent dosage before gradually decreases and approaching equilibrium at 10000 mg/L dosage. Continuous increase of dosage does not increase the boron removal percentage because the effective contact surface area of the adsorbent decreased at higher adsorbent dosage which

results in a decreasing of unit adsorption capacity as too large amount of adsorbent will reduce the adsorption saturation sites besides create particle aggregates which cause a decrease in the total surface area that results in a decrease of adsorption capacity.

### 3.5 Adsorption Isotherm

The distribution of metal ions between liquid phase and the solid phase can be described by several isotherm models such as Langmuir and Freundlich [23]. The equilibrium data for Freundlich and Langmuir isotherm models were presented in Table 1 and 2, respectively while the linearized graph of the two Freundlich and Langmuir models was plotted as shown in Fig. 5 and Fig. 6, respectively.

Table 1: Equilibrium data for Freundlich isotherm model

$Q_e$ (mg/g)	$C_e$ (mg/L)	$\ln Q_e$ (mg/g)	$\ln C_e$ (mg/L)
1.9595	3.8103	0.6727	1.3377
2.1524	4.1595	0.7666	1.4254
2.2087	4.6543	0.7924	1.5378
2.3175	4.9421	0.8405	1.5978

Table 2: Equilibrium data for Langmuir isotherm model

$Q_e$ (mg/g)	$C_e$ (mg/L)	$C_e/Q_e$ (g/mg)
4.6231	21.76	4.7067
4.5584	26.63	5.8421
5.5645	34.50	6.2001
5.4297	39.61	6.9267
5.1818	45.6	8.8011

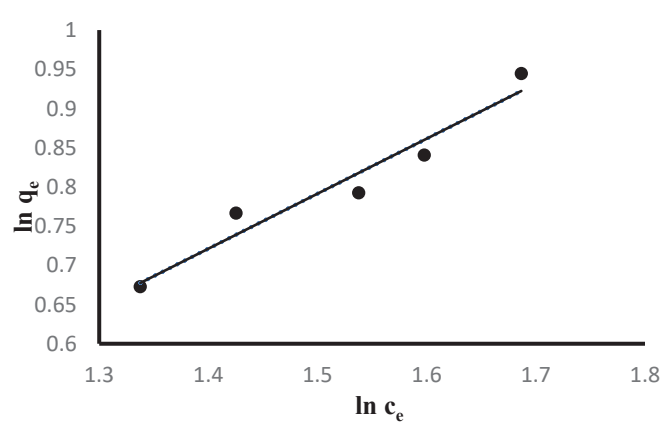


Fig. 5: Freundlich isotherm for boron removal using *M. oleifera* seeds.

From the plots, the estimated isotherm parameters were calculated and presented on Table 3. From the data,  $R^2$  for Freundlich adsorption isotherm was 0.9422 whereas that of Langmuir isotherm was 0.9115. The results showed that adsorption process evidently fitted well with the Freundlich isotherm model with high regression value. This expression predicted that the boron uptake takes place on a heterogeneous surface by monolayer sites adsorption of *M. oleifera* seeds.

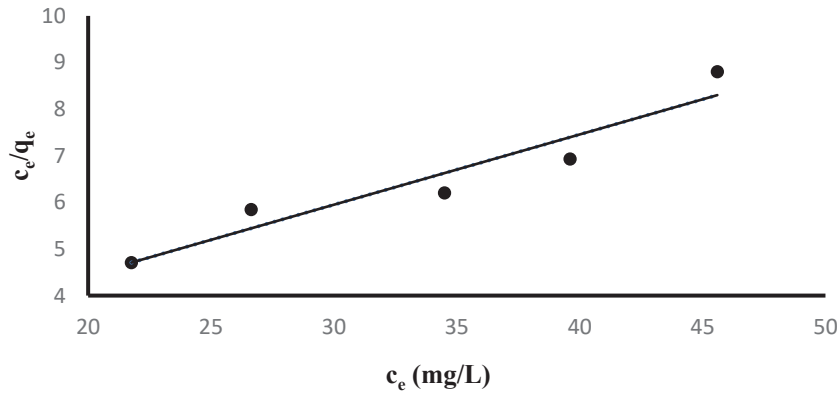


Fig. 6: Langmuir isotherm for boron removal using *M. oleifera* seeds.

From the plots, the estimated isotherm parameters were calculated and presented on Table 3. From the data,  $R^2$  for Freundlich adsorption isotherm was 0.9422 whereas that of Langmuir isotherm was 0.9115. The results showed that adsorption process evidently fitted well with the Freundlich isotherm model with high regression value. This expression predicted that the boron uptake takes place on a heterogeneous surface by monolayer sites adsorption of *M. oleifera* seeds.

Table 3 Isotherm parameters for adsorption of boron into *M. oleifera* seeds

Isotherm model	Estimated isotherm parameter		
	Freundlich	$n$	$K_f$
	0.7014	1.8231	0.9422
Langmuir	$q_{max}(\frac{mg}{g})$	$b(\frac{L}{mg})$	$R^2$
	6.6357	0.1055	0.9115

The standard curve equation,  $y = 0.0054x + 0.0363$  was used to find the final concentration of boron with  $R^2 = 0.9702$  by measuring absorbance at 657 nm.  $y$ -value is indicated by the measured absorbance value at 657 nm of solution after each batch experiment, whereas  $x$ -value is the final concentration of boron.

### 3.4 Modelling by Statistical Analysis

In this study, the model was structured by Design Expert version 6.0.8 and created by Factorial Central Composite Design (FCCD) under Response Surface Method. The three parameters which were optimized using FCCD are pH, contact time and dosage of adsorbent. Other parameters such as agitation speed were fixed at 200 rpm and the experiment was conducted at room temperature. From the 20 experimental runs, the results were analysed using the analyses of variance (ANOVA) (Table 4). The highest removal efficiency of 65 % was found at pH 8, adsorbent dosage of 6000 mg/L and contact time of 60 min. Table 5 shows the ANOVA for Boron adsorption by *M. oleifera* seeds.

Table 4: Results for batch adsorption experiment using *M. oleifera* seeds

Run	A: pH	B: Adsorbent dosage (gram)	C: Contact time (min)	Percentage boron removal (%) $\frac{C_i - C_f}{C_i} \times 100$
1	8	0.6	120	65
2	9	0.4	180	35
3	7	0.8	180	40
4	7	0.4	60	20
5	8	0.6	120	65
6	9	0.8	60	45
7	8	0.6	120	65
8	7	0.4	180	30
9	9	0.4	60	30
10	7	0.8	60	45
11	9	0.8	180	50
12	8	0.6	120	65
13	8	0.8	120	58
14	8	0.6	60	40
15	8	0.6	120	65
16	8	0.4	120	30
17	9	0.6	120	59
18	8	0.6	120	65
19	8	0.6	180	53
20	7	0.6	120	30

Table 5: ANOVA analysis for the adsorption using *M. oleifera* seeds

Source	Sum of square	DF	Mean square	F value	Prob > F	
Model	2744.60	9	304.96	4.00	0.0319	significant
<i>A</i>	291.60	1	291.60	3.82	0.0863	
<i>B</i>	864.90	1	864.90	11.34	0.0098	
<i>C</i>	78.40	1	78.40	1.03	0.3404	
<i>A</i> <sup>2</sup>	175.60	1	175.60	2.30	0.1677	
<i>B</i> <sup>2</sup>	197.98	1	197.98	2.59	0.1459	
<i>C</i> <sup>2</sup>	99.49	1	99.49	1.30	0.2865	
<i>AB</i>	3.13	1	3.13	0.041	0.8447	
<i>AC</i>	3.13	1	3.13	0.041	0.8447	
<i>BC</i>	28.13	1	28.13	0.37	0.5606	
Residual	610.40	8	76.30			not significant
Lack of Fit	534.40	5	106.88	4.22	0.1328	
Pure Error	76.00	3	25.33			
Cor Total	3534.55	19				

Based on the analysis of the model in Table 5 above, the Model F-value of 4.00 implies the model is significant. There is only a 3.19% chance that a "Model F-Value" this large could occur due to noise. Values of "Prob > F" less than 0.0500 indicate the model are significant. In this case B is a significant model term. Values greater than 0.1000 indicate the model terms are not significant. The "Lack of Fit F-value" of 4.22 implies the Lack of Fit is not significant relative to the pure error. There is a 13.28% chance that a "Lack of Fit F-value" this large could occur due to noise. Non-significant lack of fit is good as it shows that the model is in a good fit.

Table 6 Overall analysis of the model

Std. Dev.	8.73	R-Squared	0.8181
Mean	46.15	Adj R-Squared	0.6134
C.V.	18.93	Pred R-Squared	-1.1132
PRESS	7089.85	Adeq Precision	6.450

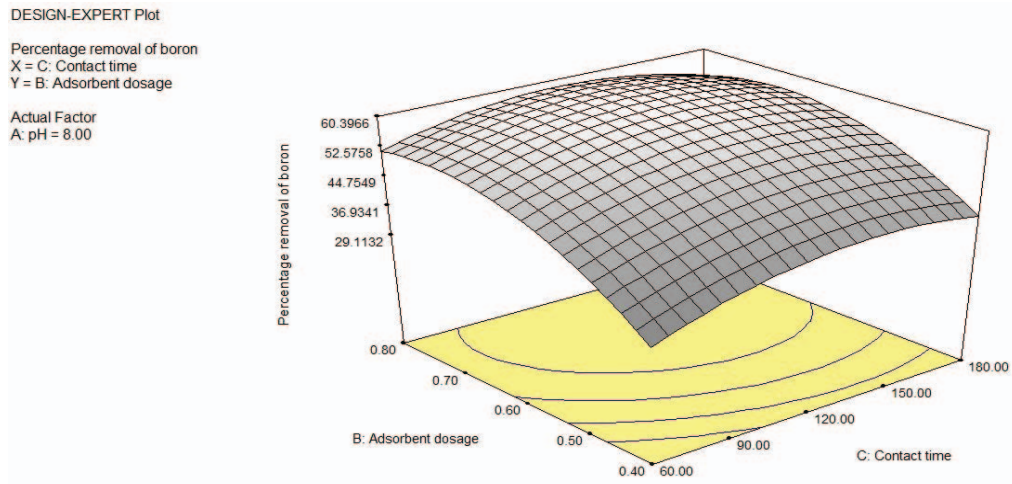
A negative "Pred R-Squared" implies that the overall mean is a better predictor of the response than the current model. "Adeq Precision" measures the signal to noise ratio. A ratio greater than 4 is desirable. The ratio of 6.450 indicates an adequate signal. This model can be used to navigate the design space. The coefficient of variation % (CV%) which can be used to measure the reliability and precision of the experiment was found to be 18.93 which is quite reliable. The higher the value of CV%, the less reliable is the experiment. The CV value is a measure of residual variation of the data relative to the size of the mean. The value of predicted residual sum of squares (PRESS) is found to be 7089.85. It is a measurement of how fit of each point in the design. The smaller the PRESS value, the better the model fits the data points.

According to the model equation generated by Design Expert 6.0 software, the 3D plots were plotted to investigate the interaction between variables. The 3D plots were generated by plotting the response (boron percentage removal) on the Z-axis against any two independent variables (Fig. 6). These plots hold a single constant variable at its centre, while the other two variables were varied in the range of experimental values. From the 3D plot indicated that it is possible to increase the percentage removal of boron further when the contact time, pH value and adsorbent dosage increased.

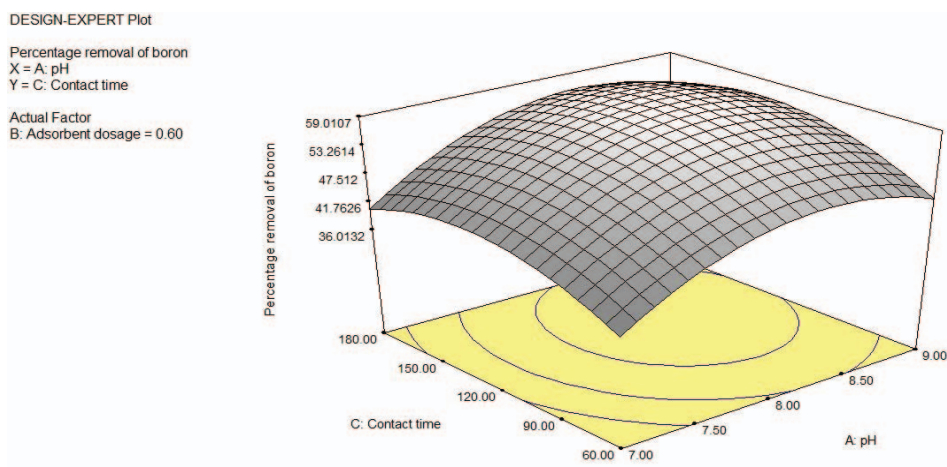
Previous studies on optimization of boron removal that adsorbed by different adsorbent are compared with the *M. oleifera* adsorption in terms of pH and adsorption capacity. The optimum pH value for *M. oleifera* was in agreement with other adsorbents such as rice husk, date seed ash, chitosan and magnesite-bentonite clay where the values were in the range of pH 7 to 10 which was in an alkaline environment [27-30]. Meanwhile, *M. oleifera* presented higher adsorption capacity than chitosan and magnesite-bentonite clay [27,30].

#### 4. CONCLUSION

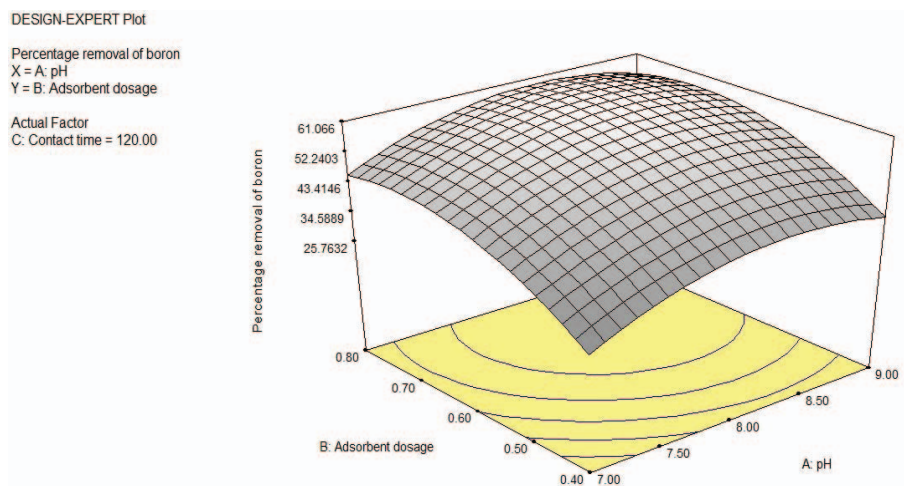
In conclusion, the results indicated that the highest percentage of boron removal was achieved up to 65% from Table 4 at optimum values of pH 8, 120 min of contact time and 6000 mg/L of adsorbent dosage. The decrease in removal rate after the optimum time of 120 min was probably due to continuous aggregation at the adsorption sites. The effect of pH variation with boron removal was associated with weak electrostatic forces between the adsorbate and the adsorbents, which manifested much at pH greater than 8. It was shown that boron removal increases with increase in adsorbent dosage with climax at 6000 mg/L. However, removal plummeted beyond this range due to decrease in the contact surface area available. The adsorption studies showed that the expressions were well fitted to Freundlich isotherm compared to Langmuir isotherm model. Statistical analysis modelling showed that the model was significant and thus confirm the effect of the combination parameters and conditions for the removal of boron from the solution.



a)



b)



c)

Fig. 6: (a) 3D plot for percentage removal of boron as a function of contact time and adsorbent dosage; (b) 3D plot for percentage removal of boron as a function of pH and adsorbent dosage; (c) 3D plot for percentage removal of boron as a function pH and contact time.

## ACKNOWLEDGEMENT

The authors express their thanks to Ministry of Higher Education (MOHE) Malaysia for granting a Fundamental Research Grant Scheme (FRGS), project no. FRGS-19-194-0803 for the financial support for this work.

## REFERENCES

- [1] Princi MP, Lupini A, Araniti F, Longo C, Mauceri A, Sunseri F, Abenavoli MR (2016). Boron Toxicity and Tolerance in Plants: Recent Advances and Future Perspectives. In *Plant Metal Interaction*, Edited by Parvaiz A. Elsevier; pp 115–147.
- [2] Zhang J, Cai Y, Liu, K. (2019). Extremely Effective Boron Removal from Water by Stable Metal Organic Framework ZIF-67. *Industrial & Engineering Chemistry Research*, 58: 4199–4207. doi.org/10.1021/acs.iecr.8b05656
- [3] Khaliq H, Juming Z, Ke-Mei P (2018). The Physiological Role of Boron on Health. *Biological Trace Element Research*, 186: 31-51. doi:10.1007/s12011-018-1284-3
- [4] Guan Z, Lv J, Bai P, Guo X. (2016). Boron removal from aqueous solutions by adsorption - A review. *Desalination*, 383: 29-37. doi.org/10.1016/j.desal.2015.12.026
- [5] Guidelines for drinking-water quality, 2nd ed. Addendum to Vol. 2. Health criteria and other supporting information. (1998) World Health Organization, Geneva.
- [6] Kabu M, Akosman M S. (2013). Biological Effects of Boron. *Reviews of Environmental Contamination and Toxicology*, Edited by Whitacre D M. Springer; pp 57-75. doi:10.1007/978-1-4614-6470-9\_2
- [7] Tu K L, Nghiem L D, Chivas A R (2010). Boron removal by reverse osmosis membranes in seawater desalination applications. *Sep. Purif. Technol*, 75: 87-101. doi:10.1016/j.seppur.2010.07.021
- [8] Kim BC, Hung P V X, Moon S H (2010). Boron removal from seawater by combined system of seawater reverse osmosis membranes and ion exchange process: a pilot-scale study. *Desalination and Water Treatment*, 15: 178–182. doi:10.5004/dwt.2010.1683
- [9] Kabay N, Bryjak M (2015). Boron Removal from Seawater Using Reverse Osmosis Integrated Processes. In *Boron Separation Processes*, Elsevier 219–235. doi:10.1016/b978-0-444-63454-2.00009-5
- [10] Biniaz P, Torabi Ardekani N, Makarem M, Rahimpour M (2019). Water and Wastewater Treatment Systems by Novel Integrated Membrane Distillation (MD). *ChemEngineering*, 3: 1-36. doi:10.3390/chemengineering3010008
- [11] Tagliabue M, Reverberi A P, Bagatin R (2014). Boron removal from water: needs, challenges and perspectives. *Journal of Cleaner Production*, 77: 56-64. doi:10.1016/j.jclepro.2013.11.040
- [12] Ozturk N, Kavak D (2005). Adsorption of boron from aqueous solutions using fly ash: Batch and column studies. *Journal of Hazardous Materials*, 127: 81-88. doi:10.1016/j.jhazmat.2005.06.026
- [13] Yüksel S, Yürüm Y (2009). Removal of Boron from Aqueous Solutions by Adsorption Using Fly Ash, Zeolite, and Demineralized Lignite. *Separation Science and Technology*, 45: 105-115. doi:10.1080/01496390903256042
- [14] Montalvo-Andia J P, Yokoyama L, Cesar Teixeira L A (2018). Study of the Equilibrium, Kinetics, and Thermodynamics of Boron Removal from Waters with Commercial Magnesium Oxide. *International Journal of Chemical Engineering*, 2018: 1-10. doi:10.1155/2018/6568548.
- [15] Wibowo E, Rokhmat M, Abdullah M (2017). Reduction of seawater salinity by natural zeolite (Clinoptilolite): Adsorption isotherms, thermodynamics and kinetics. *Desalination*, 409:146-156. doi.org/10.31436/iiumej.v21i1.1254
- [16] Anjorin T B, Ikokoh P, Okolo S (2010). Mineral composition of *Moringa oleifera* leaves, pods and seeds from two regions in Abuja, Nigeria. *Int. J. Agric. Biol.* 12: 431- 434.

- [17] Kansal S K, Kumari A (2014). Potential of *M. oleifera* for the treatment of water and wastewater. Chem Rev.114: 4993-5010. doi: 10.1021/cr400093w
- [18] Reddy D H K, Harinatha Y, Seshaiha K, Reddy A V R (2010). Biosorption of Pb(II) from aqueous solutions using chemically modified *Moringa oleifera* tree leaves. Chem. Eng. J. 162: 626-634.
- [19] Camacho F P, Sousa V S, Bergamasco R, Teixeira M R (2017). The use of *Moringa oleifera* as a natural coagulant in surface water treatment. Chem. Eng J., 313: 226-237.
- [20] Reck I M, Paixão R M, Bergamasco R, Vieira M F, Vieira A M S (2018). Removal of tartrazine from aqueous solutions using adsorbents based on activated carbon and *Moringa oleifera* seeds. J. Clean Prod., 171: 85-97.
- [21] Zarei A R, Nobakht S, Zaree M A (2012). A New Separation and Preconcentration System Based on Dispersive Liquid-Liquid Microextraction for Spectrophotometric Determination of Trace Amounts of Boron in Water Samples, JTAFD, 1: 1-13.
- [22] Ahmad M M, Azoddein A A M, Zahari M A K M, Seman M N bin A, Saedi M J, Olalere O A, Alara O R (2019). Optimization of Process Parameters in Mixed Sulfide Oxidation Bacterial Culture Using Response Surface Methodology as a Tool. Journal of King Saud University, 31: 836 - 843. doi.org/10.1016/j.jksus.2017.11.001
- [23] Glass B, Using S, Techniques M B, Shimada K, Kobayashi M, Tominaga G. (2016). Adsorption Study on *Moringa Oleifera* Seeds and Musa Cavendish as Natural Water Purification Agents for Removal of Lead, Nickel and Cadmium from Drinking Water. IOP Conf. Series: Materials Science and Engineering 136: 1-10. 012044 doi:10.1088/1757-899X/136/1/012044
- [24] Mahvi A H, Ghanbarian M, Nasserli S, Khairi A (2009). Mineralization and discoloration of textile wastewater by TiO<sub>2</sub> nanoparticles. Desalination, 239: 309-316. doi:10.1016/j.desal.2008.04.002
- [25] Al Haddabi M, Ahmed M, Al Jebri Z, Vuthaluru H, Znad H, Al Kindi M (2016). Boron removal from seawater using date palm (*Phoenix dactylifera*) seed ash. Desalination and Water Treatment, 57: 5130–5137. <https://doi.org/10.1080/19443994.2014.1000385>
- [26] Mohammed S J, Nur Syahirah Z, Moussa M A, Mohammed N, Mani M A (2018), Optimization of Process Parameters for Boron Adsorption from Sea Water Using *Moringa oleifera* Seeds, 5th International Conference on Biotechnology Engineering ICBioE, Kuala Lumpur, Malaysia 19 - 20.
- [27] Copello G J, Villanueva M E, González J A, López Egües S, Diaz L E (2014). TEOS as an improved alternative for chitosan beads cross-linking: A comparative adsorption study. Journal of Applied Polymer Science, 131: 1-8. doi.org/10.1002/app.41005
- [28] Guan Z, Lv J, Bai P, Guo X (2016). Boron removal from aqueous solutions by adsorption - A review. Desalination, 383: 29-37. doi.org/10.1016/j.desal.2015.12.026
- [29] Al Haddabi M, Ahmed M, Al Jebri Z, Vuthaluru H, Znad H, Al Kindi M (2016). Boron removal from seawater using date palm (*Phoenix dactylifera*) seed ash. Desalination and Water Treatment, 57: 5130 -5137. doi.org/10.1080/19443994.2014.1000385
- [30] Masindi V, Gitari M W, Tutu H, Debeer M (2016). Removal of boron from aqueous solution using magnesite and bentonite clay composite. Desalination and Water Treatment, 57: 8754-8764. doi.org/10.1080/19443994.2015.1025849

# NITROGEN AND PHOSPHORUS REMOVAL EFFICIENCY OF THREE HELOPHYTES IN CONSTRUCTED SURFACE FLOW WETLANDS FOR URBAN WASTEWATER TREATMENT

ABDESLAM ENNABILI<sup>1,2\*</sup> AND MICHEL RADOUX<sup>2\*\*</sup>

<sup>1</sup>MHEA® International Network, Nobressart, Belgium

<sup>2</sup> Department of Process Engineering, Superior School of Technology, Sidi Mohamed Ben Abdellah University, Fez, Morocco.

\*Corresponding author: [abdeslam.ennabili@usmba.ac.ma](mailto:abdeslam.ennabili@usmba.ac.ma)

\*\*died on June 3, 2017

Received: 22<sup>nd</sup> July 2019; Accepted: 13<sup>th</sup> March 2020; Published on-line: 4<sup>th</sup> July 2020)

**ABSTRACT:** Nutrient absorption is a function, among others, aimed at macrophytes for wastewater treatment. In this work, *Typha angustifolia*, *Phragmites australis*, and *Sparganium erectum* were multi-annually compared in secondary and tertiary treatment of urban wastewater under Mediterranean climate. *Phragmites* shows higher growth in height and density during the vegetative period of 1.83-2.09 cm.d<sup>-1</sup> and 29-49 times the planting density, respectively. Aerial biomass records 52.2-54.3, 38.1-41.0, and 19.4 t dw.ha<sup>-1</sup> in *Phragmites*, *Typha*, and *Sparganium* in the same order. The underground biomass fluctuates depending on the rooting vigour from 1.45 t dw.ha<sup>-1</sup> for *Sparganium* to 44.49 t dw.ha<sup>-1</sup> for *Phragmites* in tertiary treatment. Nitrogen and phosphorus aerial mineralomasses are more important in *Phragmites* (787 kg N.ha<sup>-1</sup>) and *Typha* (107 kg P.ha<sup>-1</sup>) in secondary treatment. *Phragmites* is, by far, the most cumulative of N and P in its underground part. The N and P retention by the vegetated mesocosms apparently has overall relationship with N-NH<sub>4</sub><sup>+</sup> and P-PO<sub>4</sub><sup>3-</sup>. Compared to mesocosm input, *Phragmites* assimilates one's maximum of 6.39% N in its aerial tissues and 7.86% P in the underground ones, whereas *Typha* records maxima of 14.8% N and 33.6% P in its aerial part with respect to corresponding mesocosm removal.

**ABSTRAK:** Penyerapan nutrien adalah satu fungsi, antara lain, bertujuan untuk makrofit merawat sisa air. Kajian ini menggunakan *Typha angustifolia*, *Phragmites australis* dan *Sparganium erectum* bagi membandingkan pelbagai-jenis rawatan sekunder dan tertiar sisa air bandar pada iklim Mediterranean. *Phragmites* menunjukkan pertumbuhan tertinggi dalam ketinggian dan ketumpatan dalam tempoh vegetatif iaitu 1.83-2.09 cm.d<sup>-1</sup> dan 29-49 kali ketumpatan penanaman, masing-masing. Rekod biojisim udara mencatatkan 52.2-54.3, 38.1-41.0, dan 19.4 t dw.ha<sup>-1</sup> dalam *Phragmites*, *Typha*, dan *Sparganium* pada susunan sama. Biojisim bawah tanah berubah-ubah bergantung kepada kekuatan akar dari 1.45 t dw.ha<sup>-1</sup> untuk *Sparganium* hingga 44.49 t dw.ha<sup>-1</sup> untuk *Phragmites* dalam rawatan tertiar. Nitrogen dan Fosforus Mineralomassa udara adalah lebih penting untuk *Phragmites* (787 kg N.ha<sup>-1</sup>) dan *Typha* (107 kg P.ha<sup>-1</sup>) dalam rawatan sekunder. *Phragmites*, setakat ini, paling kumulatif bagi N dan P pada bahagian bawah tanah. Pembendungan N dan P oleh mesokisme tumbuh-tumbuhan secara nyata berkaitan dengan N-NH<sub>4</sub><sup>+</sup> dan P-PO<sub>4</sub><sup>3-</sup>. Berbanding input mesokisme, *Phragmites* mengasimilasi maksimum pada N 6.39% tisu udara dan P 7.86% bahagian bawah tanah, manakala *Typha* mencatatkan maksima N 14.8% dan P 33.6% pada bahagian udara dengan penyingkiran mesokisme sepadan.

**KEYWORDS:** wastewater; constructed wetland; surface flow; nitrogen; phosphorus

## 1. INTRODUCTION

The use of native macrophytes in constructed wetlands for wastewater treatment has often considered the biology of the species, particularly its life cycle, the tolerance of relatively high pollutant loads, a high productivity of valuable biomass, and local criteria such as climate, wastewater quality, and operating facilities of the treatment process [1-3].

Macrophytes obviously contribute directly or indirectly to the wastewater treatment process [3,4], and the direct absorption of nutrients is one of the desired functions in this regard. Harvesting aerial biomass of helophytes at the end of the growing season could enhance their productivity during the following season, and generally further increase the retention of nutrients, including nitrogen and phosphorus [5, 6].

The macrophytes most commonly used in the world in constructed surface flow wetlands (CSFW) correspond to species of *Typha*, *Scirpus*, *Schoenoplectus*, *Phragmites*, *Juncus* and *Eleocharis* genera [3], in addition to *Canna*, *Cyperus*, *Paspalum* and *Iris* for Mediterranean countries [7]. In Mediterranean Morocco, three helophytes were selected and tested in urban wastewater treatment within the framework of the "MHEA® experimental centre of M'Diq (NW of Morocco)" project, financed by the Walloon Region through the Agence de la Francophonie [8-10], *Typha angustifolia* L., *Phragmites australis* (Cav.) Trin. ex Steud. and *Sparganium erectum* L. These three species have been tested around the world to treat municipal, agricultural, industrial, and drainage waters [3].

Based on overall treatment performance, the experiments carried out in this respect focused on the development and optimization of new extensive wastewater treatment technologies, adapted to the regional climatic and socio-economic conditions (MHEA® processes), with three successive stages each composed of an artificial ecosystem or mesocosm [10].

This work specifically exposes for the first time a multi-year comparison of the three helophytes (*T. angustifolia*, *P. australis* and *S. erectum*) in secondary and tertiary treatments of urban wastewater, based on development descriptors with annual harvesting of biomass, and their direct contribution to the nitrogen and phosphorus removal in CSFW.

## 2. MATERIALS AND METHODS

### 2.1 Mesocosms

By imitating their respective habitats in natural or polluted environments, *T. angustifolia* (T), *P. australis* (Pr), and *S. erectum* (S), were grown separately, just before the vegetative period (VP), at a density of 10 rhizomatous fragments per m<sup>2</sup> in mesocosms by simulating macrophyte bioreactors: 2.2 m<sup>3</sup> of wet volume, including 1.8 m<sup>3</sup> of substrate and 0.4 m<sup>3</sup> of surface water, and an identical non-planted pond was designed for comparison. The substrate used consists of washed river sand with a particle size of about 38% (diameter <2 mm), 31.6% (2-5 mm), 30% (>5 mm) and 0.4% (<80 µm). The feeding of these mesocosms in pre-treated wastewater is done semi-continuously and in translation (CSFW). The three planted mesocosms are compared beforehand as secondary treatment, then in the presence of a control (non-planted mesocosm); the mesocosms with T or Pr are compared in secondary and tertiary treatments (Table 1).

The climate prevailing in the experimental site is of Mediterranean type: rainfall of 523 to 683 mm (1999-2002), average daily temperatures of 14°C to 26°C, maximum of the warmest months of about 35 °C (July and August), and minimum of the coldest months above 7°C (December and January). The strongest winds are recorded during the months of September (W-E), and November-December (S-N), with negative transient effects of salt spray and plant collapse. Water losses due to mesocosm evapotranspiration vary with planting type and treatment stage, from 5.28 to 19.0% of inlet flow (Table 2).

Table 1: Characteristics of inlets feeding mesocosms per treatment stage. Sources: [11-12]; unpublished data.

Mesocosms group	Secondary inlets (I2)		Tertiary inlet (I3)
	<i>T. angustifolia</i> (T2)	Unvegetated control (L2)	Unvegetated control (L3)
	<i>P. australis</i> (Pr2)	<i>T. angustifolia</i> (T2)	<i>T. angustifolia</i> (T3)
	<i>S. erectum</i> (S2)	<i>P. australis</i> (Pr2)	<i>P. australis</i> (Pr3)
DCO (mg O <sub>2</sub> .l <sup>-1</sup> )	402.9±236.2	292.2±148.9	34.81±14.63
DBO <sub>5</sub> (mg O <sub>2</sub> .l <sup>-1</sup> )	115.8±51.94	110.3±57.95	32.67±16.54
TN (mg N.l <sup>-1</sup> )	39.48±9.446	38.65±9.906	22.60±8.332
TP (mg P.l <sup>-1</sup> )	6.769±1.908	6.803±2.553	4.896±1.525
T (°C)	22.0±5.57	22.0±5.65	20.1±4.43
pH	8.24±0.58	8.07±0.61	7.48±0.19
O <sub>2</sub> (mg.l <sup>-1</sup> )	10.9±13.2	10.7±10.3	5.29±7.42
Conductivity (µS.cm <sup>-1</sup> )	1043.8±92.463	991.49±105.19	1136.9±120.23

On the other hand duckweed coming to settle in unplanted mesocosms, or in those planted after biomass harvesting, were regularly removed. *Diptera* and *Coleoptera* spontaneously succeed in the aquatic and aerial mesocosm compartments, with an affinity of *Cladocera* and *Gastropoda* for the first, and *Hemiptera* and *Hymenoptera* for the second. Furthermore, the Mosquito Fish [*Gambusia affinis* (Baird and Girard, 1853), *Poeciliidae*] was introduced throughout the VP into each of the three mesocosms in secondary treatment: T, Pr and into the un-vegetated one.

Table 2: Water balance in mesocosms per treatment stage. Sources: [11-12]; unpublished data.

Mesocosm group		Inlet flow (l.d <sup>-1</sup> )	Evapotranspiration (mm.d <sup>-1</sup> )	Retention time (d <sup>-1</sup> )
Secondary treatment	<i>T. angustifolia</i> (T2)	186.2±21.87	16.03±10.91	2.351±0.296
	<i>P. australis</i> (Pr2)	170.8±19.17	25.92±13.90	2.673±0.311
	<i>S. erectum</i> (S2)	210.2±23.60	23.55±13.39	2.152±0.272
	Unvegetated control (L2)	243.0±39.22	12.84±17.86	1.810±0.407
	<i>T. angustifolia</i> (T2)	217.7±42.16	16.80±19.79	2.096±0.592
	<i>P. australis</i> (Pr2)	224.9±50.46	16.03±17.53	2.072±0.715
Tertiary treatment	Unvegetated control (L3)	132.9±20.72	22.45±6.19	3.430±0.565
	<i>T. angustifolia</i> (T3)	137.1±21.37	16.57±11.36	3.254±0.642
	<i>P. australis</i> (Pr3)	144.4±22.50	27.47±10.91	3.244±0.629

## 2.2 Experimental Monitoring

Water samples are taken on each mesocosm inlet and outlet approximately every two weeks for analyses of nitrogen compounds (total nitrogen, ammonium, nitrates and nitrites) and phosphorus ones (total phosphorus and orthophosphates). In addition, water samples were also collected to quantify phytoplankton, and macrophyte development parameters were measured.

### 2.2.1 Nitrogen

Total nitrogen (TN) and total non-particulate nitrogen (TNf) are determined after digestion of the sample in an alkaline medium (NaOH) in the presence of persulfate whereby the nitrogen compounds convert to nitrates. Undigested persulfate is reduced by sodium metabisulfite. Nitrates react with chromotropic acid in a strong acid medium (H<sub>2</sub>SO<sub>4</sub>) to form a yellow complex with maximum absorbance at 410 nm. Two ranges are proposed by the Hach firm: the low range (0.2-25 mg N.l<sup>-1</sup>) and the high range (7-150 mg N.l<sup>-1</sup>).

Ammonium ions (NH<sub>4</sub><sup>+</sup>) are determined according to the Nessler method on filtered samples. The hardness of the sample is complexed by a mineral stabilizer. The polyvinyl alcohol, a dispersing agent, helps to form a yellow colour with the Nessler reagent in the presence of the ammonium ions. The colouring developed is proportional to the concentration of ammonia. The reading is at 425 nm for a concentration range 0.05 to 2.5 mg N.l<sup>-1</sup>.

Nitrite ions (NO<sub>2</sub><sup>-</sup>) are determined according to the sulfanilamide method whose principle is the formation of a diazonium compound by the reaction of nitrites with sulfanilamide. This compound gives, by coupling with N-(1-naphthyl)-ethylenediamine dichloride, a red-mauve colour measured at 540 nm. The range used is 0.003 to 0.3 mg N.l<sup>-1</sup>. Nitrate ions (NO<sub>3</sub><sup>-</sup>) are reduced by cadmium to nitrite ones which react in acidic medium with sulfanilic acid to form an intermediate diazonium salt. The latter reacts with gentisic acid and forms an amber colour determined at 500 nm for the high range (0-30 mg N.l<sup>-1</sup>) and at 400 nm for the medium range (0-5 mg N.l<sup>-1</sup>). For the low range (0-0.5 mg N.l<sup>-1</sup>), the diazonium reagent reacts with chromotropic acid and develops a yellow colour measured at 507 nm.

### 2.2.2 Phosphorus

Total phosphorus (TP) and total non-particulate phosphorus (TPf) are oxidized as orthophosphate ions in acidic medium in the presence of persulfate. Two ranges are used: (i) the low range (0-3.5 mg P.l<sup>-1</sup>) for which orthophosphate reacts with molybdate in an acid medium to produce a phosphomolybdic complex which, in turn, is reduced by ascorbic acid giving an intense molybdenum blue coloration determined at 890 nm; (ii) the high range (0-100 mg P.l<sup>-1</sup>) for which the phosphomolybdic complex forms in the presence of vanadium the yellow vanadomolybdophosphoric complex measured at 420 nm.

Orthophosphate ions (PO<sub>4</sub><sup>3-</sup>) react, in acid medium, with the ammonium molybdate producing the molybdophosphoric acid. This complex is then reduced by the amino acid reagent to form the blue-molybdenum intensely coloured to determine at 530 nm. The method range is 0 to 9.8 mg P.l<sup>-1</sup>.

### 2.2.3 Phytoplankton

According to the algae density in mesocosms, an adequate volume is taken at a depth of 10 cm. The phytoplankton biomass was evaluated by the chlorophyll-a determination in accordance with the spectrophotometric method specified in Standard Methods [13].

### 2.2.4 Helophytes

Macrophyte development parameters include stem density and height, biomass production, and N and P contents in their tissues. At the end of the VP the aerial part of each helophyte is cut above the water level, and its dead parts are collected separately to estimate respectively the above-ground biomass, and the necromass inside the mesocosm.

In addition during each VP, cuttings of the plant aerial part beyond mesocosms were sometimes required because of accessibility.

At the end of the 3<sup>rd</sup> VP, the mesocosms are emptied, and the rhizomes and roots of the middle 3<sup>rd</sup> are gently recovered and washed on stacked sieves with a regressive mesh for the estimation of the underground biomass. Representative subsampling of collected biomass is adopted, and the following analytical steps (drying, grinding, and N and P determination) were conducted according to Ennabili et al. [14].

### 2.3 Analytical Methods

Data are presented depending on three periods: vegetative period (VP), vegetative rest (VR) and "VP+VR". The one-way analysis of variance (ANOVA) of normal distribution data was performed using the STATISTICA software, V.5, otherwise only averages and standard deviations were calculated using Microsoft Excel software.

## 3. RESULTS AND DISCUSSION

### 3.1 Helophyte Development

#### 3.1.1 Growth

Pr develops more in height especially in tertiary treatment (Pr3), successively followed by T and S (Table 3). These values greatly exceed those previously reported in T, Pr, and S grown in constructed wetlands, under polluted environments, or those developed in greenhouses, specifically 1.79-2.50 m for Pr, 0.90-1.99 m for T and 0.91 m for S [15-18], and are close to those underlined in natural or polluted environments, 3.2-3.5 m for Pr, 2.8 m for T and 1.70 m for S [6,14].

Table 3: Growth characteristics and above (A-) and underground (U-) biomass of helophytes studied per treatment level.

Mesocosms	T2	T3	Pr2	Pr3	S2
Height (m)	3.47±0.59	3.15±0.49	3.90±0.87	4.45±0.71	1.96±0.98
Stems.m <sup>-2</sup>	86±52	38±24	494±217	289±140	79±31
Fertile stems (%)	17.58	43.59	20.43	17.49	34.78
	±14.00	±67.48	±10.61	±8.044	±26.65
A-dry weight (% wet weight)	19.47	19.60	39.33	43.13	15.17
	±4.969	±4.623	±1.343	±3.721	±6.536
A-Biomass (t dw.ha <sup>-1</sup> )	41.009	38.098	54.284	52.209	19.436
	±13.785	±15.286	±30.850	±36.400	±12.125
A-Necromass (t dw.ha <sup>-1</sup> )	5.850	6.220	7.310	2.745	9.075
	±5.459	±7.269	±9.914	±3.627	±10.60
A-partial pre-cutting (t dw.ha <sup>-1</sup> )	0.951	0.927	4.021	3.413	0.538
	±0.369	±0.773	±2.396	±3.787	±0.371
Net productivity (t dw.ha <sup>-1</sup> .y <sup>-1</sup> )	59.895	52.428	70.113	50.098	22.272
	±4.2172	±20.601	±65.025	±54.739	±6.6706
U-Biomass (% ww)	6.80	18.47	22.20	22.27	6.78
U-Biomass (t dw.ha <sup>-1</sup> )	4.363	7.998	25.008	44.486	1.454
"U/A-Biomass" ratio	0.22	0.34	0.38	0.65	0.04

The average growth rate during the VP is 1.83-2.09, 1.48-1.63 and 0.92 cm.d<sup>-1</sup> for P, T, and S in the same order, vs. 0.77-1.9 cm.d<sup>-1</sup> underlined in Pr by Zheng et al. [6] and Zhang et al. [17]. The shoot collapse is spectacular in S especially during the "August-October" period as it was noted in a polluted environment by Ennabili and Gharnit [19], due to the cumulated effect of sludge discharge and wind. Asaeda et al. [20] point out that

collapsed shoots disappear in 40-60 days and constitute a large fraction of the floating organic matter.

Horizontal stems of Pr sometimes robustly branch out from rhizomes during fruiting (July), reaching 9 m in length with an average of 3 sprouts.m<sup>-1</sup> (September), and becoming rhizome once into the inlet piped water of mesocosms. Aquatic stolons are also observed in T during the flowering-fruiting period.

Typically more apparent at the mesocosm margins, stem density at the end of VP increased by about 29-49, 3.8-8.6, an 7.9 times for Pr, T, and S, respectively, compared to the initial planting, exceeding for Pr the range of 130-175 plants.m<sup>-2</sup> (17-18 times the planting density) highlighted by Zheng et al. [6], and the 107 plants.m<sup>-2</sup> cited in a polluted environment [15]. The increased rates of "post-planting density" obtained by this author in greenhouse approach noted in this work, 53.0 and 8.47 times the planting density of Pr and S respectively, but substantially different from that of T (21.9 times). Those high values of densities are related, inter alia, to the high tillering rate in these species, particularly 15, 6 and 3 sprouts.plant<sup>-1</sup>, respectively for Pr, T, and S [15], and to the annual cut of helophyte aerial parts [6].

Although peak flowering occurs in September, secondary flowering cohorts are noted along the VP: T (April, June-August), Pr (April, August), and S (April-May, July-August, October). The flowering rate is likely to vary inversely with the treatment stage, contrary to Pr (Table 3), and it is negatively affected in S by the shoot collapse just before flowering. However, this species completes more than one development cycle per VP, with a maximum of 3 during the 3<sup>rd</sup> year of mesocosm functioning. In addition, S seeds massively germinate from the mesocosm bottom or on water surface (Fig. 1). In addition, the sucking of S is also more remarkable in the canopy openings created by the shoot collapse in mid-summer.

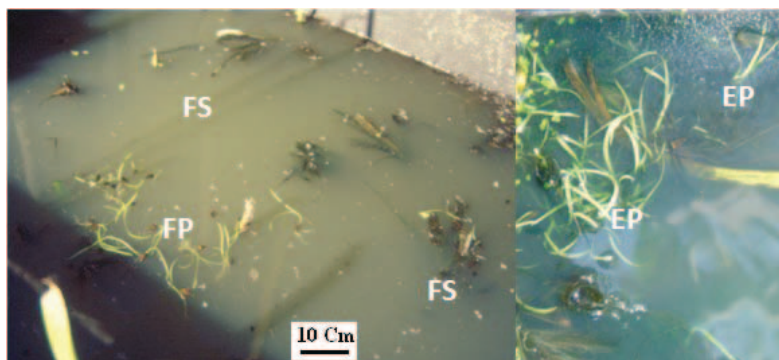


Fig. 1: Seed germination and development of *S. erectum*. FP, floating plantlets; FS, floating seeds; EP, emergent plantlets.

Moreover, the root bed is thicker in Pr, followed successively by T and S, and overwhelmingly achieves about 107, 56.7 and 20.6 cm deep from the level of substrate in the mesocosm middle part, respectively (Fig. 2). Liffen et al. [21] found that the biomass of S roots and rhizomes was highest at a depth of 0-10 cm, with a gradual decrease to 20-25 cm.

Rhizomes and roots of Pr go through the whole mesocosm substrate, forming root plaques at the bottom, and oxygenating the full height of the mesocosm bed except a slightly anoxic intermediate layer in appearance. The oxygen release from the Pr roots in the rhizosphere is qualitatively marked by a reddish colour, associated with the oxidized

forms of iron [4]. Pr rhizomes sometimes damage the mesocosm outlet by penetrating duct junctions.

### 3.1.2 Biomass

The above-ground biomass of helophytes is found to be slightly disadvantaged in tertiary treatment, with lower hydraulic loads (Table 2) and nutrients (Table 1), and ranges from 19.44 t dw.ha<sup>-1</sup> for S2 to 52.21-54.28 t dw.ha<sup>-1</sup> for Pr2, according to the lignification gradient, especially dry weights (dw) of 15.2 to 39.3-43.1% of the wet weight (ww) in the same order (Table 3). Which corresponds to a production in VP of about 0.193, 0.179, 0.255, 0.245 and 0.091 t dw.ha<sup>-1</sup>.d<sup>-1</sup> for T2, T3, Pr2, Pr3 and S2, vs. 0.14, 0.16 and 0.10 reported by Ennabili [15] in glasshouse, respectively for T, Pr and S.

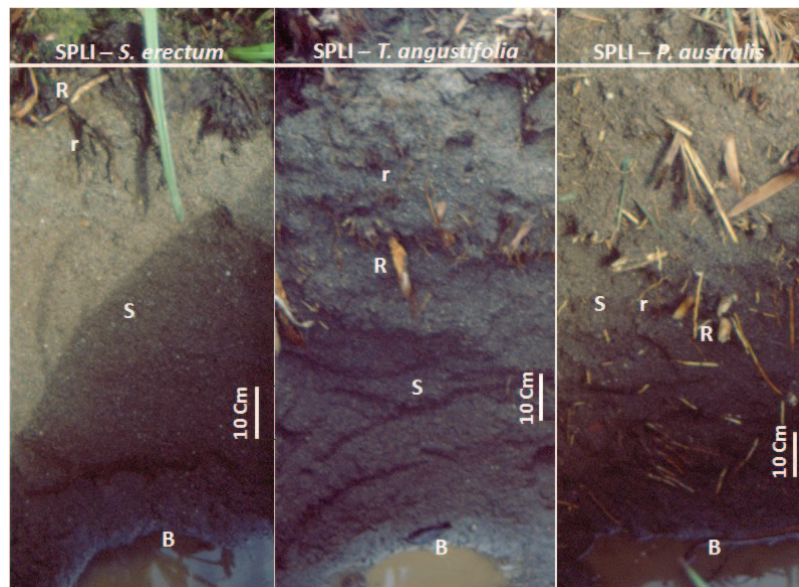


Fig. 2: Side view of dewatered mesocosm substrate after three vegetation periods. B, mesocosm bottom; R, rhizome; r, root; S, sand; SPLI, “sand/plant litter” interface.

Disregarding the role of study conditions, the aboveground biomass values obtained exceed those underlined in Pr (5.40-37.2 t dw.ha<sup>-1</sup>, vs. 52.2-54.3 t dw.ha<sup>-1</sup>) [6,14-16,18, 22-25], were similar to those reported for T (7.76-33.0 t dw.ha<sup>-1</sup>, vs. 38.1-41.0 t dw.ha<sup>-1</sup>) [14-15,18,26], and were part of the range of values highlighted in S [14-15,20-21].

The above-ground biomass during three successive years with harvesting of helophyte aerial parts at the end of each VP shows that Pr has a relative stability of production in tertiary treatment, a resilience for Pr and S in secondary treatment, while the T biomass increases in the first two years and falls steeply in the third year compared to the 3-year average (Fig. 3). The positive impact of harvesting on biomass production has been demonstrated in Pr [6,25]. Due to non-harvesting of biomass de los Reyes et al. [26] showed that the T biomass improved by about 39 to 48% in the 3<sup>rd</sup> year for the above-ground and below-ground parts respectively, suggesting an inadequacy of medium and long-term harvest for these species growing in CSFW.

The partial cut of helophytes for accessibility along the VP exports from 0.075 t dw.ha<sup>-1</sup> for S2 to 4.021 t dw.ha<sup>-1</sup> for Pr2. The specific necromass collected after harvesting is higher for S (9.075 t dw.ha<sup>-1</sup>), due especially to the shoot collapse, followed in descending order by those of Pr2, T3, T2 and Pr3 (Table 3), which would probably be a source of mesocosm enrichment during the forthcoming seasons. The net aboveground

productivity varies from more than 22 t dw.ha<sup>-1</sup>.year<sup>-1</sup> for S to over 70 t dw.ha<sup>-1</sup>.y<sup>-1</sup> for Pr in secondary treatment (Table 3), exceeding the estimated total biomass by Maucieri et al. [27] in Pr (49.2-58.9 ±9.1 t dw.ha<sup>-1</sup>) in CSFW for agricultural wastewater treatment.

As far as the underground biomass, it fluctuates from 1.454 t dw.ha<sup>-1</sup> for S to 44.486 t dw.ha<sup>-1</sup> for Pr in tertiary treatment, approximately 4 to 65% of the respective aboveground biomasses (Table 3). These values overlap with those underlined for Pr (16.0-29.7 t dw.ha<sup>-1</sup>, vs. 25.0-44.5 t dw.ha<sup>-1</sup>) [14-15,23], but are outperformed by those reported for T (12.3-34.95 t dw.ha<sup>-1</sup>, vs. 4.36-8.00 t dw.ha<sup>-1</sup>) and S (6.49-23.5 t dw.ha<sup>-1</sup>, vs. 19.4 t dw.ha<sup>-1</sup>) [14-15, 21, 26].

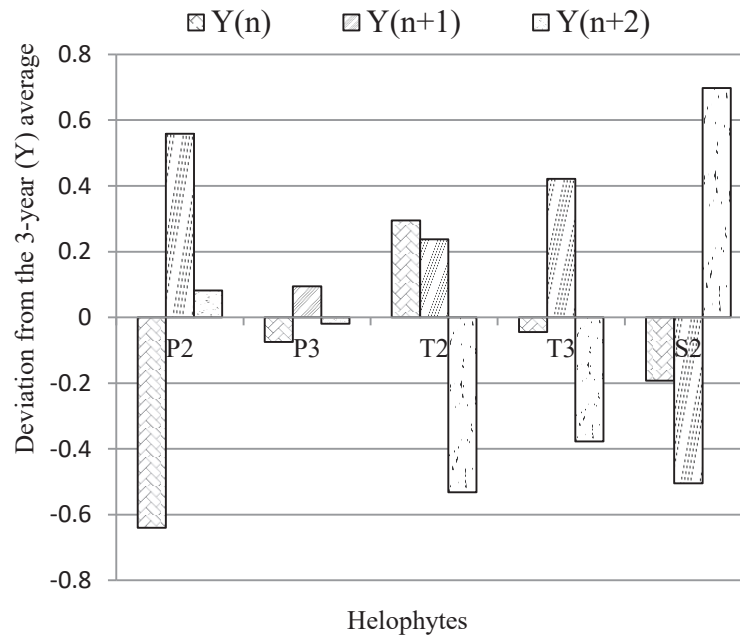


Fig. 3: Annual aboveground biomass in relation to the 3-year average one.

The above-ground biomass apparently is more favoured in CSFW (U/A of 0.04 to 0.65 depending on the species and the treatment stage) in comparison with the underground biomass (Table 3), contrary to the ratios obtained in polluted environments: 1.62, 1.62 and 0.55 for T, Pr and S in the same order [14]. However, by referring to the biomass averages obtained in these species from the same source by the same authors, and considering the harvest conditions at the end of each VP, CSFW systematically favour the aboveground biomass production (Fig. 4). The underground biomass is also favoured but with a lower intensity in Pr and T in tertiary treatment.

### 3.1.3 Mineralomass

The N/P contents in aerial tissues of helophytes are more apparent in Pr and T in secondary treatment, specially 787 kg N.ha<sup>-1</sup>/89.6 kg P.ha<sup>-1</sup>, and 670 kg N.ha<sup>-1</sup>/107 kg P.ha<sup>-1</sup> in the same order. The lowest rates for these two nutrients were recorded in T in tertiary treatment (Table 4). As regards the underground mineralomass Pr is the most cumulative of N and P, apparently due to its high underground biomass in CSFW.

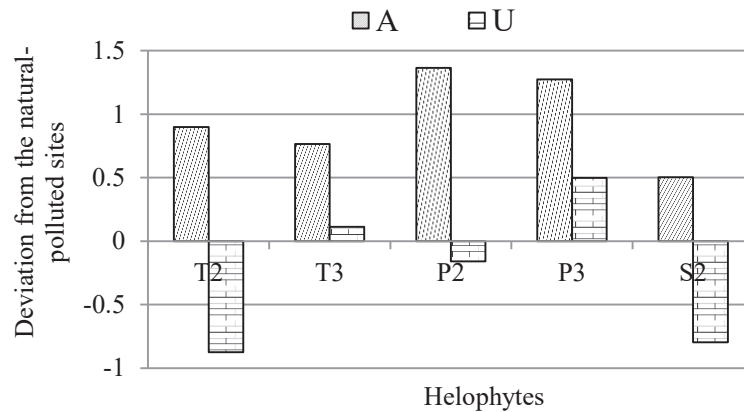


Fig. 4: Helophyte above-(A) and underground (U) biomass in relation to natural-polluted sites [14] and CSFW (the present study).

Table 4: Nitrogen and phosphorus contents and mineralomass in above (A-) and underground (U-) parts of helophytes studied per treatment level.

Mesocosms	T2	T3	Pr2	Pr3	S2
A-N (%)	1.64± 0.83	0.92± 0.25	1.45± 0.85	1.26± 0.47	1.90± 0.29
A-P (%)	0.26± 0.10	0.16± 0.08	0.17± 0.05	0.13± 0.01	0.45± 0.13
U-N (%)	1.23	0.62	1.00	1.08	1.08
U-P (%)	0.21	0.14	0.19	0.23	0.19
A-N (kg N.ha <sup>-1</sup> )	670.49±225.38	348.60±139.87	787.12±447.33	657.84±458.64	368.31±229.76
A-P (kg P.ha <sup>-1</sup> )	106.62±35.840	59.052±23.693	89.569±50.903	67.872±47.320	86.490±53.955
U-N (kg N.ha <sup>-1</sup> )	53.669	49.589	250.08	480.45	15.703
U-P (kg P.ha <sup>-1</sup> )	9.1629	11.197	47.515	102.32	2.7625

Compared to the dw, the N/P contents in helophyte tissues intersect those reported by other authors in Pr, except the low values of N in the underground part (Table 4), respectively 1.10-3.11/0.09-0.27% dw of the aerial part, and 1.44-1.73/0.22-0.32% dw of the underground one [2, 5-6,14,18]. For T and S the values underlined by other works are 1.94/0.09-0.17% and 1.94/0.35% dw of the aerial tissues, and 1.04/0.15% and 1.73/0.55% of the aerial tissues in the same order [14,18].

The mineralomass values reported by other studies clearly distinguish the N/P aboveground mineralomasses of Pr (658-787 kg N.ha<sup>-1</sup>/68-90 kg P.ha<sup>-1</sup>), vs. 111-502 kgN.ha<sup>-1</sup>/17-37.4 Kg P.ha<sup>-1</sup> [6, 14, 16, 24, 25, 27-29], and show an harmony of its N/P underground mineralomasses (250-480 kg N.ha<sup>-1</sup>/48-102 kg P.ha<sup>-1</sup>) vs. 503.3 kgN.ha<sup>-1</sup>/32.02-76.9 kg P.ha<sup>-1</sup> [6,14].

When compared with other authors, the N/P aboveground mineralomasses of T and S are similar (Table 4), vs. 74-420 kgN.ha<sup>-1</sup>/20-55 kg P.ha<sup>-1</sup> for T and 251-300 kgN.ha<sup>-1</sup>/45.3-50 kg P.ha<sup>-1</sup> for S [14, 26, 28, 29-31], while the N/P belowground ones are largely disadvantaged in this respect (Table 4), vs. 310-822 kgN.ha<sup>-1</sup>/5-147 kg P.ha<sup>-1</sup> for T and 124.3 kgN.ha<sup>-1</sup>/39.5 kg P.ha<sup>-1</sup> for S [14,26].

### 3.2 Phytoplanktonic Chlorophyll-a

The chlorophyll-a content in mesocosm water varies widely throughout the growing cycle. In secondary treatment and as compared to T and S (Fig. 5), the Pr-mesocosm generally reduces more phytoplankton (0.0171±0.0200 mg Chlorophyll-a.l<sup>-1</sup>) and especially during the VR (0.0066±0.0069 mg.l<sup>-1</sup>); this fact is more apparent in the T-

mesocosm in the VP ( $0.0174 \pm 0.0196 \text{ mg.l}^{-1}$ ). In tertiary treatment, the Pr-mesocosm forcefully reduces phytoplankton ( $0.0038 \pm 0.0105 \text{ mg.l}^{-1}$ ), compared to a lesser role of T-mesocosm, and an algae enrichment of the un-vegetated one (Fig. 5). This particular behaviour of the Pr-mesocosm is apparently in relation with, among other things, its leaf canopy more developed throughout the year.

In addition to the indirect role of helophyte shading on phytoplankton contraction, authors have shown allelopathic interferences of macrophytes with phytoplankton development. For example, extracts of leaves, stems and rhizomes of Pr can have negative effects on the growth of freshwater phytoplankton, *Microcystis* and *Scenedesmus* [32]. T and its allelochemicals can control phytoplankton blooms in eutrophic waters [33]. *Cyanobacteria* can also produce effective allelochemicals that interfere with the growth of competitive *Cyanobacteria* and algae [34].

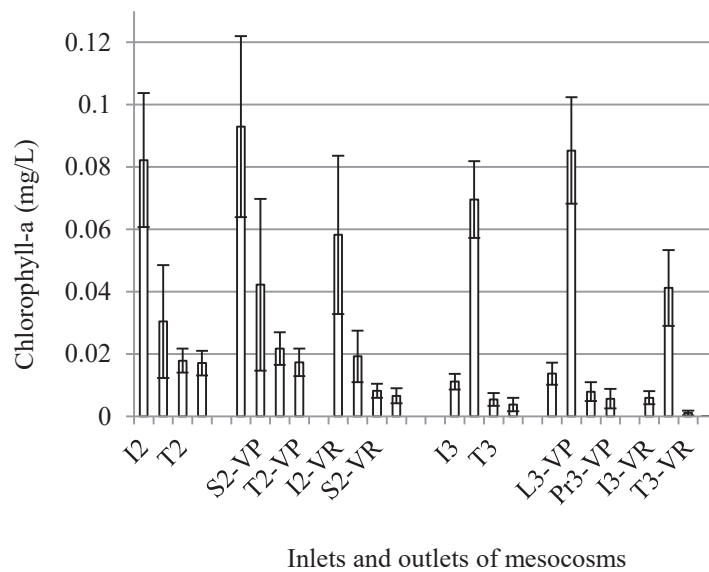


Fig. 5: Chlorophyll-a content of mesocosm inlet (I) and outlets (June 99-Sep.00).

### 3.3 Nitrogen and Phosphorus Removal Efficiency

In secondary treatment, the Pr-mesocosm has an advantage for the retention of TN, TNf and  $\text{NH}_4^+$  in comparison with the T and S ones (Table 5), but it's similar to T-mesocosm and the non-planted one (L) for TN and TNf (Table 6). In tertiary treatment, it generates the best TN removal, and aggregates with L for TNf and  $\text{NH}_4^+$ , and with L and I (mesocosm inlet) for  $\text{PO}_4^{3-}$  (Table 7). S- and T-mesocosms would be of interest for the retention of  $\text{NO}_3^-$  and  $\text{NO}_2^-$  in secondary and tertiary treatments in the same order (Table 5 and 7).

The L-mesocosm shows significant removal of  $\text{NH}_4^+$  and TPf respectively in secondary and tertiary treatments, and generates similar concentrations of  $\text{NO}_3^-$  and  $\text{PO}_4^{3-}$  to those of I in secondary treatment (Tables 6 and 7). Depending on the I-water quality, planting of mesocosms apparently has no effect on the retention of  $\text{NO}_3^-$  and  $\text{PO}_4^{3-}$  in secondary treatment, and of  $\text{PO}_4^{3-}$  in tertiary treatment (Tables 5, 6 and 7). The impact of the VP on the N and P retention likely has a general relationship with the direct plant uptake of  $\text{N-NH}_4^+$  and  $\text{PO}_4^{3-}$ , but remains without clear trend for TNf,  $\text{NO}_2^-$ ,  $\text{NO}_3^-$  and TPf (Tables 5, 6 and 7), seemingly due to other factors such as bacterial activity, substrate composition, hydraulic retention time, etc.

Table 5: Nitrogen and phosphorus contents (mg.l<sup>-1</sup>) of inlet and outlets of T-, Pr-, and S-mesocosms (Secondary treatment; Jan. 99 – Sep. 00).

	Inlet		Outlets		ANOVA significance (p<0.05)		
	I2	T2	Pr2	S2	F-ratio	F-prob.	Effet
<b>TN</b>	39.5±9.45 a	31.6±8.33 b	22.8±10.36 c	31.2±8.96 b	21.37	0.0000	***
<b>VP</b>	38.3±9.39 a	31.6±8.07 b	22.9±10.74 c	30.1±8.56 b	13.62	0.0000	***
<b>VR</b>	42.5±9.35	31.5±9.37	22.6±9.77	34.0±9.79	-	-	-
<b>TNf</b>	26.6±8.09 a	25.7±6.91 a	19.0±7.67 b	25.5±10.36 a	6.597	0.0003	***
<b>VP</b>	26.0±8.83 a	26.3±7.16 a	19.5±7.85 b	25.7±10.54 a	3.852	0.0117	*
<b>VR</b>	28.1±6.02	24.1±6.28	17.9±7.48	24.8±10.4	-	-	-
<b>NH<sub>4</sub><sup>+</sup></b>	21.6±5.89 a	21.0±8.06 a	13.3±6.20 b	20.5±7.59 a	12.89	0.0000	***
<b>VP</b>	21.4±5.67 a	22.4±6.37 a	14.1±5.70 b	21.1±6.12 a	12.55	0.0000	***
<b>VR</b>	22.0±6.74	17.3±11.1	11.2±7.26	18.7±10.9	-	-	-
<b>NO<sub>2</sub><sup>-</sup></b>	0.016±0.021	0.014±0.020	0.019±0.018	0.008±0.008	-	-	-
<b>VP</b>	0.022±0.024	0.017±0.024	0.014±0.012	0.008±0.009	-	-	-
<b>VR</b>	0.005±0.005	0.008±0.007	0.030±0.023	0.007±0.006	-	-	-
<b>NO<sub>3</sub><sup>-</sup></b>	0.252±0.236 a	0.340±0.317 a	0.217±0.214 a	1.056±1.894 b	3.318	0.0243	*
<b>VP</b>	0.235±0.192	0.278±0.273	0.149±0.090	0.141±0.102	-	-	-
<b>VR</b>	0.278±0.303	0.432±0.372	0.320±0.301	2.428±2.477	-	-	-
<b>TP</b>	6.77±1.91 a	7.05±1.54 a	6.53±1.81 a	7.00±1.61 a	0.782	0.5058	NS
<b>VP</b>	7.00±1.72 a	7.31±1.30 a	7.02±1.73 a	7.20±1.68 a	0.242	0.8671	NS
<b>VR</b>	6.13±2.32	6.34±1.97	5.19±1.33	6.47±1.32	-	-	-
<b>TPf</b>	3.88±1.75	5.09±2.07	4.18±1.95	4.87±1.77	-	-	-
<b>VP</b>	4.27±1.56	5.64±1.64	4.60±1.88	5.11±1.81	-	-	-
<b>VR</b>	2.95±1.90	3.72±2.43	3.17±1.81	4.28±1.62	-	-	-
<b>PO<sub>4</sub><sup>3-</sup></b>	2.15±1.83 a	3.77±2.78 b	2.77±2.21 a	4.06±2.12 b	6.264	0.0004	***
<b>VP</b>	2.15±1.81	3.89±2.84	2.71±2.30	4.11±2.22	-	-	-
<b>VR</b>	2.18±1.99	3.45±2.71	2.93±2.03	3.92±1.90	-	-	-

For each variable, means followed by the same letter are not significantly different at 5%. Non-significant (NS), significant (\*), and very highly significant (\*\*\*) effects.

The N/P retention in helophyte tissues compared to the I-mesocosm vary sharply and reaches maxima of 6.39%/7.86% in Pr for the aboveground/underground parts (Fig. 6), whereas by referring to the N/P removal rate by the corresponding mesocosms, T recorded maxima of 14.8%/33.6% for the aboveground (Fig. 7), suggesting a greater retention of N and P by the Pr-mesocosm compared to the T-one, contrary to the confirmation of Song et al. [18] for P.

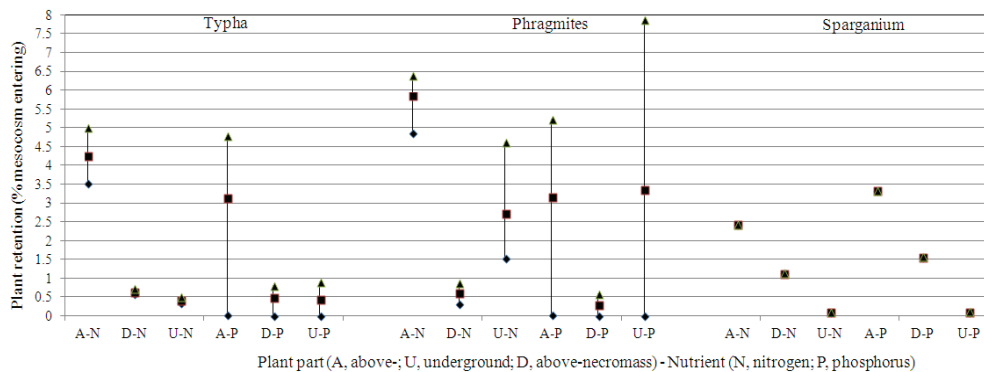


Fig. 6: Nitrogen and phosphorus retention in plant tissues in relation to the corresponding mesocosm inlet.

Table 6: Nitrogen and phosphorus contents (mg.l<sup>-1</sup>) of inlet and outlets of L-, T-, and Pr-mesocosms (Secondary treatment; May 01 – Sep. 03).

	Inlet		Outlets		ANOVA significance (p<0.05)		
	I2	L2	T2	Pr2	F-ratio	F-prob.	Effet
<b>TN</b>	38.7±9.91 a	32.6±9.46 b	31.4±9.17 b	28.5±9.35 b	11.18	0.0000	***
<b>VP</b>	41.0±10.2 a	34.7±10.3 b	33.7±9.44 b	29.8±10.1 b	7.289	0.0001	***
<b>VR</b>	34.9±8.38 a	29.1±6.77 b	27.7±7.52 b	26.4±7.81 b	5.053	0.0030	**
<b>TNf</b>	29.1±8.78 a	23.8±7.64 b	23.0±8.25 b	25.6±8.13 b	6.209	0.0005	***
<b>VP</b>	31.3±9.29 a	25.0±8.17 b	23.9±9.33 b	27.6±8.02 b	4.756	0.0035	**
<b>VR</b>	25.9±6.91 a	21.9±6.47 a	21.5±6.13 a	22.5±7.43 a	1.889	0.1377	NS
<b>NH<sub>4</sub><sup>+</sup></b>	23.8±7.57 a	18.2±6.73 b	21.3±9.00 a	22.8±8.39 a	5.756	0.0008	***
<b>VP</b>	26.0±7.97 a	19.4±7.28 b	23.2±10.4 a	25.6±8.55 a	4.881	0.0029	**
<b>VR</b>	19.8±4.77 a	16.0±5.10 a	17.8±4.23 a	17.8±5.35 a	2.156	0.0993	NS
<b>NO<sub>2</sub><sup>-</sup></b>	0.023±0.045	0.037±0.042	0.023±0.044	0.015±0.032	-	-	-
<b>VP</b>	0.023±0.042	0.030±0.035	0.022±0.042	0.010±0.022	-	-	-
<b>VR</b>	0.022±0.050	0.049±0.050	0.026±0.050	0.023±0.043	-	-	-
<b>NO<sub>3</sub><sup>-</sup></b>	2.80±1.82 a	2.62±2.16 a	3.91±2.03 b	3.85±1.73 b	7.301	0.0001	***
<b>VP</b>	3.28±2.00 a	3.31±2.31 a	4.43±2.29 b	4.39±1.80 b	3.530	0.0165	*
<b>VR</b>	1.98±1.10 a	1.43±1.13 a	3.00±1.00 b	2.91±1.10 b	10.81	0.0000	***
<b>TP</b>	6.80±2.55 a	6.57±2.76 a	5.96±2.37 a	6.03±2.07 a	1.731	0.1612	NS
<b>VP</b>	7.75±2.53 a	7.72±2.71 a	6.75±2.51 a	6.84±1.93 a	1.936	0.1261	NS
<b>VR</b>	5.12±1.55 a	4.54±1.31 a	4.55±1.18 a	4.58±1.42 a	0.910	0.4398	NS
<b>TPf</b>	4.20±1.87 a	3.84±2.09 a	4.59±2.23 a	4.47±1.83 a	1.653	0.1779	NS
<b>VP</b>	4.95±1.69 a	4.67±2.09 a	5.22±2.48 a	5.09±1.90 a	0.510	0.6756	NS
<b>VR</b>	2.88±1.39	2.36±1.01	3.46±1.02	3.36±1.04	-	-	-
<b>PO<sub>4</sub><sup>3-</sup></b>	2.94±2.01 a	2.71±2.16 a	4.02±2.15 b	3.95±1.84 b	6.751	0.0002	***
<b>VP</b>	3.47±2.22 a	3.40±2.31 a	4.59±2.42 b	4.52±1.94 b	3.300	0.0221	*
<b>VR</b>	2.00±1.08 a	1.48±1.11 a	3.03±0.99 b	2.94±1.08 b	10.86	0.0000	***

For each variable, means followed by the same letter are not significantly different at 5%. Non-significant (NS), significant (\*), highly significant (\*\*), and very highly significant (\*\*\*) effects.

For the whole plant, Pr assimilates in its tissues 10.9% N and 13.1% P compared to the I-mesocosm load. These values of N/P accumulated in aboveground plant tissues are far below than those obtained by de los Reyes et al. [26] in T (29.6% N) and Zheng et al. [6] in Pr (16.2-17.04% N). Besides, T is more effective in the N retention in its aerial tissues in secondary treatment and P in the whole plant in secondary treatment. Pr offers more efficiency of N absorption in its aerial part in secondary treatment and N and P in its underground part in tertiary treatment.

The underground part of Pr retains at most 5.23% N and 15.1% P of the general elimination rate of the corresponding mesocosm, and can be released progressively because of tissue death and decomposition during the forthcoming seasons. The S necromass in water is valued at up to 2.94% N and 7.96% P the general retention of the corresponding mesocosm, and will recover more rapidly in the treatment system given the relatively rapid decomposition of its collapsed shoots [31].

#### 4. CONCLUSION

This work focused on the monitoring of *T. angustifolia*, *P. australis* and *S. erectum* grown in constructed surface flow wetlands for urban wastewater treatment in a Mediterranean climate, based on growth and functional criteria, and allowed an interspecific comparison under the same growing conditions on the one hand, and within each species by reference to natural-polluted environments on the other hand.

Table 7: Nitrogen and phosphorus contents (mg.l<sup>-1</sup>) of inlet and outlets of L-, T-, and Pr-mesocosms (Tertiary treatment; Jan. 99 – Sep. 00).

	Inlet		Outlets				ANOVA significance (p<0.05)		
	I3	L3	T3	Pr3	F-ratio	F-prob.	Effet		
<b>TN</b>	22.8±8.45 a	12.4±6.10 b	12.9±6.42 b	7.45±5.96 c	35.80	0.0000	***		
<b>VP</b>	24.4±9.38 a	14.2±6.65 b	15.4±6.34 b	7.68±4.92 c	24.23	0.0000	***		
<b>VR</b>	20.1±5.97	9.53±3.66	8.73±3.97	7.07±7.56	-	-	-		
<b>TNf</b>	17.7±5.29 a	7.26±3.92 b	10.4±6.02 c	5.84±4.41 b	43.00	0.0000	***		
<b>VP</b>	18.4±5.39 a	6.88±3.57 b	12.0±6.23 c	5.56±3.68 b	36.29	0.0000	***		
<b>VR</b>	16.3±5.01	8.00±4.56	7.38±4.37	6.38±5.69	-	-	-		
<b>NH<sub>4</sub><sup>+</sup></b>	14.0±4.81 a	3.17±2.23 b	7.30±4.51 c	2.74±2.54 b	82.06	.00000	***		
<b>VP</b>	15.2±4.27 a	3.42±2.57 b	8.53±4.81 c	2.99±2.63 b	68.87	0.0000	***		
<b>VR</b>	11.18±4.92	2.61±1.05	4.73±2.45	2.38±2.35	-	-	-		
<b>NO<sub>2</sub><sup>-</sup></b>	0.065±0.053	0.121±0.090	0.021±0.034	0.024±0.028	-	-	-		
<b>VP</b>	0.073±0.064	0.116±0.099	0.020±0.040	0.018±0.025	-	-	-		
<b>VR</b>	0.051±0.018	0.132±0.073	0.024±0.022	0.035±0.030	-	-	-		
<b>NO<sub>3</sub><sup>-</sup></b>	0.779±0.598 a	0.743±0.951 a	0.448±0.731 a	0.245±0.344 a	2.694	0.0519	NS		
<b>VP</b>	0.679±0.653	0.428±0.773	0.122±0.047	0.132±0.114	-	-	-		
<b>VR</b>	0.929±0.507	1.214±1.044	0.936±0.996	0.413±0.497	-	-	-		
<b>TP</b>	4.94±1.52	4.24±1.81	4.46±1.56	3.82±1.81	-	-	-		
<b>VP</b>	5.49±1.48	4.75±2.08	5.13±1.49	4.41±1.99	-	-	-		
<b>VR</b>	4.14±1.17	3.48±0.81	3.50±1.04	3.01±1.06	-	-	-		
<b>TPf</b>	3.05±1.42	2.31±1.09	3.15±1.30	2.66±1.71	-	-	-		
<b>VP</b>	3.40±1.30	2.38±1.09	3.56±1.24	3.11±1.85	-	-	-		
<b>VR</b>	2.46±1.47	2.18±1.13	2.47±1.15	1.90±1.10	-	-	-		
<b>PO<sub>4</sub><sup>3-</sup></b>	2.32±1.39 a	2.17±0.93 a	3.07±1.30 b	2.26±0.84 a	5.360	0.0015	**		
<b>VP</b>	2.41±1.33	2.29±0.97	3.43±1.31	2.49±0.78	-	-	-		
<b>VR</b>	2.14±1.56	1.91±0.80	2.29±0.92	1.77±0.79	-	-	-		

For each variable, means followed by the same letter are not significantly different at 5%. Non-significant (NS), highly significant (\*\*), and very highly significant (\*\*\*) effects.

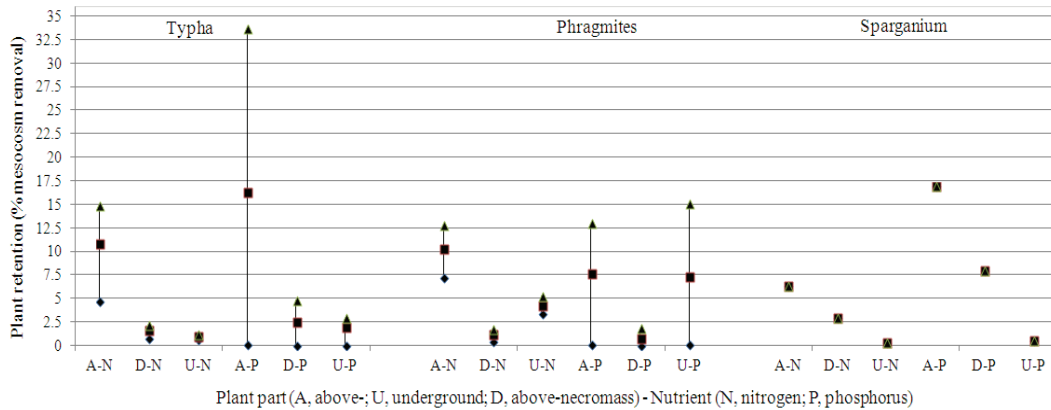


Fig. 7: Nitrogen and phosphorus retention in plant tissues in relation to the corresponding mesocosm efficiency.

In Mediterranean climate the *Phragmites* mesocosm is more effective in plankton reduction especially in tertiary treatment, compared to a lesser role of the *Typha* and *Sparganium* ones. By helophyte harvesting at the end of each vegetative period, there is relative stability of biomass production by *Phragmites* in tertiary treatment, resilience for *Phragmites* and *Sparganium* in secondary treatment, while *Typha* increases biomass

production the first two years and falls steeply the third year. Moreover, the aerial biomass of the three helophytes seems to be slightly disadvantaged in tertiary treatment.

Given the development magnitude of its underground biomass, *Phragmites* is by far the most cumulative of nitrogen and phosphorus in this part, in addition to the indirect benefit of substrate oxygenation, an interesting aspect for wastewater treatment. *Phragmites* also accumulates more nitrogen in its aboveground part in secondary treatment, and the nitrogen and phosphorus in its underground part in tertiary treatment. In secondary treatment *Typha* shows a specific interest in the assimilation of nitrogen in aerial tissues, and phosphorus in the whole plant.

## ACKNOWLEDGEMENT

This study was carried out as part of the MHEA® project, achieved in M'Diq (NW of Morocco) via the Agence de la Francophonie (Walloon Region-Morocco).

## REFERENCES

- [1] Radoux M. (1989) Epuration des eaux usées par hydrosère reconstituée. Trib. CEBEDEAU, 42(8):62-68.
- [2] Greenway M. (2003) Suitability of macrophytes for nutrient removal from surface flow constructed wetlands receiving secondary treated sewage effluent in Queensland, Australia. Water Sci. Technol., 48(2):121-128. <https://doi.org/10.2166/wst.2003.0101>
- [3] Vymazal J. (2013) Emergent plants used in free water surface constructed wetlands: A review. Ecol. Eng., 61(Part B):582-592. <https://doi.org/10.1016/j.ecoleng.2013.06.023>
- [4] Brix H. (1997) Do macrophytes play a role in constructed treatment wetlands? Water Sci. Technol., 35(5):11-17. <https://doi.org/10.2166/wst.1997.0154>
- [5] Greenway M, Woolley A. (1999) Constructed wetlands in Queensland: Performance efficiency and nutrient bioaccumulation. Ecol. Eng., 12(1-2):39-55. [https://doi.org/10.1016/S0925-8574\(98\)00053-6](https://doi.org/10.1016/S0925-8574(98)00053-6)
- [6] Zheng Y, Wang XC, Ge Y, Dzakpasu M, Zhao Y, Xiong J. (2015) Effects of annual harvesting on plants growth and nutrients removal in surface-flow constructed wetlands in northwestern China. Ecol. Eng., 83:268-275. <https://doi.org/10.1016/j.ecoleng.2015.06.035>
- [7] Korkusuz EA. (2005) Manual of practice on constructed wetlands for wastewater treatment and reuse in mediterranean countries; AVKR 5 - Technical Report Med-Reunet II (INCO-CT-2003-502453): Agbar Foundation Barcelona.
- [8] Ezzahri J, Ennabili A, Ater M, Radoux M. (2001) Epuration des eaux usées urbaines : Expérimentation sous climat méditerranéen (M'Diq, Nord-ouest du Maroc). Ann. Chim. Sci. Mat., 26:S297-311.
- [9] Ezzahri J, Ennabili A, Radoux M (2010) Artificial ecosystems for wastewaters treatment under Mediterranean conditions (Morocco). Biol. Divers. Conserv. 3/2:145-150. Retrieved from <http://www.biodicon.com/YayinlananMakaleler/7.15.pdf>
- [10] Radoux M, Cadelli D, Nemcova M, Ennabili A, Ezzahri J. (2003) Optimisation of extensive wastewater treatment systems under Mediterranean conditions (Morocco): compared purification efficiency of artificial ecosystems. In Wetlands: nutrients, metals and mass Cycling; Vymazal, J., Ed. Backhuys Publishers: Leiden, NL, pp. 143-168.
- [11] Ennabili A. (1999) Végétation hygrophile du Maroc méditerranéen: écologie, socio-économie et rôle potentiel dans l'épuration des eaux usées. PhD thesis. University of Liege, Department of Environmental Sciences and Management.
- [12] Ezzahri J. (2005) Optimisation de l'épuration naturelle des eaux usées domestiques urbaines dans le contexte climatique et socio-économique du Nord du Maroc (M'Diq). PhD thesis. University of Liege, Department of Environmental Sciences and Management.

- [13] Standard Methods. (1995) Standard Methods for the Examination of Water and Wastewater, 19<sup>th</sup>edn, American Public Health Association/American Water Works Association/Water Environment Federation: Washington D.C.
- [14] Ennabili A, Ater M, Radoux M. (1998) Biomass production and NPK-retention in macrophytes from wetlands of the Tingitan Peninsula. *Aquat. Bot.* 62(1):45-56. [https://doi.org/10.1016/S0304-3770\(98\)00075-8](https://doi.org/10.1016/S0304-3770(98)00075-8)
- [15] Ennabili A. (2008) Régénération in vivo de macrophytes originaires des zones humides du Maroc méditerranéen. *Rev. Assoc. Forum Nord Maroc*, 2-3:116-124. Retrieved from <http://revue-afnm.org/b2e/numero-2-3/regeneration-in-vivo-de-macrophytes>
- [16] Abou-Elela SI, Golinielli G, Abou-Taleb EM, Hellal MS. (2013) Municipal wastewater treatment in horizontal and vertical flows constructed wetlands. *Ecol. Eng.*, 61(Part A):460-468. <https://doi.org/10.1016/j.ecoleng.2013.10.010>
- [17] Zhang J, Sun H, Wang W, Hu Z, Yin X, Ngo HH, Guo W, Fan J. (2017) Enhancement of surface flow constructed wetlands performance at low temperature through seasonal plant collocation. *Bioresour. Technol.*, 224:222-228. <https://doi.org/10.1016/j.biortech.2016.11.006>
- [18] Song U, Waldman B, Park JS, Lee K, Park SJ, Lee EJ. (2018) Improving the remediation capacity of a landfill leachate channel by selecting suitable macrophytes. *J. Hydro-Environ. Res.*, 20:31-37. <https://doi.org/10.1016/j.jher.2018.04.005>
- [19] Ennabili A, Gharnit N. (2003) Effets d'aménagements du littoral tétouanais (Nord-ouest du Maroc) sur la végétation hygrophile (*Spermatophyta*). *Acta Bot. Barc.*, 48:199-216.
- [20] Asaeda T, Rajapakse L, Kanoh M. (2010) Fine sediment retention as affected by annual shoot collapse: *Sparganium erectum* as an ecosystem engineer in a lowland stream. *River Res. Appl.*, 26(9):1153-169. <https://doi.org/10.1002/rra.1322>
- [21] Liffen T, Gurnell AM, O'Hare MT. (2013) Profiling the below ground biomass of an emergent macrophyte using an adapted ingrowth core method. *Aquat. Bot.*, 110:97-102. <https://doi.org/10.1016/j.aquabot.2013.05.008>
- [22] Asaeda T, Rajapakse L, Manatunge J, Sahara N. (2006) The effect of summer harvesting of *Phragmites australis* on growth characteristics and rhizome resource storage. *Hydrobiologia*, 553:327-335. <https://doi.org/10.1007/s10750-005-1157-6>
- [23] Maddison M, Soosaar K, Muring T, Mander Ü. (2009) The biomass and nutrient and heavy metal content of cattails and reeds in wastewater treatment wetlands for the production of construction material in Estonia. *Desalination*, 246(1-3):120-128. <https://doi.org/10.1016/j.desal.2008.02.040>
- [24] Boyd MC, Brown MT, Brandt-Williams S. (2015) Addressing pollutant load reduction goals for impaired waterbodies through biomass harvest of Gulf Coast type *Phragmites australis* (common reed). *Wetlands Ecol. Manage.*, 23:519-533. <https://doi.org/10.1007/s11273-015-9406-6>
- [25] Tanaka TST, Irbis C, Kumagai H, Inamura T. (2016) Timing of harvest of *Phragmites australis* (CAV.) Trin. ex Steudel affects subsequent canopy structure and nutritive value of roughage in subtropical highland. *J. Environ. Manag.*, 166:420-428. <https://doi.org/10.1016/j.jenvman.2015.10.055>
- [26] de los Reyes CP, Villamar CA, Neubauer ME, Pozo G, Vidal G. (2013) Behavior of *Typha angustifolia* L. in a free water surface constructed wetlands for the treatment of swine Wastewater. *J. Environ. Sci. Health, Part A: Toxic/Hazard. Subst. Environ. Eng.*, 48(10):1216-224. <https://doi.org/10.1080/10934529.2013.776852>
- [27] Maucieri C, Salvato M, Tamiazzo J, Borin M. (2014) Biomass production and soil organic carbon accumulation in a free water surface constructed wetland treating agricultural wastewater in North Eastern Italy. *Ecol. Eng.*, 70:422-428. <https://doi.org/10.1016/j.ecoleng.2014.06.020>
- [28] Borin M, Tocchetto D. (2007) Five year water and nitrogen balance for a constructed surface flow wetland treating agricultural drainage waters. *Sci. Total Environ.*, 380(1-3):38-47. <https://doi.org/10.1016/j.scitotenv.2006.12.039>

- [29] Li EH, Li W, Wang XL, Xue HP, Xiao F. (2010) Experiment of emergent macrophytes growing in contaminated sludge: Implication for sediment purification and lake restoration. *Ecol. Eng.*, 36(4):427-434. <https://doi.org/10.1016/j.ecoleng.2009.11.009>
- [30] Das SC, Tanaka N (2007) Estimating nitrogen budgets of *Typha angustifolia* by considering the regrowth shoot productivity and nitrogen content after harvesting aerial organs in different growing seasons. *Landsc. Ecol. Eng.*, 3:99-108. <https://doi.org/10.1007/s11355-007-0024-1>
- [31] Asaeda T, Rashid MH. (2015) Nutrient retention associated with phenological features in *Sparganium erectum* stands in a lowland stream. *River Res. Appl.*, 31(2):207-215. <https://doi.org/10.1002/rra.2733>
- [32] Chicalote-Castillo D, Ramírez-García P, Macías-Rubalcava ML. (2017) Allelopathic effects among selected species of phytoplankton and macrophytes. *J. Environ. Biol.*, 38(Special issue):1221-227. [http://dx.doi.org/10.22438/jeb/38/6\(SI\)/07](http://dx.doi.org/10.22438/jeb/38/6(SI)/07)
- [33] Zhang TT, Hu W, Zhang D. (2012) Allelopathic effect of *Typha angustifolia* L. on phytoplankton. *Adv. Mater. Res.-Switz.*, 383-390:3724-728. <http://dx.doi.org/10.4028/www.scientific.net/AMR.383-390.3724>
- [34] Gross EM. (2003) Allelopathy of aquatic autotrophs. *Crit. Rev. Plant Sci.*, 22(3-4):313-339. <https://doi.org/10.1080/713610859>

## ANALYSIS AND CORRELATIONS OF DIMENSIONLESS NUMBERS RELEVANT TO ORIFICES' CAVITATING FLOW

ABDUL-FATTAH MOHAMMED ALI<sup>1,2</sup>  
AND MOHANAD JASIM MOHAMMED-RIDHA<sup>1\*</sup>

<sup>1</sup>Department of Environmental Engineering, University of Baghdad, Baghdad, Iraq

<sup>2</sup>Department of Oil and Gas Refining Engineering,  
Al-Farabi University College, Baghdad, Iraq

\*Corresponding author: [muhannadenviro@coeng.uobaghdad.edu.iq](mailto:muhannadenviro@coeng.uobaghdad.edu.iq)

(Received: 5<sup>th</sup> December 2019; Accepted: 13<sup>th</sup> May 2020; Published on-line: 4<sup>th</sup> July 2020)

**ABSTRACT:** The aim of this work was to establish a general design basis for pilot-scale units to treat textile dyeing wastewater containing recalcitrant organic chemicals by hydrodynamic cavitation (HC) using orifices of various geometries. Relevant tabulated data available in the literature were analyzed and correlated to obtain universal relationships to this end. In spite of extensive effort, most of the obtained correlations were system-specific, which still can be used for design using their respective orifice geometries as demonstrated. However, one salient general relationship links the pipe's dimensionless loss coefficient ( $K_{LP}$ ) to the pipe's Reynolds number ( $Re_P$ ), encompassing all data under consideration, which may serve as an additional design option to optimize such units. The implication of this relationship is a lower upstream pressure ( $P_1$ ) value with an increase in pipe diameter while using the same specified orifice and achieving the same desired cavitation number ( $C_v$ ). The ratio of  $P_1$  value in the larger pipe to its value in the smaller pipe is a function of the smaller pipe diameter ( $D_S$ ) to the larger pipe diameter ( $D_L$ ) ratio:  $(P_1 \text{ in } D_L) / (P_1 \text{ in } D_S) = (D_S / D_L)^{2.33}$ . A lower  $P_1$  value will increase the cavitation yield by decreasing the expended energy, especially if the required number of passes is large. Additionally, the variation of the orifices' hole loss coefficient ( $K_{Lh}$ ) with the ratio of the holes area to the pipe cross-sectional area ( $A_h/A_p$ ) for cavitating flow is compared with that for non-cavitating/incipient cavitation flow reported in the literature.

**ABSTRAK:** Tujuan kajian ini diadakan bagi mereka bentuk dasar umum unit skala-pandu bagi merawat pewarnaan air buangan tekstil yang mengandungi kimia organik rekalsitran daripada peronggaan hidrodinamik (HC) menggunakan orifis pelbagai geometri. Data berjadual berkaitan yang ada dalam kajian lepas dianalisa dan dikaitkan bagi mendapatkan kaitan universal hingga akhir. Walaupun pelbagai usaha telah dijalankan, banyak kaitan didapati mengguna pakai sistem-tertentu, di mana boleh digunakan bagi mereka cipta menggunakan geometri orifis yang ditunjukkan. Walau bagaimanapun, bagi menghubungkan kait pekali langsung tanpa dimensi ( $K_{LP}$ ) kepada paip nombor Reynolds ( $Re_P$ ), meliputi semua data di bawah pertimbangan, di mana membantu pilihan rekaan tambahan bagi mengoptimum unit tersebut. Implikasi hubungan ini adalah nilai tekanan hulu sungai bawah ( $P_1$ ) dengan penambahan diameter paip dengan menggunakan orifis sama yang sebenar dan mendapati nombor peronggaan yang sama diinginkan ( $C_v$ ). Nisbah nilai  $P_1$  dalam paip besar kepada nilai paip kecil adalah berkadaran pada nisbah diameter paip kecil ( $D_S$ ) kepada diameter paip besar ( $D_L$ ):

$$(P_1 \text{ dalam } D_L) / (P_1 \text{ in } D_S) = (D_S / D_L)^{2.33}$$

Nilai  $P_1$  yang lebih kecil akan menambah jumlah peronggaan dengan pengurangan tenaga pengembangan, terutama jika nombor laluan yang diperlukan adalah besar. Tambahan, variasi orifis pekali langsung lubang ( $K_{Lh}$ ) dengan nisbah keluasan lubang kepada ruang keratan-rentas paip ( $A_h/A_p$ ) bagi alur rongga dibandingkan dengan bukan rongga / permulaan rongga alur telah dilapor dalam kajian

---

**KEYWORDS:** *hydrodynamic cavitation; orifice geometry; cavitation numbers; upstream pressure; loss coefficients*

## 1. INTRODUCTION

Hydrodynamic cavitation (HC) is a well-established technique for a variety of applications including the treatment of wastewater containing pharmaceuticals [1], insecticides [2], phenolic compounds [3], and textile dyes [4-8]. HC is usually combined with the addition of an oxidizing agent ( $H_2O_2$ ,  $NaOCl$ , etc.) or with acoustic cavitation to achieve an acceptable cavitation yield (CY) which is defined as the cavitation effect per unit energy supplied to the system.

Over the last two decades, many HC research studies have been published, some with detailed tabulated data. Their size-scale ranged from 1 L lab units to 50 L pilot ones. Various devices were used to induce HC in these units such as single-/multi-hole orifices, venturis, stator-rotor equipment, etc. The operational mode was batch-wise based either on fixed time or on a specified number of passes (turnovers) where the wastewater volume was recirculated many times through the HC device to achieve an acceptable CY. This could be hundreds of times, lasting over two hours depending on the system's flow rate (e.g. 260 passes lasting 130 min [7]).

Single-/multi-hole orifices as HC inducing devices are simpler to manufacture and install than other alternatives which explain their wide use in HC studies. Their hole size generally ranges from 1 to 5 mm with multi-hole counts of 8, 16, 20, 25, or 33, although some studies used sizes and counts outside these values. The pipes in which the aforementioned orifices were placed had inside diameters ranging from 4 to 53 mm.

The results obtained in all previously published HC studies were system-specific; a generalized or unifying approach were markedly lacking. Reviews stated only general trends based on the published works. Consequently, it is difficult to make practical use of available information, specifically a priori design of a functional wastewater-treating HC unit, save adopting a given system with all its particulars. The present work is an attempt at a unifying approach, relying entirely on tabulated data from a number of published research studies. The outcome of this endeavor was only partially productive as will be illustrated later by the obtained results. This research did not receive any specific grant from funding agencies in the public, commercial, or not-for-profit sectors.

## 2. GEOMETRICAL DETAILS AND REFERENCES OF ORIFICES WHOSE HC PUBLISHED DATA WERE USED IN THIS WORK

Two categories of published data were excluded from the analysis and correlations performed in this study. The first concerned orifices with a hole size of one mm or less, whether single- or multi-hole ones. One mm holes or smaller are difficult/expensive to produce locally while ensuring their integrity (sharp edge, lack of burrs, etc.). The second category concerned a HC system in which the fully-recovered orifice's downstream pressure ( $P_2$ ) was higher than atmospheric pressure (i.e.  $P_2 > \text{one atm. abs. or zero gage}$ ).

Data with  $P_2 > 0$  gage did not match those with  $P_2 \approx 0$  gage. Table 1 gives the details of the orifices whose HC data were used in this work along with their references.

The data of Testud et al. [10] and that of Mancuso et al. [7] were excluded due to  $P_2$  values being greater than one atm. abs. as pointed out earlier. It should be stressed that all the HC data of the references cited in Table 1 are relevant to pilot-scale units with  $P_2 \approx$  one atm. abs. Hence, all the obtained correlations of this work are only relevant to such systems.

Table 1: Geometrical details and references of orifices whose HC data were employed in the analysis and correlations of this work.

Hole dia. [mm]	No. of holes	Pipe I.D [mm]	$A_h/A_p$	Reference
2	1	25.4	$6.2 \times 10^{-3}$	[6]
2	1	25	$6.4 \times 10^{-3}$	[9]
2	1	19	0.011	[8]
2	1	19	0.011	[17]
2	8	38	0.02216	[11]
2	8	38	0.02216	[4]
2	33	38	0.0914	[11]
2	33	38	0.0914	[4]
3	1	25.4	0.01395	[6]
3	1	19	0.02493	[17]
3	16	38	0.099723	[11]
3	16	38	0.099723	[4]
3	20	38	0.12465	[11]
3	20	38	0.12465	[4]
5	8	38	0.1385	[11]
5	8	38	0.1385	[4]

Notes: (i)  $A_h/A_p$  is the ratio of the total area of holes to the cross-sectional area of the pipe. (ii) Thicknesses of orifices in Table 1 references were not mentioned, apart from Pawar et al. [9] which was 4 mm leading to an aspect ratio of 2 (aspect ratio = orifice thickness/hole dia.). (iii) HC data listed in Table 1 references are extensive and can be referred to; they shall not be repeated in this article. (iv) A 4-mm single hole orifice datum from Madhu et al. [6] was excluded due to lack of 4-mm multi-hole data.

### 3. DIMENSIONLESS NUMBERS RELEVANT TO ORIFICE'S CAVITATING FLOW AND THEIR INTER-RELATIONSHIPS

#### 3.1 Cavitation Number or Index

There are several definitions for this parameter, the two most widely used ones are  $C_v$  and  $\sigma$  (notations used are similar to those in the cited references) defined as follows:

$$C_v = (P_2 - P_v) / (0.5 \rho_L u_0^2) \quad \text{and} \quad \sigma = (P_2 - P_v) / (P_1 - P_2)$$

where  $P_1$ ,  $P_2$  are the orifice's upstream and fully-recovered downstream pressures, respectively.  $P_v$  is the liquid-vapor pressure and  $\rho_L$  is its density, both at the operating temperature.  $u_0$  is the average liquid velocity at the orifice's hole (single hole or one hole in a multi-hole geometry).

Cavitating flow occurs when the value of  $C_v$  (or  $\sigma$ ) is usually  $< 1$ , with an increase in cavitation intensity as the value of the index is lowered. Very low values of the index ( $<$

0.1) may induce a regime called supercavitation which is counterproductive and should be avoided.

A modification of  $C_v$  (called  $C_v^{\text{prime}}$ ) was introduced and used by Vichare et al. [11] and Sivakumar and Pandit [4] as a unifying approach for comparison of HC data of orifices with various multi-hole geometries.  $C_v^{\text{prime}}$  was defined as:

$$C_v^{\text{prime}} = C_v / [(\text{total perimeter of holes}/\text{perimeter of pipe})]$$

### 3.2 Flow Head Loss Coefficients and Reynolds Numbers

Two dimensionless flow head loss coefficients were used in this work. Their definitions are:

$$K_{Lh} = (P_1 - P_2) / (0.5 \rho_L u_o^2) \quad \text{and} \quad K_{LP} = (P_1 - P_2) / (0.5 \rho_L u_p^2)$$

$K_{Lh}$  is based on the hole's dynamic pressure, whereas  $K_{LP}$  is based on the pipe's dynamic pressure with  $u_p$  being the average flow velocity in the pipe. Additionally, two Reynolds numbers were used, one based on the hole average velocity and the other one on the pipe average velocity:

$$Re_o = \rho_L u_o d_o / \mu_L \quad \text{and} \quad Re_p = \rho_L u_p D / \mu_L$$

where  $d_o$  and  $D$  are the hole diameter and the pipe inside diameter, respectively.  $\mu_L$  is the liquid dynamic viscosity at the operating temperature.

### 3.3 Inter-relationships Among the Aforementioned Dimensionless Numbers

$K_{Lh}$  is related to  $K_{LP}$  by (Maynes et al. [12]) Eq. (1):

$$K_{Lh} = (A_h/A_p)^2 K_{LP} \quad (1)$$

and  $Re_p$  is related to  $Re_o$  by Eq. (2):

$$Re_p = Re_o [n (A_h/A_p)]^{0.5} \quad (2)$$

where  $n$  is the number of holes in the orifice (hole count) and  $A_h/A_p$  is the ratio of the total area of holes to the pipe cross-sectional area as pointed out earlier. Additionally,  $\sigma$  is related to  $C_v$  by Eq. (3):

$$\sigma = C_v / K_{Lh} \quad (3)$$

The relationships represented by Eqs. (1) to (3) can be easily obtained by considering the given definitions of the dimensionless numbers involved.

The orifices' HC tabulated data of Table 1 references constituted experimental values of  $P_1$ ,  $C_v$ ,  $u_o$ ,  $A_h/A_p$ , flow rate, and temperature.  $P_2$  values were either given or calculated using the above relationships, where it was confirmed that its value was virtually one atm. abs. in all cases. Eq. (3) was used to calculate the corresponding  $\sigma$  values.

## 4. SPECIFIC CORRELATIONS OF ORIFICES' CAVITATING FLOW DIMENSIONLESS NUMBERS AND THEIR UTILITY IN DESIGN

Cavitating flow is a complex phenomenon that is still not-well understood and whose theoretical basis has not been fully established. Consequently, an empirical approach is usually adopted (Burzio et al. [18]). Accordingly, Eqs. (4) to (18) are empirical; only

characterized by values of the determination coefficient  $R^2 > 0.9$ . Furthermore, the data upon which they are based (Table 1) lacked standard deviation bounds which compromise their accuracy. Notwithstanding these limitations, the equations are of use in a priori design of HC pilot-scale units (as elucidated in section 4.5) where plus or minus 5% off specification is usually acceptable.

Table 2 expounds the types of correlations employed and equations designation as related to five orifice geometries. Two other geometries pertaining to the 2mm and 3mm single hole orifices were excluded from the said correlations due to their trend-lacking scattered data. Additionally, Eqs. 13 to 15 were also excluded from Table 2 because they represent a test for  $C_v^{prime}$  as a unifying parameter.

Table 2: Types of correlation, equations designation and corresponding orifice geometries

Correlation type	2mm-8h	2mm-33h	3mm-16h	3mm-20h	5mm-8h
$K_{Lh}$ vs. $Re_o$	Eq. (4)	-----	-----	Eq. (5)	-----
$K_{Lh}$ vs. $C_v$	Eq. (6)	-----	-----	Eq. (7)	-----
$\sigma$ vs. $Re_o$	Eq. (8)	Eq. (9)	-----	-----	Eq. (10)
$\sigma$ vs. $C_v$	Eq. (11)	Eq. (12)	Eq. (16)	Eq. (17)	Eq. (18)

Notes: (i) In the design procedure, the value of  $C_v$  is initially assumed depending on the application (see sec. 4.5) which leads to the calculation of  $Re_o$ . (ii) For a selected geometry,  $K_{Lh}$  or  $\sigma$  is then determined from an appropriate equation(s) leading to the value of  $P_1$  (a prime design parameter). (iii) There are 4 choices to accomplish note (ii) for 2mm-8holes, 3 choices for 3mm-20holes, 2 choices for either 2mm-33holes or 5mm-8holes, but only one choice for the 3mm-16holes geometry.

#### 4.1 $K_{Lh}$ vs $Re_o$ Correlations

For this category, only two specific correlations were obtained as shown in Fig. 1.

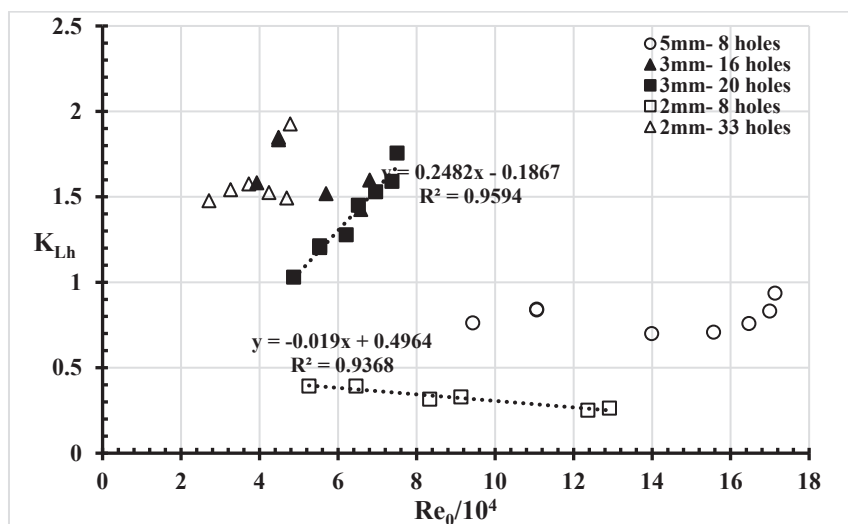


Fig. 1:  $K_{Lh}$  vs  $Re_o/10^4$ .

$$K_{Lh} = 0.4964 - 0.019 (Re_o/10^4) \quad (4)$$

$$(2mm-8holes, 5 \leq Re_o/10^4 \leq 13, R^2 = 0.9368)$$

$$K_{Lh} = 0.2482 (Re_o/10^4) - 0.1876 \quad (5)$$

$$(3mm-20holes, 4.5 \leq Re_o/10^4 \leq 8, R^2 = 0.9594)$$

The trends of Eqs. (4) and (5) are opposite to one another. The 2mm-8holes  $K_{Lh}$  decreases with increasing  $Re_o$  ( $A_h/A_p = 2.2\%$ ) whereas the 3mm-20holes  $K_{Lh}$  increases ( $A_h/A_p = 12\%$ ). Also shown in Fig. 1 are the data of the 2mm-33holes ( $A_h/A_p = 9.1\%$ ) and the 5mm-8holes ( $A_h/A_p = 13.85\%$ ). The former reflects an increasing-decreasing trend, whilst the latter depicts a clearly non-linear increasing trend for  $Re_o > 16 \times 10^4$ . Maynes et al. [12] had shown an increasing  $K_{Lh}$  trend with increasing  $u_o$  for two multi-hole orifices with  $A_h/A_p$  values of 22% and 44% which they attributed to cavitating flow, since according to their results for non-cavitating flow  $K_{Lh}$  was constant and independent of  $u_o$ . Any explanation for the above observations would be premature at this stage.

#### 4.2 $K_{Lh}$ vs $C_v$ Correlations

The following specific correlations were obtained for this category.

$$K_{Lh} = 1.0192 C_v + 0.2095 \quad (6)$$

(2mm-8holes,  $0.045 \leq C_v \leq 0.56$ ,  $R^2 = 0.9956$ , Fig. 2)

$$K_{Lh} = 0.862 C_v^{-0.567} \quad (7)$$

(3mm-20holes,  $0.3 \leq C_v \leq 0.75$ ,  $R^2 = 0.9681$ , Fig. 3)

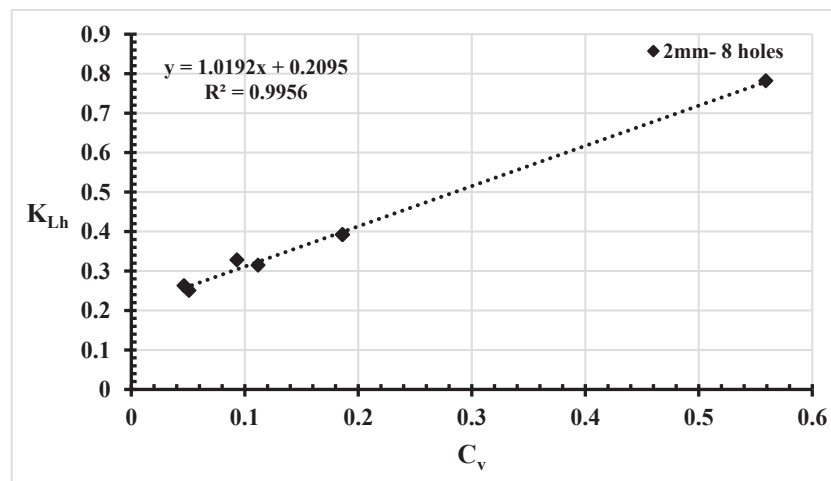


Fig. 2:  $K_{Lh}$  vs  $C_v$  2mm-8holes.

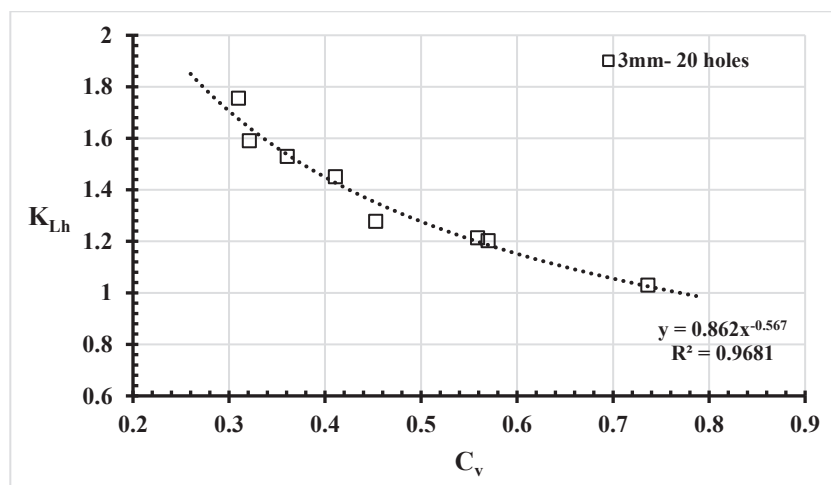


Fig. 3:  $K_{Lh}$  vs  $C_v$  3mm-20holes.

The trends represented by Eqs. (6) and (7) are opposite to one another. For each geometry, the above trend is the reverse of its  $K_{Lh}$  vs  $Re_o$  trend [Eqs. (4) and (5)]. Hence,  $K_{Lh}$  increases with increasing  $C_v$  for the geometry of the 2mm-8 holes [Eq. (6)] whereas it decreases for the 3mm-20holes one [Eq. (7)].

### 4.3 $\sigma$ vs $Re_o$ Correlations

For this category, the following specific relationships were obtained:

$$\sigma = 0.8139 - 0.0159 (Re_o/10^4) \quad (8)$$

(2mm-8holes,  $3.7 \leq Re_o/10^4 \leq 13$ ,  $R^2 = 0.9095$ , Fig. 4)

$$\sigma = 1.0317 - 0.1757 (Re_o/10^4) \quad (9)$$

(2mm-33holes,  $3 \leq Re_o/10^4 \leq 5$ ,  $R^2 = 0.9644$ , Fig. 4)

$$\sigma = 65.504 (Re_o/10^4)^{-2.027} \quad (10)$$

(5mm-8holes,  $9 \leq Re_o/10^4 \leq 17.5$ ,  $R^2 = 0.9559$ , Fig. 5)

Equations (8) to (10) indicate a decreasing trend of  $\sigma$  with increasing  $Re_o$  for different geometries. This was expected since higher  $Re_o$  values imply higher  $P_1$  values making  $\sigma$  smaller since  $P_2$  and  $P_v$  are fixed, [ $\sigma = (P_2 - P_v)/(P_1 - P_2)$ ].

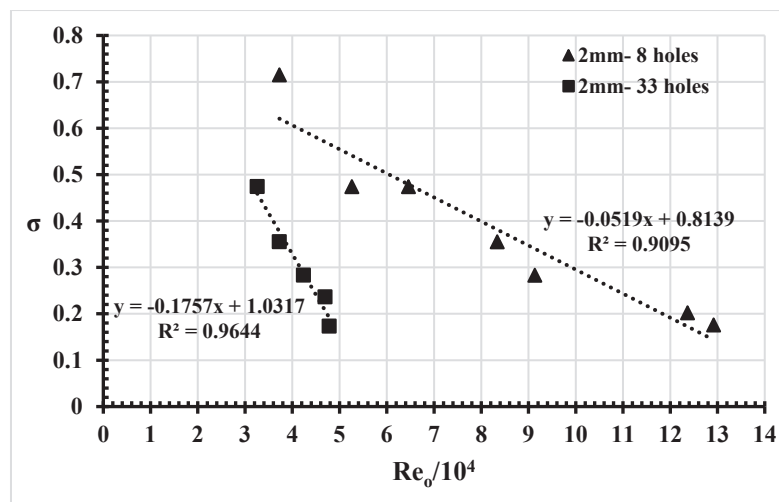


Fig. 4:  $\sigma$  vs  $Re_o/10^4$  for 2 mm-8, 33holes.

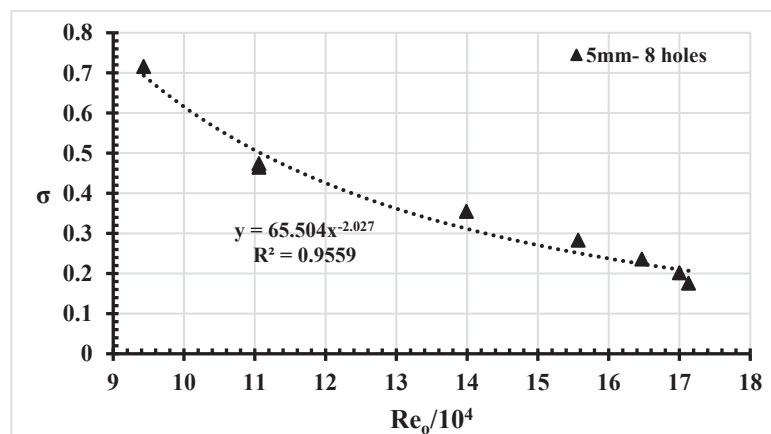


Fig. 5:  $\sigma$  vs  $Re_o/10^4$  for 5mm-8holes.

#### 4.4 $\sigma$ vs $C_v$ or $C_v^{\text{prime}}$ Correlations

Specific correlations linking the two most widely-used definitions of cavitation number were as follows:

$$\sigma = 1.016 C_v^{0.5509} \quad (11)$$

(2mm-8 holes,  $0.045 \leq C_v \leq 0.56$ ,  $R^2 = 0.9647$ , Fig. 6)

$$\sigma = 0.6848 C_v - 0.0262 \quad (12)$$

(2mm-33 holes,  $0.35 \leq C_v \leq 0.75$ ,  $R^2 = 0.9799$ , Fig. 6)

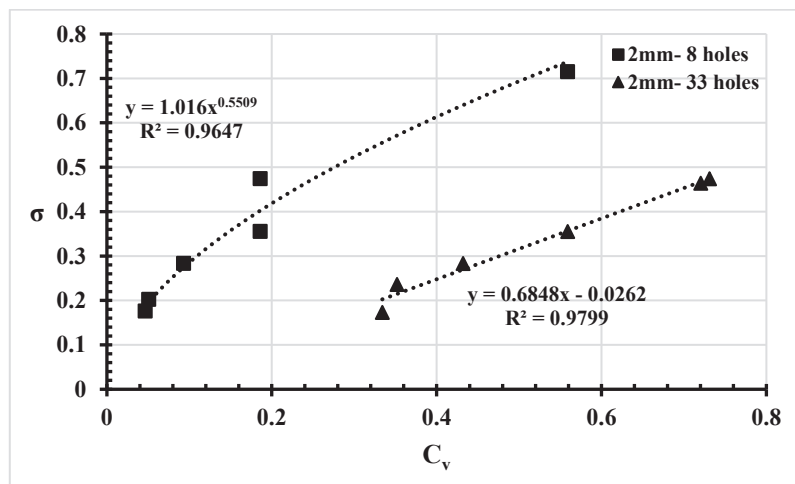


Fig. 6:  $\sigma$  vs  $C_v$  for 2mm-8, 33holes.

The two geometries of Eqs. (11) and (12) were combined by a single  $\sigma$  vs  $C_v^{\text{prime}}$  correlation:

$$\sigma = 0.9478 C_v^{\text{prime}} + 0.0593 \quad (13)$$

(2mm-8, 33 holes,  $0.1 \leq C_v^{\text{prime}} \leq 0.45$ ,  $R^2 = 0.9388$ , Fig. 7)

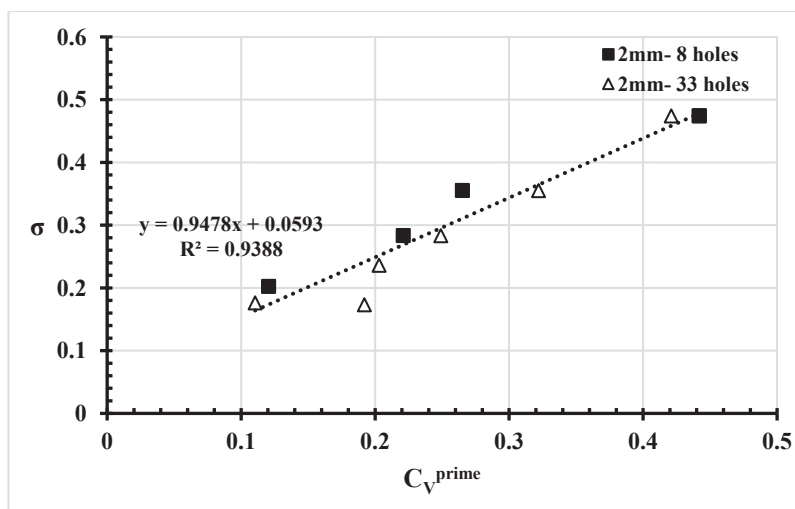


Fig. 7:  $\sigma$  vs  $C_v^{\text{prime}}$  for combined 2mm-8, 33holes.

Equation (13) is the only case where  $C_v^{prime}$  acted as a unifying parameter. Consequently, two additional  $\sigma$  vs  $C_v$  specific relationships were deduced for imaginary geometries of 2mm-16holes and 2mm-20holes:

$$\sigma = 1.1255 C_v + 0.0593 \quad (14)$$

$$(2\text{mm-16holes}, 0.0842 \leq C_v \leq 0.379)$$

$$\sigma = 0.9004 C_v + 0.0593 \quad (15)$$

$$(2\text{mm-20holes}, 0.1053 \leq C_v \leq 0.477)$$

Additionally, the following specific  $\sigma$  vs  $C_v$  correlations were obtained:

$$\sigma = 0.5995 C_v - 0.0081 \quad (16)$$

$$(3\text{mm-16holes}, 0.37 \leq C_v \leq 1.15, R^2 = 0.9602, \text{ Fig. 8})$$

$$\sigma = 1.2227 C_v - 0.206 \quad (17)$$

$$(3\text{mm-20holes}, 0.3 \leq C_v \leq 0.75, R^2 = 0.9936, \text{ Fig. 8})$$

$$\sigma = 1.2676 C_v \quad (18)$$

$$(5\text{mm-8holes}, 0.15 \leq C_v \leq 0.55, R^2 = 0.9732, \text{ Fig. 9})$$

Equations (11) to (18) reflect a trend of increasing  $\sigma$  with increasing  $C_v$  for the various orifice geometries. This trend was also expected since an increase in  $C_v$  value means a lower  $u_0$  value which entails a lower  $P_1$  value leading to an increase in the value of  $\sigma$ .

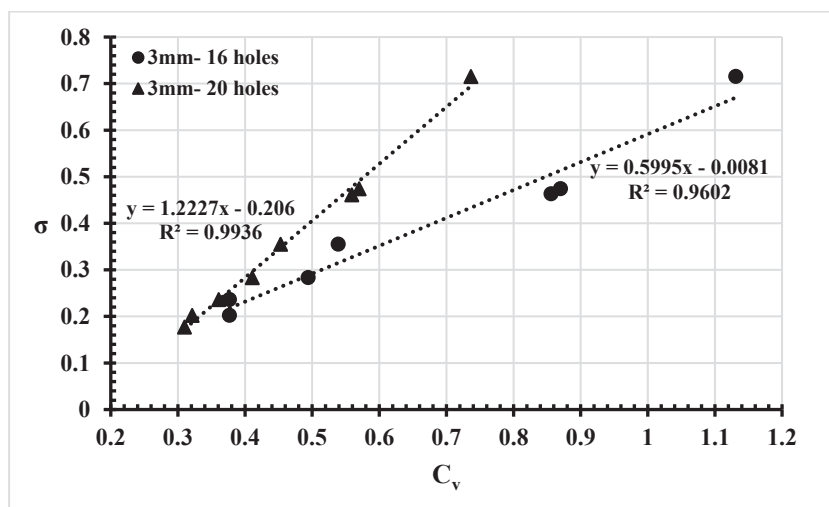


Fig. 8:  $\sigma$  vs  $C_v$  for 3mm-16, 20holes.

Yan and Thorpe [13] derived a theoretical equation linking  $\sigma$  to  $C_v$  for a single hole orifice. Their relationship included the orifice's discharge coefficient  $C_d$ , its contraction coefficient  $C_c$ , and  $A_h/A_p$ . It was not possible to compare Eqs. (11) to (18) with their equation because  $C_d$  and  $C_c$  were not given for the orifices under consideration in this work. Estimating the values of  $C_d$  and  $C_c$  from correlations available in the literature would be uncertain since they are related to the aspect ratio, which is also missing for all the multi-hole orifices of Table 1.

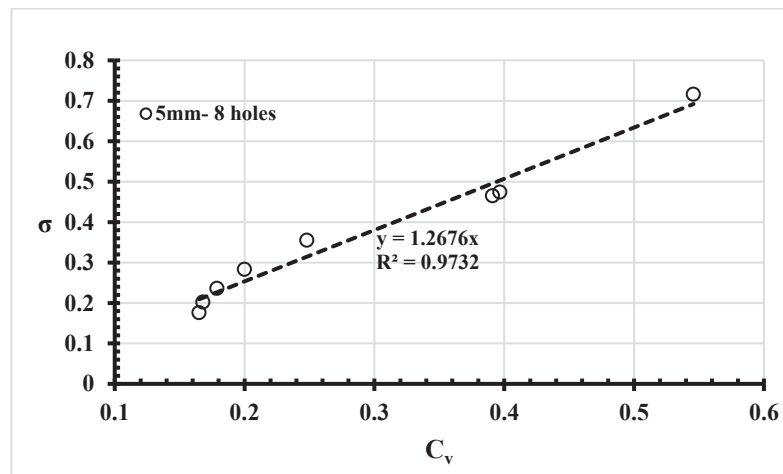


Fig. 9:  $\sigma$  vs  $C_v$  for 5 mm-8holes.

#### 4.5 Outline of a Priori Design Procedure Utilising the Specific Correlations

- Initially an appropriate  $C_v$  value for the intended application is chosen, e.g. for wastewater containing bio-refractory organic dyes, a suitable range is  $0.2 \leq C_v \leq 0.4$  (Rajoriya et al. [19])
- Since  $C_v = (P_2 - P_v)/(0.5 \rho_L u_o^2)$ ,  $u_o$  can be determined after an operating temperature is set, fixing the values of  $P_v$ ,  $\rho_L$ , and  $\mu_L$ . Hence the value of  $Re_o$  can be established.
- After selecting an orifice geometry, one or more correlation may be used to calculate either  $K_{Lh}$  or  $\sigma$  from which the value of  $P_1$  can be determined. This  $P_1$  value is based on 38 mm (1.5 inch) pipe diameter (see Table 1).
- The 38mm-based  $P_1$  value can be lowered by specifying a larger pipe diameter, e.g. 53mm (2 inch) according to the findings of sec. 5 below.  $(P_1 - P_2)$  represents the main pressure drop of the system whose volumetric flow rate ( $Q$ ) can be calculated from the value of  $u_o$  and the selected geometry leading to the estimation of the system's total pressure drop ( $\Delta P$ ).
- A centrifugal pump whose best efficiency point (BEP) matches the system's  $Q$ - $\Delta P$  point should be employed. Conversely, if a pump is already available, an appropriate  $C_v$  value, the ensuing  $P_1$  and reduced  $P_1$  values, and selected geometry should be manipulated to achieve the pump's BEP-system's  $Q$ - $\Delta P$  match.

### 5. GENERAL $K_{LP}$ vs $Re_p$ CORRELATION AND ITS IMPLICATIONS

Figure 10 shows a plot of  $K_{LP}$  vs.  $Re_p$  for all the HC data of the orifices listed in Table 1, including the single hole data which were excluded from the specific correlations of sec. 4 due to their trend-lacking scatter. It is noteworthy that four pipe sizes are included in Fig. 10 with a range of  $19 \leq I.D. \leq 38$  mm, which is in contrast with the specific correlations where only a single pipe size of  $I.D. = 38$  mm was involved. The unifying characteristic of  $K_{LP}$  vs  $Re_p$  is clear, resulting in the following general correlation Eq. (19):

$$K_{LP} = 4228.5 (Re_p/10^4)^{-1.6707} \quad (19)$$

$$\{(Re_p/10^4) \leq 18, R^2 = 0.9353\}$$

Retrieving the definitions of  $K_{LP} = (P_1 - P_2)/(0.5 \rho_L u_p^2)$  and  $Re_p = (\rho_L u_p D)/\mu_L$ , Fig. 10 indicates that increasing  $Re_p$  by increasing  $u_p$ , which can only come about by increasing  $P_1$  reduces  $K_{LP}$  in a nearly exponential decay manner. If the definitions of  $K_{LP}$  and  $Re_p$  are substituted into Eq. (19) and noting that  $(P_1 - P_2)$  may be replaced by  $P_1$  as gage pressure, then Eq. (19) can take the following form:

$$P_1 = 1.0185 \times 10^5 \rho_L^{-0.6707} \mu_L^{1.6707} u_p^{0.3293} D^{-1.6707} \quad (20)$$

where  $P_1$  has units of bar gage.

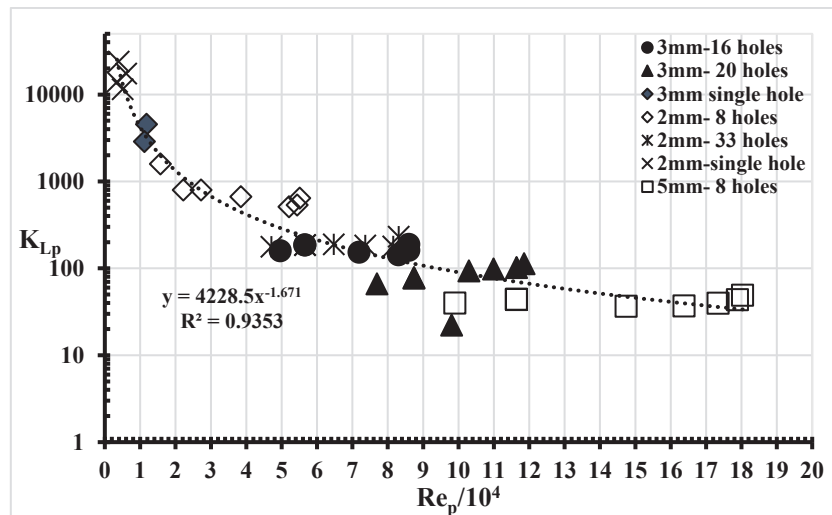


Fig. 10:  $K_{LP}$  vs  $Re_p/10^4$  for all single and multi-hole orifices.

If for a specific orifice geometry and a desired  $C_v$  value, two pipes are considered (in which the specified orifice is to be installed in one of them) one pipe with a smaller inside diameter  $D_S$  and the other with a larger inside diameter  $D_L$ , then the application of Eq. (20) and the equation of continuity (conservation of mass flow rate) for the two pipes will result in the following ratio Eq. (21): (see Appendix A),

$$(P_1 \text{ in } D_L \text{ pipe} / P_1 \text{ in } D_S \text{ pipe}) = (D_S / D_L)^{2.33} \quad (21)$$

Hence, a lower value of  $P_1$  is required to obtain the desired  $C_v$  value by installing the specified orifice in a larger I.D pipe compared to a smaller I.D. pipe. It is emphasized that this result is limited to the applicability range of Eq. (19) and the data upon which it is based.

An additional advantage of using a relatively larger inside diameter pipe is the lower pressure drop in the system, apart from the orifice's pressure drop  $(P_1 - P_2)$ , especially when the required number of passes is large. This will have a positive effect on the expended energy and consequently on the cavitation yield.

A possible drawback of lowering  $P_1$  value by using a larger inside diameter pipe is the ensuing decrease in the value of the cavity collapse pressure given by the following empirical correlation [14-16] Eq. (22).

$$P_{\text{collapse}} = 7527 [100 (A_h/A_p)]^{-2.55} P_1^{2.46} R_o^{-0.8} d_o^{2.37} \quad (22)$$

which is related to the cavitation yield by Eq. (23):

$$CY = K ( P_{collapse} )^W \quad (23)$$

where  $R_o$  is the initial cavity size,  $K$  and  $w$  are constants whose values depend on the system's particulars (device geometry, operating parameters, type of reaction). However, the possible negative effect of lower  $P_1$  value may be partially or totally offset by the decrease in the value of  $A_h/A_p$  with a larger inside diameter pipe and/or the value of  $w$  being positive or negative.

Applying Eq. (22) with  $D_s$  or  $D_L$  leads to:

$$(P_{collapse \text{ in } D_L \text{ pipe}})/(P_{collapse \text{ in } D_s \text{ pipe}}) = (D_s/ D_L)^{0.632} \quad (24)$$

## 6. COMPARISON WITH FINDINGS OF MAYNES et al. [12]

Maynes et al. [12] showed a graphical representation of  $K_{Lh}$  vs  $A_h/A_p$  in which data points pertaining to 16 multi-hole orifices of their work plus data points from three references were all bounded by two theoretical models, namely Eqs. (25) and (26):

$$(K_{Lh})_{Detached} = [C_c^{-1} - (A_h/A_p)]^2 \quad (25)$$

$$(K_{Lh})_{Attached} = 2 [1 - (A_h/A_p) - C_c^{-1}] + C_c^{-2} + (A_h/A_p)^2 \quad (26)$$

These models were derived by Testud et al. [10] for single hole orifice using Bernoulli's principle and conservation of momentum for non-cavitating flow. Eq. (25) is relevant to a thin orifice where the flow does not reattach within the hole, whereas Eq. (26) is for a thick orifice where the flow is reattached.  $C_c$  value for Eq. (25) was determined from Busemann theoretical relation cited by Maynes et al. [12] (a function of  $A_h/A_p$ ) whilst for Eq. (26) it was given a fixed value of 0.75. Maynes et al. emphasized that all the shown data were non-cavitating/incipient-cavitation points. However, the two included points from Testud et al. are developed cavitation results (one for a single hole and the other for multi-hole orifices with aspect ratios of 0.64 and 4.67, respectively).

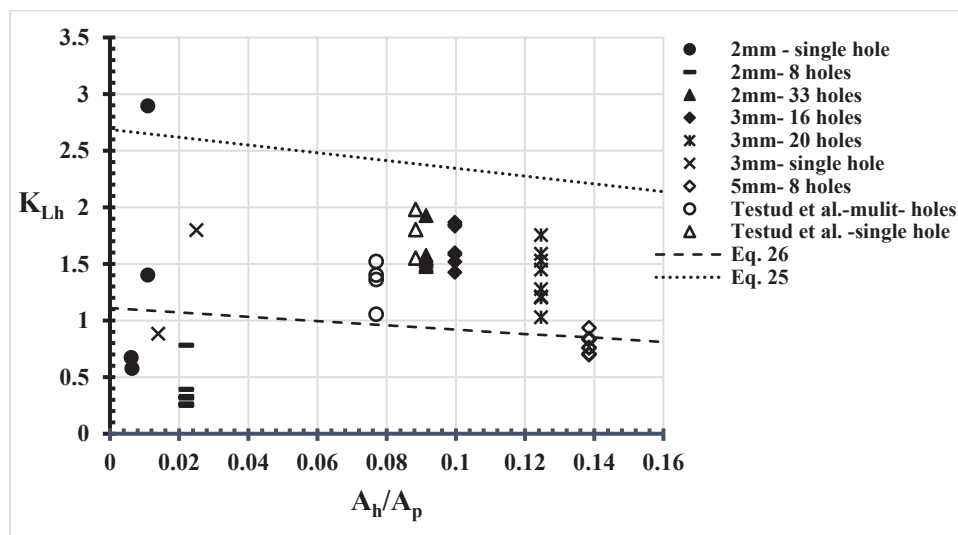


Fig. 11:  $K_{Lh}$  vs  $A_h/A_p$  for all single and multi-hole orifices.

Figure 11 is a reproduction of Maynes et al. [12] presentation where the upper line represents Eq. (25) and the lower line Eq. (26). The plotted points are all the data of Table

1 plus all the developed cavitation results of Testud et al. [10]. Hence, all the points in Fig. 11 are cavitating flow results. The 2 mm and 3 mm single hole points having very small  $A_h/A_p$  values lie mainly below or in-between the bounds representing Eqs. (25) and (26). As for the multi-hole orifices data and that of Testud et al. [10], there seems to be a trend with increasing value of  $A_h/A_p$  starting below the lower bound (2mm-8holes), then in-between the two bounds and finally back to the lower bound (5mm-8holes). It is therefore concluded that results falling in-between these two bounds are not necessarily non-cavitating/incipient cavitation data and could very well be developed cavitation results.

## 7. CONCLUSIONS

Correlations represented by Eqs. (4) to (12) and Eqs. (16) to (18), although specific to their respective orifice geometries, can be used to design and/or predict the performance of pilot-scale HC units for wastewater treatment. This includes a priori determination of  $P_1$  and  $(P_1 - P_2)$  values for the desired  $C_v$  value using a specific orifice geometry. Furthermore, they can be used to design systems to suit available pumps in order to obtain operating points at or very close to the pump's best efficiency points. This will increase the cavitation yield by lowering the value of the expended energy.

The pipe's loss coefficient  $K_{LP}$  and the pipe's Reynolds number  $Re_p$  were the only dimensionless parameters that unified all the HC data of orifices of various geometries and pipe sizes in a single general correlation with  $R^2 = 0.9353$ . This resultant correlation, Eq. (19), implies that for the same specified orifice geometry and desired  $C_v$  value, using a relatively larger pipe inside diameter entails a reduction in the value of the required upstream pressure  $P_1$ . The ratio of  $P_1$  value in the larger pipe to its value in the smaller pipe is a function of the ratio of the smaller pipe diameter ( $D_s$ ) to the larger pipe diameter ( $D_L$ ):  $(P_1 \text{ in } D_L) / (P_1 \text{ in } D_s) = (D_s / D_L)^{2.33}$ . A lower  $P_1$  value will increase the cavitation yield by decreasing the expended energy especially if the number of passes is large. However, a lower  $P_1$  value will also decrease the value of the cavity collapse pressure which may affect the cavitation yield negatively, positively, or not at all depending on  $A_h/A_p$  variation and on constants whose values are system-specific.

The findings of Maynes et al. [12] that non-cavitating/incipient cavitation orifices'  $K_{Lh}$  vs  $A_h/A_p$  data fall in-between two theoretical models, Eqs. (25) and (26), are not exclusive. Orifices' cavitating flow results may also behave likewise, but with a discernible trend.

## REFERENCES

- [1] Braeutigam P, Franke M, Schneider RJ, Lehmann A, Stolle A, Ondruschka B. (2012) Degradation of carbamazepine in environmentally relevant concentrations in water by hydrodynamic-acoustic cavitation (HAC). *Water Res.*, 46:2469-2477.
- [2] Patil PN, Bote SD, Gogate PR. (2014) Degradation of imidacloprid using combined advanced oxidation processes based on hydrodynamic cavitation. *Ultrason. Sonochem.*, 21:1770-1777.
- [3] Pradham AA, Gogate PR. (2010) Removal of p-nitrophenol using hydrodynamic cavitation and Fenton chemistry at pilot scale operation, *Chem. Eng. J.*, 156:77-82.
- [4] Sivakumar M, Pandit AB. (2002) Wastewater treatment: a novel energy efficient hydrodynamic cavitation technique. *Ultrason. Sonochem.*, 9:123-131.
- [5] Saharan VK, Pandit AB, Kumar PSS, Anandan S. (2012) Hydrodynamic Cavitation as an Advanced Oxidation Technique for the Degradation of Acid Red 88 Dye. *Ind. Eng. Chem. Res.*, 51:1981-1989.

- [6] Madhu GM, Thomas A, Deepak S, Preetham HS, Rajanandam KS. (2015) Escalation of degradation of malachite green and methyl violet using hydrodynamic cavitation using different orifice geometry. *Int. J. Env. Sci.*, 5(4):880.
- [7] Mancuso G, Langone M, Laezza M, Andreottola G. (2016) Decolourization of Rhodamine B: A swirling jet-induced cavitation combined with NaOCl. *Ultrason. Sonochem.*, 32:18-30.
- [8] Rajoriya S, Bargole S, Saharan VK. (2017) Degradation of reactive blue 13 using hydrodynamic cavitation: Effect of geometrical parameters and different oxidizing additives. *Ultrason. Sonochem.*, 37:192-202, DOI:<http://doi.org/10.1016/j.ultsonch.2017.01.005>
- [9] Pawar SK, Mahulkar AV, Pandit AB, Roy K, Moholkar VS. (2017) Sonochemical Effect Induced by Hydrodynamic Cavitation: Comparison of Venturi/Orifice Flow Geometries. *AIChE Journal*, 63(10):4705-4716.
- [10] Testud P, Moussou P, Hirschberg A, Auregan Y. (2007) Noise generated by cavitating single-hole and multi-hole orifices in a water pipe. *J. Fluids and Structures*, 23:163-189.
- [11] Vichare N P, Gogate PR, Pandit AB. (2013) Optimization of hydrodynamic cavitation using a model reaction. *Chemical Engineering Technology*, 23:683-690.
- [12] Maynes D, Holt GJ, Blotter J. (2013) Cavitation Inception and Head loss Due to Liquid Flow Through Perforated Plates of Varying Thickness. *J. Fluids Eng.*, 135: 031302-1—031302-11.
- [13] Yan Y, Thorpe RB. (1990) Flow Regime Transitions Due to Cavitation in the Flow Through an Orifice. *Int. J. Multiphase Flow*, 16 (6):1023-1045.
- [14] Gogate PR, Pandit AB. (2000) Engineering Design Methods for Cavitation Reactors II: Hydrodynamic Cavitation. *AIChE J.*, 46 (8):1641-1649.
- [15] Gogate PR, Shirganokar IZ, Sivakumar M, Senthilkumar P, Vichare NP, Pandit AB. (2001) Cavitation Reactors: Efficiency Assessment Using a Model Reaction. *AIChE J.*, 47 (11):2526-2538.
- [16] Gogate PR, Pandit AB. (2005) A review and assessment on hydrodynamic cavitation as a technology for the future. *Ultrason. Sonochem.*, 12:21-27.
- [17] Carpenter J, Badve M, Rajoriya S, George S, Saharan VK, Pandit AB. (2017) Hydrodynamic cavitation: An emerging technology for the intensification of various chemical and physical processes in a chemical process industry. *Reviews in Chemical Engineering*, 33(5):433-468. <https://doi.org/10.1515/revce-2016-0032>.
- [18] Burzio E, Bersani F, Caridi GCA, Vesipa R, Ridolfi L, Manes C. (2020) Water disinfection by orifice-induced hydrodynamic cavitation. *Ultrasonics-Sonochemistry*, 60, 104740: 1-13.
- [19] Rajoriya S, Carpenter J, Saharan VK, Pandit AB. (2016) Hydrodynamic cavitation: an advanced oxidation process for the degradation of bio-refractory pollutants. *Rev. Chem. Eng.*, 32: 379-411.

## APPENDIX A

The mass flow rate and volumetric flow rate (Q) will be the same in both  $D_L$  and  $D_S$  pipes, therefore,

$$P_1 \text{ in } D_L \text{ pipe} = 1.0185 \times 10^5 \rho_L^{-0.6707} \mu_L^{1.6707} (4Q/\pi D_L^2)^{0.3293} D_L^{-1.6707}$$

$$P_1 \text{ in } D_S \text{ pipe} = 1.0185 \times 10^5 \rho_L^{-0.6707} \mu_L^{1.6707} (4Q/\pi D_S^2)^{0.3293} D_S^{-1.6707}$$

$$\begin{aligned} \text{Dividing: } (P_1 \text{ in } D_L \text{ pipe} / P_1 \text{ in } D_S \text{ pipe}) &= (D_L^{-0.6586} D_L^{-1.6707}) / (D_S^{-0.6586} D_S^{-1.6707}) \\ &= D_L^{-2.33} / D_S^{-2.33} = (D_S / D_L)^{2.33} \end{aligned}$$

## BIODELIGNIFICATION OF LEMON PEELS USING *Aspergillus sp.* TO IMPROVE YIELD AND COMPOSITION OF EXTRACTED LEMON OIL

MUHAMMAD YUSUF ABDUH\*, ENJELINA NABABAN, FIRDANTA GINTING,  
JENNY JULIATI AND HUSNA NUGRAHAPRAJA

*School of Life Sciences and Technology, Institut Teknologi Bandung (ITB)  
Jalan Ganesha No. 10 Bandung 40132 Indonesia*

*\*Corresponding author: yusuf@sith.itb.ac.id*

*(Received: 24<sup>th</sup> December 2019; Accepted: 12<sup>th</sup> April 2020; Published on-line: 4<sup>th</sup> July 2020)*

**ABSTRACT:** Lemon oil obtained from lemon peels has a high market value. However, the presence of lignocellulose composed of cellulose, hemicellulose, and lignin, can inhibit the extraction process. This study aimed to determine the effect of biodelignification on lemon peels using *Aspergillus sp.* towards lignin content, yield, chemical composition, and productivity of lemon oil. A solid-state fermentation was carried out under controlled relative humidity of 99% and a light intensity of  $\sim 0$  W/cm<sup>2</sup> for 0, 3, 6, and 9 days. The number of spores used was in the range of  $0.3-5 \times 10^5$  spores/gram substrate with a ratio of spore solution and substrate of 1:1. Extraction was performed using a steam distillation method at 97-98°C for 6 hours. The results showed that the lignin content decreased with an increased fermentation time: 8.01%, 6.97-7.28%, 5.83-7.28%, and 4.35-5.44% dry weight for day 0, 3, 6, and 9, respectively. Lemon oil yield increased as the period of fermentation increased up to 0.27%, 0.29-0.31%, 0.30-0.46%, and 0.67-0.79% for day-0, 3, 6, and 9, respectively. A major component of lemon oil is d-limonene. The d-limonene content reached 72,54% for day-0, 73-99% for day-3, 75,09-84.59% for day-6, and 88,03-99% for day-9.

**ABSTRAK:** Minyak lemon yang terhasil dari kupasan lemon mempunyai nilai tinggi dalam pasaran. Walau bagaimanapun, kehadiran lignoselulosa yang terdiri daripada selulosa, hemiselulosa dan lignin, boleh merencatkan proses pengekstrakan. Kajian ini bertujuan memperolehi kesan biodelignifikasi pada kulit lemon menggunakan *Aspergillus sp.* terhadap kandungan lignin, hasil, komposisi kimia, dan penghasilan minyak lemon. Penapaian keadaan-pepejal dijalankan di bawah 99% kawalan kelembapan relatif dan keamatan cahaya  $\sim 0$  W/cm<sup>2</sup> bagi 0, 3, 6 dan 9 hari. Bilangan spora yang digunakan adalah dalam lingkungan substrat  $0.3-5 \times 10^5$  spora/gram dengan nisbah larutan spora kepada substrat adalah 1:1. Pengekstrakan dijalankan menggunakan kaedah penyulingan stim pada suhu 97-98°C selama 6 jam. Keputusan menunjukkan kandungan lignin berkurangan dengan pertambahan masa penapaian: 8.01%, 6.97-7.28%, 5.83-7.28%, dan 4.35-5.44% berat kering pada hari 0, 3, 6, dan 9, masing-masing. Hasil minyak lemon bertambah dengan pertambahan masa penapaian sehingga 0.27%, 0.29-0.31%, 0.30-0.46%, dan 0.67-0.79% pada hari 0, 3, 6, dan 9, masing-masing. Komponen major minyak lemon adalah d-limonina. Kandungan d-limonina mencapai 72,54% pada hari-0, 73-99% pada hari-3, 75,09-84.59% pada hari-6, dan 88,03-99% pada hari-9.

**KEYWORDS:** *Aspergillus sp.*; biodelignification; lemon oil; lemon peels; lignin content

## 1. INTRODUCTION

Essential oils are volatile aromatic compounds that can be obtained from natural sources, usually plants [1]. Essential oils contain the characteristic fragrance of the plant from which it is derived. The market of essential oils was valued at USD 3.4 billion in 2016 and it was projected to expand at a Compound Annual Growth Rate (CAGR) of 9.7% from 2016 to 2024 [2]. This growth was driven by increasing market demand of fragrance and flavouring.

Essential oils have high economic potential in Indonesia, one of the major sources of raw materials for essential oils including lemon [3]. Lemon (*Citrus limon* (L.) Osbeck) is an evergreen tree that belongs to the family Rutaceae with an annual production of 123 million metric ton [4]. Most lemon processing industries used lemon flesh and juice as sellable products, but other parts were thrown away as wastes. The wastes consist of peel, seed, and leftover of lemon juice [5]. The lemon peels can be further valorised as a raw material for producing essential oil, particularly lemon oil.

Lemon oil is one of the essential oils that have high demand worldwide. In 2007, lemon oil world production reached up to 9,200 metric tons [6] and the market is anticipated to expand at a 5.5% CAGR for the period of 2018-2027 [7]. Lemon oil is typically produced via steam distillation of the lemon peels and primarily composed of d-limonene which lies in the range of 72.4-94.5% [8,9]. Limonene is a relatively stable monoterpene that can find applications as a stress reliever, antibacterial, antifungal, antioxidant, and neuroprotection [10].

One of the key issues in the production of lemon is its relatively lower yield which lies in the range of 0.65-1.3% on a dry weight basis [9] due to the presence of the rigid structure of the cell wall that consists of lignin, cellulose, and hemicellulose. According to Janati et al. [11], lemon peel contains approximately 15.2% lignin which will hinder the isolation of lemon oil during the distillation process. The presence of lignin in lemon peel may be degraded by the use biological agents such as fungus to increase the lemon oil yield.

*Aspergillus sp.* can degrade complex carbohydrates into monosaccharides and disaccharides. *Aspergillus sp.* is one of the most effective fungi in terms of utilizing simple saccharides as an organic carbon source to help its growth [12]. Therefore, *Aspergillus sp.* is expected to degrade lignin and carbohydrates in order to facilitate the isolation of lemon. *Aspergillus sp.* is reported to contain lignin degradation enzymes such as laccase, lignin peroxidase, and manganese peroxidase [13-15].

A previous study on the solid-state fermentation of *Aspergillus niger* with coir waste had been carried out by Mrudula and Murugammal [16] for optimum production of cellulase. The fermentation was carried out at pH 6, 30°C, and moisture ratio of 1:2 (weight: volume) for 72 hours to optimize the biosynthesis of cellulase with an enzyme activity of 8.89 U per g of dry mycelial bran. Botella et al. [17] also has investigated the effect of particle size, initial moisture, and supplementation with carbon sources for the solid-state fermentation of grape pumice with *Aspergillus awamori* to produce high-value hydrolytic enzymes. It has been reported that xylanase activity reached a maximum value of  $40.4 \pm 15.6$  IU/gds after 24 hours of fermentation whereas cellulase reached a maximum value of  $9.6 \pm 0.76$  IU/gds within the first 24 hours of the fermentation period.

In another study, *Aspergillus oryzae*, was used in a solid-state fermentation of wheat bran and other substrates for producing glucoamylase. Optimum production of glucoamylase 1986  $\mu$ moles of glucose produced per minute per gram of dry fermented

substrate) was obtained when the fermentation was carried out at pH 6, 30°C with 1% starch and 0.25% urea on a weight basis and 100% (volume: weight) initial moisture for 120 hours. Other studies also reported that optimum conditions for the growth of *Aspergillus sp.* are at a light intensity of  $\sim 0$  W/cm<sup>2</sup> and controlled humidity of 99% [18,19].

Although previous studies on the solid-state fermentation of *Aspergillus sp.* have been reported, systematic studies that report on the biodelignification of lemon peels using different species of *Aspergillus sp.* are still very scarce. Hence, this study aims to investigate effect of solid-state fermentation of lemon peels with three different species of *Aspergillus sp.* namely *Aspergillus oryzae*, *Aspergillus niger*, and *Aspergillus awamori* on the yield and chemical composition of lemon oil.

## 2. MATERIALS AND METHODS

### 2.1 Preparation of Lemon Peels

Approximately 13.1 kg fresh lemons were squeezed to remove the lemon juice. Lemon peels were then separated from the pulps. Lemon peels were cut into square-shapes with a size of 0.5 cm x 0.5 cm. Finally, lemon peels were sterilized using an autoclave for 15 minutes at 121°C and 1.5 atm [17].

### 2.2 Preparation of Inoculum for *Aspergillus sp.*

*Aspergillus sp.* cultures in 39 g/L potato dextrose agar were mixed with 5 mL of NaCl (0.85%). Subsequently, an inoculating loop was used to retrieve spores on the medium surface. NaCl solution mixed with the spores was moved to beaker glasses and the number of spores was counted using a haemocytometer. The spores solution was finally diluted using distilled water to reach a concentration of  $0.3-5 \times 10^5$  spores/g substrate [17]. This preparation was carried out under aseptic conditions.

### 2.3 Fermentation of Lemon Peels with *Aspergillus sp.*

Sterilized lemon peels were moved into punctured trays. After that, the spore solution was added with a ratio of 0.1 mL for one g of substrate into trays and mixed [20]. Trays were then covered using black coloured plastics. Rami yarns were used to attach plastics to the trays. Subsequently, these substrate-containing trays were moved onto container trays to reduce water loss (Figure 1). Fungus inoculation on lemon peels were carried out using 2 trays for each fungi species with each tray containing approximately 2.2 kg of lemon peels. The inoculation was carried out under aseptic conditions. The fermentation was conducted for 0, 3, 6, and 9 days and the relative humidity was set constant (99%) [20,21]. Excess water collected in the container trays was returned to the substrate tray once a day throughout the fermentation process.

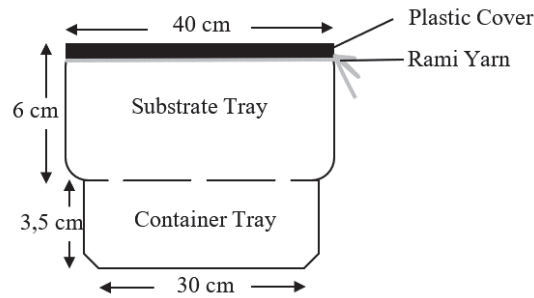


Fig. 1: Fermentation of lemon peels with *Aspergillus sp.* using two level trays (light intensity:  $\sim 0 \text{ W/cm}^2$ , relative humidity: 99%)

## 2.4 Measurement of Lignin Content in Lemon Peels

Lignin content in the lemon peels was determined using a Klason method [22]. Lemon peels were cut and dried in an oven until a moisture content of 4%. Dried lemon peels were then mashed up using a blender. After that, dried lemon peel powders were sieved using mesh 35 (a size of 0.5 mm). Subsequently, 1 g of sieved powders was added with 15 mL of  $\text{H}_2\text{SO}_4$  (72%) in a beaker glass at room temperature ( $25^\circ\text{C}$ ) while being stirred for 2-3 minutes. Afterwards, the beaker glass was covered using a watch crystal for 2 hours and stirred occasionally. The sample was then removed from the beaker glass and mixed with distilled water and  $\text{H}_2\text{SO}_4$  to achieve an  $\text{H}_2\text{SO}_4$  concentration of 3%. After that, the mixture was heated for 4 hours and the volume was kept constant followed by settling at room temperature and filtered with a Büchner funnel. The lignin content in the sample was calculated using equation (1).

$$\text{Lignin content (\%)} = \frac{m_{\text{studge}}(\text{g})}{m_{\text{initial sample}}(\text{g})} \times 100\% \quad (1)$$

where m is mass in gram (g).

## 2.5 Measurement of Moisture Content in Lemon Peels

The moisture content of the lemon peels was measured using an oven-drying method. Lemon peels were weighed before the oven-drying process. The drying was carried out at a temperature of  $105^\circ\text{C}$  until the weight remained constant [23]. The moisture content in the sample can be calculated using equation (2).

$$\text{Moisture content (\%)} = \frac{m_{\text{initial}}(\text{g}) - m_{\text{final}}(\text{g})}{m_{\text{initial}}(\text{g})} \times 100\% \quad (2)$$

where m is mass in gram (g).

## 2.6 Extraction of Lemon Oil using a Steam-Distillation Method

Fermented lemon peels were dried using an oven at  $50^\circ\text{C}$  until the moisture content lies in the range of 70-80%. Approximately 200 g of dried fermented lemon peels were mixed with distilled water (2:5 on a weight to volume basis). The distillation was carried out at  $96\text{-}98^\circ\text{C}$  for 6 hours [9]. The mixture of lemon oil and hydrosol were separated using a separatory funnel. Subsequently, the separated lemon oil phase was weighed, and its volume was measured. Lemon oil yield was calculated on dry weight basis using equation (3). The productivity of lemon oil can be calculated using equation (4).

$$\text{Essential oil yield (\% dry weight)} = \frac{m_{\text{lemon oil}}(\text{g})}{m_{\text{dried lemon peel}}(\text{g}) \times (1 - \text{moisture content})} \times 100\% \quad (3)$$

where m is mass in gram (g).

$$\text{Lemon oil productivity (g/day)} = \frac{m_{\text{lemon oil (g)}}}{\text{distillation time (day)} + \text{fermentation time (day)}} \times 100\% \quad (4)$$

where m is mass in gram (g) with distillation time and fermentation period in day.

## 2.7 Characterization of Lemon Oil

The density of lemon oil was calculated by measuring the weight and volume of the lemon oil. The lemon oil mass was weighed using an analytical balance whereas the volume was measured using a 5 mL graduated cylinder. The density was calculated using equation (4).

$$\text{Density (g/mL)} = \frac{m_{\text{lemon oil (g)}}}{V_{\text{lemon oil (mL)}}} \quad (5)$$

where m is mass in gram (g) and V is volume in millilitre (mL)

## 2.8 Determination of composition using a Gas Chromatography-Mass Spectrometry Method

The composition of lemon oil was analysed using a Gas Chromatography-Mass Spectrometry (GC-MS) method at the Forensic Laboratory Centre of Bareskrim Polri, Jakarta. A Shimadzu GCMS-QP2010 Ultra instrument was used for the analysis with the oven temperature of was set an initial temperature of 80°C and final temperature of 100°C in 25 minutes. The front inlet used a split model condition of 290°C, 19.23 psi, and total flow 202.2 mL/minute. The capillary column has nominal length 60 m and set at constant flow mode with a maximum temperature of 350°C, initial pressure of 19.24 psi and initial flow of 1 mL/minute. The thermal aux was operated at an initial temperature of 290°C. The MS equipment was set under a quad MS of 150°C (maximum 200°C) and a source MS of 250°C (maximum 300°C).

# 3. RESULTS AND DISCUSSION

## 3.1 Effect of Moisture Content on Lemon Oil Yield

After oven-drying at 50°C for 3-24 hours, the moisture content of the lemon peels lies in the range of 45-81%. Figure 2 shows that the lemon yield is highly influenced by the moisture content with an optimum moisture content of 77% producing a lemon oil yield of 0.71% dry weight (% dw). Drying of essential oil-bearing plants prior to distillation is important to increase the yield of isolated essential oil [24]. Low temperature and short drying time have been reported to increase essential oil yield whereas high temperature (>50°C) and long drying period (>24 hours) will decrease essential oil yield due to diffusion of the oil to the surrounding [25]. In this study, lemon peels were oven-dried at 50°C prior to the distillation to increase the lemon oil yield because the presence of water in the cells impedes the extraction of essential oil [27]. Hence, reducing the presence of water by oven-drying at 50°C increased the lemon oil yield. However, prolonged drying may result in a moisture content that too low that will disrupt the oil gland and essential oil losses along with water vapour [28,29].

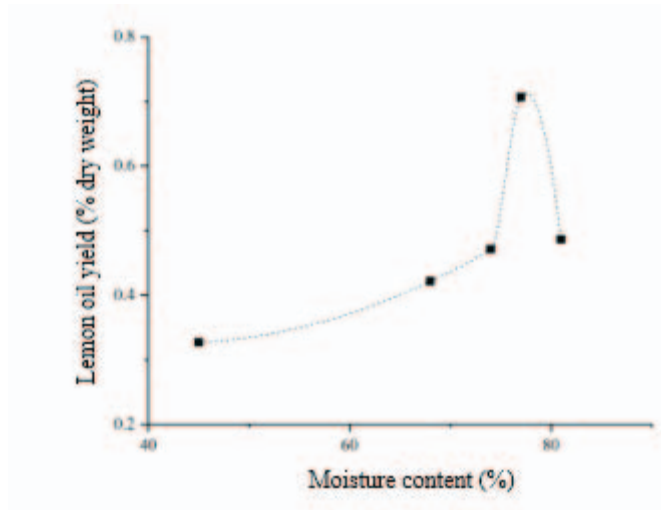


Fig. 2: Effect of moisture content on lemon oil yield

### 3.2 Effect of Fermentation Time on Lignin Content and Lemon Oil Yield

The fermentation of lemon peels using *Aspergillus niger*, *Aspergillus awamori*, and *Aspergillus oryzae* was carried out for 3, 6, and 9 days as suggested by Ferreira et al. [30] that the activity of lignin degradation enzyme (ligninase) of *Aspergillus sp.* increased along with fermentation time and reached an optimum value on the 7<sup>th</sup> day of incubation. Figure 3 shows that the lignin content in lemon peel decreased with the incubation period whereas Fig. 4 highlights that the lemon oil yield increased with the incubation period.

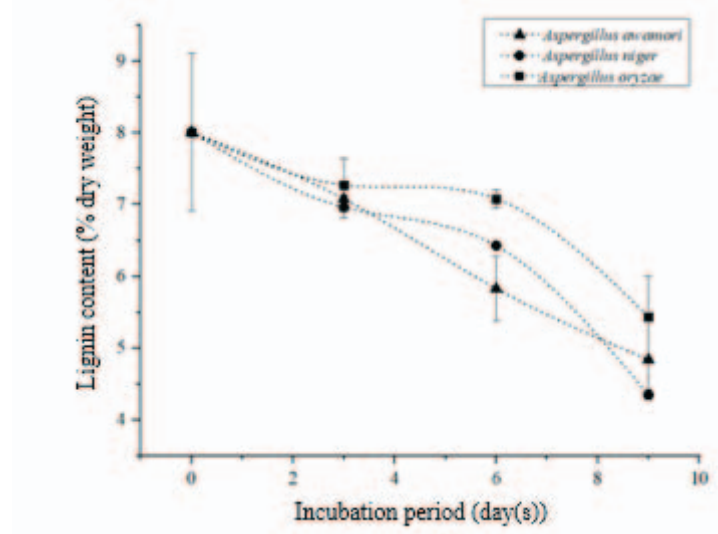


Fig. 3: Effect of fermentation with different species of *Aspergillus sp.* on lignin content in lemon peels.

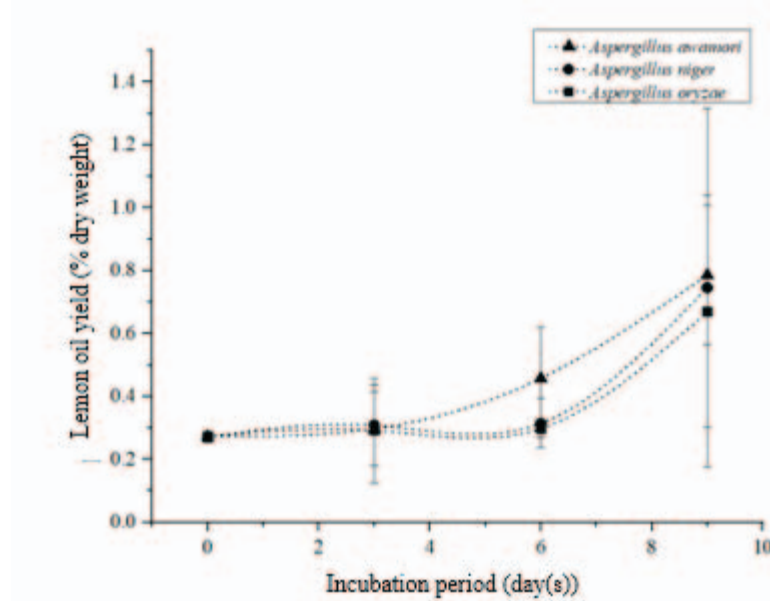


Fig. 4: Effect of fermentation with different species of *Aspergillus sp.* on lemon oil yield.

Initially, the lemon peels contained approximately  $8\% \pm 1.1\%$  dw lignin. This value resembles a lignin content of 7.6% dw reported in the literature [31]. After 9 days of fermentation with *Aspergillus sp.*, the lignin content in the lemon peels decreased to 4.4 – 5.4% dw. This may be due to the presence of various lignin degradation enzymes such as lignin peroxidase, manganese peroxidase, and laccase secreted by the *Aspergillus sp.* that were able to attack the lignin structure and caused an oxygen molecule reduction process to become water [32].

As a result of the biodegradation process, the lemon oil yield increased from  $0.3\% \pm 0.02\%$  dw up to 0.67 – 0.79% dw. The increased in lemon oil yield may also be caused by the presence of other enzymes such as cellulase and pectinase that can facilitate the secretion of essential oil from lemon peels [17,33]. González et al. [33] had previously demonstrated that pre-treatment of lemon peels with cellulase increased the lemon oil yield up to 100% from 0.009 to 0.017% on a weight basis after the 3 hours of pre-treatment at 30°C [33]. Although the lemon yield reported by González et al. [33] was lower as compared to the lemon oil yield reported in other studies, a significant amount of fermentable sugars such as glucose were also produced for further valorisation.

### 3.4 Characterization of Lemon Oil

The lemon oil has a pale-yellow colour that resembles the results reported by Boughendjioua and Djeddi [34] and in line with the specification for lemon oil. The lemon oil has a density of  $0.856 \pm 0.001$  g/mL which lies in the range of 0.845-0.870 g/mL as reported in the literature [34]. The composition of lemon oil was also analysed by gas chromatography-mass spectrometry (GC-MS) and the results are shown in Table 1. From Table 1, it can be seen that the composition of lemon oil produced from the solid-state fermentation of lemon peels with different species of *Aspergillus* vary from one another. The major composition of lemon oil in the non-fermented sample (control) is d-limonene (72.5%) which resembles the composition reported in the literature. Solid-state fermentation of lemon peels with *Aspergillus awamori*; *Aspergillus niger*, *Aspergillus oryzae* increased the content of d-limonene to 73.1-99%. According to a previous study by Wilkins et al. [35], fermentation of lemon peels increased the percentage of limonene

secretion up to 38-60% due to its inhibitory effect. The secreted limonene would allow more lemon oil to be isolated during the distillation process. In another study by Lota et al. [36], *Citrus sp.* cultivated under different soil conditions and different areas proved to contain different d-limonene compositions which lie in the range of 38.1 to 95.8%.

The composition of d-limonene in the lemon oil increased from 73.1% (day-3) to 99% (day-9) when the lemon peels were incubated with *Aspergillus awamori*. In contrast, the composition of d-limonene reached its maximum value on day-3 of fermentation when the lemon peels were incubated with *Aspergillus niger* and *Aspergillus oryzae* before slightly decreasing on day-6 and slightly increasing again on day-9. The data shows that the biosynthesis of d-limonene is highly affected by the presence of *Aspergillus sp.* Nevertheless, reported studies that can explain the mechanism that results on different d-limonene compositions when lemon peels were incubated using different *Aspergillus sp.* are still very scarce. Hence, further studies are required to explain the possible mechanism of the biosynthesis of d-limonene.

### 3.5 Productivity of Lemon Oil in a Laboratory Scale

The productivity of lemon oil produced through solid-state fermentation of lemon peel followed by a steam distillation is estimated using equation (4) and the results are shown in Table 2. The estimated productivity of lemon in a laboratory scale for the non-fermented sample (control) is of 0.5 g/day which resembles a lemon oil productivity of 0.48 g/day reported by Ferhat et al. [37]. From table 1, it can be observed that the productivity of lemon oil decreased with fermentation since a longer time was required to isolate the lemon oil. The highest productivity of lemon oil for the fermented samples is 0.044 g/day, which is around 91% lower when the lemon peel was incubated with *Aspergillus niger* for 3 days with a d-limonene content of 93.7%. The productivity of lemon oil decreased as a result of long fermentation time that was incomparable to the increase of lemon oil as suggested by Díaz [38]. Although the productivity of lemon oil decreased for the fermented samples, but the composition of d-limonene in the oil increased up to 37.7% as a result of biodegradation of lignocellulosic component by the *Aspergillus sp.* [39]. After the 9<sup>th</sup> day of fermentation with *Aspergillus awamori*, the productivity of lemon oil is 0.039 g/day with a d-limonene content of approximately 99%. Hence, a compromise is required between productivity and quality of the desired lemon oil.

Table 1: Composition of lemon oil for non-fermented and fermented lemon peel with *Aspergillus sp.*

No.	Compounds	Composition (%)									Ref. [8]	
		Day-0	Day-3			Day-6			Day-9			
			<i>Aa</i> <sup>1</sup>	<i>An</i> <sup>2</sup>	<i>Ao</i> <sup>3</sup>	<i>Aa</i> <sup>1</sup>	<i>An</i> <sup>2</sup>	<i>Ao</i> <sup>3</sup>	<i>Aa</i> <sup>1</sup>	<i>An</i> <sup>2</sup>		<i>Ao</i> <sup>3</sup>
1	$\alpha$ -Thujene	-	-	-	-	-	-	-	-	0.12	-	0.27
2	$\alpha$ -Pinene	-	-	-	-	-	0.23	-	-	-	0.54	0.98
3	$\beta$ -Pinene	-	-	2.32	-	0.30	-	-	-	0.58	-	6.60
4	Mycrene	1.33	-	1.04	-	1.65	1.16	1.33	-	3.15	2.69	1.73
5	Limonene	72.54	73.10	93.66	99.00	81.97	75.09	84.56	99.00	88.03	89.43	72.48
6	(Z)- $\beta$ -Ocimene	1.59	6.30	-	-	-	4.42	1.46	-	-	-	0.07
7	Linalool	-	-	-	-	-	-	-	-	-	-	0.13

8	Nonanal	0.84	-	-	-	-	-	-	-	-	-	<0.05
9	Citronellal	0.86	-	-	-	-	-	-	-	-	-	0.07
10	Decanal	-	-	-	-	0.50	-	-	-	-	-	0.05
11	Nerol	6,13	-	-	-	0.28	-	-	-	-	-	0.07
12	Undecanal	0.29	-	-	-	0.27	-	-	-	-	-	<0.05
13	Neryl acetate	-	-	-	-	-	0.56	-	-	0.15	-	1.21
14	Geranyl acetate	-	-	-	-	2.41	-	-	-	-	-	0.59
15	trans- $\alpha$ -Bergamotene	1.42	-	1.66	-	2.74	4.89	2.09	-	2.39	2.30	0.41
16	(E)- $\beta$ -Farnesene	-	-	-	-	0.55	0.38	-	-	0.35	0.16	<0.05
17	$\beta$ -Bisabolene	2.12	-	1.32	-	4.78	7.29	2.96	-	3.07	2.82	1.22
18	Spathulenol	-	-	-	-	-	-	-	-	-	-	0.05
19	Caryophyllene oxide	-	-	-	-	-	-	0.22	-	-	0.22	<0.05
20	1,6-Octadien-3-ol, 3,7-dimethyl-, formate	2.18	-	-	-	-	-	-	-	-	-	-
21	1-nonanol	0.50	-	-	-	-	-	-	-	-	-	-
22	$\beta$ -Fencyl-alkohol	2.52	-	-	-	-	0.71	-	-	-	-	-
23	2,6-Octadienal, 3,7-dimethyl-, (Z)	7.28	-	-	-	2.26	1.09	-	-	-	-	-
24	Siklooktana	0.39	9.49	-	-	-	-	-	-	-	-	-
25	2-(5-methyl-5-vinyltetrahydro-2-furanyl)-2-propanol	-	11.11	-	-	-	-	-	-	-	-	-
26	1,6-Octadien-3-ol, 3,7-dimethyl-, propanoate	-	-	-	-	-	-	-	-	-	-	-
27	Dodecanal	-	-	-	-	0.44	0.49	0.28	-	-	0.28	-
28	$\alpha$ -Bisabolene	-	-	-	-	0.45	0.77	0.26	-	0.11	0.26	-
29	$\alpha$ -Bisabolol	-	-	-	-	0.68	0.97	0.44	-	0.38	0.44	-
30	1,5,9-Decatriene, 2,3,5,8-tetramethyl	-	-	-	-	0.43	-	-	-	0.33	-	-
31	2,6,10-Dodecatrien-1-ol, 3,7,11-trimethyl	-	-	-	-	0.28	-	-	-	-	-	-
32	Decanol	-	-	-	-	-	1.27	-	-	-	-	-
33	1,6-Octadien-3-ol, 3,7-dimethyl-, acetate	-	-	-	-	-	0.69	-	-	0.14	-	-
34	Santolina epoxide	-	-	-	-	-	0.52	-	-	-	-	-
35	4-(2,2-Dimethyl-6-methylene-cyclohexyl) butanal	-	-	-	-	-	0.68	-	-	-	-	-
36	2,3-Dehydro-1,8-cineole	-	-	-	-	-	-	-	-	0.14	-	-
37	1,3-Cyclohexadiene, 1-methyl-4-(1-methylethyl)	-	-	-	-	-	-	-	-	0.12	-	-
38	Bicyclo[2.2.1]heptane, 2-methyl-3-methylene-2-(4-methyl-3-pentenyl)	-	-	-	-	-	-	-	-	0.35	-	-
39	Patchouli alcohol	-	-	-	-	-	-	2.95	-	0.12	-	-

40	Cyclohexanebutanal, 2,2-dimethyl-6-methylene-	-	-	-	-	-	-	-	-	0.27	2.95	-
41	1-vinyl-1-(4-methyl)pentan-3-enyl-cyclopropane	-	-	-	-	-	-	-	-	0.13	-	-
42	1,2,4-Methenoazulene, decahydro-1, 5,5,8a-tetramethyl-	-	-	-	-	-	-	-	-	0.09	-	-
43	Nonadienol	-	-	-	-	-	-	0.42	-	-	-	-

Note: <sup>1</sup>*Aspergillus awamori*; <sup>2</sup>*Aspergillus niger*; <sup>3</sup>*Aspergillus oryzae*

Table 2: Estimated productivity of lemon oil for non-fermented and fermented lemon peel with *Aspergillus sp.*

Parameter	Day-0	Day-3			Day-6			Day-9		
		<i>Aa</i> <sup>1</sup>	<i>An</i> <sup>2</sup>	<i>Ao</i> <sup>3</sup>	<i>Aa</i> <sup>1</sup>	<i>An</i> <sup>2</sup>	<i>Ao</i> <sup>3</sup>	<i>Aa</i> <sup>1</sup>	<i>An</i> <sup>2</sup>	<i>Ao</i> <sup>3</sup>
Oil mass (g)	0,125	0,137	0,142	0,134	0,211	0,145	0,137	0,362	0,343	0,308
Oil yield (% dry weight)	0,27	0,30	0,31	0,29	0,46	0,32	0,30	0,79	0,75	0,67
Oil productivity (g /day)	0,5	0,042	0,044	0,041	0,034	0,023	0,022	0,039	0,037	0,033

Note: <sup>1</sup>*Aspergillus awamori*; <sup>2</sup>*Aspergillus niger*; <sup>3</sup>*Aspergillus oryzae*

#### 4. CONCLUSION

A solid-state fermentation of lemon peels using *Aspergillus sp.* has been carried out to investigate the effect of biodelignification towards yield and chemical composition of lemon oil isolated from the lemon peels. The results show that the lignin content in lemon peel decreased from 8% to 4.4–5.4% whereas the yield increased from 0.27% to 0.67-0.79% as the fermentation time increased. The results obtained in this study highlights that the fermentation of lemon peels with *Aspergillus oryzae*, *Aspergillus niger*, and *Aspergillus awamori* increased the yield of lemon oil isolated from lemon peels. The major content of lemon oil, particularly d-limonene, also increased from approximately 73% up to 99%, depending on the species of *Aspergillus* used in the fermentation. The largest reduction of lignin content (49%) and increment of yield (193%) were obtained when the lemon peels were subjected to fermentation with *Aspergillus awamori* for 9 days which results to an increase of d-limonene up to 99%.

#### REFERENCES

- [1] Pratiwi A, Utami L. (2018) Isolasi dan Analisis Kandungan Minyak Atsiri pada Kembang Leson. *Bioeksperimen* 4 (1): 42-47. <https://doi.org/10.23917/bioeksperimen.v4i1.5930>
- [2] Grand View Research. (2018) Essential Oils Market Size, Share & Trends Analysis Report by Product (Orange, Corn, Mint, Eucalyptus, Citronella, Pepper Mint, Lemon, Clove Leaf, Lime, Spearmint), by Application, and Segment Forecasts, 2018-2025. <https://www.grandviewresearch.com>
- [3] Rosiantiningsih D. (2017) Minyak Atsiri, Emas Terpendam Indonesia. <http://marketplus.co.id/2017/03/minyak-atsiri-emas-terpendam-indonesia/>.
- [4] González-Molina E, Domínguez-Perles R, Moreno DA, García-Viguera C. (2010) Natural Bioactive Compounds of Citrus limon for Food and Health. *J. Pharmaceutical and Biomedical Analysis*, 51 (2): 327-345. <https://doi.org/10.1016/j.jpba.2009.09.049>
- [5] Nurlaila A. (2001) Upaya Pemanfaatan Limbah Jus Jeruk Lemon (*Citrus limon* (Linn) Burm. F.) sebagai Bahan Baku Pengolahan Jeruk Lemon. Bogor, Institut Pertanian Bogor. <http://repository.ipb.ac.id/handle/123456789/13152>
- [6] Sonneman T. (2012) *Lemon A Global History*. London, Reaktion Books Ltd.

- Transparency Market Research. (2019) Lemon Essential Oil Market to Expand at 5.5% CAGR During 2018-2027. <https://www.prnewswire.com>
- [7] Gök A, Kirbaşlar IFGK. (2014) Comparison of Lemon Oil Composition After Using Different Extraction Method. *Journal of Essential Oil Research*, 27(1): 17-22. <https://doi.org/10.1080/10412905.2014.982872>
- [9] Sikdar D, Nikila R. (2017) Extraction of Citrus Oil from Lemon (*Citrus limon*) Peels by Steam Distillation and Its Characterizations. *International Journal of Technical Research and Applications*, 5(2): 29-33. <https://pdfs.semanticscholar.org>
- [10] Dosoky NS, Setzer WN. (2018) Biological Activities and Safety of *Citrus spp.* Essential Oils. *International Journal of Molecular Sciences*, 19 (7): 1966-1991. <https://doi: 10.3390/ijms19071966>.
- [11] Janati SSSF, Beheshti H, Feizy J, Fahim N. (2012) Chemical Composition of Lemon (*Citrus limon*) and Peels Its Consideration as Animals Food. *GIDA-Journal of Food*, 37(5): 267-271. <https://dergipark.org.tr>
- [12] Chen H. (2014) *Biotechnology of Lignocellulose: Theory and Practice*. Dordrecht, Springer.
- [13] Ahammed S, Prema P. (2002) Influence of media nutrients on synthesis of lignin peroxidase from *Aspergillus sp.* *Applied Biochemistry and Biotechnology*, 327-336. <https://doi.org/10.1385/ABAB:102-103:1-6:327>
- [14] dos Santos TC, dos Santos RN, Silva TP, Machado FD, Bonomo RC, Franco M. (2016) Prickly palm cactus husk as a raw material for production of ligninolytic enzymes by *Aspergillus niger*. *Food science and biotechnology*, 25(1): 205-211. <https://doi.org/10.1007/s10068-016-0031-9>
- [15] Shah MP, Reddy GV, Banerjee R, Babu PR., Kothari IL. (2005) Microbial degradation of banana waste under solid state bioprocessing using two lignocellulolytic fungi (*Phylosticta spp.* MPS-001 and *Aspergillus spp.* MPS-002). *Process Biochemistry*, 40(1): 445-451. <https://doi.org/10.1016/j.procbio.2004.01.020>
- [16] Mrudula S, Murugammal R. (2011) Production of cellulase by *Aspergillus niger* under submerged and solid state fermentation using coir waste as a substrate. *Brazilian Journal of Microbiology*, 7:1119-1127. <https://doi.org/10.1590/S1517-83822011000300033>
- [17] Botella C, Diaz A, de Ory I, Webb C, Blandino A. (2007) Xylanase and Pectinase Production by *Aspergillus awamori* on Grape Pomace in Solid State Fermentation. *Process Biochemistry* 42 (1): 98-101. <https://doi.org/10.1016/j.procbio.2006.06.025>
- [18] Steviani S. (2011) Pengaruh penambahan molase dalam berbagai media pada jamur tiram putih (*Pleurotus ostreatus*). Surakarta, Universitas Sebelas Maret. <https://digilib.uns.ac.id>
- [19] Silva R. (2016) *Mycology: Current and Future Developments: Fungal Biotechnology for Biofuel Production Volume 1*. Sharjah, Benthan Science Publishers.
- [20] Zambare V. (2010) Solid state fermentation of *Aspergillus oryzae* for glucoamylase production on agro residues. *International Journal of Life Sciences*, 16-25. <https://doi.org/10.3126/ijls.v4i0.2892>
- [21] Abduh MY, Zuliansyah W, Aprina L, Arazella N. (2019) Effect of pectin biodegradation with *Aspergillus niger* on total flavonoid content of *Citrus limon* L. *J Biodjati*, 4(2):194-203. <https://doi.org/10.15575/biodjati.v4i2.4537>
- [22] Gwalingo E, Rahman NSA, Al-Marzouqi AH, Omar MMA, Khaleel AA. (2018) Klason method: an effective method for isolation of lignin fractions from date palm biomass waste. *Chemical and Process Engineering Research*, 57:46-58. <https://www.iiste.org/Journals/index.php/CPER/article/view/41830>
- [23] Carneiro JD, Nogueira RM, Martins MA, Valladão DM, Pires EM. (2018) The Oven-Drying method for Determination of Water Content in Brazil Nut. *Bioscience Journal* 34 (3), 595-602. <https://doi.org/10.14393/BJ-v34n3a2018-37726>
- [24] Kandi M, Sefidkon F. (2011) The influence of drying methods on essential oil content and composition of *Laurus nobilis* L. *Journal of Essential Oil Bearing Plants*, 14 (3), 302-308. <https://doi.org/10.1080/0972060X.2011.10643938>

- [25] Rahimmalek M, Goli SA. (2013) Evaluation of Six Drying Treatments with Respect to Essential Oil Yield, Composition and Color Characteristics of *Thymys daenensis* subsp. daenensis. Celak Leaves. Industrial Crops and Products, 42(1): 613-619. <https://doi.org/10.1016/j.indcrop.2012.06.012>
- [26] Ambrose DC, Annamalai S, Naik R. (2013) Effect of Drying on Volatile Oil Yield of Patchoulli. Indian Journal of Science and Technology, 6(12): 5559-5562. <http://52.172.159.94/index.php/indjst/article/view/43613>
- [27] Hobir Y, Nuryani E, Anggraeni. (2003) Peningkatan Produktivitas dan Mutu Minyak Nilam Melalui Perbaikan Varietas dan Teknik Pengolahan. Balitro, Bogor.
- [28] Hamrouni-Sellami I, Wannas WA, Bettaieb I, Berrima S, Chahed T, Marzouk B, Limam F. (2011) Drying Sage (*Salvia officinalis* L.) Plants and Its Effects on Content, Chemical Composition, and Radical Scavenging Activity of the Essential Oil. Food and Bioprocess Technology, 5(8): 2978-2989. <https://pubag.nal.usda.gov/catalog/448611>
- [29] Hasmita I, Adisalamun A, Alam PN, Satriana S, Mahlinda M, Supardan, M. D. (2015) Effect of Drying and Hydrodistillation Time on the Amount of Ginger Essential Oil. International Journal on Advanced Science, Engineering, and Information Technology, 5(5): 300-303. <http://dx.doi.org/10.18517/ijaseit.5.5.567>
- [30] Ferreira FL, Dall'Antonia CB, Shiga EA, Alvim LJ, Pessoni RA. (2018) Sugarcane Bagasse as a Source of Carbon for Enzyme Production by Filamentous Fungi. Hoehnea, 45(1): 134-142. <https://doi.org/10.1590/2236-8906-44/2017>
- [31] Mamma D, Christakopoulos P. (2013) Biotransformation of *Citrus* By-Products into Value Added Products. Waste Biomass Valorization, 5(4): 529-549. <https://doi.org/10.1007/s12649-013-9250-y>
- [32] Brijwani K, Rigdon A, Vadlani PV. (2010) Fungal Laccases: Production, Function, and Applications in Food Processing. Enzyme Research, 1: 1-10. <https://doi.org/10.4061/2010/149748>
- [33] Chávez-González ML, López LI, Rodríguez-Herrera R, Contreras-Esquivel JC, Aguilar CN. (2015) Enzyme-Assisted Extraction of *Citrus* Essential Oil. Chemical Papers, 70(4): 1-10. <https://doi.org/10.1515/chempap-2015-0234>
- [34] Boughendjioua H, Djeddi S. (2017) Organoleptic and Physicochemical Properties of Algerian Lemon Essential Oil. World Journal of Applied Chemistry, 2(3): 96-100. <https://doi.org/10.11648/j.wjac.20170203.14>
- [35] Wilkins MR, Grohmann K, Widmer WW. (2006) Effect of d-limonene on the Fermentation of *Citrus* Peel Waste. American Society of Agricultural and Biological Engineers, 1(1): 1-7. <https://doi.org/10.1080/15435075.2017.1307753>
- [36] Lota ML, de Rocca SD, Tomi F, Jacquemond C, Casanova J. (2002) Volatile Components of Peel and Leaf Oils of Lemon and Lime Species. Journal of Agricultural and Food Chemistry, 50(4): 796-805. <https://doi.org/10.1021/jf0109241>
- [37] Ferhat MA, Meklati BY, Smadja J, Chemat F. (2006) An Improved Microwave Clevenger Apparatus for Distillation of Essential Oils from Orange Peel. Journal of Chromatography A, 1112 (1): 121-126. <https://doi.org/10.1016/j.chroma.2005.12.030>
- [38] Díaz AB, Ory ID, Caro I, Blandino A. (2012) Enhance Hydrolytic Enzymes Production by *Aspergillus awamori* on Supplemented Grape Pomace. Food and Bioprocess Processing, 90(1): 72-78. <https://doi.org/10.1016/j.fbp.2010.12.003>
- [39] Tang PL, Hassan O, Maskat MY, Badri K. (2015) Production of Monomeric Aromatic Compounds from Oil Palm Empty Fruit Bunch Fiber Lignin by Chemical and Enzymatic Methods. Biomed Research International, 5: 1-14. <https://doi.org/10.1155/2015/891539>

## STATISTICAL ANALYSIS OF GROWTH CONDITIONS OF NEWLY ISOLATE *BACILLUS* SP. PRODUCING L-ASPARAGINASE

DZUN NORAINI JIMAT<sup>1\*</sup>, INTAN BAIZURA FIRDA MOHAMED<sup>1</sup>, AZLIN SUHAIDA AZMI<sup>1</sup> AND  
AZURA AMID<sup>2</sup>

<sup>1</sup>*Department of Biotechnology Engineering, Kulliyah of Engineering, International Islamic University Malaysia (IIUM), P.O. Box 10, 50728 Kuala Lumpur, Malaysia.*

<sup>2</sup>*International Institute for Halal Research and Training, International Islamic University, Malaysia (IIUM), P.O. Box 10, 50728 Kuala Lumpur, Malaysia.*

\*Corresponding author: [jnoraini@iium.edu.my](mailto:jnoraini@iium.edu.my)

(Received: 4<sup>th</sup> February 2019; Accepted: 13<sup>th</sup> June 2020; Published on-line: 4<sup>th</sup> July 2020)

**ABSTRACT:** The concentrations of nutrient elements together with several physical parameters were screened to find out the significant factors for the production of L-asparaginase from newly isolated strain, *Bacillus* sp. from Sg Klah, Hot Spring, Perak. Then, the significant factors were optimized for enhancing L-asparaginase production from the bacterium strain. Two statistical designs, Two Level Factorial Design and Face Centered Composite Design (FCCD), Design expert @version 8.0 were employed in screening and optimization of the process variables, respectively. The results for all experiment runs were analyzed by analysis of variance (ANOVA). Peptone (nitrogen source) concentration and temperature were found as significant factors, positively influenced the production of L-asparaginase. The two factors were then optimized to increase the desired enzyme production. The optimum peptone concentration and the temperature were found at 1.4 g/L and 30°C, respectively. The L-asparaginase production under optimized conditions increased from 0.15±0.023 U/mL to 0.19 ± 0.03 U/mL. The kinetic studies showed that the biomass production dropped after 24 hours while L-asparaginase activity is active and positively increased until the fermentation period ended.

**ABSTRAK:** Kepekatan unsur-unsur nutrien bersama-sama dengan beberapa parameter fizikal telah diteliti untuk mengetahui faktor-faktor penting untuk pengeluaran L-asparaginase dari spesies baru diasingkan, *bacillus* sp. dari kolam air panas tempatan. Kemudian, faktor penting dioptimumkan untuk meningkatkan pengeluaran L-asparaginase daripada bakteria tersebut. *Two Level Factorial Design* dan *Face Centered Composite Design* (FCCD), Design expert @version 8.0 telah digunakan dalam penyaringan dan pengoptimuman pembolehubah proses dalam kajian ini. Keputusan untuk semua eksperimen dianalisis dengan analisis varians (ANOVA). Kepekatan dan suhu peptone (sumber nitrogen) didapati sebagai faktor penting, secara positif mempengaruhi pengeluaran L-asparaginase. Kedua-dua faktor ini dioptimumkan untuk meningkatkan pengeluaran enzim yang dikehendaki. Kepekatan peptone dan suhu optimum didapati masing-masing pada 1.4 g / L dan 30°C. Pengeluaran L-asparaginase di bawah keadaan yang dioptimumkan meningkat dari 0.15 ± 0.023 U / mL kepada 0.19 ± 0.03 U/mL. Kajian kinetik menunjukkan bahawa pengeluaran biojisim menurun selepas 24 jam manakala aktiviti L-asparaginase aktif dan meningkat secara positif sehingga tempoh penapaian berakhir.

**KEYWORDS:** *Bacillus* sp., L-asparaginase activity, screening, optimization, peptone, temperature

## 1. INTRODUCTION

L-asparaginase catalyzes the hydrolysis of L-asparagine into L-aspartic acid and ammonia. L-asparaginase is widely used in food industry as an acrylamide reducing agent especially in baked and fried food products [1] as when the temperature in processing food is getting higher, the acrylamide compound is formed [2]. This enzyme is also known as a microbial therapeutic approach for cancer treatment [3]. This enzyme helps in reducing the amount of L-asparagine present in patients' blood by hydrolyzing the amino acid to two end products in leukemic cells [4]. Tumor cell needs L-asparagine to build proteins. However, these cells cannot synthesize its own L-asparagine because of the absent or low expression of asparagine synthase in the cells. Therefore, the cells use exogenous L-asparagine that obtains from the human diet to meet its needs. This enzyme is also used as a diagnostics biosensor for monitoring asparagine levels in leukemia [4]. L-asparaginase serves to destroy all the L-asparagine that does not manage to get synthesized in a tumor cell or that comes from the other sources [5]. L-asparaginase is an important component for cancer therapy, but it still has some limitations for clinical utility due to its side effect, short half-life and low-level enzyme production [6]. The current microbial strains producing L-asparaginase that are used for therapeutic are from *Escherichia coli* and *Erwinia sp.* [7]. The therapeutic response of L-asparaginase from these bacteria strains usually occurs with the evidence of toxicity [8]. A native form of the enzyme has a short half-life [9]. The fast progress of clinical resistance (the failure of cancer to shrink after treatment) is the key problem of L-asparaginase usage in treating acute leukemia. A long term administration of L-asparaginase into patients may cause the production of the corresponding antibody in the tissues. This condition may result in anaphylactic shock or neutralization of the drug effect. It was found that different types of microbial strains exhibit different biochemical and kinetic properties of L-asparaginase [10]. Previous studies have discovered new strains that able to produce asparaginase such as *Helicobacter pylori* [11, 12], *Serratia marcescens* [13, 14] and *basidiomycetes*, *Flammulina velutipes* [15]. However, alternative L-asparaginase sources are a necessity to meet a great demand that is expected in the coming years. It is because microbes are preferable sources than animals and plants due to their fast and easily grow and low-cost of culture nutrient requirements [16]. Thus, this study aimed to screen the significant factors in enhancing L-asparaginase production by newly isolated *Bacillus sp.* obtained from our previous study [17]. The significant factors were then optimized to maximize enzyme production. The growth kinetic of the bacterial strain under optimum conditions was investigated. In this study, face-centered central composite design (FCCD) from Response Surface Methodology (RSM) using Design expert @version 8.0 was selected as through this approach optimum values could be discovered effectively within the designated range of the independent variable. Furthermore, a previous study reported that the effect of several process variables on the prediction of the optimum response yield could be observed as well [18].

## 2. MATERIALS AND METHODS

### 2.1 Microorganisms

A bacteria strain producing L-asparaginase from *Bacillus sp.* was used in the present study. The wild strain of *Bacillus sp.* was isolated previously from Sg. Klah, Hot Spring, Perak [17]. The pure bacterial strain was maintained in glycerol stock at -20°C to preserve it. Then it was subcultured on nutrient agar before use. The culture plates were then stored at 4°C and subcultured every two weeks.

## 2.2. Identification of the isolate bacteria

Molecular identification using 16S rRNA gene sequencing analysis was performed by 1st BASE Molecular Biology Services. BLAST program was used to identify the gene sequence.

## 2.3. Inoculum preparation

A bacteria suspension was prepared from 24 hours old culture grown on modified M9 agar medium as described by Gulati and co-workers (1997) [19]. This modified M9 medium containing (per 1000 mL of distilled water): Na<sub>2</sub>HPO<sub>4</sub>·2H<sub>2</sub>O, 6.0 g ; KH<sub>2</sub>PO<sub>4</sub>, 3.0g ; NaCl, 0.5 g ; L-asparagine, 5.0 g ; 1M MgSO<sub>4</sub>·7H<sub>2</sub>O, 2.0 mL ; 0.1M CaCl<sub>2</sub>·2H<sub>2</sub>O, 1.0 mL ; 20% glucose stock, 10.0 mL ; agar 20.0 g at pH 7. A colony from the culture plates was suspended in 5 mL of sterile liquid M9 medium. It was grown overnight at 37°C.

## 2.4. Cultivation of newly isolates, *Bacillus sp.*

Sterilized modified M9 media (50 mL) was inoculated with 2% (1.46 x 10<sup>8</sup> CFU/mL) of inoculums (*Bacillus sp.*) which placed in 250 mL Erlenmeyer flasks and incubated at 37°C at 150 rpm for 48 hours. The uninoculated medium was used as a control. The same experiment was carried out in three times. L-asparaginase activity was determined by taking the culture broth sample after 48 hours of incubation time.

## 2.5.L-asparaginase assay

The collected sample cultures were analyzed as described in previous studies [17, 19]. The bacteria cultures were harvested by centrifugation at 6,000 rpm for 15 min. A mixture of 0.1 ml sample of enzyme extract with 0.2 ml of 0.05M Tris-HCL (pH 8.6), 1.7 ml of 0.01M L-asparagine was incubated for 10 min at 37°C. 5 ml of 1.5M trichloroacetic acid (TCA) was added to the mixture to stop the reaction. This mixture was centrifuged at 10,000 rpm for clarification then 0.5 ml of the supernatant was diluted to 7 ml with distilled water and treated with 1 ml of Nessler reagent and left for 10min. The absorbance of color changes was measured at 480 nm. The optical density (OD) readings were then compared to the standard curve of ammonia. One unit (U) of L-asparaginase was defined as that amount of enzyme which liberating 1 μmole of ammonia per minute at 37°C under the assay conditions.

## 2.6.Protein concentration

Protein concentration was determined using reagent (Pierce™ 660nm Protein Assay Reagent) and compared to a standard curve of Bovine Serum Albumin (BSA) concentration as described by Bradford, (1976)[21].

## 2.7.Screening of carbon and nitrogen concentrations and operating culture conditions by Two-Level Factorial Design

Two-Level Factorial Designs, Design expert @version 8.0 was applied for screening of significant concentration of carbon and nitrogen sources. Based on the previous part of our study [17], it was found that sucrose and peptone positively enhanced the L-asparaginase activity from the used bacterial strain, *Bacillus sp.* The concentrations of the two nutrient components were screened together with the other culture operating conditions such as pH, inoculum sizes, agitation speed, and temperature to determine the most significant parameters for L-asparaginase production by the strain. Sucrose and peptone were supplemented at certain

concentrations into the production medium as reported in the previous study [22]. The design contains 32 experimental runs where the factors were taken at two levels (high and low values) as illustrated in Table 1.

Table 1: Controllable factors and their coded levels for screening the significant factors using Two-Level Factorial Design

Factor	Code	Variable levels	
		-1(Low)	+1(High)
Carbon (g/l)	A	1.50	3.00
Nitrogen (g/l)	B	1.50	3.00
Temperature (°C)	C	37	60
pH	D	5	9
Agitation speed (rpm)	E	150	250
Inoculum sizes (%)	F	2	3.5

### 2.8. Optimization of significant factors using Face Centered Composite Design (FCCD) from Response Surface Methodology (RSM)

Face Centred Composite Design (FCCD) from Response Surface Methodology (RSM) using Design expert @version 8.0 was employed to optimize the response (enzyme activity) which was influenced by the independent variables such as medium components (carbon and nitrogen sources) and operating parameters (pH, inoculum sizes and agitation speed). The significant factors were selected based on the results obtained in section 2.7. All results were analyzed by ANOVA and validated.

### 3.0. RESULTS AND DISCUSSION

The most potent isolate (I3) with high potential for L- asparaginase production was selected and identified using 16S rRNA gene sequence analysis for classification and to further confirm the subspecies level.

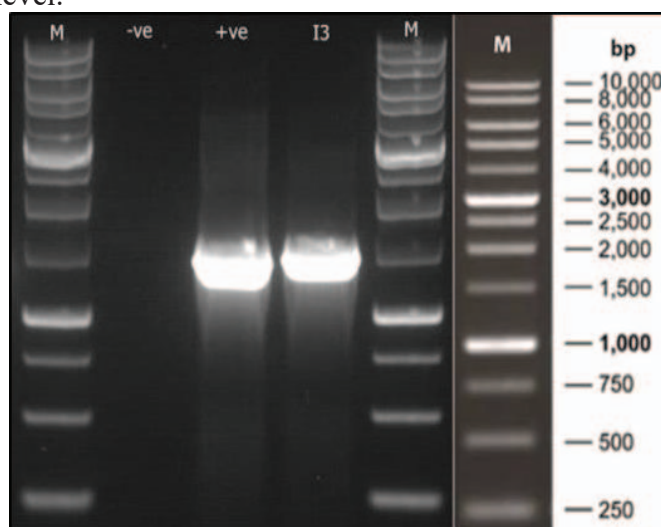


Fig. 1. PCR products for 16S rRNA gene sequence (M: DNA marker; -ve: PCR non template control (water); +ve: DNA extracted from *E.coli* ; I3: isolated strain)

Based on Fig. 1, a single band of the DNA appeared between 1000 and 1500 bp sequence. The result revealed a single band of amplified DNA products of approximately 1373 base pairs was recorded. The complete sequence data of the 16S ribosomal RNA gene were aligned and analyzed for finding the closest homologous microbes. The gene sequence was compared to nucleotide databases using the BLAST program.

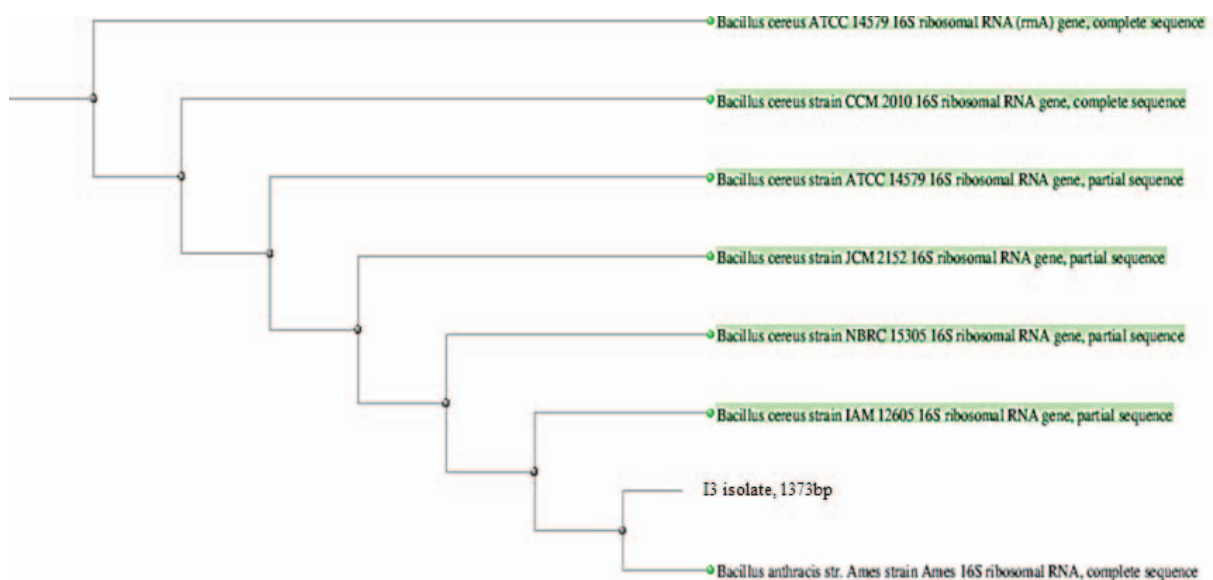


Fig. 2. A Phylogenetic tree of I3 strain. Neighbor-joining tree based on 16S rRNA gene sequences showing the positions of the selected strain.

A phylogenetic tree (Fig. 2) was constructed by taking the sequences obtained in the blast search. It was constructed to illustrate the evolutionary relationship between the unknown strains and the most closely related strains of species of the genus. As illustrated in Fig. 2, I3 strain was clustered into two major clades. The analysis of 16S rDNA sequences showed the sequences of the selected strain that very closely related to *Bacillus* sp. Therefore, based on Fig. 2, I3 isolate was identified as *Bacillus anthracis*. The sequence of the selected strain was most closely related to *Bacillus anthracis* strain Ames with a sequence similarity of 98%.

Sucrose and peptone were found as the best nutrients to boost L-asparaginase activity based on our previous study [17]. The varied concentration of the two elements together with four operating parameters like temperature, agitation speed, pH, and inoculum sizes were screened to investigate the significant factors influencing L-asparaginase activity from the *Bacillus* sp. strain. The experiment was designed under Two-Level Factorial Designs. The concentration of nutrients elements is vital to enhance bacterial growth as well as metabolites production during the fermentation process.

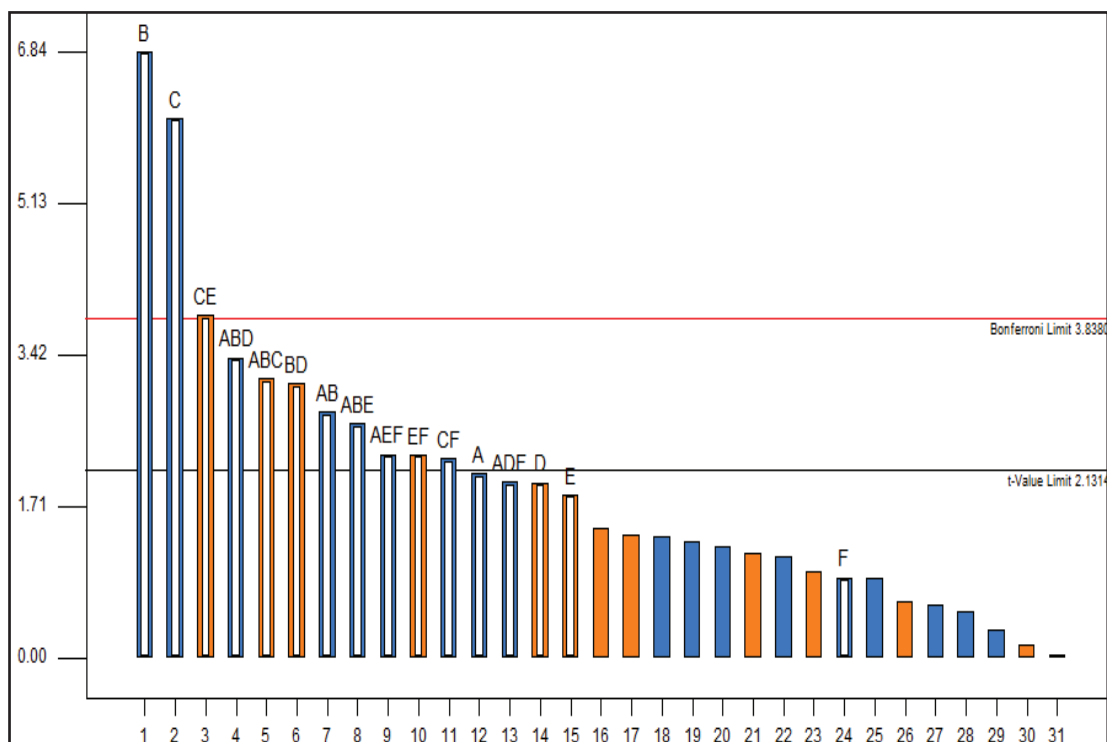


Fig. 3. Pareto chart of significant variables

The most significant factors were determined based on the analyzed results shown by the Pareto chart (Fig. 3). The factors that are above Bonferroni limit, factor B (peptone concentration), and C (temperature) are the most significant factors. The factors that are between Bonferroni and t-value limit line can be considered as significant too. Meanwhile, the parameters which are below the t-value limit line are insignificant factors and those variables can be ignored. The concentration of peptone and temperature enhanced L-asparaginase activity.

Table 2: Analysis of variance (ANOVA) for the screening of significant factors

Sources	Sum of Squares	df	Mean Square	F Value	p-value Prob >F
Model (significant)	0.46	16	0.029	11.03	< 0.0001
A: Carbon	0.011	1	0.011	4.36	0.0543
B: Nitrogen	0.12	1	0.12	46.72	< 0.0001
C: Temperature	0.097	1	0.097	37.02	< 0.0001
D: pH	0.01	1	0.01	3.92	0.0664
E: Agitation speed	8.91E-03	1	8.91E-03	3.4	0.0849
F: Inoculum sizes	2.16E-03	1	2.16E-03	0.83	0.3776
R <sup>2</sup>	0.9217	Adjusted R <sup>2</sup>	0.8381	Predicted R <sup>2</sup>	0.6436

Table 2 shows a summary of the ANOVA analysis. The F-value of the Model was 11.03 and its p-value was < 0.0001 which was less than 0.05 implies the model was significant. All of the values of p-value or Prob > F less than 0.05 indicate model terms are significant whereas the values greater than 0.1 indicate the model terms are not significant. The p-values were the indicator of the importance of each correlation among the tested variables [23]. As shown in the Pareto chart, factor B (peptone concentration; nitrogen source) and C (temperature) were important factors since the p-value for that variable were less than 0.05 while the others were greater than 0.05.

Table 3: Controllable factors and their coded levels for the Face Centered Composite Design (FCCD)

Factor	Code	Variable levels	
		-1(Low)	+1(High)
Peptone (g/l)	A	1.00	2.00
Temperature (°C)	B	30	40

In present work, Face Centered Composite Design (FCCD) from (RSM) was employed to optimize the effective parameters with a minimum number of trials. This method helps to analyze the interaction between the tested parameters. The two significant factors obtained from the previous experiment were optimized. The low (-1) and high (+1) levels of each variable were designated respectively as illustrated in Table 3. High and low levels of the substrate may lead to the fluctuation of the yield of the process [14]. As illustrated by them, the decreased L-asparaginase activity was due to the substrate inhibition when the substrate used in a high level. Meanwhile, when a low level of substrate is used, it may decrease the yield because of less nutrient availability for microbial growth and metabolite synthesis. pH 7 was selected as previous studies revealed that the pH condition was the most suitable for the growth of any *Bacillus* sp.[24]. The same observation also found for the isolate *Streptomyces* ABR2 at this pH of 7.0 [25]. While inoculum size and agitation speed were fixed at 2% and 150rpm respectively. Both factors were insignificantly influenced to the culture, thus, the lowest level value was used in the optimization condition of the culture.

The complete experimental results are listed in Table 4.

Table 4: Experimental results of FCCD

Run	Peptone (g/L)	Temperature (°C)	L-asparaginase activity (U/mL)	Protein concentration (mg/mL)	Specific activity (U/mg)
1	1.00	40.00	0.13 ±0.082	0.02±0.012	6.5
2	1.50	35.00	0.16±0.129	0.01±0.098	16.0
3	1.50	30.00	0.15±0.054	0.02±0.120	7.5
4	1.50	40.00	0.16±0.100	0.02±0.011	8.0
5	1.00	30.00	0.13±0.024	0.01±0.044	13.0
6	1.00	35.00	0.13±0.071	0.01±0.004	13.0
7	2.00	40.00	0.07±0.090	0.01±0.011	7.0
8	1.50	35.00	0.17±0.110	0.01±0.014	17.0
9	1.50	35.00	0.19±0.010	0.01±0.068	19.0
10	2.00	30.00	0.11±0.017	0.02±0.049	5.5
11	1.50	35.00	0.18±0.018	0.01±0.113	18.0
12	2.00	35.00	0.06±0.032	0.02±0.012	3.0
13	1.50	35.00	0.20±0.013	0.01±0.002	20.0

Table 5: Analysis of variance (ANOVA) for optimization of response function

Sources	Sum of Squares	df	Mean Square	F Value	p-value Prob >F
Model (significant)	0.021	3	6.860E-003	22.02	0.0002
A: Peptone conc.	3.758E-003	1	3.758E-003	12.07	0.0070
B: Temperature	1.226E-004	1	1.226E-004	0.39	0.5460
A <sup>2</sup>	0.017	1	0.017	53.61	< 0.0001
Residual	2.803E-003	9	3.115E-004		
Lack of Fit (not significant)	2.081E-003	5	4.162E-004	2.30	0.2194
C.V (%)	12.33				
R <sup>2</sup>	0.8801	Adjusted R <sup>2</sup>	0.8402	Predicted R <sup>2</sup>	0.7228

ANOVA for the quadratic model for optimization process parameters is shown in Table 5. The Model F-value of 22.02 implies the model is significant. The values of the p-value less than 0.05 reflect that the model terms were significant. In this case, A and A<sup>2</sup> were significant variables. Values more than 0.1000 show the model terms are not significant. The lack of fit of the model is not significant indicated that it was reasonable for the present work. The CV value is also considered as an important value since it determines the reproducibility of the model and helps to determine statistical reliability. The estimation is less accurate when the CV ratio is large. If the value is less than 15%, the model reliability is good. In the present work, the CV value was 12.33 showing reliability and reproducibility of the model. The accuracy of the model developed can be determined by the R<sup>2</sup>, adjusted R<sup>2</sup>, and standard deviation values. R<sup>2</sup> or known as the coefficient of determination is a number indicates how well data fit a statistical model. Generally, when the R<sup>2</sup> value is closer to 1, the linear regression fits the data is better. Based on Table 5, the R<sup>2</sup> value for the model was 0.8801. The predicted R<sup>2</sup> of 0.7228 was in reasonable agreement with the adjusted R<sup>2</sup> of 0.8402. The value of the “Adeq Precision” obtained was 10.824. This value measures the signal to noise ratio. The ratio of 10.824 indicated an adequate signal. Thus, the model could be used to navigate the design space.

A multiple regression analysis was used to relate the response of L-asparaginase activity (Y) with the two variables studied using a second-order polynomial. It can be represented by the following equation of (1) in terms of coded factors:

$$Y = -0.36398 + 0.81268A - 9.04033 \times 10^{-4} B - 0.28758A^2 \quad (1)$$

In Eq. (1), the coded factors A and B represent peptone concentration and temperature, respectively. A positive sign in front of the A-code represents good effect, while negative sign in front the B code can be deduced as a bad effect on the response function (Y). The positive value of the main effect denotes that higher activity of the enzyme would result in at a higher level of the factor whereas a factor with negative sign denotes that its lower level would provoke higher L-asparaginase activity. Previous studies confirmed that when the effect of a factor was positive, an increase in the value of the enzyme activity efficiency was observed [23]. Besides, a coefficient close to zero value means that the factor has little impact or no

impact on the response. The A term of peptone concentration had the highest effect indicating that it was the most important component for L-asparaginase production. The linear term of peptone concentration (A) has a higher effect value than the square term ( $A^2$ ), indicating that the variable has more influence on enzyme production. It means that any alteration in the level could influence the production in a significant manner. Based on the above equation, the coefficient of B (temperature) is close to zero. Only peptone concentration influenced L-asparaginase activity produced by the strain positively.

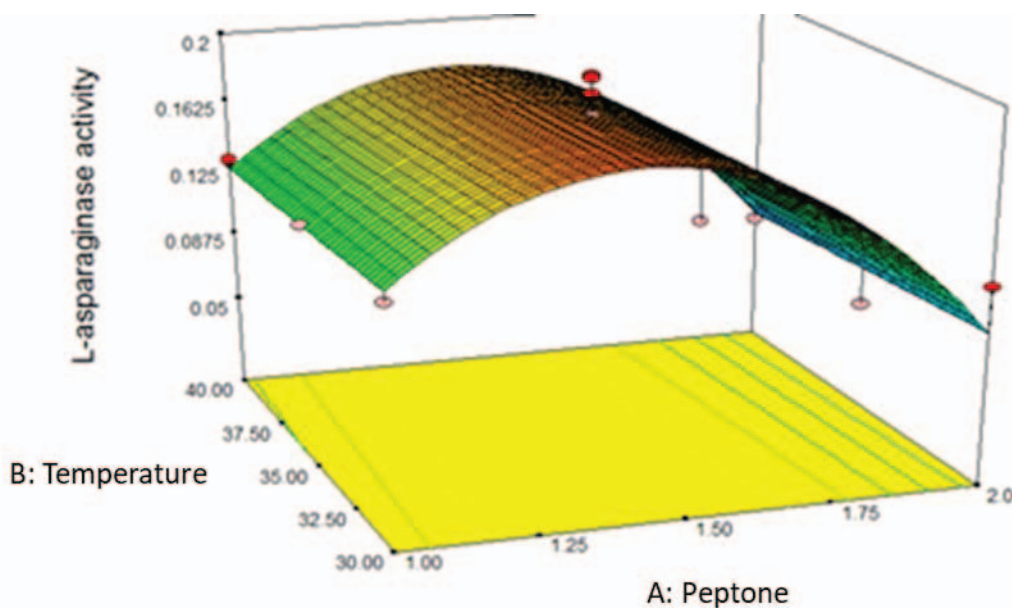


Fig. 4. A three-dimensional response surface plot showing the effect of peptone and temperature on the L-asparaginase activity.

The contour plot and Three-Dimensional (3D) graph are used to show the interaction between the involved variables. The curvature observed in a three-dimensional surface plot represents the prominent effect of peptone concentration on L-asparaginase activity (Fig. 4). The plot reveals that peptone concentration is proportional to the L-asparaginase activity. It seems like up to certain limits, the increased concentration of peptone will improve the enzyme activity. The activity of L-asparaginase was the highest at the middle level of peptone and lower level of temperature. The contour is slightly inclined towards temperature indicating that nitrogen source concentration; peptone was a slight influenced on temperature. Fig. 3 demonstrated that peptone at a concentration range of 1.40-1.50 g/l is optimum (middle level). The contour is elliptical indicating that both were independent of each other.

The predicted L-asparaginase activity for a particular set of operating culture conditions was numerically showed in the same Fig. 4. Based on the analysis of the contour plot, L-asparaginase activity increases to a maximum value with the increasing level of peptone to 1.40 g/L where the temperature was at its lower level (30°C). Further increment of the variables beyond the previously mentioned level shows an inhibitory effect on enzyme activity.

Table 6: Optimum-operating conditions for maximizing L-asparaginase

Peptone concentration (g/L)	Temperature (°C)	L-asparaginase activity (U/mL)		Percentage difference (%)
		Predicted	Experimental	
1.41	30.00	0.183	0.19 ± 0.03	3.83

Model validation was performed according to the condition generated by the software. The optimal values of parameters are as follows: peptone concentration 1.41 g/L and temperature 30°C, with corresponding L-asparaginase production at 0.183 U/mL (as shown in Table 6). The validation experiments were performed (triplicates) to find out the experimental results for enzyme activity. On conducting the experiments under these conditions, 0.19 ± 0.03 U/mL of L-asparaginase activity was recorded. According to Saeed Gholamian and co-worker, the optimum temperature for growth of *Bacillus* sp. and L-asparaginase production was 37°C [24]. Deshpande and co-workers found that the addition of peptone into the medium growth favored maximum enzyme production by *Streptomyces ginsengisoli* [26]. Other studies reported that the presence of peptone enhanced the growth of *Bacillus* sp. because it increased the dry weight of the cell and shortened the lag period where the bacteria are adjusting to the new environment and [27]. While Farag and co-workers reported that L-asparagine was the best nitrogen source for the new fungal isolate, *A. terreus* [28]. The maximum growth of the bacterial strain and L-asparaginase activity were recorded at the temperature. The experimental results were compared to the predicted L-asparaginase activity and the percentage error was calculated. It found that the values given by the software were following by with the experimental values with a small percentage difference (3.83%).

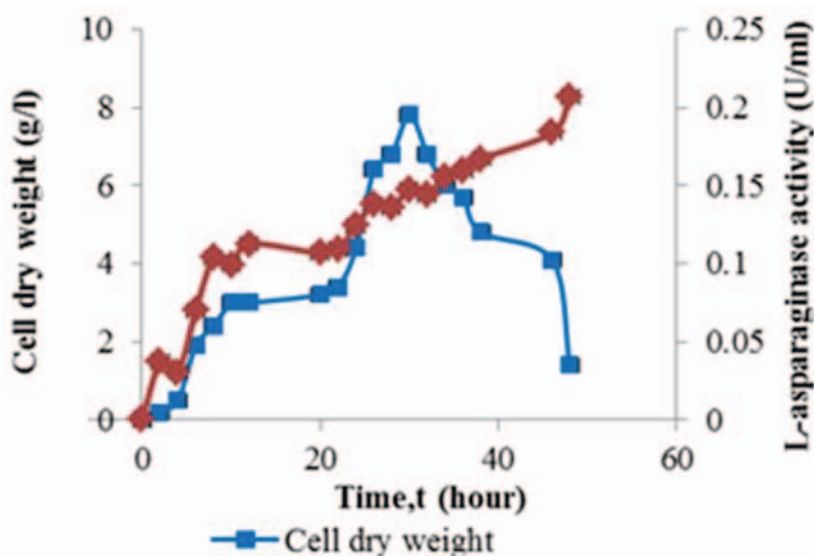


Fig. 5. A graph showing the correlation between cell dry weight (g/l) and L-asparaginase activity at different interval times.

The relationship between biomass concentration and L-asparaginase activity within 48 hours fermentation is shown the Fig. 5. The biomass concentration was increased gradually with the culture duration from 2 to 30 hours. At the 30th hour of incubation, it showed the maximum (7.8 g/l) biomass production. The biomass concentration sharply declined beyond 30 hours toward 48 hours. In this study maximum, L-asparaginase metabolite production occurred at the

end of the exponential growth phase. The L-asparaginase production declined to indicate its accumulation after a certain period of growth [29]. It found that the specific rates are high in the early part of the fermentation and later it declined steadily as the fermentation proceeds due to the disappearance of nutrients and the accumulation of toxic products.

#### 4.0. CONCLUSION

Peptone concentration and temperature were the most influential parameters in stimulating L-asparaginase activity from *Bacillus* sp. The optimal conditions for L-asparaginase activity were at 30°C with 1.41 g/L of peptone concentration. The L-asparaginase production under optimized conditions increased from 0.15±0.023 U/mL to 0.19 ± 0.03 U/mL. This study showed that the optimization of L-asparaginase production has been successfully achieved through Face Centred Composite Design (FCCD) of Response Surface Methodology (RSM).

#### REFERENCES

- [1] Cachumba JJM, Antunes FAF, Peres GFD, Brumano LP, Santos JCD, Silva SSD. (2016) Current applications and different approaches for microbial L-asparaginase production. *Brazilian J Microbiol*, 47S:77–85. <https://doi.org/http://dx.doi.org/10.1016/j.bjm.2016.10.004>
- [2] Kumar NSM, Shimray CA, Indrani D. (2014) Reduction of Acrylamide Formation in Sweet Bread with L -Asparaginase Treatment. *Food Bioprocess Technol*, 7:741–748. <https://doi.org/10.1007/s11947-013-1108-6>
- [3] Amena S., Vishalakshi N., Prabhakar M., Dayanand A. LK. (2010) Production, purification and characterization of l-asparaginase from *treptomyces gulbargensis*. *Brazilian J Microbiology*, 41:173–178. <https://doi.org/doi 10.1590/S1517-838220100001000025>
- [4] Verma N, Kumar K, Kaur G, Anand S. (2007) L-asparaginase: A promising chemotherapeutic agent. *Crit Rev Biotechnol*, 27:45–62. <https://doi.org/doi:10.1080/07388550601173926>
- [5] Jha, S K, Pasrija D., Sinha RK, Singh HR, Nigam VK VAS. (2012) Microbial L-asparaginase: A review on current scenario and future prospects. *Int J Pharm Sci Res*, 3:3076–3090. [https://doi.org/http://dx.doi.org/10.13040/IJPSR.0975-8232.3\(9\).3076-90](https://doi.org/http://dx.doi.org/10.13040/IJPSR.0975-8232.3(9).3076-90)
- [6] Zuo S, Zhang T, Jiang B, Mu W. (2014) Recent research progress on microbial l-asparaginases. *Appl Microbiol Biotechnol*, 99:1069–1079. <https://doi.org/10.1007/s00253-014-6271-9>
- [7] Pieters R, Hunger SP, Boos J, Rizzari C, Silverman L, Baruchel A, Goekbuget N, Schrappe M, Pui C. (2011) L-Asparaginase Treatment in Acute Lymphoblastic Leukemia. *Cancer*, 117:238–249. <https://doi.org/10.1002/cncr.25489>
- [8] Jha SK, Pasrija D., Sinha RK, Singh HR, Nigam VK, Vidyarthi AS. (2012) Microbial L-asparaginase: A review on current scenario and future prospects. *Int J Pharm Sci Res*, 3:3076–3090
- [9] Jain R, Zaidi KU, Verma Y, Saxena P. (2012) L-Asparaginase : A Promising Enzyme for Treatment of Acute Lymphoblastic Leukemia. *People's J Sci Res*, 5:29–35
- [10] Prakasham RS, Hymavathi M, Rao CS. (2010) Evaluation of Antineoplastic Activity of Extracellular Asparaginase Produced by Isolated *Bacillus circulans*. *Appl Biochem Biotechnol*, 160:72–80. <https://doi.org/10.1007/s12010-009-8679-8>

- [11] Shibayama K, Takeuchi H, Wachino J ichi, Mori S, Arakawa Y. (2011) Biochemical and pathophysiological characterization of *Helicobacter pylori* asparaginase. *Microbiol Immunol*, 55:408–417. <https://doi.org/10.1111/j.1348-0421.2011.00333.x>
- [12] Cappelletti D, Chiarelli LR, Pasquetto MV, Stivala S, Valentini G, Scotti C. (2008) *Helicobacter pylori* asparaginase: A promising chemotherapeutic agent. *Biochem Biophys Res Commun*, 377:1222–226. <https://doi.org/doi:10.1016/j.bbrc.2008.10.118>
- [13] Agarwal A, Kumar S, Veeranki VD, Kumar Æ. (2011) Effect of chemical and physical parameters on the production of L -asparaginase from a newly isolated *Serratia marcescens* SK-07. *Letter in Applied Microbiology*, 52:307–313. <https://doi.org/10.1111/j.1472-765X.2011.03006.x>
- [14] Ghosh S, Murthy S, Govindasamy S, Chandrasekaran M. (2013) Optimization of L-asparaginase production by *Serratia marcescens* (NCIM 2919) under solid state fermentation using coconut oil cake. *Sustainable Chemical Process*, 1(9):1–8 . <https://doi.org/DOI:10.1186/2043-7129-1-9>
- [15] Eisele N, Linke D, Bitzer K, Na’ammieh S, Nimtze M, Berger RG. (2011) The first characterized asparaginase from a basidiomycete, *Flammulina velutipes*. *Bioresour Technol*, 102:3316–3321 . <https://doi.org/10.1016/j.biortech.2010.10.098>
- [16] Lopes AM, Oliveira-Nascimento L de, Ribeiro A, Tairum CA, Breyer CA, Oliveira MA de, Monteiro G, Souza-Motta CM de, Magalhães P de O, Avendaño JGF, Cavaco-Paulo AM, Mazzola PG, Rangel-Yagui C de O, Sette LD, Converti A, Pessoa A. (2017) Therapeutic l-asparaginase: upstream, downstream and beyond. *Crit Rev Biotechnol*, 37:82–99 . <https://doi.org/10.3109/07388551.2015.1120705>
- [17] Jimat DN, Baizura I, Mohamed F, Azmi AS, Zainudin Z. (2015) Isolation and Characterization of Thermophilic Bacteria Producing L-Asparaginase from Malaysia Hotspring and Enzyme Activity Using Different Carbon and Nitrogen Sources. *J Appl Sci Agric*, 10:69–77
- [18] Ahmad T, Danish M, Kale P, Geremew B, Adeloju SB, Nizami M, Ayoub M. (2019) Optimization of process variables for biodiesel production by transesterification of flaxseed oil and produced biodiesel characterizations. *Renew Energy*, 139:1272–1280. <https://doi.org/10.1016/j.renene.2019.03.036>
- [19] Gulati R, Saxena RK, Gupta R. (1997) A rapid plate assay for screening L -asparaginase producing. *Lett Appl Microbiol*, 24:23–26
- [20] Jimat DN, Mohamed IBF, Azmi AS, Jamal P. (2017) Purification and partial characterization of L- asparaginase enzyme produced by newly isolated *Bacillus* sp. *IIUM Eng J*, 18:1–10 <https://doi.org/10.31436/iiumej.v18i2.654>
- [21] Bradford MM. (1976) A Rapid and Sensitive Method for the Quantitation Microgram Quantities of Protein Utilizing the Principle of Protein-Dye Binding. *Anal Biochem*, 72:248–254
- [22] Hymavathi M, Sathish T, Brahmaiah P, Prakasham RS. (2010) Impact of Carbon and Nitrogen Sources on L-Asparaginase Production by Isolated *Bacillus circulans* (MTCC 8574 ): Application of Saturated Plackett-Burman Design. *Chem Biochem Eng Q*, 24:473–480
- [23] Mungi H, Carvalho R, Ilegar S. (2014) Optimization of L-asparaginase production from *Pseudomonas fluorescens* by Response Surface Methodology. *Int J Curr Microbiol Appl Sci*, 3:350–362
- [24] Gholamian, S.; Gholamian, S.; Nazemi, A.; Nargesi MM. (2013) Optimization of Culture Media for L Asparaginase Production by Newly Isolated Bacteria , *Bacillus* sp. GH5 1. *Microbiology*, 82:856–863 . <https://doi.org/10.1134/S0026261714010032>
- [25] Sudhir AP, Dave BR, Trivedi KA, Subramanian RB. (2012) Production and

- amplification of an L-asparaginase gene from actinomycete isolate *Streptomyces* ABR2. *Ann Microbiol*, 62:1609–1614 . <https://doi.org/10.1007/s13213-011-0417-0>
- [26] Deshpande N, Choubey P, Agashe M. (2014) Studies on Optimization of Growth Parameters for L-Asparaginase Production by *Streptomyces ginsengisoli*. *The Scientific World Journal*, :1–6 . <https://doi.org/10.1155/2014/895167>
- [27] Fooladi J, Sajjadian A. (2010) Screening the thermophilic and hyperthermophilic bacterial population of three Iranian hot-springs to detect the thermostable  $\alpha$ -amylase producing strain. *Iran J Microbiol*, 2:49–53
- [28] Farag AM, Hassan SW, Beltagy EA, El-Shenawy MA. (2015) Optimization of production of anti-tumor l-asparaginase by free and immobilized marine *Aspergillus terreus*. *Egypt J Aquat Res*, 41:295–302 . <https://doi.org/10.1016/j.ejar.2015.10.002>
- [29] Thaer, T.A. and Ellaiah P. (2013) L-Asparaginase production by a *streptomycete* and optimization of production parameters. *J Pharm Biomed Sci*, 29:859–869

## A COMPARATIVE STUDY ON TREATMENT TECHNOLOGIES FOR SEWAGE RECLAMATION: A FOCUS ON THE DISINFECTION PROCESS

NOORINI IZZATI MOHAMAD MAZUKI<sup>1</sup>, TEOW YEIT HAAN<sup>1,2\*</sup>  
AND ABDUL WAHAB MOHAMMAD<sup>1,2</sup>

<sup>1</sup>Department of Chemical Engineering and Process,

<sup>2</sup>Research Centre for Sustainable Process Technology (CESPRO),  
Faculty of Engineering and Built Environment,  
Universiti Kebangsaan Malaysia, 43600 UKM Bangi,  
Selangor Darul Ehsan, Malaysia

\*Corresponding author: [yh\\_teow@ukm.edu.my](mailto:yh_teow@ukm.edu.my)

(Received: 24<sup>th</sup> September 2019; Accepted: 8<sup>th</sup> April 2020; Published on-line: 4<sup>th</sup> July 2020)

**ABSTRACT:** Selection of suitable disinfection technology is necessary with regards to wastewater reclamation goals. In this work, the performance of various disinfection technologies - single disinfection units and integrated disinfection systems - on local sewage was studied for non-potable reuse. Disinfection units used as stand-alone units include ultraviolet (UV) disinfection, chlorination, microfiltration (MF), and ultrafiltration (UF). The integrated disinfection system consists of UV or chlorination as the primary disinfection unit incorporated with either MF, UF, multi-media or granular activated carbon as pre-treatment. The performance of these disinfection units and integrated processes were evaluated based on the percentage of removal of biochemical oxygen demand, chemical oxygen demand, total suspended solids, ammoniacal nitrogen, nitrate nitrogen, phosphorus, *Escherichia coli*, and trihalomethane in bench-scale disinfection systems. The single unit of PES20kDa membrane and the integrated disinfection system of UF-Cl showed the most effective treatment among single disinfection units and integrated systems, respectively. The results showed that almost all disinfection units and integrated disinfection processes were useable for restricted and unrestricted area non-potable applications according to United State Environmental Protection Agency (US EPA) water reuse guidelines and managed to fulfil Singapore grey water quality for recycling.

**ABSTRAK:** Pemilihan teknologi penyahjangkitan kuman yang sesuai adalah perlu selaras dengan matlamat pemuliharaan air buangan. Kajian ini adalah tentang prestasi pelbagai teknologi penyahjangkitan kuman - unit tunggal penyahjangkitan kuman dan sistem penyahjangkitan kuman bersepadu pada air sisa kumbahan tempatan dikaji bagi penggunaan semula air minuman. Unit tunggal penyahjangkitan kuman yang digunakan mempunyai penyahjangkitan kuman ultraungu (UV), pengklorinan, mikro penurasan (MF), dan ultra penurasan (UF). Manakala, sistem penyahjangkitan kuman bersepadu terdiri daripada UV atau pengklorinan sebagai unit penyahjangkitan kuman utama yang digabungkan bersama samada dengan MF, UF, multi-media atau karbon teraktif berbutir sebagai proses pra-rawatan. Prestasi unit tunggal penyahjangkitan kuman dan proses-proses bersepadu dinilai berdasarkan pada peratus penyingkiran keperluan oksigen biokimia, permintaan oksigen kimia, jumlah pepejal terampai, nitrogen ammonia, nitrogen nitrat, fosforus, *Escherichia coli*, dan trihalometana dalam sistem penyahjangkitan kuman berskala-makmal. Unit tunggal penurasan ultra membran PES20kDa dan sistem penyahjangkitan kuman bersepadu UF-Cl menunjukkan masing-

masing paling efektif dalam rawatan unit tunggal dan sistem penyahjangkitan kuman bersepadu. Keputusan menunjukkan bahawa hampir semua unit tunggal penyahjangkitan kuman dan proses penyahjangkitan kuman bersepadu boleh diguna pakai bagi aplikasi terhad dan tidak terhad mengikut garis panduan penggunaan semula air sisa rawatan yang ditetapkan oleh Agensi Pelindungan Alam Sekitar Amerika Syarikat (US EPA) dan kualiti kitar semula air sisa Singapura.

---

**KEYWORDS:** *sewage reclamation; single disinfection unit; integrated disinfection system; water reuse; Escherichia coli*

## 1. INTRODUCTION

Sewage reclamation has been widely practiced in various regions around the world, in line with increasing water demand and public awareness related to safe and clean water issues. Meanwhile, various studies are still on-going on the potential of wastewater reclamation and reuse in Malaysia. In early 2015, Malaysia faced water shortages that affected more than seven million users in the Klang Valley, due to drought which led to the reduction of the water level at the Sungai Selangor dam [1]. This issue indicates the importance of sustainable water management since there is no guarantee of constant water supply even for high rainfall countries. About 4,500 MLD of sewage equivalent to 25% of national potable water is being treated in Indah Water Konsortium (IWK) sewerage treatment plant (STP) in Malaysia per day with 96.7% sanitation coverage available in urban areas [2-4]. Hence, sewage effluent should be considered as a valuable resource and can provide important positive trade-off to overcome the water crisis in this country.

Sewage in Malaysia is commonly allowed to undergo preliminary, primary, and secondary treatments before being discharged into the environment. Typically, centralized STPs produced high-quality final discharge effluent that is well below the Department of Environment (DOE) Malaysia Standard A limit [5]. Given the intent to promote the reuse of treated sewage, which is considered to be a green technology initiative, the treated effluent could be used as a water resource for non-potable applications. However, the raw effluent is unsafe for direct use as it still contains high concentration of pathogens (both *Salmonella spp.* and *Escherichia coli (E. coli)* that were present at  $10^5$  CFU/100 mL in Malaysia sewage discharged effluent) [6]. Therefore, it is important to disinfect the final discharge effluent prior to its supply to end users to lower the risk of biological hazard.

Chlorination and ultraviolet (UV) processes are the most extensively used disinfection technologies. Chlorination has been widely investigated in the past several decades for wastewater applications. Despite numerous advantages offered by chlorination, its potential generation of carcinogenic disinfection by-products (DBPs) has made it a less favourable disinfectant [7]. On the other hand, the adoption of UV light for wastewater disinfection has grown significantly to compete with chlorination since it would not produce toxic treated effluent, is safe in operation, and has a small footprint [8,9]. Today, thousands of municipalities in North America have converted from chemical-based disinfection technology such as chlorine gas to UV [10].

As the efficiency of chlorination and UV disinfection varied depending on the characteristics of sewage's discharged effluent, both systems were suggested to be coupled with an advanced technology that could act as a physical pre-treatment prior to the primary disinfection process in order to enhance the effectiveness of chlorination or UV disinfection and improve the quality of the treated effluent to meet with the stringent wastewater reuse limit established by United State Environmental Protection Agency (US

EPA) and by other countries [11]. Membrane filtration and adsorption process could be applied as the pre-treatment to reduce the colloidal and particulate constituents in wastewater to enhance the effectiveness of the primary disinfection unit.

Adsorption technology using granular activated carbon (GAC) is a good option for the removal of macro-contaminants. GAC could perform dual functions - as an adsorbent and filter to the influent. Its ability as a macrofilter-adsorbent medium has attracted strong interest from many parties to utilize at various wastewater treatment plants [12-15]. On the other hand, membrane filtration applying a physical separation mechanism in its operating process is well-known to be able remove microbial and contaminants in sewage. Microfiltration (MF) and ultrafiltration (UF) are the membranes commonly used to remove microorganisms and turbidity. The selection on the feasible disinfection technology must be done accordingly, suitable to the target sewage reclamation's objective. Unfortunately, there are still limited numbers of studies that provide technical feasibility information on the implementation of disinfection technology in Malaysia for sewage reclamation. Hence, this research aims to study and evaluate the performance of various commercially available single disinfection units and integrated disinfection systems on Malaysia sewage for non-potable water reuse applications.

## 2. MATERIALS AND METHODS

### 2.1 Sampling of Final Discharge Effluent

Effluent used in this study was collected from a secondary effluent discharge drain at STP located in Selangor, Malaysia. Currently, the plant operates up to secondary treatment using sequencing batch reactor (SBR) system. The raw effluent discharged from this plant was stipulated under Standard B limits based on the Department of Environment (DOE) standard. Characterization of raw effluent was done immediately after each sampling to ensure the reliability of the measurements. In this study, 30 L volume of sample was required for each experiment. Hence each experiment was conducted using different batches of raw effluent.

### 2.2 Materials

A calcium hypochlorite [ $\text{Ca}(\text{ClO})_2$ ] tablet manufactured by Tosoh Corporation, Japan was used as the chlorine source. Four different types of commercial flat sheet membranes: two MF membranes and two UF membranes were used in this study. HVL P00010 and PVDF021M membranes having membrane pore size of 0.45  $\mu\text{m}$  and 0.2  $\mu\text{m}$  were used to represent the MF membranes, respectively. Meanwhile, PVDF1001M and PES20kDa membranes having molecular weight cut-off (MWCO) at 100 kDa and 20 kDa each were selected to represent UF membranes, respectively. GAC (mesh size: 8 $\times$ 30, iodine value: 1000 to 1200 mg/g, ash content: < 3%) synthesized by Laju Carbon Products Sdn. Bhd, Malaysia was used as the adsorbent for pre-treatment prior to the disinfection process. Environ multi-media (EMM) capsule (height: 6 cm, diameter: 2 cm) acted as the housing for GAC was supplied by EnviroSource (M) Sdn. Bhd, Malaysia.

### 2.3 Bench-scale Integrated Disinfection System

The single disinfection units involved in this study include UV, chlorination, MF, and UF. Whereas, for integrated disinfection processes, UV disinfection and chlorination acted as the primary disinfection unit incorporated with MF, UF, EMM or GAC as the pre-treatment unit.

Figure 1 shows the schematic diagram of the bench-scale integrated disinfection system comprising of MF/UF-chlorination and MF/UF-UV. Fig. 2 shows the schematic diagram of a bench-scale integrated disinfection system comprising of GAC/EMM-chlorination and GAC/EMM-UV.

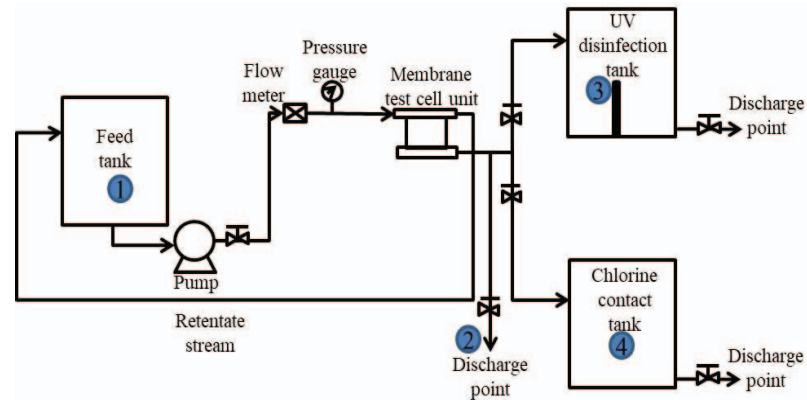


Fig. 1: Schematic diagram of bench-scale integrated disinfection system (MF/UF-chlorination and MF/UF-UV) with sampling points: (1) at feed tank (2) at discharge point after the membrane unit (3) at UV disinfection tank (4) at chlorine contact basin.

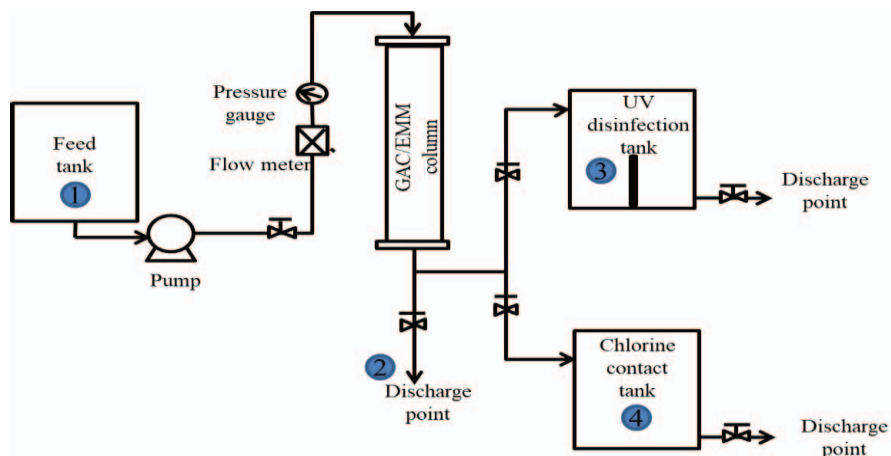


Fig. 2: Schematic diagram of bench-scale integrated disinfection system (GAC/EMM column-chlorination and GAC/EMM column-UV) with sampling points: (1) at feed tank (2) at discharge point of GAC/EMM column (3) at UV disinfection tank (4) at chlorine contact basin.

### 2.3.1 Preliminary Study

Preliminary study was conducted for UV disinfection and chlorination to investigate the optimum UV dosage and chlorine dosage in treating raw effluent. The selection of optimum UV dosage and chlorine dosage was determined at the condition when there was no *E. coli* detected in the treated effluent.

#### a) UV Disinfection

UV exposure time in treating raw effluent was varied for 5 minutes, 30 minutes, 60 minutes, 120 minutes, and 180 minutes while the intensity of UV lamp was kept constant at 15 Watts.

### **b) Chlorination**

Chlorine dosage applied for the raw effluent ranged from 0 mg/L to 30 mg/L while the contact time for chlorine treatment was kept constant at 30 minutes.

### **2.3.2 Disinfection Technology**

#### **a) GAC**

GAC/EMM adsorption column was filled with GAC at a filling ratio of 0.5. Next, the raw effluent was fed into GAC/EMM adsorption column from the top at constant flow rate of 50 L/day with empty bed contact time (EBCT) at 12.73 minutes.

#### **b) EMM**

EMM capsules used for EMM pre-treatment were half-filled with GAC and closed tightly. EMM pre-treatment was carried out in a GAC/EMM adsorption column where the EMM capsules were used to replace GAC in adsorption column at a filling ratio of 0.5. Subsequently, the raw effluent was fed into the GAC/EMM adsorption column from the top at constant flow rate of 50 L/day. The pre-treated raw effluent was then transferred to the primary disinfection unit for further treatment.

#### **c) Membrane Filtration**

The commercial flat sheet membrane was cut into a rectangular shape (19.1 cm × 14.0 cm) with membrane effective surface area of 155 cm<sup>2</sup>, laid on top of the cross-flow stainless steel membrane test cell unit and clamped tightly. Operating pressure for both MF and UF membranes was 2 bar. The permeate flux (J) was determined using Eq. (1):

$$J = \frac{V}{At} \quad (1)$$

where V is the permeate volume (L), A is the membrane effective surface area (m<sup>2</sup>), and t is the permeation time (h).

#### **d) UV Disinfection**

UV disinfection was carried out in the UV disinfection tank by immersing a 15 Watt UV-C lamp (Dolphin KW, China) at the centre of UV disinfection tank. The effective exposure area for UV disinfection was 0.3 m in diameter and 0.3 m in height. The intensity of UV light at 254 nm was measured using the PM100D optical power and energy meter with S120VC photodiode (Thorlabs, Germany) after the low-pressure UV-C lamp was switched on for 30 minutes. UV exposure time in single UV disinfection unit and integrated UV disinfection system was based on the results obtained from the preliminary study for UV disinfection. The applied UV dosage was calculated using Eq. (2) and Eq. (3) [16, 17].

$$I_{avg} = I_o \left( \frac{1 - e^{-d \times \ln \frac{1}{T}}}{d \times \ln \frac{1}{T}} \right) \quad (2)$$

$$UV \text{ Dosage} = I_{avg} \times t \quad (3)$$

where  $I_{avg}$  is the UV-C intensity per unit area (mW/cm<sup>2</sup>),  $t$  is the UV exposure time,  $I_o$  is the UV-C incident irradiance (mW/cm<sup>2</sup>),  $d$  is the depth of the raw effluent perpendicular to the UV lamp, and  $T$  is the UV-C transmittance at 254 nm with cell path length of 1 cm.  $I_o$  is constant at 0.475 mW/cm<sup>2</sup>.

### e) Chlorination

The chlorination process was carried out in a chlorination tank for 30 minutes. The chlorine dosage added to the single chlorination unit and integrated chlorination system was according to the results obtained from the chlorination preliminary study. Next, the treated raw effluent was added with 4 w/w% of Na<sub>2</sub>S<sub>2</sub>O<sub>5</sub> solution for de-chlorination purposes after 30 minutes of chlorination process.

## 2.4 Water Quality Analysis

Efficiency of commercially available disinfection units and integrated disinfection processes in treating the raw effluent was assessed based on the treated effluent quality. The measured parameters included temperature, pH, biochemical oxygen demand (BOD<sub>5</sub>), chemical oxygen demand (COD), total suspended solids (TSS), ammoniacal-nitrogen (NH<sub>3</sub>-N), nitrate-nitrogen (NO<sub>3</sub>-N), phosphorus (P), *E. coli*, and trihalomethanes (THM). The percentage of removal for each parameter was calculated using Eq. (4):

$$\text{Percentage of removal} = \frac{(C_f - C_p)}{C_f} \times 100\% \quad (4)$$

where  $C_f$  and  $C_p$  are the specific parameter's concentration in the feed water sample and treated effluent, respectively. The measurement for each sample was tested in triplicates.

## 3. RESULTS AND DISCUSSION

### 3.1 Characterization of the Raw Effluent

The characteristics of the raw effluent samples were summarized in Table 1. The data was obtained from 17 samples to minimize analytical error. The raw effluent contained a high quantity of *E. coli* in that had far exceeded the water reuse standard for any non-potable applications. High quantity of *E. coli* has high potential to be a health hazard. Hence, direct use of the raw effluent for any purpose is not suggested without an appropriate disinfection treatment. On the other hand, the wide range of the raw effluent quality indicated the need for a pre-treatment process prior to the primary disinfection unit for better disinfection performance.

Table 1: Characteristics of the raw effluent samples

Parameter	Unit	Effluent quality
Temperature	°C	21.93-28.90
pH	-	7.05-8.21
TSS	mg/L	2-21
NH <sub>3</sub> -N	mg/L	10.00-24.03
NO <sub>3</sub> -N	mg/L	0.02-1.11
P	mg/L	0.50-3.71
COD	mg/L	27-59
THM	µg/L	112.00-246.98
<i>E. coli</i>	CFU/100 mL	608-635000
BOD <sub>5</sub>	mg/L	4-8

## 3.2 Preliminary Study

### 3.2.1 UV Disinfection

Two raw effluent samples: Sample 1 with low number of *E. coli* (~700 CFU/100 mL) and Sample 2 with high number of *E. coli* (~26000 CFU/100 mL) were sampled at different sampling periods and used as the feed water samples for the UV disinfection preliminary study. Figure 3 depicted the results obtained from the UV disinfection preliminary study. As shown in Fig. 3, 5 minutes of UV exposure time is sufficient to totally disinfect *E. coli* in Sample 1. For 5 minutes of UV exposure time, 28.14 mWs/cm<sup>2</sup> of UV dosage has been transmitted with average UV transmittance (UVT) of 72.27%. Previous study conducted by Wahid et al (2012) reported that the UV dosage needed to inactivate 1-3 log of *E. coli* in secondary wastewater effluent was in the range of 27.80 – 83.40 mWs/cm<sup>2</sup> [18]. Hence, UV dosage of 28.14 mWs/cm<sup>2</sup> used in this study was in good agreement for the UV dosage applied for disinfection.

However, 5 minutes of UV exposure time is not able to produce *E. coli* free effluent for Sample 2. 500 CFU/100 mL *E. coli* still remained in the treated effluent after exposure to 5 minutes of UV light. Hence, the UV exposure time was further prolonged. By referring to Fig. 3, 30 minutes of UV exposure time is required to fully disinfect raw effluent which contained a high quantity of *E. coli* (4.4 log). The UV dosage applied for 30 minutes of exposure time was 168.86 mWs/cm<sup>2</sup>. It was in line with the finding obtained by Anastasi et al (2013), where 40-80 mWs/cm<sup>2</sup> of UV dosage was required to inactivate 1.7-1.9 log *E. coli* from secondary treated effluent [19]. Hence, approximately 160 mWs/cm<sup>2</sup> of UV dosage is required to inactivate 4 log of *E. coli* in raw effluent.

As a conclusion for the UV disinfection preliminary study, UV dosage of 28.14 mWs/cm<sup>2</sup> produced from 5 minutes of UV exposure time is sufficient for effluent containing low quantity of *E. coli*. On the other hand, UV dosage of 168.86 mWs/cm<sup>2</sup> produced from 30 minutes of UV exposure time is recommended to be applied for the single UV disinfection unit, where high UV radiation was required to penetrate through the effluent with low water quality or having huge quantity of *E. coli*.

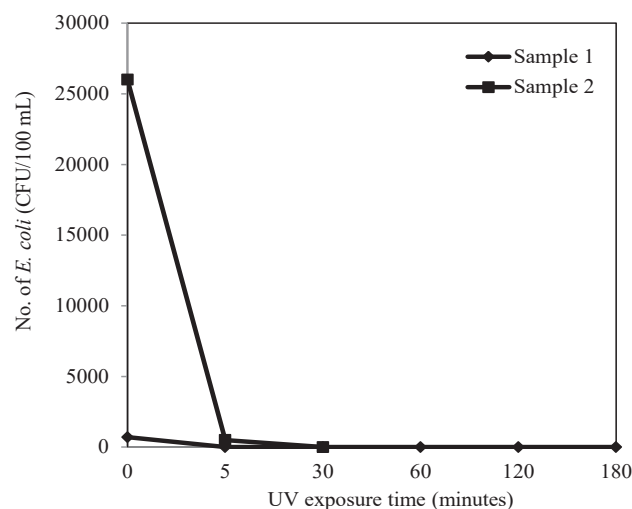
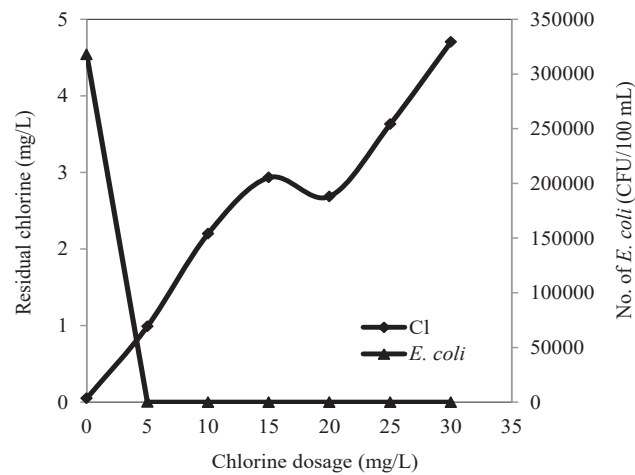


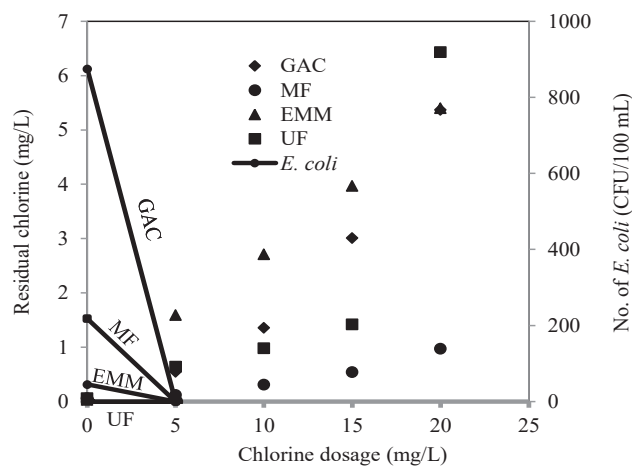
Fig. 3: Effect of UV exposure time towards *E. coli* removal for different raw effluent quality.

### 3.2.2 Chlorination

The raw effluent samples underwent a chlorination breakpoint study to determine the optimum chlorine dosage applied for the single disinfection unit and subsequently, the integrated disinfection system. Figure 4 showed the chlorination curve profile for both the raw effluent and the samples pre-treated with GAC, EMM, MF, and UF. As presented in Fig. 4, the chlorination curve profile for a single chlorination unit showed a typical “hump-and-dip” pattern. The “hump” zone with a peak appeared at 15 mg/L chlorine dosage corresponded to the formation of chloramines compounds in chlorinated raw effluent after chlorine reacted with inorganic reducing compounds [20]. Chloramine compounds were formed through the oxidation-reduction and substitution reactions between hypochlorite available in  $\text{Ca}(\text{ClO})_2$  (chlorine source in this study) and ammonia or ammonia-like compounds, such as amines groups, present in the raw effluent [20]. The destruction of chloramine compounds subsequently occurred at higher chlorine dosage as the chlorination curve profile switched to the “dip zone”. The ammonia or ammonia-like compounds were oxidized by chlorine and produced nitrogen-free gas [21]. This phenomenon caused the concentration of residual chlorine in raw effluent to decline.



(a)



(b)

Fig. 4: Chlorination curve profile for (a) raw effluent and (b) pre-treated raw effluent.

The minimum point of the “dip zone” in the chlorination curve profile is known as the chlorination breakpoint. It indicated the minimum chlorine dosage required in a chlorination process to react with organic and inorganic substances contained in the water sample and to disinfect the bacteria as it contained persistent chloramines that had not yet been destroyed. By referring to the chlorination curve profile in Fig. 4(a), the chlorination breakpoint for the single chlorination unit is 20 mg/L. The feasibility of using 20 mg/L chlorine dosage to disinfect raw effluent in the single chlorination unit is confirmed with the absence of *E. coli* in the treated effluent after 30 minutes of chlorination contact time.

On the contrary, a distinct chlorination curve profile was observed for the raw effluent pre-treated with GAC, EMM, MF, and UF in Fig. 4(b) where no chlorination breakpoint was detected. Pre-treatment using GAC, EMM, MF, and UF was expected to improve the quality of the raw effluent, thus reducing the chlorine dosage to react with reducing compounds, ammonia, and nitrogenous organics in the pre-treated effluent. Referring to chlorination curve profile in Fig. 4(b), no *E. coli* was detected in pre-treated raw effluent dosed with 5 mg/L of chlorine after 30 minutes chlorination contact time. Hence, 5 mg/L of chlorine dosage is recommended to treat the pre-treated raw effluent in the integrated disinfection system that had been pre-treated with GAC, EMM, MF, or UF.

### 3.3 Performance Study of the Single Disinfection Unit

Table 2 summarizes the treated effluent quality for single disinfection unit, while Fig. 5 shows the performance of the single disinfection unit on each measuring parameters. As shown in Fig. 5, most of the single disinfection units achieved outstanding performance on *E. coli* removal where no *E. coli* was detected in the treated effluent. The UV dosage (168.86 mWs/cm<sup>2</sup>) and chlorine dosage (20 mg/L) determined from preliminary study were effective in producing treated effluent free with *E. coli*. Similarly, MF and UF membranes that have smaller pore diameter than the size of *E. coli* (2.1 µm in length and 0.6 µm in width) also successfully acted as barrier to prevent the penetration of *E. coli* and suspended solids (> 0.45 µm) through the membrane filtration unit [22]. The performance of MF and UF membranes in removing particulate matters such as *E. coli* and TSS from feed water is not affected by feed water quality. Both MF and UF membranes used in this study showed a superior performance for TSS removal where the percentage of removal was 100%. Meanwhile, no significant TSS removal was observed for chlorination and UV disinfection. This is expected since the mechanism of both chlorination and UV disinfection are just to destroy pathogens in the feed water sample. Unfortunately, the PVDF021M membrane failed to achieve total removal of *E. coli* in treated effluent even though its membrane diameter was smaller than that of the HVLP00010 membrane. This is because the PVDF021M membrane has a very porous surface morphology as compared to other commercial flat sheet membranes used in this study (depicted in Fig. 6). On the other hand, although the HVLP00010 membrane has a membrane pore diameter that is larger than the pore diameter of the PVDF021M membrane, the gridded morphology structure of the HVLP00010 membrane provided a better trapping capability than the HVLP00010 membrane, where the *E. coli* was not able to penetrate through the membrane with non-straight channels.

The trend of COD removal is analogous to TSS removal where membrane filtration has shown predominant impact compared to chlorination and UV disinfection. Similar trend is observed for both COD and TSS removal since COD is considered as part of TSS. According to Falsanisi et al. [23] the reduction of COD from feed solution using a membrane filtration process is attributed to the retaining of organic compounds by molecular sieving mechanism. It is surprising that the PVDF021M membrane (MF

membrane) rejects a higher percentage of COD than the PVDF1001M membrane and the PES20kDa membrane (UF membranes) with smaller membrane pore diameters. High permeate flux of the PVDF021M membrane could be the reason for this phenomenon. High permeate flux of the PVDF021M membrane contributed to fast development of a fouling layer on top of the PVDF021M membrane surface. The developed fouling layer acted as an additional barrier to the PVDF021M membrane, eventually leading to higher removal efficiency by prohibiting more organic matter from passing through the membrane. Meanwhile, no significant COD removal was observed for chlorination and UV disinfection.

Table 2: Raw effluent quality after treated with single disinfection unit obtained from two samples.

Parameter	Unit	MF		UF		UV	Chlorination
		HVLP00010	PVDF021M	PVDF1001M	PES20kDa		
Temperature	°C	26.27±2.67	24.49±1.29	26.05±0.75	27.13±2.03	27.08±0.82	22.96±0.41
pH	-	7.55±0.53	7.82±0.13	7.56±0.38	7.82±0.19	7.58±0.11	7.42±0.14
TSS	mg/L	0±0	0±0	0±0	0±0	15±4	12±5
NH <sub>3</sub> -N	mg/L	10.37±1.23	13.09±1.15	12.22±1.58	9.71±1.23	18.96±1.78	13.65±1.04
NO <sub>3</sub> -N	mg/L	0.83±0.28	0.55±0.27	0.93±0.19	0.79±0.28	1.55±0.57	0.33±0.23
P	mg/L	0.87±0.11	2.18±1.13	0.76±0.13	1.60±0.11	3.51±0.36	1.99±0.18
COD	mg/L	20±0	15±3	20±2	18±4	43±1	57±8
THM	µg/L	NA	NA	NA	NA	NA	223.84±49.84
<i>E. coli</i>	CFU/ 100 mL	ND < 1	341±176	ND < 1	ND < 1	ND < 1	ND < 1
BOD <sub>5</sub>	mg/L	2±0	4±1	1±0	1±0	2±1	1±0

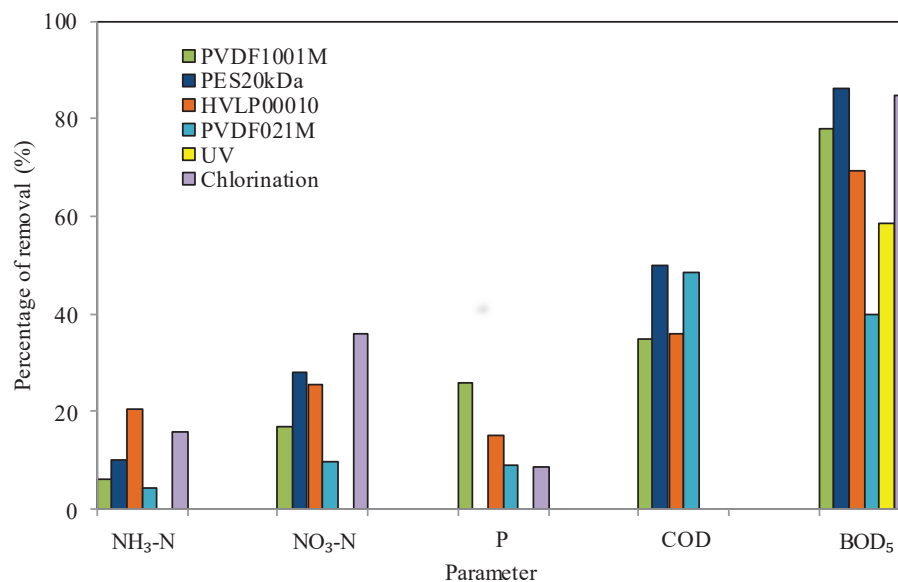


Fig. 5: Performance of single disinfection unit.

With regards to the BOD<sub>5</sub> removal illustrated in Fig. 5, the PVDF021M membrane contributed to the lowest BOD<sub>5</sub> removal, followed by UV disinfection, HVLP00010 membrane, PVDF1001M membrane, chlorination, and PES20kDa membrane with the removal percentage of 39.38, 58.70, 69.24, 77.95, 84.79, and 86.28%, respectively. Low

BOD<sub>5</sub> removal by the PVDF021M membrane is probably due to large membrane pore diameter and non-gridded structure of the membrane. Hence, the trapping capability of the PVDF021M membrane towards *E. coli* is the weakest among the other membranes. Whereas, the PES20kDa membrane with the smallest membrane pore diameter is most vulnerable for the rejection of microorganisms among other membranes. Meanwhile, the average removal of BOD<sub>5</sub> concentration by UV disinfection could have been influenced by the presence of activated *E. coli* after UV disinfection. The presence of residual organic substrate that has not been removed during UV disinfection supported the regrowth of *E. coli* in the treated effluents. In contrast, chlorination accomplished considerably high BOD<sub>5</sub> removal, which proved its capability as an oxidizing agent to oxidize organic compounds. In addition, unlike UV disinfection, microorganisms that have been inactivated by chlorination cannot undergo major repair mechanisms of damaged cells.

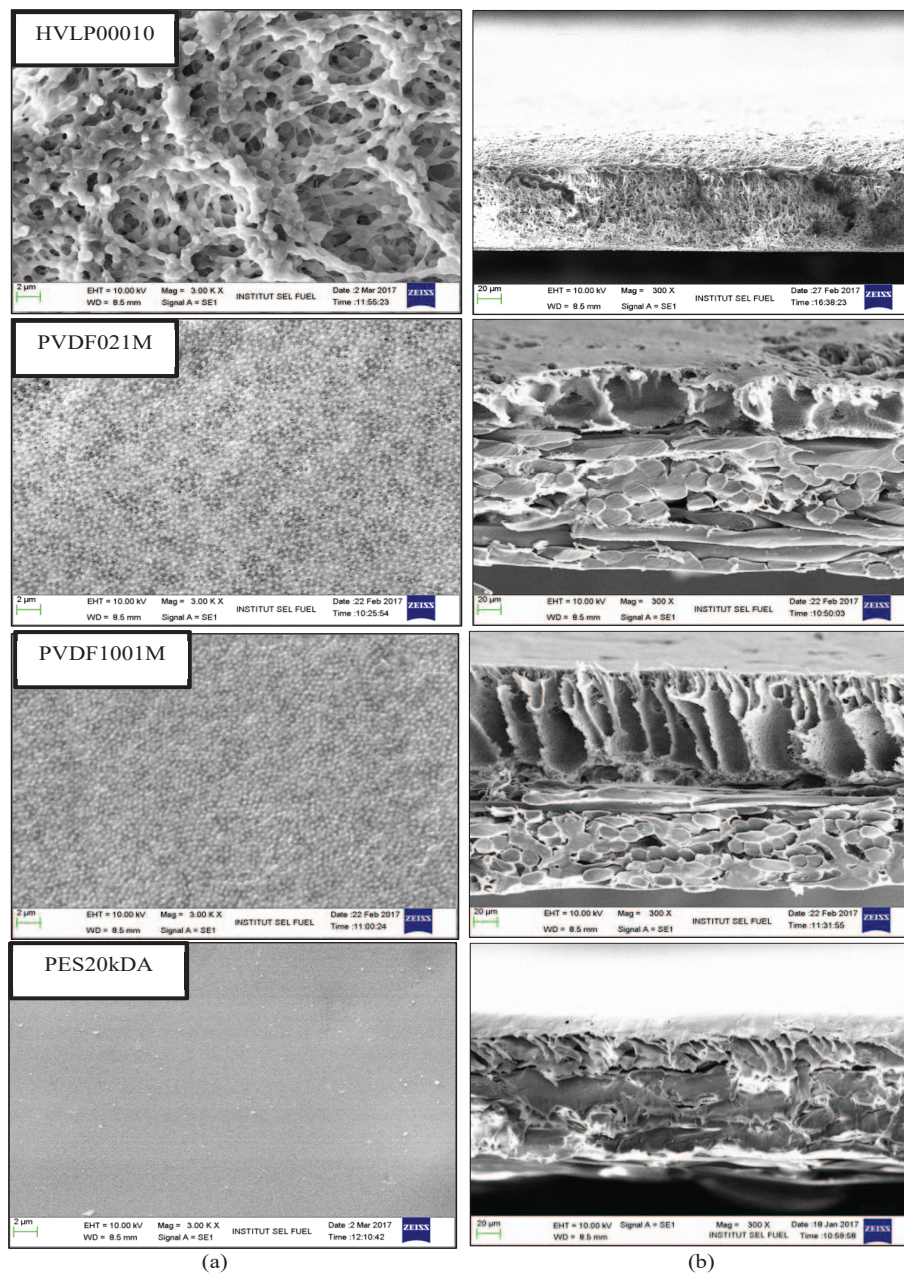


Fig. 6: (a) Surface morphology and (b) cross-sectional micrographs of flat sheet commercial membranes at the magnification of 3000x and 300x, respectively.

On the other hand, single disinfection units used in this study were not able to achieve a high percentage of nutrient ( $\text{NH}_3\text{-N}$ ,  $\text{NO}_3\text{-N}$ , and P) removal. Generally, both MF and UF membranes are not effective for the removal of dissolved natural organic matter (NOM), where the hydrodynamic particle size of dissolved NOM is smaller than the MF and UF membrane pore diameters [24]. However, the slight removal of the nutrients could be attributed to nitrogen-containing anions ( $\text{NO}_3^-$ ) and orthophosphate ( $\text{PO}_4^{3-}$ ) that are possibly rejected due to the partial repulsion caused by the negatively charged membranes. Membrane surface charge was indicated by the surface zeta potential value presented in Fig. 7 [25]. As presented in Fig. 7, all flat sheet commercial membranes used in this study were negatively charged and increased at the trend of PVDF021M < PVDF1001M < PES20kDa < HVLP00010. Although the HVLP00010 membrane is a MF membrane with larger pore diameter, the segmented morphology of the HVLP00010 membrane has provided good trapping capability to the membrane in improving its rejection efficiency. Meanwhile, UV radiation, which only affects the pathogens, is not able to contribute in nutrient removal. Chlorination showed a better performance on nutrient removal as compared to UV radiation in which the percentage of removal for  $\text{NH}_3\text{-N}$ ,  $\text{NO}_3\text{-N}$ , and P was 15.71, 36.00, and 8.67%, respectively. Still, the percentage of removal of  $\text{NH}_3\text{-N}$ ,  $\text{NO}_3\text{-N}$ , and P is still not as high as expected. Theoretically, the destruction of chloramine by free chlorine at chlorination breakpoint concentration will release nitrogen ( $\text{N}_2$ ) gas and allowed for the oxidation of  $\text{NH}_3$ . However, there is only a slight “dip” zone in the chlorination curve profile for our study. As a result, less chloramine was destructed by the limited available free chlorine, resulting in slight removal of  $\text{NH}_3\text{-N}$  and  $\text{NO}_3\text{-N}$  (15.71 and 36.00% of removal, respectively).

The effectiveness of the chlorination process is always compensated by the coupling of carcinogenic disinfection by-products such THM [26]. Table 3 showed the concentration of four THM compounds including chloroform ( $\text{CHCl}_3$ ), bromodichloromethane ( $\text{CHBrCl}_2$ ), dibromochloromethane ( $\text{CHBr}_2\text{Cl}$ ), and bromoform ( $\text{CHBr}_3$ ) presented in raw effluent and chlorination treated effluent. High concentration of  $\text{CHCl}_3$  in the feed solution has contributed to the high concentration of  $\text{CHCl}_3$  in the treated effluent after the chlorination process, exceeding the Ministry of Health (MOH) Malaysia guidelines. Thus, the utilization of chlorination treated effluent could be risky and harmful. Therefore, pre-treatment prior chlorination is necessary where a suitable pre-treatment method is expected to reduce the THM value of feed solution.

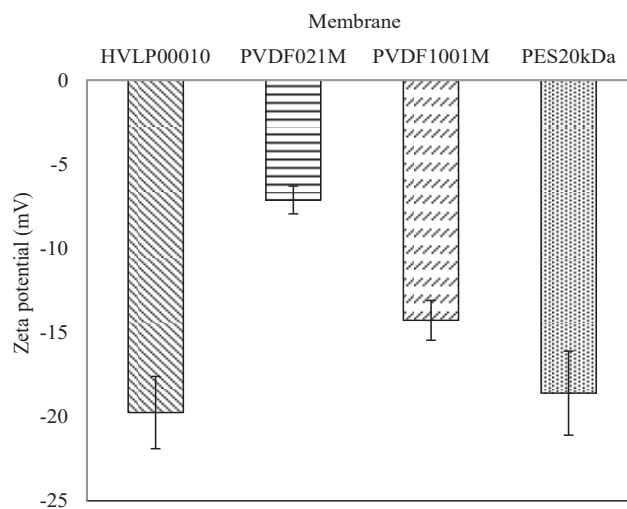


Fig. 7: Membrane surface charge for the commercial flat sheet membranes.

Table 3: THM concentration in raw effluent, chlorination treated effluent, and MOH guidelines

Compound	Raw effluent [µg/L]	Chlorination treated effluent [µg/L]	MOH guidelines [µg/L]
CHCl <sub>3</sub>	213.70±33.07	222.02±51.66	200
CHBrCl <sub>2</sub>	0.45±0.24	1.11±1.11	100
CHBr <sub>2</sub> Cl	0.28±0.28	0.65±0.65	100
CHBr <sub>3</sub>	0.61±0.61	0.07±0.07	60

Among the single disinfection units, the PES20kDa membrane with the smallest membrane pore diameter had shown the highest rejection in most of the parameters where the percentage of removal for *E. coli*, TSS, COD, BOD<sub>5</sub>, NH<sub>3</sub>-N, NO<sub>3</sub>-N, and P was recorded as 100.00, 100.00, 49.77, 86.28, 9.80, 27.88, and 42.27%, respectively. Since PES20kDa membrane filtration unit was able to remove part of the nutrients and suspended solids, it was used as the pre-treatment coupled with either UV disinfection or chlorination unit (primary disinfection process) in integrated disinfection system to further enhance the effectiveness of the primary disinfection process and to improve the water quality of the treated effluent.

### 3.4 Performance Study of the Integrated Disinfection System

Table 4 and Table 5 summarize the treated effluent quality from the integrated disinfection system using chlorination as primary disinfection unit and treated effluent quality from the integrated disinfection system using UV as primary disinfection unit. Meanwhile, the performance of both integrated disinfection systems is illustrated in Fig. 8.

Table 4: Treated effluent quality from integrated disinfection system using chlorination as primary disinfection unit obtained from two samples.

Parameter	Unit	UF-CI		GAC-CI		EMM-CI	
		Influent	Effluent	Influent	Effluent	Influent	Effluent
Temp.	°C	25.67±2.93	25.03±1.97	23.12±0.12	22.90±0.80	26.17±2.93	22.10±0.60
pH	-	7.70±0.18	7.20±0.04	7.33±0.11	7.69 ±0.05	7.21±0.22	7.13±0.38
TSS	mg/L	2±0	0±0	4±2	1±1	4±1	2±1
NH <sub>3</sub> -N	mg/L	12.08±2.08	1.92±1.79	11.50±3.80	7.25±4.45	7.76±7.54	6.00±6.00
NO <sub>3</sub> -N	mg/L	0.70±0.39	1.13±0.00	1.10±0.00	0.62±0.47	0.74±0.32	0.80±0.31
P	mg/L	1.63±1.13	1.70±0.02	1.99±1.21	3.82±0.15	2.05±1.15	1.75±0.87
COD	mg/L	35±2	23±5	31±1	15±1	63±31	27±0
THM	µg/L	215.04±34.20	171.81±2.73	215.04±34.20	161.52±37.04	215.04±34.20	177.44±2.54
<i>E. coli</i>	CFU/ 100 mL	9004±8396	ND < 1	26850±26150	ND < 1	22276±4276	ND < 1
BOD <sub>5</sub>	mg/L	7±1	0±0	5±1	0±0	3±1	0±0

With regards to the *E. coli* removal presented in Fig. 8, almost all integrated disinfection systems are successful in producing treated effluent with no *E. coli* contamination. This result indicated that 5 mg/L chlorine dosage and 58.43 mWs/cm<sup>2</sup> UV dosage determined from preliminary study are able to disinfect all *E. coli* detected in raw effluent with the assistance of a pre-treatment unit. It is known that the performance of chlorination and UV disinfection greatly depends on the turbidity of the feed solution [27]. As mentioned by Winward et al (2008), the removal of TSS constituents from water

samples could reduce the shielding effect which restricted the chlorine from accessing the cellular components of *E. coli* [28]. Similarly, low TSS content in the water sample allow the direct transmittance of UV light towards the targeted microorganisms for disinfection purposes. Hence, PES20kDA, GAC, and EMM pre-treatment units which help to reduce the TSS content in raw effluent had eventually helped in increasing the efficiency of chlorination and UV disinfection processes in integrated disinfection systems.

Table 5: Treated effluent quality from integrated disinfection system using UV as primary disinfection unit obtained from two samples.

Parameter	Unit	UF-UV		GAC-UV		EMM-UV	
		Influent	Effluent	Influent	Effluent	Influent	Effluent
Temp.	°C	25.67±2.93	26.35±2.25	26.17±2.93	22.10±2.00	26.17±2.93	26.50±2.80
pH	-	7.70±0.18	7.63±0.17	7.21±0.22	7.54±0.29	7.21±0.22	7.59±0.32
TSS	mg/L	2±0	0±0	4±1	1±1	4±1	3±2
NH <sub>3</sub> -N	mg/L	12.08±2.08	6.72±0.62	7.76±7.54	5.60 ±5.60	7.76±7.54	7.07±7.07
NO <sub>3</sub> -N	mg/L	0.70±0.39	1.11±0.01	0.74±0.32	0.11±0.07	0.74±0.32	0.66±0.46
P	mg/L	1.63±1.13	0.42±0.91	2.05±1.15	2.21±1.35	2.05±1.15	0.97±0.82
COD	mg/L	35±2	23±2	63±31	50 ±40	63±31	56±27
<i>E. coli</i>	CFU/ 100 mL	9004±8396	ND < 1	35500±17500	ND < 1	22276±4276	9±9
BOD <sub>5</sub>	mg/L	7±1	2±1	3±1	3±1	3±1	1±1

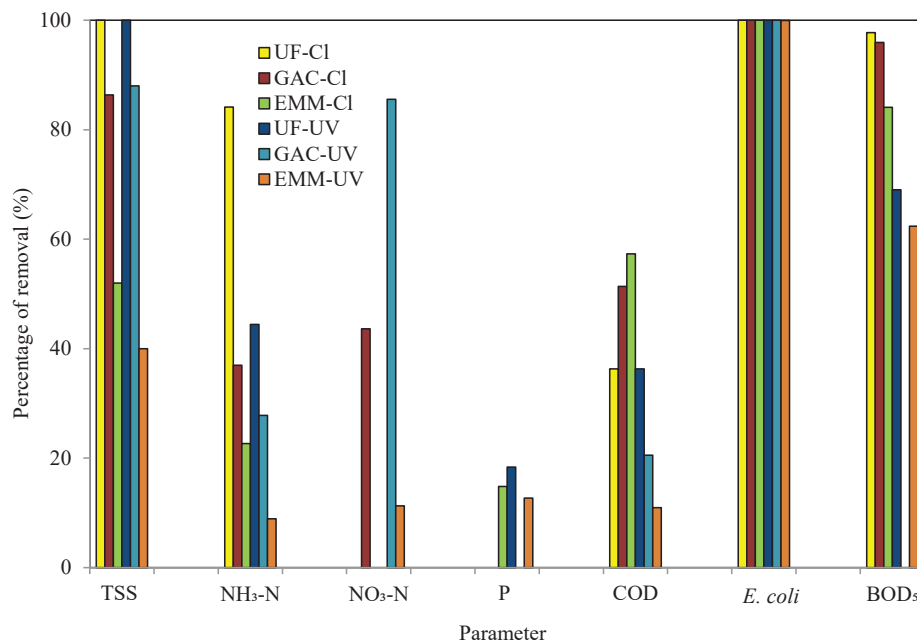


Fig. 8: Performance of integrated disinfection system.

As a comparison for TSS removal, the UF membrane is the most promising pre-treatment unit that had greatly reduced the TSS content in raw effluent through sieving effect. Therefore, greatest TSS removal is achieved by the integrated disinfection system using the UF membrane as a pre-treatment unit. The performance of an integrated disinfection system on TSS removal is followed the trend of EMM < GAC < UF. EMM and GAC pre-treatment units use the same type of adsorbent. However, the percentage of TSS removal for the EMM pre-treatment unit is slightly lower as compared to the GAC

pre-treatment unit due to the loose packing of adsorbents in the EMM column. Fewer adsorption sites are available for the attachment of suspended solids, thus contributing to lower efficiency of the EMM pre-treatment unit.

With regards to the COD removal presented in Fig. 8, the integrated disinfection system using chlorination as primary disinfection unit revealed higher COD removal as compared to the integrated disinfection system using UV as primary disinfection. Besides, it is found that the trend of COD removal by integrated disinfection system using UV as primary disinfection unit is analogous to the trend of TSS removal. Hence, with higher TSS removal by UF membrane filtration unit, greater COD removal is observed for UF-UV. However, a different trend of COD removal is observed for the integrated disinfection system using chlorination as a primary disinfection unit, where the COD removal is decreased in the sequence of EMM-Cl < GAC-Cl < UF-Cl. This trend basically depends on chlorine demand needed by the system. High removal efficiency of UF pre-treatment towards organic matters has contributed to higher quality of pre-treated effluent. With the same chlorine dosage in each integrated disinfection system using chlorination as a primary disinfection system, there will be excess free residual chlorine in UF-Cl. This will eventually lead to higher COD value in UF-Cl as the excess free residual chlorine is part of the factor contributing to COD concentration. Whereas, for EMM and GAC pre-treatment where the efficiency is not so high, the remaining organic matter in the pre-treated effluent are bonded with free chlorine, therefore greatly reducing the COD concentration in the treated effluent.

For BOD<sub>5</sub> removal, all integrated disinfection systems using chlorination as a primary disinfection unit successfully resulted in treated effluent with high BOD<sub>5</sub> removal. The BOD<sub>5</sub> removal followed the trend of EMM-Cl < GAC-Cl < UF-Cl. High removal of BOD<sub>5</sub> by integrated disinfection systems using chlorination as the primary disinfection unit is due to the effectiveness of the pre-treatment unit and also the chlorination process, where the chlorination process is able to disinfect the microorganisms contained in the raw effluent. Comparatively, integrated disinfection systems using UV as a primary disinfection unit had lower BOD<sub>5</sub> removal than integrated disinfection systems using chlorination as a primary disinfection unit. This is because although UV has the function of disinfecting the microorganisms in the raw effluent, its efficiency is not as high as chlorination. On the other hand, low percentage removal of BOD<sub>5</sub> for GAC-UV is influenced by the high P content in GAC-UV treated effluent. High P content in treated effluent will speed up eutrophication, support the microorganisms (recovered *E. coli* or non-disinfected pathogens) for cell synthesis and energy transport, thus accelerating the microbial activity to consume more DO and lower the BOD<sub>5</sub> removal [29,30].

With regards to nutrient (NH<sub>3</sub>-N, NO<sub>3</sub>-N, and P) removal as depicted in Fig. 8, a wide range of nutrient removal was obtained by the integrated disinfection systems used in this study. The percentage of NH<sub>3</sub>-N, NO<sub>3</sub>-N, and P removal was at the range of 8.90-84.15, 0.00-85.55, and 0.00-18.36%, respectively. The percentage of nutrient removal greatly depended on the pre-treatment efficiency and dosage applied in the primary disinfection unit. UF-UV presented the greatest NH<sub>3</sub>-N removal among integrated disinfection system using UV as primary disinfection. Nitrification process (depicted in Eq. (5)) is expected to occur during pre-treatment of UF-UV. Long membrane filtration time increased the DO level in pre-treated effluent due to continuous flow of retentate back to the inlet tank. With the added oxygen into the effluent, NH<sub>3</sub>-N is converted into NO<sub>3</sub>-N.



This postulation is supported by the addition of  $\text{NO}_3\text{-N}$  content in treated effluent by UF-UV and UF-Cl, in which no  $\text{NO}_3\text{-N}$  removal was achieved. Whereas, GAC and EMM pre-treatment showed inconsistent performance in treating nutrients. This could be because GAC and EMM are insufficient in providing effective adsorption sites for the nutrient adsorption. However, more activated carbon contained in the GAC column provided larger effective adsorption sites for the nutrients to adsorb onto it and therefore had greater adsorption capacity as compared to the EMM column. Comparatively, the integrated disinfection system using chlorination as primary disinfection unit generally exhibited higher  $\text{NH}_3\text{-N}$  removal than integrated disinfection system using UV as primary disinfection unit. The addition of  $\text{Ca}(\text{OCl})_2$  in the chlorination process has increased the oxidation level in pre-treated effluent [10]. Hence, a higher amount of  $\text{NH}_3\text{-N}$  was removed from the raw effluent through the nitrification process (as indicated by Eq. (5)).

With regards to P removal, only a low amount of P is able to be removed by integrated disinfection systems using EMM as pre-treatment. Although much research reported that GAC has the capability to adsorb P, the leaching of P from the GAC surface into treated effluent due to weak physical attachment of P onto the GAC surface during its synthesis process has opposed the removal of P from raw effluent. However, P leaching effect was less significant in the EMM pre-treatment unit as the GAC content in the EMM column was less than that of the GAC column. Meanwhile, the inconsistent P removal by integrated disinfection system using UF as a pre-treatment unit could be due to the PES20kDa membrane surface defect.

As compared to single the disinfection unit, the integrated disinfection system using chlorination as a primary disinfection unit is able to reduce the THM content in the treated effluent. This could be attributed to the existence of a pre-treatment unit in the integrated disinfection system. Pre-treatment such as UF, GAC, and EMM manage to remove part of THM and NOM from raw effluent either by physical sieving mechanism or adsorption. NOM is the precursor for THM formation [31]. Lower THM concentration in pre-treated effluent and less NOM for the further formation of THM will therefore reduce the THM concentration in treated effluent from the integrated disinfection system using chlorination as a primary disinfection unit. The treated effluent from the integrated disinfection system using chlorination as primary disinfection unit is able to comply with MOH guidelines. Thus, the treated effluent is safe for recycle and reuse purposes.

### 3.5 Treated Effluent Quality Compared to Water Reuse Guidelines

To date, no water reuse guideline has been developed by Malaysian authorities to facilitate the recycling and reuse of treated water in Malaysia. Attributed to this, several water reuse guidelines presented in Table 6 - United States Environmental Protection Agency (US EPA) water reuse guidelines and Singapore grey water quality were chosen as the benchmark to determine the adaptability of treated water quality for reuse purposes [11,32]. The US EPA water reuse guidelines is an international guideline that has been widely recognized for water reuse in restricted area applications and unrestricted area applications. As these US EPA water reuse guidelines might not be representative of the Asia climate, Singapore grey water is a water reuse program tailored strictly for flushing of water closets and urinals, general washing (excluding high pressure jet washing and general washing at market and food establishments), irrigation (excluding irrigation sprinklers), and cooling tower makeup water [32].

Table 6: Water reuse guidelines

Parameter	US EPA [11]		Singapore grey water [32]
	Restricted area	Unrestricted area	
pH	6-9	6-9	6-9
BOD <sub>5</sub> [mg/L]	≤ 30	≤ 10	< 5
COD [mg/L]	-	-	-
Turbidity [NTU]	-	≤ 2	< 2
TSS [mg/L]	≤ 30	≤ 5	-
<i>E. coli</i> [CFU/100 mL]	-	-	ND
Fecal coliform [CFU/100 mL]	≤ 200	ND	-
NO <sub>3</sub> -N [mg/L]	-	-	-
NH <sub>3</sub> -N [mg/L]	-	-	-
Total THMs [µg/L]	-	-	-

Table 7: Adaptability of treated effluent from each system for water recycling and reuse

System	USEPA		Singapore grey water
	Restricted area	Unrestricted area	
HVLP00010	✓	✓	✓
PVDF021M			
PVDF1001M	✓	✓	✓
PES20kDa	✓	✓	✓
Chlorination	✓		✓
UV	✓		✓
UF-UV	✓	✓	✓
GAC-UV	✓	✓	✓
EMM-UV	✓		
UF-CI	✓	✓	✓
GAC-CI	✓	✓	✓
EMM-CI	✓	✓	✓

Table 7 summarizes the adeptness of treated effluent from each system for water recycling and reuse. As presented in Table 7, almost all treated effluent from single disinfection complied with the US EPA water reuse guidelines at restricted areas except for the final effluent given by the PVDF021M membrane. This means that treated effluents from the HVLP0010 membrane, PVDF1001M membrane, PES20kDa membrane, chlorination, and UV disinfection are suitable for reuse as irrigation water (restricted area), agricultural reuse (food crops commercially processed and non-food crops), landscape impoundments, and construction. However, only treated effluents by the HVLP0010 membrane, PVDF1001M membrane, and PES20kDa membrane are able to meet US EPA water reuse guidelines for unrestricted areas. These treated effluents have added value for urban reuse, recreation, and agricultural purposes (food crops commercially processed and food crops not commercially processed). UV and chlorination are only recommended for restricted area applications due to the presence of high TSS content in treated effluent. Whereas, permeate filtered from the PVDF021M membrane did not comply with US EPA water reuse guidelines for both unrestricted areas and restricted areas. There was still a high number of *E. coli* ( $341 \pm 176$  CFU/100 mL)

remaining in the treated effluent after filtering with the PVDF021M membrane. For integrated disinfection systems, almost all integrated disinfection systems complied with US EPA water reuse guidelines for unrestricted area applications except the integrated disinfection system of EMM-UV due to the presence of *E. coli*.

The adaptability of treated effluent with Singapore grey water quality presented the same trend as its adaptability with US EPA water reuse guidelines for restricted area. All disinfection units and integrated disinfection systems complied with the parameter range except the PVDF021M membrane, and integrated disinfection system of EMM-UV. Although single PVDF021M membrane and integrated disinfection system of EMM-UV complied with pH and BOD<sub>5</sub> parameters of the Singapore grey water quality, high *E. coli* content in treated effluents make them fail to comply. Thus, treated effluent from these disinfection systems are not recommended for grey water reuse purposes [32].

#### 4. CONCLUSION

- The PES20kDa membrane with the smallest membrane pore diameter was the most effective single disinfection unit with the highest rejection in most of the parameters where the percentage of removal for *E. coli*, TSS, COD, BOD<sub>5</sub>, NH<sub>3</sub>-N, NO<sub>3</sub>-N, and P were 100.00, 100.00, 49.77, 86.28, 9.80, 27.88, and 42.27%, respectively.
- Almost all single disinfection units complied with the US EPA water reuse guidelines at restricted areas for the application of irrigation (restricted area), agricultural reuse (food crops commercially processed and non-food crops), landscape impoundments, construction, and industrial reuse except the PVDF021M membrane filtration unit.
- Additionally, high quality treated effluent by the HVLP0010 membrane, PVDF1001M membrane, and PES20kDa membrane are able to meet Singapore grey water quality, and US EPA water reuse guidelines at unrestricted area for urban reuse, recreation, and agricultural (food crops commercially processed and food crops not commercially processed) purposes.
- All integrated disinfection systems were effective in disinfecting the raw effluent where almost all of it achieved 100% *E. coli* removal in treated effluent. Comparatively, the integrated disinfection system using chlorination as primary disinfection unit has better performance than the integrated disinfection system using UV as primary disinfection unit.
- UF-Cl is the preferable integrated system for the greatest removal of most of the parameters from raw effluent. The percentage of removal for *E. coli*, TSS, COD, BOD<sub>5</sub>, NH<sub>3</sub>-N, NO<sub>3</sub>-N, and P by UF-Cl is 100.00, 100.00, 36.32, 97.74, 84.15, 0.00, and 0.00%, respectively.
- All integrated disinfection systems complied with the US EPA water reuse guidelines for restricted area application. However, only integrated disinfection systems of EMM-UV did not manage to fulfil the Singapore grey water quality, and US EPA water reuse guidelines for unrestricted area applications.

#### ACKNOWLEDGEMENTS

The authors wish to gratefully acknowledge the financial support of this work by Indah Water Konsortium (IWK) Sdn. Bhd. (KK-2018-005) and Dana Penyelidikan Strategik

(KRA-2017-06). The authors also wish to acknowledge Fuel Sel Institute, UKM for SEM analysis.

## REFERENCES

- [1] Mohamed RMSR, Nazmi AM, Arief MM, Hashim MKA. (2016) Conventional water filter (sand and gravel) for ablution water treatment, reuse potential, and its water savings. *J. Sustain. Dev.*, 9:35–43. doi:10.5539/jsd.v9n1p35
- [2] Academy of Sciences Malaysia. (2015) Study on the Current Issues and Needs for Water Supply and Wastewater Management in Malaysia. Volume 2. Kuala Lumpur. Retrieved from [https://issuu.com/asmpub/docs/wswm\\_volume\\_2](https://issuu.com/asmpub/docs/wswm_volume_2)
- [3] Alternative Water Resource to Potentially Reduce Water Footprint [<http://ensearch.org/wp-content/uploads/2013/10/PAPER-11-ALTERNATIVE-WATER-RESOURCES-AS-A-POTENTIAL-TO-REDUCE-WATER-FOOTPRINT.pdf>]
- [4] Cleaning the Unseen [<https://www.thestar.com.my/news/nation/2016/12/04/cleaning-the-unseen-from-the-tidak-apa-attitude-of-users-to-financial-gaps-former-indah-water-konsor/>]
- [5] Looking For Water [<https://www.thestar.com.my/news/environment/2014/06/16/looking-for-water/>]
- [6] Wahid MA, Tanaka H. (2012) Potential implementation of wastewater reclamation and reuse in Malaysia urban area. *Int. Sustain. Civ. Eng. J.*, 1(1):75–83.
- [7] Abarnou A, Miossec L. (1992) Chlorinated waters discharged to the marine environment chemistry and environmental impact. An overview. *Sci. Total Environ.*, 126:173–197. doi:10.1016/0048-9697(92)90490-J
- [8] Turtoi M. (2013) Ultraviolet light potential for wastewater disinfection. *Ann. Food Sci. Technol.*, 14(1):153–164. Retrieved from [https://www.researchgate.net/publication/264002288\\_Ultraviolet\\_light\\_potential\\_for\\_wastewater\\_disinfection](https://www.researchgate.net/publication/264002288_Ultraviolet_light_potential_for_wastewater_disinfection)
- [9] Rodriguez-Chueca J, Ormad MP, Mosteo R, Sarasa J, Ovelleiro JL. (2015) Conventional and advanced oxidation processes used in disinfection of treated urban wastewater. *Water Environ. Res.*, 87(3):281–288. doi:10.2175/106143014X13987223590362
- [10] UV Disinfection for Wastewater [<http://www.trojanuv.com/applications/wastewater/>]
- [11] U.S. Environmental Protection Agency. (2004) Guidelines for Water Reuse. Washington.
- [12] Grover D, Zhou J, Frickers P, Readman J. (2011) Improved removal of estrogenic and pharmaceutical compounds in sewage effluent by full scale granular activated carbon: impact on receiving river water. *J. Hazard Mater.*, 185(2-3):1005–1011. doi:10.1016/j.jhazmat.2010.10.005
- [13] Kim SD, Cho J, Kim IS, Vanderford BJ, Snyder SA. (2007) Occurrence and removal of pharmaceuticals and endocrine disruptors in South Korean surface, drinking, and waste waters. *Water Res.*, 41(5):1013–1021. doi:10.1016/j.watres.2006.06.034
- [14] Margot J, Kienle C, Magnet A, Weil M, Rossi L, de Alencastro LF, Abegglen C, Thonney D, Chevre N, Scharer M, Barry DA. (2013) Treatment of micropollutants in municipal wastewater: ozone or powdered activated carbon? *Sci Total Env.*, 461:480–498. doi:10.1016/j.scitotenv.2013.05.034
- [15] Gonzalez O, Bayarri B, Acena J, Perez S, Barcelo D. (2016) Treatment technologies for wastewater reuse: Fate of contaminants of emerging concern. In *Advanced Treatment Technologies for Urban Wastewater Reuse The Handbook of Environmental Chemistry*. Volume 45. Edited by Fatta-Kassinos D, Dionysiou D, Kummerer K. Cham, Springer; pp 5–38.
- [16] Morowitz HJ. (1950) Absorption effects in volume irradiation of microorganisms. *Science*, 111(2879):229–230. doi:10.1126/science.111.2879.229-a
- [17] Hallmich C, Gehr R. (2010) Effect of pre- and post-UV disinfection conditions on photoreactivation of fecal coliforms in wastewater effluents. *Water Res.*, 44: 2885–2893. doi:10.1016/j.watres.2010.02.003

- [18] Wahid MA, Kim I, Yamashita N, Tanaka H, Baki A. (2012) UV based process for *E. coli* and coliphage in secondary effluent for wastewater reclamation and reuse. Inst. Eng. Malaysia, 73:18–24. Retrieved from [https://www.myiem.org.my/content/iem\\_journal\\_2012-361.aspx](https://www.myiem.org.my/content/iem_journal_2012-361.aspx)
- [19] Anastasi EM, Wohlsen TD, Stratton HM, Katouli M. (2013) Survival of *Escherichia coli* in two sewage treatment plants using UV irradiation and chlorination for disinfection. Water Res, 47(17):6670-6679. doi:10.1016/j.watres.2013.09.008
- [20] March JG, Gual M. (2007) Breakpoint chlorination curves of greywater. Water Environ. Res, 79(8):828–832. doi:10.2175/106143007X156736
- [21] Jorgensen SE. (1993) Breakpoint chlorination. In The Removal of Nitrogen Compounds from Wastewater. Edited by Halling-Sorensen B, Jorgensen SE. Netherlands, Elsevier Science Publishers; pp. 295–304.
- [22] Martins JM, Majdalani S, Vitorge E, Desaunay A, Navel A, Guine V, Daian JF, Vince E, Denis H, Gaudet JP. (2013) Role of macropore flow in the transport of *Escherichia coli* cells in undisturbed cores of a brown leached soil. Environ. Sci. Process. Impact, 15(2):347–356. doi:10.1039/c2em30586k.
- [23] Falsanisi D, Liberti L, Notarnicola M. (2009) Ultrafiltration (UF) pilot plant for municipal wastewater reuse in agriculture: Impact of the operation mode on process performance. Water, 1:872–885. doi:10.3390/w2040872
- [24] Ang WL, Mohammad AW, Hilal N, Leo CP. (2015) A review on the applicability of integrated/hybrid membrane processes in water treatment and desalination plants. Desalination, 363: 2–18. Doi:10.1016/j.desal.2014.03.008
- [25] Mandzy N, Grulke E, Druffel T. (2005) Breakage of TiO<sub>2</sub> agglomerates in electrostatically stabilized aqueous dispersions. Powder Technology, 160(2):121-126. doi:10.1016/j.powtec.2005.08.020
- [26] Shah AD, Mitch WA. (2012) Halonitroalkanes, halonitriles, haloamides, and N-nitrosamines: A critical review of nitrogenous disinfection byproduct formation pathways. Environ. Sci. Technol., 46:119–131. doi:10.1021/es203312s
- [27] Farrell C, Hassard F, Jefferson B, Leziart T, Nocker A, Jarvis P. (2018) Turbidity composition and the relationship with microbial attachment and UV inactivation efficacy. Sci. Total Environ., 624:638–647. doi:10.1016/j.scitotenv.2017.12.173
- [28] Winward GP, Avery LM, Stephenson T, Jefferson B. (2008) Chlorine disinfection of grey water for reuse: Effect of organics and particles. Water Res., 42:483–491. doi:10.1016/j.watres.2007.07.042
- [29] Phosphorus and water. [<http://water.usgs.gov/edu/phosphorus.html>]
- [30] Zhang Y, Zhang G, Wang P, Wang Q. (2017) Disinfection of municipal secondary effluents with microwave-induced electrodeless ultraviolet irradiation for water reuse. J. Chem. Technol. Biotechnol., 92(5):1017–1025. doi:10.1002/jctb.5077
- [31] Hua G, Yeats S. (2010) Control of trihalomethanes in wastewater treatment. Florida Water Resour. J., April. Retrived from [https://www.fwrj.com/techarticles/0410\\_FWRJ\\_tech1.pdf](https://www.fwrj.com/techarticles/0410_FWRJ_tech1.pdf)
- [32] Technical Guide for Greywater Recycling System [<https://www.pub.gov.sg/Documents/greywaterTech.pdf>]

## INFLUENCE OF PALM OIL BIOMASS CLINKER AND EMPTY FRUIT BUNCH FIBERS ON CONCRETE PROPERTIES

MOHD HAZIMAN WAN IBRAHIM<sup>1\*</sup>, SAJJAD ALI MANGI<sup>2</sup>,  
SHARIFAH SALWA MOHD ZUKI<sup>1</sup>, RAMADHANSYAH PUTRA JAYA<sup>3</sup>,  
DADANG SUPRIYATNO<sup>4</sup>

<sup>1</sup>Jamilus Research Center, Faculty of Civil Engineering and Built Environment,  
Universiti Tun Hussein Onn Malaysia, 86400, Parit Raja, Johor, Malaysia

<sup>2</sup>Department of Civil Engineering, Mehran University of Engineering and Technology,  
SZAB Campus Khairpur Mir's, Sindh, Pakistan

<sup>3</sup>Department of Civil Engineering, College of Engineering,  
Universiti Malaysia Pahang, 26300, Kuantan, Pahang, Malaysia

<sup>4</sup>Faculty of Engineering, Universitas Negeri Surabaya, Indonesia.

\*Corresponding author: [haziman@uthm.edu.my](mailto:haziman@uthm.edu.my)

(Received: 3<sup>rd</sup> November 2019; Accepted: 22<sup>nd</sup> March 2020; Published on-line: 4<sup>th</sup> July 2020)

**ABSTRACT:** This study aims to evaluate the influence of palm oil empty fruit bunch (EFB) fibers on flexural strength performance of concrete in the presence of palm oil biomass clinker (POBC). This study considered various proportions of palm oil EFB fibers as 0%, 0.2%, 0.4%, and 0.6% in concrete with fixed amount of POBC as 10%. It was investigated that there is substantial influence of palm oil EFB fibers on properties of concrete containing 10% POBC as sand replacement. The experimental findings of this study indicated that the workability of fresh mix concrete decreases as palm oil EFB fiber content increased. Besides that, hardened properties of concrete were found to be improved as the amount of palm oil EFB fibers increased in the concrete. It was noticed that flexural strength was improved with addition of 0.2% palm oil EFB fibers that act as reinforcement and deliver growth in flexural strength for concrete containing 10% of POBC. Hence, it was concluded that palm oil EFB fiber could be utilized as fiber reinforcement in concrete to improve flexural strength performance of the concrete.

**ABSTRAK:** Kajian ini bertujuan mengkaji pengaruh gentian tandan kelapa sawit (EFB) terhadap kekuatan lentur pada konkrit dengan kehadiran klinker minyak kelapa sawit biomas (POBC). Kajian ini mengguna pakai pelbagai peratus serat EFB kelapa sawit dalam konkrit iaitu sebanyak 0%, 0.2%, 0.4%, dan 0.6% dengan jumlah tetap POBC sebanyak 10%. Didapati bahawa gentian tandan kelapa sawit EFB yang mengandungi 10% POBC berpengaruh besar sebagai pengganti pasir dalam bahan konkrit. Penemuan eksperimen menunjukkan bahawa keboleherjaan campuran baru konkrit berkurangan apabila kandungan gentian EFB minyak sawit meningkat. Selain itu, sifat-sifat mengeras pada konkrit didapati bertambah baik apabila jumlah gentian EFB minyak sawit meningkat dalam konkrit. Di samping itu, kekuatan lenturan meningkat dengan penambahan sebanyak 0.2% serat EFB minyak kelapa sawit, berfungsi sebagai penguat dan penambah kekuatan lenturan pada konkrit yang mengandungi 10% POBC. Oleh itu, serat EFB minyak kelapa sawit boleh digunakan sebagai penguat gentian dalam konkrit bagi meningkatkan kekuatan lenturan konkrit.

**KEYWORDS:** *bunch fiber; biomass clinker; compressive strength; flexural strength*

## 1. INTRODUCTION

The production of palm oil has been increased over the years. According to a recent report by the Malaysia Palm Oil Board (MPOB), crude palm oil production has increased from 24.91 to 28.64 million tons in a year [1]. This huge quantity of palm oil production left behind the waste by-products known as palm oil biomass clinker (POBC) and palm oil empty fruit bunch (EFB). In Malaysia, EFB is being utilized as a fertilizer for the agricultural field and POBC is being considered in concrete as cement and sand replacement material. POBC is a waste material produced through incineration of oil palm shells and mesocarp fiber as fuel for stream turbines in mills [2]. A massive quantity of POBC is usually dumped into landfills, which causes environmental problems. However, use of sustainable materials should be given immediate attention and emphasis on the sustainable development through adopting waste by-products into the potential construction material [3].

The POBC has a lower value of specific gravity and higher crushing value, which indicates its potentiality to be considered as an alternative source of fine aggregate. There is no pre-treatment or modification required for this material. The adoption of POBC as fine aggregate to some extent could save the depletion of natural resources [2]. Recent study was conducted by Wan Ibrahim et al. [4] on POBC as fine aggregate replacement in concrete with hooked-end steel fibers. They considered a 10% proportion of POBC to be an optimum replacement level of fine aggregates in concrete. However, this method can reduce the self-weight of concrete, which delivers lightweight and green and sustainable concrete. Beside that palm oil EFB fiber is one of the local natural fibers, which can easily be obtained at low cost and low level of energy either in manpower or technology. Hence, this study aims to investigate the influence of palm oil EFB fiber on the fresh and hardened concrete properties with 10% POBC as fine aggregate.

## 2. PREVIOUS RELATED RESEARCH

### 2.1 Effects of POBC on Concrete Properties

Concrete containing POBC as fine aggregate is influenced by the physical properties of POBA. However, POBC is a porous material that absorbs more water than normal aggregates, its water absorption was noted in the range of 4.7-26.5%, which deliver low workability concrete [5]. It was also declared by Ahmmad, et al. [6] that lightweight concrete can integrate more waste materials like crushed oil palm shell (OPS) as coarse aggregate and palm oil clinker (POC) as a replacement of fine aggregate. They declared that the modulus of elasticity was 23% higher in OPS concrete. The lower compressive strength of self-compacting concrete was observed when fully or partially coarse and fine aggregate were replaced with POC [2].

Gunasekaran et al. [7] considered Coconut shell concrete (CSC). They declared that workability and tensile and flexural strength were improved. Overall, CSC bond strength is comparable to that of normal and lightweight aggregate concretes. However, they further declared that coconut shells fulfil the provisions to be used as aggregate for lightweight concrete.

Abutaha et al. [8] investigated the compressive strength of concrete with palm oil clinker (POC) as coarse and fine aggregate. They declared that the amount of POC in the mix reduces the compressive strength of the concrete as shown in Fig. 1, which shows that the targeted compressive strength of Grade 40 concrete was achievable with 10% coarse aggregate replacement with POC. The strength declined by 11.73%, 16.79%, 18.94%,

19.66%, 21.60% and 30.37% at the replacement levels of 10%, 20%, 40%, 60%, 80% and 100% respectively. The maximum drop of strength was noticed with full replacement of coarse aggregate. Nevertheless, the compressive strength performance of concrete with POC as fine aggregate is far better than coarse aggregate replacement. It was observed that POC as fine aggregate can enhance the compressive strength as shown in Fig. 2. It indicated that at the replacement level of 10%, 20%, 40%, 60% and 100% the compressive strength was noticed as decreased by 4.07%, 4.43%, 0.15%, 0.80%, and 5.17%, respectively. However, compressive strength was found to be 5% improved at 80% replacement. These results show the potentiality of POC to be utilized as replacement of fine aggregate. Therefore, this study also considered the 10% replacement.

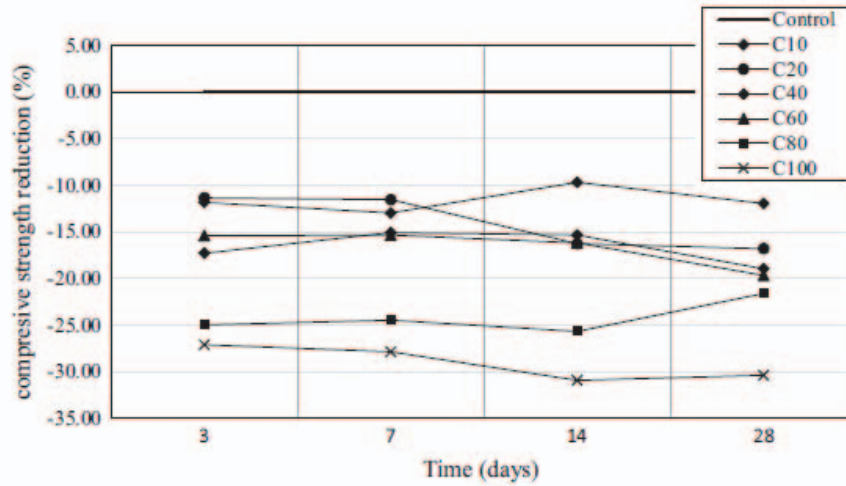


Fig. 1: Concrete strength performance with POC as replacement of coarse aggregates [8].

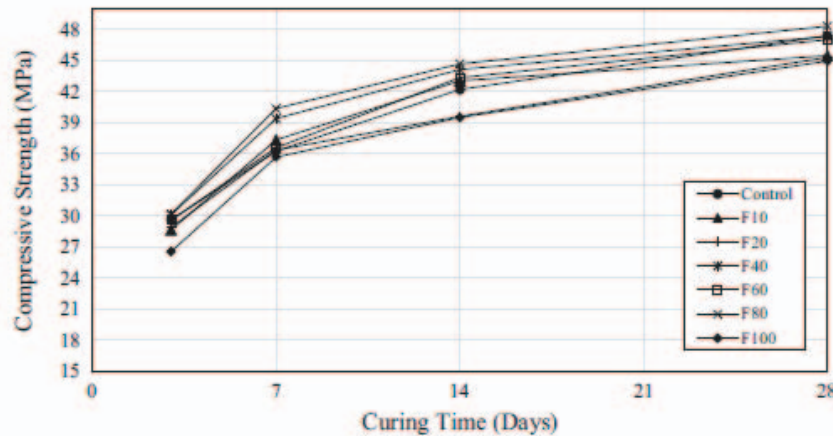


Fig. 2: Concrete strength performance with POC as replacement of fine aggregates [8].

Furthermore, Shahreen et al. [9] examined the flexural strength of concrete comprising POC as fine aggregate replacement. It showed a positive increment in flexural strength at early ages due to the presence of POC fine particles, which creates a pozzolanic reaction and densification of the concrete mix and enhanced internal bonds among aggregates and cement paste, resulting in the development of strength as seen in the results provided in Fig. 3. They declared that fine particles of POC occupy the free spaces in the

concrete and fill the voids, which delivers high density and also increases the stability of the concrete mix. It was noticed that the flexural strength of concrete was increased around 28% and 33% with incorporation of 5% and 10% of POBC as fine aggregates, respectively [9]. However, the opposite results were found with more than 10% of POBC [10]. The adverse influence was noticed with the utilization of POBC as coarse and fine aggregates in concrete.

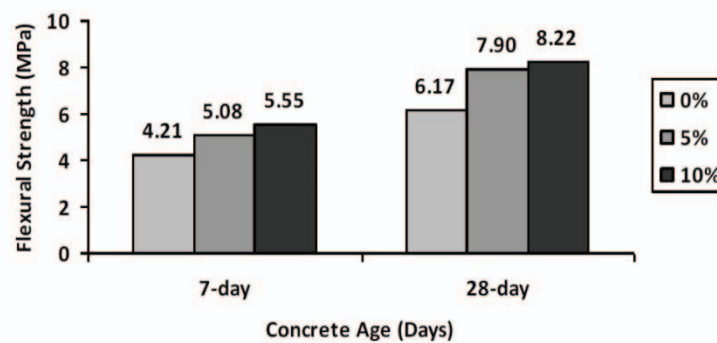


Fig. 3: Flexural strength result of POC concrete and conventional concrete [9].

From the literature review it can be concluded that the presence of POBC can affect the performance of concrete. Therefore, the flexural strength performance would be improved with the addition of fiber along with the 10% proportion of POBC as fine aggregate replacement.

## 2.2 Effects of Natural Fiber to Concrete

Particularly in tropical states like Malaysia and Indonesia, palm oil EFB are the abundant waste that is left behind after the fruits are stripped from fruit bunches for the oil extraction process [11]. EFB fiber is a type of fiber that is clean and free from pesticides. This fiber could be utilized in concrete to improve its performance. It was previously well known that the inclusion of fibers in concrete creates reinforced concrete that delivers better strength than normal concrete. For instance, previous research work has been summarized below on the fiber proportion and performance of concrete.

Sim et al. [12] investigated the influence of basalt fiber on structural concrete and found that basalt fiber is a good substitute for strengthening concrete structures. In addition, Kim et al. [13] considered two type of concretes; normal concrete and high-fluidity concrete. Whereas, they found that the addition of 1% jute fiber by volume in the normal strength concrete does not deliver significant increment, but in high-fluidity concrete it gives a substantial rise in compressive strength, around 55%, as compared to one without fiber. The compressive strength of 0% jute fiber content for high-fluidity concrete gives 25 MPa and for 0.5% of jute fiber content deliver about 42 MPa, which indicated that the presence of fibers could positively influence the concrete performance. Hence, it was generally observed that the flexural strength can be increased as the fiber content increased in concrete. However, presence of fiber can resist tensile load and increase the flexural strength.

### 3. MATERIALS AND METHODOLOGY

#### 3.1 Materials

Ordinary Portland cement (OPC) was used in this study. The coarse aggregates were collected from Muar, Johor, Malaysia. This study considered a 10 mm average of coarse aggregate. After collection, coarse aggregates were dried under open sun for few days so as to achieve saturated surface dry (SSD) conditions. However, the fine aggregates (sand) were transported from a river in Kahang, Johor, Malaysia. The fine aggregates were also dried for a few days under open sunlight so as to achieve saturated surface dry (SSD) conditions. Before mixing, the sand was sieved through a 5 mm sieve.

#### 3.2 Palm Oil Biomass Clinker

This study considered palm oil biomass clinker (POBC) as shown in Fig. 4, which was collected from a biomass steam plant located in Tanjung Langsat, managed by TPM Technopark Sdn Bhd. Initially, it was partially replaced by the fine aggregate (sand). The optimum replacement percentages of sand with POBC was chosen as 10% based previous studies [4]. Afterward, POBC were passed through a 5 mm sieve size. Furthermore, a random sample of POBC was investigated with a scanning electron microscope (SEM) for an understanding of its microstructure, as shown in Fig. 5. It was observed that POBC has micro voids that could affect the properties of concrete and create weak regions in the form of free voids. The presence of voids is the significant cause of reduction in strength of concrete. These voids also provide a gap between particles and result in weaker bonds in the hardened concrete. Some organic compounds were noticed on the surface of the POBC. It can be concluded that POBC contains voids and organic compounds that affect its porosity and low value of specific gravity.



Fig. 4: Palm oil biomass clinker.

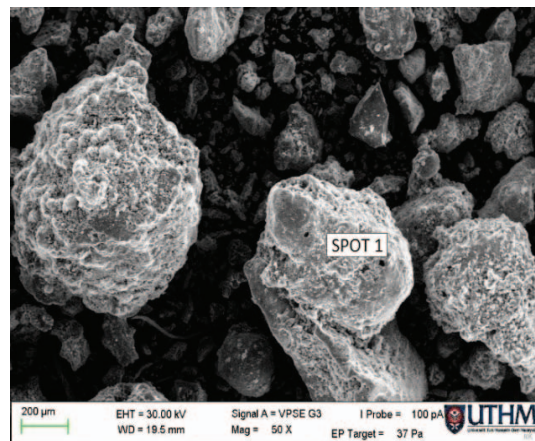


Fig. 5: SEM image of POBC.

#### 3.3 Palm Oil Empty Fruit Fibers

Palm oil empty fruit bunch (EFB) fibers, as shown in Fig. 6, were used in this study. The length of the palm oil EFB fiber was fixed at the range of 30 mm to 50 mm with a diameter of around 0.05 mm. The aspect ratio of the palm oil EFB fibers was in the range of 60 to 100 for better strength development.

#### 3.4 Experimental Procedure

In this study, normal concrete mix design was prepared for 25 MPa at 28 days with a fixed water-to-cement ratio of 0.50. A total of four mixes were prepared; one was the

reference mix with 10% POBC but without fibers and the other three contained varying amounts of palm oil EFB fiber at 0.2, 0.4 and 0.6% by weight total batch mix. The quantity of fiber was calculated by multiplying the overall weight of ingredients of the concrete mix with the percentage of fiber content. The concrete mix details are provided in Table 1.



Fig. 6: Palm oil empty fruit bunch fibers.

Table 1: Mix design detail (kg/m<sup>3</sup>) for concrete containing POBC with palm oil EFB fiber

Sample Notation	Cement	Sand	CA	POBC	Water	EFB Fibers
0% EFB	18.24	37.80	28.62	0.00	9.12	-
0.2% EFB	18.24	34.02	28.62	3.78	9.12	0.195
0.4% EFB	18.24	34.02	28.62	3.78	9.12	0.390
0.6% EFB	18.24	34.02	28.62	3.78	9.12	0.585

Overall, 48 specimens were prepared to explore the compressive and flexural strength of the concretes at 7 and 28 days, as mentioned in Table 2. Concrete cubes of 100 mm size were cast for the purpose of compressive strength. The prisms of 100 mm in cross-section and 500 mm in length were cast for the evaluation of flexural strength. Furthermore, curing of concrete was observed under water immersion conditions.

Table 2: The Specimen prepared for strength performances

Palm Oil EFB fibers (%)	7 days		28 days	
	Compressive	Flexural	Compressive	Flexural
0	3	3	3	3
0.2	3	3	3	3
0.4	3	3	3	3
0.6	3	3	3	3
Sub Total	12	12	12	12
Total Samples	48			

## 4. RESULTS AND DISCUSSION

### 4.1 Particle Size Distribution

Particle size distribution has been done through sieve analysis. Figure 7 illustrates the cumulative percentages passing for sand and POBC at various sieve sizes. However, the

sand and POBC particle size distribution curve did not exceed the upper and lower limits. Both sand and POBC used in the experiment fulfil the particle size behaviour stated in BS 882: 1992, the required percentage by mass passing BS sieve for sand. In this study, aggregates used were air dried to obtain saturated dried surface. To achieve this condition, aggregates were dried at room temperature for 24 hours.

Coarse aggregates of 10 mm size were used, and less than 5 mm were removed through sieving. The specific gravity for sand and POBC used in this study has the average specific gravity of 2.07 and 2.63 respectively. The specific gravity of POBC is 21% lower than the average specific gravity of sand.

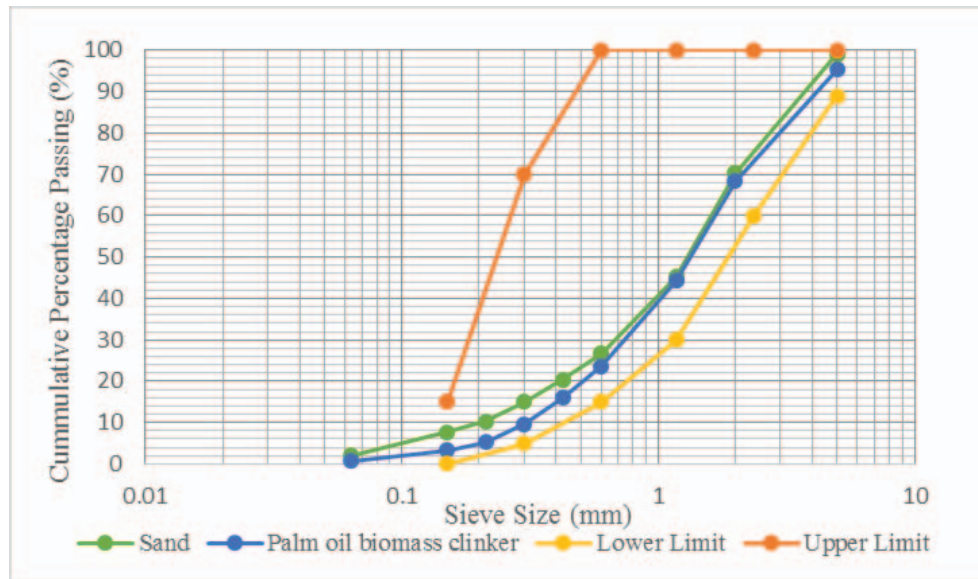


Fig. 7: Particle size distribution of sand and POBC.

## 4.2 Workability of Concrete

Workability is an aspect of concrete, which indicates flow without mechanical shaking. The workability performance of concrete containing 10% POBC along with various proportions of palm oil EFB fiber are presented Fig. 8. It shows a reduction in workability due to the addition of fiber content. The slump value dropped from 20 mm to 18, 12, and 8 mm at fiber contents of 0.2, 0.4, and 0.6%, respectively. The results showed a substantial decrease in workability due to presence of fiber. As the fiber content increased, workability was reduced. However, the presence of fiber absorbed more water in the concrete mix [14] and resulted in the drop in workability. An adequate performance was noticed with 0.2% fiber. It was also previously noticed by Ahmad et al. [15] that the addition of fibers cause the reduction in workability. However, the palm oil EFB fiber is an organic fiber that could reduce the quantity of free water in a concrete mixture and affect the mobility of concrete.

## 4.3 Compressive Strength

Compression strength test performances of concrete with 10% POBC as a fine aggregate replacement with the addition of 0.2%, 0.4%, and 0.6% of palm oil EFB fiber has been presented in Fig. 9. The experimental findings indicate that compressive strength was reduced as fiber quantity increased in the concrete. The control sample without fiber shows the highest compressive strength of 27.23 MPa at 28 days. Compressive strength results with the addition of 0.2%, 0.4% and 0.6% palm oil EFB fiber show a reduction in

strength of 12.6%, 17.7%, and 21.7% respectively. Comparatively, the strength performances with 0.2% fiber is considered to be satisfactory, due to the lower reduction in the strength [4,16,17]. This study clarifies that there is a continual decrease in compressive strength as palm oil EFB fibers increase in the concrete mix. It shows that concrete becomes more porous and delivers lower strength. This study also validated that in the presence of both materials, POBC and palm oil EFB fiber, concrete depletes its water content, since more water is absorbed by these two materials. As a result, reduction in water content could slow the hydration process of concrete and ultimately cause it to exhibit lower strength, even at 28 days.

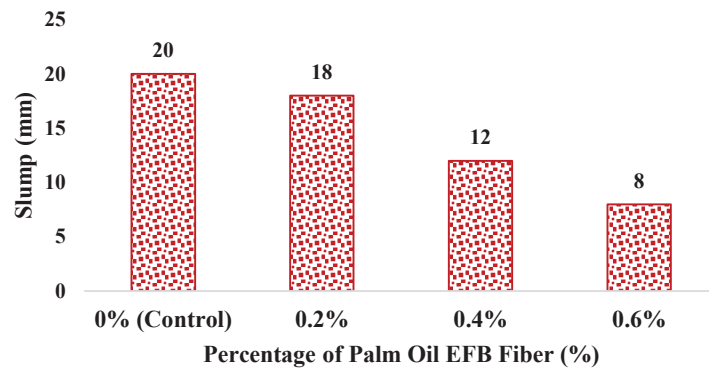


Fig. 8: The slump value with various percentage of reinforced palm oil EFB fiber.

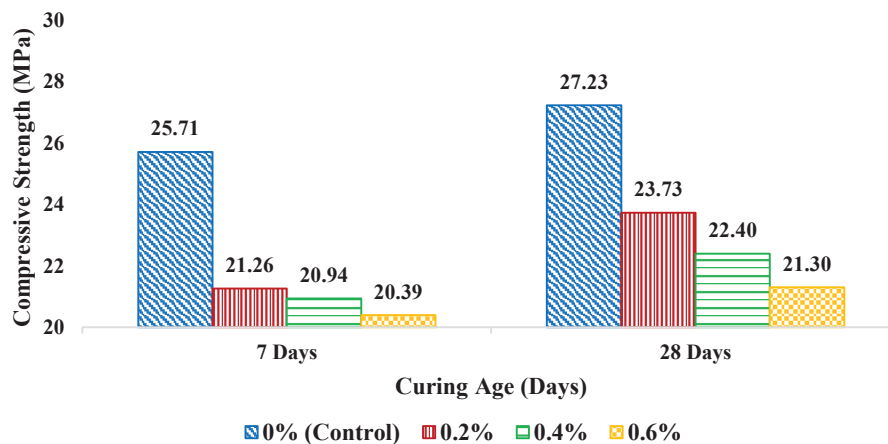


Fig. 9: Compressive strength of fiber reinforced concrete at different curing periods

#### 4.4 Flexural Strength

Experimental results of flexural strength of concrete incorporating 10% POBC as fine aggregate replacement along with the addition of 0.2%, 0.4% and 0.6% of palm oil EFB fiber has been demonstrated in Fig. 10. It was observed that flexural strength of concrete was better in the presence of fibers. It was noticed that flexural strength was increased from 2.18 MPa to 2.43 MPa with the addition of 0.2% fiber, which is almost 11.47% rise in flexural strength at 28 days. However, 0.4% and 0.6% fiber content also delivers around 5.96% and 4.59% improvement in the flexural strength of concrete. Hence, it is worth noting here that the increase in palm oil EFB fiber content causes a reduction in flexural strength. It was previously acknowledged that the addition of supplementary materials along with fibers enhances the flexural strength of concrete [4,18,19,20,21]. This study

also experimentally validated that 0.2% proportion of fiber enhances the concrete properties in terms of flexural strength, and it is hereby recommended as an appropriate proportion of fibers in a concrete mix.

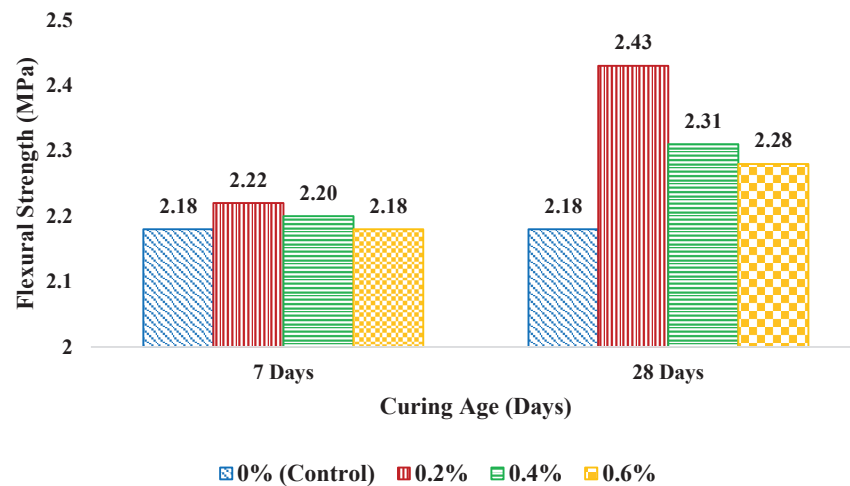


Fig. 10: Concrete flexural strength at curing periods of 7 and 28 days.

## 5. CONCLUSIONS

This experimental study confirmed that POBC has a good potential to be utilized as a fine aggregate replacement. Based on the performance of concrete containing 10% POBC as fine aggregate with addition of palm oil EFB fiber, the following conclusions can be made:

- Concrete containing 10% POBC as a fine aggregate along with addition of palm oil EFB fiber delivers lower workability performances and around 10% reduction in workability with the addition of 0.2% fiber in concrete.
- Concrete compressive strength was also reduced with addition of 0.2%, 0.4% and 0.6% palm oil EFB fiber, which gives around 12.6%, 17.7%, and 21.7% reduction in compressive strength, respectively. However, 0.2% fiber content is considered to be optimum, due to minimum reduction in the strength.
- The flexural strength performances of concrete were found to be increased from 2.18 MPa to 2.43 MPa with the addition of 0.2% fiber, which is almost an 11.47% rise in flexural strength at 28 days. Therefore, based on the experimental outcomes, the appropriate proportion of fiber is recommended to be 0.2%.

## ACKNOWLEDGEMENTS

This study was supported by Universiti Tun Hussein Onn Malaysia (UTHM) and Ministry of Education Malaysia through Fundamental Research Grant Scheme (FRGS) Vot No. K054.

## REFERENCES

- [1] Kushairi A, Loh SK, Azman I, Hishamuddin E, Abdullah MO, Mohd Noor Izuddin ZB, Razmah G, Sundram S, Ahmad Parveez MK. (2018) Oil Palm Economic Performance in Malaysia and R&D Progress in 2017 – Review Article. *Journal of oil palm research* 30(2):163-195. DOI: <https://doi.org/10.21894/jopr.2018.0030>
- [2] Kanadasan J, Razak HA. (2015) Engineering and sustainability performance of self-compacting palm oil mill incinerated waste concrete, *J. Clean. Prod.*, 89:78-86. <https://doi.org/10.1016/j.jclepro.2014.11.002>
- [3] Alengaram UJ, Al Muhit BA, Jumaat MZB. (2013) Utilization of oil palm kernel shell as lightweight aggregate in concrete – A review, *Constr. Build. Mater.*, 38:161–172. <https://doi.org/10.1016/j.conbuildmat.2012.08.026>
- [4] Wan Ibrahim, MH, Mangi SA, Ridzuan MB, Burhanudin MK, Jamaluddin N, Li KH., Shahidan S, Sheikh KF, Arshad MF, Ramadhansyah PJ. (2019) Compressive and Flexural Strength of Concrete Containing Palm Oil Biomass Clinker with Hooked-End Steel Fibers, *Int. J. Integr. Eng.*, vol. 10(9):152–157. <https://publisher.uthm.edu.my/ojs/index.php/ijie/article/view/2559>
- [5] Aslam M, Shafiq P, Jumaat MZ. (2016) Oil-palm by-products as lightweight aggregate in concrete mixture: A review, *Journal of Cleaner Production*, 126:56-73. <https://doi.org/10.1016/j.jclepro.2016.03.100>
- [6] Ahmmad R, Jumaat MZ, Bahri S, Saiful Islam ABM. (2014) Ductility performance of lightweight concrete element containing massive palm shell clinker, *Constr. Build. Mater.*, 63:234-241. <https://doi.org/10.1016/j.conbuildmat.2014.04.022>
- [7] Gunasekaran K, Kumar PS, Lakshmi pathy M. (2011) Mechanical and bond properties of coconut shell concrete, *Constr. Build. Mater.*, 2:592-98. <https://doi.org/10.1016/j.conbuildmat.2010.06.053>
- [8] Abutaha F, Razak HA, Kanadasan J. (2016) Effect of palm oil clinker (POC) aggregates on fresh and hardened properties of concrete, *Constr. Build. Mater.*, 112:416–423. <https://doi.org/10.1016/j.conbuildmat.2016.02.172>
- [9] Shahreen E, Wahab A, Omar R, Che Osmi SF, Muhamad Khairussaleh NA, Abdullah A. (2012) Preliminary study on Mechanical Properties of Concrete added with Fine Palm Oil Clinker, in *Jordan Engineers Association Conferences*. <http://www.jeaconf.org>
- [10] Shafiq P, Mahmud HB, Jumaat MZB, Ahmmad R, Bahri S. (2014) Structural lightweight aggregate concrete using two types of waste from the palm oil industry as aggregate, *J. Clean. Prod.*, 80. 187–196. <https://doi.org/10.1016/j.jclepro.2014.05.051>
- [11] Gunawan FE, Homma H, Brodjonegoro SS, Hudin ABB, Zainuddin AB. (2009) Mechanical Properties of Oil Palm Empty Fruit Bunch Fiber, *J. Solid Mech. Mater. Eng.*, 3(7):943–951. <https://doi.org/10.1299/jmmp.3.943>
- [12] Sim J, Park C, Moon DY. (2005) Characteristics of basalt fiber as a strengthening material for concrete structures, *Compos. Part B: Eng.*, 36(6–7):504–512. <https://doi.org/10.1016/j.compositesb.2005.02.002>
- [13] Kim J, Park C, Choi Y, Lee H, Song G. (2012) An Investigation of Mechanical Properties of Jute Fiber-Reinforced Concrete. In: Parra-Montesinos G.J., Reinhardt H.W., Naaman A.E. (eds) *High Performance Fiber Reinforced Cement Composites 6*. RILEM State of the Art Reports, vol 2. Springer, Dordrecht. [https://doi.org/10.1007/978-94-007-2436-5\\_10](https://doi.org/10.1007/978-94-007-2436-5_10)
- [14] Shreesail BH. (2015) Effects of Coconut Fibers on The Properties of Concrete, *Int. J. Res. Eng. Technol.*, 04(01):5–11.
- [15] Ahmad Z, Saman HM, Tahir PM. (2010) Oil palm trunk fiber as a bio-waste resource for concrete reinforcement, *Int. J. Mech. Mater. Eng.*, 5(2):199-207
- [16] Mangi SA, Wan Ibrahim MH, Jamaluddin N, Arshad MF, Memon FA, Ramadhansyah PJ, Shahidan S. (2019) A Review on Potential Use of Coal Bottom Ash as a Supplementary Cementing Material in Sustainable Concrete Construction, *Int. J. Integr. Eng.*, 10(9):127–135. <https://publisher.uthm.edu.my/ojs/index.php/ijie/article/view/2496>
- [17] Mangi SA, Wan Ibrahim MH, Jamaluddin N, Arshad MF, Ramadhansyah PJ. (2018) Effects of Ground Coal Bottom Ash on the Properties of Concrete, *J. Eng. Sci. Technol.* 14 (1):338–

350.  
[http://jestec.taylors.edu.my/Vol%2014%20issue%201%20February%202019/14\\_1\\_24.pdf](http://jestec.taylors.edu.my/Vol%2014%20issue%201%20February%202019/14_1_24.pdf)
- [18] Dullah H, Akasah ZA, Nik Soh NMZ, Mangi SA. (2017) Compatibility improvement method of empty fruit bunch fibre as a replacement material in cement bonded boards: A review, IOP Conf. Ser. Mater. Sci. Eng., 271: 1–7.  
<https://iopscience.iop.org/article/10.1088/1757-899X/271/1/012076>
- [19] Jamaluddin N, Hamzah AF, Wan Ibrahim MH, Ramadhansyah PJ, Arshad MF, Zainal Abidin NE, Dahalan, NH. (2016) Fresh Properties and Flexural Strength of Self-Compacting Concrete Integrating Coal Bottom Ash, MATEC Web Conf., 47:01010.  
<https://doi.org/10.1051/mateconf/20164701010>
- [20] Ramadhansyah PJ, Abu Bakar BH, Megat Azmi MJ, Wan Ibrahim MH (2011) Engineering properties of normal concrete grade 40 containing Rice husk ash at different grinding times, Int. J. Technol., 2(1):10–19.
- [21] Mangi SA, Wan Ibrahim MH, Jamaluddin N, Shahidan S, Arshad MF, Memon SA, Ramadhansyah PJ, Mudjanarko SW, Setiawan MI. (2019) Influence of Ground Coal Bottom Ash on the Properties of Concrete, Int. J. Sustain. Constr. Eng. Technol., 9(2):26–34.  
<https://publisher.uthm.edu.my/ojs/index.php/IJSCET/article/view/3296>

## THE CHARACTERISTICS OF REED LIGHTWEIGHT CLAY BRICKS AFTER DRYING PROCESS

GHAZWAN ABDULSAMAD SALMAN

*Ministry of Higher Education and Scientific Research,  
Contract Department, Baghdad, Iraq*

*\*Corresponding author: ghazwan\_salman@yahoo.com*

*(Received: 16<sup>th</sup> November 2019; Accepted: 11<sup>th</sup> February 2020; Published on-line: 4<sup>th</sup> July 2020)*

**ABSTRACT:** The drying procedure is one of the basic stages in the brick making process, particularly when utilizing the extrusion framing technique. This stage decides the quality and amount of the brick samples. One of the characteristic waste vegetable materials is reed, which is found in huge amounts in Iraq and numerous other nations. Five weight proportions of reed crumbs (5,10,15,20 and 25%) were utilized to produce lightweight clay bricks. Lab samples were shaped with dimensions of (25×38×76mm) using the vacuum extraction method. Brick properties were tested after drying to determine the values of longitudinal drying shrinkage, bulk density, and compression strength. In order to check the property of lightweight clay brick samples, the samples were burned in the furnace at a temperature of 1000°C with a burning rate of 2°C per minute. The significance of this research is to know the optimal proportions of the reed crumbs that prompts exact control of the drying procedure. This fine control brings about samples of lightweight bricks of the required dimensions and without cracks that influence their properties after drying and become more visible after burning. This knowledge will prompt the decrease of waste in raw materials and energy utilized in the manufacturing of a particular amount of lightweight bricks and, along these lines, reduce the expense of production.

**ABSTRAK:** Prosedur pengeringan merupakan salah satu peringkat asas dalam proses membuat bata, terutamanya apabila menggunakan teknik pembersihan penyemperitan. Peringkat ini memutuskan kualiti dan jumlah sampel bata. Salah satu daripada bahan-bahan sayur-sayuran sisa buatan adalah buluh, ia didapati dalam jumlah besar di Iraq dan banyak negara yang berbeza. Sebanyak 5 buah berat serbuk reed (5,10,15,20 dan 25%) digunakan untuk menghasilkan bata tanah liat yang ringan. Model makmal dibentuk dengan dimensi (25 × 38 × 76mm) dengan menggunakan kaedah pengekstrakan vakum. Ciri-ciri bata telah diuji selepas pengeringan untuk menentukan nilai-nilai kepekatan pengeringan longitudinal, ketumpatan pukal dan kekuatan mampatan. Untuk memeriksa sampel tanah liat ringan tanahpropertyof, model-model tersebut dibakar dalam relau pada suhu 1000 ° C dengan kadar pembakaran 2°C seminit. Kepentingan kajian ini adalah untuk mengetahui perkadaran optimum serbuk reed yang menimbulkan kawalan tepat terhadap prosedur pengeringan. Kawalan halus ini membawa model-model bata yang ringan dari dimensi yang diperlukan dan tanpa retak yang mempengaruhi sifatnya selepas pengeringan dan menjadi lebih terlihat selepas terbakar. Pengetahuan ini akan mendorong penurunan sisa bahan mentah dan tenaga yang digunakan dalam pembuatan sejumlah bata ringan dan di sepanjang garisan ini mengurangkan perbelanjaan pengeluaran.

**KEYWORDS:** *drying process; optimal proportions; vacuum extraction method; reed; lightweight clay bricks*

## 1. INTRODUCTION

The drying procedure is a means of preparing thermally-shaped samples for a specific time frame at a temperature of 110°C with the goal that the humidity does not surpass (25%) of the initial moistness. This procedure builds the mechanical strength of the samples, which facilitates the process of transfer and placing into the furnaces. The drying procedure is completed in stages where in the primary stage free water among the particles of the clays is lost, causing a convergence of particles with each other leading to the occurrence of dry shrinkage. The shrinkage in the body is equivalent to the measure of vanished water. In the following stage, the thin water surrounding the clay particles vanishes, causing more combinations of the particles and some additional shrinkage. In the last stage, the water in the pores is lost and the water travels through the pores to the particle surface to replace the vanished water from the surface. This stage is described by no shrinkage and the air in the long run replaces the water in the capillary pores, making the dried mass permeable. The drying stages cannot be set and isolated from one another obviously on the grounds that they are overlapping.

Numerous scientists considered the effect of adding agricultural waste to soil in order to create lightweight bricks. One of the most well-known agricultural wastes is rice husk. It has been found that, the perfect proportion of the rice husk ranges from 10-20% by weight. Adding rice husk to the clay is restricted because it reduces the compression strength of the brick as the rice husk content increases [1,2].

Demir [3,4,5] discovered that the compression strength of the dried brick samples containing sawdust, tobacco, and grass remained unequivocally increased in spite of the increased drying shrinkage of the clay body and these results led to a reduced use of the scraps because of handling issues of unburned blocks.

Similar conclusions were reached by Samia et al. [6], they found that the drying shrinkage and the compression strength before firing were also increased after raising the content of two types of organic waste, namely olive stones and hay, at 1-10% replacement-to-clay in order to manufacture clay bricks. This behaviour was due to the binding effect of the agricultural waste in the block's structure before burning and that increase was found useful in reducing cracks while transporting bricks to kilns and in maintaining brick dimensions.

Ahmad et al. [7] produced clay samples within the limits allowed for most of the recommended standards by including 5-15% by weight of coal and wheat peel additives to the clay, moreover the drying shrinkage was found to be lower than 8% within the limits and decreased with the increase of percentage of additives.

In addition, porosity of the sample can be constrained by the proportion of sawdust mixture and for structural purposes where compression strength is significant, the level of sawdust ought not surpass 10 to 15 percent by weight of the insulating fired bricks [8].

The use of reed morsels for manufacturing of lightweight clay bricks has been exploited in Iraq by the addition of 5-25% by weight of reed morsels to the clay and the mixes burned at different temperatures of 800,900 and 1000°C, respectively. The results showed the possibility of manufacturing lightweight clay bricks with comparatively good properties such as bulk density and compression strength in the brick samples containing 5% by weight of reed crumbs. On the other hand, the results of the studies indicated a decrease in thermal conductivity and longitudinal shrinkage. Moreover, the produced bricks can be made in the same factories that manufacture the ordinary brick clay and in the same step of producing ordinary clay bricks [9,10].

The purpose of this research was to determine the effects of the addition of reed crumbs in the brick mixture on the drying technique. The bulk density, drying shrinkage and compression strength properties were examined.

## 2. MATERIALS

Physical, chemical and metallic tests were conducted to evaluate the raw materials used in the production of this brick.

### 2.1 Soil

Soil (100 kg) from two unique quarries was fetched from Al-Nahrawan quarry in the Baghdad zone. The soil was moist and contained masses with a maximum diameter of 5 cm. The soil was cleaned by removing foreign and organic materials from it and then dried in large containers outside the laboratory as a result of exposure to sunlight. After that, the masses of soil were transferred to the oven for drying at a temperature of 110 °C for 48 hours and pounded with an iron ball plant to be passed through sifter No. 22 (710) micron. Chemical and physical analyses were carried out on the soil sample. The chemical investigation of the clay was done by X-ray fluorescence. Table 1 and 2 show the chemical and physical characteristics of the clay utilized in this research. To decide the grain size distribution of soil utilized, wet sieving and hydrometer technique were utilized based on ASTM D422[13] and ASTM D2487[14]. Table 3 demonstrates the grain size distribution of the clay utilized.

Table 1: chemical compounds of the soil utilized

Chemical compound	Content in soil (%)	Standard requirement [11,12] (%)
SiO <sub>2</sub>	40.80	50-60
CaO	16.04	5-10
Al <sub>2</sub> O <sub>3</sub>	10.49	20-30
Fe <sub>2</sub> O <sub>3</sub>	4.90	5-7
MgO	2.42	1
K <sub>2</sub> O	1.3	2-2.76
Na <sub>2</sub> O	1.08	0.1
SO <sub>3</sub>	2.0	-
T.S.S	2.28	-
L.O.I	18.6	3-4

Table 2: physical characteristics of the soil utilized

Type of Test	Result	Test Specification	Specification Limit
Moisture Content		ASTM D 4318 [12]	
% Atterberg			
Liquid Limit	32		Not more than 55
Plastic Limit	21.3		Not more than 55
Plastic Index	11.3		Not more than 30

Table 3: The grain size distribution of the soil utilized

Grain size of soil (%)	Results (%)	Typical Range (%) [13,14]
sand	21	20-45
silt	45	25-45
clay	34	20-35

## 2.2 Reeds

The reeds were transported from the banks of a stream in Baghdad as shown in Fig. 1. The reed was cut with a target length of approximately 4 cm. The principal attributes of the reeds utilized appear in Table 4. A manual system was utilized to produce reed crumbs with a little mallet and an electric saw. The reeds were shredded utilizing an electric saw as can be seen in Fig. 2, at that point they were dried in a stove at a temperature of 110°C for 48 hours. After the reeds were granulated, the dried reeds were changed over to crumbs using a little mallet and went through strainer 52, size 300 to be prepared for use as an added substance to deliver lightweight blocks, as seen in Fig. 3.



Fig. 1: The reed plants from the banks of the stream.

Table 4: properties of the reeds [15]

Characterization	Shortened form	Value
Specific gravity	S.G	2.44
Silica (%)	SiO <sub>2</sub>	65.2
Sulfur trioxide (%)	SO <sub>3</sub> ***	1.52
Calcium (%)	CaO	6.4
Alumina (%)	Al <sub>2</sub> O <sub>3</sub>	12.3
Iron (%)	Fe <sub>2</sub> O <sub>3</sub>	2.6
Potassium (%)	K <sub>2</sub> O**	2.5
Chloride (%)	Cl	N.R
Sodium (%)	Na <sub>2</sub> O	N.R
Phosphorus (%)	P <sub>2</sub> O <sub>5</sub>	0.03
Magnesium (%)	MgO	N.R
Titanium (%)	TiO <sub>2</sub>	0.19
Manganese (%)	MnO	0.08
Moisture Content (%)	w	0
Loss on Ignition (%)	L.O.I	1.47

\*Chemical compound values are determined utilizing EDX-7000 instrument.

\*\*K<sub>2</sub>O value is determined utilizing XRD-6000 instrument.

\*\*\*SO<sub>3</sub> value is determined utilizing MXF-2400 instrument.



Fig. 2: Electrical saw



Fig. 3: The reed crumbs produced in this study.

Table 5: Plasticity coefficients of soil with and without different percentages of reeds crumbs.

Mix symbol	Raw materials	Plasticity index (%)
S	Soil (reference)	31
S1	Soil + 5% RC	34
S2	Soil + 10% RC	38
S3	Soil +15% RC	44
S4	Soil + 20% RC	49
S5	Soil + 25% RC	52

\*Where RC=reed crumbs

### 3. MIX PROPORTIONS AND MIXING PROCESS

The production of lightweight clay block mixtures was done by adding (5, 15, and 25%) by weight of the reed crumbs to the clay. The Pefferkorn method was used for deciding the measure of water required for changing the plasticity index with the different percentage of the reed additions. Table 5 shows the plasticity coefficients for mixes of soil with and without various rates of the additional reeds crumbs. The blending procedure was done in a bigpan and the mixture bowl was cleaned before each blending procedure. To set up the reference blend, the clay was soaked with the fundamental water (as indicated by the plasticity coefficient) and the blending procedure was done in the big pan for 15minutes so as to acquire a homogeneous blend. Concerning blends containing reed crumbs, the specified quantities of soil and reed morsels were blended into the skillet for 10 minutes without adding any water in order to get a homogeneous blend. Then the water was added to the dry blend and blended for another 15 minutes. After the blending procedure is finished, the blend is set in a closed loop container for 24 hours to guarantee the homogeneity of water and soil in the blend.

#### 4. SAMPLE PREPARATION, DRYING AND FIRING

The soil blocks were produced in the lab by an extruded expulsion of air technique, using a vacuum extruder (Fig. 4). Specimens of 75 mm length, 38 mm width, and thickness of 25 mm height measurements were made. The drying method was started by leaving the framed soil samples in the lab for 7 days and then drying them in a stove at a temperature of  $110\pm 5^{\circ}\text{C}$  for 48 hours. Later the block samples were taken away from the stove and left to cool at a lab temperature of  $23\pm 2^{\circ}\text{C}$  for 48 hours. The dried specimens were transferred to an electric kiln to start the firing procedure where the warming rate and the soaking time were constant.

The dried blocks were sorted inside the kiln, (Fig. 5) in an effort to guarantee that the warmth reached all surfaces of the samples uniformly. The dried clay blocks were burned at a  $1000^{\circ}\text{C}$  degree of firing by electrical kiln (Fig. 6). The dried blocks of every blend were burned independently using a similar firing program and at the time of drenching for two hours until arriving at the planned firing temperature  $1000^{\circ}\text{C}$ . The firing rate was  $2^{\circ}\text{C}$  per minute, to guarantee adequate time for firing of every natural material with the complete arrival of carbon dioxide. After the firing procedure was finished, the kiln was turned off and the block samples were left inside until the temperature decreased to the temperature of the lab. In order to ensure a lightweight block, bulk density and compression strength tests were performed.



Fig. 4: Clay extrusion device.



Fig. 5: Curing and drying furnace.



Fig. 6.: Burning furnace.

## 5. TEST PROCEDURE

### 5.1 Longitudinal Shrinkage Test

One of the significant properties after the drying process of reed lightweight clay bricks is the shrinkage of the clay mass, which mainly affects the accuracy of the final brick dimensions and the bulk density. The longitudinal shrinkage test was carried out according to specification [16] after drying the brick samples at a temperature of 110°C for 48 hours and then cooling to the laboratory temperature of 23±2°C. The length of the sample was measured before and after drying from two different sides and the average length was recorded. The length of brick blocks was measured after and before the drying process to determine the longitudinal shrinkage proportion. The following equation was used to calculate the longitudinal shrinkage:

$$(L.S)\% = \left(\frac{H_d - H_r}{H_d}\right) \times 100 \quad (1)$$

where: (L.S)= Longitudinal shrinkage,  $H_d$ =Sample length before drying process (mm) and  $H_r$ =Sample length after drying process (mm). An average of 10 specimens was used.

### 5.2 Bulk Density Test

The bulk density of the samples was determined based on the specification [14] and after drying process by weighing them with a high sensitivity electric balance and accuracy up to ±0.01 g. Dimension measurements were performed on two sides with a Vernier caliper and the rate was recorded. An average of 10 specimens was used. The bulk density of the dried lab samples was estimated using equation (2):

$$B.D = \frac{W}{V} \quad (2)$$

where:  $B.D$ =Bulk density (g/cm<sup>3</sup>),  $W$ = weight of samples after drying (g) and  $V$ = Volume of samples after drying (cm<sup>3</sup>).

The same equation was used to calculate the bulk density after the burning process. The bulk density of the firing block samples was determined as per ASTM C373 [17].

### 5.3 Compression Strength Tests

The values of the compression strength tests after drying are influenced by cracks and defects that show up in the sample bricks and are considered to be a primary measure of the final compression strength of these samples after burning. The increase in the compression strength of the dried samples is an indication of the lack of cracks and other

defects in the brick samples, which helps not to damage them during the loading and transporting process before burning. This test began after the samples were dried at 110°C and cooled to the laboratory temperature. The test was carried out by covering the top and bottom surfaces of the sample with two pieces of 3 mm-thick plywood to ensure uniform distribution of the load on the loading surface as seen in Fig. 7 and Fig. 8. A load of 15 N/mm<sup>2</sup> per minute was applied until failure occurred. Compression strength for each sample was calculated from the following relationship:

$$C = \frac{P}{A} \quad (3)$$

where:  $C$ =Compression strength (N/mm<sup>2</sup>),  $P$ =The applied loading when the sample fails and  $A$ = The area of the sample which exposed to the applied load.

An average of 10 specimens was used. The compression strength after firing process was determined according to ASTM standard ASTM C373-88[17] using Eq. 3.



Fig. 7: Compressive strength test machine.



Fig. 8: Sample under compressive strength test.

## 6. RESULTS AND DISCUSSION

From these experiments, it was observed that the amount of moisture increased for the formation of brick samples with the addition of reed crumbs. This behaviour was due to the addition of reed crumbs which resulted in more difficult extrusion. This is due to the fibrous nature of the reed crumbs and their internal water channels that lead to increased water absorption which is the main reason for the increasing demand for water. Some difficulties occurred during the mixing and extrusion process when the percentage of the reed crumbs reached 20% - 25% due to the fibrous nature of the reed. No defects were observed after the drying process of the samples except for the samples with the addition of 20 and 25% of reed crumbs, where small cracks occurred and increased with the percentage of reed crumbs added during the drying process, resulting in failure during firing. Splits, swelling, and other perceptible deformities are seen after the burning procedure for the samples with 20 and 25% of reed crumbs. After combustion, an increase in weight loss when ignition is observed in block samples containing high levels of reed crumbs compared to samples with little or no additive ratio. Increased demand for energy was also noted during the firing process due to the high amount of water needed to form the brick samples. No black cores were seen in broken samples after the compression strength test. Lightweight clay bricks were created by merging no more than 5% (by weight) of reed crumbs into soil which met the compression strength prerequisites of blocks utilized for partitions, as indicated in ASTM Standard C62 [18].

### 6.1 Longitudinal Shrinkage

The drying shrinkage property is influenced by the method used to form the bricks. The extrusion method used in the formation of bricks needs a higher water content than the critical water content and an increase in the formation water content leads to increased drying shrinkage causing contraction in the body of the brick [19]. The results of the longitudinal shrinkage after drying process were shown in Fig. 9. A high increase in the drying shrinkage values was observed in the samples compared to the control (clay only). The percentage of increase for longitudinal drying shrinkage were 7.3, 17.08, 34.15, 43.90, and 68.29% for S1, S2, S3, S4, and S5 samples respectively compared to reference mix S. This linear increase in longitudinal drying shrinkage is attributed to the increase in the percentage of reed crumbs that led to an increase in the formation water content and plasticity index due to the fibrous nature of reeds that absorb water, which results in higher shrinkage values after drying as plotted in Fig. 9. However, despite of increment in the plasticity index, the longitudinal drying shrinkage does not increase to the same degree, as we can see in Fig. 10. This condition is because of the hollow and sorbent nature of the reed crumbs which somewhat balances out the drying conduct of the clay body notwithstanding the increment in water demand with the increment of reed crumbs. In general, the longitudinal drying shrinkage values of the clay mixtures containing reed crumbs were higher than the longitudinal drying shrinkage value of the reference mixture samples. This conclusion was reached by a group of researchers who used different types of agricultural waste in a number of lightweight brick industry research [3,4,5,6]. This behaviour continues after burning the brick samples as can be seen of the longitudinal shrinkage results in Fig. 10. The percentage of increase in longitudinal shrinkage values of the fired samples was 11.98, 21.87, 32.30, 41.15 and 52.08% for the mixes S1, S2, S3, S4, and S5 respectively compared to the reference mix S. Accordingly, there is a direct increment in the drying and complete longitudinal shrinkage as the quantity of reed crumbs in the blend increases. Brick samples containing 20-25% of reed crumbs were found to be unsuitable due to high shrinkage after drying which caused large cracks after burning.

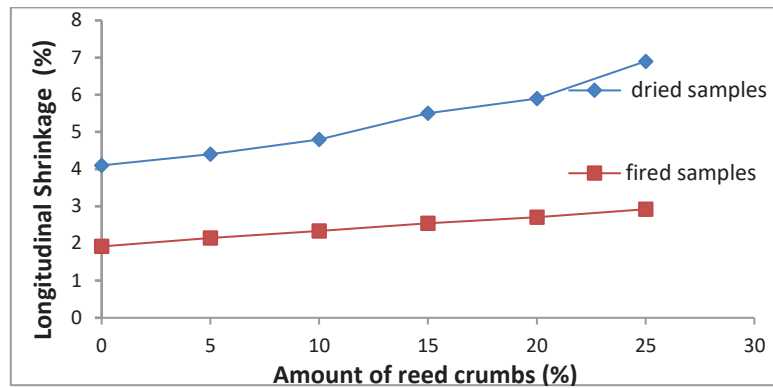


Fig. 9: Effects of % reed addition on longitudinal shrinkage of dried and fired clay brick samples

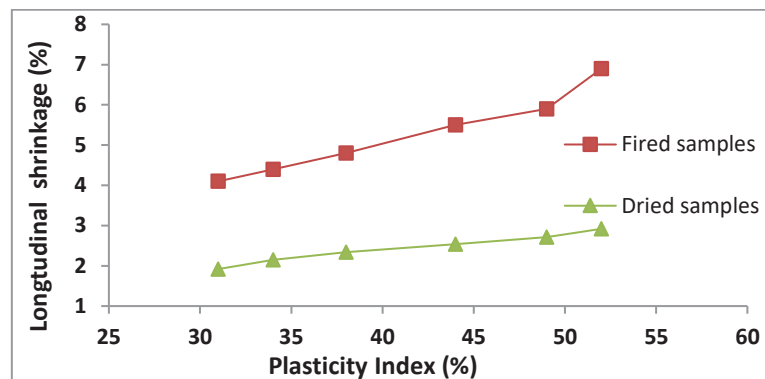


Fig. 10: The relationship between longitudinal shrinkage and the plasticity index of dried and fired brick samples.

## 6.2 Bulk Density

The results of the bulk density tests after the drying are shown in Fig. 11. These results showed that the values of bulk density after drying gradually decreased for mixing samples S1, S2, S3, S4 and S5 compared to the reference mixture samples (S). The percentage of decrease was 8.13, 16.06, 21.83, 27.68, and 30.24% for S1, S2, S3, S4, and S5 respectively compared to reference sample S. This indicates that bulk density after drying of samples containing reed crumbs is lower than that of samples manufactured from brick clay only as shown in Fig. 11. A rise in the quantity of reed crumbs brings about more decreases in bulk density values. This reduction in the bulk density of the samples containing reed crumbs is due to the decrease in the proportion of clay in the blend, which was replaced by reed crumbs with less density than the clay. In addition, the increase in the amount of water to maintain the plasticity required for the mixture with an increase in the proportion of reed crumbs, which subsequently evaporates after the end of the drying process, leads to more decrease in the dry density. Similar findings were reached in several previous studies that used different types of agricultural waste as clay replacement material in brick. According to [3,4,5,6] the addition of different agricultural waste such as Kraft pulp production residues, processed waste tea, sawdust, tobacco, grass, olive stones, and hay to the soil used for the production of clay bricks leads to a reduction in the bulk density of the brick samples. This is due to the partial replacement of high density of soil with a low density additive such as the agricultural waste in addition to the high plasticity coefficients of the mixing samples S1, S2, S3, S4 and S5 with increasing ratios of

addition, which leads to a decrease in density of the samples. In addition, bulk densities of the samples containing reed crumbs after firing have a lower value compared to the reference samples made from clay only. The bulk density test results of samples containing reed crumbs after firing are plotted in Figure 11. The level of reduction was 12.73, 23.35, 25.90, 36.77 and 41.93% for S1, S2, S3, S4, and S5 samples individually contrasted with S. Further reed crumbs increase in mixes S1-S5 caused just a slight further decrease. The burning of reed crumbs through the sintering time is the main reason behind this behaviour.

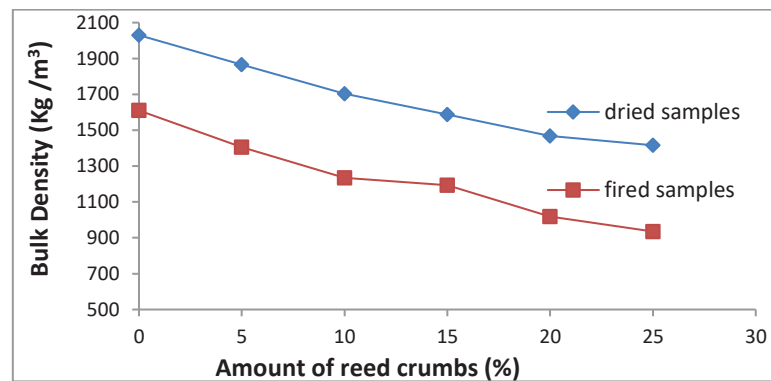


Fig. 11: Effects of amount of reed on bulk density of dried and fired clay brick samples.

### 6.3 Compression Strength

Compression strength after drying is influenced by several factors, the most important factors are the type and percentages of additives. Agricultural waste additives are characterized by their fibrous nature. The compression strength depends on the strength of these fibers. Compression strength increases with the increase of the fiber's strength and decreases with lower strength [5]. Another factor affecting compression strength after drying is formation water content. An increase in formation water content leads to the separation of the clay molecules from each other and the decrease of body strength, in addition to the increase in the proportion of capillary cracks formed due to drying shrinking with the increase of the formation water content which causes the weakening of the body and leads to reduced strength. The results of compression strength tests after drying are shown in Fig. 12. As can be seen in Fig. 11, mixes S1, S2, and S3, which contain 5, 10 and 15% of reed crumbs, have higher compression strength after drying compared to the reference mixture (S), which is made solely from soil. The level of increment of the blends of S1, S2, and S3 was 29.26, 42.89 and 7.95% contrasted with a reference blend S. This behaviour was due to the fibre strengthening effect of the of reed crumbs with low porosity which increase compression strength of samples S1, S2, and S3. This result is similar to the findings of the group of researchers who pointed to the increase in compression strength with 5 – 10% clay replacement with different types of agricultural waste in a number of lightweight clay brick industry research. According to [3-6], the addition of 5 – 10% of different agricultural waste such as Kraft pulp production residues, processed waste tea, sawdust, tobacco, grass, olive stones and hay to the soil used for production clay bricks leads to increase in compression strength after drying. As they discovered, this phenomenon is due to the fibre strength of agricultural waste with low porosity that leads to increase the compression strength after drying. This increase in compression strength after drying was discovered to be extremely valuable in avoiding the handling problems of the lightweight clay brick. Subsequently, the increase in reed crumbs to 20% of weight and then 25% of weight resulted in reduced compression strength after

drying of mixtures S4 and S5 respectively compared to the reference mixture S. The level of decrease in compression strength was 28.98 and 48.86% for blends S4 and S5 in comparison with a reference blend S. This decrease in compression strength after drying is due to the increase in porosity of the brick body to a high degree due to the high content of the formation water which overcomes the strength of the fibrous nature of reed crumbs. As shown in Fig. 12, the compression strength values after burning was decreased with the increase of the addition of reed crumbs to soil. The level of reduction was 19.1, 36.8, 49, 66.56, and 75.23% for blends S1, S2, S3, S4, and S5 individually comparing with a reference blend S. The reduction in compression strength after burning with the increase in the rate of addition of reeds crumbs was due to the increase in the amount of carbon dioxide gas caused by the combustion of carbon materials as well as the gaps left by the penetrating gas, which increase the porosity of the body and thus reduce the resistance of the brick body. Replacing part of the soil with reed crumbs also reduces the clay content in the mass, this clay content is responsible for forming the crystalline minerals which increasing the compression strength of the product [6,9].

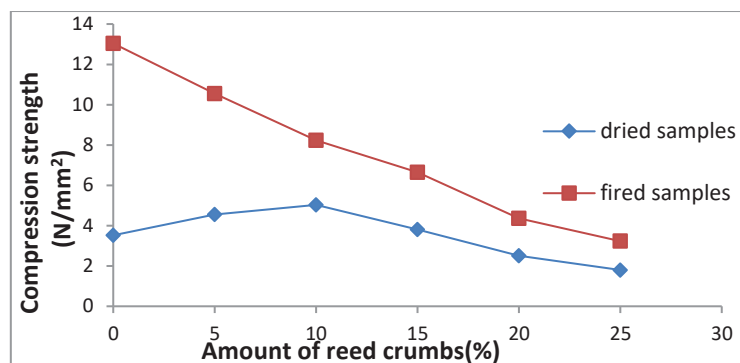


Fig. 12: Effects of % reed addition on compression strength of dried and fired clay brick samples.

## 7. CONCLUSION

Lightweight clay brick samples were manufactured by incorporating 5-25% (by weight) of reed crumbs into soil. Lightweight clay bricks samples meeting the requirements for blocks used for partitions, as indicated by ASTM Standard C62 [18], were made by adding 5% of reed crumbs into soil. The following conclusions were reached based on the results of laboratory tests on the manufactured brick samples:

- The addition of reed crumbs to the mixes of clay bricks caused no difficulties during the blending and extrusion process, but at the same time increased the required water content to keep the plasticity of the reed clay mixture. Hence, this leads to an increase of the water content and plasticity coefficient simultaneously. The increase in plasticity coefficient ranged from 9.7 to 22.58% when the reed crumbs were added in percentages ranging from 5 to 25% to the brick mixture. The ability of water channels within cellulose fibres to naturally absorb water is believed to be the main reason for the increased water demand in order to maintain the plasticity.
- A higher increase was found in the longitudinal drying shrinkage of reed-containing specimens than that of the brick clay sample only. The level of increment was discovered to range from 7.3 to 68.29% when the addition of reed crumbs ranged from 5 to 25%. This action is due to the increase in the water content needed to maintain the plasticity of the mixture when adding reed crumbs. Ratios of addition

- of 20 and 25% of reed crumbs to brick mixtures was found unsuitable for brick making due to high shrinkage after burning.
- The rate of increase in the longitudinal drying shrinkage is less than the rate of increase in plasticity coefficient when the same percentage of reed crumbs are added to the slurry mixture of the brick samples.
  - The bulk density values for dried samples containing reed crumbs were lower than that of clay samples only. The percentage decrease in bulk density values for brick samples with an added 5, 10, 15, 20 and 25% of reed crumbs was 8.13, 16.06, 21.83 and 27.68% respectively compared to samples made from clay only. This behaviour is due to the replacement of part of the high-density clay with low-density reed crumbs which increased plasticity coefficient of these mixtures.
  - The ratios of adding up to 15% of reed crumbs were discovered to considerably increase the dry compression strength of the clay samples. The ratio of increase in compression strength values was 29.26, 42.89, and 7.95% when including 5, 10, and 15% of the reed crumbs to the clay blends respectively compared with the reference samples produced from the clay only. This behaviour was due to the fibre strength of reed crumbs which increase the dry compression strength; this increase was found very valuable in avoiding handling problems.
  - Increasing the additives of reed crumbs more than 15% causes a reduction in compression strength after drying. The ratio of reduction in compression strength values was 28.98 and 48.86% when adding 20 and 25% of the reed crumbs to the clay blends respectively compared with the reference samples produced from the clay only. This reduction in compression strength after drying was found due to the increase of water content and plasticity coefficient in order to keep the plasticity of clay mixture which increased porosity and cracks after drying.
  - Generally, the reed crumbs can be used as a type of additive to form pores in the clay body without any detrimental effect on the drying process of lightweight clay bricks. Conversely, the addition of these reed crumbs was found very valuable in preventing handling problems of the lightweight clay bricks due to the increases in the compression strength after drying caused by the strength of the reed fibres.
  - The percentage of the scraps resulting from the handling problems of unfired bricks were found to be low when the reed crumbs were added by no more than 10%. A high percentage of the scraps were seen when the addition of reed crumbs was more than 15%. This knowledge is very important in order to maintain the raw materials from loss when using high percentages of reed crumbs.

## ACKNOWLEDGEMENT

The researcher would like to express profound thanks and appreciation to Prof. Dr. Shakir Ahmed Salih for his support and encouragement during the planning of this research.

## REFERENCES

- [1] Görhan G, Şimşek O. (2013) Porous clay bricks manufactured with rice husks. *Construction and Building Material*, 40:390-396.
- [2] Carter GW, Cannon AM, Mansell DS. (1982) Properties of bricks incorporating ungrounded rice husks. *Build Environmental*, 17(4): 285-291.

- [3] Ismail D, Serhat B, Mehmet O. (2004) Utilization of kraft pulp production residues in clay brick production. *Building and Environment*, 40: 1533–1537.
- [4] Demir I. (2005) An investigation on the production of construction brick with processed waste tea. *Building and Environment*, 41: 1274-1278.
- [5] Demir I. (2007) Effect of organic residues addition on the technological properties of clay bricks. *Waste Management*, 28: 622-627.
- [6] Arezki S, Chelouah N, Tahakourt A. (2015) Study of the influence of agricultural waste on the porosity of clay brick, Available online: <http://fstroj.uniza.sk/journal-mi/PDF/2015/03-.pdf>.
- [7] Safer A, Yaseen I, Raz M. (2017) Effects of coal and wheat husk additives on the physical, thermal and mechanical properties of clay bricks, *Boletín De La Sociedad Española De Cerámica Y Vidrio*, 56: 131-138.
- [8] Kumar, A. Mohanta, K. Kumar, D. and Parkash, O. (2012). Properties and industrial applications of rice husk. *J. Engineering Technology and Advanced Engineering*, 2: 5-10.
- [9] Ghazwan S, Shakir S. (2019) Effect of firing temperatures on physico-mechanical properties of clay bricks containing reeds. *International Journal on Advanced Science, Engineering and Information Technology*, 9(1): 321-238.
- [10] Ghazwan S, Shakir S. (2018) Effect of burning temperature of clay bricks containing reeds on its longitudinal shrinkage, modulus of rupture and thermal conductivity. *International Journal of Civil Engineering and Technology*, 9(9): 1388-1402.
- [11] ASTM D 4327 (2013) Determining chloride and sulfate contents in soils. ASTM International, West Conshohocken, PA, USA.,
- [12] ASTM D 4318 (2006) Standard test method for liquid limit, plastic limit, and plasticity index of soils. Annual book of ASTM standards.
- [13] ASTM D 422 (2006) Standard test method for particle size analysis of soils. Annual book of ASTM standards.
- [14] ASTM D 2487 (2011) Standard practice for classification of soils for engineering purposes (Unified System)". ASTM International, West Conshohocken, PA, USA.
- [15] Karim HH, Samuel ZW, Ahmed SF. (2015) Geotechnical properties of soft clay soil stabilized by reed ashes, 2nd International conference on Buildings, Construction and Environmental Engineering.
- [16] Beech, DG (1974). Testing methods for brick and tile manufacture, Britain Ceramic Research Association. Publication (84).
- [17] ASTM C 373 (2006) Standard test method for water absorption, bulk density, apparent density and apparent specific gravity of fired whitewares products", Annual book of ASTM standards.,
- [18] ASTM Standard C 62. (2006) Standard Specification for Building Brick (Solid Masonry Units Made From Clay or Shale), Annual book of ASTM standards, 2006.
- [19] Clews FH. (1969) Heavy Clay Technology, 2<sup>nd</sup> ed., New York, pp 9-16.

## INFLUENCE OF WIND WAVES ON THE FLOW IN FLOWING RESERVOIRS

SOBIR SAMATOVICH ESHEV, ALISHER NORMURODOVICH KHAZRATOV\*,  
ASHRAF RASUL O'GLI RAHIMOV AND SHAHBOZ ALISHER O'GLI LATIPOV

*"Operation of Hydraulic Structures and Pumping Stations" Department,  
Karshi Engineering Economics Institute, Karshi, Uzbekistan*

*\*Corresponding author: Khazratov@gmail.com*

*(Received: 4<sup>th</sup> January 2019; Accepted: 18<sup>th</sup> February 2020; Published on-line: 4<sup>th</sup> July 2020)*

**ABSTRACT:** Methods are given for calculating the formation of wind waves in flowing reservoirs, taking into account oncoming and associated currents and the limitation of acceleration by the banks.

**ABSTRAK:** Kaedah diberikan bagi mengira pembentukan gelombang angin dalam takungan aliran, dengan mengambil kira arus datang dan aliran berkaitan dan kekurangan pecutan pada tebing.

**KEYWORDS:** *wave action; spectral component; method of characteristics; acceleration length; wave beam*

### 1. INTRODUCTION

Additional factors that determine the generation of wind waves at large watercourses (flowing reservoirs, large rivers, and large canals) in comparison to the open sea are the current and the limited acceleration by the coasts. The combined effect of both factors was studied in [1-10]. We will review the corresponding theory that underlies the methodology for calculating the formation of wind waves on watercourses.

For wind waves on a large-scale flow, the main dynamic equation is the conservation equation, which with respect to the problem under consideration can be written as:

$$\frac{\partial N}{\partial t} + \vec{r} \frac{\partial N}{\partial \vec{r}} = 0 \quad (1)$$

where:

$$N(\vec{r}, \vec{k}, t) = S(\vec{r}, \vec{k}, t) / \omega_r \quad (2)$$

spectral density of the wave action  $S(\vec{r}, \vec{k}, t)$  is the spatial amplitude spectrum of the waves,  $\omega_r$  – is the frequency corresponding to the spectral component  $\vec{k}(k_x, k_y)$  at the point  $\vec{r}(x, y)$  at time  $t$  in the reference frame moving with the flow velocity  $\vec{U}(\vec{r}, t)$ . The principle of conservation of wave action is valid for waves in a moving environment, was established by Bretherton, Garret in 1969 [9], and was developed for waves on water by Uizem.

In the one-dimensional case, equation (1) is simplified as follows:

$$\frac{\partial N}{\partial t} + \frac{\partial x}{\partial t} \frac{\partial N}{\partial x} + \frac{\partial k}{\partial t} \frac{\partial N}{\partial k} = \dots \quad (3)$$

Characteristics of equation (3):

$$\begin{aligned} \frac{\partial x}{\partial t} &= \frac{\partial \omega}{\partial k} = C_{ag} \\ \frac{\partial k}{\partial t} &= \frac{\partial \omega}{\partial x} = 0 \end{aligned} \quad (4)$$

where  $C_{ga}$  is the absolute group velocity,  $C_{ag} = C_{gr} = U$ . In accordance with (3) and (4), the condition on the characteristics has the form:

$$\frac{\partial N}{\partial t} + C_{ag} \frac{\partial N}{\partial x} = Q_{act} \quad (5)$$

In the steady state, when sufficient time is reached, the wave action ceases to depend on time, but is only a function of acceleration. Moreover, equation (5) takes a very simple form:

$$C_{ag} \frac{\partial N}{\partial x} = Q_{act} \quad (6)$$

Therefore, using the method of characteristics and dividing the variables in equation (6), we can write the solution of equation (3) in the following implicit form:

$$\int_{N_0}^N \frac{dN}{Q_{act}} = \int_{x_0}^x \frac{dx}{C_{ag}}, \quad (7)$$

where

$$N = N_0 \Big|_{x=x_0} \quad (8)$$

is a boundary condition. Under the initial condition  $x_0$ , the wave factor  $N_0$  corresponds to  $x_0 \rightarrow N_0$ , in a certain section  $x$ , the wave factor  $N$  corresponds  $x \rightarrow N$ .

Since the group velocity at constant depth and flow velocity does not depend on the coordinate, the right-hand side of equation (7) is reduced to:

$$\int_{x_0}^x \frac{dx}{C_{ag}} = t - t_0 = \frac{x - x_0}{C_{ag}}, \quad (9)$$

where  $t - t_0$  is the propagation time of waves with a group velocity from the boundary alignment. From (7) and (9) it follows that the following coordinate transformation (for  $x_0 = 0$ ) is:

$$\frac{x}{C_{ag}} = \frac{X}{C_{g0}} \quad \text{or} \quad \frac{X}{x} = \frac{C_{g0}}{C_{ag}} \quad (10)$$

where  $C_{g0}$ , the group velocity on still water, gives a wave action value  $N(x)$  equal to  $N_0(x)$  at the acceleration distance  $x$  along the flow, which is the amount of wave action

on the take-off run  $X$  on still water. Thus, relation (10) determines the effective acceleration length for wind waves in the flow.

The definition of the effective acceleration length for waves in a flow was considered in more detail in [6], where, in particular, it was shown that if the angle between the wind and current vectors is equal to  $\alpha$ , then the effective acceleration length is determined by the relation:

$$\frac{X}{x} = \frac{C_{g0}}{C_{gr} + U \cos \alpha}, \quad (11)$$

where  $C_{gr}$  is the group velocity of the waves in the coordinate system associated with the flow.

The concept of the effective acceleration length for waves in a flow gives the correct qualitative tendency for the influence of the flow on the development of waves. Indeed, in deep water  $C_{ga} = C_{g0} + U$  and in the associated stream ( $U > 0$ ) it follows from (10) that  $X/x < 1$ , i.e. effective acceleration length is less than actual. On the contrary, in the opposite flow ( $U < 0$ ) it follows from (10) that  $X/x > 1$ , i.e. effective acceleration length is greater than the actual geometric length. Such a flow effect corresponds to the data obtained in aero hydrodynamic channels [11–13], where the wind waves in the passing current are less and are more in the opposite flow than in the absence of the flow, in other equal conditions.

The effective acceleration length can be determined from equation (11), in which it is necessary to set the value of the relative group velocity. For this, the experimental dependence for the frequency of the maximum of the wave spectrum in the coordinate system of the flow can be used [13]:

$$\frac{u_* f_{pr}}{g} = 0,939 \left( \frac{gX}{u_*^2} \right)^{-0,354}, \quad (12)$$

where  $u_*$  is the wind friction velocity in a fixed coordinate system. If we go in relation (12) to the wind speed and the average frequency in the spectrum using the following relations [14]:

$$W = 25u_* \quad \bar{f} = 1,17f_p, \quad (13)$$

then the expression (12) takes the form:

$$\frac{\bar{\omega}_r W}{g} = 14,28 \left( \frac{gX}{u_*^2} \right)^{-0,354}, \quad (14)$$

where  $\bar{\omega}_r$  is the average relative circular frequency. Then for the average group speed we get:

$$\bar{C}_{gr} = \frac{0,44W}{4\pi} \left( \frac{gX}{u_*^2} \right)^{-0,354}. \quad (15)$$

For the effective acceleration length, from the relation (11) the following implicit equation is obtained:

$$\frac{X}{x} = \frac{1}{\left(\frac{X}{x}\right)^{0,354} + \frac{4\pi}{0,44} \frac{U \cos \alpha}{W} \left(\frac{gx}{W^2}\right)^{-0,354}} \quad (16)$$

The numerical solution of equation (16) is shown in Fig. 1. In Fig. 1a, the solution relates to the associated flow, when  $U \cos \alpha / W > 0$  and  $X/x < 1$ . Figure 1b shows the solution for the oncoming flow:  $U \cos \alpha / W < 0$  and  $X/x > 1$ . The curves in Fig. 1 clearly demonstrate how important the flow factor can be, which can increase or decrease the acceleration length, especially at limited acceleration lengths.

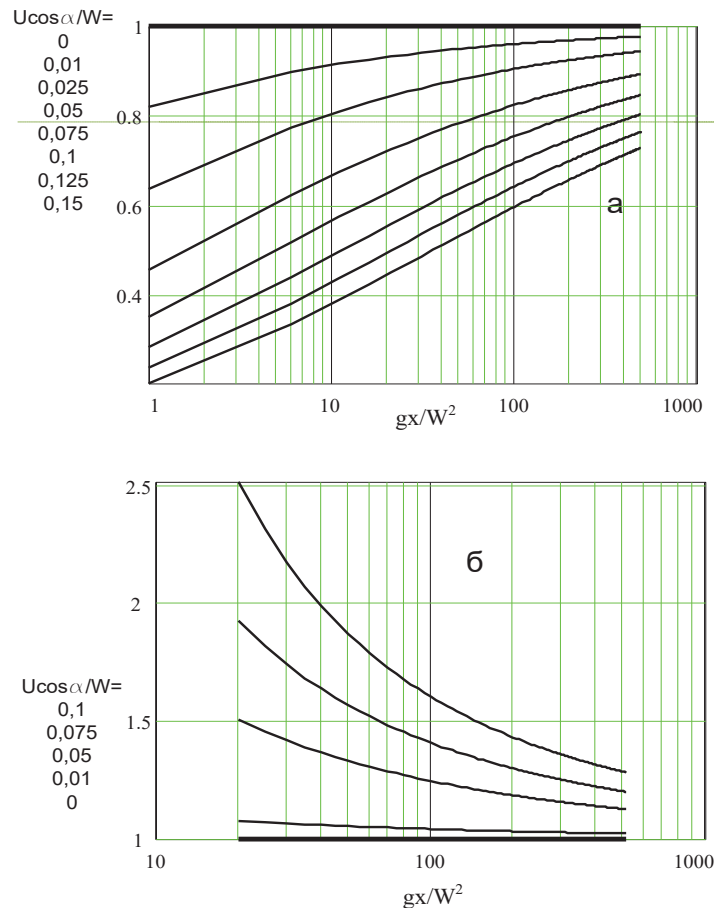


Fig. 1: The dimensionless acceleration length for wind waves in the flow:  
 a) on the passing flow, b) on the oncoming flow.

The introduction of an effective acceleration length allows the following formulas of GOIN-SoyuzMorNIIproekt [5] to be used to calculate the average height and period of waves in flows [5]:

$$\frac{g\bar{H}}{W^2} = 0,16 \left\{ 1 - \left[ \frac{1}{1 + 6,0 \times 10^{-3} (gX/W^2)^{0,5}} \right]^2 \right\}^{th} \left\{ 0,625 \frac{(gd/W^2)^{0,8}}{1 - \left[ \frac{1}{1 + 6,0 \times 10^{-3} (gX/W^2)^{0,5}} \right]} \right\}, \quad (17)$$

$$\frac{g\bar{T}_r}{W} = 3,1 \times 2\pi \left( \frac{g\bar{H}}{W^2} \right)^{0,625}$$

where  $T_r$  is the period of waves in a moving coordinate system (in the flow system),  $d$  - is the water depth at acceleration. As shown in [5], dependences (17) are consistent for the absence of flow with a large amount of data from field measurements of waves.

When predicting wind waves in limited water areas (large rivers, canals, reservoirs, or the coastal zone of the sea), it is necessary to take into account the limitation of acceleration by the coastline. This factor in conditions of narrowness or complex configuration of the coastline can be no less important than the current.

The principle of taking into account the influence of the coastline on acceleration limitation is known. For the coastal zone of the sea, the corresponding techniques are given in [15]. For estuaries, straits, and canals that can be approximated in plan by a rectangle, a technique for accounting for the limited channel width is given in [16].

The effective acceleration length is also used, which we will call effective to limit acceleration. The latter value is determined by the integration of the acceleration lengths measured from the design point to the intersection with the coastline, along the angle between the local and general directions of the wind speed:

$$\frac{F}{x} = \int_{-\theta'}^{\theta'} p(\theta)x(\theta)d\theta \Big/ \int_{-\theta'}^{\theta'} x d\theta \quad , \quad (18)$$

where  $\theta'$  is the raster of angles of the effective wave-forming action of the wind,  $p(\theta)$  – is the weight function.

The effective wave formation raster is set at 90 degrees on both sides of the general direction for the complex outline of the coastline and from 30 to 90 degrees in the case of watercourses. The type of weight function depends on the distribution of wind speed in the directions and on local conditions. So with  $\theta'=30^\circ$  and  $p(\theta)=1$ , we get a solution often used for channels:

$$\frac{F}{x} = \frac{6}{\pi} \left[ \ln \operatorname{tg} \left( \frac{1}{2} \operatorname{arctg} \frac{b}{2x} + \frac{\pi}{4} \right) - 1,317 \frac{b}{2x} - \frac{b}{2x} \ln \operatorname{tg} \left( \frac{1}{2} \operatorname{arctg} \frac{b}{2x} \right) \right] \quad , \quad (19)$$

where  $b$  is the channel width. The form of the function (19) is shown in Fig. 2.

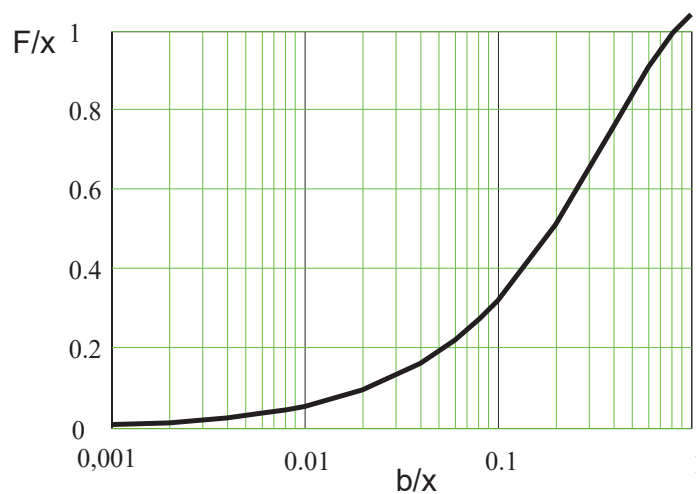


Fig. 2: The influence of the relative width of the channel on the acceleration of waves.

## 2. METHODOLOGY

The calculation method, taking into account the influence of both the current and the complex configuration of the coastline, is as follows and is used further to calculate the size of wind waves in the region of the investigated transition. The principles of the technique are described in detail in [7,8].

The algorithm is a generalization of the method of calculating wind waves with a complex coastline configuration. From the calculated point with an interval of 22.5 degrees on both sides of the main beam with number  $n = 1$ , additional rays with numbers  $n = \pm 2, \pm 3, \pm 4$  are drawn. Then, for each beam, the effective acceleration length along the stream is determined:

$$X(\alpha) = \Delta \sum_{i=1}^n \left( \frac{X}{x} \right)_i, \quad (20)$$

where  $\Delta$  is the length of the calculated section,  $(X / x)_i$  is determined by formula (16), in which the corresponding projection of the flow velocity takes part. The beam continues until it crosses the shoreline. In the case of relatively small accelerations, we can neglect the curvature of the wave beam and use relation (20) for the beam as a whole.

Further, for each wave beam, the average wave height is calculated according to the first formula (17), the average wave height for the studied water area is determined by weighted averaging in accordance with the recommendations [13]:

$$\bar{H} = 0,1 \left\{ 25\bar{H}_1^2 + 21(\bar{H}_2^2 + \bar{H}_{-2}^2) + 13(\bar{H}_3^2 + \bar{H}_{-3}^2) + 3,5(\bar{H}_4^2 + \bar{H}_{-4}^2) \right\}^{\frac{1}{2}}. \quad (21)$$

Then, according to the second formula (17), the average wave period is determined.

To move from the average height and period of the waves to the height and period of the specified provision, the system uses the distribution function of the heights of the wind waves in the form of the Rayleigh distribution, which is assumed to be valid for effective acceleration. In particular, to determine the height and period of significant waves, the following ratio can be applied:

$$\bar{H} = 0,625H_s \quad \bar{T} = 0,9T_s. \quad (22)$$

As measurements show, for the oncoming flow, there is a feature related to the initial acceleration section. In this area, the generated wind waves propagate along the downstream, and in the wind, i.e. groups of waves propagate upstream. It is natural to assume that for a given wave the length of the initial section is determined by the relation:

$$C_{gr} = U |\cos \alpha|, \quad (23)$$

That, using expression (15) for group velocity, can be written as:

$$\left( \frac{X}{x} \right)^{0,354} - \frac{4\pi}{0,44} \frac{U}{W} \left( \frac{gx}{W^2} \right)^{-0,354} |\cos \alpha| = 0. \quad (24)$$

If we solve equations (24) and (16) together for a ray in the opposite flow, then we can take into account the effect of the initial section.

### 3. RESULTS AND CONCLUSION

The developed methodology is confirmed by field measurements made at the Karakum channel (on the 110-120 km section of the canal) by the authors of the report, as well as by the SANIIRI measurement data on several Central Asian channels [6]. For an idea of the ranges of the comparison, the author's measurement data along with the calculation data are presented in Table 1. The table shows that a comparison of the results of calculating the heights of the wind waves with the measurement data give a good ratio.

Table 1: Comparison of wind wave height calculation results with measurement data

Acceleration length [m]	Channel width [m]	Water depth [m]	Wind speed [m / s]	Flow velocity [m]	Mass [kg]	
					Measured	Estimated
256	134	4.6	5.3	-0.42	4.5	4.3
258	134	4.6	6.9	-0.42	5.8	6.7
258	134	4.6	4.1	-0.42	3.3	3.0
795	167	3.8	5.7	0.42	6.0	6.1
795	167	3.8	5.8	0.42	6,3	6.2
137	55	3.2	9.4	-0.55	8.0	5.8
198	55	3.2	6.1	-0.55	5.6	3.7
180	50	2.1	15.8	-0.53	14.0	14.0
125	50	2.1	17.2	-0.53	13.0	11.0
180	50	2.1	6.0	-0.53	1.6	1.5

It can be concluded that when calculating the formation of wind waves on a stream in flowing reservoirs, large and small rivers, and large channels, the proposed calculation method can be used. The proposed methods have scientific justification and allow you to get the results needed to estimate the turbidity fields during dredging, determine the safe depth of the pipeline, predict possible erosion along the route, and calculate the wave deformation of the bottom and coastal slopes of the watercourse. The presented calculation methods and models can be applied to various areas of large watercourses or the coastal zone of the sea for the scientific justification of works on the construction of crossings by pipelines.

### REFERENCES

- [1] Atazhanov A, Kantargi IG, Sapova NO. (1989) Development of a method for predicting wind waves on streams. Proceedings of the VNII VODGEO, M., VODGEO, 40-45.
- [2] Zairov HI, Listrova PP, Masumov RR. (1986) Prediction of wind wave elements in large channels. Hydraulic Engineering, 12:44-46.
- [3] Kantargi IG (1987) A method for predicting wind waves on streams. Tr. VNII VODGEO, M, VODGEO, 60-68.
- [4] Kantargi IG, Dreisis YuI., Chebotkevich VO. (1987) The forecast of wind waves in large canals and flowing reservoirs. Hydraulic Engineering and Land Reclamation, 2: 24-27.
- [5] Krylov YuM., Strekalov SS, Tsyplukhin VF. (1976) Wind waves and their impact on structures. Leningrad, Gidrometeoizdat.
- [6] Mass EI, Kantargi IG. (1988) Method for calculating wind waves in large channels. Water Resources, 1:60-67.

- [7] Mass EI, Kantargi IG. (1986) Recommendations for the calculation of wind waves and sediment transport in large channels. Central Scientific Research Institute of Scientific Research, 1986, pp 1-63.
- [8] Rzhanitsyn NA, Altunin VS, Voynich-Syanozhentsky TG, Mass EI, Debolsky VK, Kantargi IG and others. Recommendations for the hydraulic calculation of large channels. GKNT USSR, Soyuzgiprovodkhoz, (1986), pp 1-153.
- [9] Bretherton FP, Garret CJR. (1969) Wave trains in inhomogeneous moving media. Proc. Roy. Soc. A, 302: pp 1-529.
- [10] Kato H, Tsuruya H, Doi T, Mijarari Y. (1976) Experimental study of wind waves generated on water currents. 2nd report, Rep. Port Harbor Res. Inst., 15(4):3-46.
- [11] Kato H, Tsuruya H, Terakawa H. (1981) Experimental study of wind waves generated on water currents. 3rd report. Wave forecasting methods and its experimental confirmation. Rep. Port Harbor Res. Inst., 20(3):94-129.
- [12] Kato H, Tsuruya H. (1978) Experimental study of wind waves generated on currents. Proc. 16th Coastal Eng. Conf. ASCE, 1:742-755.
- [13] Mitsuyasu H, Rikiishi. (1975) On the growth of duration-limited wave spectra. Rep. Res. Inst. Appl. Mech., Kuishi Univer., v. 23, 31-60.
- [14] US Army (1984) Shore protection manual v. 2, 4th ed., Coast. Eng. Res. Center, Washington, D.C.
- [15] Wood AMM. (1969) Coastal Hydraulics. Pitman Press, Both.
- [16] Willis DH. (1978) Sediment Load under Waves and Current. Proc. 16th Int. Conf. on Coastal Eng. August 27-September 3, 1978; Hamburg, Germany.

## IMPROVE THE EFFICIENCY OF THE POWER TRANSMISSION SYSTEM USING THE GENETIC ALGORITHM TO DETERMINE THE OPTIMUM LOCATION AND FACTS DEVICES

HUSAM HASAN MOHAMMED<sup>1\*</sup>, HIBA ZUHAIR ABDUL KAREEM<sup>1</sup>,  
AND WAFAA MOHAMMED RIDHA<sup>2</sup>

<sup>1</sup>Department of Electronic Technologies,

<sup>2</sup>Department of Computer Systems,  
Babylon Technical Institute,

Al-Furat Al-Awsat Technical University, 51015, Babylon, Iraq

\*Corresponding author: [husam171984@gmail.com](mailto:husam171984@gmail.com)

[Husam10@atu.edu.iq](mailto:Husam10@atu.edu.iq)

(Received: 23<sup>rd</sup> October 2019; Accepted: 4<sup>th</sup> January 2020; Published on-line: 4<sup>th</sup> July 2020)

**ABSTRACT:** As the world's energy consumption increases, the expansion of the energy system becomes increasingly important. However, the creation of new transmission lines requires excessive costs and time if the same transmission capacity is to be added to the existing network. Today's electrical networks are faced with high risks of voltage instability and real power losses. This development tends to occur due to the lack of reactive control power (RPL) in heavily stressed operating conditions caused by increased demand for loads and the rapid development of power systems worldwide. This paper has adopted the setting of FACTS (flexible AC transmission system) devices as additional control parameters for reducing transmission losses in power system static types of two FACTS devices consisting of SVC (static VAR compensators) while the TCSC (thermistor controlled series compensator) is included in the issue formulation. During this paper, the proposed algorithm was to determine the optimal placement of power network devices by genetic algorithm to manage reactive power, reduce losses, increase the transmission capacity and power lines, and help simulate the IEEE 24 bus control system and also the position of FACTS devices.

**ABSTRAK:** Apabila penggunaan tenaga dunia semakin meningkat, penambahan sistem tenaga sangat penting. Walau bagaimanapun, penciptaan talian penghantaran terkini memerlukan kos yang berlebihan dan had masa jika kapasiti penghantaran yang sama digunakan dengan lebih tinggi. Dalam rangkaian elektrik hari ini, unit ini berhadapan dengan risiko ketidakstabilan voltan dan putus bekalan tenaga. Penambahan sistem tenaga ini cenderung berlaku disebabkan kekurangan kuasa kawalan reaktif (RPL) dalam keadaan beban operasi yang besar disebabkan oleh peningkatan beban permintaan dan perkembangan pesat sistem kuasa di seluruh dunia. Kertas ini telah menggunakan pakai peranti FACTS (sistem penghantaran AC fleksibel) sebagai parameter kawalan tambahan bagi mengurangkan kehilangan penghantaran dalam sistem kuasa statik dua peranti FACTS yang terdiri daripada SVC (pemampas VAR statik) manakala TCSC (pemampas siri termistor kawalan) adalah termasuk dalam perumusan isu. Dalam kertas kerja ini, algoritma yang dicadangkan adalah penempatan optimum peranti rangkaian kuasa oleh algoritma genetik bagi mengurus kuasa reaktif juga mengurangkan kerugian dan meningkatkan kapasiti penghantaran dan kabel elektrik dan membantu menyerupai

sistem kawalan bas IEEE 24 dan juga kedudukan peranti FACTS di mana ia terbukti berkesan.

---

**KEYWORDS:** FACTS devices; genetic algorithms; SVC; TCSC; optimal location

## 1. INTRODUCTION

Reducing oil and gas reservoirs and increasing energy consumption worldwide have encouraged researchers to consider optimizing generation and energy transmission in power grids to increase efficiency and improve plant utilization, reduce losses, and preserve the environment. Studies show that FACTS technology has increased transmission capacity, reduced losses of power and load density, and improved reliability, performance and control by maintaining the voltage profile and affecting transmission parameters [1]. In recent years, reactive power control and loss reduction in power systems are performed through optimal location of FACTS devices using smart algorithms. Genetic Algorithm (GA) is one of the computer science exploration techniques used to find approximate solutions for optimization of exploration problems [2]. FACTS devices were first presented by Electric Power Research Institute (EPRI) in 1990 in the USA [3]. These devices not only increase system loadability but also control power to a great extent. They are also able to improve system stability due to their high speed [4].

## 2. POWER LOSSES

For solving this problem, continuous variables such as generator bus voltage, and discrete variables such as parallel switching size and FACTS series devices are used, and the objective function is to reduce the power network loss index. The real power loss ( $P_{Loss}$ ) in transmission networks is calculated as the following [5]:

$$P_{Loss} = \sum_{K=1}^{N_L} G_K (V_i^2 + V_j^2 - 2V_i V_j \cos \theta_{ij}) \quad (1)$$

Where,  $N_L$  is the number of the branches of the power system,  $P_{Loss}$  is the loss of a branch,  $G_K$  is the conductance of the branch K.  $V_i$  and  $V_j$  voltages at the beginning and end of the branch.  $\theta_{ij}$  is the power angle difference between  $ij$  bus. The constraints that are considered for this problem include nonlinear equality of power flow equations and the linear inequality of various parameters [6] as the following:

$$P_{Gi} = P_{Di} + V_i \sum_{N=1}^{N_B} V_j (G_{ij} \cos \theta_{ij} + B_{ij} \sin \theta_{ij}) \quad (2)$$

$$Q_{Gi} = Q_{Di} + V_i \sum_{N=1}^{N_B} V_j (G_{ij} \sin \theta_{ij} - B_{ij} \cos \theta_{ij}) \quad (3)$$

The equation (2) and (3) follow the following constraints[6]

$$V_i^{min} \leq V_i \leq V_i^{max} \quad i \in N_B \quad (4)$$

$$T_i^{min} \leq T_i \leq T_i^{max} \quad i \in N_j \quad (5)$$

$$Q_{Gi}^{min} \leq Q_{Gi} \leq Q_{Gi}^{max} \quad i \in N_{PV} \quad (6)$$

$$Q_{Ci}^{min} \leq Q_{Ci} \leq Q_{Ci}^{max} \quad i \in N_C \quad (7)$$

Where  $P_{Gi}$  and  $Q_{Gi}$  are active and reactive powers of bus.  $P_{Di}$  and  $Q_{Di}$  are active and reactive consumption powers of bus  $i$ .  $G_{ij}$  and  $B_{ij}$  are real and imaginary parts of component  $ij$  of admittance matrix of the network.  $N_B$  is the number of buses of the network.  $N_{PV}$  is the set of buses of the generator. Indices min and max are minimum and maximum value of each parameter.  $N_C$  is the number of shunt VAR compensation  $Q_C$ .

### 3. THE MODEL OF SVC

The static var compensator (SVC) parallel compensator is a static capacitance/inductance with susceptance of BSVC shown in Fig. 1, which is, modelled as a variable susceptance in parallel with BSVC at bus  $i$ . The reactive power injected to bus of SVC is described as follows[7]:

$$Q_{SVC} = B_{SVC} \cdot V^2 \quad (8)$$

where  $V$  is the amplitude of the voltage for the bus that SVC is connected to. The main task of SVC is to regulate voltage of the bus, which is done by controlling reactive power injection at that point. As shown in Fig. 1, the equivalent circuit of SVC can be represented as a variable susceptance [8].

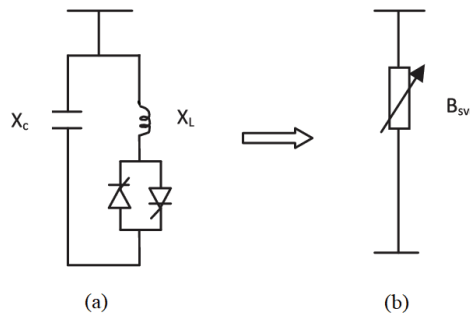


Fig. 1: The static VAR compensator (a) basic structure (b) model..

The new admittance of the system after installing SVC in the  $i$  bus can be expressed by the following matrix:

$$Y_{bus}^{SVC} = Y_{bus} + \begin{bmatrix} 0 & 0 & 0 & \dots & 0 & 0 & 0 \\ 0 & Y_{shunt} & 0 & \dots & 0 & 0 & 0 \\ 0 & 0 & 0 & \dots & 0 & 0 & 0 \\ \dots & \dots & \dots & \dots & 0 & \dots & 0 \\ 0 & 0 & 0 & \dots & 0 & 0 & 0 \\ 0 & 0 & 0 & \dots & 0 & 0 & 0 \\ 0 & 0 & 0 & \dots & 0 & 0 & 0 \end{bmatrix} \quad (9)$$

where,  $Y_{bus}$  is the admittance of the system without SVC.

For constant active power and  $V_{rms}$  source voltage, the required capacitive reactive power varies before and after the capacitive compensator is installed:

$$VAR(capacitive) = VAR(required) - VAR \quad (10)$$

As the value of  $B_{cap}$  capacitive susceptance is given by the following equation:

$$B_{cap} = \frac{VAR(required) - VAR(Uncompensated)}{V_{rms}^2} \cdot S \quad (11)$$

And capacitance required in farad is calculated as follows: [2]

$$C \text{ (Farad)} = \frac{B_{cap}}{(2\pi f)} \quad (12)$$

#### 4. THE MODEL OF THYRISTOR CONTROLLED SERIES COMPENSATOR TCSC

The TCSC is a capacitive reactance compensator that consists of a series capacitor bank shunted by a thyristor-controlled reactor. The basic conceptual TCSC module comprises a series capacitor, C, in parallel with a thyristor controlled reactor Fig. 2A [9]. The TCSC compensator is a static reactor capacitance with the impedance of  $jx_c$  with susceptance of BSVC shown in Fig. 2B [9]. The thyristor is modelled with a nonlinear resistance that is controlled by firing angle [10]. Current of inductance and voltage of capacitance are selected as two variables in state space.

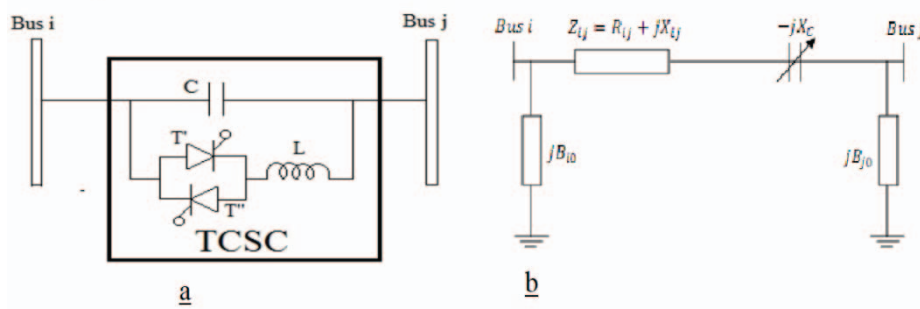


Fig. 2: Thyristor controlled series compensator presentation:  
 (a) basic structure, (b) model.

$X_{ij}$  is the line reactance,  $R_{ij}$  is the line resistance,  $jB_{jo}$ ,  $jB_{io}$  are load susceptance of half of the line at bus  $i$  and bus  $j$  of the line. The difference between the line susceptance before and after TCSC installation is as follows:

$$\Delta y_{ij} = y_{ij \text{ old}} - y_{ij \text{ new}} = (g_{ij} + jb_{ij})_{old} - (g_{ij} + jb_{ij})_{new} \quad (13)$$

$$g_{ij \text{ old}} = \frac{r_{ij}}{\sqrt{r_{ij}^2 + x_{ij}^2}}, \quad b_{ij \text{ old}} = -\frac{x_{ij}}{\sqrt{r_{ij}^2 + x_{ij}^2}} \quad (14)$$

$$g_{ij \text{ new}} = \frac{r_{ij}}{\sqrt{r_{ij}^2 + (x_{ij} + x_c)^2}}, \quad b_{ij \text{ new}} = -\frac{x_{ij} + x_c}{\sqrt{r_{ij}^2 + (x_{ij} + x_c)^2}} \quad (15)$$

The new admittance of the system after connecting TCSC between the  $i$  and  $j$  bus can be expressing by the following matrix:

$$Y_{bus}^{TCSC} = Y_{bus} + \begin{bmatrix} 0 & 0 & 0 & \dots & 0 & 0 & 0 \\ 0 & \Delta y_{ij} & 0 & \dots & 0 & -\Delta y_{ij} & 0 \\ 0 & 0 & 0 & \dots & 0 & 0 & 0 \\ \dots & \dots & \dots & \dots & 0 & \dots & 0 \\ 0 & 0 & 0 & \dots & 0 & 0 & 0 \\ 0 & -\Delta y_{ij} & 0 & \dots & 0 & \Delta y_{ij} & 0 \\ 0 & 0 & 0 & \dots & 0 & 0 & 0 \end{bmatrix} \quad (16)$$

where,  $Y_{bus}$  is The admittance of the system without TCSC. Eq. (17) shows new reactance of the line after installing TCSC.

$$x_{new} = x_{old} - n \cdot x_{old} \quad (17)$$

where,  $x_{old}$  is the reactance of the line without TCSC and the  $n$  is in the range of

$$0.25x_{line} \leq n \leq 0.75x_{line} \quad (18)$$

## 5. THE PROPOSED METHOD

One of the most important advantages of intelligent methods is that there is no specific space to find the best solution. Among the intelligent methods, we can mention Simulated Annealing (SA) [11], Tabu Search method (TS) [12] and particle swarm optimization technique [13]. We decided in this paper to use the method of GA. GA uses one of the natural Darwin's selection principles for finding an optimal formula to predict or match patterns [14]. In summary, it is said that GA is a programming technique that employs genetic evolution to solve problems. The summary of a genetic algorithm is as follows:

- **Beginning:** Create  $n$  chromosomal population randomly (appropriate solutions to **the problem**).
- **Valuation:** Assess the fitness  $f(x)$  of each chromosome  $X$  in the population.
- **New population:** Create a new population. Repeat steps below to complete the new crowd.
- **Choice:** Choose two chromosomes (parents) according to their fitness from the crowd. The higher the chances, the better the chances of being chosen.
- **Combination:** Combine the possibility of combining parents (Probability Crossover) to form new children (Offspring).
- **Mutations:** A mutation occurs with the probability of children mutation in each locas (position on the chromosome).
- **Accepting:** Include new children in the new population.
- **Replacement:** Use the new population created for the algorithm process

The main objective of this work is to find the best place for the FACTS devices, their types, and their values. Special coding was developed to achieve parameters (location, type, value). The first string represents the location of the FACTS devices, where it contains the numbers of lines. As for the second string, it is to determine the type of FACTS devices added. The value of the added device is determined by the last string, which is between 0 and 1 where 0 represents the minimum, and 1 represents the maximum. The real value of the FACTS device  $v_{realF}$  can be calculated using the following equation:

$$v_{realF} = v_{minF} + (v_{maxF} - v_{minF})v_F \quad (19)$$

where  $v_{maxF}$  and  $v_{minF}$  are respectively the maximum and the minimum setting value of the FACTS device, and  $v_F$  is the normal value. The initial population of the system depends on the following parameters:

- $n_F$  The number of FACTS devices that are selected as optimal
- Types of FACTS devices that will be determined
- $n_v$  Represents the number of special settings for each device
- $n_i$  Represents the number of individuals of the population.

At each of the three stages is created:

- In the first string, a set of numbers of branches of the network are randomly placed.
- The second step is to draw random numbers indicating the types of devices and placed in the second string
- In the third step, the values of the devices are chosen randomly within the possible limits.

The objective function will be calculated for each individual population previously configured and the objective function in this paper is the effect of the FACTS devices in the power system. A slice will be allocated in the roulette wheel for each individual population. The size of the slice is proportional to each individual and the appropriate individual will occupy a larger slice, as in Fig. 3. The wheel will be rotating many times and after the wheel stops, the individual to which it refers will be selected.

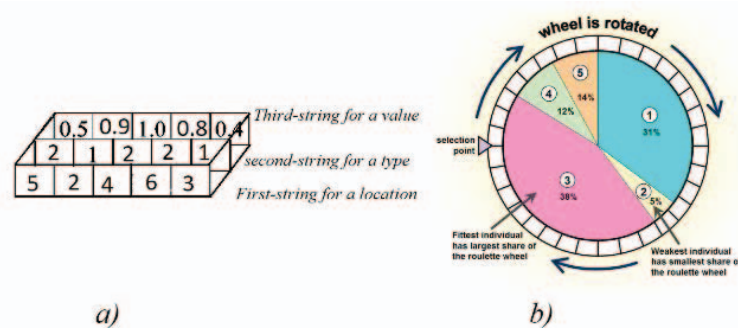


Fig. 3: Arrangement of 2 FACTS devices (a) Individual, (b) Roulette wheel to select individuals.

## 6. DETERMINE THE LOCATION AND VALUE OF THE FACTS DEVICES WITH THE GENETIC ALGORITHM (GA)

- First, initial conditions are considered for system loads. This initial condition might be based on the basic load of the system.
- For generator buses (except reference bus), an initial active power proportionate to the load is determined.
- The power flow program is executed.
- The power flow program might diverge due to excess increase in load condition of the system. In this case, the previous load condition is considered as the maximum load condition and step 6 is performed.
- GA and the employed devices are used to define the objective function (reducing losses).
- Real genetic program is executed.
- The algorithm represents optimal size and location of TCSC and SVC and the considered index through iterative and random selection.
- The program is finished.

## 7. SIMULATION AND RESULTS

In this section, location of SVC and TCSC in a standard IEEE 24-bus system is investigated using GA and the results are presented. Performance of the system is first



for TCSC. Encoding region would be 38 integers from 1 to 38. Compensation percentage using TCSC is 60%. After using real GA, it is seen that considering line 27 which is between buses 15 and 24 as the optimal location of TCSC with magnitude of 0.581, loss index is reduced to 208.865 MVA.

#### 7.4 Losses Index by Installing a Combination Of SVC and TCSC in the IEEE 24-Bus System

In this case, installing a combination of TCSC and SVC is studied and its results are compared with each other. After using real GA, it is seen that considering line 27, which is located between buses 15 and 24, as the optimal location for installing TCSC with magnitude of 0.581 and bus 10 as the best location for installing SVC with capacity of 225.69MVAR, loss index is reduced to 201.765MVA. The voltage profile curve for IEEE 24-bus system is shown in Fig. 5 to Fig. 7.

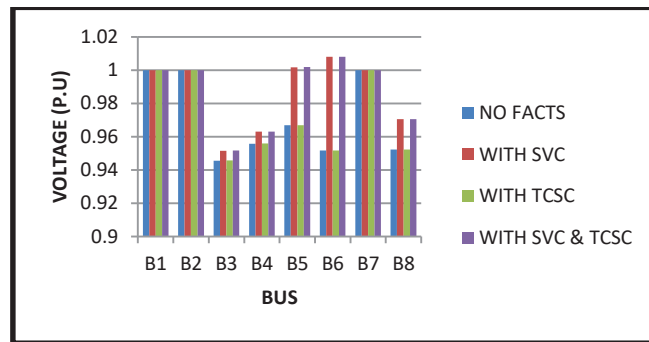


Fig. 5: Voltage profile of buses (1-8) for the IEEE 24-bus system.

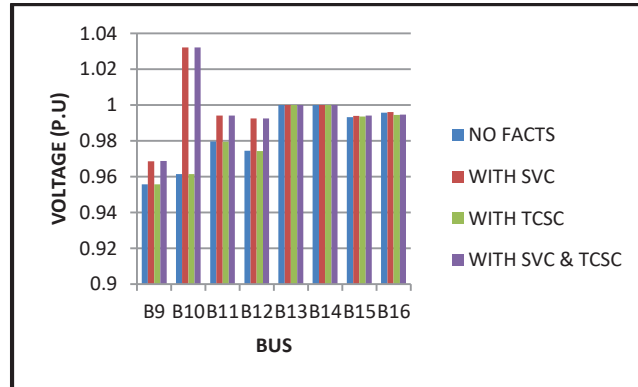


Fig. 6: Voltage profile of buses (9-16) for the IEEE 24-bus system.

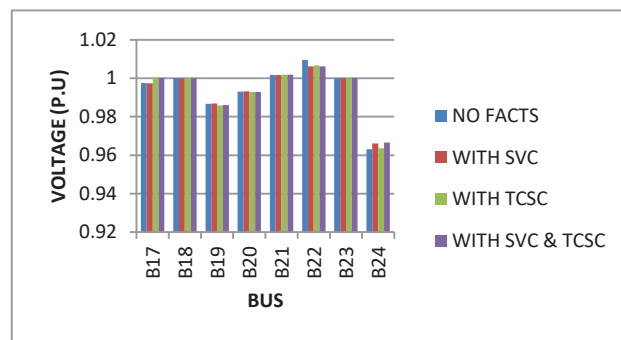


Fig. 7: Voltage profile of buses (17-24) for the IEEE 24-bus system.

When referring to Fig.5-7, we notice a significant improvement in the voltage profile of buses after installing a combination of SVC and TCSC. For example, the bus voltage number 5 was 0.9668 before the installation of SVC and TCSC, but it became 1.0018 and by installing SVC in this system, voltage profile of load buses at bus 10 increases significantly.

Table 1: Comparing loss index before and after devices in IEEE 24-bus system

Case	Without Facts	With SVC	With TCSC	With SVC and TSCS
<b>Location</b>	--	Bus 10	Line 27	Svc Bus 10 TCSC Line 27
<b>Size</b>	--	225.69 Mvar	0.581	225.69 Mvar 0.581
<b>Losses</b>	225.68 Mva	218.786 Mva	208.865 Mva	201.765 Mvar

After using the proposed GA method to find the best location and value for SVC and TCSC we find that the losses in the system decreased a lot and when looking at Table 1. We find that the losses became 201.765 Mva after installing TCSC and SVC after it was 225.68Mva without FACTS devices. In other words, this index was improved.

## 8. CONCLUSION

In order to study simulation, Genetic Algorithm is implemented on a sample bus of an IEEE 24-bus system with real coding and the obtained results are discussed along with corresponding diagrams and tables. Obtained results show that considering loss index and installing SVC in both systems, voltage profile of load buses increases significantly. Furthermore, considering loss index and installing a combination of SVC and TCSC in both systems, voltage profile of load buses increases. By installing a combination of SVC and TCSC, loss index becomes lower compared to when no such device is installed, SVC is installed, or TCSC is installed, which shows improvement of this index.

## REFERENCES

- [1] Dazahra MN, Elmariami F, Belfqih A, Boukherouaa J.( 2016) Optimal Location of SVC using Particle Swarm Optimization and Voltage Stability Indexes. *International Journal of Electrical and Computer Engineering*, 6(6):2581.
- [2] Mirjalili S. (2016) Dragonfly algorithm: a new meta-heuristic optimization technique for solving single-objective, discrete, and multi-objective problems. *Neural Computing and Applications*, 27(4):1053-1073.
- [3] Jordehi AR. (2016) Optimal allocation of FACTS devices for static security enhancement in power systems via imperialistic competitive algorithm (ICA). *Applied Soft Computing*, 48:317-328.
- [4] Darabian M, Jalilvand A. (2017) A power control strategy to improve power system stability in the presence of wind farms using FACTS devices and predictive control. *International Journal of Electrical Power & Energy Systems*, 85:50-66.
- [5] Nwohu MN, Isah A, Usman AU, Sadiq AA. (2016) Optimal placement of Thyristor Controlled Series Compensator (TCSC) on Nigerian 330kV transmission grid to minimize real power losses. *International Journal of Research studies in Electrical and Electronics Engineering*, 2:18-26.
- [6] Raj S, Bhattacharyya B.( 2018) Optimal placement of TCSC and SVC for reactive power planning using Whale optimization algorithm. *Swarm and Evolutionary Computation*,

- 40:131-143.
- [7] Yu M, Xie H, Song W, WANG H, HE J, XIN H. ( 2017) Impact of SVC control mode on voltage abnormal oscillation in wind power influx area. *Autom Electr Power Syst*, 41(1):73-78.
  - [8] Sen D, Ghatak SR, Acharjee P. (2019) Optimal allocation of static VAR compensator by a hybrid algorithm. *Energy Systems*, 10(3):677-719.
  - [9] Zare K, Hagh MT, Morsali J.( 2015) Effective oscillation damping of an interconnected multi-source power system with automatic generation control and TCSC. *International Journal of Electrical Power & Energy Systems*, 65:220-230.
  - [10] Sahoo DK, Sahu RK, Sekhar GTC, Panda S. (2018) A novel modified differential evolution algorithm optimized fuzzy proportional integral derivative controller for load frequency control with thyristor controlled series compensator. *Journal of Electrical Systems and Information Technology*, 5(3):944-963.
  - [11] Sodeifian G, Sajadian SA, Ardestani NS. (2017) Experimental optimization and mathematical modeling of the supercritical fluid extraction of essential oil from *Eryngium billardieri*: application of simulated annealing (SA) algorithm. *The Journal of Supercritical Fluids*, 127:146-157.
  - [12] Martí R, Martínez-Gavara A, Sánchez-Oro J, Duarte A. (2018) Tabu search for the dynamic Bipartite Drawing Problem. *Computers & Operations Research*, 91:1-12.
  - [13] Babu TS, Rajasekar N, Sangeetha K. (2015) Modified particle swarm optimization technique based maximum power point tracking for uniform and under partial shading condition. *Applied Soft Computing*, 34:613-624.
  - [14] Gubin A V, Borzunov DY, Marchenkova LO, Malkova TA, Smirnova IL. (2016) Contribution of GA Ilizarov to bone reconstruction: historical achievements and state of the art. *Strategies in Trauma and Limb Reconstruction*, 11(3):145-152.
  - [15] Kia M, Nazar MS, Sepasian MS, Heidari A, Siano P.( 2017) Optimal day ahead scheduling of combined heat and power units with electrical and thermal storage considering security constraint of power system. *Energy*, 120:241-252.

# BORDER SURVEILLANCE USING FACE RECOGNITION, MOBILE OTP AND EMAIL

NARESH KUMAR<sup>1</sup> AND DEEPALI GUPTA<sup>2</sup>

<sup>1</sup>*Department of Computer Science and Engineering,  
MSIT, Janakpuri, New Delhi, India.*

<sup>2</sup>*Chitkara University Institute of Engineering and Technology,  
Chitkara University, Punjab, India.*

\*Corresponding author: [narsumsaini@gmail.com](mailto:narsumsaini@gmail.com)

(Received: 24<sup>th</sup> December 2019; Accepted: 13<sup>th</sup> March 2020; Published on-line: 4<sup>th</sup> July 2020)

**ABSTRACT:** Expanding strains over Indian borders with illegal crossings and examining past assaults on the nation, it is clear that in a large portion of the cases, security powers are uninformed of the movement of these interlopers. For this reason, a framework is needed to manage the border issue that would be equipped for working in sloping landscapes where there is no power. This paper manages identification and situating of interlopers crossing the border utilizing PIR sensors and cameras. In the event of any undesirable crossing in the area, the sensor quickly detects it and the camera will stream pictures to the base station (BS). Relying upon the guidance originating from the BS, the sensor will either activate the camera for further streaming or turn it off. The objective of this paper is to give a framework that will help the Border Security Force (BSF) in controlling all sorts of illicit activities near the outskirt in a superior and precise manner.

**ABSTRAK:** Merentas isu sempadan India dengan kegiatan pencerobohan sempadan dan dengan mengambil kira kutukan lepas terhadap bangsa kami, adalah jelas dalam banyak-banyak kes ini pegawai keselamatan tidak diberitahu tentang bahagian yang dicerobohi. Dalam keadaan ini, kita memerlukan rangka kerja bagi mengurus masalah sempadan di mana kelengkapan perlu dipasang di tebing landskap yang tidak mempunyai sumber tenaga. Kajian ini mengurus identiti pengenalan dan kedudukan kegiatan haram yang berleluasa di sempadan dengan mengguna pakai pengesan PIR dan kamera. Apabila terdapat perubahan pergerakan yang tidak diingini di sempadan, PIR akan mengesan pergerakan dengan cepat dan kamera akan menggaris arus gambar-gambar ke stesen utama (BS) dan bergantung kepada panduan pengkalan di BS, pengesan akan membuat kamera lebih bergaris arus atau berhenti merekod. Kajian ini penting bagi menunjukkan rangka yang membantu Penguatkuasaan Keselamatan Sempadan (BSF) dalam mengawal semua kegiatan haram berhampiran sempadan dengan bermutu dan tepat.

**KEYWORDS:** *Eigenface; face detection; face recognition, training set*

## 1. INTRODUCTION

Outskirt Security System is a creative plan to verify wildernesses insightfully without the mediation of humans. It gives protection to the nation and simultaneously reduces manpower and asset usage. The outskirt security framework recognizes any interloper and also monitors every one of the activities occurring close to the territory. Because the border area is an enormous and perilous region, it is difficult to secure a constant power supply for the system. Nonetheless, an effective national shield requires a constant

monitoring of the border areas, with the associated labour and equipment costs. For this reason, an automated framework for surveillance is fundamental. The automated system must include specialized issues and use of legitimate calculation with the goal that any interruption identified in the outskirts can easily be transmitted to inform vital responses from authorities. Appropriate use of the framework may help Border Security Force (BSF) to control those exercises in a superior and increasingly exact manner. A report of [1] in the US in 2014 showed 1.7% of aggressive offense and robbery cases increased by 1% from total of 311936 cases of 2014. Lots of research has been carried out on face recognition border security systems and the information is available in [2-7]. Similar home security systems are also mentioned in [8-11].

Facial discovery is a PC innovation that decides the area and size of human face in a self-assertive (advanced) picture. The facial highlights are identified and some other items like trees, structures and bodies and so on are overlooked from the computerized picture. It can be seen as classification of instances where one can find the area with size of all the places and its class. Face recognition is basic element of face limitation. In face confinement, the errand is to discover the areas and sizes of a known number of appearances (normally one). Essentially there are two sorts of ways to deal with the distinguished facial part in the given picture for example highlight base and picture base approach. Feature base methodology attempts to remove highlights of the picture and compare it with the information on the face highlights. The method is based on the image to provide the best match between training and the image to be tested.

Faces are a factor that is exceptionally simple to recall, all things considered. For the most part, people can recall and perceive an individual dependent all over. It is proven that a face is one of a mind boggling set of variations when seen from the point of view of PC vision. Human countenances have various highlights and qualities of every individual with the goal that face acknowledgment is generally excellent to be applied in different territories, including excitement, savvy cards, data security, and so forth.

The essential idea of PC vision is as valuable data from a solitary picture or a succession of pictures, generally utilizing the technique of programmed extraction, investigation and learning. Probably the best technique to perform facial acknowledgment is to utilize the Principal Component Analysis (PCA) calculation. PCA is likely the most prevalent multivariate measurable procedure and it is utilized by practically all logical orders. It is additionally liable to be the most seasoned multivariate strategy. Multivariate investigation can essentially be translated as a strategy related with enormous factors in at least one examination. This strategy can separate the fundamental trademark information from different information that we have. PCA is a multivariate procedure that breaks down an information table wherein perceptions are depicted by a few between corresponded quantitative ward factors. The Eigen face based approach is used by PCA.

In this paper, the proposed approach uses a human face with an Eigen face approach to provide security at border.

## **2. RELATED WORKS**

Face acknowledgment has been considered by numerous specialist utilizing different calculation and approach. Biometric use is the most noteworthy security framework contrasted with conventional frameworks (utilizing secret word or different Identity Card for verification) on the security framework. Face acknowledgment itself has two fundamental strides as a rule [12], namely face discovery and face acknowledgment. To

perform face identification, Cascade Classifier technique is used. In [13] the Feed Forward Neural Networks (FFNW) is used to accomplish face acknowledgment. Face recognition was performed in [12] and [13] by Principal Component Analysis (PCA).

By watching the writing, particularly [12,13], and PCA calculation is chosen to play out the face acknowledgment. This exploration is likewise bolstered by another examination like [14].

### **3. CHALLENGES OF BORDER SECURITY**

Some of the challenges encountered in border security are as follows:

- a) Infiltration and ex-filtration of armed militants
- b) Narcotics and armed smugglers
- c) Illegal migrations
- d) Export of fundamentalist terrorism

### **4. OBJECTIVES OF BORDER SECURITY**

Based on literature review and challenges identified in section II and III, the following are the major objectives of this paper:

- a) To identify intruders with cameras and sensors like PIR and IR sensors.
- b) To effectively eliminate the intruder using a gun firing mechanism.
- c) To eliminate the need for being physically present in any location for security of the border.

### **5. PROPOSED METHOD**

The architecture of proposed method is shown in Fig. 1, which elaborates the complete process of how the work in the proposed approach is accomplished. The architecture shown in Fig.1 utilizes Red Green Blue (RGB) images captured by webcam as essential information and can use optional information, such as xml classifier documents, for facial identification and recognition. It comprises info factors of the initial face picture and the prepared face picture. The yield factors of this examination are level of similarity and recognition of a suspect's face [15]. The module-wise explanation of architecture is:

#### **5.1 Object Detection**

The initial step to accomplish for face location is to get to the camera that will be utilized for face identification and acknowledgment. The detection process is shown in Fig. 2. This stage will also check whether the webcam is on. On the off chance that the camera is turned off, the procedure cannot be continued.

The recognition procedure begins by identifying objects utilizing `CASCADE_FIND_BIGGEST_OBJECT` as a course classifier that will only look through the one biggest item. Moreover, the underlying information picture of RGB arrangement is converted to grayscale design. The following stage is to contract the camera picture to a sensible size on the grounds that the speed of face discovery depends on the size of the picture. It will be delayed for enormous pictures and will be quick for little pictures. It is likewise still genuinely dependable to identify faces even at low resolution.

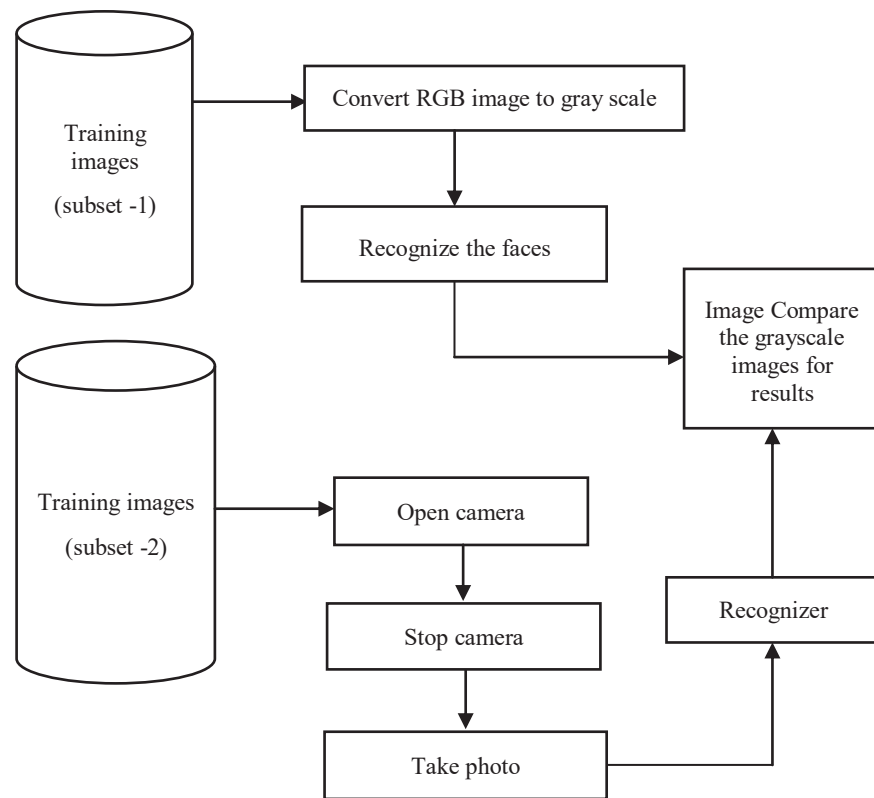


Fig. 1: Architecture of the face detection system.

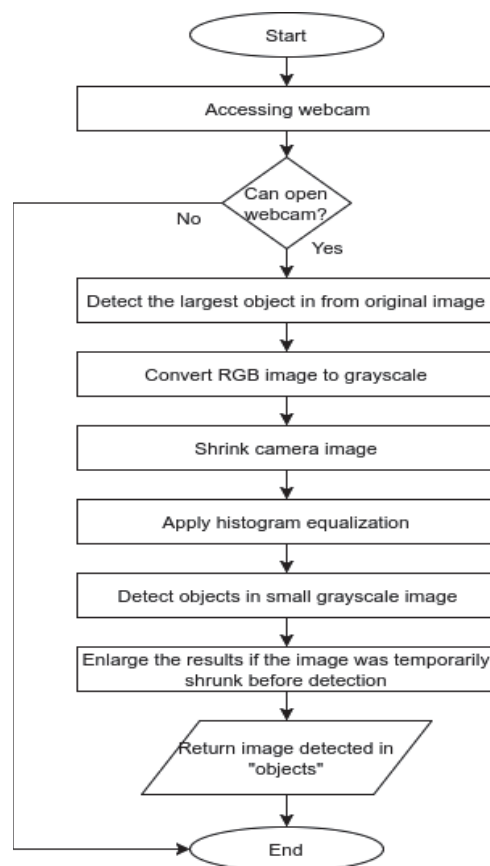


Fig. 2: Face detection process.

To improve the contrast and sharpness, histogram adjustment is applied. From that point onward, we can at last recognize the face from a little improved grayscale picture. The next significant step is to grow the outcomes if the picture was briefly contracted due to a past contracting step. The last advance of distinguishing an object as a face is to restore the face recognized and put it away in "objects".

Pre-processing is done to limit disappointment in the acknowledgment process. It starts by recognizing the area of the eye from the underlying information picture. It is graphically represented in Fig. 3. The captured eye area has been retained. The geometric change process is then completed by turning, scaling, and interpreting the pictures with the goal that the eyes are adjusted, trailed by the expulsion of the foundation from the face picture. To have a better arrangement, the recognized eyes are utilized to adjust the face so that the location of the two eyes line up consummately in the desired positions.

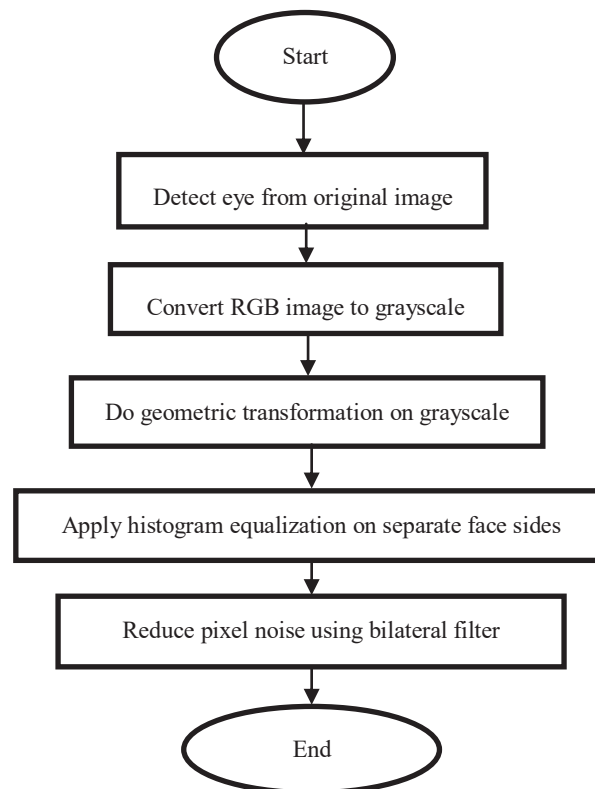


Fig. 3: Face preprocessing.

The turning stage pivots the face with the goal that the two eyes are even. The scaling stage will make the separation between the two eyes consistent and equivalent. Then, the interpreting stage will decipher the face with the goal that the eyes are constantly focused on a level plane and at an ideal height.

A significant number of the cases wherein face acknowledgment failed, were due to the lighting factor, both the absence of lighting, the light just originating from one side, or as unreasonable lighting. In this manner, it is important to do a histogram evening out independently on the left and right parts of the face, to have institutionalized sharpness and complexity on each side of the face.

The two histogram balances will be applied bit by bit from the left or right towards the middle and blend it in with an entire face histogram adjustment, so the inside utilizes a

smooth blend of left or right value and the entire face adjusted value. The last phase of this procedure is to apply the respective channel, which is valuable for smoothing the vast majority of a picture while keeping edges sharp.

## 5.2 Collect and Train the Faces

Face information assortment is determined and information is prepared for the model. Each face capture takes place at a time interval of one second and should surpass the limit estimation of similarity  $> 0.3$ . The edge likeness esteem is helpful for checking whether recently captured and subsequent face pictures have variations, supposing that the information is increasingly changed the better the consequence of face acknowledgment is finished.

To provide variation in the facial training data set, a mirror version is also added. Then the data is saved in the "Data" folder in .pgm format and the process of training is performed which converts the data into a model and then stores it in xml format. At the final average face value, eigenvector and Eigen values are calculated using a PCA algorithm whose steps are explained in Fig. 4.

The possibility of an Eigenface is a movement of eigenvectors used to see human faces in a PC vision. Eigenvectors are obtained from covariance order which has a high probability scattering and vector space estimation to see the likelihood of a face [12].

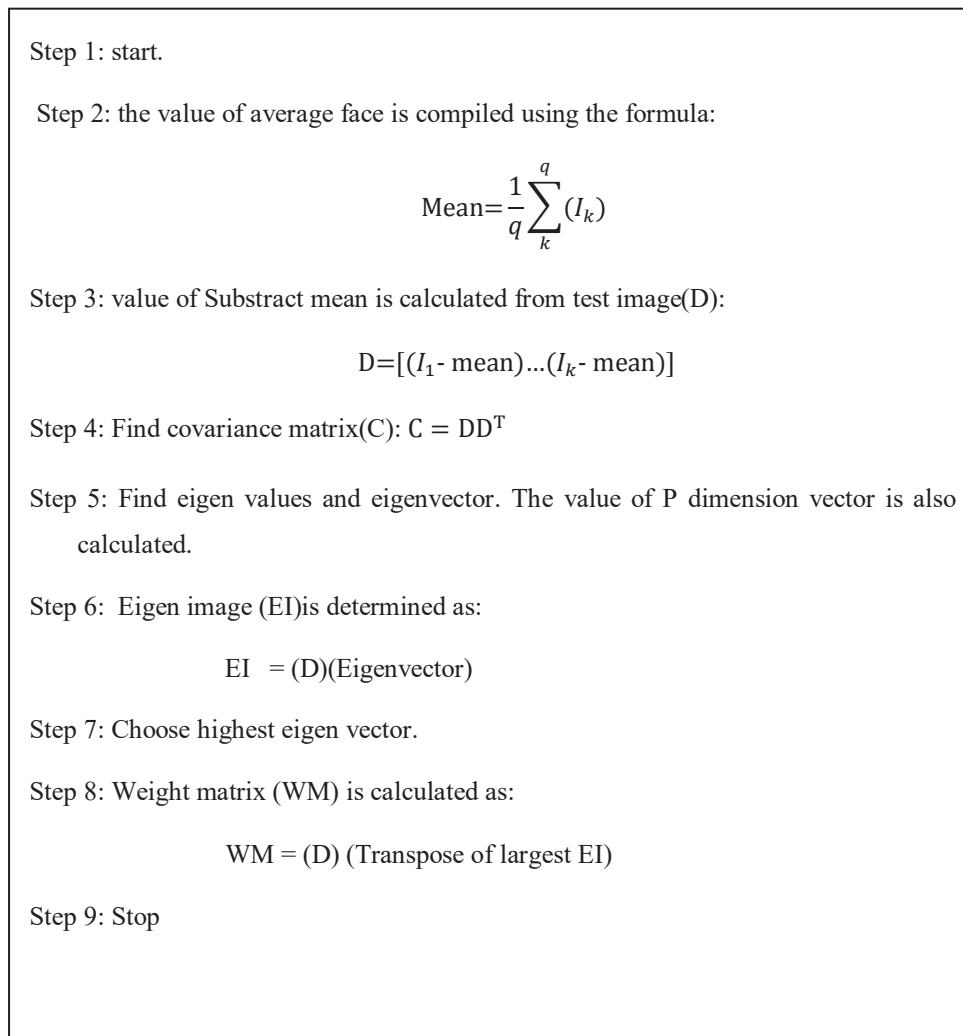


Fig. 4: PCA algorithm.

### 5.3 Recognition

To play out a face acknowledgment process, the initial step to do is to stack the .xml document from the prepared facial picture of the past procedure and the .xml record of the course classifier that will be utilized to recognize faces and eyes. In the event that the .xml document has been effectively stacked, at that point check whether the webcam is available. On the off chance that the webcam isn't available, the procedure will consequently stop and exit, generally the framework will continue the discovery process.

The aftereffects of face pre-processing will be contrasted and the preparation model that has been handled into a reproducible face by back-anticipating the eigenvectors and eigenvalues [16]. The edge esteem utilized for examination is 0.5. In the event that the estimation of comparability/estimation of the correlation results is not exactly the edge esteem, then the client's face can be perceived by the framework, otherwise it will be considered as an "Obscure" client.

## 6. EXPERIMENTAL SETUP AND RESULTS DISCUSSION

The proposed approach is implemented in Python. Some other circuitry used includes:

- **Arduino Uno** is a microcontroller dependent on the ATmega328P with 14 computerized input pins with 6 information sources, 16 MHz, USB, a power jack, an ICSP header and a reset mechanism.
- **The HOG** highlights are broadly used for object recognition. Hoard disintegrates a picture into little squared cells, figures a histogram of arranged angles in every cell, standardizes the outcome utilizing a square shrewd example, and returns a descriptor for every cell. Stacking the cells into a squared picture area can be utilized as a picture window descriptor for object identification, for instance by methods for a SVM.
- **Servo engine** is an electric device to push an item with exactness.
- A **Cascade Classifier** is prepared with two or three hundred example perspectives on a specific article (i.e., a face or a vehicle), called positive models, that are scaled to a similar size (say, 20x20), and negative models - subjective pictures of a similar size. A short image of complete setup is shown in Fig. 5.

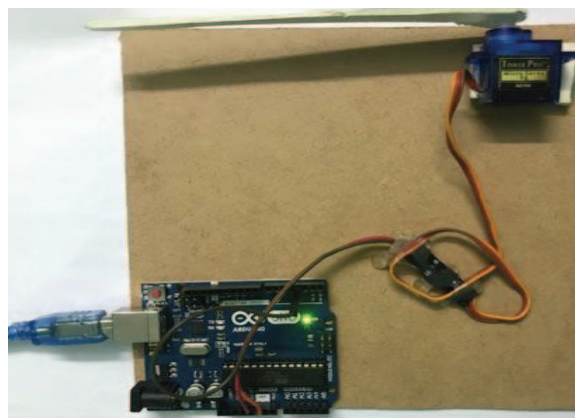


Fig. 5: Hardware setup of proposed architecture.

The proposed approach is tested by making a data set of 100 different human faces and the results found are extremely good. The whole process of the project is also explained with the help of snapshots. The facial recognition provides accurate results, so the initial step is to detect the face as shown in Fig. 6. Fig. 7 shows the finest Eigenface images available in the database. Eigen values can be used to reconstruct the initial input image. The reconstructed image is shown in Fig. 8. The face recognition by taking live image is performed on the system and is shown in Fig. 9. If the system recognizes the person then the barrier will open and allows the person to go on. If the person is not recognized, it means an unauthorized person as shown in Fig. 10, it will then restrict the person and display a message as shown in Fig. 11.



Fig. 6: Average face detection.

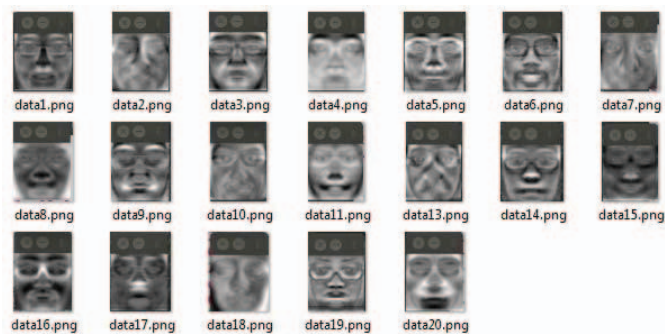


Fig. 7: Finest Eigenface images.



Fig. 8: Reconstructed image.

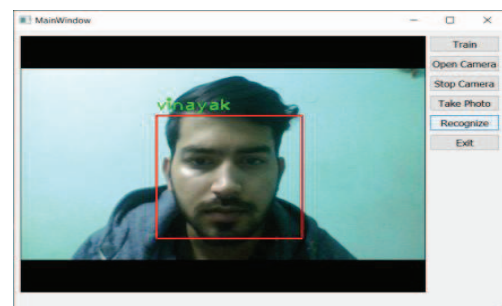


Fig. 9: Face recognition at barrier.

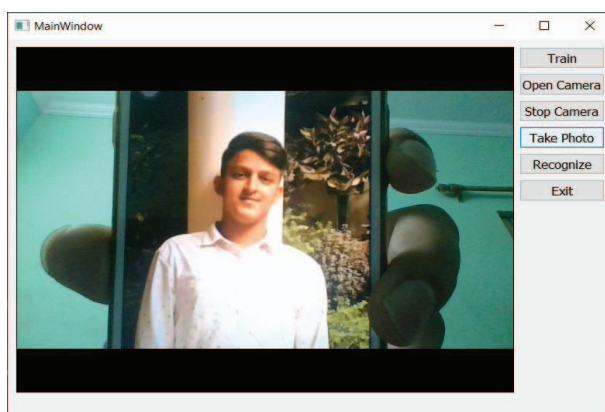


Fig. 10: Unauthorized person

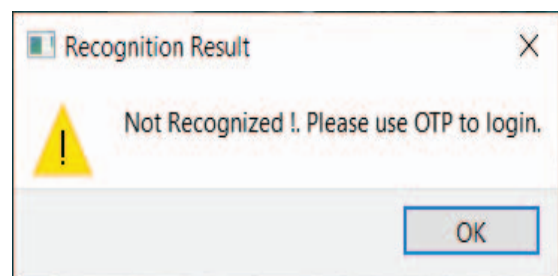


Fig.11: Dialogue box showing unauthorized access

In parallel, it sends a message to higher authorities to warn of unauthorized access. If higher authorities know the person, they will send an OTP on user mobile, then the user will enter this OTP on the provided interface (as shown in Fig. 12) within a specified time limit and the motor will rotate to 90 degrees (as shown in Fig. 13) and the person will be allowed to go ahead. If the OTP is incorrect or not entered, the system will send an email to higher authorities as shown in Fig. 14.

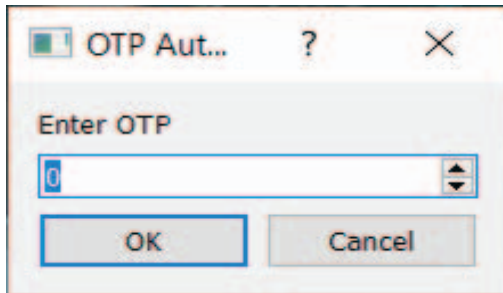


Fig. 12: OTP authentication.

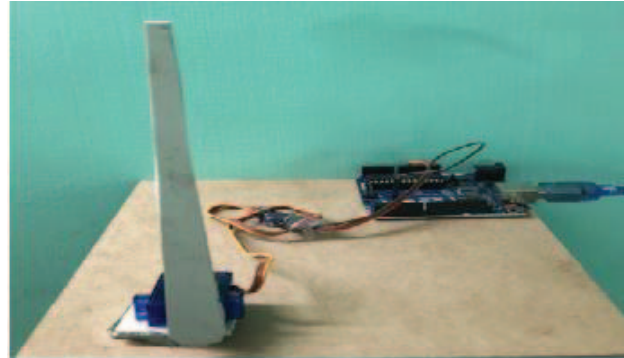


Fig. 13: Servo motor rotating at 90 degree.

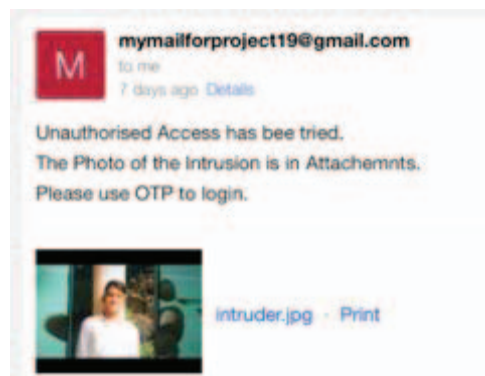


Fig. 14: Email for unauthorized access.

## 7. CONCLUSION AND FUTURE SCOPE

The conclusion of the complete approach for the paper has been explained as below:

- Face recognition utilizing course classifier technique has an awesome and quick capacity to distinguish between faces of human.
- Light & edge feature identification process is compelling in support of the acknowledgment procedure, hence the pre-processing of faces must be complete that comprises of RGB shading varied nearly to grayscale picture and geometric picture change comprising of turning, scaling, and deciphering the picture, and perform histogram balance independently on the two sides of appearances to compose it balance among differentiate and brilliance.
- The varieties in faces preparing information about the framework has improved after effects of face acknowledgment and that can limit the acknowledgment of vague faces as one of the recognized face in the framework.

- Acknowledgment procedure determination admirable when the discovery of caught face outcome is obvious and not hidden.
- Person face acknowledgment utilizing an Eigenface approach runs quite well and fast.
- The utilization of Eigen values and Eigen vectors in produces excellent facial pictures and can be presented as an examination of recently prepared pictures.

In the current scenario, governments all over the world are looking the ways to tighten the security of respective borders. For this purpose they are inventing and experimenting different approaches and technologies to lower the occurrence of terrorism. A versatile human identification interface may become very important in the future. Face recognition can provide quick and accurate information in identification of any unauthorized access. We are currently working on this idea by incorporating biometric identification and eye retina to make it more successful.

## REFERENCES

- [1] Federal Bureau of Investigation United States Department of Justice. Crime in the United States, 2015.
- [2] Phillip IW, John F. (2006) Facial feature detection using haar classifiers. *Journal of Computing Sciences in Colleges*, 21(4):127-133.
- [3] Richard JQ, Ibrahim MS, Kristine EM. (1998) A robust real-time face tracking algorithm. In *proceedings of Image Processing, 1998 International Conference on*, volume 1, 131–135.
- [4] Ha MD, Craig M, Meiqin L, Weihua S. (2014) Humanrobot collaboration in a mobile visual sensor network. In *Robotics and Automation (ICRA), 2014 IEEE International Conference on*, pp 2203-2208.
- [5] Weihua S, Yongsheng O, Duy T, Eyosiyas T, Meiqin L, Gangfeng Y. (2013) An integrated manual and autonomous driving framework based on driver drowsiness detection. In *Intelligent Robots and Systems (IROS), 2013 IEEE/RSJ International Conference on*, 4376–4381.
- [6] Duy T, Eyosiyas T, Weihua S, Yuge S, Meiqin L, Senlin Z. (2016) A driver assistance framework based on driver drowsiness detection. In *Cyber Technology in Automation, Control, and Intelligent Systems (CYBER), 2016 IEEE International Conference on*, 173-178.
- [7] Davis EK., Dlib-ml. (2009) A machine learning toolkit. *Journal of Machine Learning Research*, 10:1755–1758.
- [8] ADT. Security systems, home automation, alarms and surveillance. [visited: 08-12-2019].
- [9] Vivint Smart Home Security Systems. Smart home security solutions. 2016. [visited: 08-12-2019].
- [10] Protect America. Affordable home security systems for everyone., 2016. [visited: 08-12-2019].
- [11] Jeffrey SC, Darryl I. (1999), Facial recognition system for security access and identification, US Patent 5,991,429.
- [12] Singh A, Kumar S. (2012) Face recognition using PCA and Eigenface approach, Thesis: National Institute of Technology Rourkela.
- [13] Kumar D, Rajni. (2014) An efficient method of pca based face recognition using simulink, *International journal of advanced in computer science and technology*, vol. 3, pp. 364-368.
- [14] Abdi H, Williams LJ. (2010) Principal component analysis, John Wiley & Sons Inc, vol. 2, pp. 433-459.
- [15] Urifan I, Hidayat R, Soesanti I. (2010) Pengenalan wajah dengan metode Eigenface, *Jurnal Penelitian Teknik Elektro*, 3: 320-323.
- [16] Slavkovic M, Jevtic D. (2012) Face recognition using Eigenface approach. *Serbian Journal of Electrical Engineering*, 9:121-130.

## WORD SEGMENTATION OF OUTPUT RESPONSE FOR SIGN LANGUAGE DEVICES

NOR FARAHIDAH ZA'BAH\*, AHMAD AMIERUL ASYRAF MUHAMMAD NAZMI,  
AMELIA WONG AZMAN

*Department of Electrical and Computer Engineering, Kulliyyah of Engineering, International Islamic University Malaysia, Kuala Lumpur, Malaysia*

*\*Corresponding author: adah510@iium.edu.my*

*(Received: 22<sup>nd</sup> March 2020; Accepted: 11<sup>th</sup> June 2020; Published on-line: 4<sup>th</sup> July 2020)*

**ABSTRACT:** Segmentation is an important aspect of translating finger spelling of sign language into Latin alphabets. Although the sign language devices that are currently available can translate the finger spelling into alphabets, there is a limitation where the output is stored in a long continuous string without spaces between words. The system proposed in this work is meant to be used together with a text-generating glove device. The system used text input string and the string is then fed into the system, one character at a time, and then it is segmented into words that is semantically correct. The proposed text segmentation method in this work is by using the dynamic programming and back-off algorithm, together with the probability score using word matching with an English language text corpus. Based on the results, the system is able to properly segment words with acceptable accuracy.

**ABSTRAK:** Segmentasi adalah aspek penting dalam menterjemahkan ejaan bahasa isyarat ke dalam huruf Latin. Walaupun terdapat peranti bahasa isyarat yang menterjemahkan ejaan jari menjadi huruf, namun begitu, huruf-huruf yang dihasilkan disimpan dalam rentetan berterusan yang panjang tanpa jarak antara setiap perkataan. Sistem yang dicadangkan di dalam jurnal ini akan diselaraskan bersama dengan sarung tangan bahasa isyarat yang boleh menghasilkan teks. Sistem ini akan mengambil rentetan input teks di mana huruf akan dimasukkan satu persatu dan huruf-huruf itu akan disegmentasikan menjadi perkataan yang betul secara semantik. Kaedah pembahagian yang dicadangkan ialah segmentasi yang menggunakan pengaturcaraan dinamik dan kaedah kebarangkalian untuk mengsegmentasikan huruf-huruf tersebut berdasarkan padanan perkataan dengan pengkalan data di dalam Bahasa Inggeris. Berdasarkan hasil yang telah diperolehi, sistem ini berjaya mengsegmentasikan huruf-huruf tersebut dengan berkesan dan tepat.

**KEY WORDS:** Segmentation, Sign Language, Algorithm

### 1. INTRODUCTION

Sign language is the main language used by deaf people around the world. However, there is always a gap between them and people without disability, since communication is a problem between them. Sign language is a necessity for people with hearing problems to communicate and interact with others. For non-disabled people, learning sign language is optional. Even if they learn sign language, it is difficult for them to be able to grasp it well as they do not use it frequently unless they are around the deaf community. This is the reason why a sign language device is needed. The device may help to improve communication and reduce the language barrier between them.

In order to solve this problem, numerous research and studies were performed to make a sign language device possible. Although there are many research papers on the topic, there are still many challenges and still there are no perfect solutions for translating sign language into other languages due to various constraints.

One of the biggest challenges in making a sign language device is the segmentation issue [1]. This issue is faced differently based on the types of input for the device. For example, camera-based sign language devices must be able to detect the hand sign made by the user correctly to ensure a proper translation [1]. Glove-type devices [2][3], on the other hand, are based on digital text output but face issues to segment the text and sentences properly. Therefore, it is difficult for these devices to determine what kind of output to produce and what the user intends to do, without a proper segmentation system.

Currently, a glove-type device that can produce character output based on hand signs is being researched. However, it is not working properly as it faces the text segmentation issue. All the alphabet character outputs from the device are stored in a long continuous string of text without spaces. For example, if the user intends to say “*word of the day*”, the output that will be produced is ‘*wordoftheday*’. Therefore, in order to split this string, word segmentation needs to be performed to ensure that the output is correct and will be understood by humans [4]. There are a number of segmentation systems proposed using different approaches and algorithms to improve the accuracy of the output due to the challenges faced in many areas such as language translation and spelling correction. Table 1 shows a summary of some previous work on segmentation.

Table 1: Summary of some previous work on segmentation

Reference	Application	Input	Technique
G. A. Rao, P. Kishore [1]	Sign language translation	Video captured with camera	Used Gaussian filtering for pre-processing and segmentation. Then, hand and head contour are segmented with morphological subtraction.
Peter Norvig [4]	Word segmentation, spelling correction	Text input, URL	Proposed a general method of word segmentation based on Google n-gram dataset using python programming.
W. Jiang [5]	Word segmentation	Text input from user	Proposed a method of word segmentation using dynamic programming to improve performance. Divide and conquer algorithm is introduced so there will be no maximum length character limit for the input.
S. N. Nawaz [6]	Word segmentation	Urdu text	Proposed word segmentation model using Conditional Random Field (CRF) algorithm.
D. Tanaya and M. AdrianI [7]	Language transcription	Text in Javanese script and Latin character	Used a dictionary-based model with Maximal Matching Algorithm modified with additional steps. Performed character statistics on the dictionary to improve the output score.
S. Srinivasan, S. Bhattacharya [8]	Web-domain and hashtag segmentation	Capturing URL from website and twitter hashtag from twitter API	Used multiple corpora from different sources to improve the accuracy of segmentation and used dynamic programming to implement inference algorithm.
Y. Bassil, M. Alwani [9]	Spelling correction for Optical Character Recognition (OCR)	Optical Character Recognition (OCR) output text	Proposed an error correction algorithm based on Google spelling suggestion. The output from OCR will be fed to Google search engine and triggers “did you mean” feature if there is at least one error. Google search is capable of segmenting words properly in case the OCR output text has spacing error.
S. P. Panda and A. K. Nayak [10]	Speech recognition system	Voice recorded in .wav file	Proposed a model that performs segmentation at syllable boundaries using vowel offset point (VOP) identification and zero-crossing rate (ZCR) technique.

Reference	Application	Input	Technique
Y. Bassil, M. Alwani [11]	Error Correction for Automatic Speech Recognition (ASR)	ASR output text	An error correction algorithm based on Bing spelling suggestion. The output of ASR will be fed to Bing search engine as an input.
S. S. Chawathe [12]	Word segmentation	Sanskrit text	Proposed a dictionary-based model with dynamic programming to match the input with the dictionary word with the inclusion of Aho-Corasick algorithm

## 2. METHODOLOGY

### 2.1. Overview

For the proposed word segmentation system, three main components are required as shown in Fig. 1; the text input, the processing algorithm that contains the text dictionary, and the output. While the input and output are simple and self-explanatory, the processing algorithm involves some steps and procedures in order to process the data and produce the intended output. This will be discussed in the next section.

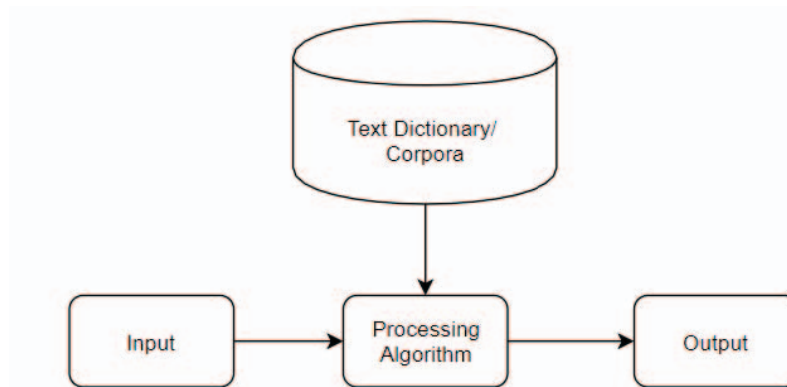


Fig. 1. Block diagram for the word segmentation model

For the input, a text-generating glove device is used to produce the alphabet characters to be fed into the system. However, in this work, a keyboard input will be used to emulate the glove device to produce the alphabet characters when the wearer makes a proper hand sign. Since the glove can only produce alphabet characters, all the non-alphabet keyboard keys such as “Spacebar”, “Enter”, “Backspace” and all non-alphabet keys will be ignored. The flowchart for the model is illustrated in Fig. 2. Since the “Enter” key is ignored, the string will be continuously fed into the system every time a character is added.

Secondly, for the processing of the input, Python programming language will be used to write and implement the segmentation algorithm. Also, for this work, a pre- installed dataset called text corpus will be used as the word library for the word matching mechanism. This text corpus is used to provide a vocabulary of words to the processor and “guide” the system with the correct words for segmentation. This is similar to the work done by Jiang [5] and Jenks [13] on the general word segmentation algorithm.

For the output, it will be directly shown on display as soon as a character is added into the string. When the user stops entering an input for more than 3 seconds, the system will reset the input in order to allow the user to enter the next line of strings.

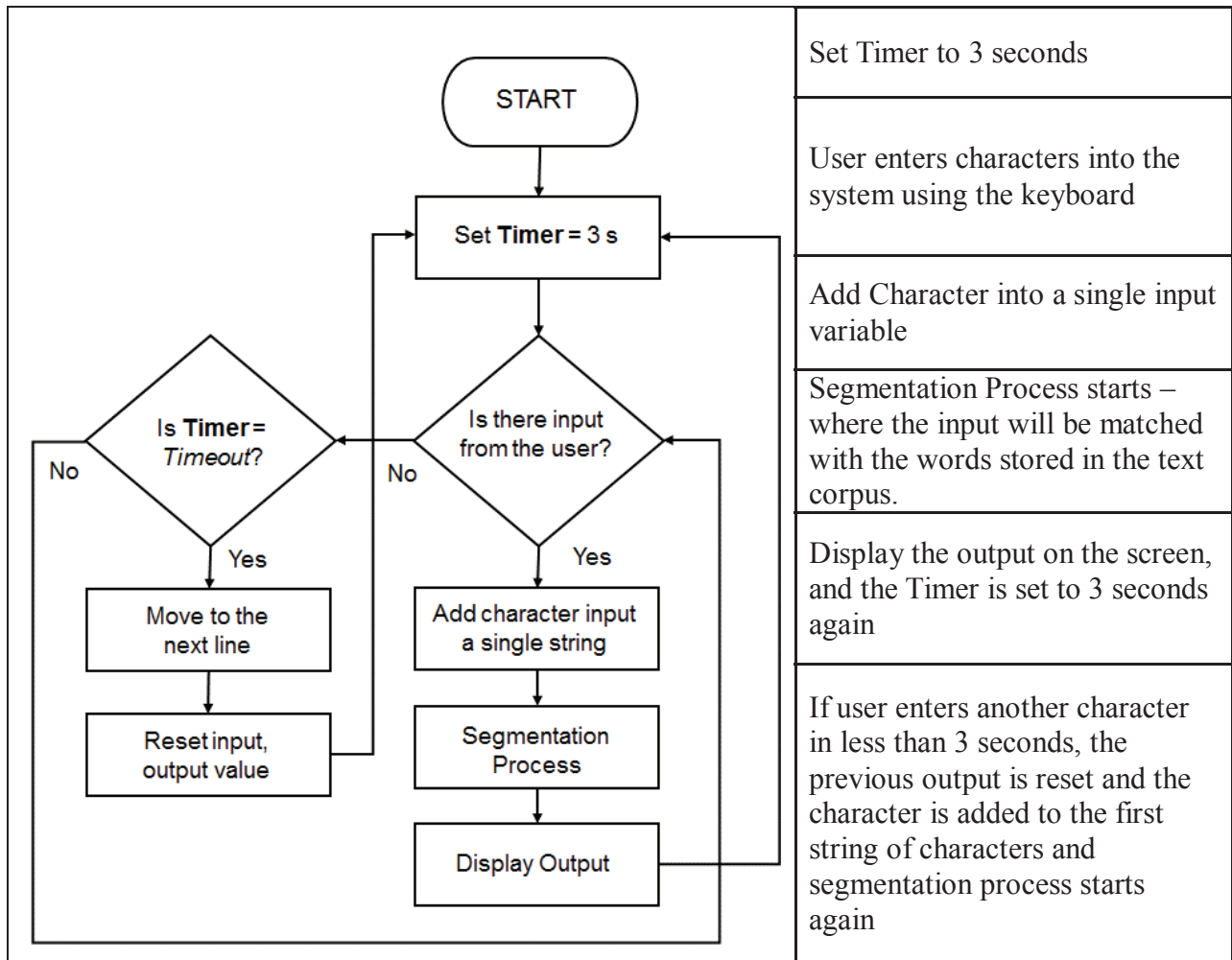


Fig. 2. Flowchart of the segmentation system

## 2.2. Segmentation Algorithm

There are some steps involved in implementing the word segmentation system, which involves the division of characters into possible words and then matching the words with the words contained in the text corpus. This part takes place after the input string is being fed into the processor.

### 2.2.1. Dynamic Programming

The process of matching strings with words inside the text corpus is performed using dynamic programming. Dynamic programming is a well-known method used in programming to solve complex problems by breaking them into smaller and simpler sub-problems. In the case of word segmentation, a long continuous string entered by the user is split into two substrings by matching the string with the proper word inside the text corpus [5]. The first string will be the matched word and the latter will become the character strings that are not yet processed. Then, the system recurs multiple times until the last character of the string, then splitting it into possible words, as shown in Fig. 3. If no word can be found due to typing error, it will either separate the string into single character or simply return the input as the output.

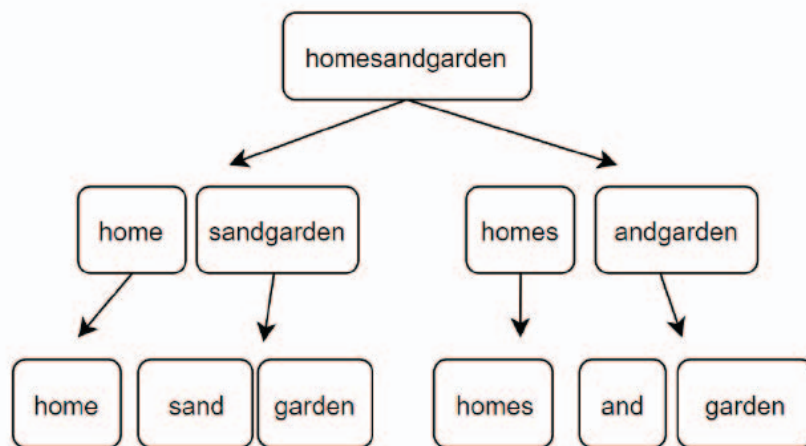


Fig. 3. Dynamic programming example

### 2.2.2. Word Matching Algorithm Using Probability Score

After the division of characters, the process of matching strings with words inside the text corpus is done using a word matching algorithm. Basically, when the user enters a string, the system will try to match the string with the words contained in the dictionary. Using a word dictionary is one of the common ways for creating a word segmentation model [7]. If the model finds a matched word, then that part of the string will be segmented. Then, the process is iterated until it reaches the end of the string.

The matching algorithm will also rely on the probability of the word as well as the whole sentence. As shown in Fig. 4, the frequency is stored together with the word in the dictionary. If there are multiple ways of segmenting the string, it will prioritize the word with higher probability. Also, longer words will be prioritized compared to shorter words. For example, the string “strawberry” will be segmented as “strawberry” instead of “straw” and “berry” although these two words are stored in the dictionary, and “berry” has a higher probability compared to “strawberry”. This is because the system will consider the total probability of the string, which is the multiplication of probability for each word [4]. In theory, it can be calculated by using Equation 1 [4] shown below.

$$P(W_{1:n}) = \prod_{k=1:n} P(W_k | (W_{1:k-1})) \quad (1)$$

Equation 1 is highlighted in Norvig [4] states that, based on the context of a particular word, the probability of a sequence of words  $[P(W_{1:n})]$  is the product of the probabilities of all the preceding words  $[\prod_{k=1:n} P(W_k | (W_{1:k-1}))]$  within the same context. It means that, for example, using a 5-word sequence – “Honesty is the best policy” - the probability of this word sequence would be the product of each word given the four previous words.

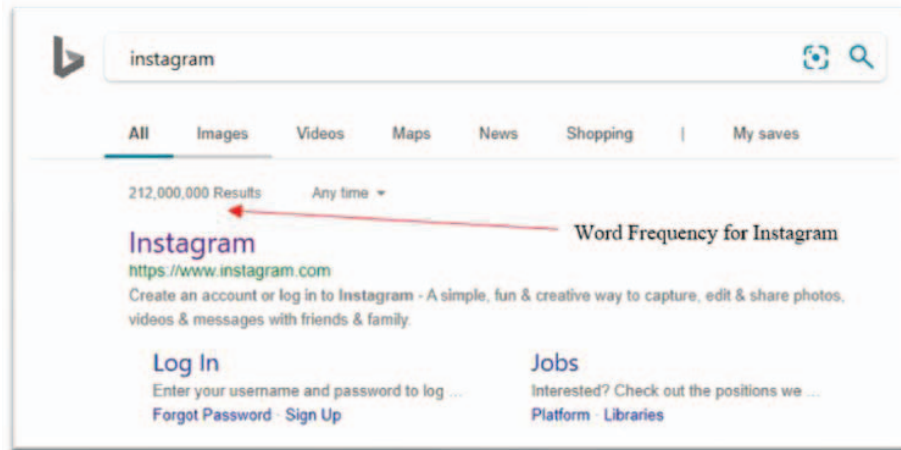


Fig. 4. The word 'instagram' and its frequency is obtained using a search engine

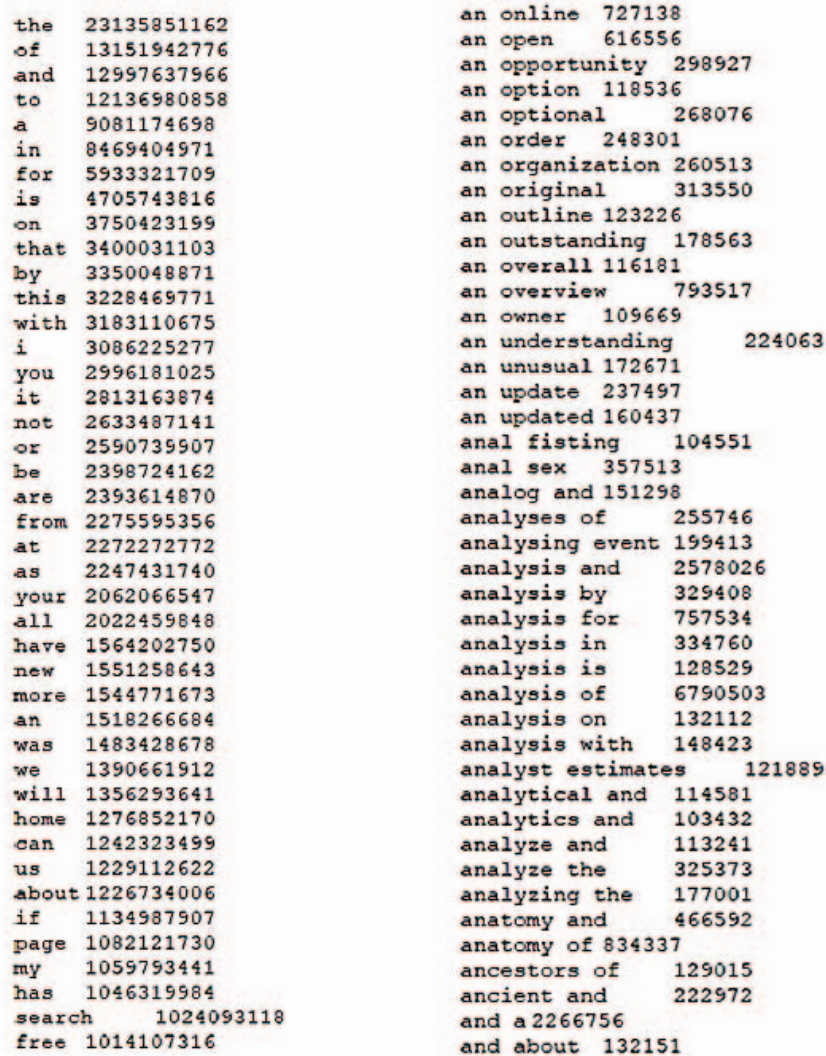
### 2.2.3. Back-off Algorithm

For every word segmented, the algorithm will check whether there is any bigram probability for the next word to occur. A bigram dataset is used in the system to ensure better accuracy of the segmentation. However, since there are chances that the probability of the bigram is zero, a back-off algorithm is included in the system to ensure no error in probability calculation due to multiplication by zero [4]. The back-off algorithm will simply ignore the bigram probability and continue the segmentation using unigram probability, or the probability for every single word. However, one of the disadvantages in implementing this is that the system will take a longer time to match each word in the unigram database, whereas if the bigram probability score is included, the computation time may be shorter.

### 2.2.4. Text Corpus

Text corpus (plural: corpora) is a huge collection of structured text stored in electronic form. It is used as a dataset for the word matching process so that the string input can be segmented into the correct output. In this work, the text corpus is massively important because the matching word will solely rely on it for segmentation purposes. In order to obtain a highly accurate output, a huge file of text corpus or multiple collection of corpora is required. Therefore, the corpus is taken from the Google n-gram dataset where it contains billions of words that are collected by Google's users around the world, which is stored in multiple ways; a single word (unigram), 2-word phrase (bigram), 3-word phrase (trigram) and so on. Since the file size of the n-gram corpus is so big that it may consist of hundreds of gigabytes of memory, this work only considers the unigram and the bigram database. However, it is not difficult since all this data is provided by Norvig [4] and is also being used for other word segmentation models. Fig. 5 shows some of the words contained in the unigram and bigram dataset.

This text corpus also contains the word frequency for each word for the purpose of increasing accuracy to determine the correctness of a word for a certain input. As shown in Fig. 3, "home" and "homes" are both valid words that are the candidates for the output. Here, the probability is calculated to ensure that the word with the higher probability is chosen. The term "homes and" generally has higher word frequency compared to "home sand", hence the former is chosen.



the	23135851162	an online	727138
of	13151942776	an open	616556
and	12997637966	an opportunity	298927
to	12136980858	an option	118536
a	9081174698	an optional	268076
in	8469404971	an order	248301
for	5933321709	an organization	260513
is	4705743816	an original	313550
on	3750423199	an outline	123226
that	3400031103	an outstanding	178563
by	3350048871	an overall	116181
this	3228469771	an overview	793517
with	3183110675	an owner	109669
i	3086225277	an understanding	224063
you	2996181025	an unusual	172671
it	2813163874	an update	237497
not	2633487141	an updated	160437
or	2590739907	anal fisting	104551
be	2398724162	anal sex	357513
are	2393614870	analog and	151298
from	2275595356	analyses of	255746
at	2272272772	analysing event	199413
as	2247431740	analysis and	2578026
your	2062066547	analysis by	329408
all	2022459848	analysis for	757534
have	1564202750	analysis in	334760
new	1551258643	analysis is	128529
more	1544771673	analysis of	6790503
an	1518266684	analysis on	132112
was	1483428678	analysis with	148423
we	1390661912	analyst estimates	121889
will	1356293641	analytical and	114581
home	1276852170	analytics and	103432
can	1242323499	analyze and	113241
us	1229112622	analyze the	325373
about	1226734006	analyzing the	177001
if	1134987907	anatomy and	466592
page	1082121730	anatomy of	834337
my	1059793441	ancestors of	129015
has	1046319984	ancient and	222972
search	1024093118	and a	2266756
free	1014107316	and about	132151

Fig. 5. Unigram and Bigram count inside the text corpus [4]

### 3. RESULT AND ANALYSIS

#### 3.1. Python Programming

Python coding was developed specifically for word segmentation systems. It involves the process of loading the text corpora -unigram as well as bigram text- to improve the accuracy of word segmentation. When the user starts the program, it will automatically load all these three text files into the program and store every word and its frequency in the dictionary. This is completed in a couple of seconds when the program is executed. Then, the user can start entering the text using a keyboard.

Since this work is specifically made for the sign language device, it is programmed to accept only lower-case alphabet characters and numbers. All other buttons and symbols will be ignored, including the spacebar, enter, and delete buttons. If the user presses these keys, nothing will happen. However, for required functions such as 'moving to next line' or spacing between words, a delay time of 3 seconds is used as described in Fig. 2. Fig. 6 illustrates the graphical interface of the segmentation program. When the program is executed, two windows will be opened; one for the main windows for displaying the input and output and the other is to display the timer.

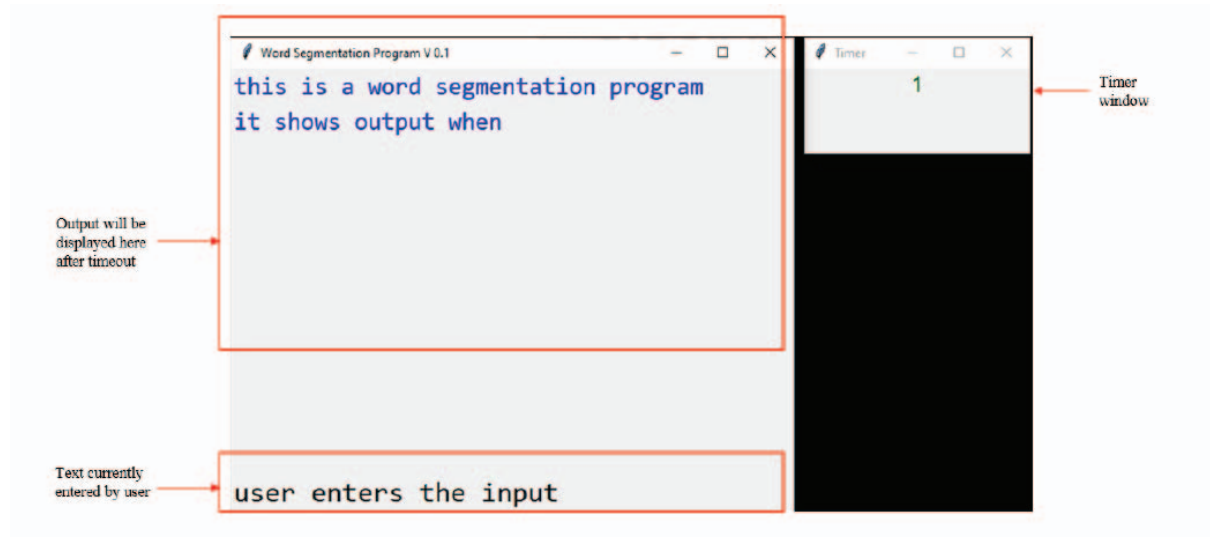


Fig. 6. The graphical interface of the segmentation program

By referring to Fig. 6, when a user enters the string “*thisisawordsegmentationprogram*”, the program will automatically split the text and generate a correctly spaced text output. However, as mentioned earlier, the system will accept the input per character and the segmentation process occurs simultaneously as the user continues to key in the character. If the whole process were to be displayed, it would show a list of outputs as illustrated in Fig. 7, where it illustrates that during the segmentation process, the segmentation output may change while user enters the input; such as “word” and “words”. This behavior is caused by the change of probability score of the whole sentence during the process. The system will choose the highest probability score for the whole sentence as the chosen output.

### 3.2. Challenges in the segmentation system

While testing the system, some errors in segmentation may occur due to the following issues.

#### 3.2.1. Incorrect Input

One of the reasons for error in segmentation is the user may enter an incorrect character and due to the continuous mode of the system, the incorrect character will be stored in the string. As the system can neither delete the character in the string nor have any kind of error correction mechanism, a timer is used to tackle this issue as shown in Fig. 8. It shows that a user needs to wait for 3 seconds to allow a timeout, at which the system will reset the input and output of the system and move to the next line where the user can basically start again. However, the incorrect string or word will still be displayed and hence, this might not be an efficient way to fix the incorrect input error.

```
t
th
thi
this
this i
this is
this is a
this is aw
this is awo
this is awor
this is a word
this is a words
this is a words e
this is a word seg
this is a word segm
this is a word segme
this is a word segmen
this is a word segment
this is a word segment a
this is a word segment at
this is a word segmentati
this is a word segmentatio
this is a word segmentation
```

Fig.7. The word segmentation process flow



Fig. 8. The output of the segmentation process after timeout

### 3.2.2. Missing Words in Corpus

Another limitation of the system is the database used in this work. Although it contains 330,000 unigram words and around 250,000 bigram phrases, many highly specific words such as scientific terms and specific words like “*instagram*” are not available because the text corpora used were compiled in 2009. The system will also have issue in detecting uncommon human names and places, as these are too specific.

However, there are only a handful of words that are not stored in the corpora and it rarely needs

to be updated. Nevertheless, a function to add words into the unigram or bigram corpus is added in the system. It is done simply by adding the word “*addunigram*” into the unigram file. When the system detects the user entering “*addunigram*”, it will interrupt the segmentation process, triggering a popup window that allows the user to key in the word and its frequency, as shown in Fig. 9 and 10

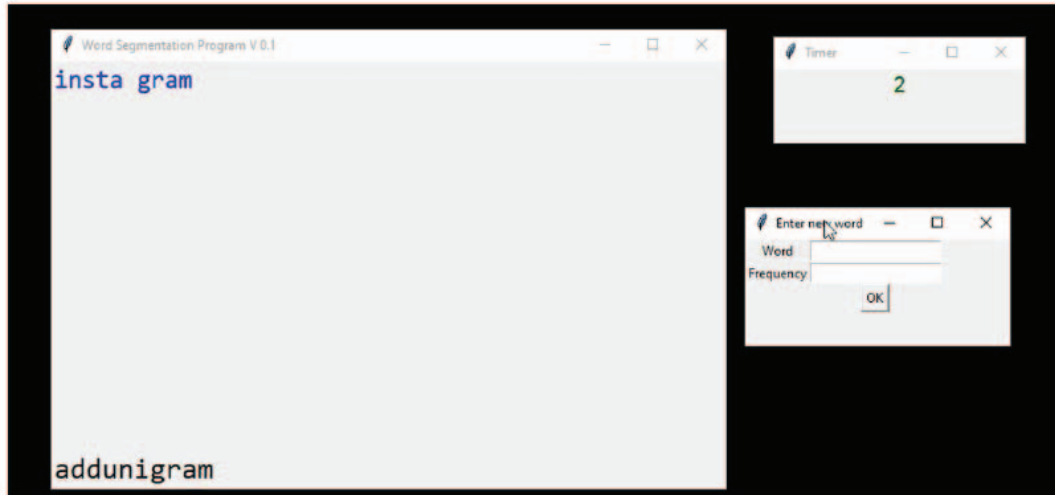


Fig. 9. The system does not recognize the word ‘*instagram*’ and by using the command *addunigram*, a pop-up windows appears to key in the word and its frequency



Fig. 10. The system now recognizes the word ‘*instagram*’

## 4. CONCLUSION

In this work, a text segmentation algorithm for sign language was implemented using Python programming. The system is able to segment a string of characters correctly for all the input strings tested and thus, it is proven that the system is working properly as a word segmentation system for English words. Although, the system is unable to segment some specific words such as long scientific terms and special nouns, this can be fixed by adding a function to add words into the text corpus together with its frequency. One of the main limitations of this work is that the system is made specifically for a text-generating glove device assuming that it will only generate single alphabet characters. As of now, the system is not able to detect and process hand gestures in sign language that represents phrases such as “hello” and “thank you”. Another observation is that the system can be a bit slow in producing the output if the string is too long (more than 30 characters) as it has to go through the words in the text corpus. Future work is required to address this challenge and in addition, the system may also include creating corpora for other languages that use Latin alphabets, such as the Malay Language.

## REFERENCES

- [1] G. A. Rao, P. Kishore (2016) Sign Language Recognition System Simulated for Video Captured with Smart Phone Front Camera, *International Journal of Electrical and Computer Engineering (IJECE)*, vol. 6, no. 5, p. 2176
- [2] Boon Giin Lee and Su Min Lee (2019) Smart Wearable Hand Device for Sign Language Interpretation System with Sensors Fusion, *IEEE Sensors Journal* pp (99):1-1
- [3] Ahmad Zaki Shukor *et al.*, (2015) A New Data Glove Approach for Malaysian Sign Language Detection, *Procedia Computer Science*, vol. 76, pp 60-67
- [4] Norvig, Peter (2009), *Natural Language Corpus Data*
- [5] W. Jiang (2015), *Word-Segmentation* [<http://pypi.org/project/wordsegmentation>]
- [6] Sadiq Nawaz Khan *et al.*, (2018) Urdu Word Segmentation using Machine Learning Approaches, *International Journal of Advanced Computer Science and Applications(IJACSA)*, 9(6) <http://dx.doi.org/10.14569/IJACSA.2018.090628>
- [7] D. Tanaya and M. Adriani (2016), Dictionary-based Word Segmentation for Javanese, *Procedia Computer Science*, vol. 81, pp. 208–213
- [8] S. Srinivasan, S. Bhattacharya, R. Chakraborty (2012), Segmenting web-domains and hashtags using length specific models, In *Proceedings of the 21st ACM International Conference on Information and Knowledge Management*, Oct 2012, Maui.
- [9] Y. Bassil, M. Alwani (2012), OCR Post-Processing Error Correction Algorithm using Google Online Spelling Suggestion., *Journal of Emerging Trends in Computing and Information Sciences*, vol. 3, no. 1
- [10] S. P. Panda, A. K. Nayak (2015), Automatic speech segmentation in syllable centric speech recognition system, *International Journal of Speech Technology*, vol. 19, no. 1, pp. 9–18
- [11] Y. Bassil, M. Alwani (2012), Post-Editing Error Correction Algorithm for Speech Recognition using Bing Spelling Suggestion, *International Journal of Advanced Computer Science and Applications*, vol. 3, no. 2
- [12] S. S. Chawathe (2018), Lexical text segmentation using dictionaries, 2018 IEEE 8th Annual Computing and Communication Workshop and Conference (CCWC)
- [13] Jenks, G. (2017), *Python Word Segmentation* [<http://grantjenks.com/docs/wordsegment>]

## SPACE MAPPING OF HIP AND WRISTS MOTIONS FOR DIFFERENT TRANSFER DISTANCES IN MANUAL MATERIAL HANDLING TASK

RADIN ZAID RADIN UMAR<sup>1,2\*</sup>, FATIN AYUNI MOHD AZLI LEE<sup>1</sup>, MUHAMMAD  
NAQUIDDIN KHAFIZ<sup>1</sup>, NADIAH AHMAD<sup>1,2</sup>, NAZREEN ABDULLASIM<sup>3</sup>

<sup>1</sup>Fakulti Kejuruteraan Pembuatan,

<sup>2</sup>Center of Smart System and Innovative Design,

<sup>3</sup>Fakulti Teknologi Maklumat dan Komunikasi,  
Universiti Teknikal Malaysia Melaka, Malaysia

\*Corresponding author: [radinzaid@utem.edu.my](mailto:radinzaid@utem.edu.my)

(Received: 16<sup>th</sup> July 2019; Accepted: 9<sup>th</sup> March 2020; Published on-line: 4<sup>th</sup> July 2020)

**ABSTRACT:** Manual material transfer tasks are common in occupational settings. Repetitive lifting tasks usually involve twisting and bending which are associated with occupational lower back injuries. One of the approaches to reduce bending and twisting is to separate the distance between lifting origin and destination, which will encourage lifters to step and turn entire bodies. However, adding lifting distances is likely to affect space usages and requirements. A study was conducted to investigate how the transfer distances influence space usage during the lifting task. Raw data of hip and hand wrists motion of 26 male subjects during transfer in 4 different distances were captured using X-Sens motion capture system. MVN Studio software was used to process and extract positional data. Tabulated space mapping revealed limited hip movement and semicircular shaped hand motions for short transfer distances. The pattern changes into a more stretched-curve shape as the distance increases. Overall, it was observed that shorter transfer distance caused participants to adopt more twisting and less bending postures, while further transfer distances resulted in more bending and less twisting. This study may provide industrial practitioners with information to design a space requirement for manual material transfer tasks.

**ABSTRAK:** Kerja-kerja pemindahan barang secara manual adalah biasa dalam persekitaran kerja. Kerja-kerja mengangkat barang yang kebiasaannya melibatkan badan membengkok dan berpusing boleh menyebabkan kecederaan tulang belakang. Salah satu cara bagi mengurangkan risiko ini adalah dengan memisahkan jarak antara tempat asal dan tempat tuju pemindahan barang. Pemindah barang digalakkan untuk melangkah dan memusingkan seluruh badan. Namun, cara ini menyebabkan penggunaan ruang yang banyak. Satu kajian telah dijalankan bagi mengkaji bagaimana jarak pemindahan barang mempengaruhi penggunaan ruang ketika kerja-kerja pemindahan. Data asal pergerakan pinggul dan pergelangan tangan daripada 26 subjek lelaki ketika pemindahan barang pada 4 jarak berbeza diperolehi menggunakan sistem rakaman gerakan X-Sens. Perisian MVN Studio digunakan bagi memproses dan mengekstrak data ini. Ruang pemetaan berjadual mendedahkan pergerakan pinggul yang terhad dan pergerakan tangan berbentuk separa bulat pada jarak pemindahan terdekat. Corak ini berubah kepada bentuk lengkung memanjang apabila jarak bertambah. Keseluruhannya, jarak pindahan yang kurang menyebabkan para peserta lebih terdedah kepada postur memusingkan badan berbanding membengkok, sementara jarak yang jauh menyebabkan peserta lebih membengkok berbanding memusingkan badan. Kajian ini memberikan maklumat untuk

penggiat industri mereka cipta keperluan ruang bagi kerja-kerja pemindahan barang secara manual.

---

**KEYWORDS:** *space mapping; ergonomics; manual material handling; transfer distance*

## 1. INTRODUCTION

Application of ergonomic principles has shown good results in increasing productivity and decreasing health issues [1]. Ergonomics consideration in early stages of workplace design has been shown to yield better outcomes compared to considerations at later design stages. Front end ergonomics involves looking into interfaces between workers and workplace elements such as workstation, task, and work environment. One of the components of front-end ergonomics is the evaluation of work layout, which specifically looks into space requirements.

Manual material handling (MMH) activities are one of the most common tasks in workplaces. High frequency and long duration of exposure to MMH, especially in the industry that still relies on manual labour, can directly impact the workers as they are more likely to be exposed to ergonomic risk factors related to MMH activities [2]. Multiple studies have discussed potential methods to minimize ergonomic risk factors due to MMH such as training [3], assisting devices [4], and workplace layout design [5,6]. However, there have been publications suggesting limited effectiveness of training for preventing lower back pain [7,8]. Assisting devices may also minimize ergonomic related risks, however high tech devices may come at a cost, and there might be resistance to adopt them due to unfamiliarity and slowing down the processes [9].

Workplace layout and space play a direct role in influencing workers' movements and postures. Poor layout and limited space may contribute to poor work postures for the workers [10]. Lavender and Johnson [6] argued that consideration of good workplace layout allows some degree of control on asymmetric lifting behaviour. In another study, Mehta et. al. [5] outlined that separating the origin of the lift station and the destination at a certain distance may nurture workers to step and turn their whole body which may help reduce bending and twisting during the manual handling activity. It was suggested that distancing the location between lifts can limit the twisting of body. In an experimental study conducted in the United States of America, Lavender & Johnson [6] revealed that lateral bending and twisting of the spine were minimized when a separation distance of 1 meter was created between the lift's origin and the destination. Poor work postures in combinations of repetitive and long exposure durations can increase risks of ergonomics issues like sprain, strain, and work-related musculoskeletal disorders [11,12]. Therefore, a good design that focuses on optimizing interaction between workplace setup and workers can contribute to increased efficiency and productivity in a workplace [13].

In workstation design options to control ergonomic risk factors, existing ergonomics guidelines have been primarily focused on space clearances. There have also been generic guidelines on manual material handling activities [14,15] than can be referred prior to the design process. However, there has not been much information that specifically focuses on space requirement for manual material handling tasks. The objective of this study is to capture and map the hip and wrist motions during the manual material handling task. Specifically, box transfer processes of different transfer distances and their effect on the space requirement during the handling task have been selected as the focus of study. It is envisioned that space mapping of motions during manual material handling tasks can provide engineers and designers with space requirement information during the front-end

manual material handling workstation design process. Thus, a deeper study focusing on interaction of workers and their space requirement may provide insights that can be utilized in the front-end design of workplaces.

## 2. METHODOLOGY

### 2.1 Overview

A randomized repeated design of experiment was conducted to map the space requirement behaviours of different transfer distances during manual handling activities. Space mapping data was collected through the use of 3D body motion capture system Xsens (Xsens Technologies, Netherlands). The system consisted of accelerometers that captured acceleration data at a sampling frequency of 30 data per second. The raw acceleration data were then converted into velocity data, and then positional data through a series of customized programming algorithms developed using Processing software.

### 2.2 Subject Participants

26 healthy male participants, age ranging from 23-24 years old (Mean = 23.88, SD=0.35) were recruited in this study. The subjects were screened to ensure that they were free of any history of musculoskeletal disorders or prior injuries that could affect the way they performed the tasks of interest. Other exclusion criteria include any injury within the past 12 months that caused them to restrict any work or non-work activity, and existence of current pain or other musculoskeletal symptoms.

### 2.3 Data Collection

Each subject signed consent forms and filled demographic data before wearing the Xsens sensor-integrated suit. The subject was then asked to transfer boxes of fixed weight (10.9 kg) between two stations, the heights of which were set so that the beginning and ending heights were at the 5th percentile of Malaysian population elbow height (0.913 m) [16]. Lifting load and height were controlled to minimize their effect on experimental outcomes. Each subject was briefed on the simulated task, before being asked to practice transferring the boxes. After the practice session, subject was asked to continuously transfer 4 boxes in 4 different transfer distances of 0.50 m, 0.75 m, 1.00 m, and 1.25 m, as shown in Fig. 1. No specific instructions were given with regards to transfer techniques. Figure 2 shows an example of one subject performing the box transfer task.

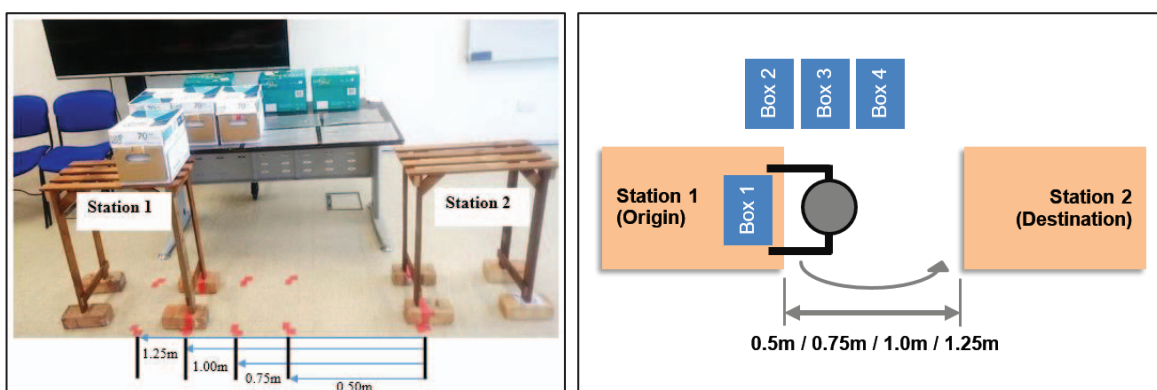


Fig. 1: Workstation setup (left), top view of experimental setup (right).

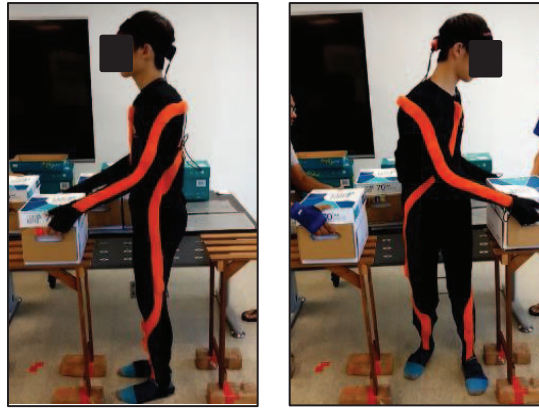


Fig. 2: Subject wearing motion capture system performing the box transfer task at 0.5 m distance set up.

## 2.4 Data Processing and Analysis

### 2.4.1 Image Analysis

Raw data from the Xsens motion capture system were extracted and visualized in MVN Studio software (Xsens Technologies, Netherlands). The 3D simulation was run for each subject to observe obvious trends and patterns on postural behaviours. Screen captures were taken at the 4th cycle at both origin and destination of lifting for the purpose of image analysis. The observation of 4th cycle data is to represent work postures during continuous transfer, as well as to allow subjects to be more at ease as task familiarization started to take place.

### 2.4.2 Space Mapping Analysis

Positional data of the hip and right and left wrists were obtained for each subject. These positional data, in X and Y planes were extracted using Cinema 4D software (MAXON Computer GmbH, Germany) that were then tabulated and mapped using Microsoft Excel.

The tabulation allows an overview of the motions from the top view. Each data was colour-coded to differentiate between the body parts (hip, right wrist, and left wrist), and between transfer distances (0.5 m, 0.75 m, 1.0 m, and 1.25 m).

### 2.4.3 Analysis on Width Requirements

The maximum width distance requirements of each cycle from all transfer distances, across all subjects, were captured through identification of furthest positional data in an excel file. Descriptive statistics were used to analyse the differences in width requirements and consequently, in the area used by each subject. Repeated ANOVA measures were conducted using a JASP statistics package (Wagenmakers, Amsterdam) to see if there were significant differences on width requirements between different transfer distances. Mauchly's test was used for sphericity assumption. A post hoc comparison test was performed using Bonferroni correction to analyse the pairwise comparisons of experimental conditions.

### 3. RESULTS

#### 3.1 Image Analysis

Qualitative analysis was conducted through observation of images captured using MVN Studio software. It was conducted to identify the relation between bending and twisting postures with transfer distance from different subjects. Figure 3 and 4 show the bending postures whereas Fig. 5 and Fig. 6 show twisting postures of one of the subjects. Both were captured during the box lifting and placing at four different distances. For the twisting posture, the images were captured from the top view. It can be seen that the small transfer distance caused the subject to adopt more twisting but less bending posture. The observation was opposite for greater transfer distances.

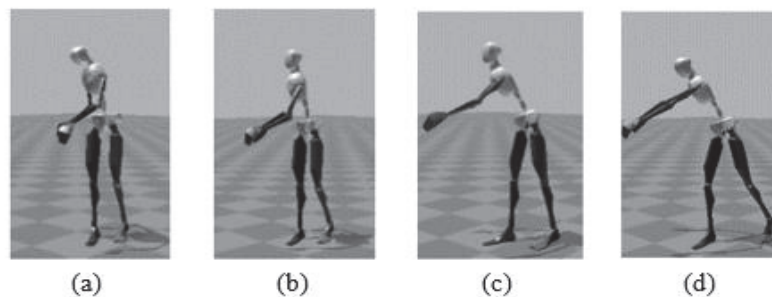


Fig. 3: Forward bending of a subject during the start of box lifting (origin) at four different transfer distances: (a) 0.50 m, (b) 0.75 m, (c) 1.00 m, and (d) 1.25 m.

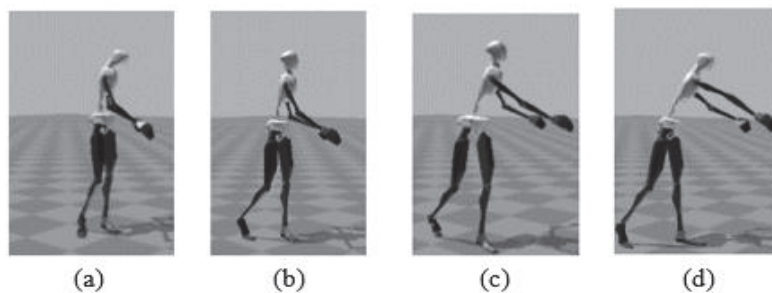


Fig. 4: Forward bending of a subject during the start of box placement (destination) at four different transfer distances: (a) 0.50 m, (b) 0.75 m, (c) 1.00 m, and (d) 1.25 m.

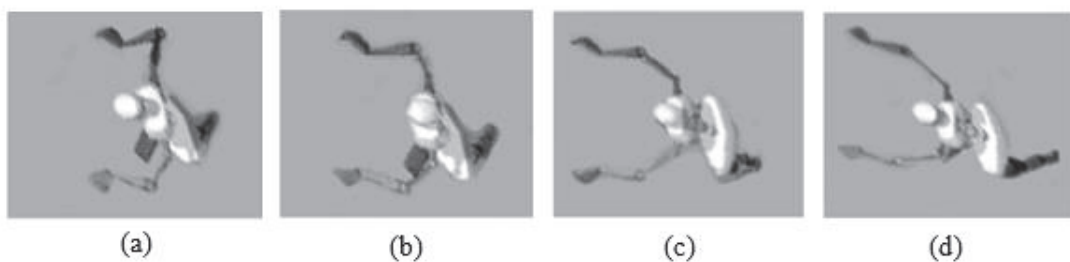


Fig. 5: Lower back twisting of a subject during the start of box lifting (origin) at four different transfer distances: (a) 0.50 m, (b) 0.75 m, (c) 1.00 m, and (d) 1.25 m.

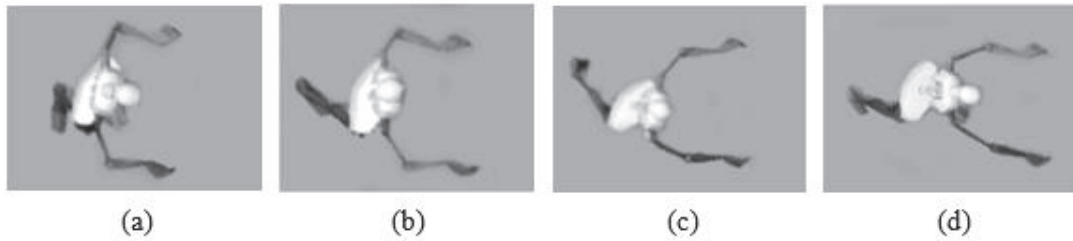


Fig. 6: Lower back twisting of a subject during the start of box placement (destination) at four different transfer distances: (a) 0.50 m, (b) 0.75 m, (c) 1.00 m, and (d) 1.25 m.

### 3.2 Space Mapping Analysis

In order to see the patterns of hip and wrist motions, graphs were plotted based on the maximum and minimum points of the hip and wrists for all subjects. Figure 7 shows the graphs of space mapping data for one subject at different transfer distances while Fig. 8 shows the graphs of space mapping of hip and wrists positional data for all subjects during the material handling activity. The starting point of each subject is facing the positive x-axis from the origin.

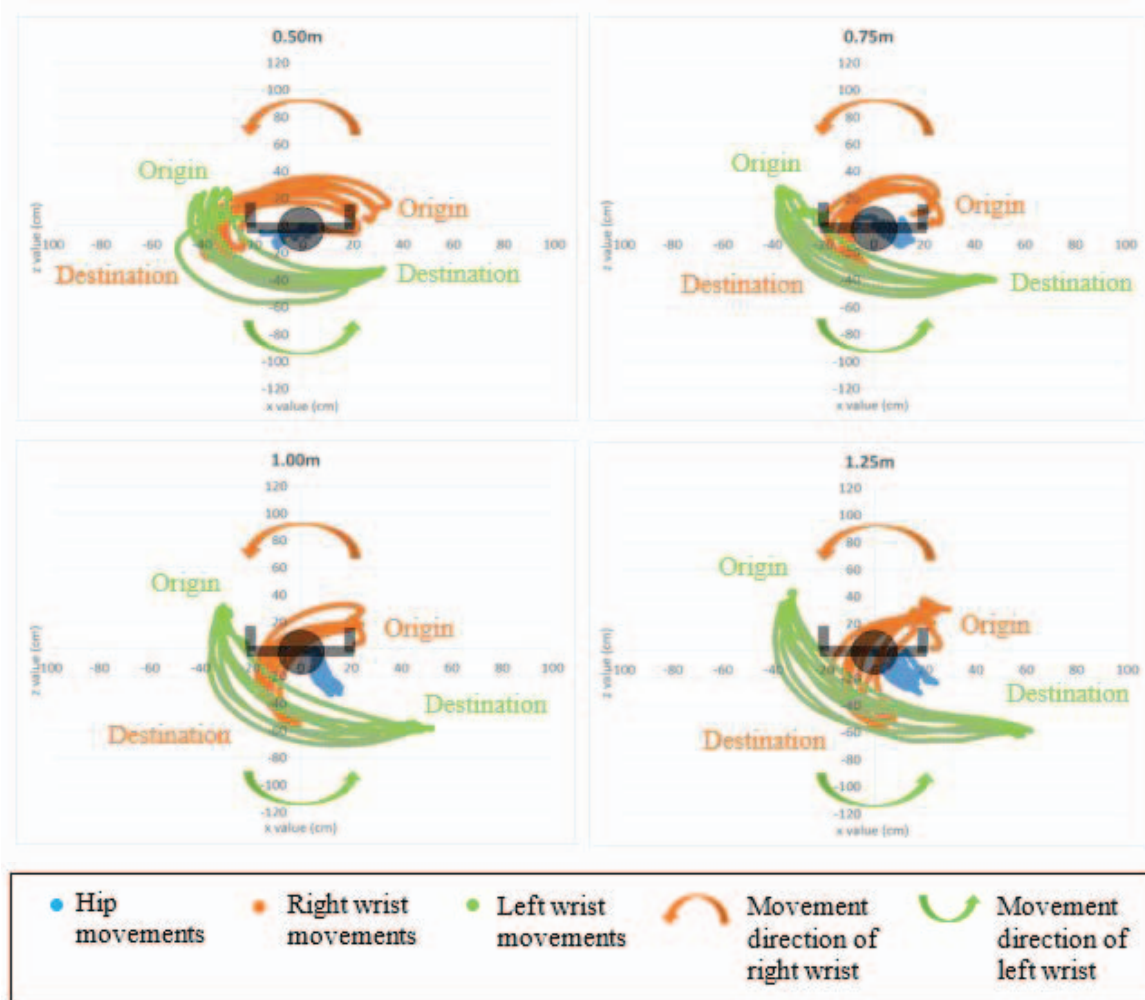


Fig. 7: Space mapping of wrists and hip motion of manual transfer for Subject 23 at 0.50 m, 0.75 m, 1.00 m, and 1.25 m transfer distances.

It can be seen from the space mapping analysis that more space was utilized during the transfer as the transfer distances increased. The hip movements in 0.5 m transfer distance were seen to be localized in the same area, between 20 cm in both x and y axis. As the transfer distance increased, the hip movements were seen to be distributed over larger areas. At 1.25m transfer distance, the hip movements were shown to be the largest compared to other distances, as shown in Fig. 8. A similar trend was observed with both right and left wrist movements. The space mapping data shows that movements of hip, right wrist, and left wrist occupied larger areas as the transfer distances increased from 0.5 m to 1.25 m. In addition to the larger occupied area, it can also be seen that different transfer distances affected the movement direction and shape. As transfer distance increased, the hip tended to move further in the y axis direction. In terms of wrists, the movements expended from a semi-circular shape into stretched-out semi-circular shape.

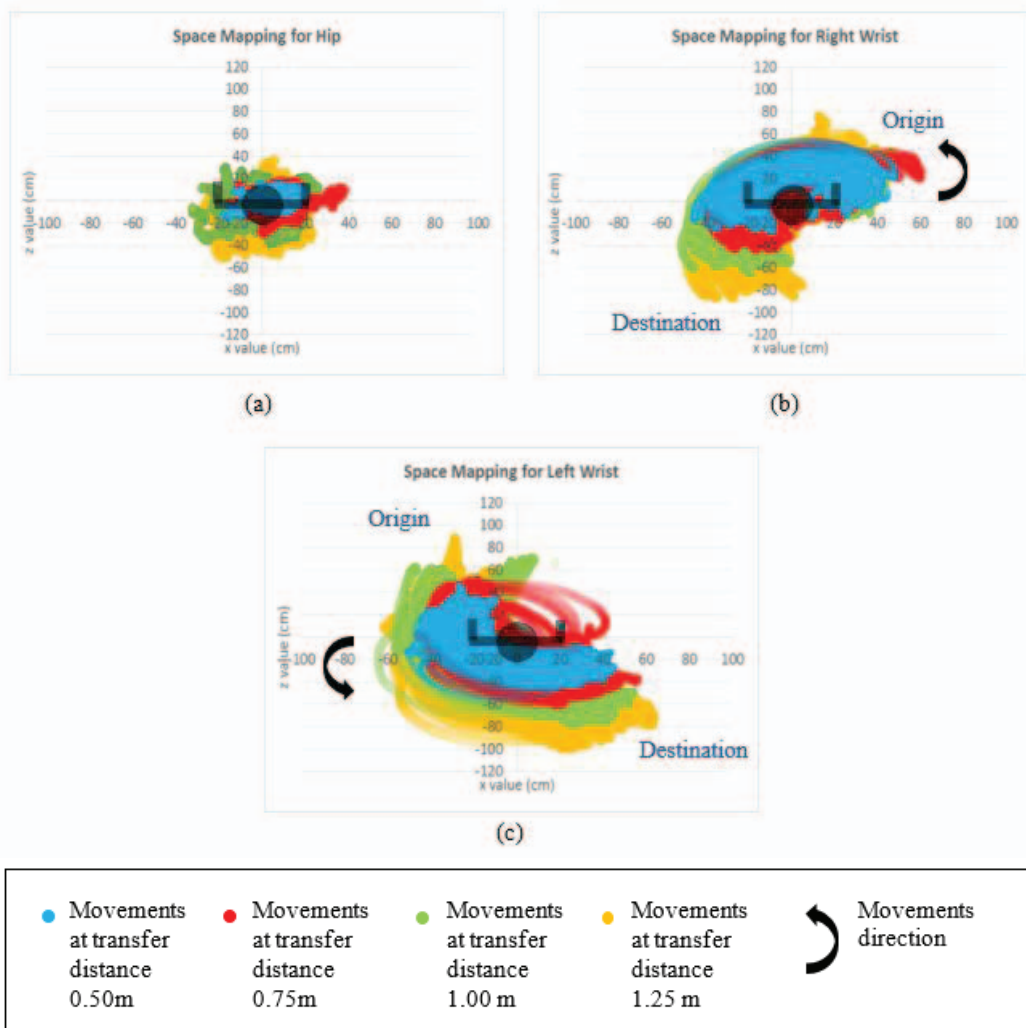


Fig. 8: Mapping of (a) hip, (b) right wrist, and (c) left wrist movements for all 26 subjects at 0.50 m, 0.75 m, 1.00 m, and 1.25 m transfer distances.

### 3.3 Analysis on Width Requirements

The positional data involved to map the top view of hip and wrist motions were x and z points. The maximum value, average, and standard deviation of width at each transfer distance from all subjects were calculated and tabulated in Table 1. The values showed

increase in space width from the shortest (0.50 m) to greatest (1.25 m) transfer distance. Figure 9 shows the graph of width average for subject 23.

Mauchly's test showed good sphericity assumption ( $p=0.129$ ), which indicated that the variances of the differences were equal. Repeated ANOVA measures showed that there was a significant effect of transfer distances ( $p<0.001$ ) on width requirements. The post hoc Bonferroni test to analyse the pairwise comparisons between the transfer distances showed significant differences between 0.5 m vs 1.25 m, and 0.75 m vs 1.25 m at  $\alpha=0.05$ . The width requirements for transfer distances between 0.5 m vs 0.75 m, 0.50 m vs 1.0 m, and 1.0m vs 1.25m were not statistically significant, as shown in Table 2. It should be noted that the 0.75 m vs 1.0 m transfer distance showed marginal significance ( $p=0.055$ ).

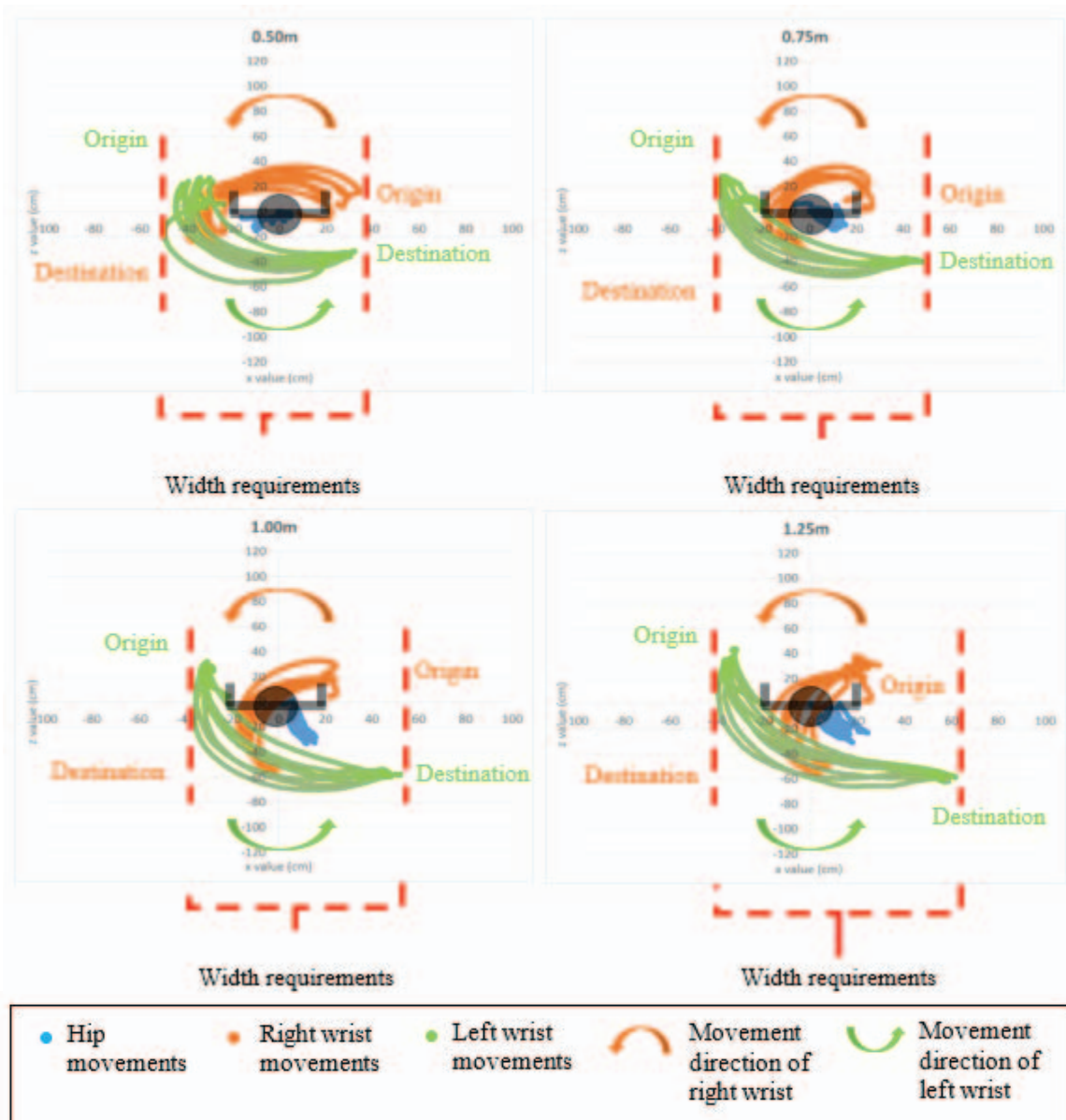


Fig. 9: Width requirements of wrists and hip motion of manual transfer for different distances for Subject 23.

Table 1: Maximum value, mean and standard deviation of width requirements for all subjects (n=26) at different transfer distances.

Transfer distance(m)	Width requirements (cm)		
	Maximum	Mean	Standard Deviation
0.50	92.02	74.84	10.26
0.75	93.73	74.18	8.81
1.00	109.41	78.95	12.07
1.25	108.02	83.42	14.01

Table 2: Post Hoc analysis to compare significance differences in width requirements between transfer distances.

Comparison of transfer distances		Mean Difference	Standard Error	t	P bonferroni
0.5 m	0.75 m	0.654	1.818	0.360	1.000
	1.0 m	-4.111	2.060	-1.996	0.342
	1.25 m	-8.586	2.660	-3.228	<b>0.021*</b>
0.75 m	1.0 m	-4.765	1.686	-2.827	0.055
	1.25 m	-9.240	2.502	-3.693	<b>0.007*</b>
1.0 m	1.25 m	-4.474	2.089	-2.142	0.253

Note: \* signifies statistical significant difference

#### 4. DISCUSSION

Comparing images visualized from MVN Studio software, it was found that the 0.50m transfer distance encourages twisting the most, compared to longer transfer distances. The limited space and clearance encouraged subjects to stand relatively static at one place and twist the body while transferring the box. When the transfer distance increased, subjects were able to make some movements while transferring the box causing less possession of twisting, but it was observed that bending posture was more prominent. In general, hip movement is more dynamic at larger space but the hip position is still within the same relative area (not spread around). This indicates that the subjects tended to move more but were still standing on the same spot. In order to complete the transfer task, subjects tended to bend more during lifting and placing the box in order to reach the stations.

The positional data of hip and wrists for different transfer distances during manual transfer were mapped to give an overview of the space requirements. Overall, the result showed that in the shortest setup (0.5 m), hip positional data are mostly localized in one area, while the wrist motions are in a semi-circular shape. The relatively static hip data suggested that the subjects were adopting twisting motion during the transfer process. As the transfer distances increased, the curve pattern for hip and wrists positional data stretched out and resulted in a more stretched curve pattern. This suggests more dynamic motions occur during the transfer process, comprising of both body movements and bending, compared to primarily twisting movements in the shortest setup at 0.5 m transfer distance.

Body postures during material handling can be influenced by the distance between the lifting origin and the destination stations. Findings from this study show that the magnitude of lower back bending increases as the transfer distance increases. This result is in agreement with a study by Metha et al. [5] which found that the increase of separation

distance might increase forward flexion of the spine. This posture pose may happen due to the tendency of the workers to reach rather than stepping toward to the destination station. The authors added that longer transfer distance can also increase physiological cost and transfer time of the handlers. Meanwhile, if the transfer distances between the origin and destination stations were too close to each other, workers were more likely to adopt a twisting motion due to limited space and clearances. In another study, Kuorinka and Ilkka [10] also found that limited workspaces and clearances may result in workers adopting incorrect material handling methods. Overall, results in this study are aligned to findings from other researchers that suggest increase in lower back bending magnitude, and decrease in lower back twisting magnitude, as the transfer distances increased. However, the detailed analyses on these trends were not the primary focus of this manuscript. The detailed measurement, analysis, and description on the trends of lower back bending and twisting during different transfer distances had been documented in the authors' other manuscript.

The principle of correct manual carrying is by holding the object as close to the body as possible while keeping the back straight [15]. A study conducted by Dolan et al. [17] found that the activity of lifting a weight that is farther in front of the body as one of the parameters contributing to a substantial increment in extensor moment of the spine. Extensor moment is the tension in the thin muscle groups running at every side of the vertebral column of the body, and can be an indirect measure of the compressive force acting on the spine. In addition, multiple studies have established that lower back bending and twisting cause biomechanical load on lower back, hence increasing the risk for lower back pain [18,19]. For example, a case study in Malaysian automotive manufacturing company reported that lower back pain is the highest prevalence of MSD among workers [20]. The authors claimed that the workers were found to perform the MMH tasks with improper work postures and incorrect techniques. Poor handling, in combination with poor postures may affect the function and efficiency of muscle forces. Muscle forces are increased when there are asymmetrical postures during bending and twisting of lower back [21]. The asymmetry in muscle activity occurs due to generation of mechanical stiffness by different sets of muscles for spine stabilization process, and this may eventually lead to unequal stress concentrations on the different component structures of the spine. Cholewicki and McGill [22] in a lumbar spine modelling study showed that reduction in passive joint and muscle stiffness in various postures may affect mechanical stability of the spine, consequently increasing the risk of development of chronic back pain.

Marras and Granata [18] reported that bending and twisting can cause compressional and shear force loadings on spine discs. Compressive force and shear force exerted on the intervertebral discs increase as the velocity and acceleration of the trunk increase, which may happen due to sideways bending and twisting activities. During material handling tasks, the gravitational force, initial force of body segments and hand load notable to L5-S1 of spine may cause the upper body to torque-tilt at the lumbosacral (L5-S1) joint [23]. This torque depends on the motion of the spine and on the acceleration of the body segments, as well as the load. As such, transfer distances at two extremes (too short or too far away) would increase risks to musculoskeletal strain. An appropriate transfer distance that can balance between bending and twisting would reduce biomechanical load, musculoskeletal strain, and ultimately risks to musculoskeletal disorders or injuries. Even though many industries have been providing supporting devices and techniques on proper material handling to their workers, they may not be effective enough in preventing back pain among workers [24]. As such, practitioners may also include consideration of

appropriate transfer distance as it can influence the magnitude of bending and twisting activities in manual handling tasks.

The positional data showed that the different transfer distances may also affect width requirements, consequently the overall space requirement. The data across subjects showed similar width requirements between 0.5 m and 0.75 m transfer distances (mean = 74.84 cm, SD = 10.26 cm for 0.5 m, and mean = 74.18 cm, SD = 8.81 cm for 0.75 m). These two transfer distances encourage more twisting, due to limited clearance. As such, this might result in the subjects to naturally pulling the box close to the body during the transferring process of both 0.5 m and 0.75 m transfer distances, hence explaining why the width requirements were similar. As the transfer distance increases, the data trend suggests that the width requirement increases as well (mean = 78.95 cm, SD = 12.07 cm for 1.0 m, and mean = 83.42 cm, SD = 14.01 cm for 1.25 m). At further transfer distance, the body posture seems to shift from primarily twisting to twisting plus forward bending. As subjects were bending forward, the hands naturally extended out in an effort to span the reaching distances. This is likely to explain the extension of the width requirements in further transfer distances.

The repeated measures ANOVA found that there were significant differences in width requirements between transfer distances of 0.5 m vs 1.25 m, and 0.75 m vs 1.25 m at  $\alpha=0.05$ . Since width requirements for transfer distances of 0.5 m and 0.75 m were similar, it can be argued that 0.75 m transfer distance does not take significantly larger areas than 0.5 m, but at the same time provide larger clearance between the transfers. On the other hand, the 1.25 m transfer distance showed significant difference in width requirement as compared to 0.5 m, 0.75 m, and 1.0 m transfer distances, which indicates that it will take larger space area. When translated to area requirements, 1.25 m transfer distance on average consumed 64% larger area than 0.5 m, 46% larger area than 0.75 m, and 24% larger area than 1 m transfer distances. Larger space area requirement resulted in additional real estate, which indirectly translated to higher capital and costs. As such, it can be interpreted from data obtained in this study that the optimum transfer distance may be between 0.75 and 1.0 m. In this range, there is a middle ground in which the lifters do not have to adopt extreme twisting and forward bending. In addition, the differences in width requirements are marginal. This can provide the trade-off between postural adoption and space requirements when performing the manual transfer task. It should be noted that study by Lavender and Johnson [6] suggest that twisting and lateral movement would be minimized when the transfer distances were between 1 and 1.25 meters. The differences may come due to experimental setups, measures, and subject populations.

## 5. CONCLUSION

This study provides a visual mapping of hands and hip movements of manual transfer at four different distances, 0.50 m, 0.75 m, 1.00 m and 1.25 m. Based on observation of twisting and bending of subjects in motion capture software, and through visualization of hip and hand wrists motion top view mapping, it can be seen that the pattern of the hip motion changes from mostly static to more dynamic movements as the distance increases. In addition, patterns for wrists motions change from a semi-circular shape to a more stretched semi-circular shape as the transfer distance increases. Shorter transfer distance encourages low back twisting while minimizing bending, whereas the increase of transfer distance reduces the magnitude of low back twisting while individuals adopt more bending postures. As such, the motions of the hip and wrists during the manual handling process were affected by the transfer distance. In addition, the study also found that transfer

distances affect space requirements. As transfer distance increases, the data trend suggests that the width requirement also increases, due to shifting from primarily twisting to twisting plus forward bending. Forward bending and arm extension were adopted by subjects to increase their reaching range in further transfer distances, which consequently affect the space requirements. The study suggests that the optimum transfer distance may be between 0.75 and 1.0 m, in which there is a balance between extreme twisting and bending. In summary, it can be concluded that the difference in transfer distance does affect the space requirement as well as the postures possessed during manual handling activity. This provides guidance for engineers in designing workplace layouts as well as space requirements related to manual transfer tasks, especially in the early engineering design stage.

## ACKNOWLEDGEMENTS

The authors are grateful to the Malaysian government, Universiti Teknikal Malaysia Melaka (UTeM) for supporting this study. The study is partially funded by research grant INDUSTRI (IRMG) / ERGOWORKS / 2019 / FKP-COSSID / I00037. The authors acknowledge Lee Poh Yan and Nur Izzati Azri for their contributions in this study.

## REFERENCES

- [1] Duly J, Neumann WP. (2009) Ergonomic contributions to company strategies. *Applied Ergonomics*, 40(4):745-752.
- [2] Coenen P, Gouttebauge V, van der Burght AS, van Dieën JH, Frings-Dresen MH, van der Beek AJ, Burdorf A. (2014) The effect of lifting during work on low back pain: a health impact assessment based on a meta-analysis. *Occupational and Environmental Medicine*, 71(12): 871-877.
- [3] Deros BM, Daruis DDI, Rosly AL, Aziz IA, Hishamuddin NS, Hamid NHA, Roslin SM. (2017) Ergonomic risk assessment of manual material handling at an automotive manufacturing company. *Press Academia Procedia*, 5:317-324.
- [4] Mital A. (2017) *Guide to manual materials handling*, London.
- [5] Mehta JP, Kim TH, Weiler MR, Lavender SA. (2014) Effects of transfer distance on spine kinematics for de-palletizing tasks. *J. of Occupational and Environmental Hygiene*, 11(1):1-8.
- [6] Lavender SA, Johnson M. (2009) Is there a transfer distance that minimizes twisting and bending motions of the spine?. In *Proceedings of the Human Factors and Ergonomics Society Annual Meeting*, 53(14):882-882.
- [7] Lavender SA, Lorenz EP, Andersson GB. (2007) Can a new behaviorally oriented training process to improve lifting technique prevent occupationally related back injuries due to lifting?. *Spine*, 32(4):487-494.
- [8] Daltroy LH, Iversen MD, Larson MG, Lew R, Wright E, Ryan J, Liang MH. (1997) A controlled trial of an educational program to prevent low back injuries. *New England J. of Medicine*, 337(5):322-328.
- [9] Karwowski W. (2005) Ergonomics and human factors: the paradigms for science, engineering, design, technology and management of human-compatible systems. *Ergonomics*, 48(5):436-463.
- [10] Kuorinka I, Lortie M, Gautreau M. (1994) Manual handling in warehouses: the illusion of correct working postures. *Ergonomics*, 37(4):655-661.
- [11] Shamsuddin KA, Ani MNC, Ab-Kadir AR, Osman MH. (2014) Analysis on the work-related musculoskeletal disorders (WMSD's) based on ergonomic study in case of industry study. *International J. of Engineering Research*, 3(4):190-195.

- [12] Yahya NM, Zahid MNO. (2018) Work-related musculoskeletal disorders (WMDs) risk assessment at core assembly production of electronic components manufacturing company. In IOP Conference Series: Materials Science and Engineering, 319(1):012036.
- [13] Kazmierczak K, Neumann WP, Winkel J. (2007) A case study of serial-flow car disassembly: ergonomics, productivity and potential system performance. *Human Factors and Ergonomics in Manufacturing & Service Industries*, 17(4):331-351.
- [14] Cheung Z, Feletto M, Galante J, Waters T, Centers for Disease Control and Prevention. (2007) Ergonomic guidelines for manual material handling. In NIOSH Publication, 2007-131.
- [15] Department of Occupational Safety and Health. (2018) Guidelines for manual material handling at workplace 2018, Malaysia.
- [16] Mohamad D, Deros BM, Ismail AR, Daruis DDI. (2010) Development of a malaysian anthropometric database. In Conference on Manufacturing Technology and Management.
- [17] Dolan P, Earley M, Adams MA. (1994) Bending and compressive stresses acting on the lumbar spine during lifting activities. *J. of Biomechanics*, 27(10):1237-1248.
- [18] Marras WS, Granata KP. (1997) The development of an EMG-assisted model to assess spine loading during whole-body free-dynamic lifting. *J. of Electromyography and Kinesiology*, 7(4):259-268.
- [19] Plamondon A, Denis D, Delisle A, Larivière C, Salazar E, IRSST MMH research group. (2010) Biomechanical differences between expert and novice workers in a manual material handling task. *Ergonomics*, 53(10):1239-1253.
- [20] Deros BM, Daruis DD, Ismail AR, Sawal NA, Ghani JA. (2010) Work-related musculoskeletal disorders among workers' performing manual material handling work in an automotive manufacturing company. *American J. of Applied Sciences*, 7(8):1087.
- [21] Pope MH, Andersson GBJ, Broman H, Svensson M, Zetterberg C. (1986) Electromyographic studies of the lumbar trunk musculature during the development of axial torques. *J. of Orthopaedic Research*, 4(3):288-297.
- [22] Cholewicki J, McGill SM. (1996) Mechanical stability of the in vivo lumbar spine: implications for injury and chronic low back pain. *Clinical Biomechanics*, 11(1):1-15.
- [23] Jager M, Luttmann A. (1992) The load on the lumbar spine during asymmetrical bi-manual materials handling. *Ergonomics*, 35(7-8):783-805.
- [24] Verbeek JH, Martimo KP, Karppinen J, Kuijper PPF, Viikari-Juntura E, Takala EP. (2011) Manual material handling advice and assistive devices for preventing and treating back pain in workers. *Cochrane Database of Systematic Reviews*, (6).

## CUTTING TOOL PERFORMANCE IN TURNING OF AL 7075-T651 ALUMINIUM ALLOY

NUR SOFWATI DAUD @ AB AZIZ<sup>1</sup>, NATASHA A. RAOF<sup>1\*</sup>,  
ABDUL RAHMAN A. GHANI<sup>2</sup>, AISHAH NAJIAH DAHNEL<sup>1</sup>, SUHAILY MOKHTAR<sup>1</sup>,  
NOR KHAIRUSSHIMA MUHAMAD KHAIRUSSALEH<sup>1</sup>

<sup>1</sup>*Department of Manufacturing and Materials Engineering,  
International Islamic University Malaysia, Kuala Lumpur, Malaysia.*

<sup>2</sup>*Production Technology, German Malaysian-Institute, Kuala Lumpur, Malaysia.*

\*Corresponding author: [natashar@iium.edu.my](mailto:natashar@iium.edu.my)

(Received: 28<sup>th</sup> August 2019; Accepted: 22<sup>nd</sup> January 2020; Published on-line: 4<sup>th</sup> July 2020)

**ABSTRACT:** Recently, almost 70% of a commercial jetliner's airframe is made of aluminium alloys. It is predicted that the application of aluminium alloy is to increase up to 65% by the year 2025. They are typically used because of their high strength to weight ratio. However, there are some drawbacks during machining aluminium alloy such as the adhesion wear and built-up edge (BUE) formation that can shorten tool life. As the tool wears, the machining performance, surface roughness, and cutting tool life are affected significantly. A lot of studies were conducted in order to minimize this critical issue. This project presents a study of the cutting tool performance of an uncoated carbide tool in dry turning operation on Al 7075-T651, in which the tool wear rate, volume of material removed, wear mechanism, and surface roughness were investigated. The machining tests were conducted on a CNC lathe machine to obtain the tool wear and surface roughness of the machined work piece. The average flank wear was measured using a digital microscope, whereas the wear mechanism was observed using a Scanning Electron Microscope (SEM). The average surface roughness (Ra) was measured using a surface roughness tester. The cutting time for this experiment was fixed at 40 minutes and all the results were analysed within this time range to evaluate the tool performance in the turning of Al 7075-T651. The results revealed that the tool performs better at low cutting speed, 250 m/min, by reducing the tool wear rate by 33%. The cutting speed of 250 m/min also contributed to 71% higher volume of material removed during the machining tests. The dominant type of wear found was flank wear, while the main principal of wear mechanism is adhesion. At higher cutting speed, the surface roughness was improved. Based on the results, it can be concluded that high cutting tool performance is achieved when low tool wear growth rate, high volume of material removal, and low surface roughness during turning operation are obtained.

**ABSTRAK:** Kebelakangan ini, hampir 70% kerangka pesawat udara komersil diperbuat daripada aloi aluminium. Penggunaan aloi aluminium ini dijangka meningkat sehingga 65% pada tahun 2025. Ia biasa digunakan kerana nisbah kekuatan kepada berat yang tinggi. Walau bagaimanapun, terdapat beberapa kekurangan semasa pemesinan aloi aluminium ini iaitu pemakaian pelekat dan pembentukan binaan tepi (BUE) yang mengurangkan jangka hayat mata alat. Apabila mata alat menjadi haus, prestasi mesin, kekasaran permukaan, dan jangka hayat mata alat pemotong terjejas dengan ketara. Banyak kajian telah dijalankan bagi mengurangkan isu kritikal ini. Projek ini mengkaji prestasi mata alat pemotong karbida tidak bersalut dalam operasi mesin larik kering pada Al 7075-T651, di mana kadar haus mata alat, kuantiti bahan yang dibuang, mekanisme haus dan kekasaran permukaan telah diselidiki. Ujian pemesinan dijalankan pada mesin

CNC mesin larik bagi mendapatkan kadar haus mata alat dan kekasaran permukaan material yang dimesin. Purata haus pengapit mata alat diukur dengan menggunakan mikroskop digital, manakala mekanisme haus dipantau menggunakan Mikroskop Elektronik Pengimbas (SEM). Purata kekasaran permukaan (Ra) diukur menggunakan alat penguji kekasaran permukaan. Tempoh masa pemotongan bagi eksperimen ini telah ditetapkan pada 40 minit dan semua keputusan telah dianalisa dalam tempoh masa ini bagi menilai prestasi mata alat dalam melarik Al 7075-T651. Hasil menunjukkan prestasi mata alat lebih baik pada kelajuan pemotongan rendah, 250 m/min dengan mengurangkan kadar haus mata alat sehingga 33%. Kelajuan pemotongan 250 m/min juga menyumbang kepada 71% peningkatan ke atas jumlah bahan yang dibuang semasa ujian pemesinan. Jenis haus yang dominan telah ditemui pada pengapit mata alat, manakala mekanisme haus yang utama adalah lekatan. Pada kelajuan pemotongan yang tinggi, kekasaran permukaan didapati lebih baik. Berdasarkan keputusan, dapat disimpulkan bahawa prestasi mata alat pemotong yang bagus dapat dicapai apabila kadar haus mata alat adalah rendah, jumlah penyingkiran bahan yang tinggi dan kekasaran permukaan yang rendah semasa operasi pelarikan dijalankan.

---

**KEYWORDS:** *tool wear; cutting tool performance; surface roughness; wear mechanism; Al 7075*

## 1. INTRODUCTION

Aluminium alloy is one of the common metal alloys used to manufacture products in industries such as automotive, aircraft, sporting equipment, food packaging, and building construction. Various applications of aluminium products include bicycle frame, rudder of aircraft, truck frames, kitchen utensils, and food wrapper [1]. It is favoured in industry owing to the excellent combination of high strength-to-weight ratio and excellent mechanical properties such as hardness and good machinability found in various series of aluminium alloy [2]. Aluminium alloy consists of different elements with different chemical compositions where the Aluminium is the dominant component with different main alloying elements. Different alloy elements in the composition of aluminium alloys determine its characteristics and properties. Among the Aluminium alloy groups, Al 7075 containing 5.6% Zinc in weight of Aluminium was marked as the highest strength of Aluminium alloy with 570MPa tensile strength, comparable to other steels [3]. The research claimed that, aluminium alloy has its drawbacks in machining operation despite its high machinability. The formation of a built-up edge (BUE) tends to affect the machined surface and alter the cutting tool geometry. BUE also tends to increase the tool wear significantly [3]. Thus, numerous studies were conducted in order to minimize the problem encountered during machining aluminium alloy and solve the critical issues. Recently, many studies were done on aluminium alloy to investigate its machinability. Researchers are looking into various machining parameters on some criteria such as tool life, chip formation, and surface roughness to provide a vast overview on the machinability of aluminium alloys [4]. Nevertheless, research on the cutting tool analysis and performance is a bit lacking compared to the study on the surface integrity and optimization of cutting conditions especially for turning operations. Most of the research concentrated on the milling operation. Therefore, further studies on this problem are necessary, particularly in turning operations. This study aims to evaluate the cutting tool performance in terms of tool wear rate, wear mechanism, volume of material removed, and the quality of machined surface in dry turning Al 7075-T651 aluminium alloy using KW10 Kyocera uncoated carbide tool.

## 2. METHODOLOGY

### 2.1 Workpiece and Cutting Tool Material

The workpiece material used in the machining tests was 100 mm x 200 mm Al 7075-T651 cylindrical bar. T651 is the tempered designation in which the material is solution heat treated, stress relieved, and artificially aged. The chemical composition and mechanical properties of the work material are given in Table 1 and Table 2, respectively.

Table 1: Chemical Composition of Al 7075 (%wt)

Si	Fe	Cu	Mn	Mg	Cr	Zn	Ti	Others
0.04	0.10	1.3	0.07	2.3 – 2.4	0.10	6.7 – 6.8	0.05	Balance

Table 2: Mechanical properties of Al 7075

Properties	Values
Tensile strength (ksi)	78 - 85
Yield strength (ksi)	68 – 78
Elongation (%)	7 – 12

The cutting tool used was a KW10 Kyocera uncoated carbide tool with the ISO designation TNGG 160408AH. This cutting tool is suitable for use in cutting non-ferrous material such as Al 7075 for medium to finishing operations. The tool holder was selected according to the cutting tool with the ISO designation MTJNR 2525M-16.

### 2.2 Machining Experiments

The turning operation was conducted in dry conditions using a ROMI M420 CNC lathe machine. The parameters and values used in the experiment are shown in Table 3.

Table 3: Parameters used in the experiment

Parameters	Value
Cutting speed (m/min)	250, 450
Feed rate (mm/rev)	0.05
Depth of cut	1.0

The average tool flank wear,  $VB_{ave}$  was measured using a Dino-Lite Edge Digital Microscope at 227x magnification at each 1 minute of the cutting time. The turning operation was then stopped when the cutting time reached 40 minutes. The recorded data was used to determine the tool flank wear progression with cutting time and tool wear rate for both cutting speeds. The wear also was used to calculate the volume of material removed within 40 minutes of machining time.

When 40 minutes of cutting time was achieved, the average surface roughness of workpiece ( $R_a$ ) was measured using a Mitutoyo SurfTest surface roughness tester. The surface roughness of both cutting speeds were recorded and analysed.

Then, the cutting tool was examined under scanning electron microscope (SEM) JEOL JSM-5600 in order to determine the type of wear and wear mechanism that occurred during the machining operation.

### 3. RESULTS AND DISCUSSION

#### 3.1 Effect of Cutting Speed On Tool Wear Rate and Volume of Material Removed

Figure 1 shows the progression of flank wear versus cutting time for turning Al 7075-T651 using KW10 uncoated carbide tool at cutting speed of 250 m/min and 450 m/min, while other parameters are kept constant, as tabulated in Table 3. The average flank wear of uncoated carbide tool increased with the increase in cutting time within 40 minutes of cutting time.

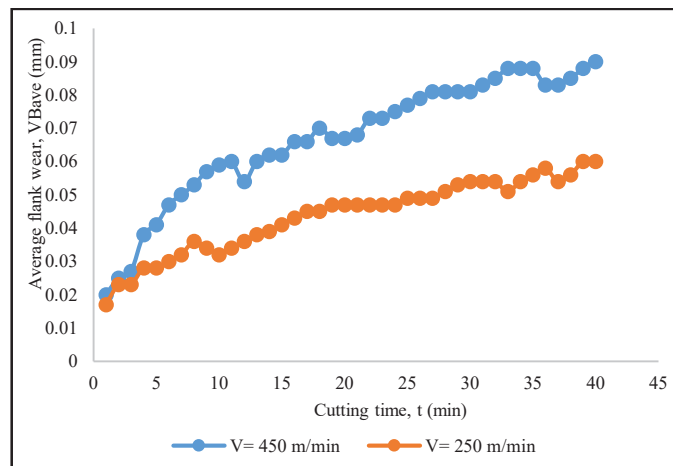


Fig. 1: Comparison of tool average flank wear progression versus cutting time at cutting speeds 250 m/min and 450 m/min in dry condition ( $f = 0.05\text{mm/rev}$ ,  $d = 1.0\text{ mm}$ ).

Although similar trends of flank wear were observed, it is noted that at 40 minutes of machining time, the uncoated carbide tool used at 450 m/min had 50% higher average flank wear which is 0.090 mm compared to 0.060 mm of  $VB_{ave}$  when cutting at 250 m/min. Due to that, it can be concluded that the uncoated carbide tool wears rapidly at high cutting speed especially on the flank face. This might be caused by the high intensity of cutting temperature at high cutting speed because of the rubbing of the tool and the machined surface and the sliding of the chip along the tool's rake face. This is supported with the findings by other researchers that were reviewed by [5], who stated that the increment of cutting speed results in higher rate of material deformation at the cutting zone, which consequently elevates the degree of heat generation hence accelerating the tool wear formation.

The graph presented in Fig. 1 has a similar trend to the tool wear growth curve that was reported in [6]. For 40-minutes machining time, the two phases of wear progression trend, which are break-in period and steady-state wear regions, can be observed. The rate of tool wear growth for each phase at both cutting speeds was calculated as shown in Table 4.

The rate of flank wear growth using a KW10 uncoated carbide tool in the first phase is higher than the second phase and the tool wear rate is relatively high at higher cutting speed (450 m/min). This means that the wear occurred rapidly in the first phase, especially at high cutting speed. This rapid increment was due to the increase in the tool's material removal resulting from the elevation of the machining temperature. This result is aligned with the findings reported by [6] that some of tool materials can be removed easily when the cutting edge experienced high cutting temperature due to the high cutting speed.

Table 4: The rate of flank wear growth using uncoated carbide tool

Tool Wear Progression Phase	Rate of Flank Wear Growth	
	V = 250 m/min	V = 450 m/min
Break-in period (first phase)	2.375E-3	3.636E-3
Steady-state wear region (second phase)	0.774E-3	1.28E-3

The varied cutting speeds also have an influence on the volume of material removed in the turning operation. The volume of material removed was calculated using Eq. (1) at the same average flank wear, which is 0.060 mm.

$$v(\text{mm}^3) = (\pi)(D_{avg})(d)(f)(N) \times \text{tool travel}(\text{min}) \quad (1)$$

At cutting speed 250 m/min, the volume of material removed was found to be 507 461.46 mm<sup>3</sup> for 40 minutes of machining time ( $V_{b_{ave}} = 0.060$  mm), whereas the volume of material removal at cutting speed 450 m/min for 11 minutes of machining time ( $V_{b_{ave}} = 0.060$  mm) was 296 161.71 mm<sup>3</sup>.

The lower speed (250 m/min) has 71% higher volume of material removal with longer cutting time compared to the high cutting speed (450 m/min). According to Rao [8], they stated that the relationship between tool life and cutting speed affects the decrease of material removal rate (MRR). MRR is the volume of material removed per unit time. Hence, it can be decided that, the decrease of MRR leads to a decrease in material removal volume as the volume of material removed is directly proportional to MRR.

### 3.2 Tool Wear and Wear Mechanism

Table 5 shows the views of wear area for the KW10 uncoated carbide tool used in the machining test for 40 minutes under SEM. From Table 5, it can be noted that the flank wear, crater wear, and nose wear were found on the cutting tool edges for both cutting speeds within 40 minutes of the turning operation of Al 7075-T651 using KW10 uncoated carbide under dry conditions.

The flank wear occurred at the front relief and side relief faces, whereas the crater wear was formed at the rake face. The nose wear was formed at the nose area of the tool. Flank wear is the main type of wear observed in this machining experiment. The friction caused by the rubbing action of the tool and the machined surface resulted in high cutting temperature; thus, the flank wear formation was promoted [9]. Despite both cutting conditions having similar types of wear, the severity in tool wear formation differed. With the increment of cutting speed, the flank wear was affected and increased significantly.

The main wear mechanism observed in this study was adhesion wear mechanism. It was formed due to the high cutting temperature at the tool-chip interface during machining of aluminum alloy. The heat generation was influenced by the cutting speed. However, the effect of the cutting speed on the adhesion wear mechanism is not severely affected as the flank wear does.

Adhesion wear was formed due to the welding of the workpiece material which was concentrated at the rake, front relief, and side relief faces. The cutting temperature that was generated in both conditions was predicted to be high enough to melt the work material at the cutting interface. The welded material was then developed to form BUE. The tearing of unstable BUE from the cutting tool surface caused a small quantity of tool material to be removed. The frequent building and breaking away of BUE increased the high wear rate

[7]. The result was in agreement with the findings reported by Jurado et al. [9], as the adhesion wear occurred when material was transferred by chip onto the tool surface and modified the cutting conditions.

Table 5: The views of wear area for KW10 uncoated carbide tool used in machining test at cutting speed at  $V = 250$  m/min and  $V = 450$  m/min after 40 minutes of cutting time

	$V = 250$ m/min	$V = 450$ m/min
Nose		
Front relief face		
Side relief face		

### 3.3 Effect of Cutting Speed on Surface Roughness

The surface roughness of the machined workpiece was measured to evaluate the cutting tool performance of the uncoated carbide tool in turning Al 7075-T651. Fig.2 shows the relationship between cutting speed and average surface roughness ( $R_a$ ) at 40 minutes of cutting time.

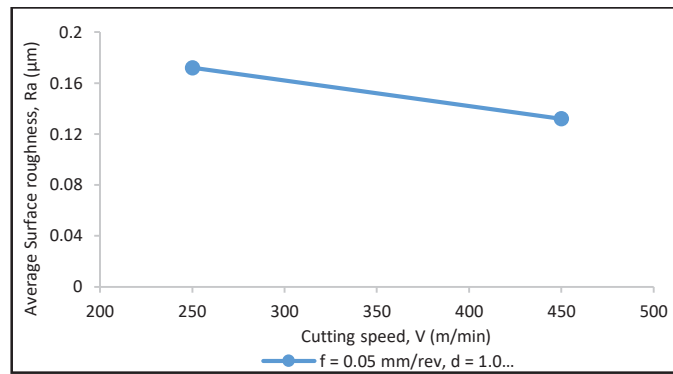


Fig. 2: The average surface roughness (Ra) of the machined surface of Al 7075-T651 for cutting speeds 250 m/min and 450 m/min using the KW10 uncoated carbide tool at  $t = 40$  minutes in dry conditions ( $f = 0.05\text{mm/rev}$ ,  $d = 1.0$  mm).

Referring to Fig. 2, the best surface finish was achieved at high cutting speed with  $0.132 \mu\text{m}$  within 40 minutes of cutting time. The surface roughness value produced decreased as the radius of chip curl increased with the increment of the cutting speed. Figure 3 shows the difference in degree of chip curl produced at cutting speed = 250 m/min and 450 m/min in turning Al 7075-T651.

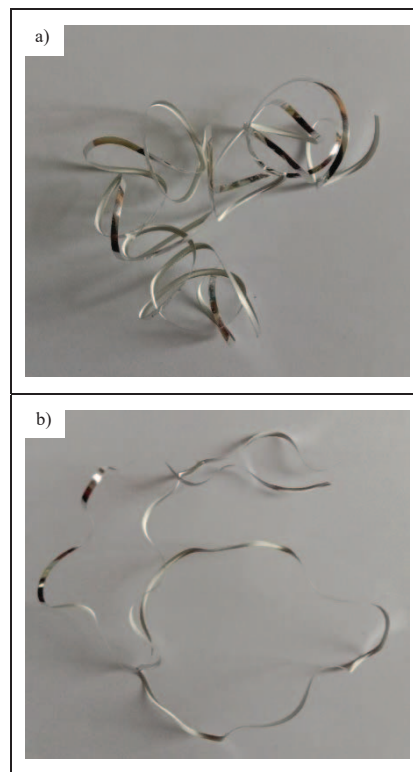


Fig. 3: Chips produced in turning Al 7075-T651 using a KW10 uncoated carbide tool under dry conditions,  $f = 0.05$  mm/rev,  $d = 1$  mm at, (a)  $V = 250$  m/min, and (b)  $V = 450$  m/min.

A high surface roughness was obtained due to this low radius of chip curl, which tends to tangle and accumulate around the machined surface and scratches the freshly cut workpiece. Consequently, the surface roughness increases as the accumulation of chips caused the unevenness in the machined surface. Similar findings were discussed by [10],

the radius of the chip curvature increased with increase in the cutting speed which led to chips wrapping around the cutting tool, tool holder, and workpiece.

#### 4. CONCLUSION

From the analysis on the cutting tool performance of KW10 uncoated carbide tool in turning Al 7075-T651, the following can be concluded:

- The tool at lower cutting speed (250 m/min) performed better in having lower average tool wear rate within 40 minutes of operation. The percentage of average tool wear reduction was about 33% when turning at cutting speed 250 m/min compared to 450 m/min.
- A rapid wear growth rate was achieved in the first phase (break-in phase) especially at a high cutting speed. The tool wear rate at cutting speed 250 m/min is 34%-40% slower than the tool wear rate at 450 m/min in both phases (break-in and steady-state wear phases). The rapid increment was due to the high intensity of cutting temperature at higher cutting speed.
- At the same average flank wear measurement,  $V_{\text{bave}} = 0.6$  mm, the low cutting speed (250 m/min) produced about 71% higher volume of material removed compared to high cutting speed (450 m/min), in which high volume of material removed may increase the machining productivity.
- The most significant type of wear observed on the cutting edges in both conditions at 250 m/min and 450 m/min is the flank wear. The severity in tool wear formation increased with the increment of cutting speed.
- The main wear mechanism identified was adhesion during the turning operation at both cutting speeds. The welded material on the cutting edge caused the adhesion to form in all conditions. The building and tearing of BUE promotes higher tool wear.
- The KW10 uncoated carbide tool used in turning Al 7075-T651 at cutting speed 450 m/min performed better than at 250 m/min in producing low surface roughness due to the high radius of chip curl. It has low tendency for the chip to tangle around the freshly cut surface of the workpiece and leave scratches and marks on it.

#### ACKNOWLEDGEMENTS

This project is supported by the Government of Malaysia and the International Islamic University Malaysia under these research grants, FRGS/1/2018/TK03/UIAM/03/4 and RIGS17-157-0732.

#### REFERENCES

- [1] Ng CH, Yahaya SN, Majid AA. (2017) Reviews on aluminum alloy series and its applications. *Academia Journal of Scientific Research*, 708–716.
- [2] Das DK, Mishra PC, Sahoo AK, Ghosh D. (2015) Experimental investigation on cutting tool performance during turning AA 6063 using uncoated and multilayer coated carbide inserts. *International Journal of Machining and Machinability of Materials*, 17(3/4):277.
- [3] Santos MC, Machado AR, Sales WF, Barrozo MAS, Ezugwu EO. (2016) Machining of aluminum alloys: a review. *International Journal of Advanced Manufacturing Technology*, 86(9–12):3067–3080.

- [4] Kouam J, Songmene V, Balazinski M, Hendrick P. (2015) Effects of minimum quantity lubricating (MQL) conditions on machining of 7075-T6 aluminum alloy. *The International Journal of Advanced Manufacturing Technology*, 79(5–8):1325–1334.
- [5] Santos MC, Machado AR, Barrozo MAS. (2018) Temperature in Machining of Aluminum Alloys. *Temperature Sensing*.
- [6] SV Alagarsamy NR. (2014) Analysis of Influence of Turning Process Parameters on MRR & Surface Roughness Of AA7075 Using Taguchi's Method and Rsm. *International Journal of Applied Research and Studies*, Volume 3(4):1–8.
- [7] Zagórski I, Warda T. (2018) Effect of Technological Parameters on the Surface Roughness of Aluminium Alloys After Turning. *Advances in Science and Technology Research Journal*, 12(2):144–149.
- [8] Rao CJ, Sreemulu D, Mathew AT. (2014) Analysis of Tool Life during Turning Operation by Determining Optimal Process Parameters. *Procedia Engineering*, 97:241–250.
- [9] Jurado DG, Martínez JMV, Gámez AJ, Batista M, Puerta FJ, Marcos M. (2017) Analysis of secondary adhesion tool wear effects on surface roughness in dry turning process of UNS A92024 aluminium alloy. *International Journal of Mechatronics and Manufacturing Systems*, 10(1):23.
- [10] Xu D, Feng P, Li W, Ma Y, Liu B. (2014) Research on chip formation parameters of aluminum alloy 6061-T6 based on high-speed orthogonal cutting model. *International Journal of Advanced Manufacturing Technology*, 72(5–8):955–962.

## INVESTIGATION ON INFLUENCE OF ANIONIC SURFACTANT FOR HOMOGENISATION OF MWCNT IN ALUMINIUM 6065 MATRIX

SAVINA JADDINAGADHE PUTTASWAMY\* AND  
RAGHAVENDRA BOMMANAHALLI VENKATAGIRIYAPPA

*Department of Mechanical Engineering, JSS Academy of Technical Education,  
Bangalore-560060, India*

*\*Corresponding author: mailtosavin@gmail.com*

*(Received: 21<sup>st</sup> December 2019; Accepted: 13<sup>th</sup> March 2020; Published on-line: 4<sup>th</sup> July 2020)*

**ABSTRACT:** In the proposed work, sodium dodecyl sulfate (SDS) is used as a surfactant for carbon nanotubes, to fabricate multi walled carbon nanotube-aluminium metal matrix composites (MMCs). This paper presents the comparison study of SDS coated and non-coated multi walled carbon nanotube (MWCNT) mixed with Al6065 by stir casting technique. The presence of low molecular weight surfactant treated with MWCNT was investigated by Fourier Transform Infrared (FTIR) spectroscopy analysis. About 1 wt. % of MWCNT is used as a filler metal in Aluminium and the dispersion characteristics of SDS coated and non-coated Carbon Nanotubes in the composite is examined using a scanning electron microscope (SEM). The comparison study of SEM analysis showed that the MWCNT coated with SDS has good dispersion stability and considerable reduction in agglomeration to obtain agglomeration free composites. The mechanical properties and wear characteristics of the MWCNT-Aluminium matrix were studied as per the American Society for Testing and Materials (ASTM) standards. The results of SDS coated MWCNT exhibits exceptional properties with increase in the tensile strength, compressive strength, hardness, and wear characteristics of the reinforced metal matrix.

**ABSTRAK:** Natriumdodesilsulfat (SDS) digunakan sebagai surfaktan pada karbon nanotub, bagi menghasilkan multi dinding karbon nanotub-komposit matriks logam aluminium (MMCs). Perbandingan dibuat dalam kajian ini dengan membandingkan salutan SDS dengan bukan-salutan multi dinding karbon nanotub (MWCNT) yang bercampur A16065 melalui teknik kacauan acuan. Kehadiran berat surfaktan molekul ringan terawat dengan MWCNT dikaji mengguna pakai analisis spektroskopi Penjelmaan Fourier Inframerah (FTIR). Kira-kira 1 wt.% MWCNT digunakan sebagai pengisi besi dalam Aluminium dan ciri-ciri penyebaran salutan SDS dan bukan-salutan karbon nanotub dalam komposit diteliti menggunakan pengimbas mikroskop elektron (SEM). Perbandingan analisis SEM menunjukkan, salutan MWCNT dengan SDS mempunyai kestabilan penyebaran dan berkurang dengan banyak dalam pengaglomeratan bagi mendapatkan komposit bebas pengaglomeratan. Ciri-ciri mekanikal dan haus matrik Aluminium-MWCNT dikaji berdasarkan piawai Persatuan Pengujian Bahan Amerika (ASTM). Keputusan MWCNT salutan SDS mempunyai ciri-ciri luar biasa dengan kenaikan kekuatan tegangan, kekuatan mampatan, kekerasan, dan ciri-ciri haus pada kekuatan matrik logam.

**KEYWORDS:** *MWCNT (multi-walled carbon nanotube); aluminium matrix; SDS (sodium dodecyl sulfate); mechanical properties*

## 1. INTRODUCTION

Several manufacturing industries are facing challenges for attaining a stable and uniform dispersion of carbon nanotube (CNT) in a metal matrix [1]. It is important to understand the manipulation of the particles at micro or nano level to accomplish a yield with the desired qualities.

An exponential growth is found in the properties of ceramic, metallic, and polymeric composites with the introduction of CNTs as reinforcements. The improved mechanical properties, including the average elastic modulus within the range of 1 to 2TPa, the tensile strength from 11GPa to 63GPa, and the integration of CNTs with aluminium-based metal matrix nano-composites (Al-MMCs), has attracted researchers all across the globe. The research mainly focuses on obtaining high thermal stability, good strength to weight ratio, and stiffness with higher electrical conductivity in engineering material applications [2,3].

The aluminium based metal matrix is used as a lightweight component in manufacturing industries and is popular for its low density and high stiffness. Various reinforcing materials like silicon carbide, aluminium oxide, graphite, and CNTs are best suited for aluminium based metal matrix composites. The uniform dispersion of particulate matter along with high stability plays an important role in many industrial applications. Thus, the surface modification and various complementary strategies must be incorporated in order to obtain compatibility between CNTs and aluminium matrices. This will guarantee the homogenous dispersion and will introduce densification in the composite materials [4]. The complexity of dispersion tends to increase when the micro or nano sized particles are injected. Within the specified ranges, the dispersion state of particles in the final product is controlled by the surface chemistry.

The manipulation of surface properties thus becomes important to achieve a product of desired properties. Of the various methods involved, the stir casting method is one of the more prominent and cost effective methods followed by researchers [5]. In this method, the particulate reinforcements are evenly mixed with the molten metal, which is later subjected to solidification. With the help of a rotating impeller, the pre-treated particles are inserted into the vortex of the molten alloy. During this process the issue that arises is sedimentation (also called agglomeration of reinforcements). That is, the reinforcements do not disperse uniformly. The poor dispersion of the reinforcements due to agglomeration with large Van-der Waals forces within the nano tubes and their poor wettability between aluminium and CNTs, are thought to be the major challenges that researches come across while trying to improve the material properties of the composite [6]. They have noticed that the addition of surfactants to the CNTs is one of the techniques to overcome the agglomeration of the nanoparticles in the matrix. They act as coupling agents that introduce a repulsive force between the individual CNTs. These forces are larger in comparison with the van der Waals attractive forces of the CNTs. With low surfactant to multi walled carbon nanotubes (MWCNTs) ratio, the surfactant is unable to form an effective coating, which introduces an electrostatic repulsion (also called as steric hindrance effect) in order to counter-balance the van der Waals force of attractions [7]. Hence sufficient addition of surfactant becomes crucial.

Anionic surfactants are most commonly used for effective dispersion of CNTs. SDS, which is a well-known anionic detergent, has a unique property of binding forces, making it a suitable choice as a surfactant in the CNT filler materials. For good mechanical properties of the metal matrix material, a uniform dispersion of the nanoparticles is necessary. In addition to this, the influence of sodium dodecyl sulfate (SDS) surfactant enhances the dispersion properties in the metal matrix composites [8,9]. Therefore, the

study is focused on enhancing the mechanical properties of aluminium metal matrix composite along with uniform dispersion of surfactant coated on MWCNT.

## 2. MATERIALS AND METHODS

### 2.1 Preparation of SDS Coated MWCNT

The reinforced Al6065-MWCNT composites were fabricated using the stir casting method. The Aluminium 6065 ingots, casted as per the chemical composition represented in the Table 1, were used as the matrix material. MWCNT with respective properties of Shear modulus of 26 GPa, Young's Modulus of 1TPa, Poisson's ratio 0.33 and density of  $1.3\text{g/cm}^2$  were used.

Table 1: Composition of Aluminium 6065

Component	Si	Cu	Fe	Zn	Mg	Ti	Mn	Cr	Pb	Al
Amount (wt %)	0.6	0.36	0.3	0.1	1.0	0.1	0.1	0.1	0.08	Balance

MWCNTs were later treated with an anionic SDS surfactant in a ratio of 1:1 with 300ml distilled water. This mixture was stirred continuously using a magnetic stirrer to obtain a homogeneous mixture. Furthermore, to ensure better homogenization, the mixture was subjected to ultra-sonication for 1 hour at room temperature as shown in Fig. 1(a).

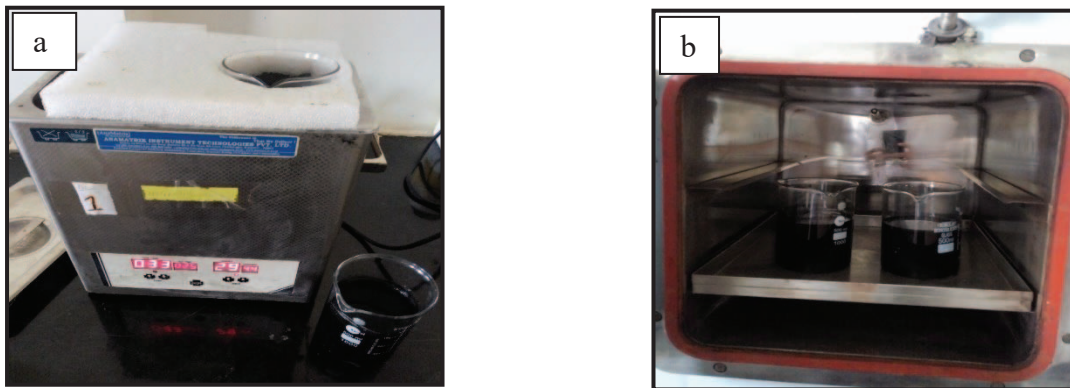


Fig. 1: (a) CNT-SDS mixture placed for ultra-sonication, (b) CNT-SDS mixture placed in hot air-oven at  $80^{\circ}\text{C}$ .

Figure 1(b) shows the CNT-SDS mixture placed in a hot air oven to remove the water content at  $80^{\circ}\text{C}$  for 12 hours and to decrease the Van der Waals force between CNTs and to facilitate their ease of dispersion. The CNT-SDS flakes acquired after drying were grinded to obtain fine particles with the use of a mortar and pestle, as shown in Fig. 2. The final product obtained was stored in sealed container for further use. The products were later checked for FTIR analysis to examine the functional groups present in the product.

### 2.2 Fabrication of MWCNT-Al Matrix

The stir casting method is simple, highly efficient, and the most cost effective method for manufacturing of AMMCs in mass production. Thermodynamic factors like temperature, physical, metallurgical principles, and foundry techniques, are the most important factors involved in the conversion of metallic raw material(s) into composite materials using the stir casting method. The Al6065 ingot-castings were preheated and

then placed into the electric furnace. The temperature of the crucible in the furnace is raised to 800°C and is maintained at the same temperature for uniform heating of the entire molten metal.

The molten metal was further stirred continuously for about 15 minutes to create a vortex and the SDS coated with CNT particulate were mixed as shown in Fig. 3(a, b). The same procedure is repeated for the reinforced material of 99% Al-6065 and 1 wt. % of CNT without SDS coating. This takes place with a radial type stirrer with three wings that is moved down to a depth of 70mm inside the furnace and is rotated with a speed of 500 rpm. This mixes the reinforced powder uniformly. The molten metal in the crucible was then degassed by adding a suitable amount of scum powder, which separates the impurities and accumulates at the surface. These impurities were later extracted and removed. During casting of aluminium, the solidification process involves the evolution of hydrogen gases that leads to porosity in the molten aluminium. The degassing is very much essential to produce high-quality castings [10,11]. In order to do this, solid dry hexachloroethane ( $C_2Cl_6$ ) degasser tablets were added, that remove the gases from the molten alloy; thus eliminating the presence of blow hole defects in the casting metal [12]. The molten metal was later poured into the die to obtain three separate sample sets of MWCNT with and without SDS coating Reinforced-Al matrix composite as shown in Fig. 3.

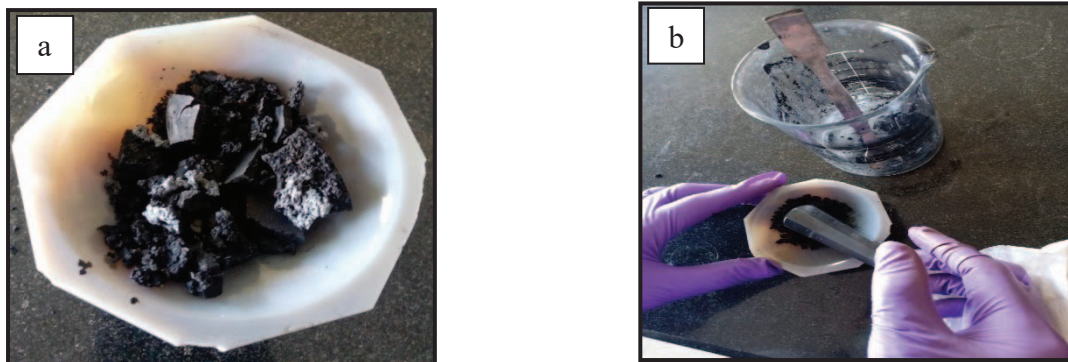


Fig. 2: (a) CNT-SDS flakes obtained after drying. (b) Powdering CNT-SDS flakes using a mortar and pestle.



Fig. 3: (a) Stirring of molten metal and (b) Pouring the molten metal in to the die.

Figure 4 shows samples of aluminium ingots with SDS coated 1% CNT and another non-SDS coated 1% MWCNT. The samples were later investigated for their microstructure, using SEM and radiography apparatus.

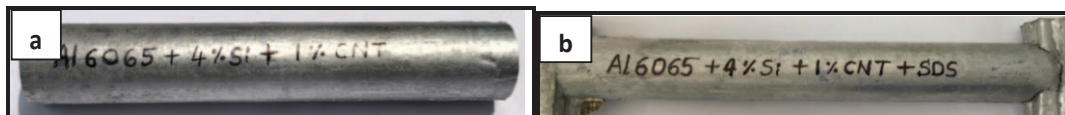


Fig. 4: (a) CNT+Al molten metal ingots with and (b) without SDS coating.

### 3. RESULTS AND DISCUSSION

#### 3.1 Fourier Transform Infrared Spectroscopy (FT-IR) Analysis of SDS Coated and Non-Coated CNT.

FT-IR is one of the prominent analytical techniques that are used for identifying organic materials present in samples. It spots the chemical bonds in the molecules using an infrared absorption spectrum. This approach determines the transmission of infrared radiation into the sample material versus wavelength. The FT-IR results obtained confirmed the presence of SDS with CNT. The infrared absorption bands detect molecular components and structures. The presence of SDS substitution in the obtained sample is a significant data to be retrieved for the study and to evaluate the efficiency of the process.

The transmittance-comparison plot of CNT coated with SDS and CNT non-coated with SDS was plotted as shown in Fig. 5. It displays a peak around 1100, 1281, 2961, 2980 and 3445  $\text{cm}^{-1}$ . The peaks around 2961 and 2980  $\text{cm}^{-1}$  are accredited to C-H stretching frequencies. The band at 3445  $\text{cm}^{-1}$  is allocated to stretch and bend vibrations of O-H bands due to absorbed water molecules. The band at 1281  $\text{cm}^{-1}$  is attributed to C-H bending frequencies. The peaks around 1100  $\text{cm}^{-1}$  refer to the  $\text{SO}_4$  group, whereas these peaks are absent in non-coated MWCNT.

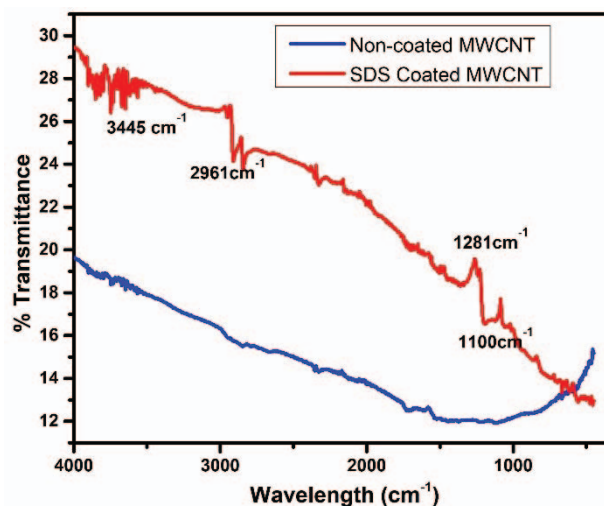


Fig. 5: Transmittance comparison plot for non-coated and SDS coated CNT.

#### 3.2 Microstructure Analysis

The distribution of CNT nanotubes in the Al matrix was extensively analysed using SEM analysis. In Fig. 6(a) few distinct CNTs were detected for the untreated MWCNT-Al matrix, which were entangled and overlapped together, whereas this arrangement differed for the MWCNT-Al matrix. This introduces defects in the Al matrix thus reducing the

mechanical properties of the composite. In Fig. 6(b) the MWCNTs are seen discretely and effectively dispersed in the Al matrix.

The SEM image with the scale range of 500nm depicts the more porous structures for the non-coated Al matrix with uneven distribution of CNTs leading to the formation of clusters, as shown in Fig. 6(a). Inter-granular porosity is extensively observed with the absence of the SDS in the Al matrix [13]. Fewer porosities are observed and the porosity between the grains is not seen in Fig. 6(b) for the SDS coated MWCNT Al matrix. As shown in Fig.6(b), the quality of dispersion for MWCNT was enhanced with the help of added surfactant of a thin SDS layer. Thus, SEM analysis proves that SDS coated CNT dispersion when compared to non-coated CNT is better.

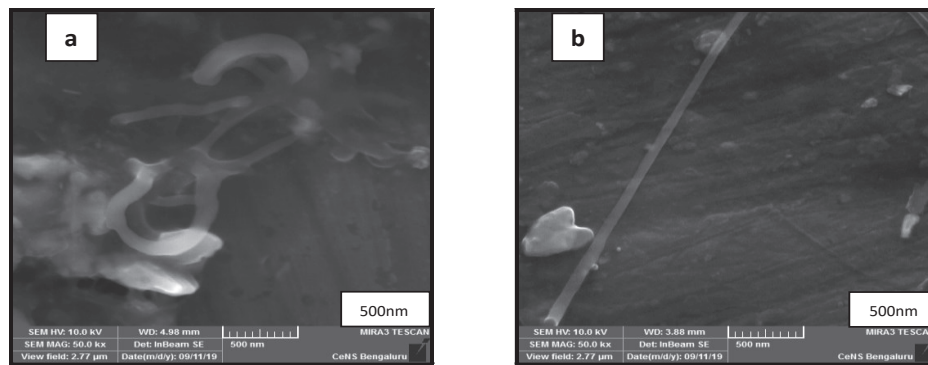


Fig. 6: (a) SEM image of MWCNT-Al matrix and (b) SDS-MWCNT-Al matrix.

### 3.3 X-Ray Radiography

Radiography is one of the best non-destructive methods to study the internal defects and volumetric discontinuities present in casting materials using radiography. This method is also implemented for non-planar materials.

Dark regions are observed in Fig. 7 (a), indicating that blow holes were formed in the non-coated MWCNT -Al matrix and it is insignificant in the SDS coated Al matrix. This defect might be the result of voids created during the casting process for the non-coated MWCNT-Al matrix. No cracks or fine lines were observed for both the non-coated and SDS coated MWCNT-Al matrix. Hence, it can be concluded that internal stress had less impact to cause cracks in the present specimens. Segregations are detected in the mid region for non-coated MWCNT-Al and this observation is absent in the SDS coated MWCNT-Al matrix.



Fig. 7: (a) Radiography image of MWCNT-Al matrix and (b) SDS-MWCNT-Al matrix.

### 3.4 Hardness Testing

Specimens are tested for hardness using a Vickers Hardness testing machine. The Vickers hardness tester (Model-BV 250) follows ASTM E92 standards. Figure 8 shows the comparison plot of hardness for the non-coated and SDS coated MWCNT-Al matrix. It was evident that the SDS coated MWCNT-Al matrix showed a better average value of

49.26 HV, than that of untreated MWCNT-Al matrix, which showed 45.23 HV. This significant improvement in the hardness might be ascribed to the solitary strengthening effect of nanotubes [14]. The percentage variation of hardness was increased by 8.91% for the SDS coated MWCNT-Al matrix.

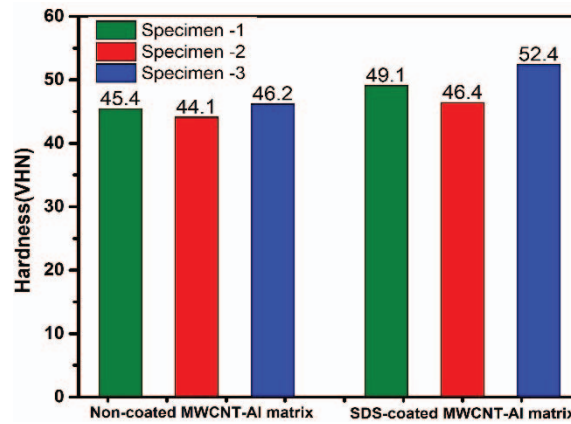


Fig. 8: Hardness comparison plot of non-coated and SDS coated MWCNT-Al matrix.

### 3.5 Tensile Strength

The tensile analysis was accomplished by the use of a Universal Tensile Testing Machine (UTM). Specimens were prepared as per ASTM E8 standards. From the graph in Fig. 9, it is evident that the tensile strength value is greater for the SDS coated MWCNT Al matrix. The excellent tensile strength value of the CNT contributes to significant improvement in tensile strength in Al matrix. The enhanced UTS values can be attributed to the presence of the well dispersed MWCNT that reduce the mobility of dislocations present in the matrix, thereby obstructing the plastic deformation. These results in remarkable progress in UTS percentage value of 7.48% for SDS coated MWCNT Al matrix.

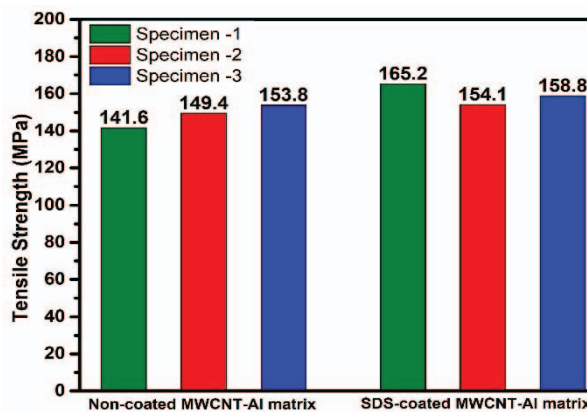


Fig. 9: Tensile strength comparison plot of non-coated and SDS coated MWCNT-Al matrix.

### 3.6 Compressive Strength

The compressive strength was tested by UTM according to the ASTM E9 standards as shown in Fig. 10. The strength reduction in the non-coated MWCNT Al matrix may be due to the presence of agglomeration and clusters.

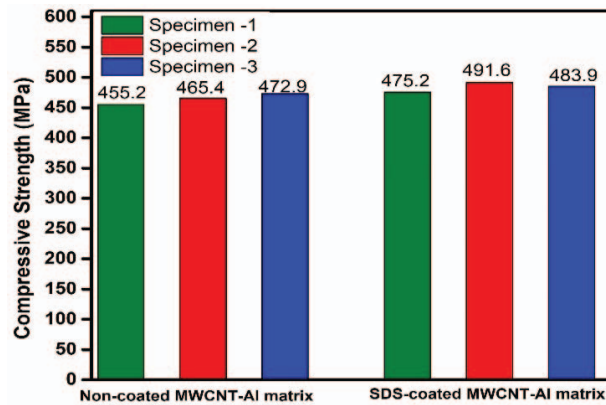


Fig. 10: Compressive strength comparison plot of non-coated and SDS coated MWCNT-Al matrix.

One of the main concerns for the reduced compression strength is the brittle behaviour of agglomerated CNTs so that the maximum strain was determined to be very low. The agglomeration in the non-coated MWCNT-Al matrix hindering the establishment of a dense sample in the course of densification process [15]. Consequently, the absence of clusters in the SDS coated MWCNT-Al matrix leads to 3.87% increase in the compressive strength over the non-coated MWCNT Al matrix.

### 3.7 Wear Analysis

A computational approach called the pin on disc test was used to study the tribological condition of the MWCNT-Al Matrix. Per the ASTM G99 standards of specimens, 8mm in diameter and 30mm in length were taken into consideration. The plot in Fig. 11 displays the wear characteristics of SDS-coated and Non-coated MWCNT-Al matrix. The tests were carried out with a load of 5kgs and the specimen sliding on the disc at a rotation speed of 600rpm. The amount of wear in microns was measured for a duration of 900sec and was plotted as a function of time, as indicated in Fig. 11.

The amount of wear of SDS coated MWCNT-Al matrix is lesser than non-coated matrix by 10.62%. The graph indicates that the coated specimen gives uniform wear but non coated specimen gives abnormal fluctuations in the wear. This happens due to its poor wear resistance. The wear resistance (inverse of specific wear rate) of SDS-coated MWCNT-Al matrix was significantly improved by the homogeneous dispersion of MWCNT in Al matrix.

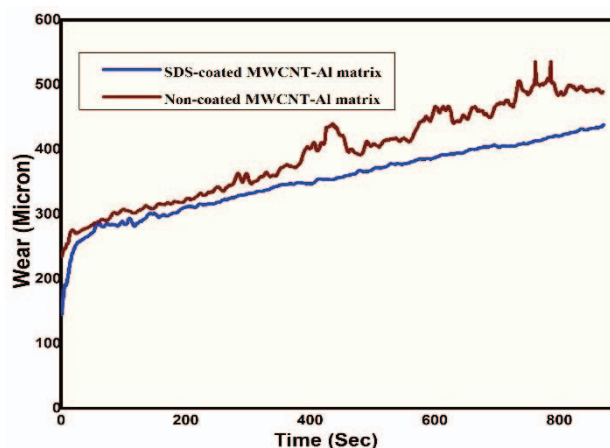


Fig. 11: Wear comparison plot of non-coated and SDS coated MWCNT-Al matrix.

### 3.8 Frictional Force

Frictional force generated between two surfaces is mainly affected by the surface texture and amount of force impelling them together. Hence to evaluate the difference in the frictional force of the developed SDS coated and Non-Coated MWCNT-Al matrix, pin-on-disc test method was considered. The sliding took place under dry frictional conditions with normal load of 5 kg; sliding velocities of 2.2 m/s and for constant sliding distance of 1.98 km. The test results of frictional force were reported as a function of time, indicated in Fig. 12.

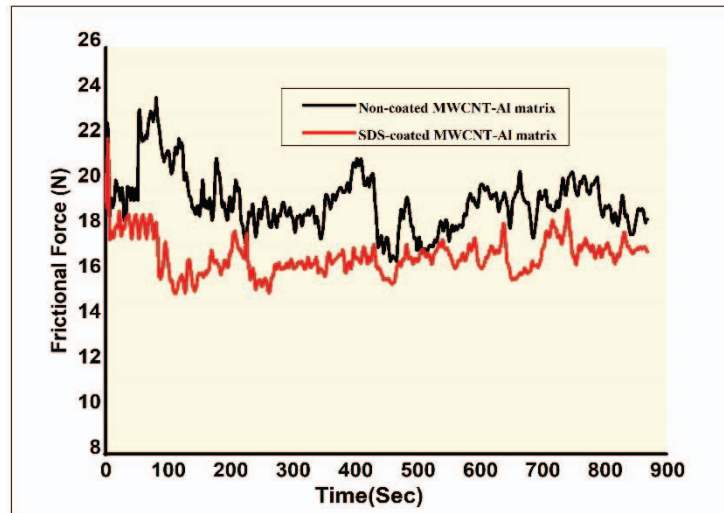


Fig. 12:Frictional force comparison plot of non-coated and SDS coated MWCNT-Al matrix.

As per the graph, the SDS coated MWCNT-Al matrix has better surface texture and offers high wear resistance as compared to that of the non-coated specimen. Thus, the SDS coated MWCNT-Al matrix offers reduced frictional force in comparison with that non-coated matrix and this reduces the amount of wear of the coated material.

## 4. CONCLUSION

The SDS-coated and non-coated MWCNT-Al MMC were fabricated. Tests on the specimens were conducted to study the dispersion of reinforcement in the base metal and further study extended to mechanical properties. The FT-IR study was conducted to ensure SDS coating on CNT. Radiography tests were conducted and observed that there were no traces of voids and blow holes in the SDS coated MWCNT-Al matrix. Fig. 5 exhibits that the infrared absorption percentage is more with the SDS coated MWCNT as compared to the non-coated MWCNT-Al MMCs. SEM tests for microstructure study were conducted. Figure 6b shows that the SDS coated MWCNT-Al MMC found fairly good dispersion of reinforcement as compared to Fig. 6a, which is the non-coated MWCNT. Tensile strength, compression strength, wear rate, resistance to wear tests were conducted to study the mechanical properties. These tests were conducted on each of three specimens for each coated and non-coated MWCNT-Al MMC. It is observed that tensile strength and compression strength is increased to 7.48% and 4.1% respectively with SDS coated MWCNT-Al MMC. Figure 11 shows the wear rate evaluated at 900sec for the SDS coated MWCNT-Al MMC is about 10.62% less as compared to the non-coated MWCNT.

Surface texture test were conducted and found (Fig. 12) that the coated MWCNT-Al MMC gives superior surface texture as compared to the non-coated MWCNT-Al MMC. The augmentation of dispersion and interfacial bonding of the SDS coated MWCNT-Al composite, proves to be more effective in improving the wear resistance along with high tensile strength and compressive strength. It is evident from the study that the SDS coated MWCNT improves the dispersion of reinforcement in the Aluminium thereby improving the mechanical properties.

## ACKNOWLEDGEMENT

We would like to thank the Research Centre, Department of Nano-Technology, Visvesvaraya Technological University, Chickaballapur, India for providing research facilities to carry out the research.

## REFERENCES

- [1] Esawi A., Morsi K (2007). Dispersion of carbon nanotubes (CNTs) in aluminum powder. *Composites Part A. Applied Science and Manufacturing* 38(2): 646-650. DOI: 10.1016/j.compositesa.2006.04.006.
- [2] Thomas S, Umasankar V(2019). Review of Recent Progress in the Development and Properties of Aluminum Metal Matrix Composites Reinforced with Multiwalled Carbon Nanotube by Powder Metallurgy Route, *Materials Performance and Characterization*, 8(3): 371-400. <https://doi.org/10.1520/MPC20180140>.
- [3] Rajesh Jesudoss Hynes N, Sankaranarayanan R, Kathiresan M, Senthamaraikannan P, Khan A, Asiri A M, & Khan I (2019). Synthesis, properties, and characterization of carbon nanotube-reinforced metal matrix composites. *Nanocarbon and Its Composites*, 805–830.
- [4] F. Rikhtegar, S.G. Shabestari, H. Saghafian(2015). The homogenizing of carbon nanotube dispersion in aluminium matrix nanocomposite using flake powder metallurgy and ball milling methods. *Powder Technology*, 280: 26–34. DOI: 10.1016/j.powtec.2015.04.047.
- [5] Hanizam H, Salleh M S, Omar M Z, Sulong A. B(2019).Optimisation of mechanical stir casting parameters for fabrication of carbon nanotubes–aluminium alloy composite through Taguchi method. *Journal of Materials Research and Technology*, 8(2): 2223-2231. DOI: 10.1016/j.jmrt.2019.02.008.
- [6] Awotunde M A, Adegbenjo A O, Ayodele O O, Okoro A M, Shongwe M B, Olubambi P A (2019). Interdependence of carbon nanotubes agglomerations, its structural integrity and the mechanical properties of reinforced nickel aluminide composites. *J. Alloys and Compound*,803:514–526. <https://doi.org/10.1016/j.jallcom.2019.06.297>.
- [7] Li J, Fan T, Xu Y, Wu X(2016). Ionic liquids as modulators of physicochemical properties and nanostructures of sodium dodecyl sulfate in aqueous solutions and potential application in pesticide microemulsions. *Physical Chemistry Chemical Physics*, 18: 29797-29807. <https://doi.org/10.1039/C6CP04722J>.
- [8] Hansen J H, Petersen S V, Andersen K K, Enghild J J, Damhus T, Otzen D(2009). Stable intermediates determine proteins primary unfolding sites in the presence of surfactants. *Biopolymers*, 91(3): 221–231. Doi: 10.1002/bip.21125.
- [9] Matarredona O, Rhoads H, Liu Z, Harwell J H, Balzano L, Resasco D E(2003). Dispersion of Single-Walled Carbon Nanotubes in Aqueous Solutions of the Anionic Surfactant NaDDBS, *The Journal of Physical Chemistry B*, 107:13357-13367. <https://doi.org/10.1021/jp0365099>.

- 
- [10] Zhao L, Pan Y, Liao H, Wang Q(2012). Degassing of aluminum alloys during re-melting. *Materials Letters*, 66: 328-331.  
<https://doi.org/10.1016/j.matlet.2011.09.012>.
- [11] Haghayeghi R, Bahai H, Kapranos P(2012). Effect of ultrasonic argon degassing on dissolved hydrogen in aluminum alloy. *Materials Letters*, 82: 230-232.  
<https://doi.org/10.1016/j.matlet.2012.05.112>.
- [12] Adat R, Kulkarni S, Kulkarni S(2015). Manufacturing of particulate reinforced aluminum metal matrix composites using stir casting process, *International Journal of Current Engineering and Technology*, 5(4):2808-2812.
- [13] Shahrdami L, Sedghi A, Shaeri M H(2019). Microstructure and mechanical properties of Al matrix nanocomposites reinforced by different amounts of CNT and SiCW. *Composites Part B: Engineering*, 175:107081.  
<https://doi.org/10.1016/j.compositesb.2019.107081>.
- [14] Muhammad Mansoor, Muhammad Shahid(2016). Carbon nanotube-reinforced aluminum composite produced by induction melting, *Journal of Applied Research and Technology* 14(4): 215-224.  
DOI: 10.1016/j.jart.2016.05.002.
- [15] Jafari M, Abbasi M H, Enayati M H, Karimzadeh F(2012). Mechanical properties of nanostructured Al<sub>2024</sub>-MWCNT composite prepared by optimized mechanical milling and hot pressing methods. *Advanced Powder Technology.*, 23(2), 205–210.

## EFFECT OF SPINNING PARAMETERS ON PLA/PPC/CURCUMIN MICROFIBER DIAMETER: AN INVESTIGATION VIA RESPONSE SURFACE METHODOLOGY

SHARIFAH IMIHEZRI SYED SHAHARUDDIN<sup>1\*</sup>, AMIRUL AKMAL FAUZAN<sup>1</sup>,  
MOHAMAD FARIS IZZUDIN MOHAMAD JAZI<sup>1</sup>, NUR ATIQA MOHD. AKHIR<sup>1</sup>,  
MAIZATULNISA OTHMAN<sup>1</sup>, NOR KHAIRUSHIMA MUHAMAD KHAIRUSSALEH<sup>1</sup>,  
NORHASHIMAH SHAFFIAR<sup>1</sup> AND ZAIMAH HASAN<sup>2</sup>

<sup>1</sup> Department of Manufacturing and Materials Engineering,

Kulliyah of Engineering International Islamic University Malaysia, Gombak, Malaysia

<sup>2</sup>Mechanical Engineering Department, College of Engineering, Universiti Tenaga Nasional,  
Kajang, Malaysia

\*Corresponding author: [shaimihezri@iium.edu.my](mailto:shaimihezri@iium.edu.my)

(Received: 16<sup>th</sup> January 2020; Accepted: 4<sup>th</sup> March 2020; Published on-line: 4<sup>th</sup> July 2020)

**ABSTRACT:** The initial phase of this study was to investigate the effect of polypropylene carbonate (PPC) additions in polylactic acid (PLA)/curcumin (Cur) blends. It was observed that the presence of curcumin particulates behaved as a reinforcement filler for PPC additions up to 30 wt%. A specific composition was then invested to find the correlation between the fiber diameter and melt-spinning process parameters using central composite design (CCD), a subset of response surface methodology (RSM). Results showed that the spinning temperature had a greater effect than the spinning speed on the diameter of PLA/PPC/curcumin fiber. The response model indicated a good correlation between experimental and predicted values since the ANOVA analysis demonstrated high  $F$ -value of model adequacy at 10.34, non-significant lack of fit, precision adequacy of 9.94 and  $R^2$  value of 0.80. Therefore, this model can be used in a future study to establish the processing parameters for controlled fiber production.

**ABSTRAK:** Fasa awal kajian ini adalah bagi mengkaji kesan penambahan karbonat polipropilin ke dalam campuran asid prolaktik (PLA)/kurkumin (Cur). Didapati kehadiran zarah-zarah kurkumin bertindak sebagai pengisi bantuan pada penambahan PPC sehingga 30 wt%. Komposisi tertentu kemudian dikaji bagi mencari kaitan diameter fiber dan parameter proses putaran-cair menggunakan rekaan komposit utama (CCD), dan subset metodologi gerak-balas permukaan (RSM). Keputusan menunjukkan suhu putaran berpengaruh besar berbanding kelajuan putaran pada diameter fiber PLA/PPC/kurkumin. Model yang bertindak balas ini menunjukkan kaitan yang baik antara eksperimen dan nilai yang dijangka kerana analisis ANOVA menunjukkan nilai- $F$  yang tinggi pada 10.34 kecukupan model, tidak-ketara kurang padanan, kecukupan ketepatan pada 9.94 dan nilai  $R^2$  sebanyak 0.80. Oleh itu, model ini boleh digunakan pada kajian akan datang bagi menghasilkan parameter proses pengeluaran fiber kawalan.

**KEYWORDS:** *poly(lactic acid); curcumin; poly(propylene carbonate); fiber; RSM*

## 1. INTRODUCTION

Poly(lactic acid) (PLA) biopolymer has been extensively studied for biomedical applications due to its high mechanical strength and modulus [1]. PLA can be used with non-toxic and non-carcinogenic effects in the human body [2,3] since its by-products such as lactic acid and its short oligomers, H<sub>2</sub>O and CO<sub>2</sub>, are internally metabolized. However, brittleness has been one of its main drawbacks since it limits the flexibility of the polymer [4]. The physical properties of PLA can be attuned for specific applications by blending (solvent or melt blending techniques) [5] with biodegradable polymers such as polypropylene carbonate (PPC) [6]. PPC is produced through a copolymerization process of CO<sub>2</sub>/propylene oxide (PO) [7]. The resulting copolymer chains are comprised of homopolymer propylene oxide and alternating carbon dioxide and propylene segments [8]. Despite the similar chemical structure between PLA and PPC [9], Ning et al. [10] and Ma et al. [11] studies on PLA/PPC blends suggested that the two polymers are partially miscible when mixed.

Curcumin, a naturally active compound derived from turmeric (*Curcuma longa*), is well known for its antibacterial, antitumor, and antioxidant properties [12-14]. Antimicrobial agent derived from natural sources does not display typical side effects as observed for synthetically produced chemicals [15]. *In-vivo* and *in-vitro* studies revealed that curcumin promotes bioactivities by inducing cell apoptosis, inhibiting cell proliferation, anti-cell adhesion and motility, and imparting anti-microbe properties [16]. PLA membranes loaded with curcumin (1-5 wt %) have been previously reported [17,18]. The incorporation of bioactive particulates into polymer fiber, however, affects the strength of the fiber with increasing particulate content [19]. Thus, one of the greatest challenges in manufacturing these novel therapeutic-eluting fibers lies in attaining considerable drug amounts and therapeutic properties without compensating the suture's mechanical and release kinetic properties.

Response surface methodology is prevalently used to develop a mathematical low-order polynomial expression by approximating physical experimental data [20]. One of the main advantages of RSM is the ability to establish a true relationship between the dependent variable or response (*Y*) and a range of independent variables (*X*). RSM also gives a low standard of error and thus has been considered as a reliable optimization tool [21]. Previously, RSM has been employed in an abundant number of works to study the correlation between process/materials and fiber properties that were produced via the melt spinning process [22,23] as well as the electrospinning process [20,24,25].

This study was spurred by our previous success in the melt-spinning of PLA/curcumin microfiber [26]. However, the addition of curcumin filler into PLA resulted in a more viscous blend and the resultant melt-spun fibers were also found to be brittle and lack the desired flexibility. Thus, this study aims to address the brittle issue of PLA/curcumin by adding plasticizer such as PPC. The resultant polymer blends were characterized via tensile test. A specific composition with reasonable strength and modulus was then selected to investigate the interactive effects of the melt spinning process parameters (spinning speed and spinning temperature) on the fiber diameter using RSM. This work provides a processing route for mass production of biodegradable fibers containing therapeutic agents that can potentially be used for suture, ligament reconstruction, and in self-reinforced composite [27,28].

## 2. METHODOLOGY

### 2.1 Materials Preparation

PLA (IngeoTM Biopolymer 3052D) from Natureworks (USA), PPC (QPAC 40) from Empower Materials (Malaysia) and curcumin (Pahang Pharmacy Sdn. Bhd., Malaysia) were dissolved in chloroform (R&M Chemicals, United Kingdom). Before the solvent blending process, both PLA and PPC pellets were dried at 70°C and 40°C respectively for 2 hours in an oven. The PLA/curcumin/PPC blends at different weight % ratios as shown in Table 1 were dissolved in chloroform at a ratio of 1:10 and stirred for 1 hour at room temperature. The completely dissolved mixture was then poured into a tray. The polymer blend solutions were reduced into thin films once the chloroform has fully evaporated.

Table 1: Composition of PLA/curcumin/PPC used in this study.

Code	Ratio (wt.%)		
	PLA	Curcumin	PPC
PLA_Cur_PPC 10	89	1	10
PLA_Cur_PPC 20	79	1	20
PLA_Cur_PPC 30	69	1	30
PLA_Cur_PPC 40	59	1	40
PLA_Cur_PPC 50	49	1	50

### 2.2 Tensile Test

Thin films were cut according to the ASTM D882 dimension of 50 mm x 10 mm x 0.80 mm with an extra 10 mm at both ends for clamping purposes. The tests were performed using a Shimadzu Universal Tensile Machine (AGS-10K NXD) at a crosshead speed of 20 min/mm and a load cell of 5kN. The average and standard deviation of tensile strength, modulus and percent elongation were calculated from the load-elongation curve based on 5 samples.

### 2.2 Mutivariate Design of Experiment

Before determining the design space, the range of available spinning speed as well as the temperature range for continuous fiber spinning was determined. The in-house built mini fiber drawing tower has the capacity to spin fiber from 250 to 390 rpm. Preliminary experimental works showed that the intended composition can be successfully drawn/spun within a melt viscosity region corresponding to 160 °C – 173 °C.

In this study, central composite design (CCD) which is a subset of RSM was used to develop the regression model. The model represents the response of fiber diameter ( $Y$ ) for two design factors or independent variables represented by  $X_1$ , spinning temperature and  $X_2$ , spinning speed. The total number of runs suggested by CCD was based upon the following equation:

$$N = 2^k + 2k + n_0 \quad (\text{Eq. 1})$$

where  $2^k$  = represents the two-level factorial points,

$k$  = axial points located at “ $\pm\sqrt{k}$ ” from the centre points of experimental domain

$n_0$  = central point replicates.

The  $2k$  (axial points) is used during screening and readability for variance of model prediction and the  $n_0$  (central points) is very crucial to obtain an independent estimate of the

design experimental error [29]. The design factors or independent variables (in this study,  $k=2$  for spinning temperature and spinning speed) were considered at two levels; low (-) and high (+) as shown in Table 2. Therefore, the total number of proposed experiments is 13 based on:  $2^k$  ( $2^2 = 4$ : factorial points) +  $2k$  ( $2 \times 2 = 4$  axial points) + 5 ( $n_0 = 5$  replications). Fig. 1 shows the schematic of the experimental design. The CCD design matrices in coded/uncoded values for the design of experiment are listed in Table 3. The ANOVA analysis and statistical values were determined using Design Expert software (version 6.0.8).

Table 2: CCD coded and uncoded values of the input variables for the experimental design

Variables	Codes levels	Lowest	Low	Center	High	Highest
		$-\sqrt{2}$	-1	0	1	$\sqrt{2}$
$(X_1)$ Spinning temperature ( $^{\circ}\text{C}$ )		157	160	166.5	173	176
$(X_2)$ Spinning speed (rpm)		221	250	320	390	419

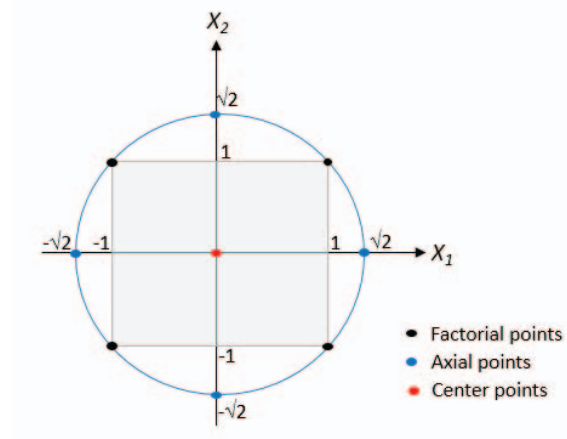


Fig. 1: Schematic diagram of central composite design (CCD) with  $2^2$  factorial design based on  $X_1$ (spinning temperature) and  $X_2$  (spinning speed) variables.

Table 3: CCD design matrices in coded and uncoded values for the design of experiment of melt spinning process.

Run No.	Design factor in coded value		Design factor in uncoded value	
	$X_1$	$X_2$	Spinning temperature ( $^{\circ}\text{C}$ )	Spinning speed (rpm)
1	0	$-\sqrt{2}$	166.5	221
2	1	1	173	390
3	-1	1	160	390
4	-1	-1	160	250
5	$\sqrt{2}$	0	176	320
6	$-\sqrt{2}$	0	157	320
7	0	0	166.5	320
8	0	$\sqrt{2}$	166.5	419
9	0	0	166.5	320
10	0	0	166.5	320
11	0	0	166.5	320
12	0	0	166.5	320
13	1	-1	173	250

### 2.3 Melt-drawn Spinning Setup

The fibers from PLA\_Cur\_PPC 30 were spun via an in-house built melt spinning process as shown in the schematic representation in Fig. 2. In this process, the crushed thin film was melted above the melting temperature for extrusion through a circular shaped orifice at the nozzle and then stretched into monofilament fiber by the speed of the take-up rotating wheel. The fibers were rapidly cooled by the ambient air as they emerged from the nozzle. The melt spinning process used is also known as vertical spinning since no mechanical means such as extruder is used to force the flow through the nozzle. Instead, the polymer moves simply by the force of gravity.

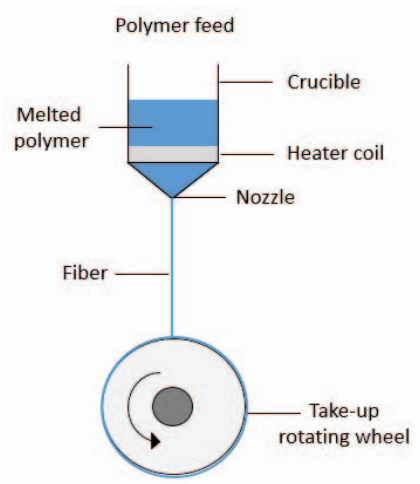


Fig. 2: Schematic representing the melt spinning experimental setup.

### 2.3 Fiber Morphology

The diameter of PLA\_Cur\_PPC 30 fibers was measured via optical microscope (BX41M) (Olympus Microscopes, UK). The diameter was taken as an average of 20 different fibers for each composition. The resulting fiber physical structure was then observed via scanning electron microscope (SEM) (JEOL, JSM-IT 100; Japan) with 200x magnifications at 10 kV. All fibers were prepared by sputter coating with palladium using Polaron SC7620.

## 3. RESULTS AND DISCUSSION

### 3.1 Tensile Test

The amount of filler particulates significantly affects the ease of processing and quality of the fibers obtained [26]. In this study, the amount of curcumin was limited to only 1 wt% since previous studies [26,30] had shown that increasing the curcumin content corresponds with a further decrease in strength. The tensile test was performed to determine the effect of PPC on PLA/curcumin blend.

In this study, it can be seen from Fig. 3 that the strength was maintained as PPC was incorporated up to 30 wt %. However, previous studies have shown that there was an immediate decrease in strength and modulus when PPC was incrementally added into neat PLA [9,31,32]. Thus, it is postulated that the observed strength retention was attributed to the presence of curcumin particulate that had behaved as a reinforcing filler [33,34]. PPC also has an inherently lower tensile strength in comparison to PLA [35]. Thus, further

additions of PPC (>30 wt%) are believed to have weakened the intermolecular strength of the polymer blend which subsequently cancelled the curcumin reinforcement effect [11,31].

A comparison between Fig. 4 and Fig. 5 revealed that the elongation % trend is inversely proportional to Young's modulus trend. It is also observed that at 30 wt% PPC, reversal trend occurred for both modulus and elongation. Other than the contribution of Young's modulus of each constitutive polymer in the blend, other factors may have contributed to the observed modulus and elongation trend such as phase morphology and selective localisation [11]. In most cases, the major constituent in the polymer blend will form the continuous phase whilst the minor constituent will form as scattered spherical droplets [36]. SEM studies on binary PLA/PPC system [37,38] revealed that at 30 wt% PPC addition, the blend resembles typical sea-island morphology in which the PLA phases coalesce together and surround the PPC droplets. At 50 wt% PPC, the existing sea-island morphology is transformed into co-continuous morphology. Consequently, the PPC phase progressed from droplets into elongated and interconnected structures. Particulates or fillers added into the polymeric blend may be dispersed at the phase interphase or in either phase of the multi-component blend. Studies have shown that during mixing, particulates behave in a manner of selective localization whereby the particulates prefer to move and reside in the polymer phase that has sufficiently low viscosity [39,40]. Such selective localization tendency induces better particulate dispersion and has been observed in various systems of filler/matrix composites [42,42].

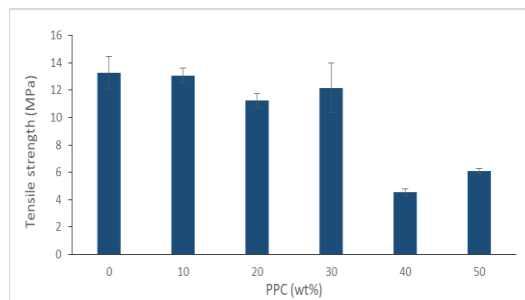


Fig. 3: Tensile strength properties of PLA/curcumin/PPC blends.

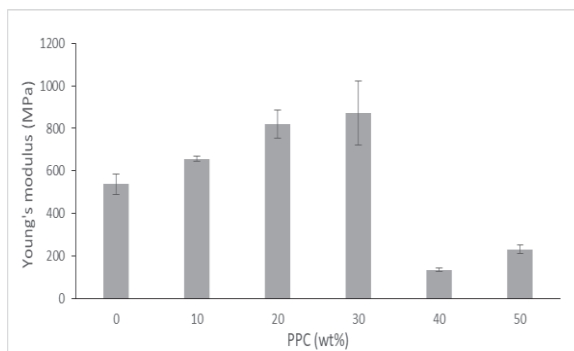


Fig. 4: Young's modulus properties of PLA/curcumin/PPC blends.

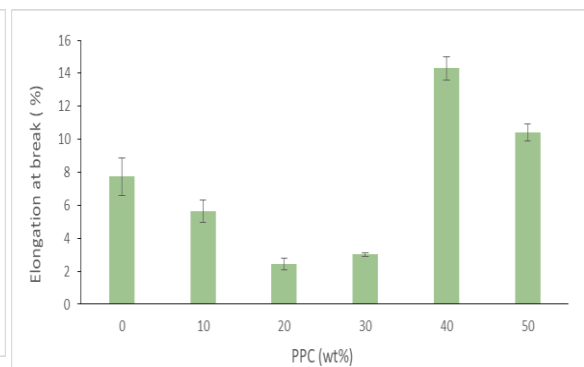


Fig. 5: Elongation at break properties of PLA/curcumin/PPC blends.

Thus, it is proposed that the parallel increase of Young's modulus with the increasing amount of PPC (inversely proportional effect on elongation %) up to 30 wt% PPC, encourages better curcumin dispersion in the PPC phase since it is less viscous than PLA. The presence of these particulates impedes the slippage movement of PPC molecular chains. A study by Ning et al. [10] on PLA/PPC/carbon black (CB) particulate blend also revealed

that greater particle dispersion was achieved in the PPC phase. At 40 wt% PPC, the size of the PPC droplets further increases [38] and the modulus drops drastically by 85% whilst the elongation % increased tremendously by 400%. Further additions of PPC at 50 wt% decrease the elongation % of the blend. A similar drop in elongation % was also observed by Gao et al. [37]. Hence, it is proposed that the localization of curcumin particles in the co-continuous phase has contributed to the decrease in elongation %. In this work, PLA\_Cur\_PPC 30 was selected as a case study for RSM due to its reasonably high strength and modulus properties.

### 3.2 ANOVA Analysis and Response Model

Fabrication of biopolymer fiber via the melt spinning process offers a simple, efficient and economical approach since solvent-free monofilament fiber can be manufactured at a fairly high rate [43,44]. Theoretically, the region of melt viscosity suitable for most polymer processing such as extrusion and melt spinning varies from  $10^2$  Pa·s to  $10^5$  Pa·s [44]. The obtained responses (fiber diameter) for the CCD design matrices are tabulated in Table 4.

Table 4: Design factors in coded and uncoded values and their responses.

Run No.	Design factor in coded value		Design factor in uncoded value		Response
	$X_1$	$X_2$	Spinning temperature (°C)	Spinning speed (rpm)	Average fiber diameter (µm)
1	0	$-\sqrt{2}$	166.5	221	26.2
2	1	1	173	390	28.7
3	-1	1	160	390	14.7
4	-1	-1	160	250	28.5
5	$\sqrt{2}$	0	176	320	36.7
6	$-\sqrt{2}$	0	157	320	30.4
7	0	0	166.5	320	25.6
8	0	$\sqrt{2}$	166.5	419	21.1
9	0	0	166.5	320	23.5
10	0	0	166.5	320	26.3
11	0	0	166.5	320	27.9
12	0	0	166.5	320	28.4
13	1	-1	173	250	39.4

The initial ANOVA analysis for the design factors for PLA\_Cur\_PPC 30 is shown in Table 5. The constructed response model was evaluated for its suitability to represent the experimental data based on the following criteria; model adequacy, lack-of-fit test, precision adequacy, and  $R^2$  value. The  $p$ -value statistically represents the significance measures of each design factor or parameter in explaining the variability for the response model. The parameter is considered to have an adequate or significant effect if its  $p$ -value is lower than 0.05 ( $p < 0.05$  degree of confidence limit).

The  $F$ -value for ‘model adequacy’ of 6.20 implies that the response model is significant and there is only a 1.65% chance that a “model  $F$ -value” this large could occur due to noise. The result also shows that the  $F$ -values for both terms (spinning temperature  $X_1$  and spinning speed  $X_2$ ) was significantly effective on the response trend with probability values of nearly 99%. The quadratic terms ( $X_1^2$ ) were also significantly effective with a probability of more than 96%. However, the quadratic term,  $X_2^2$  and cross-product term  $X_1X_2$  were greater than the significance level of  $p = 0.05$  and thus have no significant impact on

the response trend. The  $p$ -value for the lack-of-fit test was not significant at 0.06 ( $p > 0.05$ ), hence it was deduced that the model was able to satisfactorily fit the data. The signal-to-noise ratio or “adequacy precision” for the response model indicates an adequate signal at 9.032 since a value greater than 4 is highly desirable.

Table 5: Initial analysis of variance based on two design factors (spinning temperature, spinning speed) for the melt spinning process of PLA\_Cur\_PPC 30

Source	F value	P value
Temperature: $X_1$	11.66	0.0112
Speed: $X_2$	10.25	0.0150
$X_1^2$	6.60	0.0370
$X_2^2$	1.34	0.2844
$X_1X_2$	0.20	0.6713
Model adequacy	6.20	0.0165
Lack of fit	6.15	0.0559
Adequate precision (ratio>4)	= 9.032	
$R^2$	= 0.8157	

The initial fitted second-order equation for the response and design factors is as follows:

$$Y = 26.34 + 4.23X_1 - 3.96X_2 + 3.41X_1^2 - 1.54X_2^2 + 0.78X_1X_2 \quad (\text{Eq. 2})$$

where  $Y$  is the average fiber diameter, and  $X_1$  and  $X_2$  respectively represent the coded terms for spinning temperature and spinning speed. Both negative and positive signs respectively represent antagonistic effect and synergistic effect. The insignificant terms of  $X_2^2$  and cross-product term  $X_1X_2$ , were removed and ANOVA analysis was performed for the second time, yielding the results shown in Table 6.

Table 6: Reduced analysis of variance based on two design factors (spinning temperature, spinning speed) for the melt spinning process of PLA\_Cur\_PPC 30.

Source	F value	P value
Temperature: $X_1$	12.28	0.0067
Speed: $X_2$	10.81	0.0094
$X_1^2$	7.94	0.0201
Model adequacy	10.34	0.0028
Lack of fit	4.68	0.0801
Adequate precision (ratio>4)	= 9.941	
$R^2$	= 0.7752	

The reduced fitted second-order equation for the response and design factors is as follows:

$$Y' = 25.27 + 4.23X_1 - 3.96X_2 + 3.61X_1^2 \quad (\text{Eq. 3})$$

The  $F$ -value for ‘model adequacy’ in  $Y'$  increases to 10.34, with a 0.28% chance that the  $F$ -value obtained may occur due to noise. The ‘lack-of-fit’ value was not significant at 0.08 ( $p > 0.05$ ) and the adequacy precision is 9.941. The increase of  $p$ -values for the reduced model,  $Y'$  for ‘lack-of-fit’ and the increase of adequate precision respectively means that the model is now better fitted and has a higher signal-to-noise ratio. The correlation coefficient,  $R^2$  is a criterion that is obtained from the fitted linear plot for a set of predicted values versus observed values and is used to evaluate the ability of the model to predict the result. The value of  $R^2$  for the final response model in this study statistically indicates that the model

can explain reasonably well up to approximately 80% of the variation in the fiber diameter due to the two design factors.

The  $F$ -value associated with the  $X_1$  term (spinning temperature) is higher than the  $X_2$  term (spinning speed) and thus comparatively has a more significant effect on the response model (fiber diameter). Kong et al. [45] had also observed the pronounced effect of temperature on fiber diameter since it directly influences the physiochemical properties (melt viscosity, surface tension) of the polymer blend. On its own, PPC lacks the viscous flow necessary to produce continuous fiber due to its terminal chain of hydroxyl groups [46]. Thus, the addition of PPC is expected to lower the melt viscosity of the PLA/curcumin blend in this study [10]. Hypothetically, it was anticipated that the fabrication of nano-sized fibers of this composition may be slightly difficult since polymer melts are more viscous [45] in the order of one magnitude in comparison to the viscosity of polymer solutions [47]. Fig. 6 depicts an approximately linear probability plot and thus supports the condition that the error terms were distributed normally. The plot of predicted results against observed results is shown in Fig. 7. It can be seen from the graph that there is a satisfactory correlation between the diameter of the fiber with spinning temperature and spinning speed.

Fig. 8 visualizes the contoured plot of the predicted mean fiber diameter due to the effect of spinning temperature and spinning speed. The propitious condition for fiber fabrication via melt spinning process dictates that both the gravitational force and elongation force provided by the spinning speed must be able to overcome the combined forces exerted by viscosity and surface tension [48]. It can be seen that at any given spinning temperature, the fiber diameter decreases with increasing spinning speed due to the increasing elongation stress. It was also observed that at any constant spinning speed, the diameter of the fiber progressively increases with increasing temperature. In general, the increase in spinning temperature lowers the surface tension. As a result, the cohesive forces between the molecules to resist the increasingly fluidic polymer flow from the gravitational force and elongation force decrease. Eventually, more volume of the polymer is drawn which leads to an increase in the fiber diameter. A similar correlation effect between spinning temperature and fiber diameter was also observed by Ko et al. [48]. The contour plot suggests that the optimum range of temperature and speed to draw thin microfiber occur within the spinning temperature region of 160-163 °C and 285 rpm- 340 rpm respectively.

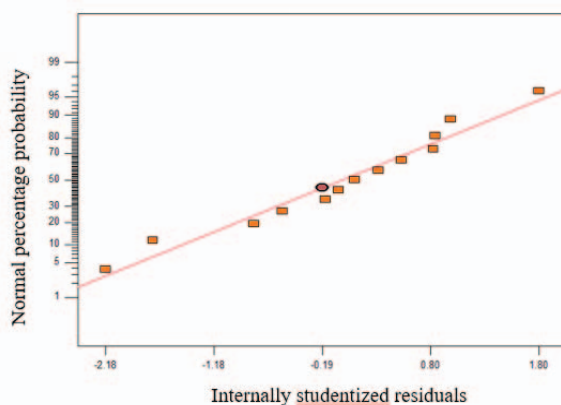


Fig. 6: Studentized residuals and normal percentage probability plot for the melt spinning of PLA\_Cur\_PPC 30 fibers.

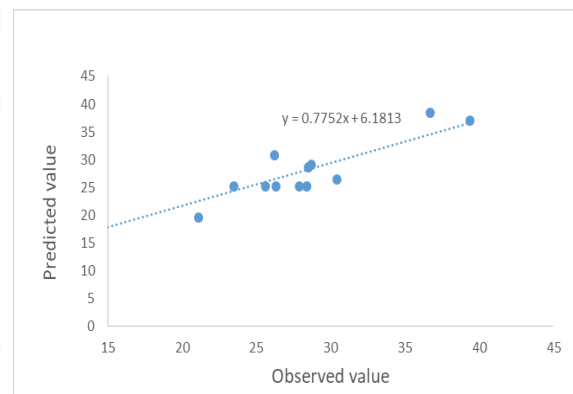


Fig. 7: Plot of observed values versus the predicted values obtained from the reduced fitted regression line obtained for

the melt spinning of PLA\_Cur\_PPC 30 fibers.

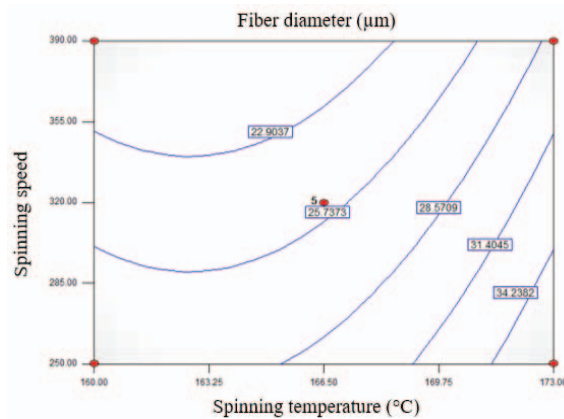


Fig. 8: Contour plot in the design space for Y' (fiber diameter) with respect to X<sub>1</sub> (spinning temperature) and X<sub>2</sub> (spinning speed) for PLA\_Cur\_PPC 30 fiber.

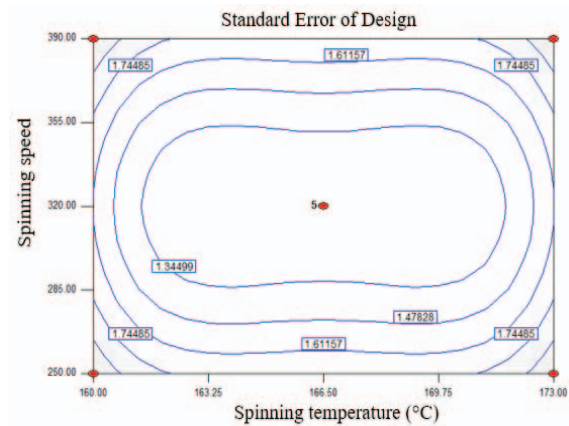


Fig. 9: Plot of standard error of design in the design space for Y' (fiber diameter) with respect to X<sub>1</sub> (spinning temperature) and X<sub>2</sub> (spinning speed) for PLA\_Cur\_PPC 30 fiber.

Fig. 9 represents the standard error estimation based on several numbers of observations made at the centre point (0,0) (Aslan, 2007) of the two-factor CCD approach. If the number of observations/replicates at the centre point is too high, then the farther points from the centre will yield a rapid increase in standard error estimations (Clark & Williges, 1973). On the contrary, if the number of replicates is too low at the centre point, this would yield a reversing effect in which the error estimation would be greater at the centre compared to other data points. Having a constant error contour throughout the design space is highly desirable as this would justify that the error estimate calculated at the centre point is a good representative of the error estimate throughout the design space. It can be observed from Fig. 9 that the error estimation is not the same throughout the experimental domain. The standard error is reasonably uniform over a large design space near the centre and the error contours slowly increase as the data points reach the design space boundaries which suggest that the response model may not deliver accurate predictions for diameter governed by extreme values of the design space.

### 3.3 Fiber Morphology

The fiber diameter measured using optical microscope revealed that they averaged between 15 to 40 microns (see Fig. 10). Fig. 11 shows the fiber bundle from each test run observed via SEM. It was also noted that there was irregular formation of bead-like structure on the lateral surface of the fiber as shown in Fig. 12. It is postulated that such surface condition occurred due to the partial dispersion of curcumin particles in the PLA/PPC blend. A similar textured or bead-like surface effect was also obtained for melt-spun fibers from the polypropylene/soy particle blend [51] and the polypropylene/talc blend [52]. Contrary to the perception that such textured surface is undesirable, this bead-like surface is actually a unique feature because it imitates the tactile feel of the irregular cross-section and highly crenulated structure of natural fibers such as those found in cotton [51].

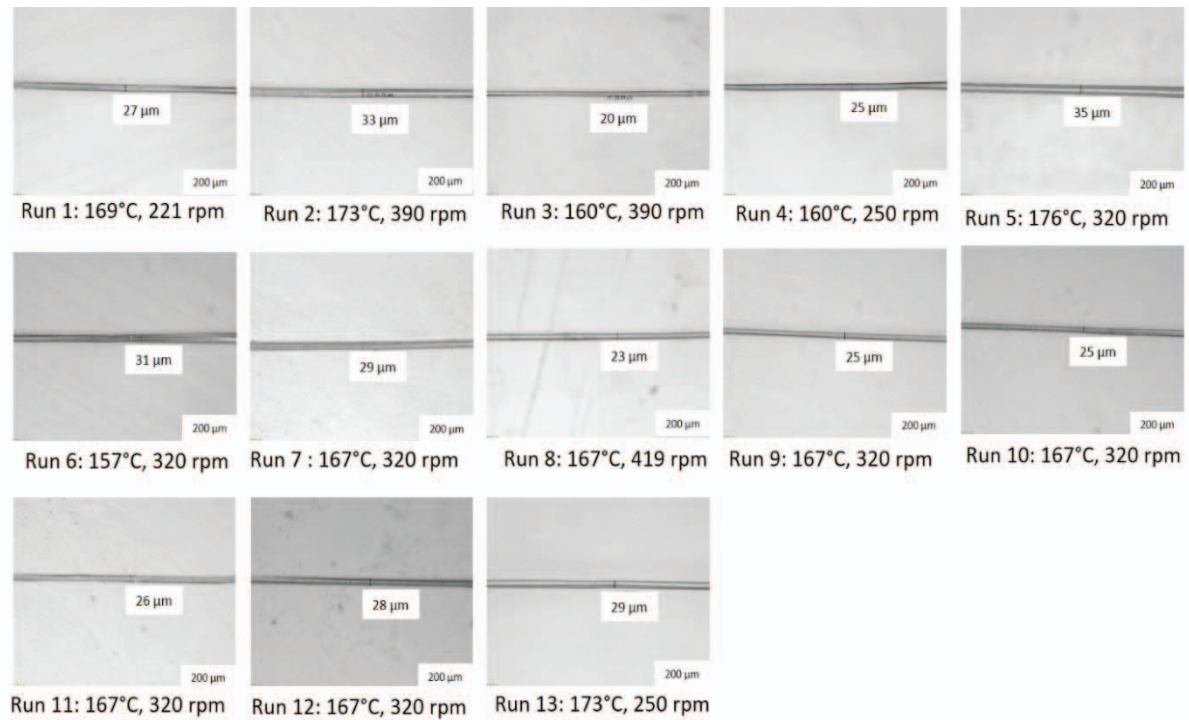


Fig. 10: SEM images (200x) of PLA\_Cur\_PPC 30 fiber spun at each CCD design matrix.

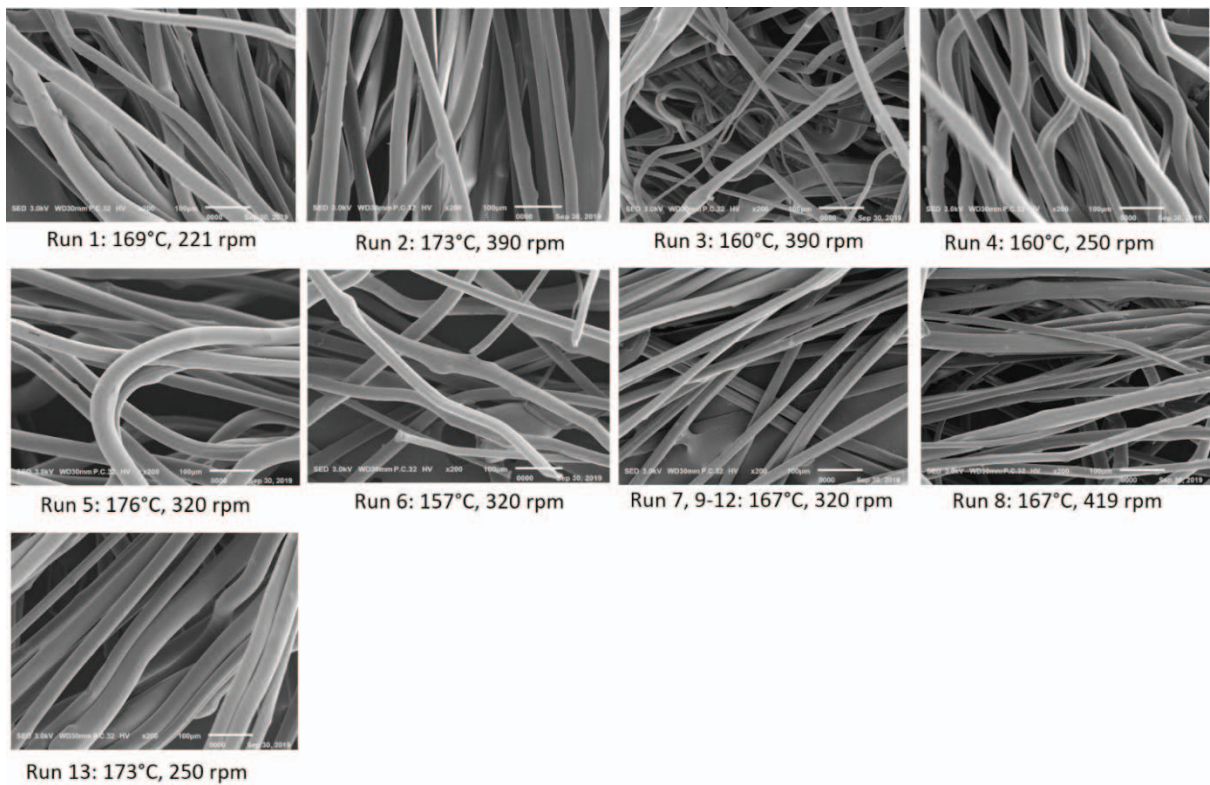


Fig. 11: Images of randomly taken fiber diameter measured via optical microscope for PLA\_Cur\_PPC 30 fiber.

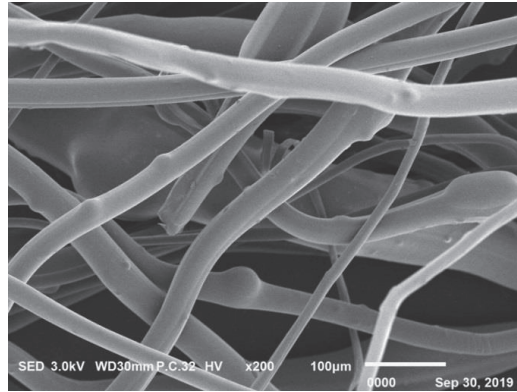


Fig. 12: SEM image showing the irregular formation of bead-like structure on the lateral surface of the fiber.

#### 4. CONCLUSION

This study revealed that the substantial inclusion of PPC up to 30 wt % into PLA/curcumin blends did not result in appreciable change in strength due to the reinforcement effect of curcumin. The modulus values increased due to favourable dispersion of curcumin in the less viscous PPC, which aids in constraining the polymer chain movement. However, further additions of the more flexible PPC at 40 wt% were accompanied by an increasing toughness and vice versa effect in strength and modulus. PLA\_Cur\_PPC 30 was then identified for further study via RSM. It was concluded from the response model that spinning temperature had a more dominant effect on the fiber diameter in comparison to spinning speed due to its direct influence on the surface tension and melt viscosity. The response model also indicated a good correlation between experimental and predicted values based on all the criteria defined in this study.

#### ACKNOWLEDGEMENTS

This work was fully supported by International Islamic University Malaysia, IIUM (RIGS17-052-0627). The authors would like to express their deepest gratitude to facilities and technical assistance provided by International Institute for Halal Research and Training (INHART), IIUM.

#### REFERENCES

- [1] Lyu S, Untereker D. (2009) Degradability of polymers for implantable biomedical devices. *Int. J. Mol. Sci.*, 9:4033-4065.
- [2] Xiaon L, Wang B, Yang G, Gauthier M. (2011) Poly(lactic acid)-based biomaterials: Synthesis, modification and applications. *Biomedical Science, Engineering and Technology, Intech, Croatia*.
- [3] Casalini T, Rossi F, Castrovinci A, Perale G. (2019) A perspective on polylactic acid-based polymers use for nanoparticles synthesis and application. *Front. Bioeng. Biotechnol.*, 7:1-16.
- [4] Liu L, Wei H, Wang Z, Li Q, Tian N. (2018) Simultaneous enhancement of strength and toughness of PLA induced by miscibility variation with PVA. *Polymers*, 10(10):1178.
- [5] Saini P, Arora M, Kumar MR. (2016) Poly(lactic acid) blends in biomedical applications. *Adv. Drug Deliv.*, 107: 47-59.

- [6] Qin SX, Yua CX, Chen XY, Zhoua HP, Zhao LF (2018) Fully biodegradable poly(lactic acid)/poly(propylene carbonate) shape memory materials with low recovery temperature based on in situ compatibilization by dicumyl peroxide. *Chinese J Ploym Sci.*, 36:783-790.
- [7] Gao L, Huang M, Wu Q, Wan X, Chen X, Wei X, Yang W, Deng R, Wang L, Feng J. (2019) Enhanced poly(propylene carbonate) with thermoplastic networks: A cross-linking role of maleic anhydride oligomer in CO<sub>2</sub>/PO copolymerization. *Polymers.*, 11:1467-1479.
- [8] Wang S, Huang Y, Liao B, Lin G, Cong G, Chen L. (1997) Structure and properties of poly(propylene carbonate). *Int J Polym Ch.* 3(2):131-143.
- [9] Yao M, Deng H, Ma F, Wang K, Zhang Q, Chen F, Fu Q. (2011) Modification of poly(lactic acid)/poly(propylene carbonate) blends through melt compounding with maleic anhydride. *Polym Lett*, 5(11):937-949.
- [10] Ning W, Xingxiang Z, Jiugao Y, Jianming F. (2008) Partially miscible poly(lactic acid)blend-poly(propylene carbonate) filled with carbon black as conductive polymer composite. *Polym Int.*, 57:1027–1035.
- [11] Ma X, Yu J, Wang N. (2006) Compatibility characterization of poly(lactic acid)/poly(propylene carbonate) blends. *J Polym Sci Phys.*, 44(1):94-101.
- [12] Aggarwal B, Sung B. (2009) Pharmacological basis for the role of curcumin in chronic diseases: An age-old spice with modern targets. *Trends Pharmacol Sci.*, 30(2):85-94
- [13] Prasad S, Tyagi AK, Aggarwal BB. (2014) Recent developments in delivery, bioavailability, absorption and metabolism of curcumin: the golden pigment from golden spice. *Cancer Res Treat.*, 46(1):2-18.
- [14] Ramalingam N, Natarajan TS, Rajiv S. (2015) Preparation and characterization of electrospun curcumin loaded poly(2-hydroxyethyl methacrylate) nanofiber--a biomaterial for multidrug resistant organisms. *J. Biomed. Mater. Res. Part A*, 103(1):16-24.
- [15] Morais DS, Guedes RM and Lopes MA. (2016) Antimicrobial approaches for textiles: From research to market. *Materials*, 9(6):498.
- [16] Xia F, Chun Z, Dong-bo L, Jun Y, Hua-ping L. (2013) The clinical applications of curcumin: Current state and the future. *Curr. Pharm. Des.*, 19(11):2011-2031.
- [17] Yan C, Jie L, Yuqin W, Yanna F, Hongbo W, Weidong G. (2012) Preparation and blood compatibility of electrospun PLA/Curcumin composite membranes. *Fiber Polym.*, 13(10):1254-1258.
- [18] Chen Y, Lin J, Fei Y, Wang H, Gao W (2010) Preparation and characterization of electrospinning PLA/Curcumin composite membranes. *Fiber Polym.*, 11(8):1128-1131.
- [19] Weldon CB, Tsui JH, Shankarappa SA, Nguyen VT, Ma M, Anderson DG, Kohane DS. (2012) Electrospun drug-eluting sutures for local anesthesia. *J Control Release*, 161:903-909.
- [20] Yördem OS, Papila M, Mencelöglu Y. (2008) Effects of electrospinning parameters on polyacrylonitrile nanofiber diameter: An investigation by response surface methodology. *Mater Design*, 29:34-44.
- [21] Mohamed OA, Masood SH, Bhowmik JL. (2015) Optimization of fused deposition modeling process parameters: a review of current research and future prospects. *Adv Manuf.*, 3(1):42-53.
- [22] Ghoreishian SM, Fereydooni A, Nasser S, Asadolahi T, Beigpour N, Ghoreishian M. (2017) Optimization of melt-spinning parameters of poly(ethylene terephthalate) partially oriented multi-filament yarn in an industrial scale: Central composite design approach. *Fiber Polym.*, 18:1280-1287.
- [23] Garnier L, Duquesne S, Casetta M, Lewandowski M, Bourbigot S (2010) Melt spinning of silane–water cross-linked polyethylene–octene through a reactive extrusion process. *React Funct Polym.*, 70(10):775-783.

- [24] Shu-Ying G, Jie R. (2005) Process optimization and empirical modeling for electrospun poly(D,L-lactide) fibers using response surface methodology. *Macromol Mater Eng.*, 290 (11):1097-1105.
- [25] Dhura B, Saraswathy N, Maheswaran R, Sethupathi P, Vanitha P, Vigneshwaran S, Rameshbabu V. (2013) Electrospinning of curcumin loaded chitosan/poly (lactic acid) nanofilm and evaluation of its medicinal characteristics. *Front Mater Sci.*, 7(4):350–361.
- [26] Sharifah ISS, Qairol AAB, Noor Azlina H, Nor Khairusshima MK (2017) Thermal, structural and mechanical properties of melt drawn curcumin loaded poly(lactic acid) fibers. *Procedia Eng.*, 184:544-551.
- [27] Yuan X, Mak AF, Kwok KW, Yung BK, Yao K. (2001) Characterization of poly(L-lactic acid) fibers produced by melt spinning. *J App Polym Sci.*, 81:251-260.
- [28] Pawar RP, Tekale SU, Shisodia SU, Totre JT, Domb AJ (2014) Biomedical applications of poly(lactic acid). *Recent Pat Regen Med.*, 4:40-51.
- [29] Behera SK, Meena H, Chakraborty S, Meikap BC. (2018) Application of response surface methodology (RSM) for optimization of leaching parameters for ash reduction from low-grade coal. *Int. J. Min. Sci. Technol.*, 28 (4):621-629.
- [30] Shah SAA, Imran M, Lian Q, Shehzad FK, Athir N, Zhang J, Cheng J. (2018) Curcumin incorporated polyurethane urea elastomers with tunable thermomechanical properties. *React Funct Polym.*, 128:97-103.
- [31] Yu C, Zhao R, Wang H. (2018) Mechanical property of PLA/PPC blends. *Int J Trend Res Dev.*, 5(2):206-208.
- [32] Liu H, Zhang J. (2011) Research progress in toughening modification of poly(lactic acid). *J Polym Sci Pol Phys.*, 49:1051-1083.
- [33] Liu Y, Cai Y, Jiang X, Wu J, Le X. (2015) Molecular interactions, characterization and antimicrobial activity of curcumin-chitosan. *Food Hydrocoll.*, 52:564-572.
- [34] Kim DK, Kim JI, Sim BR, Khang G. (2017) Bioengineered porous composite curcumin/silk scaffolds for cartilage regeneration. *Mater Sci Eng C.*, 78:571-578.
- [35] Muthuraj R, Mekonnen T. (2018) Recent progress in carbon dioxide (CO<sub>2</sub>) as feedstock for sustainable materials development: Co-polymers and polymer blends. *Polymer*, 145:348-373.
- [36] Deng Y, Yu C, Wongwiwattana P, Thomas NL. (2018) Optimising ductility of poly(lactic acid)/poly(butylene adipate-co-terephthalate) blends through co-continuous phase morphology. *J Polym Environ.*, 26:3802-3816.
- [37] Gao J, Bai H, Zhang Q, Gao Y, Chen L, Fu Q. (2012) Effect of homopolymer poly(vinyl acetate) on compatibility and mechanical properties of poly(propylene carbonate)/poly(lactic acid) blends. *Polym Lett.*, 11:860–870.
- [38] Haneef INHM, Shaffiar NM, Buys YF, Hamid M, Shaharuddin SIS. (2018) Morphologies and mechanical properties of polylactic acid / polypropylene carbonate (PLA/PPC) blends by solvent casting method. In *Proceedings of the International Conference Biotechnology Engineering : September 19-20, Kuala Lumpur.*
- [39] Mofokeng J, Luyt A. (2015) Morphology and thermal degradation studies of melt-mixed poly(lactic acid) (PLA)/poly( $\epsilon$ -caprolactone) (PCL) biodegradable polymer blend nanocomposites with TiO<sub>2</sub> as filler. *Polym Test*, 45:93-100.
- [40] Nocke A, Wolf M. (2012) *Nanoparticle-based Resistors and Conductors in Bio and Nano Packaging Techniques for Electron Devices: Advances in Electronic Device Packaging.* Springer-Verlag, Berlin.
- [41] Kim SY, Noh YJ, Yu J. (2015) Thermal conductivity of graphene nanoplatelets filled composites fabricated by solvent-free processing for the excellent filler dispersion and a theoretical approach for the composites containing the geometrized fillers. *Compos Part A Appl Sci Manuf.*, 69:219-225.

- 
- [42] Wu D, Zhang Y, Zhang M, Yu W. (2009) Selective localization of multiwalled carbon nanotubes in poly( $\epsilon$ -caprolactone)/polylactide blend. *Biomacromolecules*, 10:417-424.
- [43] Asmatulu R, Khan WS. (2019) *Synthesis and applications of electrospun nanofibers*. Elsevier, Amsterdam.
- [44] Vlachopoulos J, Strutt D. (2003) The role of rheology in polymer extrusion. In *Proceedings of the Extrusion Minitex and Conference: From Basics to Recent Developments: 26<sup>th</sup> October 2004, Du'sseldorf*; pp 107–132.
- [45] Kong C, Jo K, Jo HKNK. (2009) Effects of the spin line temperature profile and melt index of poly(propylene) on melt-electrospinning. *Polym Eng Sci.*, 49(2):391-396.
- [46] M. Niaounakis (2015) *Biopolymers: Applications and Trends*, Elsevier, Oxford.
- [47] Nayak R, Padhye R, Kyratzis IL, Truong YB, Arnold L. (2013) Effect of viscosity and electrical conductivity on the morphology and fiber diameter in melt electrospinning of polypropylene. *Text Res.*, 83(6):606-617.
- [48] Ko J, Jun S, Lee JK, Lee PC, Jun MB. (2015) Effects of molecular weight and temperature on fiber diameter of poly( $\epsilon$ -caprolactone) melt electrospun fiber. *J. Korean Soc Manuf Technol Eng.*, 24(2):160-165.
- [49] Aslan N. Application of response surface methodology and central composite rotatable design for modeling the influence of some operating variables of a multi-gravity separator for coal cleaning. *Fuel*, 86(5-6):769-776.
- [50] Clark C, Williges RC. (1973) Response surface methodology central-composite design modifications for human performance research. *Human Factor*, 15(4):295-310.
- [51] Guzdemir O, Ogale AA. (2019) Influence of spinning temperature and filler content on the properties of melt-spun soy flour/polypropylene fibers. *Fibers*, 7(10):83-101.
- [52] Tascan M, Nohut S. (2016) Melt-spun talc-filled polypropylene fibers and yarns with higher thermal shock resistance. *Text Res J.*, 87(1):31-45.

# DEVELOPMENT OF LOW-COST ADDITIVE MANUFACTURING SYSTEM THROUGH SELECTIVE INHIBITION SINTERING (SIS) PROCESS AND EVALUATION OF MECHANICAL CHARACTERISTICS OF FABRICATED PARTS

MESFIN SISAY MENGESHA\*, BALASUBRAMANIAN ESAKKI, ARUNKUMAR PONNAMBALAM, SILAMBARASAN MATHIYAZHAGAN AND RAJAMANI DEVARAJ

*Centre for Autonomous System Research,  
Vel Tech Rangarajan Dr. Sagunthala R&D Institute of Science and Technology,  
Chennai - 600062, India*

*\*Corresponding author: mesfins245@gmail.com*

*(Received: 4<sup>th</sup> February 2020; Accepted: 19<sup>th</sup> May 2020; Published on-line: 4<sup>th</sup> July 2020)*

---

**ABSTRACT:** Additive manufacturing (AM) is widely being used in today's contemporary industry; however, products fabricated by the existing AM techniques are costly due to the high machine cost and low production rate. Therefore, the focus of this work is to design and fabricate a cost-effective and novel powder based selective inhibition sintering (SIS) system. Various subsystems of the machine such as the infrared heater assembly, inhibition deposition mechanism, build and feed tank assemblies, powder deposition, and the compaction system have been indigenously designed and fabricated. An electronic control system is also established through integrating sensors, linear and rotary actuators, belt and pulley mechanism, and temperature feedback control unit. The customized SIS system is developed by integrating the assembly of all the subsystems, and the electronic modules with an open-source platform to generate the necessary motion characteristics. Besides, an open source RepRap user interface firmware has been used to control the machine. Thermo-structural finite element analysis has been used to study the sintering behaviour of powder material. Inhibitor material selection and preparation have been carried out by performing an experimental investigation on the inhibition effects of various materials. The machine has been tested through fabricating parts from HDPE polymer powder. Finally, the performance of the produced parts has been evaluated by conducting an experimental investigation. The results of the investigation indicated that the fabricated parts have attained sufficient mechanical strength and, hence, the developed SIS system can be utilized to manufacture functional parts.

**ABSTRAK:** Industri pembuatan bahan tambahan (AM) banyak digunakan dalam industri kontemporer semasa; walau bagaimanapun, produk yang terhasil daripada teknik sedia ada AM adalah mahal disebabkan harga mesin yang mahal dan kadar penghasilan yang rendah. Oleh itu, tujuan kajian ini adalah bagi mereka cipta serbuk baharu dengan harga berpatutan berdasarkan sistem pensinteran rencatan pilihan (SIS). Pelbagai mesin subsistem seperti pemasangan pemanas inframerah, mekanisme pemendapan rencatan, binaan dan pemasangan tangki suapan, deposisi serbuk, dan sistem pemadatan telah direka cipta secara alami dan dipasang siap. Sistem kawalan elektronik juga diadakan melalui integrasi sensor, lurus dan penggerak putaran, jaluran dan mekanisme takal dan suhu unit kawalan suap balik. Sistem SIS yang dibuat mengikut pesanan ini dihasilkan dengan mengintegrasikan pemasangan kesemua subsistem, dan modul elektronik melalui platform sumber terbuka bagi menghasilkan ciri-ciri pergerakan bersesuaian. Selain itu, sumber terbuka RepRap perisian tegar antara muka telah digunakan bagi mengawal mesin.

Analisis unsur terhadapa struktur-terma digunakan bagi mempelajari perihal pensinteran bahan serbuk. Pilihan bahan perencat dan persediaan telah dijalankan dengan menjalankan siasatan eksperimen pada kesan perencat pelbagai bahan. Mesin diuji melalui pemasangan bahagian daripada HDPE serbuk polimer. Akhirnya, bahagian yang terhasil diuji melalui ujian eksperimen. Hasil kajian menunjukkan pemasangan bahagian telah mencapai kekuatan mekanikal mencukupi, dengan itu sistem SIS yang dibina boleh digunakan bagi mengilang bahagian berkaitan.

---

**KEYWORDS:** *additive manufacturing; selective inhibition sintering; IR heater; tensile strength; flexural strength*

## 1. INTRODUCTION

Additive manufacturing (AM) is a process that fabricates functional parts directly from three-dimensional (3D) computer-aided design (CAD) data through adhesion of materials layer-upon-layer as opposed to the subtractive methodology [1,2]. Because AM can manufacture any complex geometry in a short span of time, and production volume does not affect the cost of the fabricated part as it would in the case of the subtractive manufacturing method [3], it is widely being considered in today's contemporary industry. Moreover, unlike a traditional fabrication technique, the AM process does not require tooling such as jigs, fixtures, and cutters as well as coolants to operate [4]. Kurth et al. [5] classified the AM process based on the state of the raw materials used as solid, powder, and liquid based processes. Amongst these classifications, the Selective Inhibition Sintering (SIS) process, first invented by Khoshnevis et al. [6], at the University of Southern California, is a powder-based process that operates based on the principle of inhibiting a selected region from sintering to make a part [6-9]. SIS is a contemporary approach to Selective Laser Sintering (SLS) [10]. Unlike the SLS process, the SIS process uses a low cost infrared heat source instead of a high power laser. Hence, it is an economical powder based additive fabrication method that fabricates parts on a layer-upon-layer basis. Moreover, adaptability to various materials such as polymers, ceramics, and metals is another key advantage of the SLS and SIS processes. Unlike other AM manufacturing technologies, SLS and SIS do not require support material as the unsintered powder acts as support material.

The principal idea in the SIS system is to inhibit selected regions of powder layer from fusing using precise delivery of inhibitor material. The high melting point inhibitor material is deposited on the selected region of the powder bed to define the part profile and a ceramic heater is used to supply heat energy across the predetermined surface area of a layer. Due to the large difference between melting points of inhibitor and polymer powder, the region printed with inhibitor material will absorb heat energy and therefore be inhibited from sintering while the remaining area is sintered. Finally, the inhibitor and un-sintered powder can be washed away from the part after the building of the part is complete. As mentioned above, the major difference between the SLS and SIS processes are the heat sources and the sintering mechanisms. In addition, the SIS process has many advantages over the SLS processes. As a result of eliminating the high power heat source (the SIS system does not use high power lasers and cooling circuitry) the carbon footprint associated with SIS is much less compared to other laser enabled AM processes. Hence, compared to the existing 3D printing techniques, SIS will have a significantly less detrimental effect on the environment. It has a higher printing speed due to area sintering instead of point sintering as used in the SLS process. Moreover, similar to the SLS process, its adaptability to various materials such as polymers, ceramics, and metals is an important feature of the SIS process. Therefore, this fabrication technique can be implemented for processing a wide range of indigenously

available polymer materials such as polypropylene, HDPE, LDPE, polycarbonates, and polystyrene [6,9,11].

Since the invention of the first SIS system, improvements were done to the existing system in terms of adapting to metallic materials. Khoshnevis et al. [9] developed an Alpha selective inhibition sintering machine and characterized the process parameters of the machine by fabricating bronze parts and studying their quality features. In addition, Petros et al. [12] developed a  $\beta$ -SIS machine that fabricates metallic products. Torabi et al. [13] introduced an SIS metal machine that uses a commercial piezoelectric inkjet printer-head to deliver the inhibitor material. A bronze part was produced with the machine and the mechanical property of the fabricated part was investigated.

Some of the drawbacks of the existing SIS systems are: compaction related problems during the spreading of the powder layer, material wastage, and the presence of significantly large numbers of process variables that influence the quality characteristics of the fabricated parts [14]. Asiabanpour et al. [15] identified more than 30 factors that influence the SIS process. The presence of a large number of process parameters has complicated the optimization problem of identifying the best combinations of parameters and their settings. As a result, SIS process characterization has become a tedious task. Thus, improving the quality of the SIS fabricated part has become a cumbersome task and consequently, quality characteristics such as the mechanical properties, dimensional tolerance, and surface roughness of the SIS fabricated parts has been inferior [13]. Several research works were conducted to enhance the quality of the SIS fabricated part. Balasubramanian et al. [16] have optimized the settings of the few significant SIS process factors to improve the dry sliding wear behaviour of high-density polyethylene (HDPE). Baligheid et al. [17] studied and optimized SIS factors' settings that affect the dimensional accuracy of products. Yoozbashizadeh et al. [18] explored the effect of the inhibitor materials and the sintering phenomenon on the mechanical strength of SIS fabricated metallic parts. Rajamani et al. [19] investigated the influence of the SIS process variables on shrinkage characteristics of SIS parts. Optimization problem of SIS process was studied by various researchers. The effect of process variables on surface quality characteristics was examined by Rajamani et al [20]. As a result, impact of some process variables on part quality has been comprehended, and the result of the investigation showed that the mechanical, dimensional, and surface characteristics of the products are in acceptable ranges.

Despite the reports of the experimental studies, none of the aforementioned SIS systems are being utilized in the fabrication of functional parts. As a result, it is not commercialized and is not available in the additive manufacturing market yet. In addition, a design document for the fabrication of the SIS system has not been addressed sufficiently in the literature. However, with innovative design approach, it can be made applicable for fabricating prototypes and functional aircraft parts, UAV structures, automobile components, prosthetics, and exoskeleton devices. Thus, a new approach needs to be followed to design and develop an SIS system that eliminates the issue of the existing system.

Therefore, this work presents a comprehensive and systematic approach to the design and development of a low cost SIS system. The functionality of the developed machine has been tested by fabricating parts from HDPE polymer powder. The Polymer material used to fabricate the test specimens and prototypes has been chosen by examining the thermo-structural behaviour of various polymers through finite element analysis. In addition, the inhibitor solution was selected by conducting multiple pilot tests on their inhibition and penetration effects. Finally, the produced parts were tested for tensile and flexural strength to evaluate their performance. In this paper, the detailed design of SIS subsystems such as

the heater assembly, inhibition system, build and feed tanks, powder deposition, electronic control unit, and software and hardware integration are presented. Testing of developed SIS system and component fabrication is discussed. Furthermore, evaluation of the mechanical strength of the fabricated part was performed to determine the applicability of the developed system for fabricating useful products.

## 2. MATERIALS AND METHODS

### 2.1 Selection of Inhibitor

In the SIS process, the selected region of the powder layer is wetted through a liquid called an inhibitor which defines the part boundary. Inhibitor liquid is a saturated aqueous solution of high melting point salt with high water solubility [7,10]. Bhuvaneshwaran et al. [21] investigated a few of the salt materials as inhibition purposes. In order to reduce the surface tension of the aqueous solution, avoid the formation of droplets, and thereby achieve effective penetration into the powder layer, a small amount of isopropyl alcohol was mixed with the solution. As the amount of isopropyl alcohol added to the solution increases, salt gets precipitated [21]. Therefore, about 17% to 20 % of alcohol was an optimum amount for 100 ml of water to produce the desired effect.

Preliminary experiments were performed to evaluate the performance of each inhibitor material by applying heat energy on the polymer powder with an inhibitor at the periphery. It is observed that barium chloride ( $BaCl_2$ ) and potassium iodide (KI) produced less uniform penetration than other inhibitors, [21]. However, KI is preferable due to its high solubility to water which is essential for effective inhibition.

### 2.2 Selection of Polymer

In the present work, various polymer materials were considered as candidate materials for the SIS process, and the selection of specific polymers was carried out by evaluating their thermo-structural load carrying capacity using a finite element (FE) analysis. Figure 1 indicates the FE model of the powder bed and inhibitor solution. The polymer material and inhibitor material are represented in light grey and dark grey colours respectively. For the thermal analysis, 85% of the melting point of the polymer was used as input heat energy and the rate of heat transfer through the free surface is computed by assuming a free convection heat transfer coefficient,  $h= 30W/m^2K$ . Figure 2(a) and 2(b) show the result of the FE analysis and it indicates the coupled effect of thermal as well as structural loads on a single sintered layer as temperature distribution is applied as an input to the structure assuming a fixed bottom polymer layer.

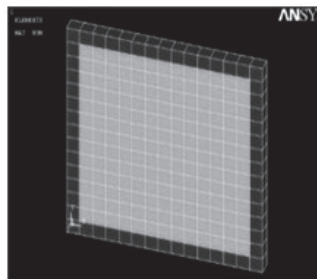


Fig. 1: FE model of polymer and inhibitor part.

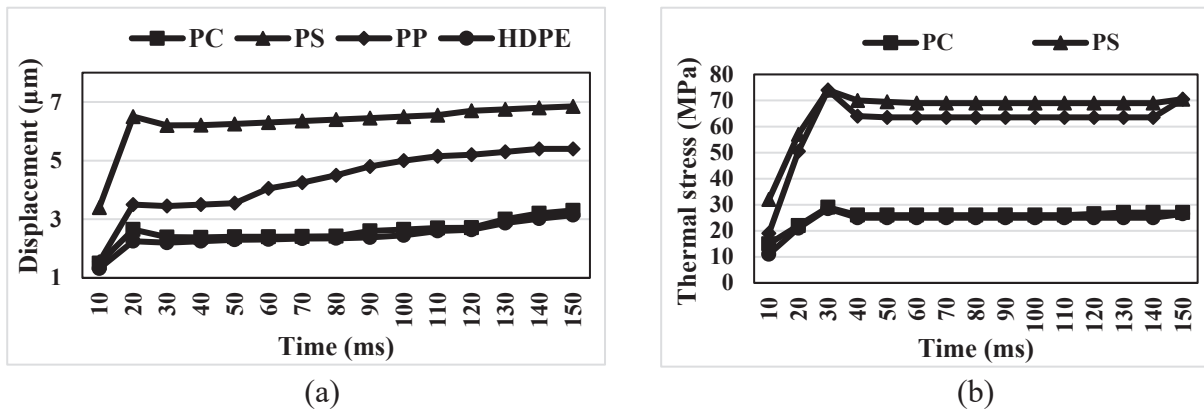


Fig. 2: (a) Displacement (b) Thermal stress of different polymer materials i) PP, ii) PC, iii) PS, iv) HDPE.

In comparison to other polymers, HDPE [22] attained minimal displacement and thermal stress as shown in Fig. 2(a) and Fig. 2(b) respectively, and hence it is considered for part fabrication.

### 3. DESIGN AND DEVELOPMENT OF THE SELECTIVE INHIBITION SINTERING (SIS) SYSTEM

The SIS system comprises the following sequence of operations to build functional parts layer by layer: How to use this document?

- Spread a thin layer of powder over the build tank from the feed tank
- Wet selected region of powder layer with inhibitor liquid to define the periphery of the part.
- Expose both the wetted and un-wetted powder layer to a heat source.
- Move down the build tank and simultaneously move up the feed tank through a small distance which defines layer thickness of the part.
- Spreading another layer of powder over the previously sintered layer.
- Repeat the process for each layer until the desired part is completed.

In order to attain the aforementioned operations, various subsystems such as build and feed tank assembly, powder deposition and compaction mechanism, inhibitor deposition, and heater assembly are ingeniously designed and fabricated.

#### 3.1 Feed, Build and Collector Tank

The SIS system is comprised of a feed and build tank. The feed tank is a reservoir that stores the powder material, and build tank is the platform where parts are constructed. These two platforms move vertically up and down in the opposite direction synchronously. When a build tank moves downward to a certain distance, the feed tank moves upward by the same distance equal to the desired layer thickness. In addition, a collector tank is provided to collect surplus powder during the powder deposition and compaction process. The platforms are made from high-grade aluminium plate machined to the required dimension using a water jet cutting process that provides precision and surface finish to avoid misalignments during assembly. A build tank of 200 x 200 x 200 mm, a feed tank of 250 x 200 x 200 mm and a collector tank of 50 x 200 mm is designed as shown in Fig. 3.

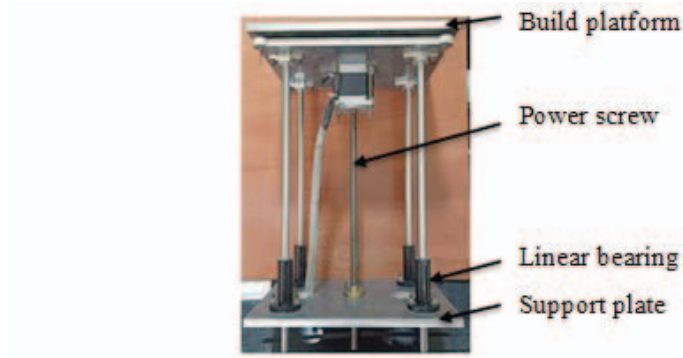


Fig. 3: Feed and build platforms assembly.

The upward and downward movement of the two tanks is achieved through a power screw driven by NEMA-23 stepper motors. Four round steel bars are used to guide the bedplates of both tanks in their upward and downward motions. The movement of the feed and build tank is designed so that the required amount of powder is made available in order to deposit a powder layer thickness with the required layer thickness. The possible swaying of the top plate as it moves vertically up and down is eliminated with the help of linear bearings fitted at the bottom of the tanks as shown in Fig. 3.

### 3.2 Powder Spreading and Compaction System

A simple mechanism (Fig. 4) that deposits a layer of powder on the build platform and compresses it to the required level of density is designed and fabricated. It is made up of a blade and a round bar. In order to reduce the number of voids and increase density, the powder bed requires compression using a roller. The blade spreads the powder on the build platform and the roller follows the blade to compact the powder bed to the required density. Hence, a round bar follows the blade during powder layer preparation.

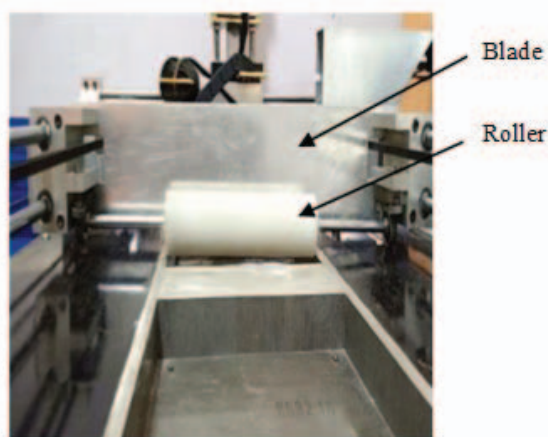


Fig. 4: Powder feeding and compacting mechanism.

The height of the roller from the build platform determines the layer thickness of parts. Therefore, depending on the strength required from the final sintered part, the height of the spreader-roller needs to be varied. As a result, the height of the spreader-roller is designed to be adjustable. In addition, the lower edge of the blade (spreader) is positioned slightly above the roller to ensure that a sufficient amount of material is provided for achieving the desired part density.

### 3.3 Inhibitor Deposition System

The inhibitor deposition mechanism consists of a syringe, a linear lead screw, and a stepper motor (Fig. 5). The stepper motor is used to drive the plunger linearly in a reciprocating manner. The rotational motion of the stepper motor is converted into a reciprocating motion of the plunger (piston) to compress the inhibitor solution through the nozzle. Two round steel bars are used to avoid sidewise swaying of the plunger thereby it moves perpendicular to the cross-sectional area of the syringe barrel without the piston head pushing the inner wall of the barrel. This enables the mechanism to deposit inhibitor solution efficiently on the powder layer. The designed inhibitor deposition system has a capacity of 60 ml of inhibitor and a plastic dispensing tip of 0.4 mm nozzle diameter [8] was used.

The flow rate of the inhibitor is influenced by the actuator's power (speed and torque). Droplet size is controlled through fitting cheap dispensing tips at the tip of the syringe. Multiple iterations were carried out to obtain an optimum printer feed rate. This mechanism is a low cost mechanism, yet it is able to dispense inhibitor solution as desired.

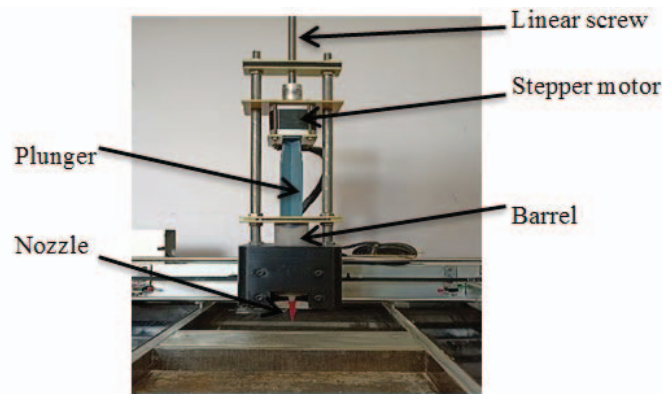


Fig. 5: Inhibitor deposition mechanism.

### 3.4 Heater Assembly

A short-wave infrared heater is used as a heat source for sintering the powder bed. The heat energy is transmitted from the source to the powder layer through electromagnetic radiation. The heating element, shown in Fig. 6, is made up of two lamps, each with 1000-Watt / 240-Volt. The lamps are fixed to a casing that is constructed from aluminium sheet metal because aluminium has better reflectivity property of infrared light and strength to weight ratio. During the sintering process, the heat source moves in a single-axis (Y-axis) over the build tank at the required speed. In addition, a 150 mm x 150 mm flat mica heater bed heater of 150-Watt / 230-Volt is fitted beneath the build tank.

Therefore, part warping during sintering is prevented by preheating the build platform with the bed heater to a temperature of approximately 90 °C - 100 °C during and prior to depositing the powder layer.



Fig. 6: Heating element.

### 3.5 X-Y Positioning Mechanism

The X-Y positioning system used in this machine is an H-Bot that uses a low cost single timing belt to guide and position the cart on which the inhibitor depositor is attached as shown in Fig. 7(a). Two low-priced NEMA-17 stepper motors are used to actuate the X-Y micro positioning mechanism. The motor mount blocks on which the actuators are fitted and the cart that hold the nozzle are also machined from low cost aluminium. Round stainless steel bars are used as a guide for the moving elements of the mechanism.

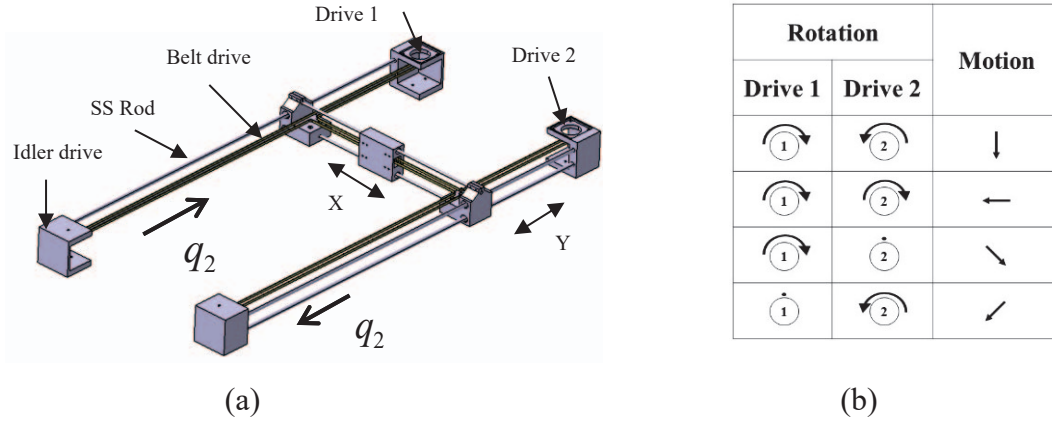


Fig. 7: X-Y positioning mechanism.

All elements of the mechanism except the belt and the stainless-steel rods are made of Al6061 and is fabricated using a CNC milling process. In this mechanism, fixed rotary drivers are connected by a single H-bar GT-2 timing belt of width 6mm via GT-2 timing pulley. As indicated in Fig.7 (a), (b), the coordinated motion of the drive motors helps the mechanism to achieve the required movement. That is the nozzle of the inhibitor depositor mechanism can be moved along the required direction (X, Y, and combination of X and Y), by controlling the motion of the drives. As can be seen from the figures, when motor 1 and motor 2 rotates in the counter-clockwise direction by  $q_1$  and  $q_2$  angles respectively, the angles  $q_1$  and  $q_2$  are shared by the linear displacement  $x$  and  $y$ . Equation (1) and (2) below show the relationship of  $q_1$  and  $q_2$  with  $x$  and  $y$  distance movement of the nozzle.

$$q_1 = \Delta x + \Delta y \quad \text{and} \quad q_2 = \Delta x - \Delta y \quad (1)$$

$$\Delta x = \frac{1}{2}(q_1 + q_2) \quad \text{and} \quad \Delta y = \frac{1}{2}(q_1 - q_2) \quad (2)$$

Therefore, when both drives rotate in the clockwise direction, the nozzle moves along the negative X direction. However, when they rotate counter-clockwise, the nozzle makes a positive X-axis movement. Similarly, when one of the motors rotates in clockwise and the other rotates in the opposite direction, the nozzle moves along Y-axis. The rotation of a single drive enables the nozzle to move diagonally in the X-Y plane. Therefore, this mechanism can precisely position the nozzle at any point in X-Y plane over the build platform.

### 3.6 Base Structure

The base structure that supports the entire setup of the SIS machine is required to be strong, tough and rigid as the kinematics of the system cannot be compromised. Most of the relatively heavy components are made from aluminium 6061 and the top support sheet is

made from mild steel. In addition, stainless steel rods are chosen to support and guide the inhibition mechanism, the heating element, and the powder spreader and compactor mechanism. Hence, the beam and column of the machine are loaded with the lumped weight of all the components that is approximately 35 kg.

The aluminium extrusion profile is chosen for the frame of the support structure as it is a lightweight and good corrosion-resistant material. It is also easy and economical to fabricate a structure from aluminium extrusion profiles than plastics or steel structures. Moreover, T-Slot aluminium profiles have high specific density than a steel structure. Hence, an aluminium extruded profile (30 mm x 30 mm) frame is chosen for the support structure to provide structural rigidity to the machine.

### 3.7 Hardware and Software Integration

Customized design of the hardware (Fig. 8) showing all the connection of the actuators, sensors and control unit is created using the Proteus platform. The circuit shown in the figure is divided into two major categories as direct and alternating current circuits. The direct current circuit is the electronic controller that guides the computer-controlled SIS system to achieve desired characteristics.

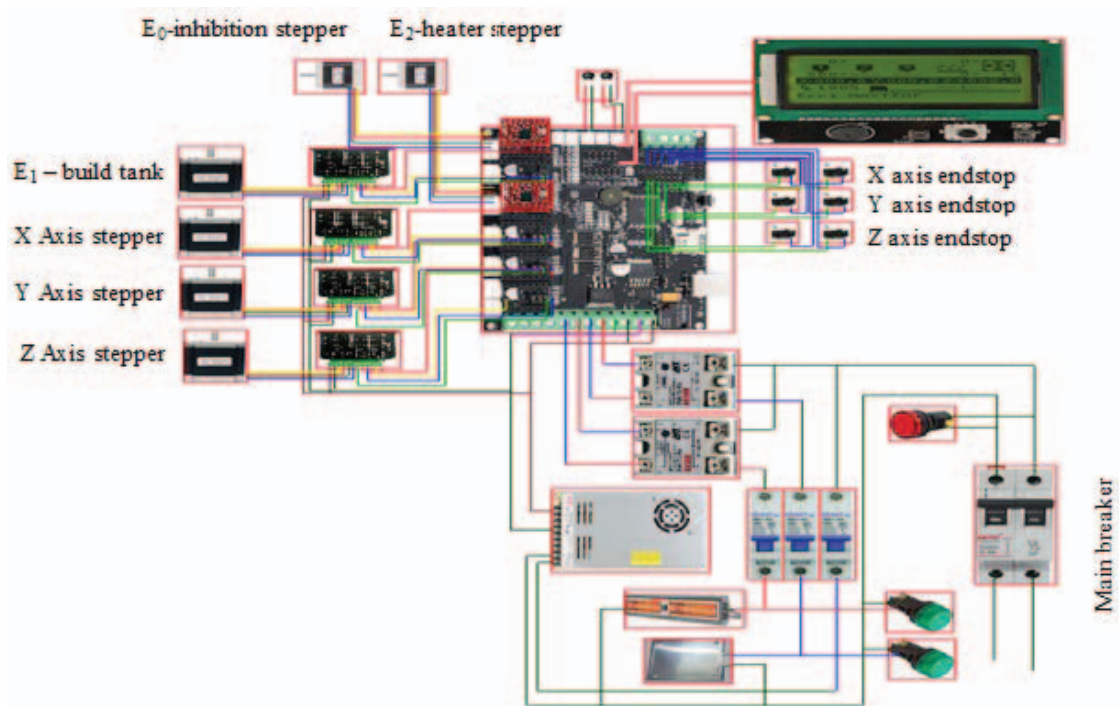


Fig. 8: Electronic control circuit.

A Megatronics V3.1 microcontroller is used to control the six stepper drivers (X, Y, Z, Extruder 1, Extruder 2 and Extruder 3) and the two heaters (Bed and IR heater). An input of 12V power is delivered to the controller board via the 30A switch mode power supply. The stepper drivers are designed to control the independent motions of the following components of the developed system: Powder deposition-compression mechanism (Y), nozzle motions (X and Y), feed tank (Z), inhibitor deposition mechanism (Extruder 1), liner movement of build tank (Extruder 2) and motion of IR heater (Extruder 3).

NEMA-23 stepper motors are used to drive X, Y, Z linear motions and Extruder 2 as they require relatively high torque motors. On the other hand, Extruder 1 and Extruder 3 are

driven using NEMA-17 stepper motor. A4988 and Tb6600 stepper drivers are used to drive the NEMA-17 and NEMA-23 stepper motors respectively. In addition, the X and Y axis travel limits are controlled using micromechanical end stops. The control system of the heating elements is a closed-loop, and the output temperature of the infrared heater and bed heater is measured using 100k thermistors and K type thermocouple temperature sensors respectively. The microcontroller controls the temperatures through an SSR-25 solid state relay.

Software was developed by customizing an open-source Marlin firmware program based on the number and types of input and output devices of the developed machine and was uploaded to the Megatronics V3.1 microcontroller. Part fabrication using the developed system begins with creating the 3D CAD model of the required part in STL format. The CAD model then sliced into desired layer thickness using Slic3r software, and corresponding G – Codes are generated. Finally, based on the generated G-codes, Pronterface software is used to generate a numerical control (NC) machine tool path.

### 3.8 Assembly of SIS Subsystems and Development of SIS System

The designed subsystems such as build and feed tanks assembly, powder deposition and compaction mechanism, inhibition deposition mechanism and heater assembly are assembled to make the SIS system which is shown in Fig. 9. Preliminary testing on linear and rotary actuators, tanks assemblies, NC tool path generation, inhibitor deposition, heater motion, temperature feedback controller and limit switch sensing is performed.

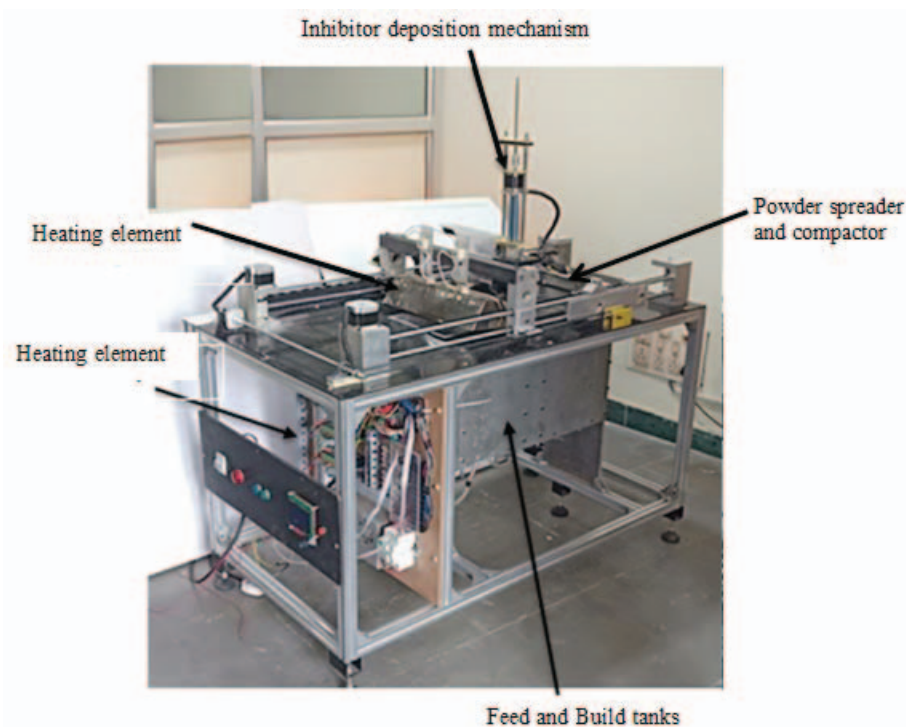


Fig. 9: Developed SIS system.

To minimize the cost of the SIS system, selection of temperature sensors, linear actuators, and belt drive systems are carried out with due consideration of cost-effectiveness and superior performance. A novel inhibition delivery mechanism is developed for the precise delivery of inhibitor. The composition of inhibitor material preparation was crucial to obtain precise inhibition effect on the polymer powder surface and is successfully achieved. The

low-cost SIS system is developed by assembling the various components. The preliminary functionality tests demonstrate that the developed SIS system is applicable in all aspects and it can be used to produce functional parts. However, one major limitations of the developed SIS system is material wastage. In the SIS part fabrication process the entire powder bed is heated by the infrared heater which fuses the whole powder layer except the region that is wetted by the inhibitor solution. Consequently, the powder that is not in the waste powder is not reusable. In this developed system the powder bed region that make up the part body as well as the region outside the part cross sectional area is sintered which causes powder loss.

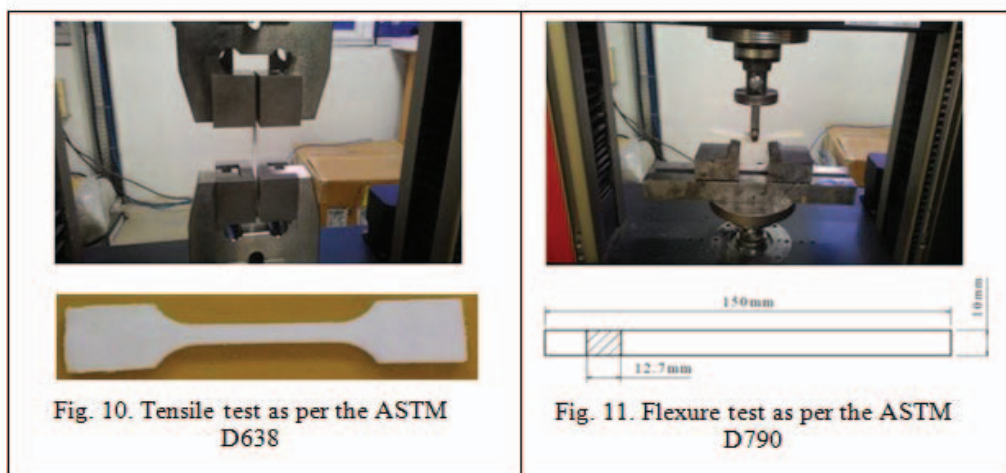
### 3.9 Mechanical Strength Testing of SIS Fabricated Parts

To evaluate the performance of the developed system and determine the influence of its process parameters such as heater feed rate, printer feed rate, layer thickness, and heat energy on the tensile and flexural strength of the fabricated part, sample parts were fabricated and their mechanical characteristics have been assessed. Specimens were fabricated from high-density polyethylene (HDPE) polymer powder, supplied by JP Polymers, India. As per the datasheet of the supplier, the grain size of the selected powder particles was in the range of 35  $\mu\text{m}$  to 80  $\mu\text{m}$ . The powder used was 100% virgin so that any possible irregularities in the sintered parts were avoided. Box-Behnken based RSM approach was followed to perform an optimal set of experiments through varying SIS process parameters [20,23]. The process parameters were varied with three levels as indicated in Table 1.

Table 1: SIS process parameters and levels

S. No.	Parameters	Units	Levels		
			Low	Medium	High
1	Layer thickness	mm	1	2	3
2	Heat energy	J/mm <sup>2</sup>	25.32	28.48	30.06
3	Heater feed rate	mm/sec	3	3.25	3.5
4	Printer feed rate	mm/min	100	110	120

The range of settings for the considered process variables were determined based on the thermal property of the polymer powder by conducting numerous preliminary tests.



The tensile strength test was performed according to the ASTM D638 standard [24] with a test speed of 5 mm/min at room temperature and 40% relative humidity. Similarly, the flexural strength test was carried out based on ASTM: D790 [25] standard with a test speed of 1.2 to 1.8 mm/min. The Instron 3369 dual column universal testing system shown in Fig. 10 and 11 were employed to carry out both tensile and flexure strength test.

#### 4. RESULTS AND DISCUSSION

The result of the experiment and the combinations of corresponding parameters and their settings are given in Table 2.

Table 2: Experimental results of tensile and flexural strengths

Run	Layer thickness (mm)	Heat energy (J/mm <sup>2</sup> )	Heater feed rate (mm/s)	Printer feed rate (mm/min)	Tensile strength (MPa)	Flexure strength (MPa)
1	3	28.48	3.5	110	23.05	25.46
2	2	30.06	3	110	21.29	26.64
3	1	28.48	3.5	110	22.53	26.34
4	2	28.48	3.25	110	25.55	28.63
5	3	25.32	3.25	100	24.39	26.35
6	1	28.48	3.25	120	24.94	27.18
7	2	30.06	3.5	120	20.53	24.20
8	2	28.48	3	120	20.41	24.11
9	2	30.06	3.5	110	25.92	27.57
10	2	28.48	3.25	110	25.12	28.55
11	2	30.06	3.25	100	24.64	28.13
12	2	25.32	3.5	100	23.97	27.90
13	3	28.48	3	110	20.86	26.18
14	2	25.32	3.25	120	21.29	27.04
15	2	25.32	3.5	110	19.34	25.24
16	3	25.32	3.25	110	23.77	28.57
17	2	28.48	3.25	110	24.29	27.22
18	1	28.48	3	110	25.87	29.60
19	2	28.48	3.5	100	21.62	26.40
20	2	30.06	3.25	110	24.90	28.22
21	2	28.48	3.25	110	24.70	22.10
22	2	25.32	3	100	24.97	28.05
23	2	30.06	3.5	120	25.25	28.19
24	1	30.06	3.25	100	24.85	27.11
25	1	28.48	3.25	110	26.54	32.08
26	1	25.32	3.25	110	23.80	27.01
27	3	30.06	3.25	110	24.97	28.94
28	2	25.32	3	110	24.47	28.71
29	3	28.48	3.25	120	22.90	26.77

From the result of the experiments, it is evident that maximum tensile strength and flexural strength of 26.54 MPa and 32.08 MPa respectively were obtained for process

variables settings: layer thickness of 1mm, heat energy of 28.48 J/mm<sup>2</sup>, printer feed rate of 110 mm/min and heater feed rate of 3.25 mm/sec.

The influence of input process parameters such as layer thickness, heat energy, heater feed rate and printer feed rate on tensile and flexure strengths were analysed as depicted in Fig. 12 and 13. The effect of each process parameter was distinctly analysed where other parameters were set at their mid-levels.

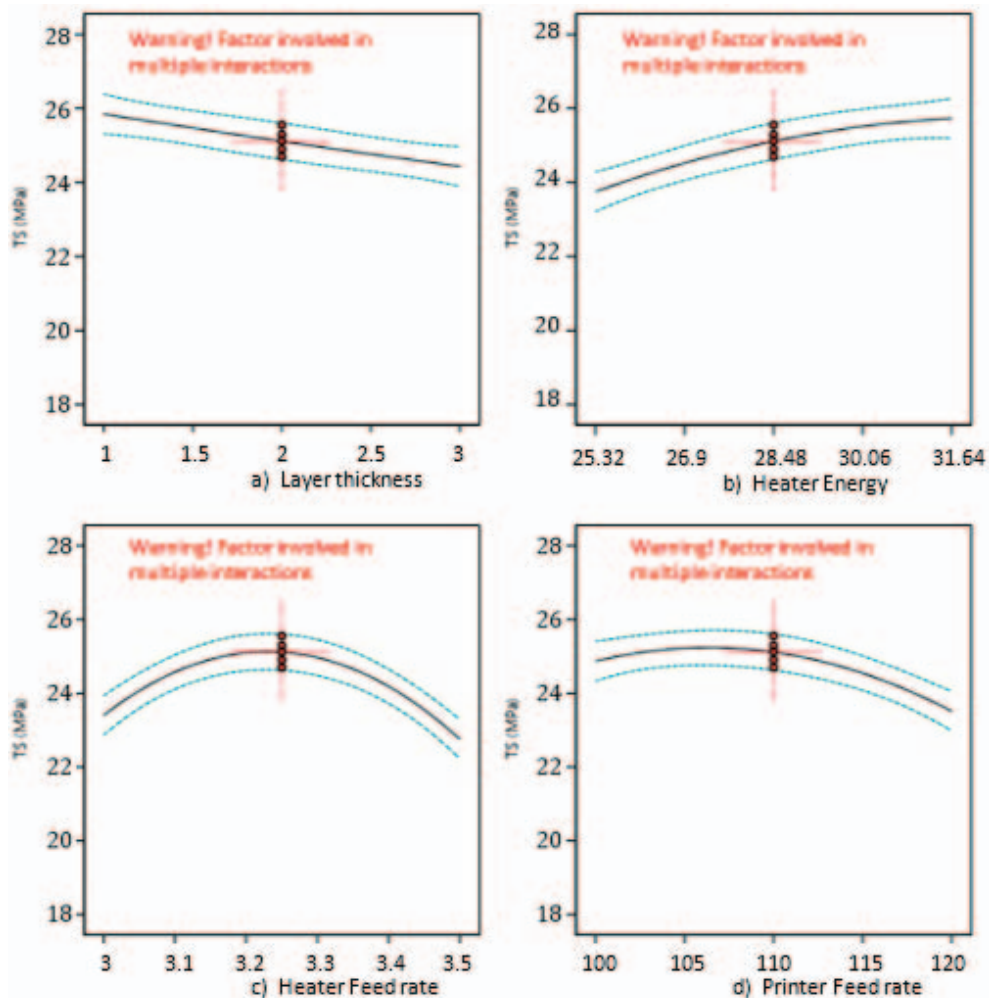


Fig. 12: Effect of process parameters on tensile strength of SIS parts.

As can be seen from Fig. 12 (a) and 13 (a) an increase in layer thickness leads to a reduction in tensile and flexural strengths. This is because at minimal layer thickness the bonding between successive layers is stronger. On the contrary, at maximum thickness of the powder layer, micro voids are developed which leads to the reduction of tensile strength [26]. Heat energy in the range of 27 J/mm<sup>2</sup> - 31 J/mm<sup>2</sup>, which is about 77 % to 85 % of the energy required to achieve the melting point of HDPE has resulted in a more compact structure due to better fusion of powder particles. Strong intermolecular attraction between the polymer particles occurs in the specified range of temperature. As a result, mechanical strength increased with an increase of heat energy as shown in Fig. 12 (b) and 13 (b) [27]. Therefore, heat energy necessary to bring strong bonding between powder particles helps to achieve high mechanical strength on the fabricated part.

Furthermore, the effect of the heater feed rate as shown in Fig. 12 (c) and 13 (c), and printer feed rate indicated in Fig. 12 (d) and 13 (d) on the mechanical strength is nonlinear. As seen from the graphs mechanical strength increases up to the optimal value of the heater feed rate and printer feed rate which then decreases drastically. An increase in heater feed rate causes porosity between layers which diminishes the mechanical strength. The printer feed rate influences the inhibition penetration effect, which affects the dimensional and geometric characteristics of the part.

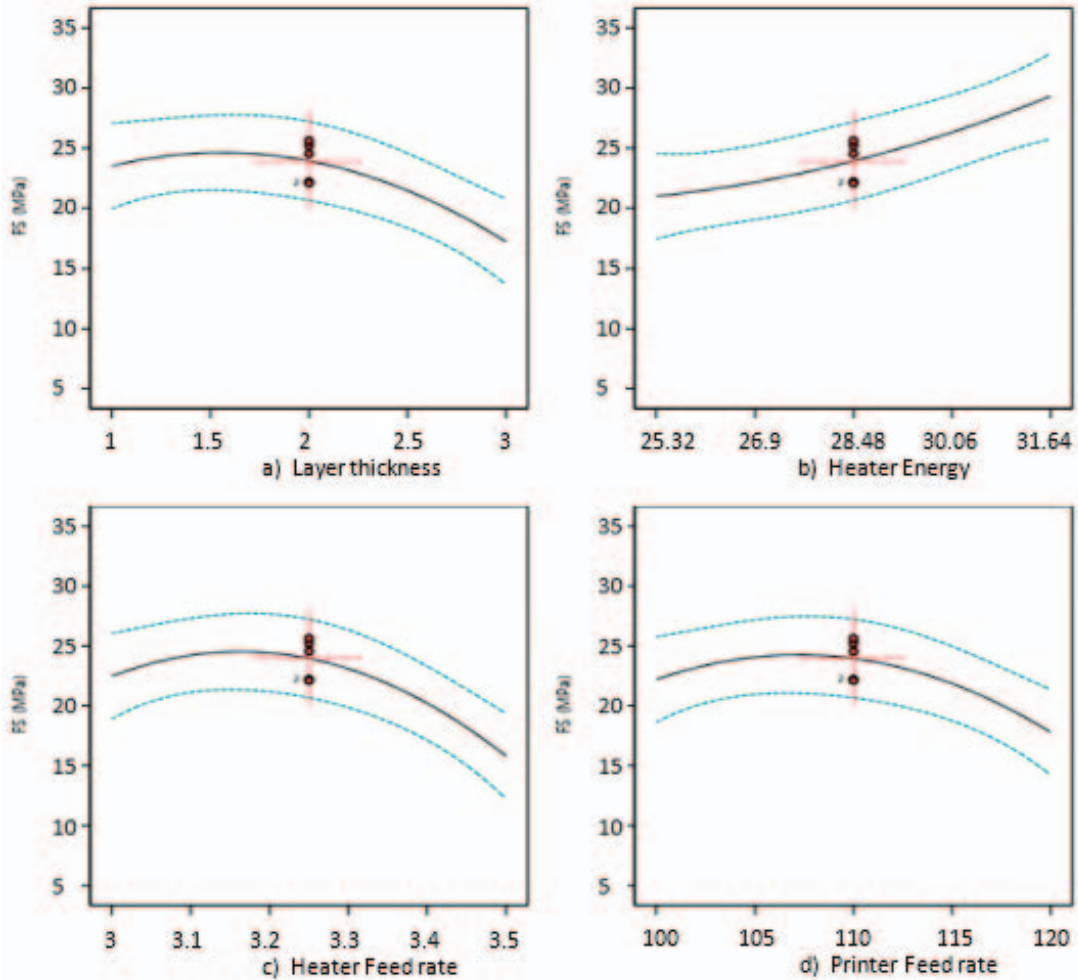


Fig. 13: Effect of process parameters on flexure strength of SIS parts.

Figure 14 (a–c) shows the SEM images of the fractured surface of the tensile test specimens fabricated with a heat energy of  $28.48 \text{ J/mm}^2$ . Analysis of the SEM images showed some porosity in the fractured surface. These voids act as stress concentrators and cause uneven distribution of the normal stress over the cross-sectional area of the test specimens. Therefore, such pores and voids observed need to be eliminated by optimizing the compaction pressure during layer making.

Figure 15 (a–c) shows the SEM micrograph of the flexural fractured surface of the specimens fabricated with heat energy of  $28.48 \text{ J/mm}^2$ . It is evident from Fig. 15 (a) that there is interphase de-lamination at the cross-section of the sintered specimen due to the applied flexural load. Voids are also observed in Fig. 15 (b) due to poor interfacial bonding between sintered particles. However, the formation of voids and uneven sintering of

polymer particles are comparatively higher in the case of specimens fabricated below the applied heat energy of  $28.48 \text{ J/mm}^2$ .

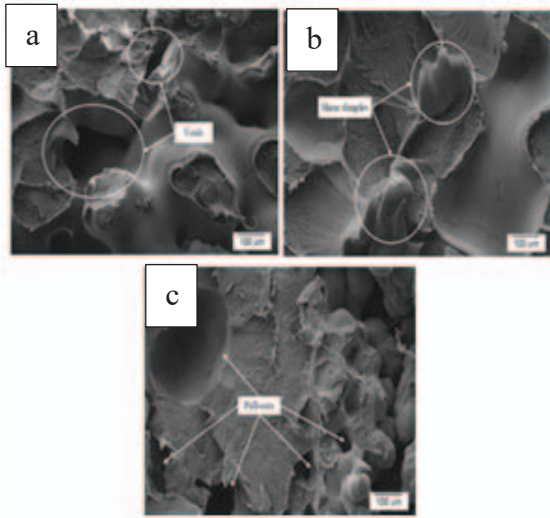


Fig. 14: Fractured surfaces of SIS fabricated tensile test specimen.

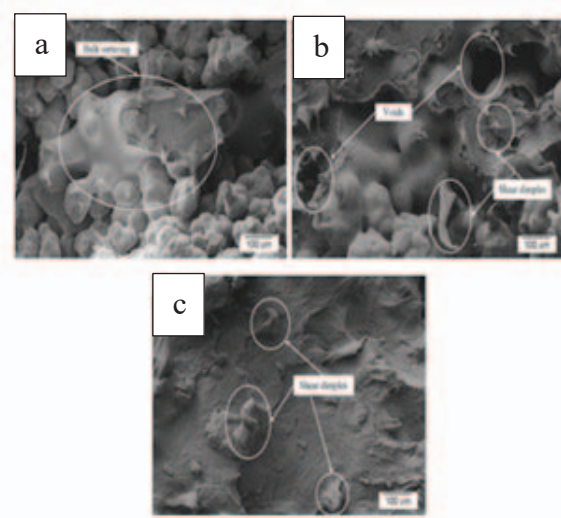


Fig. 15: Fractured surfaces of SIS fabricated flexural test specimen.

An identical load was constantly applied on the specimens' surface that created a shear band along the middle section of the specimens resulting in its breakage as seen in Fig. 15 (c). In addition, elongated dimples normal to the loading axis are observed in Fig. 15 (c). Moreover, few voids and bulk cohesion of particles are seen in the fractured surface, these can be attributed to the non-uniform heat distribution during sintering.

Response surface methodology (RSM) has been used for the optimization of mechanical strength characteristics as it handles the interaction effects of input parameters [28]. In order to validate the results obtained, confirmation experimental tests were conducted as shown in Table 3.

Table 3: Validation table

a) Comparison of predicted tensile strength with experiment result

Layer thickness (mm)	Heat energy ( $\text{J/mm}^2$ )	Heater feed rate (mm/s)	Printer feed rate (mm/min)	Predicted value (MPa)	Experimental value (MPa)	Error percentage
1	28.48	3.2	110	27.21	27.80	2.12%

b) Comparison of predicted flexural strength with experiment result

Layer thickness (mm)	Heat energy ( $\text{J/mm}^2$ )	Heater feed rate (mm/s)	Printer feed rate (mm/min)	Predicted value (MPa)	Experimental value (MPa)	Error percentage
1	28.48	3.2	110	33.60	34.59	2.86%

As can be seen from the table, the deviation of the actual tensile strength and flexural strength values from the predicted values are only by 2.12% and 2.86% respectively. Hence, it can be concluded that the predicted value is in good agreement with the experimental value. In addition, to evaluate the dimensional accuracy and geometric complexity of the

parts fabricated using the developed low cost SIS system; sample components shown in (Fig. 16) were manufactured. These samples have shown dimensional accuracy of about 1 mm which shows that the developed system has the capability of producing parts with acceptable mechanical strength as well as dimensional accuracy.



Fig. 16: Fabricated SIS parts.

Therefore, parts fabricated by the developed SIS system can be utilized as load carrying structural machine elements replacing components fabricated using another fabrication processes such as SLS and injection moulding.

## 5. CONCLUSION

The developed SIS system is custom-built through the integration of an indigenously designed H-Bot X-Y precision position mechanism, inhibition depositor, heating element and build and feed tank assemblies. To minimize the cost of the SIS system, selection of temperature sensors, linear actuators, and belt drive systems are carried out with due consideration of cost-effectiveness and superior performance. A novel inhibition delivery mechanism that minimizes the controllable process variables has been developed and implemented for the precise delivery of inhibitor. In addition, an innovative low cost powder spreader was used, and thus the cost of the current machine has been brought down significantly so that it is economically affordable. The capability of the machine was tested by fabricating various parts from polymer powder, and the mechanical and geometric characteristics of the fabricated parts were evaluated. The polymer materials used to test the performance of the developed system were selected by evaluating its thermo-structural load carrying capacity using finite element analysis. The FEA studies indicated that HDPE attains minimal displacement and thermal stress. Besides, KI was identified as the best inhibitor material because of its high solubility to water and high melting point.

Tensile and flexural specimens have been fabricated from the selected HDPE polymer powder and their mechanical property was evaluated. The result showed that the HDPE parts fabricated by the developed SIS system achieved a tensile and flexural strength of 27.8 MPa and 34.59 MPa respectively. Furthermore, the fabricated components have been found to have achieved good dimensional accuracy. Therefore, from these observations, it can be deduced that the indigenously designed and fabricated SIS system can be utilized to manufacture functional prototypes from various polymer powders of melting point up to 300°C for diverse applications. Furthermore, in this study the SIS process variable settings

have been investigated only for HDPE polymer powder. In order to use the system for materials other than HDPE, a parametric study needs to be carried out to achieve optimum part quality. In addition, more optimization research needs to be conducted on the SIS process variables in order to enhance the quality of the fabricated parts. The developed SIS system has great potential for commercialization in the additive manufacturing sector in the near future.

## REFERENCES

- [1] Achillas C, Tzetzis D, Raimondo MO. (2017). Alternative production strategies based on the comparison of additive and traditional manufacturing technologies. *International Journal of Production Research*, 55(12):3497-3509. <https://doi.org/10.1080/00207543.2017.1282645>
- [2] Gardan J. (2016). Additive manufacturing technologies: State of the art and trends. *International Journal of Production Research*, 54(10):3118-3132. <https://doi.org/10.1080/00207543.2015.1115909>.
- [3] Abdulhameed O, Al-Ahmari A, Ameen W, Mian, SH. (2019). Additive manufacturing: Challenges, trends, and applications. *Advances in Mechanical Engineering*, 11(2):1-27. <https://doi.org/10.1177/1687814018822880>.
- [4] Krassimir D. (2009). Rapid Prototyping and Engineering Applications: A Toolbox for Prototype Development. *Assembly Automation*. <https://doi.org/10.1108/aa.2009.03329cae.001>.
- [5] Kruth, JP (1991). Material Incess Manufacturing by Rapid Prototyping Techniques. *CIRP Annals - Manufacturing Technology*, 40(2):603-614. [https://doi.org/10.1016/S0007-8506\(07\)61136-6](https://doi.org/10.1016/S0007-8506(07)61136-6).
- [6] Khoshnevis B, Asiabanpour B, Mojdeh M, Palmer K. (2003). SIS—a new SFF method based on powder sintering. *Rapid Prototyping Journal*, 9(1):30-36.
- [7] Asiabanpour B, Palmer K, Khoshnevis B. (2004). An experimental study of surface quality and dimensional accuracy for selective inhibition of sintering. *Rapid Prototyping Journal*, 10(3):181-192.
- [8] Asiabanpour B. (2003). An experimental study of factors affecting the selective inhibition of sintering process.
- [9] Khoshnevis B, Yoozbashizadeh M, Chen Y. (2012). Metallic part fabrication using selective inhibition sintering (SIS). *Rapid Prototyping Journal*, 18(2):144-153. <https://doi.org/10.1108/13552541211212122>
- [10] Asiabanpour B, Khoshnevis B, Palmer K. (2006). Advancements in the selective inhibition sintering process development. *Virtual and Physical Prototyping*, 1(1):43-52.
- [11] Aravind A, Siddiqui TN, Arunkumar P, Balasubramanian E. (2017). Comparative Study of High Performance Polymers in Selective Inhibition Sintering Process through Finite Element Analysis. *Polymers and Polymer Composites*, 25(3):199-202. <https://doi.org/10.1177/096739111702500303>
- [12] Petros M, Torabi P, Khoshnevis B. (2016). The influence of build strategies in selective inhibition sintering (SIS). *International Journal of Advanced Manufacturing Technology*, 84(5-8):969-979. <https://doi.org/10.1007/s00170-015-7766-y>
- [13] Torabi P, Petros M, Khoshnevis B. (2014). Selective inhibition sintering: the process for consumer metal additive manufacturing. *3D Printing and Additive Manufacturing*, 1(3):152-155.
- [14] Asiabanpour B, Khoshnevis B, Palmer K, Mojdeh M. (2003). Advancements in the SIS process. 14th International Symposium on Solid Freeform Fabrication, Austin, TX.
- [15] Palmer K., Khoshnevis B. (2003). Performance Factors in the Selective Inhibition of Sintering Process. IIE Annual Conference. Proceedings, 1. Institute of Industrial and Systems Engineers (IISE).
- [16] Balasubramanian E, Rajamani D, Arunkumar P. (2018). Investigation on dry sliding wear behavior of Selective Inhibition Sintered HDPE parts using simulated annealing algorithm. *Materials Today: Proceedings*, 5(2):6534-6542. <https://doi.org/10.1016/j.matpr.2017.11.308>

- [17] Baligheid SM, Chandrasekhar U, Elangovan K, Shankar S. (2018). Taguchi's Approach: Design optimization of process parameters in selective inhibition sintering. *Materials Today: Proceedings*, 5(2):4778-4786. <https://doi.org/10.1016/j.matpr.2017.12.051>
- [18] Yoozbashizadeh M, Khoshnevis B (2019). The Effects of Sintering Conditions on Selective Inhibition Sintering Process for Bronze. *3D Printing and Additive Manufacturing*, 6(5):262-271.
- [19] Rajamani D, Balasubramanian E, Arunkumar P, Silambarasan M, Bhuvaneshwaran G. (2018). Experimental Investigations and Parametric Optimization of Process Parameters on Shrinkage Characteristics of Selective Inhibition Sintered High Density Polyethylene Parts. *Experimental Techniques*, 42(6):631-644. <https://doi.org/10.1007/s40799-018-0286-6>
- [20] Rajamani D, Ziout A, Balasubramanian E, Velu R, Sachin S, Mohamed H. (2018). Prediction and analysis of surface roughness in selective inhibition sintered high-density polyethylene parts: A parametric approach using response surface methodology–grey relational analysis. *Advances in Mechanical Engineering*, 10(12). 1687814018820994. <https://doi.org/10.1177/1687814018820994>
- [21] Bhuvaneshwaran G, Sisay M, Manivannan R, Arunkumar P, Silambarasan M. (2019). Development of inhibition system for SIS process. *Lecture Notes in Mechanical Engineering*, 383-389. [https://doi.org/10.1007/978-981-13-2697-4\\_42](https://doi.org/10.1007/978-981-13-2697-4_42)
- [22] Shaikh H, Anis A, Poulouse AM, Alam M, A-Otaibi MN, Alam MA, Al-Zahrani SM. (2016). Studies on High Density Polyethylene Reinforced with Phosphate Ore Particles: Thermal, Rheological, Mechanical and Morphological Properties. *Polymer-Plastics Technology and Engineering*, 55(17):1831-1841. <https://doi.org/10.1080/03602559.2016.1171875>
- [23] Esakki B. (2017). Modeling and prediction of optimal process parameters in wear behaviour of selective inhibition sintered high density polyethylene parts. *Progress in Additive Manufacturing*. <https://doi.org/10.1007/s40964-017-0033-z>
- [24] ASTM D638-14. (2014). Standard Test Method for Tensile Properties of Plastics. ASTM International, West Conshohocken, PA, 82(C):1-15.
- [25] ASTM D790-03. (2017). Standard Test Methods for Flexural Properties of Unreinforced and Reinforced Plastics and Electrical Insulating Materials. ASTM International, West Conshohocken, PA.
- [26] Shubham P, Sikidar A, Chand T. (2016). The influence of layer thickness on mechanical properties of the 3D printed ABS polymer by fused deposition modeling. *Key Engineering Materials*, 706:63-67. <https://doi.org/10.4028/www.scientific.net/KEM.706.6>
- [27] Khalil Y, Kowalski A, Hopkinson N. (2016). Influence of energy density on flexural properties of laser-sintered UHMWPE. *Additive Manufacturing*, 10:67-75. <https://doi.org/10.1016/j.addma.2016.03.002>
- [28] Şimşek B, İç, YT, Şimşek EH. (2016). A RSM-Based Multi-Response Optimization Application for Determining Optimal Mix Proportions of Standard Ready-Mixed Concrete. *Arabian Journal for Science and Engineering*, 41(4):1435-1450. <https://doi.org/10.1007/s13369-015-1987-0>

## PREPARATION AND CHARACTERIZATIONS OF LATEX/FILLER NANOCOMPOSITES

MOHAMAD FIRDAUS OMAR<sup>1,2</sup>, NURIAH MOHAMAD<sup>2</sup> AND FATHILAH BINTI ALI<sup>1\*</sup>

<sup>1</sup>*Department of Biotechnology Engineering, Faculty of Engineering, International Islamic University Malaysia, Jalan Gombak, 53100 Kuala Lumpur, Malaysia.*

<sup>2</sup>*Top Glove Sdn. Bhd., R&D Centre, Lot 64593, Jalan Dahlia KU/8, 41050 Klang, Selangor, Malaysia*

\*Corresponding author: [fathilah@iium.edu.my](mailto:fathilah@iium.edu.my)

(Received: 9<sup>th</sup> March 2020; Accepted: 14<sup>th</sup> June 2020; Published on-line: 4<sup>th</sup> July 2020)

**ABSTRACT:** Latex compounding which incorporates various types of clays as filler to the rubber can significantly give reinforcement in the rubber matrix when rubber/clay nanocomposites are formed, but the filler agglomerates. Thus, study was conducted by using Kaolin clay as the filler in the rubber nanocomposites with silane coupling agent to functionalize the surface of the filler. This study was done in order to investigate the mechanical properties of various functionalized Kaolin in latex nanocomposites, to prepare various ratios of Kaolin to rubber, and to characterize mechanical, thermal and morphological properties of the Kaolin in latex nanocomposites. To achieve these, six types of silane coupling agents was used for Kaolin filler surface functionalization purpose during the filler's incorporation in latex compounding. The optimized coupling agent, USi-7301 ( $\gamma$ -chloropropyltrimetoxysilane) – with tensile strength value of 32.77 MPa, elongation at break value of 632.589 % and force at break value of 6.737 N – was used to further functionalize Kaolin filler in different ratios so as to achieve the optimum mechanical, thermal and morphological properties of the filler in the polymer matrix. Universal tensile machine was used to analyze the mechanical properties of the nanocomposites, while the Scanning Electron Microscopy (SEM) and Differential Scanning Calorimetry (DSC) were used to observe the morphological and thermal properties of the nanocomposites, respectively. The results showed that reducing the Total Solids Content (TSC) of Kaolin filler to 26 % somehow showed the optimized properties of the nanocomposites, giving 34.00 MPa tensile strength, 576.494 % elongation at break and 6.564 N force at break. Rough surface morphology was observed under SEM suggesting the occurrence of phase separation between the hydrophilic filler and the hydrophobic rubber matrix. In the DSC plot, sample with USi-7301 and with functionalized Kaolin filler 26 % TSC showed glass transition temperature shifted to lower region compared to normal nitrile rubber. The reinforcement of nanocomposites formed will not only enhance the properties of the nanocomposites, but is also economically feasible thus brings advantages to the industry.

**ABSTRAK:** Penyebatian lateks yang menggabungkan pelbagai jenis tanah liat sebagai pengisi dalam getah dapat memberi penguatan dalam matriks getah dengan ketara apabila nanokomposit getah / tanah liat terbentuk, tetapi pengisi mengagregat. Oleh itu, kajian dijalankan dengan menggunakan tanah liat Kaolin sebagai pengisi dalam nanokomposit getah dengan ejen gandingan silan untuk menambah-fungsi permukaan pengisi tersebut. Kajian ini dilakukan untuk mengenalpasti sifat mekanik pelbagai Kaolin (yang berfungsi) dalam nanokomposit lateks, untuk menyediakan pelbagai nisbah Kaolin terhadap getah, dan untuk mencirikan sifat mekanik, haba dan morfologi Kaolin dalam nanokomposit lateks. Untuk mencapainya, enam jenis ejen gandingan silan digunakan

untuk tujuan menambah-fungsi permukaan pengisi Kaolin semasa penggabungan pengisi dalam penyebatian lateks. Ejen gandingan silan yang paling optimum, USi-7301 ( $\gamma$ -silan kloropropiltrimetoksi) - dengan nilai kekuatan tegangan 32.77 MPa, nilai pemanjangan ketika pemutusan 632.589% dan kekuatan daya ketika pemutusan 6.737 N - digunakan dengan lebih lanjut untuk menambah-fungsi pengisi Kaolin dalam nisbah yang berbeza untuk lebih mencapai sifat mekanikal, haba dan morfologi optimum pengisi dalam matriks polimer lateks. Mesin tegangan universal digunakan untuk menganalisis sifat mekanik nanokomposit, sementara Mikroskopi Elektron Pengimbasan (SEM) dan Kalorimetri Pengimbasan Berbeza (DSC) digunakan untuk menganalisa sifat morfologi dan haba nanokomposit tersebut. Hasil kajian menunjukkan bahawa pengurangan Jumlah Kandungan Pepejal (TSC) pengisi Kaolin kepada 26% menunjukkan sifat optimum nanokomposit, dengan kekuatan tegangan 34.00 MPa, pemanjangan ketika pemutusan sebanyak 576.494% dan daya ketika pemutusan sebanyak 6.564 N. Morfologi permukaan kasar diperhatikan di bawah SEM dan ia menunjukkan berlakunya pemisahan fasa antara pengisi hidrofilik dan matriks getah hidrofobik. Dalam plot DSC, sampel dengan USi-7301 dan dengan pengisi Kaolin yang difungsikan dengan 26% TSC menunjukkan suhu peralihan kaca beralih ke kawasan yang lebih rendah berbanding getah nitril biasa. Pengukuhan nanokomposit yang terbentuk bukan sahaja akan meningkatkan sifat nanokomposit, tetapi juga dapat dilaksanakan secara ekonomi sehingga memberi banyak kelebihan kepada industri.

---

**KEY WORDS:** *rubber; latex; filler; nanocomposites; silane coupling agent*

## 1. INTRODUCTION

The incorporation of clay with natural rubber has been commonly investigated in the past few years because of the structure of the nanoparticles exhibited that can significantly give reinforcement towards rubber/clay nanocomposites when the two materials are mixed [1]. Due to its improved physical or mechanical properties, thermal stability, gas permeability and so on, these rubber/clay nanocomposites have gained so much attention, especially in the rubber industry. Compared to unfilled rubber compounds, these rubber/clay nanocomposites are generally better in properties as mentioned. As the name suggests, nanocomposites are lighter in terms of weight and significantly is low cost.

There are several methods on how these nanocomposites could be formed; which include melt intercalation [2], in-situ polymerization process [3], intercalation of solution [4], and also the compounding of latex [5]. Latex compounding and melt mixing methods have been combined and rampantly used especially in the rubber industry [5], since it is considerably more environmental-friendly because no organic solvents are present in the system and has high compatibility with the system that is currently used in industries. The idea of latex compounding is that, during the initial stage of the process, the clay interlayer spacing is increased. During this stage, monomers form polymers due to the clay dispersion in the water that was happening and thus intercalation of matrix will happen within the widened spacing of the clay [6].

However, because nanocomposite itself is in nano-scale, agglomerations of particles of the filler tend to happen and therefore, the adhesion and compatibility of the filler with the polymer matrix need to be enhanced. It was proposed in this project that silane coupling agent could help in modifying the filler surface so as to induce a strong interaction between the polymer and filler, by silanization process. This process is significant in order to introduce reactions on the surface of hydroxyl ( $-OH$ ) groups abundant on the mineral (filler)

surface with the coupling agent [7]. Therefore, surface-functionalized filler was created in this project and believed to have improved the properties of the polymer from its matrix.

In this study, Kaolin filler was used as the main material, surface-functionalized with six coupling agents separately in order to investigate the best type of coupling agent to be employed in its latex compounding to produce synthetic rubber gloves. Furthermore, the surface-functionalized filler at the optimized coupling agent type – would then be prepared with different ratios or total solids content (TSC) to find the best optimized ratio or TSC for the filler for improved mechanical, morphological and thermal properties of the rubber produced.

The importance of this study is to improve the mechanical properties of synthetic rubber that will be produced with the incorporation of surface functionalized latex/filler nanocomposites from Kaolin clay as the main ingredient for filler. From the past recent studies, it has been shown that Kaolin filler could be one of the contributing agents in rubber production, during the latex compounding procedure. The present study is carried out in order to achieve the objectives as follows; to prepare Kaolin clay surface functionalized with different functionalization agents incorporated with Nitrile Butadiene Rubber (NBR) synthetic rubber and to investigate the mechanical properties of the various functionalized Kaolin filler in latex nanocomposites, to prepare various ratios or TSC of Kaolin filler to latex based on the optimized functionalized Kaolin, and to characterize mechanical, thermal and morphological properties of the optimized Kaolin filler in latex nanocomposites.

## 2. MATERIALS AND METHODS

### 2.1. Materials

Carboxylated nitrile butadiene rubber latex (NBR latex) was used as the core material to produce the rubber samples. Kaolin clay was used as the main constituents for Kaolin filler for the latex/filler nanocomposites purpose. For functionalization of the filler, six (6) silane coupling agents of product names USi-2301, USi-7301, USi-7311, USi-1212, USi-1302 and USi-5301 were used for the surface functionalization of Kaolin filler. After characterized by tensile test, USi-7301 has the highest elongation at break value, thus chosen to be the optimized sample. Then, this coupling agent is used for surface functionalization of Kaolin filler to be diluted to different ratios or TSC.

The raw chemicals for the Kaolin filler preparation as well as latex compound preparation as in Table 1 and Table 2 together with the aforementioned coupling agents in were obtained from Top Glove Sdn. Bhd via Avidco Asia Pacific Sdn. Bhd. as Top Glove's main supplier for chemicals that were purchased from China.

### 2.2. Kaolin Filler Preparation

The ingredients were mixed in a tank and stirred to produce a homogenous mixture and left to mature for 24-36 hours. Kaolin filler of appropriate mass to be used in few sets of latex compounding was made and a small portion of the filler was taken and diluted where necessary for latex compounding procedure (Table 1).

Table 1: Ingredients in preparing Kaolin filler

Ingredient (Chemical)	Mass percentage (%)
pH adjuster	< 4
Dispersing agent	1 – 5
Wetting agent	< 1
Thickener	1 – 2
Antifoam	< 1
Water	60 – 65
Calcined Kaolin clay	35

### 2.3. Latex Compounding

TSC, measured in percentage, was measured as the remaining weight of sample after drying, expressed in terms of the original weight of the wet sample as in Eq. 1.

$$\text{TSC \%} = \left[ \frac{(\text{weight of dry sample+container})-(\text{weight of empty container})}{(\text{weight wet sample+container})-(\text{weight empty container})} \right] \times 100 \% \quad (1)$$

The dosage of each chemical was measured in phr. In rubber industry, it is common to use this term to demonstrate the amount of chemicals needed to be incorporated with the raw latex for compounding purpose. Thus, the mass of each chemical with regards to their given dosage values in phr unit was as in Eq. 2.

$$\text{chemical mass (kg)} = \left[ \frac{\text{latex mass (kg)} \times \text{chemical dosage (phr)} \times \text{latex TSC}}{\text{chemical TSC}} \right] \times 100 \% \quad (2)$$

Table 2 shows the chemical formulation for the production of nitrile gloves with required dosage (phr) of each chemical. NBR latex, as the main ingredient for the synthetic glove samples production was initially stirred in the compounding tank based on its required amount. Then, the chemicals as in Table 2 were mixed with the raw latex. The compounded latex was then stirred for maturation purpose for 24-36 hours. The TSC of the compounded latex will then be checked upon maturation for clarification. The mixture was further diluted with water if necessary. Then, the samples were produced by hand-dip procedure in the production line.

Table 2: Formulation of NBR latex added with Kaolin filler and coupling agent

Ingredient (Chemical)	TSC (%)	Dosage (phr)
NBR latex	<b>44.5</b>	<b>100</b>
Kaolin filler	<b>35.0</b>	<b>7.0</b>
<b>(Variable in second objective)</b>		
Coupling agent	<b>100</b>	<b>0.3</b>
pH adjuster	25	1.4 – 2.0
Vulcanizing Accelerator	50	0.2 – 0.8
Vulcanizing agent	60	0.8 – 1.4
Vulcanizing activator	60	1.0 – 1.6
Wax	49	0.5 – 1.0
Wetting agent	25	0.2 – 0.4
Antifoam	10	0.02 – 0.06

## 2.4. Methods of Testing and Characterizations

The nitrile glove samples were produced in the factory's production line by hand-dip procedure. Hand-dip was done by plugging out of the hand-shaped ceramic mould before the latex dip process to be dipped in the lab scale-made compounded latex for 8-10 seconds before plugging in back to the production line. The ceramic mould temperature shall maintain its temperature in between 55 to 70 °C throughout the hand-dip process. The dipped moulds shall undergone processes such as leaching, chlorination, drying and cuff-beadrolling before stripping of the samples. Then, the glove samples were cut into dumbbell-shape by using the pneumatic cutter before tested for tensile properties (tensile strength, elongation at break, force at break). Universal tensile machine (Model: AI-3000) from Top Glove company was used for this purpose. Scanning Electron Microscope (SEM) was used to observe the morphological properties of the samples. The fractured surface of the samples was observed with Field Emission SEM (FESEM) (JOEL, JFC-1600) from IIUM, after the tensile test was done. The fractured samples were initially cut to an approximately 4 mm × 4 mm square shape and placed on the sample holder with the fractured surface facing upward. The microphotographs of the samples were generated at the magnification ×2300. Thermal properties of the samples were analyzed by using Differential Scanning Calorimetry (DSC) (METTLER TOLEDO DSC 3) from Top Glove, with heating rate of 10.0 °C/min, temperature range of -75 °C to 350 °C nitrogen gas, and a one-time heat process. The samples were cut into an approximately 2.0 mg.

## 3. RESULTS AND DISCUSSION

### 3.1. Tensile Properties

#### 3.1.1 Sample Tensile Properties with Different Silane Coupling Agents

Figure 1 shows tensile properties (tensile strength and elongation at break) for rubber samples incorporated with Kaolin filler functionalized with different silane coupling agents. It can be seen that the samples have the highest average tensile strength after the incorporation of USi-7311 (chloro family) silane coupling agent at 35.47 MPa, while the average tensile strength is the lowest with USi-1302 (amino family) silane coupling agent at only 28.24 MPa, when they were compared with the control samples. This could be due to the stronger bonding between the matrix and nanoparticles presented in the samples with USi-7311 compared to others [8]. USi-7301 of chloro family has elongation at break value of 632.589 % as well as considerably high tensile strength of 32.77 MPa. Here, polymer chains are believed to cross-link with each other that eventually strengthen the polymeric structure. Occasionally, the event leads to higher stress needed to elongate and rupture the sample that gives high elongation at break value [9]. The tested samples generally conform to the ASTM D639 standard requirement of minimum tensile strength and elongation at break of 14 MPa and 500 % respectively.

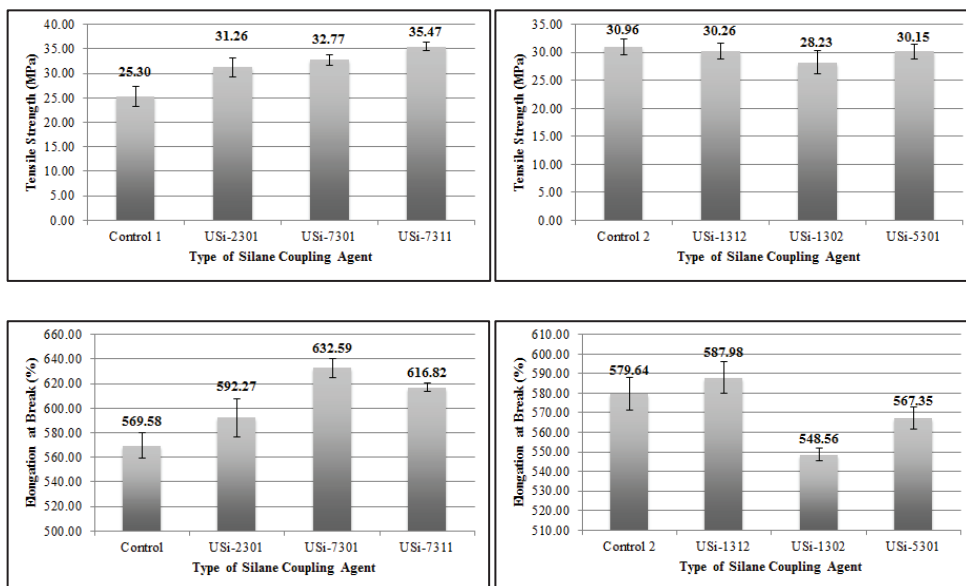


Figure 1: Tensile properties of rubber with Kaolin filler functionalized with different silane coupling agent.

### 3.1.2 Sample Tensile Properties with Different TSC of Kaolin Filler

The best optimized silane coupling agent used for the 35 % Kaolin filler is of type USi-7301 with tensile strength value of 32.77 MPa and elongation at break value of 632.589 %. This silane was further used to be incorporated with Kaolin filler of various TSC values (35, 32, 29, 26 and 23 %). Figure 2 shows the results for tensile properties (tensile strength and elongation at break) for rubber samples incorporated with different ratios or TSC Kaolin filler functionalized with USi-7301 silane coupling agent.

From Figure 2, all sets showed increase in the rubber’s tensile strength relatively with filler addition at decreasing solids content. Theoretically, better spreading of the silane coupling agent used throughout the filler surface occurs here since the solids content is lower to achieve better silane spreading on the filler surface, thus the rubber’s tensile strength improved [10].

The average elongation at break for the samples at 35 % TSC of filler is much lower than the ones with lower TSCs, and 23 % TSC of Kaolin filler loadings with the highest elongation at break value of 587.248 %. At this Kaolin filler’s TSC, it is believed that the polymer chains gives better cross-link with each other and stronger the polymeric structure which in turns giving higher stress needed to elongate and rupture the sample [8].

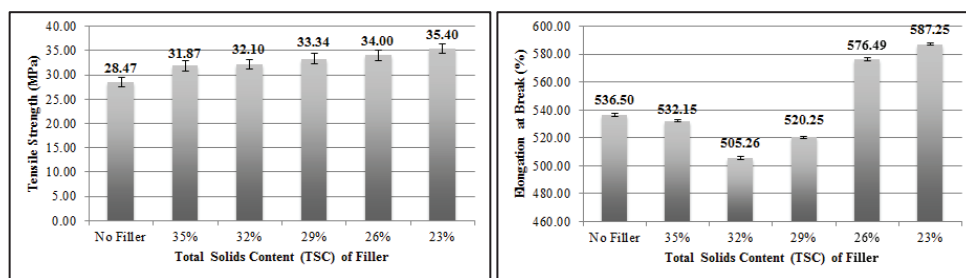


Figure 2: Tensile properties of rubber with optimized silane coupling agent in different ratios (TSC) of Kaolin filler.

### 3.2. Morphological Properties

Four (4) samples as follows were taken for characterization under SEM to analyze their surface morphology and filler behavior in the rubber matrix, respectively: (i) rubber sample without fillers, (ii) rubber sample with Kaolin filler but without silane coupling agent, (iii) rubber sample with Kaolin filler functionalized with USi-7301 silane, and (iv) rubber sample with Kaolin filler of 26 % TSC functionalized with USi-7301. Figure 3 shows FESEM analysis on the four samples under 2300× magnification.

As can be observed from Figure 3, the surfaces can be justified to be smooth in Figure 4 (a) and (b), but rough in (c) and (d). With the presence of silane coupling agent USi-7301 (Figures 4 (c) and (d)), a better adhesion between Kaolin filler and rubber matrix were believed to happen here. Kaolin filler well wetted by the rubber matrix and the pulled out of filler from rubber matrix is minimum [11]. These figures also show that the surface has many tear lines with branching. This type of failure indicates strong adhesion between filler and rubber matrix. However, the film is rougher than the control rubber sample with more pronounced undulating curves. Particles are very obviously accompanied by cracks and grooves. The formation of surface cracks suggests the occurrence of phase separation between the hydrophilic filler and the hydrophobic rubber matrix [12].

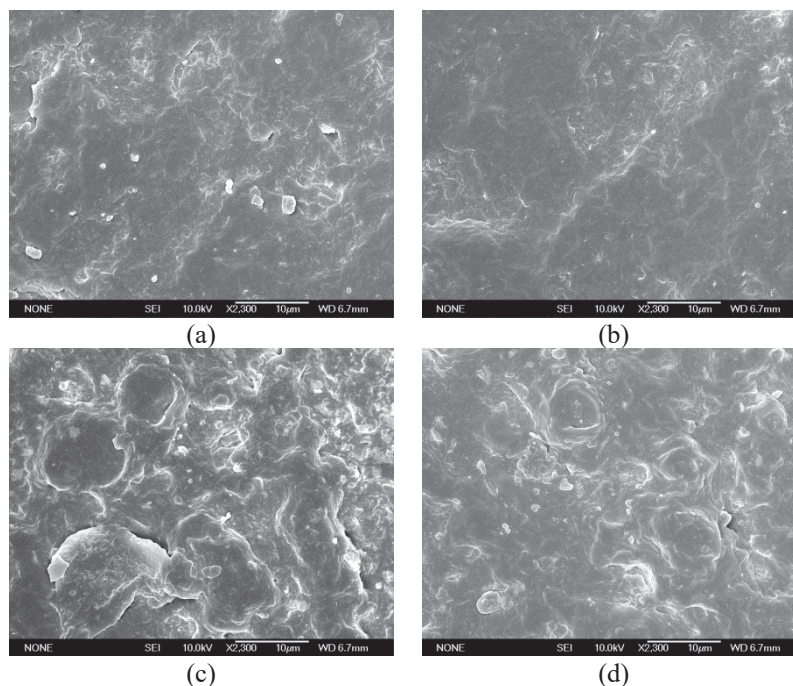


Figure 3: SEM images of the control (a, b) and the optimized samples (c, d) at ×2300 magnification.

### 3.3. Thermal Properties

The same 4 samples were taken for characterization in analyzing their thermal properties by using DSC. The results were based on the use of DSC on graph plotting. Table 3 shows the results of thermal analysis of the samples, with respective glass-transition temperatures ( $T_g$ ).

Table 3:  $T_g$  values of samples in DSC analysis.

Sample	$T_g$ value (°C)	Decomposition Temperature (°C)
Rubber sample without fillers	-20.67	244.88
Rubber sample with Kaolin filler but without silane coupling agent	-19.62	241.80
Rubber sample with Kaolin filler functionalized with USi-7301 silane	-20.98	240.19
Rubber sample with Kaolin filler of 26 % TSC functionalized with USi-7301	-20.80	236.30

From the results in the DSC curve tabulated in Table 3, on further heating the samples, the sudden shifting down of the 4 curves indicate that there is more heat flow. The onset temperature value for sample with USi-7301 silane has the absolute  $T_g$  value of -20.98 °C. Thus, there is more in the heat capacity of the sample compared to the others. In contrast, the sample without silane coupling agent functionalizing the filler has the lowest absolute  $T_g$  value -19.62 °C. Apparently, all the samples had gone through glass transition, and the change in heat capacity is more on the sample with USi-7301. However, the change doesn't occur suddenly, but takes place over a temperature range.

The curve also had shown no crystallization peak, which means the polymer cannot form crystals. Apparently, for nitrile rubber, it is amorphous, thus the samples will not show any crystallization or any melting behavior [13, 14]. Towards the end of the plots, the highest decomposition temperature is for the sample containing no filler, at 244.88 °C, and the lowest decomposition temperature 236.30 °C achieved for the samples with Kaolin filler TSC of 26 % functionalized with USi-7301 silane coupling agent. The samples are rendered safe to be used for handling materials at relatively high temperature.

#### 4. CONCLUSION

In this study, one of the fillers that have the potential to be further employed and commercialized in rubber or polymer industry – the Kaolin filler, from its clay based – was prepared and characterized with silane coupling agent and optimized. USi-7301 silane coupling agent was taken to be the optimized functionalization agent with tensile strength value of 32.77 MPa and elongation at break value of 632.589. Optimized content of 26 % TSC Kaolin filler in the rubber composites has exhibited tensile strength value of 34.00 MPa and elongation at break value of 576.494 %. USi-7301 and Kaolin filler TSC of 26 % showed rough surface morphology with glass transition temperature of -20.98 °C and -20.80 °C respectively. This sample can further be explored for its potential in the gloves production.

#### ACKNOWLEDGEMENT

The corresponding author would like to thank IIUM Faculty of Engineering and Top Glove Sdn. Bhd. and its R&D department for the supports in accomplishing this project. Not to forget, also thanks to Top Glove's main chemical and equipment suppliers for this project for samples preparation and characterizations. Top Glove company, the world's largest rubber glove manufacturer had also provided space in their production line for the samples' production.

## REFERENCES

- [1] Mohd Nor, N. A., Muttalib, S. N., & Othman, N. (2016). Synthesis of Natural Rubber/Palygorskite Nanocomposites via Silylation and Cation Exchange. *Nanoclay Reinforced Polymer Composites*, 261-289. doi:10.1007/978-981-10-1953-1\_12A.
- [2] Lu, M., Zhou, J., Wang, L., Zhao, W., Lu, Y., Zhang, L., & Liu, Y. (2010). Design and Preparation of Cross-Linked Polystyrene Nanoparticles for Elastomer Reinforcement. *Journal of Nanomaterials*, 2010, 1-8. doi:10.1155/2010/352914.
- [3] Okamoto, M., Morita, S., Taguchi, H., Kim, Y. H., Kotaka, T., & Tateyama, H. (2000). Synthesis and structure of smectic clay/poly(methyl methacrylate) and clay/polystyrene nanocomposites via in situ intercalative polymerization. *Polymer*, 41(10), 3887-3890. doi:10.1016/s0032-3861(99)00655-2.
- [4] Paul, P. K., Hussain, S. A., Bhattacharjee, D., & Pal, M. (2013). Preparation of polystyrene–clay nanocomposite by solution intercalation technique. *Bulletin of Materials Science*, 36(3), 361-366. doi:10.1007/s12034-013-0498-4.
- [5] Tan, J., Wang, X., Luo, Y., & Jia, D. (2012). Rubber/clay nanocomposites by combined latex compounding and melt mixing: A masterbatch process. *Materials & Design*, 34, 825-831. doi:10.1016/j.matdes.2011.07.015.
- [6] Mohd Nor, N. A., Muttalib, S. N., & Othman, N. (2016). Synthesis of Natural Rubber/Palygorskite Nanocomposites via Silylation and Cation Exchange. *Nanoclay Reinforced Polymer Composites*, 261-289. doi:10.1007/978-981-10-1953-1\_12.
- [7] Tatou, M., Genix, A., Imaz, A., Forcada, J., Banc, A., Schweins, R., ... Oberdisse, J. (2011). Reinforcement and Polymer Mobility in Silica–Latex Nanocomposites with Controlled Aggregation. *Macromolecules*, 44(22), 9029-9039. doi:10.1021/ma2012893
- [8] Nassar, A., & Nassar, E. (2013). Study on Mechanical Properties of Epoxy Polymer Reinforced with NanoSiC particles. *Nanoscience and Nanoengineering*, 1(2), 89–93. <https://doi.org/10.13189/nn.2013.010201>.
- [9] Nair, K. P., Nair, A. B., & Joseph, R. (2014). Carboxylated acrylo nitrile butadiene rubber latex/kaolin nanocomposites: preparation and properties. *Composite Interfaces*, 21(6), 571-583. doi:10.1080/15685543.2014.899198.
- [10] Takatoh, K., Sakamoto, M., Hasegawa, R., Koden, M., Itoh, N., & Hasegawa, M. (2005). *Alignment Technology and Applications of Liquid Crystal Devices*, 90-95. Boca Raton: CRC Press.
- [11] Alkadasi, N. A., Sarwade, B. D., Hundiwale, D. G., & Kapadi, U. R. (2004). Studies on the effect of titanate coupling agent (2.0%) on the mechanical properties of flyash-filled polybutadiene rubber. *Journal of Applied Polymer Science*, 93(3), 1293-1298. doi:10.1002/app.20548.
- [12] A. Ndabigengesere, K. B. Narasiah, and K. Subraimanian. “Quality of water treated by coagulation using Moringa oleifera seeds,” *Water Res.* Vol. 32, no. 3, pp. 781-791, 1998.
- [13] Song, Q., Tan, Z., Zhang, Y., Sha, L., Deng, X., Deng, Y., ... Yang, L. (2014). Do the rubber plantations in tropical China act as large carbon sinks? *iForest - Biogeosciences and Forestry*, 7(1), 42-47. doi:10.3832/ifor0891-007.
- [14] Shanks, R. A., & Kong, I. (2013). General Purpose Elastomers: Structure, Chemistry, Physics and Performance. *Advanced Structured Materials*, 11-45. doi:10.1007/978-3-642-20925-3\_2.

## EFFECT OF CHITIN SOURCE AND CONTENT ON PROPERTIES OF CHITIN NANOWHISKERS FILLED POLYLACTIC ACID COMPOSITES

SYAZEVEN EFFATIN AZMA MOHD ASRI<sup>1</sup>, ZAINOHA ZAKARIA<sup>1</sup>,  
AZMAN HASSAN<sup>2\*</sup> AND MOHAMAD HAAFIZ MOHAMAD KASSIM<sup>3</sup>

<sup>1</sup>Department of Chemistry, Faculty of Science,  
Universiti Teknologi Malaysia, Skudai, Malaysia

<sup>2</sup>Department of Bioprocess and Polymer Engineering,  
School of Chemical and Energy Engineering,

Faculty of Engineering, Universiti Teknologi Malaysia, Skudai, Malaysia

<sup>3</sup>School of Industrial Technology, Universiti Sains Malaysia, Penang, Malaysia

\*Corresponding author: [azmanh@cheme.utm.my](mailto:azmanh@cheme.utm.my)

(Received: 4<sup>th</sup> May 2020; Accepted: 14<sup>th</sup> June 2020; Published on-line: 4<sup>th</sup> July 2020)

**ABSTRACT:** This study investigates the use of chitin nanowhiskers (CHW) from different chitin sources to develop CHW reinforced polylactic acid (PLA) nanocomposite. Chitin sources used in this study were commercial chitin (CC), fermented chitin (FC) and treated fermented chitin (TFC) whereby FC and TFC were obtained from fermentation of prawn waste. The chitin was then undergoes acid hydrolysis to produce commercial chitin nanowhiskers (CCHW), fermented chitin nanowhiskers (FCHW) and treated fermented chitin nanowhiskers (TFCHW). PLA was chosen due to several advantages such as biodegradability, good mechanical strength and in line with global pressure to improve environmental pollution aspects. Tensile strength for PLA/FCHW, PLA/TFCHW and PLA/CCHW increased with increasing filler content until it reached optimum value at 1 phr, 2 phr and 3 phr, respectively. Young's modulus for the nanocomposites increased with increasing filler content but elongation at break decreased significantly with increasing filler content for all types of nanocomposites. TGA results indicated that PLA/CHW nanocomposites displayed better thermal stability as compared to pure PLA. The biodegradability and water absorption of nanocomposites increased with increasing filler content. The overall results confirm that PLA nanocomposites from FC are not inferior than PLA nanocomposites from CC and therefore has similar potential to be used in packaging applications.

**ABSTRAK:** Kajian ini menyelidik penggunaan nanowisker kitin (CHW) dari sumber kitin yang berbeza untuk membangunkan komposit poli(asid laktik) (PLA) bertetulang CHW. Sumber-sumber kitin yang digunakan dalam kajian ini terdiri daripada kitin komersial (CC), kitin ditapai (FC) dan kitin ditapai yang dirawat (TFC) di mana FC dan TFC diperolehi daripada penapaian sisa udang. Kitin kemudiannya menjalani proses hidrolisis asid untuk menghasilkan nanowisker kitin komersial (CCHW), nanowisker kitin ditapai (FCHW) dan nanowisker kitin ditapai yang dirawat (TFCHW). PLA dipilih kerana kelebihannya misalnya kebolehan pereputan-bio, kekuatan mekanikal yang baik dan sesuai dengan tekanan global untuk memperbaiki aspek pencemaran alam sekitar. Kekuatan regangan untuk PLA/FCHW, PLA/TFCHW dan PLA/CCHW meningkat dengan peningkatan kandungan pengisi sehingga mencapai nilai optimum masing-masing pada 1 phr, 2 phr dan 3 phr. Modulus Young bagi komposit nano meningkat dengan peningkatan kandungan pengisi tetapi ciri pemanjangan takat putus menurun dengan ketara dengan peningkatan kandungan pengisi bagi semua jenis komposit nano.

Keputusan TGA menunjukkan bahawa komposit nano PLA/CHW memaparkan kestabilan terma yang lebih baik berbanding dengan PLA tulen. Kadar pereputan-bio dan penyerapan air komposit nano meningkat dengan peningkatan kandungan pengisi. Hasil keseluruhan mengesahkan bahawa komposit nano PLA daripada FC tidak lebih rendah daripada komposit nano PLA dari CC dan berpotensi serupa untuk digunakan dalam aplikasi pembungkusan.

---

**KEYWORDS:** *chitin; nanowhiskers; prawn waste; polylactic acid; nanocomposites*

## 1. INTRODUCTION

Chitin is one of the most abundant natural polysaccharides that exist in nature and is found in the outer skeleton of crustaceans such as shrimp, lobster and crab. It is known to possess many desirable properties such as biocompatible, antibacterial [1] and is found to have desirable mechanical properties due to their natural stacks of chitin nanowhiskers (CHW) [2]. Research and development on CHW sparked new interest following the successful use of nanocrystalline fractions from cellulose as fillers in nanocomposites [3-7] since both cellulose and chitin shared similar backbone structure. Natural polymers such as chitin, starch and cellulose consist of both crystalline and amorphous region. Various methods have been employed in production of CHW. One of the methods that are widely used is through acid hydrolysis [8]. The crystalline region in nanoscale size once isolated can be used as reinforcing nanofillers in polymer nanocomposites [9-10].

Synthetic polymers have become an essential part of our lives; having wide applications in various fields including in agriculture, packaging and in medical applications [11]. Although synthetic polymers have many advantages, the lack of biodegradability is one of the setbacks and has caused serious polluting effects on the environment. Therefore interests on biopolymers which are biodegradable and are synthesized from renewable resources [12] have increased among the academicians and researchers globally as indicated by the expanding literatures [13-15].

Poly(lactic acid) (PLA) is the most promising bio-based and biodegradable thermoplastic, and is considered as a 'green' eco-friendly material. It is an aliphatic polyester and fulfils many requirements as a packaging thermoplastic and is suggested as a material for general packaging applications [16]. To enhance the competitiveness of PLA, many properties such as mechanical and thermal can be further improved. In addition, the reinforcement of PLA using natural nano-fillers is interesting to be considered as it is expected to improve biodegradability besides enhancing the mechanical and thermal properties due to their nanosize crystals. Previous report mentioned that addition of chitin nanofibrils (CNs) as reinforcing fillers do not alter the other properties of PLA based materials; hence proposing that this additive can be used in bioplastic items mainly exploiting its intrinsic anti-microbial and skin regenerating properties [17].

Several studies have reported on the use of CHW as reinforcing filler in PLA [18-19]. The earliest work was on the fabrication and characterization of melt-blended PLA/chitin composites in which the CHW was produced by an acid hydrolysis. Interestingly, the study showed that the stiffness of the composites increased with increasing chitin content while the strength decreased. In a later study, the effect of surface acetylated CHW on structure and mechanical properties of PLA was determined [20]. In the study, the miscibility between CHW and PLA was improved by surface acetylation of CHW. The acetylated CHW was incorporated into a PLA matrix by solution blending, and resulted in an increase of tensile strength and Young's modulus and they reached to the maximum value as 45 and 37% higher than neat PLA film, respectively, with the loading level of

acetylated CHW reaching to 4 wt %. The enhancement could be attributed to that acetylation improved dispersion of acetylated CHW in the PLA matrix and interfacial adhesion between acetylated CHW and PLA. Recently, the effect of CHW on crystallization of triethyl-citrate-plasticized PLA has also been reported [21]. The addition of a small amount (1 wt %) of CHW to plasticized PLA significantly affected its nucleation, crystal size, and crystallization speed. In the previous study, CHW were chosen to surface modify PLA film to better utilize and combine the advantages of PLA matrix and CHW [22]. The resulting film prepared via the vertical coating method through shearing force action has significantly better strength and modulus compared to conventional solution blending. On the other study, electrospun composite nanofibers membrane of PLA and the surface grafted chitin whiskers resulted in superior tensile strength and modulus as compared to pure PLA. This is mainly due to the hydrophilicity of PLA was improved by the introduction of CHW [23]. In a recent study, it was reported that PLA based films containing CNs resulted in biocompatibility and able to stimulate the production of cell defensins, acting as an indirect anti-microbial agent [24].

In recent years, a biotechnological approach using lactic acid fermentation to purify chitin from prawn waste [25-26] provides an environmentally friendly approach as opposed to the conventional chemical method. The biological approach produces two industrially important products namely a protein-rich liquid fraction and a chitin solid fraction. Besides reducing the usage of hazardous chemicals by the conventional methods, the biological approach is able to conveniently recover the protein-rich fraction via a suitable bioreactor [25] and has been shown to be a suitable source of protein for aquaculture feed [26]. Meanwhile, finding good use to the chitin by-product fraction will give added advantage to the fermentation process.

In the present work, CHW from the chitin fraction of fermented prawn waste is investigated as nanoscale fillers to reinforce PLA. Prawn waste is widely produced from prawn processing industries and its disposal is becoming an issue due to its high perishability. Thus, its proper disposal and putting it to good use is becoming more urgent. To date, no study has been done on using CHW obtained from fermented chitin as fillers in PLA. In this study, CHW from chitin through fermentation of prawn waste is being produced as potential material for polymer reinforcement in an attempt to replace commercial chitin produced through harsh chemical treatment. The objective of this study is to compare the effects of CHW from fermented chitin with the chitin obtained through chemical method on mechanical, physical and thermal properties of CHW reinforced PLA composites.

## 2. EXPERIMENTAL

### 2.1 Materials

PLA was obtained from NatureWork<sup>TM</sup> (PLA 300ID). The density of PLA is 1.25 g/cm<sup>3</sup>, melting temperature of 145-155°C, glass transition temperature of 55-58°C, crystallinity of up to 37% and it has an average molecular weight of Mw: 220 kDa and Mn: 101 kDa. Chitin sources are i) fermented chitin (FC) produced by fermentation treatment of tiger prawn waste, ii) treated fermented chitin (TFC) which is basically an FC that undergoes an extra mild acid and alkaline treatment and iii) chitin from prawn shells purchased from Sigma Aldrich designated as commercial chitin (CC) for comparison. All types of chitin sources underwent hydrolysis and dialysis through treatment with hydrochloric acid to produce CHW. The solvent used to dissolve the PLA is chloroform, purchased from Merck Malaysia.

## 2.2 Production of Chitin via Fermentation of Prawn Waste

Tiger prawn (*Penaeus monodon*) waste obtained from a local prawn processing industry in Johor consisted of head, exoskeleton, and tail portion were minced through a 4.5 mm die plate using an industrial mincer (Rheninghaus Meat Mincer, model EVE/ALL 22, Italy) and were fermented using effective microorganism (EM) which has been activated with palm sugar for a week prior to use [26]. Fermentation of minced prawn waste was carried with addition of 10% (w/w) of carbohydrate sources (glucose or brown palm sugar) and 10% (v/w) activated EM in a loosely covered bottle and incubated at 37°C for 72 hours. The mixture was occasionally stirred especially during the first 24 hours and pH was monitored using bench top pH meter (Hanna Instruments, Italy). The fermented product is separated into solid chitin; fermented chitin (FC) and liquid proteinaceous fraction. For the production of treated fermented chitin (TFC), FC was hydrolysed in 1M HCl at room temperature for 1 hour followed by another hour in 1M NaOH solution. Both FC and TFC were washed, dried and kept at room temperature for further use.

## 2.3 Preparation of Chitin Nanowhiskers (CHW)

CHW was prepared through acid hydrolysis method [8]. Fermented chitin (1.0 g) was hydrolyzed in boiling 3N HCl for 1 hour. After hydrolysis, chitin was diluted with distilled water (40 mL) and centrifuged at 3200 rpm for 15 minutes and this process were repeated thrice. The chitin extract was dialyzed in cellulose dialysis tubing against continuous water flow for 2 hours. The dialysis process was continued by immersing the dialysis tubing in a beaker of distilled water until it reaches pH 4. The chitin extract designated as fermented chitin nanowhiskers (FCHW) was sealed and stored at 4°C. Similar steps were repeated using treated fermented chitin (TFC) and commercial chitin (CC) producing treated fermented chitin nanowhiskers (TFCHW) and commercial chitin nanowhiskers (CCHW) respectively. All samples of nanowhiskers were characterized using FTIR and TEM.

## 2.4 Preparation of PLA and PLA/CHW nanocomposites

An amount of 10 g of PLA pellets were fully dissolved in chloroform through constant stirring in a water bath at 60°C for approximately 60 minutes [7]. The solution was evenly spread on a glass plate using a fabricated spreader and the film was left to dry by evaporation at ambient temperature for 48 hours. Dried film was kept in a desiccator until further use. The thickness of the cast film was approximately  $100 \pm 0.125 \mu\text{m}$  and designated as PLA. The PLA/CHW nanocomposites were prepared by mixing PLA with different types of CHW (FCHW, TFCHW and CCHW) at different CHW contents (1, 2, 3 and 4 phr) following the same method in production of PLA film. Nanocomposites of PLA/FCHW, PLA/CCHW and PLA/TFCHW were analysed for mechanical, thermal, water absorption properties and biodegradability.

## 2.5 Characterizations

### 2.5.1 Fourier Transform Infrared Spectroscopy

FTIR spectroscopy was performed using Perkin Elmer 1600 infrared spectrometer (USA). All types of CHW were characterized using liquid method through suspension casting. All samples were recorded at 32 scans with a resolution of  $4\text{cm}^{-1}$  and within the wavenumber range from 370 to  $4000\text{cm}^{-1}$ .

### 2.5.2 Transmission Electron Microscopy

The study of surface morphology of CNW from various sources of chitin (FCHW, TFCHW and CCHW) were evaluated using Hitachi Hd-2000 scanning transmission electron microscopy (TEM). Samples were prepared by placing 5  $\mu\text{L}$  diluted suspension of

FCHW, TFCHW and CCHW on the carbon-coated grid and was allowed to dry at room temperature. The samples were negatively stained by allowing the grids to float in a 1% uranyl diacetate solution for 3 minutes. The samples were examined at an accelerating voltage of 120kV. The TEM images were obtained by using soft imagine system software.

### 2.5.3 Tensile Testing

Tensile test was performed according to ASTM D882 using Lloyd LRX (USA) machine under ambient condition. Rectangular specimens were cut from the obtained cast film with dimension 60 x 12.6 x 0.1 mm<sup>3</sup>. The crosshead speed of 12.5 mm/min with 30 mm gauge length was used. Tensile strength, elongation at break and Young's modulus were determined. Seven specimens for each formulation were tested and mean value was recorded.

### 2.5.4 Thermogravimetric Analysis

Thermogravimetric analyses (TGA) and Derivative Thermogravimetric (DTG) were used to determine thermal stability of the PLA nanocomposites by tracking weight change during a ramp to 600°C at 20°C/min with nitrogen purge.

### 2.5.5 Water Absorption

Water absorption test was carried out according to ASTM D570-81. The sample (20 x 20 x 0.1 mm<sup>3</sup>) was dried to a constant weight (W<sub>0</sub>) in vacuum oven prior to the test and was then immersed in distilled water at ambient temperature for 2 hours and 24 hours. Wet weight after immersion (W<sub>i</sub>) were taken and percentage weight gain was taken as the water absorption values using Equation (1),

$$\text{water absorption (\%)} = [(W_i - W_0) / W_0] \times 100 \quad (1)$$

### 2.5.6 Soil Burial Test

Soil burial test was conducted with the purpose of studying biodegradation of composites in natural conditions using garden soil [25]. The garden soil used contained a balance of three soil materials namely silt, sand and clay with humus. It has a pH of 6-6.5 and high calcium levels because of its previous organic matter content. Rectangular samples (20 x 20 x 0.1 mm<sup>3</sup> dimension) were kept in a desiccator until a constant weight (W<sub>1</sub>) was achieved. The samples were buried in garden soil at a depth of 170-220 mm from the soil surface for durations of 1-8 weeks. The soils were sprayed with water every 24 hours to maintain its moisture. After selected durations, samples were washed with water to remove the soil from the surface of samples and dried at 55°C in vacuum oven and was weighed to a constant weight (W<sub>2</sub>). The percent weight loss (WL) was calculated according to Equation (2).

$$\text{WL (\%)} = [(W_1 - W_2) / W_1] \times 100 \quad (2)$$

## 3. RESULTS AND DISCUSSION

### 3.1 Fourier Transform Infrared Spectroscopy

FTIR spectroscopy is an indispensable technique and relatively simple method to obtain information on any possible changes in the chemical structure of the chitin after undergoing chemical acid hydrolysis to produce CHW. FTIR spectra of various types of CHW (FCHW, CCHW and TFCHW) are shown in Fig. 1 and their vibrational assignments are summarized in Table 1.

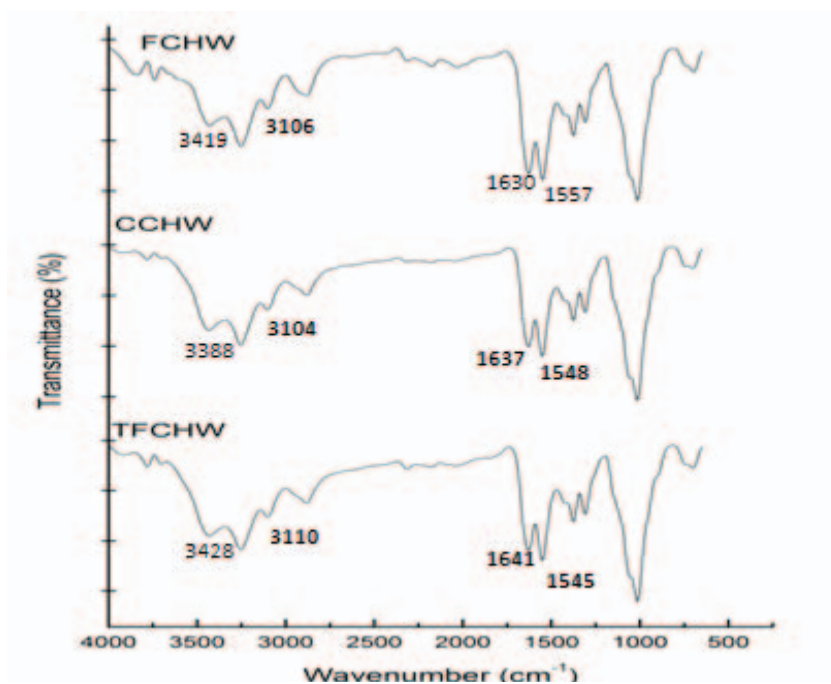


Fig.1: FTIR spectra of FCHW, CCHW and TFCHW.

Table 1: FTIR spectra peak assignments for chitin whiskers (FCHW, CCHW and TFCHW).

Peak assignment	Peak frequency (cm <sup>-1</sup> )		
	FCHW	CCHW	TFCHW
O-H groups	3419	3388	3428
N-H stretching	3106	3104	3110
C-H stretching	2923	2883	2869
C=O (Amide I)	1630	1637	1641
C=O (Amide II)	1557	1548	1545
C-H bending	1473	1380	1372
C-N groups	1384	1308	1317
C-O stretching	1112	1074	1024
N-H bending	722	762	713

Based on the FTIR spectra, all samples showed similar absorption bands at two main absorbance regions around 1600 cm<sup>-1</sup> and 2800-3500 cm<sup>-1</sup> indicating that all samples have similar chemical compositions. The characteristic carbonyl (C=O) stretching around 1640 cm<sup>-1</sup> is attributed to the carbonyl vibrations of amide functional group. Some of the carbonyl groups (Amide I) are bonded through hydrogen bonds to the amino group inside the same chain (C=O---H-N) that is responsible for the vibration mode at around 1640 cm<sup>-1</sup> while the rest creates similar bond with -CH<sub>2</sub>OH from the side chain. This additional bond created the slightly lower peak of Amide II at around 1560 cm<sup>-1</sup>. The existence of these interchain bonds is responsible for the high chemical stability of the  $\alpha$ -chitin structure [1,28,29]. The presence of amide group was further strengthened by appearance of C-N absorption band at around 1370 cm<sup>-1</sup> and N-H bending around 720-770 cm<sup>-1</sup>.

In the corresponding region of the OH and NH (3600-3000 cm<sup>-1</sup>) groups, all samples exhibit similar vibrational stretching peaks. This is attributed to the different packing

arrangements of the macromolecules. The shoulder that appears in the spectrum at  $3426\text{ cm}^{-1}$  is attributed to the intramolecular hydrogen bond involving the OH on carbon 6 and carbonyl oxygen (OH (6)---O=C). The band appears at  $3315\text{ cm}^{-1}$  corresponds to the intramolecular hydrogen bond (OH (3)---O(5) from the ring). The bands at  $3100\text{-}3270\text{ cm}^{-1}$  are assigned to the vibrational assignments of the NH of the amide (intermolecular hydrogen bond C=O—H-N and the NH groups intramolecularly bonded by H). Similar observations have been reported in the study of chitin from shrimp, prawn, king crab, squid and lobster [30].

The FTIR spectra of all samples displayed similar absorption bands denoting that there is no significant difference between the CHW from various sources of chitin and that the hydrolysis process was successful in producing CHW and did not alter the chemical structures. The hydrolysis done in a controlled condition as shown in this study was able to protect the chemical groups of chitin. On another note, it is envisaged that the milder fermentation treatment during production of fermented chitin (FC) could protect the polymeric structure of chitin which in turn will produce a higher aspect ratio chitin nanowhiskers (FCHW).

### 3.2 Transmission Electron Microscopy

Transmission electron microscopy (TEM) was performed to confirm the separation of individual crystallites into nanowhiskers. TEM is considered a powerful technique in characterization of nanomaterials. The analysis of the suspension of FCHW, CCHW and TFCHW shown in Fig. 2 (a)-(c) revealed some changes in the morphological features of the chitin after the acid hydrolysis treatment. As anticipated, TEM images showed the typical rod-like nanoparticles for FCHW, CCHW and TFCHW confirming that the treatment used was successful in producing the individual rod-like chitin nanowhiskers. Interesting observations can be seen on the size differences of various CHW.

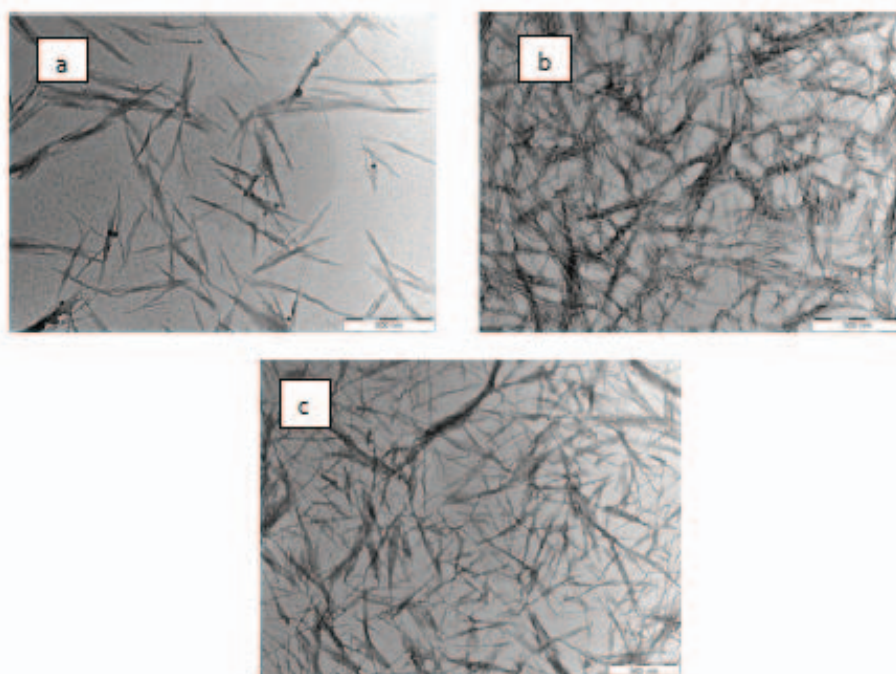


Fig.2: TEM of a) FCHW, b) CCHW and c) TFCHW.

The average size of FCHW was found to be more than 500 nm in length and 10 nm in width as compared to CCHW which recorded about 300 nm in length and 10 nm in width.

Meanwhile when the fermented chitin was chemically treated prior to hydrolysis to form whiskers, the width of TFCHW was found to be shorter than FCHW which is about 300 nm length and 20 nm widths in average. The extra chemical pretreatment of fermented chitin had probably shortened the polymeric chitin chain, hence producing a shorter CCHW. Based on the usual trend of the positive effect of using higher aspect ratio CHW, the slightly higher aspect ratio of FCHW is expected to give comparable if not a better reinforcing performance as fillers in PLA compared to using CHW from commercial chitin source (CCHW). It is also interesting to note that FCHW displayed many individual whiskers as compared to aggregated and stacked whiskers in CCHW and TFCHW. This characteristic may produce a better reinforcement to the PLA matrix.

### 3.3 Tensile Properties of PLA Nanocomposites

The effects of FCHW, CCHW and TFCHW content on the tensile strength, elongation at break and Young's modulus of PLA/FCHW, PLA/CCHW and PLA/TFCHW composites are shown in Fig. 3, 4 and 5, respectively. Figure 3 shows that incorporation of all types of CHW showed an increase in tensile strength of the nanocomposites as compared to pure PLA (11.95 MPa). For all nanocomposite samples, the tensile strength increased until a maximum value before it started to decrease. The maximum values differ for each nanocomposite. The maximum values are 1, 2 and 3 phr for PLA/FCHW (17 MPa), PLA/TFCHW (12 MPa) and PLA/CCHW (21 MPa) respectively. The highest value is PLA/CCHW nanocomposite, which increased by 91% at 3 phr compared to pure PLA. This is followed by PLA/FCHW by 54% at 1 phr and 36% increment for PLA/TFCHW at 2 phr content. However, the trend between PLA/FCHW and PLA/CCHW were different after 2 phr, whereby the tensile strength of PLA/CCHW continued to increase until it reached the maximum value at 3 phr. The tensile strength of PLA/FCHW on the other hand decreased after 2 phr.

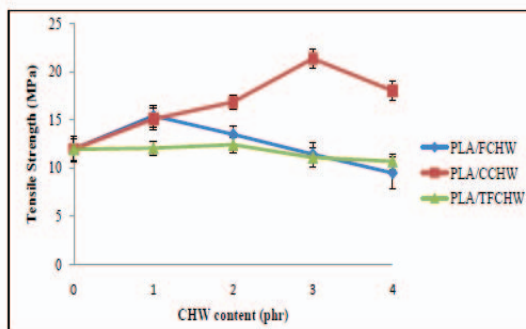


Fig. 3: Effect of FCHW, CCHW and TFCHW content on tensile strength of PLA/FCHW, PLA/CCHW and PLA/TFCHW.

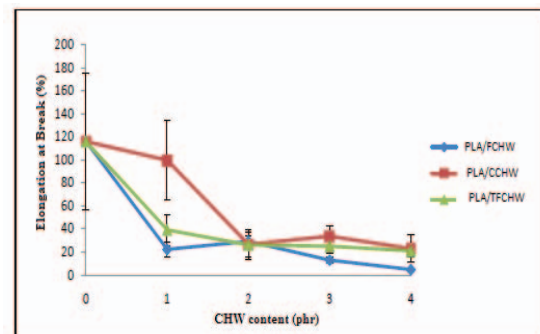


Fig. 4: Effect of FCHW, TFCHW and CCHW content on elongation at break of PLA/FCHW, PLA/TFCHW and PLA/CCHW.

The general improvement in the tensile strength of nanocomposites indicates that there is a good interfacial adhesion between the fillers (FCHW, CCHW and TFCHW) with PLA matrix leading to good stress transfer between the matrix and fillers. This is likely due to the good dispersion of fillers, stiffness of the fillers and existence of hydrogen bonding between N-H group on CHW and the lone pair of electrons on C=O of PLA matrix. In addition hydrogen bonds may also formed between terminal hydroxyl group of PLA and C=O of CHW (Fig. 6).

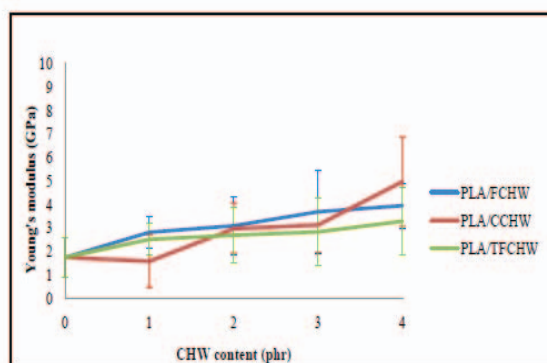


Fig.5: Effect of FCHW, TFCHW and CCHW content on Young's modulus of PLA/FCHW, PLA/TFCHW and PLA/CCHW.

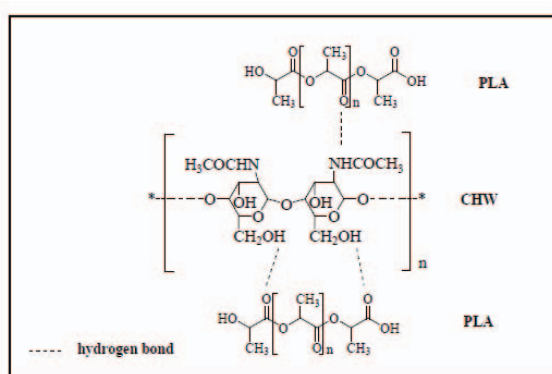


Fig. 6: Possible intermolecular interactions between PLA and CHW.

The formation of hydrogen bonding was also reported when cellulose nanowhiskers (CNW) were used as fillers in PLA nanocomposites due to the presence of polar O-H groups on CNW backbone chain [31]. Cellulose and chitin have the same molecular structure except for replacement of OH on carbon-2 with an acetyl amino (amide) group. Hence, a slightly lower intermolecular attraction between CHW with PLA is expected with CHW due to fewer amounts of OH groups on CHW.

As mentioned earlier, after the optimum filler content, the tensile strength for all nanocomposites decreased. The most likely reason is due to agglomeration among the whiskers of FCHW, CCHW and TFCHW in PLA when their content increases since hydrogen bonding between CHW-CHW molecules is more likely to form with increasing filler content. These filler-filler interactions reduce the level of filler-matrix interactions in the system. The aggregation of the filler could act as stress-centralized point and reduced surface area of interaction between filler and matrix leading in an inefficient transfer of stress from matrix to fillers resulting in low tensile strength values of PLA nanocomposites. Similar observation of reduction in strength after a certain filler content has been reported in many previous studies on PLA nanocomposites [7,32].

In terms of comparison between types of CHW from different sources, it can be concluded that CCHW had the highest increase compared to FCHW and TFCHW. CCHW is a pure chitin whereas FCHW had slight impurities of protein and minerals due to the incomplete purification of chitin during fermentation method. As for the TFCHW, it was too purified such that the polymeric chitin may have been shortened and may have affected the resulting tensile strength of the nanocomposites. Besides its poorer performance, usage of TFCHW is also not cost effective as it needed to undergo an extra

chemical treatment prior to production of CHW. FCHW is a promising material for reinforcement of PLA as it does increase the tensile strength of PLA and also relatively lower cost to produce FCHW compared to CCHW since fermented chitin is a by-product of fermentation of prawn waste for the production of protein.

In Fig. 4, results of elongation at break for PLA/FCHW, PLA/TFCHW and PLA/CCHW show that the elongation at break of the nanocomposites decreased upon the addition of FCHW, TFCHW and CCHW fillers into the PLA matrix which indicates an enhancement in brittleness of the nanocomposites. It was observed that the decrease is more dramatic for PLA/FCHW and PLA/TFCHW nanocomposites at 1 phr. At 2 phr, the elongation of break values is almost similar. Overall, it can be said that PLA/FCHW nanocomposites is the most brittle with 4 % elongation at break for 4 phr fillers content. The decrease in ductility upon addition of fillers were reported previously in many studies on PLA nanocomposites [7,25]. The reason for the decrease is that stiff reinforcements of chitin nanowhiskers had probably caused substantial local stress concentrations and failure at reduced strain. The local stress concentration can be affected by volume fraction of the added reinforcement, dispersion of the reinforcement in the matrix, and interaction between the reinforcement and the matrix [33]. The other possible reason is due to the stiffening action of chitin nanowhiskers restricting the segmental chain movement of PLA.

The Young's modulus of PLA/FCHW, PLA/TFCHW and PLA/CCHW increased with increasing of FCHW, TFCHW and CCHW content respectively (Fig. 5). The increase in the modulus with increasing CHW content can be explained by increased in hydrogen bond interaction, stiffening effect and high crystallinity index of the CHW filler which are the typical characteristics of polymer/filler composites. Similar findings have been reported in the physicochemical and mechanical properties study of PLA/cellulose nanowhiskers nanocomposites [34-36].

It is noted that the modulus continue to increase with increasing filler content while the tensile strength increase to a maximum value, after which it decreased due to filler agglomeration. The continued increase in modulus can be explained by the fact that modulus is measured at low strain and weak van der Waals forces are sufficient to bond the fillers and matrix. Therefore modulus is not affected by filler agglomeration which happens at higher filler content. These weak bonds can transfer the stress between fillers and polymer; therefore showing a higher modulus at small strains[37].

The mechanical properties of nanocomposites is dependent on several factors including: i) adhesion between the PLA matrix and reinforcements, ii) stress transfer efficiency of the interface; iii) volume fraction of the fibers; iv) aspect ratio of the reinforcements; v) fiber orientation; and vi) the degree of crystallinity of the matrix [38]. The higher tensile strength of the nanocomposites compared to pure PLA can be explained based on the aspect ratio of the three CHW. All three types of the CHW possess rod-like structures or whiskers which has high aspect ratios. The high aspect ratio would increase the effectiveness of stress transfer efficiency at the interface between the matrix and the reinforcement. It is possible in cases where the adhesion is relatively poor, effective stress transfer can still occur due to high aspect ratio of the reinforcement.

### 3.4 Thermogravimetric Analysis

The addition of fillers into PLA could help to increase the temperature region where PLA can be used. The TGA and DTG curves reveal the weight loss of material as it is heated. Figure7(a)-(c) shows the TGA and DTG (derivative thermograms) of pure PLA and its nanocomposites with various FCHW, CCHW and TFCHW content. The TGA and

DTG curves of neat PLA and all PLA nanocomposites show a similar decomposition pattern of one-step degradation process represented by a single peak in DTG curve. It can be observed that all samples showed initial weight loss at approximately 100°C. The weight loss was a result of evaporation of moisture and was previously reported in the study of PLA-cellulose whiskers composites [5,36].

Table 2 summarized the thermal stability PLA and nanocomposites based on  $T_{20}$  and  $T_{max}$  values.  $T_{20}$  is the temperature at which 20% of the nanocomposites has decomposed while  $T_{max}$  is the temperature at which the rate of decomposition is highest. Both  $T_{20}$  and  $T_{max}$  can be used to determine the thermal stability of the nanocomposites. Interestingly based on  $T_{20}$  and  $T_{max}$ , thermal stability of PLA nanocomposites for all types of CHW were seen to be significantly higher than pure PLA. Based on  $T_{20}$  values, all the three nanocomposites have almost similar values with PLA/TFCHW at 3phr being the highest at 355°C, which is 15 degrees higher than PLA. This can be considered a significant improvement due to the incorporation of CHW and is effective in enhancing the thermal stability. PLA/FCHW and PLA/CCHW has similar highest values at 353°C, which is slightly lower than PLA/TFCHW.

Meanwhile for  $T_{max}$ , the highest was obtained at 371°C by PLA/FCHW4, 13 degrees higher than pure PLA which is also quite significant. For the CCHW, the maximum values are slightly lower at 367°C and  $T_{max}$  reaching maximum values at 3 phr CHW content. However, the maximum values for PLA/TFCHW occurred at 1phr CHW content.

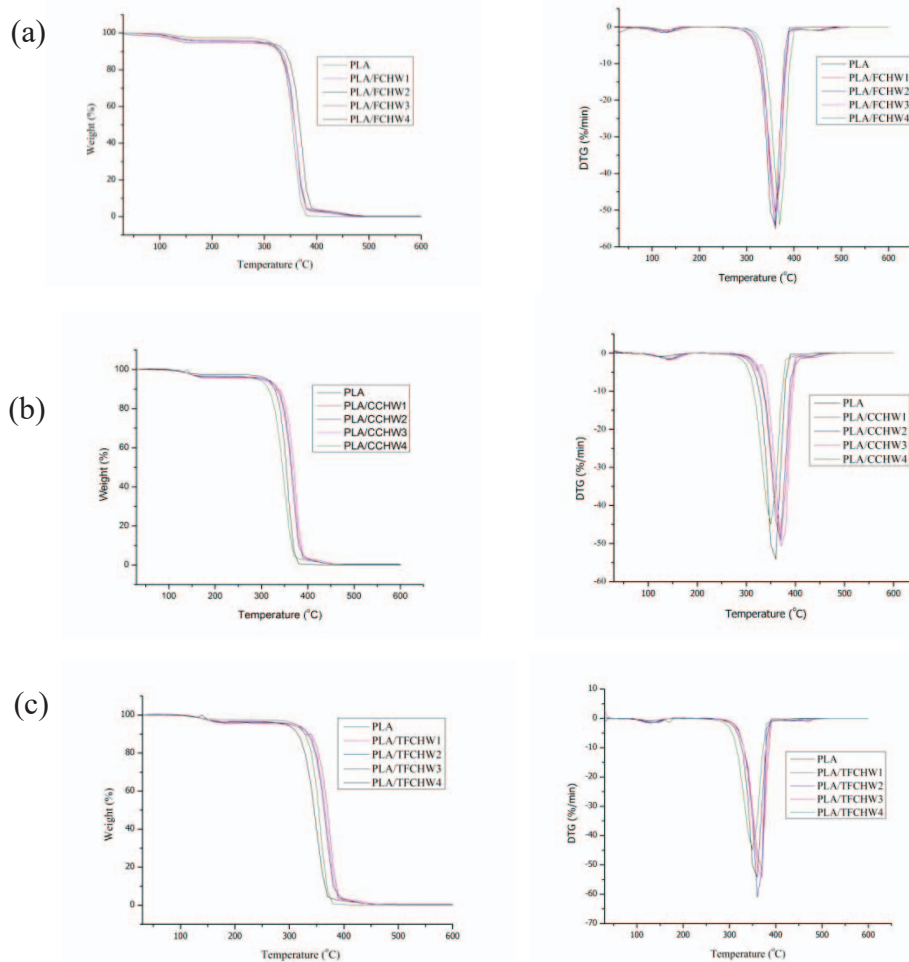


Fig.7: TGA and DTG curve of a) PLA/FCHW, b) PLA/CCHW and c) PLA/TFCHW.

From the TGA of PLA and the PLA/CHW nanocomposites, it can be concluded that all the three CHW types are effective in enhancing thermal stability of PLA nanocomposites. This improvement can be due to the good physical interaction between the PLA and CHW.

Beside that, the improvement in thermal stability could also be attributed to the uniform dispersion of the CHW in PLA matrices resulting in an increase in tortuous path for the [39-40] transfer-outmigration of degraded volatiles to the surface, thus retarding the decomposition rate [41]. Previous studies on cellulose/MMT nanocomposites also reported similar results [41-43]. From the overall results, it is difficult to conclude which type of CHW is the most effective in enhancing the thermal stability of PLA/CHW nanocomposites. It can however be said that the CHW from the fermented chitin are not inferior compared to the CHW from commercial chitin.

Table 2: Effect of CHW on thermal stability of PLA nanocomposites

Formulation	Degradation temperature (°C)	
	T <sub>20</sub>	T <sub>max</sub>
PLA	340	358
PLA/FCHW1	342	363
PLA/FCHW2	345	362
PLA/FCHW3	342	362
PLA/FCHW4	353	371
PLA/CCHW1	348	363
PLA/CCHW2	347	359
PLA/CCHW3	353	367
PLA/CCHW4	328	360
PLA/TFCHW1	353	367
PLA/TFCHW2	315	363
PLA/TFCHW3	355	365
PLA/TFCHW4	341	366

### 3.5 Biodegradability and Water Absorption Properties

An increase in biodegradability and mechanical strength at lower cost are advantage for the application of PLA/CHW as packaging materials. The effects of CHW source and content on biodegradability and water absorption properties of PLA/CHW nanocomposites are discussed together in this section since both properties are interrelated. The biodegradability of PLA, PLA/FCHW, PLA/CCHW and PLATFCHW were conducted using soil burial test. The weight loss of PLA, PLA/FCHW, PLA/CCHW and PLA/TFCHW were collected for duration ranging from 14 to 56 days and are shown in Table 3.

It can be seen that the biodegradability as indicated by the weight loss of all nanocomposites samples were higher than pure PLA at all durations. This is attributed to the presence of chitin materials on the surface of the samples which attract the microorganisms such as fungi to consume this material as nutrient source. It was also noted that prolonging the burial time lead to higher weight loss, which is as expected. Pure PLA hardly showed any weight loss after 14 days unlike the nanocomposites which had started to show some weight loss, especially PLA/CCHW and PLA/TFCHW. It was reported that the degradation of pure PLA in soil is slow and it takes a long time for degradation to start, probably because of the low temperature and water content and the

relative scarcity of PLA degrading organisms [44]. However, in a composting environment, the pure PLA is able to be hydrolyzed into smaller molecules after 45-60 days at 50-60°C.

It was also observed that biodegradability increased with increasing in the filler content for all types of nanocomposites. The highest weight loss was recorded at 4 phr CHW content for all types of nanocomposites with PLA/CCHW4 having the highest at 3.29% and PLA/FCHW4 the lowest at 2.28%. The increasing CHW content will increase chances for chitinolytic microorganisms to consume the CHW as well as increasing the interaction of CHW with water, thus increasing the biodegradation process. Therefore the ability of water to diffuse into the polymer matrix has a strong influence on the rate of degradation of PLA [45]. The degradation occurs by firstly water being diffused into the material followed by hydrolysis of C-O ester bonds and lowering of molecular weight. Rates of hydrolysis increase with water content and temperature and are catalyzed by free carboxyl groups of the hydrolyzed PLA ends. Hydrolysis occurred faster in the interior of a thick sample since carboxylic acid concentration is higher than the exterior due to leaching of the acidic PLA oligomers into the surrounding aqueous medium [46].

Table 3: Water absorption of PLA nanocomposites (%)

Formulation	Water Absorption (%)	
	2 Hours	24 Hours
PLA	0.00 ± 0.09	0.30 ± 0.09
PLA/FCHW1	1.90 ± 0.10	3.03 ± 0.09
PLA/FCHW2	3.40 ± 0.10	3.59 ± 0.03
PLA/FCHW3	3.60 ± 0.10	3.74 ± 0.07
PLA/FCHW4	4.70 ± 0.64	5.86 ± 0.18
PL/CCHW1	2.00 ± 0.10	2.97 ± 0.05
PLA/CCHW2	3.17 ± 0.15	3.20 ± 0.12
PLA/CCHW3	4.04 ± 0.25	4.84 ± 0.27
PLA/CCHW4	7.07 ± 0.52	9.35 ± 0.37
PLA/TFCHW1	1.38 ± 0.06	1.94 ± 0.07
PLA/TFCHW2	2.27 ± 0.10	2.68 ± 0.02
PLA/TFCHW3	2.51 ± 0.03	2.73 ± 0.03
PLA/TFCHW4	2.77 ± 0.11	5.15 ± 0.24

In a study by Rosdi and Zakaria [48] on the effect of chitin particles on degradation of PLA by soil burial test for duration of 10 weeks showed weight losses of 7.5% at 56 days which is higher compared to using CHW from the present study. However the study showed that addition of chitin particles did not improve the mechanical properties of PLA [47] as compared to the increase of strength with the incorporation CHW in the present study.

From the soil burial test, it can be concluded CCHW is more effective than FCHW in promoting the degradation of PLA but not significantly higher. The plausible reason is the purity of CCHW as compared to FCHW which was derived from fermented chitin. In the previous study on PLA and PLA/cellulose nanowhiskers from oil palm empty fruit bunch, it was also found that the incorporation CNW promotes the biodegradability of PLA [36]. For 5 phr of CNW, the weight loss after 56 days of soil burial is 2.1% which is less than PLA/CCHW4 reported in this study which is 3.3%. Overall it can be concluded that CHW has the potential to degrade PLA faster compared to cellulose nanowhiskers.

The water absorption of PLA, PLA/FCHW, PLA/CCHW and PLA/TFCHW after 2h and 24h immersion in distilled water at ambient temperature are shown in Table 4. As expected, amount of water absorption increased with time for PLA and all PLA/CHW nanocomposites. It was also observed that the amount of water absorption increased with increasing filler content for all types of CHW. Similar to the biodegradability results, PLA/CCHW again showed the highest water absorption at 9.35% after 24h which is around 80% higher than PLA/FCHW and PLA/TFCHW.

Materials with higher water absorptivity displayed better biodegradability mainly due to the fact that hydrophilic material will allow micro-organism to penetrate into the material, further accelerate the breakdown of polymer matrix and increased the degradation process [27]. Higher water absorption will also enable micro-organisms such as fungi and bacteria to use the CHW as their nutrient source. From both studies, it can be seen the higher the water absorption the faster the biodegradation of the composites. Comparing the PLA/CCHW and PLA/FCHW provides new knowledge on their potential as biodegradable packaging materials.

Table 4: Weight loss of PLA nanocomposites (%)

Formulation	Weight Loss (%)			
	14 Days	28 Days	42 Days	56 Days
PLA	0.02 ± 0.01	0.267 ± 0.01	0.34 ± 0.01	0.88 ± 0.02
PLA/FCHW1	0.05 ± 0.03	0.337 ± 0.03	0.838 ± 0.03	1.47 ± 0.02
PLA/FCHW2	0.36 ± 0.01	0.783 ± 0.01	1.375 ± 0.06	1.67 ± 0.03
PLA/FCHW3	0.42 ± 0.06	0.955 ± 0.06	1.61 ± 0.05	1.98 ± 0.03
PLA/FCHW4	0.44 ± 0.01	1.32 ± 0.02	1.87 ± 0.03	2.28 ± 0.03
PLA/CCHW1	0.87 ± 0.02	1.10 ± 0.02	1.44 ± 0.02	1.77 ± 0.03
PLA/CCHW2	1.15 ± 0.02	1.33 ± 0.02	2.13 ± 0.03	2.57 ± 0.10
PLA/CCHW3	1.48 ± 0.01	1.67 ± 0.03	2.34 ± 0.01	2.85 ± 0.02
PLA/CCHW4	1.83 ± 0.02	2.09 ± 0.09	2.77 ± 0.03	3.29 ± 0.01
PLA/TFCHW1	0.88 ± 0.02	1.17 ± 0.01	1.54 ± 0.02	1.85 ± 0.03
PLA/TFCHW2	1.33 ± 0.02	1.33 ± 0.01	1.75 ± 0.02	2.07 ± 0.07
PLA/TFCHW3	1.48 ± 0.02	1.88 ± 0.02	2.02 ± 0.01	2.30 ± 0.05
PLA/TFCHW4	1.77 ± 0.03	2.36 ± 0.06	2.75 ± 0.05	2.89 ± 0.01

#### 4. CONCLUSION

The objective of this study is to compare the properties PLA/CHW nanocomposites in which the source of CHW are different, which are commercial chitin and fermented chitin. Tensile strength for all nanocomposites increased with increasing filler content until it reached a certain maximum value while Young's modulus increased with increasing filler content. However, elongation at break decreased with increasing filler content for all types of nanocomposites. TGA results indicated that the all nanocomposites displayed better thermal stability as compared to pure PLA. The addition of FCHW, CCHW and TFCHW into PLA improved the biodegradability of PLA. The water absorption of all nanocomposites also increased with increasing filler content. The overall results confirm that PLA nanocomposites from FC are not inferior than PLA nanocomposites from CC and therefore has similar potential to be developed into eco-friendly packaging materials. The future areas of investigation are to further improve the mechanical properties. The ductility can be improved by using plasticisers and hybridization with other nanofillers such as graphene will help to enhance the modulus and strength.

## ACKNOWLEDGEMENT

The authors would like to thank Universiti Teknologi Malaysia (UTM) for the research facilities and Ministry of Higher Education Malaysia for financial support through FRGS Grant 4F377.

## REFERENCES

- [1] Rinaudo, M. (2006). Chitin and chitosan: Properties and applications. *Progress in Polymer Science*, 31(7):603–632. <https://doi.org/10.1016/j.progpolymsci.2006.06.001>
- [2] Mincea M, Negrulescu A, Ostafe V. (2012). Preparation, modification, and applications of chitin nanowhiskers: A review. *Reviews on Advanced Materials Science*, 30:225–242.
- [3] Azizi Samir MAS, Alloin F, Dufresne A. (2005). Review of Recent Research into Cellulosic Whiskers, Their Properties and Their Application in Nanocomposite Field. *Biomacromolecules*, 6:612-626.
- [4] Oksman K, Mathew AP, Bondeson D, Kvien I. (2006). Manufacturing process of cellulose whiskers/poly(lactic acid) nanocomposites. *Composites Science and Technology*, 66(15):2776–2784. <https://doi.org/10.1016/j.compscitech.2006.03.002>
- [5] Petersson L, Kvien I, Oksman K. (2007). Structure and thermal properties of poly(lactic acid)/cellulose whiskers nanocomposite materials. *Composites Science and Technology*, 67(11–12):2535–2544. <https://doi.org/10.1016/j.compscitech.2006.12.012>
- [6] Eichhorn SJ, Dufresne A, Aranguren M, Marcovich NE, Capadona JR, Rowan SJ, Weder C, Thielemans W, Roman M, Renneckar S, Gindl W, Veigel S, Keckes J, Yano H, Abe K, Nogi M, Nakagaito AN, Mangalam A, Simonsen J, Benight AS, Bismarck A, Berglund LA, Peijs T. (2010). Review: Current International Research into Cellulose Nanofibres and Nanocomposites. *Journal of Material Science*, 45:1-33. <https://doi.org/10.1007/s10853-009-3874-0>
- [7] Haafiz MKM, Hassan A, Zakaria Z, Inuwa I, Islam MS, Jawaid M. (2013). Properties of poly(lactic acid) composites reinforced with oil palm biomass microcrystalline cellulose. *Carbohydrate polymers*, 98(1):139–145. <https://doi.org/10.1016/j.carbpol.2013.05.069>
- [8] Nair KG, Dufresne A. (2003). Crab shell chitin whisker reinforced natural rubber nanocomposites. 1. Processing and swelling behavior. *Biomacromolecules*, 4(3):657–665.
- [9] Nishino T, Matsui R, Nakamae K. (1999). Elastic modulus of the crystalline regions of chitin and chitosan. *Journal of Polymer Science Part B: Polymer Physics*, 37(11):1191–1196. [https://doi.org/10.1002/\(SICI\)1099-0488\(19990601\)37:11<1191::AID-POLB13>3.0.CO;2-H](https://doi.org/10.1002/(SICI)1099-0488(19990601)37:11<1191::AID-POLB13>3.0.CO;2-H)
- [10] Vincent JFV, Wegst UGK. (2004). Design and mechanical properties of insect cuticle. *Arthropod Structure and Development*, 33:187–199. <https://doi.org/10.1016/j.asd.2004.05.006>
- [11] Luckachan GE, Pillai CKS. (2011). Biodegradable Polymers- A Review on Recent Trends and Emerging Perspectives. *Journal of Polymers and the Environment*, 19(3):637–676. <https://doi.org/10.1007/s10924-011-0317-1>
- [12] Singh AK, Sharma L, Mallick N, Mala J. (2017). Progress and challenges in producing polyhydroxyalkanoate biopolymers from cyanobacteria. *Journal of Applied Phycology*, 29(3):1213–1232. <https://doi.org/10.1007/s10811-016-1006-1>
- [13] Yates MR, Barlow CY. (2013). Life cycle assessments of biodegradable, commercial biopolymers—A critical review. *Resources, Conservation and Recycling*, 78:54–66. <https://doi.org/10.1016/j.resconrec.2013.06.010>
- [14] Gandini A, Lacerda TM. (2015). From monomers to polymers from renewable resources: Recent advances. *Progress in Polymer Science*, 48:1-39. <https://doi.org/10.1016/j.progpolymsci.2014.11.002>
- [15] Pretula J, Slomkowski S, Penczek S. (2016). Polylactides-Methods of synthesis and characterization. *Advanced Drug Deliveries Reviews*, 107:3-16. <https://doi.org/10.1016/j.addr.2016.05.002>

- [16] Madhavan Nampoothiri K, Nair NR, John RP. (2010). An overview of the recent developments in polylactide (PLA) research. *Bioresource technology*, 101(22):8493–8501. <https://doi.org/10.1016/j.biortech.2010.05.092>
- [17] Coltelli M, Cinelli P, Gigante V, Aliotta L, Morganti P, Panariello L, Lazzeri A. (2019). Chitin Nanofibrils in Poly(Lactic Acid) (PLA) Nanocomposites: Dispersion and Thermo-Mechanical Properties. *International Journal of Molecular Sciences*, 20(3):504-523. <https://doi.org/10.3390/ijms20030504>
- [18] Rizvi R, Cochrane B, Naguib H, Lee, P.C. (2011). Fabrication and characterization of melt-blended polylactide-chitin composites and their foams. *Journal of Cellular Plastics*, 47:283. <https://doi.org/10.1177/0021955X11402549>
- [19] Zeng, J.B., He, Y.S., Li, S.L. and Wang, Y.Z., (2012). Chitin whiskers: An overview. *Biomacromolecules*, 13(1):1–11. <https://doi.org/10.1021/bm201564a>
- [20] Zhang, Q., Wei, S., Huang, J., Feng, J., & Chang, P. R. (2014). Effect of surface acetylated-chitin nanocrystals on structure and mechanical properties of poly (lactic acid). *Journal of Applied Polymer Science*, 131(2):2-9. <https://doi.org/10.1002/app.39809>
- [21] Singh S, Maspoth ML, Oksman K. (2019). Crystallization of triethyl-citrate-plasticized poly (lactic acid) induced by chitin nanocrystals. *Journal of Applied Polymer Science*, 136(36): 47936. <https://doi.org/10.1002/app.47936>
- [22] Liu, W., Zhu, L., Ma, Y., Ai, L., Wen, W., Zhou, C. and Luo, B. (2019). Well-ordered chitin whiskers layer with high stability on the surface of poly (D,L-lactide) film for enhancing mechanical and osteogenic properties. *Carbohydrate Polymers*, 212:277-288. <https://doi.org/10.1016/j.carbpol.2019.02.060>
- [23] Liu, H., Liu, W., Luo, B., Wen, W., Liu, M., Wang, X. and Zhou, C. (2016). Electrospun composite nanofiber membrane of poly(l-lactide) and surface grafted chitin whiskers: Fabrication, mechanical properties and cytocompatibility, *Carbohydrate Polymers*, 147:216-225. <https://doi.org/10.1016/j.carbpol.2016.03.096>
- [24] Coltelli, M., Aliotta, L., Vannozzi, A., Morganti, P., Panariello, L., Danti, S., Neri, S., Fernandez-Avila, C., Fusco, A., Donnarumma G, Lazzeri A. (2020). Properties and Skin Compatibility of Films Based on Poly(Lactic Acid) (PLA) Bionanocomposites Incorporating Chitin Nanofibrils (CNs), *Journal of Functional Biomaterials*, 11(2):21-43. <https://doi.org/10.3390/jfb11020021>
- [25] Zakaria Z, Hall GM, and Shama G. (1998). Lactic Acid Fermentation of Scampi Waste in a Rotating Horizontal Bioreactor for Chitin Recovery, *Process Biochemistry*, 33:1-6. [https://doi.org/10.1016/S0032-9592\(97\)00069-1](https://doi.org/10.1016/S0032-9592(97)00069-1)
- [26] Zulkeple NM, Zakaria Z, Hamdan S, Abdul Manaf MS. (2011). Fermentation of Prawn Waste by using Effective Microorganism (EM) for Protein Production. *Journal of Fundamental Sciences*, 7(2):108-112.
- [27] Chuayjuljit S, Su-Uthai S, Tunwattanaseree C, Charuchinda S. (2009). Preparation of Microcrystalline Cellulose from Waste-Cotton Fabric for Biodegradability Enhancement of Natural Rubber Sheets. *Journal of Reinforced Plastics and Composites*, 28:1245–1254. <https://doi.org/10.1177/0731684408089129>
- [28] Lavall RL, Assis OBG, Campana-Filho SP. (2007). Beta-chitin from the pens of *Loligo* sp.: extraction and characterization. *Bioresource Technology*, 98(13):2465–2572. <https://doi.org/10.1016/j.biortech.2006.09.002>
- [29] Pereira AGB, Muniz EC, Hsieh YL. (2014). Chitosan-sheath and chitin-core nanowhiskers. *Carbohydrate polymers*, 107:158–166. <https://doi.org/10.1016/j.carbpol.2014.02.046>
- [30] Cárdenas G, Cabrera G, Taboada E, Miranda SP (2004). Chitin characterization by SEM, FTIR, XRD and <sup>13</sup>C cross polarization/mass angle spinning NMR. *Journal of Applied Polymer Science*, 93(4):1876–1885. <https://doi.org/10.1002/app.20647>
- [31] Wang Y, Cao X, Zhang L. (2006). Effects of cellulose whiskers on properties of soy protein thermoplastics. *Macromolecular bioscience*, 6(7):524–531. <https://doi.org/10.1002/mabi.200600034>
- [32] Arjmandi R, Hassan A, Haafiz MKM, Zakaria Z. (2015). Effect of Microcrystalline Cellulose on Biodegradability, Tensile and Morphological Properties of Montmorillonite

- Reinforced Polylactic Acid Nanocomposites. *Fibers and Polymers*, 16 (10):2284–2293. <https://doi.org/10.1007/s12221-015-5507-3>
- [33] Pei A, Zhou Q, Berglund LA. (2010). Functionalized cellulose nanocrystals as biobased nucleation agents in poly (l-lactide)(PLLA)—Crystallization and mechanical property effects. *Composites Science and Technology*, 70(5):815-821. <https://doi.org/10.1016/j.compscitech.2010.01.018>
- [34] Zakir KM, Ifty H, Andrew A, Rudd CD. (2012). Physico-chemical and mechanical properties of nanocomposites prepared using cellulose nanowhiskers and poly (lactic acid). *Journal of Materials Science*, 47(6):2675–2686. <https://doi.org/10.1007/s10853-011-6093-4>
- [35] Hong J, Kim DS. (2013). Preparation and physical properties of polylactide/cellulose nanowhisiker/nanoclay composites. *Polymer Composites*, 34(2):293–298. <https://doi.org/10.1002/pc.22413>
- [36] Haafiz MKM, Hassan A, Khalil H, Fazita M, Islam MS, Inuwa I, Marliana M, Hussin M. (2016). Exploring the effect of cellulose nanowhiskers isolated from oil palm biomass on polylactic acid properties. *International Journal of Biological Macromolecules*, 85:370–378. <https://doi.org/10.1016/j.ijbiomac.2016.01.004>
- [37] Bikiaris D. (2010). Microstructure and Properties of Polypropylene/Carbon Nanotube Nanocomposites. *Materials*, 3(4):2884-2946.
- [38] Dufresne A, Dupeyre D, Paillet M. (2002). Lignocellulosic flour-reinforced poly(hydroxybutyrate-co-valerate) composites. *Journal of Applied Polymer Science*, 87:1302–1315. <https://doi.org/10.1002/app.11546>
- [39] Lim JW, Hassan A, Rahmat AR, Wahit MU. (2006). Morphology, thermal and mechanical behavior of polypropylene nanocomposites toughened with poly (ethylene-co-octene). *Polymer international*, 55(2):204-215. <https://doi.org/10.1002/pi.1942>
- [40] Majeed K, Hassan A, Bakar AA, Jawaid M. (2016). Effect of montmorillonite (MMT) content on the mechanical, oxygen barrier, and thermal properties of rice husk/MMT hybrid filler-filled low-density polyethylene nanocomposite blown films. *Journal of Thermoplastic Composite Materials*, 29(7):1003-1019.
- [41] Ray SS, Okamoto M. (2003). Biodegradable polylactide and its nanocomposites: opening a new dimension for plastics and composites. *Macromolecular Rapid Communications*, 24(14):815-840.
- [42] Cerruti P, Ambrogi V, Postiglione A, Rychlý J, Matisová-Rychlá L, Carfagna C. (2008). Morphological and thermal properties of cellulose–montmorillonite nanocomposites. *Biomacromolecules*, 9(11):3004-3013. <https://doi.org/10.1021/bm8002946>
- [43] Delhom CD, White-Ghoorahoo LA, Pang SS. (2010). Development and characterization of cellulose/clay nanocomposites. *Composites Part B: Engineering*, 41(6):475-481.
- [44] Karamanlioglu M, Preziosi R, Robson GD. (2017). Abiotic and biotic environmental degradation of the bioplastic polymer poly (lactic acid): A review. *Polymer Degradation and stability*, 137:122-130.
- [45] Elsayy MA, Kim KH, Park JW, Deep A. (2017). Hydrolytic degradation of polylactic acid (PLA) and its composites. *Renewable and Sustainable Energy Reviews*. 79:1346-1352. <https://doi.org/10.1016/j.rser.2017.05.143>
- [46] Shogren R, Doane W, Garlotta D, Lawton J, Willett J. (2003). Biodegradation of starch/polylactic acid/poly (hydroxyester-ether) composite bars in soil. *Polymer Degradation and Stability*, 79:405–411.
- [47] Rosdi N, Zakaria Z. (2016). Biodegradability Properties on Chitin/Polylactic Acid Composite Films. *eProceedings Chemistry. Universiti Teknologi Malaysia*. 1:48-52.

## FORMALIZATION OF THE COTTON DRYING PROCESS BASED ON HEAT AND MASS TRANSFER EQUATIONS

YUNUSOVA SAYYORA TOSHKENBOYEVNA<sup>1\*</sup>, HALMATOV DAVRON  
ABDALIMOVICH<sup>2</sup>, ATAJONOV MUHIDDIN ODILJONOVICH<sup>1</sup>  
AND HUZANAZAROV ULUGBEK OLIMOVICH<sup>2</sup>

<sup>1</sup>*Department of Information Processing and Control Systems,  
Tashkent State Technical University, Tashkent, Uzbekistan*

<sup>2</sup>*Tashkent Institute of Textile and Light Industry, Tashkent, Uzbekistan*

\*Corresponding author: [yunusova\\_sayyora@mail.ru](mailto:yunusova_sayyora@mail.ru)

(Received: 17<sup>th</sup> April 2020; Accepted: 9<sup>th</sup> May 2020; Published on-line: 4<sup>th</sup> July 2020)

---

**ABSTRACT:** The paper deals with the construction of a mathematical model of the cotton drying process, taking into account the thermal and mass transfer properties of raw cotton components. To determine changes in the temperature of the fibre and raw cotton seeds, the application of Fourier's law is proposed. The mathematical dependence of the change on the humidity of the cotton fibre and seeds along the length of the drum is determined. The rational value of the heat agent consumption in the process of drying raw cotton is also determined. Research methods are based on the provisions of modern trends in management theory and identification. Mathematical models are constructed using analytical methods and equations that describe the physical properties of an object. Methods for constructing a mathematical model usually rely on experimental methods, in particular, the method of acceleration curves, and as a result, the mathematical description becomes a priori inaccurate. It is shown that the mathematical model used is quite adequate for the dynamics of a real object, fully describes it, and characterizes it over the entire range of changes. The analysis of the developed mathematical model based on simulation showed the adequacy of the obtained mathematical dependence of the temperature regime of the cotton drying process with the consumption of heat agent.

**ABSTRAK:** Kajian ini membincangkan tentang penciptaan model matematik bagi proses pengeringan kapas, dengan mengambil kira terma dan sifat-sifat pindah jisim komponen kapas mentah. Bagi mendapatkan perubahan suhu pabrik dan biji benih kapas mentah, penggunaan hukum Fourier telah dicadangkan. Kebergantungan matematik pada perubahan kelembapan pabrik kapas dan biji benih sepanjang drum telah diperolehi. Nilai bersesuaian menggunakan ejen haba dalam proses pengeringan kapas kering mentah didapati. Kaedah kajian berdasarkan tren moden dalam teori pengurusan dan pengenalanpastian. Model matematik dibina dengan menggunakan kaedah analisis dan persamaan yang menerangkan ciri-ciri fizikal pada objek. Kaedah bagi membina model matematik selalunya bergantung pada kaedah eksperimen, khususnya, kaedah pecutan melengkung, dan hasilnya, pernyataan penaakulan matematik menjadi tidak tepat. Model matematik yang digunakan adalah cukup bagi objek dinamik sebenar, dengan penerangan penuh dan perincian ke atas keseluruhan perubahan. Analisis model matematik yang terhasil berdasarkan simulasi, dilihat cukup kebergantungan matematik terhasil melalui proses pengeringan kapas pada aturan suhu dengan ejen haba.

---

**KEYWORDS:** *raw cotton; mass transfer; fibers; heat exchange; drying drum; process; differential equations; temperature*

---

## 1. INTRODUCTION

Raw cotton, as an object of drying, refers to capillary porous-colloidal, heterogeneous materials. Its main components are fiber, skin, and seed core. The structure of the fiber refers to capillary-porous materials.

Due to the structure of raw cotton, the removal of moisture from the core is slow and depends on many factors. Depending on the humidity between the skin and the seed core, air layers are formed, the size of which depend on the maturity and humidity of the seeds. With the presence of an air layer, the process of heat and mass exchange between the skin and the seed core changes significantly, due to the formation of additional resistance to the movement of moisture and heat between the components of raw cotton [1].

The intensification of heating of porous materials, in particular the drying of raw cotton, is determined by the laws of heat and substance transfer inside the body (internal heat and mass transfer) and between the surface of the body and the environment (external heat and mass transfer). To properly understand the mechanism of these processes under thermal influence, it is necessary to develop a thermophysical model of raw cotton that describes the heat and mass exchange processes between the components (fiber and seeds) and the thermal agent (heated air).

When exposed to heat, the thermodynamic equilibrium in the material is disturbed, resulting in internal heat and mass transfer processes associated with the transfer of heat and matter (moisture) in the raw cotton components. In this case, the exchange processes can be implemented:

- due to surface heat and mass transfer;
- internal convective heat exchange between raw cotton components according to Newton's law, according to which the flow of heat and matter will be proportional to the difference in temperature and moisture of each component;
- internal convective heat and mass exchange between the material components and the heated air mass (heat agent);
- transfer of heat and moisture as a result of flow movement in the pores of raw cotton;
- transfer of heat and moisture by diffusive phenomena occurring in each component of the material in the air.

When creating a control system for the technological processes of raw cotton processing, it is necessary to use the entire arsenal of modern theory and practice of automatic control and management, and in addition, it is necessary to have information about the behaviour of the technological control object under the influence of control actions. Effective management of processes and industrial facilities is possible when the main characteristic features inherent in the object are presented in the form of a mathematical description [2-4].

The development of a control system for the process of cotton processing that can provide the required quality of management in the conditions of rapid changes in the parameters of processed raw cotton with changes in environmental indicators is an urgent scientific and technical task. The solution to this problem will significantly improve the quality of management of technological process parameters.

To solve this problem, the processing raw cotton is functionally decomposed into sub-processes, the structure of which changes over time depending on such factors as changes

in the quality requirements of cotton fibre and raw cotton source material, as well as on the operating modes of aggregates, changes in technological regulations, and production situations.

The complexity of mathematical modelling of the technological process is caused by the insufficient level of development of the theory, the presence of a large number of factors that affect the course of the process, the difficulty of assessing the objective relationship between a set of disturbing factors, as well as the non-stationary parameters of the technological object and their weak observability in real time [4,5]. These factors determine the formalization of the processes, taking into account the main parameters that define it.

It is known that the process of cotton processing consists of interrelated sub-processes, the technological parameters of which significantly affect the quality of the produced pre-product-cotton fibre. At the same time, the most important among them is the process of drying raw cotton [6-8].

## 2. FINDING SOLUTIONS METHOD

Based on the analysis of the functioning of the drying drum, the facts of the existence of functional relationships of each parameter with others are revealed and subsets of interrelated parameters are formed based on these features. The subsets obtained in this way are combined into a common set (set) of interrelated parameters and divided into groups of input parameters  $U(t)$ , output  $y(t)$ , variable States  $x(t)$ , and the drying process. The input parameters of the drying process include: raw cotton consumption  $G_c(u_1)$ , fuel consumption  $G_T(u_2)$ , humidity of raw cotton  $B_c(u_3)$ , air flow- $G_b(u_4)$ , air temperature- $t_b(u_5)$ , air humidity- $B_b(u_6)$ . The output parameters of the object are: cotton humidity at the outlet of the drum - $B_x(y_1)$ , temperature of cotton at the exit of the drum - $t_x(y_2)$ , output of cotton from the drum- $G_x(y_3)$  temperature of the waste heat agent- $t_0(y_4)$ , and humidity of the selected heat agent- $B_0(y_5)$  output of the selected heat agent- $G_a(y_6)$ . In this case, the number of variable state parameters selected: dehumidifier in the drum-  $K_b(x_1)$  temperature in the drum- $t_b(x_2)$ , all cotton in the drum- $G_b(x_3)$ , heat agent temperature- $t_a(x_4)$ , heat agent consumption- $G_a(x_5)$ , and humidity of the heat agent- $B_a(x_6)$ .

Using the method proposed in this paper [5-9] we will make differential equations of heat and mass transfer processes in each phase of raw cotton.

Select the volume of the material  $V$  bounded by the surface  $S$  and denote by  $J_{ij}^V$ ,  $J_{il}^V$  and  $J_{i2}^V$  accordingly, the flow of moisture in the form of liquid ( $i=1$ ) and steam ( $i=2$ ) through the surface  $S$ , through  $-U_{ij}$ ,  $U_{il}$  and  $U_{i2}$  corresponding to the moisture content in each component. Changing the moisture content  $U_{ij}$  in volume  $V$  occurs due to the derivative  $\frac{\partial U_{ij}}{\partial t}$  internal moisture exchange between components according to Newton's law.

According to the law of conservation of mass of a substance a second change in the moisture content of a material in volume  $V$  is equal to the amount of liquid entering this volume per unit of time, both due to its inflow through the surface  $S$ , and due to its receipt from sources [10-14].

Find expressions for the vectors  $\mathbf{J}_{ij}$ . For this purpose, we use Fourier's law, according to which the flow vector will be collinear to the gradient of changes in moisture and temperature.

$\mathbf{J}_{ik} = -p_k(a_{mi}^{(k)} \text{grad}U_k + \tilde{a}_{mi}^{(k)} \text{grad}T_k)$ , where  $a_{mi}^{(k)}$  and  $\tilde{a}_{mi}^{(k)}$  are the transfer coefficients.

Given all this, the differential equations for the total mass of transport in the fiber-seed-air system are presented as

$$\rho_1 \frac{\partial U}{\partial t} + c_{12}(U_1 - U_2) + c_{13}(U_1 - U_3) + c^{(T)}_{12}(T_1 - T_2) + c^{(T)}_{13}(T_1 - T_3) = \text{div}[\rho_1(a_m^{(1)} \text{grad}U_1 + \tilde{a}_m^{(1)} \text{grad}T_1)]; \quad (1)$$

$$\rho_2 \frac{\partial U_2}{\partial t} + c_{12}(U_2 - U_1) + c_{23}(U_2 - U_3) + c^{(T)}_{12}(T_1 - T_2) + c^{(T)}_{23}(T_2 - T_3) = \text{div}[\rho_2(a_m^{(2)} \text{grad}U_2 + \tilde{a}_m^{(2)} \text{grad}T_2)]; \quad (2)$$

$$\rho_3 \frac{\partial U_3}{\partial t} + c_{13}(U_3 - U_1) + c_{23}(U_3 - U_2) + c^{(T)}_{13}(T_3 - T_1) + c^{(T)}_{23}(T_3 - T_2) = \text{div}[\rho_3(a_m^{(3)} \text{grad}U_3 + \tilde{a}_m^{(3)} \text{grad}T_3)], \quad (3)$$

where  $c_{23} = a_{23} + b_{23}$ ,  $c^{(T)}_{23} = a^{(T)}_{23} + b^{(T)}_{23}$ ,  $c_{lk} = a_{lk} + b_{lk}$ ,  $c^{(T)}_{lk} = a^{(T)}_{lk} + b^{(T)}_{lk}$ ,

$\rho_1 = m_1\rho_{10}$ ,  $\rho_2 = m_2\rho_{20}$ ,  $\rho_3 = m_3\rho_{30}$ ,  $\rho_{10}$ ,  $\rho_{20}$  and  $\rho_{30}$  - true densities of fibres, seeds, and air, respectively.  $a_{12}$ ,  $a^T_{12}$  - mass transfer and heat transfer coefficients between fibres and seeds for liquid moisture,  $a_{13}$ ,  $a^T_{13}$  - mass transfer and heat transfer coefficients between fibres and air,  $a_{23}$ ,  $a^T_{23}$  - coefficients of mass exchange and heat exchange between seeds and air (drying agent),  $b_{12}, b_{13}, b_{23}$ ,  $b^{(T)}_{12}, b^{(T)}_{13}, b^{(T)}_{23}$  - similar coefficients for vaporous moisture,  $U_1 = U_{11} + U_{21}$ ,  $U_2 = U_{21} + U_{22}$ ,  $U_3 = U_{31} + U_{32}$  - total mass of moisture transfer for the fibre system, seeds and air, respectively,  $a_m^{(k)} = a_{m1}^{(k)} + a_{m2}^{(k)}$ ,  $\tilde{a}_m^{(k)} = \tilde{a}_{m1}^{(k)} + \tilde{a}_{m2}^{(k)}$ .

### 3. SOLVING THE PROBLEMS

The system of equations (1) – (3) describes the process of mass transfer in raw cotton components under the known law of change in the temperature of the fiber, for which we use Fourier's law. Heat consumption for heating components, as well as heat exchange between components:

$$c_1\rho_1 \frac{\partial U_1}{\partial t} = \text{div}(\lambda_1 \text{grad}T_1) + r^{(1)}I_{11} - \alpha_{12}(T_1 - T_2) - \alpha_{13}(T_1 - T_3); \quad (4)$$

$$c_2\rho_{21} \frac{\partial U_2}{\partial t} = \text{div}(\lambda_2 \text{grad}T_2) + r^{(2)}I_{12} + \alpha_{12}(T_1 - T_2) - \alpha_{23}(T_2 - T_3); \quad (5)$$

$$c_3\rho_3 \frac{\partial U_3}{\partial t} = \text{div}(\lambda_3 \text{grad}T_2) + r^{(3)}I_{13} + \alpha_{13}(T_1 - T_3) + \alpha_{23}(T_2 - T_3), \quad (6)$$

where with  $\lambda_k$  and  $r^{(k)}$  - coefficients of thermal conductivity and specific heat of transformation (for fibre (k=1), for seeds (k=2)) and air (k=3),  $\alpha_{ij}$ - coefficients of internal heat exchange between fibres and seeds (i=1, j=2), air and fibres (i=1, j=3) and air and seeds (i=2, j=3). The power of the source when transferring vaporous moisture will be equal to

$I_{11} = I_{21}$  and is determined from the condition  $\frac{\partial \mathcal{U}_{21}}{\partial t} = 0$ , which gives

$$I_{21} = \text{div}(\mathcal{J}_{21}) + \rho_1 [b_{12}(U_1 - U_2) + b_{13}(U_1 - U_3) + b_{12}^{(T)}(T_1 - T_2)] + b_{13}^{(T)}(T_1 - T_3). \quad (7)$$

Substituting (1) in equation (4), using the expression (7), we get

$$c_1 \rho_1 \frac{\partial T_1}{\partial t} = \text{div}(\lambda_1 \text{grad} T_1) + r^{(1)} \text{div}[\rho_1 (a_{m2}^{(1)}) \text{grad} U_1 + \tilde{a}_{m2}^{(1)} \text{grad} T_1] - \alpha_{12}(T_1 - T_2) - \alpha_{13}(T_1 - T_3) - r^{(1)} \rho_1 [b_{12}(U_1 - U_2) + b_{13}(U_1 - U_3)] + b_{12}^{(T)}(T_1 - T_2) + b_{13}^{(T)}(T_1 - T_3). \quad (8)$$

Similarly, we have

$$c_2 \rho_2 \frac{\partial T_2}{\partial t} = \text{div}(\lambda_2 \text{grad} T_2) + r^{(2)} \text{div}[\rho_2 (a_{m2}^{(2)}) \text{grad} U_2 + \tilde{a}_{m2}^{(2)} \text{grad} T_2] + \alpha_{12}(T_1 - T_2) - \alpha_{23}(T_2 - T_3) r^{(2)} \rho_2 [b_{12}(U_2 - U_1) + b_{23}(U_2 - U_3)] + b_{12}^{(T)}(T_2 - T_1) + b_{23}^{(T)}(T_2 - T_3);$$

$$c_3 \rho_3 \frac{\partial T_3}{\partial t} = \text{div}(\lambda_3 \text{grad} T_3) + r^{(3)} \text{div}[\rho_3 (a_{m2}^{(3)}) \text{grad} U_3 + \tilde{a}_{m2}^{(3)} \text{grad} T_3] + \alpha_{12}(T_1 - T_2) + \alpha_{23}(T_2 - T_3) r^{(3)} \rho_3 [b_{13}(U_3 - U_1) + b_{23}(U_3 - U_2)] + b_{13}^{(T)}(T_3 - T_1) + b_{23}^{(T)}(T_3 - T_2). \quad (9)$$

Equations (1)-(3), (8)-(10) for known densities  $\rho_k$ , heat capacity  $c_k$  and transfer coefficients  $\lambda_k, r^{(k)}, a_{mi}^{(k)}, \tilde{a}_{mi}^{(k)}$ , mass transfer coefficients  $a_{ik}, b_{ik}$  and heat exchange  $a_{ik}^{(T)}, b_{ik}^{(T)}, \alpha_{ik}$  form a closed system for determining the moisture content and temperature of the fiber  $(U_1, T_1)$ , seeds'  $(U_3, T_3)$ .

Introducing the coefficients of the phase transformation of a liquid into steam  $\varepsilon_{ik}, \varepsilon_i$  and thermogradient coefficients according to  $\delta_{ik}, \delta_i$  the formulas

$$\varepsilon_{12} = \frac{b_{12}}{a_{12} + b_{12}}, \varepsilon_{13} = \frac{b_{13}}{a_{13} + b_{13}}, \varepsilon_{23} = \frac{b_{23}}{a_{23} + b_{23}}, \varepsilon_1 = \frac{a_{m2}^{(1)}}{a_m^{(1)}}, \varepsilon_2 = \frac{a_{m2}^{(2)}}{a_m^{(2)}}, \varepsilon_3 = \frac{a_{m2}^{(3)}}{a_m^{(3)}};$$

$$\delta_{12} = \frac{c_{12}^{(T)}}{c_{12}}, \delta_{13} = \frac{c_{13}^{(T)}}{c_{13}}, \delta_{23} = \frac{c_{23}^{(T)}}{c_{23}}, \delta_1 = \frac{\tilde{a}_{m2}^{(1)}}{a_{m2}^{(1)}}, \delta_2 = \frac{\tilde{a}_{m2}^{(2)}}{a_{m2}^{(2)}}, \delta_3 = \frac{\tilde{a}_{m2}^{(3)}}{a_{m2}^{(3)}} \text{ and considering the}$$

one-dimensional transfer case (flat case n=0, cylindrical symmetry n=1 and the case of spherical symmetry n=2) give the equation (1)-(3), (8)-(10) to mind

$$\rho_i \frac{\partial U_i}{\partial t} = \left( \frac{\partial}{\partial x} + \frac{n}{x} \right) [a_m^{(i)} \rho_i \left( \frac{\partial U_i}{\partial x} + \delta_i \frac{\partial T_i}{\partial x} \right)] - \rho_i \sum_{k=1}^3 c_{ik} [U_i - U_k + \delta_{ik} (T_i - T_k)]; \quad (11)$$

$$c_i \rho_i \frac{\partial T_i}{\partial t} = \left(\frac{\partial}{\partial x} + \frac{n}{x}\right) (\lambda_i \frac{\partial T}{\partial x}) + r^{(i)} \left(\frac{\partial}{\partial x} + \frac{n}{x}\right) [\varepsilon_i a_m^{(i)} \rho_i \left(\frac{\partial U_i}{\partial x} + \delta_i \frac{\partial T_i}{\partial x}\right)] - \sum_{k=1}^3 \alpha_{ik} (T_i - T_k) - r^{(i)} \rho_i \sum_{k=1}^3 c_{ik} \varepsilon_{ik} [U_i - U_k] + \delta_{ik} (T_i - T_k); \quad (12)$$

where  $i=1, 2, 3$ ,  $c_{21}=c_{12}$ ,  $c_{32}=c_{23}$ ,  $\varepsilon_{32} = \varepsilon_{23}$ ,  $\alpha_{21} = \alpha_{12}$ ,  $\alpha_{32} = \alpha_{23}$ .

To integrate equations (11) and (12), the following initial, boundary, and symmetry conditions must be met:

$$U_i = U_{i0} = const \text{ at } t=0$$

$$-\lambda_{ic} \frac{\partial T}{\partial x} + a_{ic} (T_c - T_i) - (1 - \varepsilon_{ic}) \rho_i \eta_{ic} r_c^{(i)} (U_i - U_c) = 0 \text{ at } x=R,$$

$$a_{mc}^{(i)} + \delta_{ic} \frac{\partial T_i}{\partial x} + \eta_{ic} (U_i - U_c) = 0 \text{ at } x=R, \quad \frac{\partial U_i}{\partial x} = 0, \quad -\frac{\partial T_i}{\partial x} = 0 \text{ at } x=0,$$

where  $\lambda_{ic}, -\rho_{ic}, -a_{mc}^{(i)}, -\delta_{ic}, -\varepsilon_{ic}$  - boundary values of thermal conductivity, density, substance diffusion coefficient, thermogradient coefficient and phase transformation criterion for the  $i$ -th phase,  $a_{ic}, \eta_{ic}$  coefficients of heat and mass transfer of the  $i$ -th phase with the external environment,  $T_c$  and  $U_c$  - values of temperature and humidity of the external environment.

For a moving medium, the time derivative operator  $\frac{\partial}{\partial t}$  replaced by the full derivative operator using the formula  $\frac{d}{dt} = \frac{\partial}{\partial t} + v \frac{\partial}{\partial x}$ , where  $v_i$  - is the velocity of transport of medium particles. Then the transport equations (11) and (12) for a moving medium can be written as:

$$\rho_i \left(\frac{\partial U_i}{\partial t} + v_i \frac{\partial U_i}{\partial x}\right) = \left(\frac{\partial}{\partial x} + \frac{n}{x}\right) [a_m^{(i)} \rho_i \left(\frac{\partial U_i}{\partial x} + \delta_i \frac{\partial T_i}{\partial x}\right)] - \rho_i \sum_{k=1}^3 c_{ik} [U_i - U_k + \delta_{ik} (T_i - T_k)]; \quad (13)$$

$$c_i \rho_i \left(\frac{\partial T_i}{\partial t} + v_i \frac{\partial T_i}{\partial x}\right) = \left(\frac{\partial}{\partial x} + \frac{n}{x}\right) (\lambda_i \frac{\partial T}{\partial x}) + r^{(i)} \left(\frac{\partial}{\partial x} + \frac{n}{x}\right) [\varepsilon_i a_m^{(i)} \rho_i \left(\frac{\partial U_i}{\partial x} + \delta_i \frac{\partial T_i}{\partial x}\right)] - \sum_{k=1}^3 \alpha_{ik} (T_i - T_k) - r^{(i)} \rho_i \sum_{k=1}^3 c_{ik} \varepsilon_{ik} [U_i - U_k] + \delta_{ik} (T_i - T_k),$$

where  $v_i$  is the speed of movement of fibres ( $i=1$ ), seeds ( $i=2$ ) and air ( $i=3$ )

In the case of a one-dimensional ( $n=0$ ) stationary transfer mode ( $\frac{\partial U_i}{\partial t} = 0, \frac{\partial U_i}{\partial x} = 0$ ) at constant values of travel speeds  $v_i = v_{i0} = const$ , thermal and mass transfer parameters of raw cotton components [11-17].

$$\rho_i = \rho_{i0} = const, \quad a_m^{(i)} = a_{m0}^{(i)} = const, \quad \lambda_i = \lambda_{i0} = const, \quad \delta_i = \delta_{i0} = const, \quad \varepsilon_i = \varepsilon_{i0} = const,$$

$$r^{(i)} = r_{i0}^{(i)} = const, \quad c_i = c_{i0} = const \text{ have}$$

$$\frac{d\bar{U}_i}{d\xi} = \gamma^{(i)} Lu_i \left( \frac{d^2\bar{U}_i}{d\xi^2} + \rho_i \frac{d^2\bar{T}_i}{d\xi^2} \right) - \sum_{k=1}^3 \lambda_{ik} [\bar{U}_i - \bar{U}_k + \rho_{ik} (\bar{T}_i - \bar{T}_k)]; \quad (14)$$

$$\frac{d\bar{T}_i}{d\xi} = \gamma^{(i)} (K_{11}^{(i)} \left( \frac{d^2\bar{T}_i}{d\xi^2} + \rho_i \frac{d^2\bar{U}_i}{d\xi^2} \right) - \sum_{k=1}^3 \theta_{ik} [\bar{U}_i - \bar{U}_k - \sum_{k=1}^3 \sigma_{ik} (\bar{T}_i - \bar{T}_k)], \quad (15)$$

where  $\bar{T} = \frac{T}{T_0}$ ,  $\bar{U} = \frac{U}{U_0}$ ,  $\gamma^{(i)} = \frac{a_i}{Lv_{i0}}$ ,  $Lu_i = \frac{a^{(i)}_{m0}}{a_i}$ ,  $\rho_{ni} = \frac{\delta_{i0} T_0}{U_0}$ ,  $\lambda_{ik} = \frac{c_{ik} L^2}{v_{i0}}$ ,  $\rho_{ik} = \frac{\delta_{ik} T_0}{U_0}$ ,

$$K_{11}^{(i)} = 1 + \varepsilon_{i0} K_{0i} \rho_{ni} Lu_i, K_{12}^{(i)} = \varepsilon_{i0} K_{0i} Lu_i, K_{0i} = \frac{r^{(i)}_0 U_0}{c_{i0} T_0}, \theta_{ik} = \lambda_{ik} K_{0i} \varepsilon_{ik},$$

$\sigma_{ik} = \beta_{ik} + \theta_{ik} \rho_{ik}$ ,  $\beta_{ik} = \frac{a_{ik} L^2}{\lambda_{i0} a_i}$ ,  $a_i = \frac{\lambda_{i0}}{c_{i0} \rho_{i0}}$ ,  $T_0$  i -  $U_0$  initial (equilibrium) values of temperature and moisture of any component (for example, air) of raw cotton. The system in Eq. (14) and (15) are integrated under the following boundary conditions

$$\bar{T}_i = \bar{T}_{ni}, \bar{U}_i = \bar{U}_{ni} \text{ by } \xi = 0, \quad (16)$$

$$-\frac{\partial \bar{T}_i}{\partial \xi} + \beta_{ic} (\bar{T}_c - \bar{T}_i) - (1 - \varepsilon_{ic}) \mu_{ic} (\bar{U}_i - \bar{U}_c) = 0 \text{ at } \xi = 1, \quad (17)$$

$$\frac{\partial \bar{U}_i}{\partial \xi} + \rho_{ni} \frac{\partial \bar{T}_i}{\partial \xi} + v_{ic} (\bar{U}_i - \bar{U}_c) = 0 \text{ at } \xi = 1, \quad (18)$$

where  $\xi = \frac{x}{L}$ ,  $\beta_{ic} = \frac{a_{ic} L}{\lambda_{i0}}$ ,  $\mu_{ic} = \frac{\eta_{ic} r^{(i)}_0 U_0 L}{c_{i0} T_0 a_i}$ ,  $v_{ic} = \frac{\eta_{ic} U_0 L}{a_{m0}^{(0)}}$ ,  $\bar{T}_{ni} = \frac{T_{ni}}{T_0}$ ,  $\bar{U}_{ni} = \frac{U_{ni}}{U_0}$ ,

$\bar{U}_c = \frac{U_c}{U_0} T_{ni}$  and  $U_{ni}$  - set values of temperature  $i =$  and moisture of the  $o$ -th component in the cross- section  $x = 0$ .

As an example, consider the process of drying raw cotton in a dryer in a drum, where the fibres and seeds move at the same speed  $v_{10} = v_{20} = v_0$  and equal in size  $v_0 = qv_{30}$ . The research is carried out using the following initial data, corresponding to the properties of the real properties of raw cotton and the parameters of the dryer [6]:

$$T_0 = 20, U_0 = 10, T_{n1} = 20, T_{n2} = 20, T_{n3} = 150, U_{n1} = 20, U_{n2} = 20, U_{n3} = 10, p_{12} = p_{13} = p_{23} = 0.1, \varepsilon_{12} = \varepsilon_{13} = \varepsilon_{0.5}, K_{01} = 0, K_{02} = K_{03} = 1$$

The maximum values of seed moisture are 20% at the beginning of the drum, i.e. before drying, and at the end, i.e. at the end of drying  $\approx 17.5\%$ . The pattern of removing moisture from the fibre differs significantly from similar patterns corresponding to seeds. At the beginning and end of the drying process the fibre humidity has the following limits 20% и  $\approx 12\%$ .

Based on equation. (14) and (15), a computational model of the cotton drying process has been developed (Fig. 1), which characterizes the dependence of changing parameters. Simulation experiments were conducted to study the properties of these dependencies. The

calculations were performed in the MATLAB system. The transition process graphs are shown in Fig. 2.

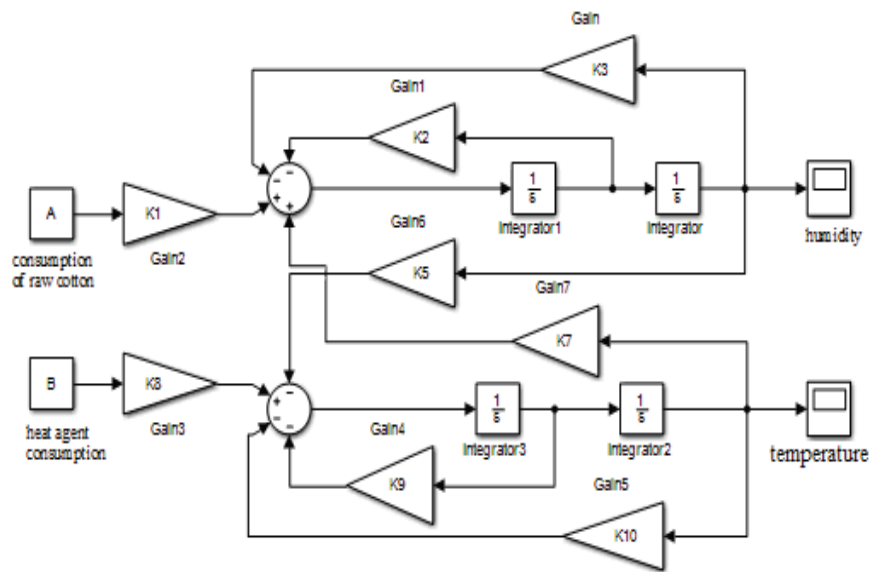


Fig.1: Modelling scheme of static mode of raw cotton drying process (with distributed parameters).

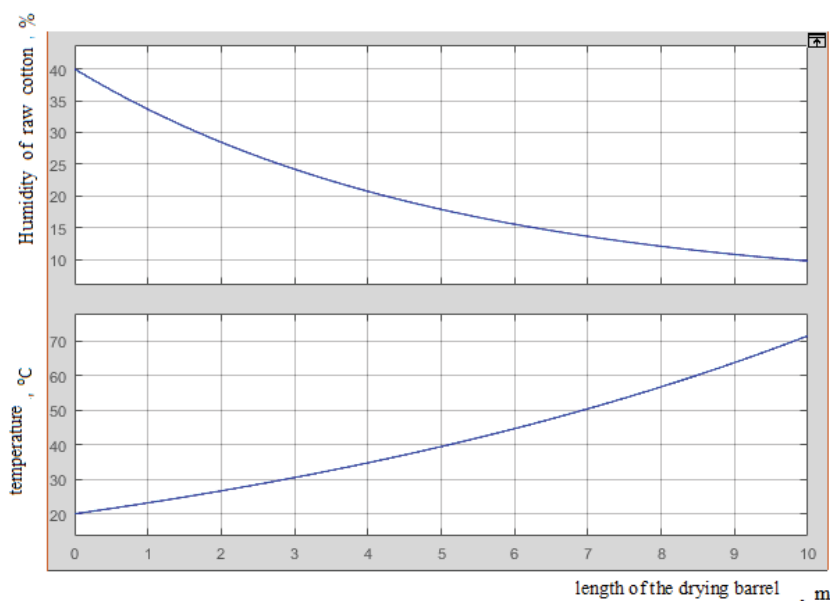


Fig. 2: Graphs of the transition process.

To calculate the processes in the computational model, the following are entered:

$$k_1 = L \cdot x_1 \cdot \gamma \quad , \quad k_2 = k_1 \rho \quad , \quad k_3 = \theta \quad , \quad k_4 = \rho \quad ,$$

$$k_5 = \gamma \cdot k \quad , \quad k_6 = k_5 \rho \quad , \quad k_7 = \theta \quad , \quad k_8 = \delta$$

Comparing the results, we conclude that the seeds at the exit of the drum have a humidity of 17,5%, and fiber – 12%. The moisture content of the seed is 2.5%, and that of the fibre

is 8%, which means that to intensify the drying of raw cotton seeds, it is necessary to improve the access of heated air to their surface.

It follows that in order to obtain high-quality fibre and seeds, it is proposed to maintain the seed temperature at the exit of the drum at about 50% of the input temperature.

#### 4. CONCLUSION

A dynamic mathematical model of the drying process is constructed, which determines the regularities of changes in the moisture content of fibre and seeds, which depend not only on the humidity of the original cotton, but also on the consumption of the supplied heat agent. Verification of the adequacy of the developed model is carried out by comparing real data with the result of simulation modelling.

Thus, a mathematical model of the raw cotton drying process is obtained, which allows us to determine the dynamic properties of the control system and choose rational modes of operation of aggregates with optimal control of the entire process and increase production productivity without compromising the natural properties of cotton fibres and seeds.

#### ACKNOWLEDGEMENTS

I thank you for giving me such an opportunity to work under your IIUM engineering journal. Huge thanks to my supervisor Dr I.H. Sidikov for providing me great insight and knowledge, for his continuous encouragement and for providing me with many of his valuable time. I would also like to thank my friends Muhiddin Atajonov, and others who have given me moral support and stayed with me at the university for many days. Without their support, I could not have spent so much time and effort on my article.

Finally, I thank goes to the Tashkent State Technical University, Department of "Information Processing and Control Systems" staffs for their support and taking me to the next level in my studies.

#### REFERENCES

- [1] Cotton: World Statistics. Bulletin of the International Cotton Advisory Committee, NY, November 2015. <http://www.ICAC.org>, <http://www.USDA.gov>.
- [2] Parpiev A.P, Mamatov A.Z, Usmankulov A.K. (2000) Maximum permissible temperatures in the drum dryer. *IzvestiyaVuzov*, 1:35-36.
- [3] Usmankulov A. (2002) Improving the efficiency of the drying process of raw cotton in a drum dryer, Diss. for the degree of candidate of technical Sciences Tashkent; pp128.
- [4] Mamatov A.Z. (1995) Modeling of raw cotton drying technology to improve the quality of fiber, Diss. On competition of a scientific degree. doctor of technical Sciences Tashkent; pp 248.
- [5] Siddikov I.X, Umurzakova D.M. (2019) Features of automatic control of technological parameters of water level in the drum steam boilers, *Journal of Southwest Jiaotong University*,54(3):1-10. DOI:10.35741/issn.0258-2724.54.3.1.
- [6] Siddikov I.X, Umurzakova D.M. (2019) Mathematical Modeling of Transient Processes of the Automatic Control System of Water Level in the Steam Generator, *Universal Journal of Mechanical Engineering*, 7(4):139-146. DOI:10.13189/ujme.2019.070401.
- [7] Siddikov I.X, Umurzakova D.M. (2019) Adaptive neuron-fuzzy regulating system of the temperature mode of the drum boiler. *International Journal of Advanced Research in Science, Engineering and Technology*, 6(1) 7869-7872. (2019).
- [8] Siddikov I.X, Umurzakova D.M, Bakhrieva H.A. (2020) Adaptive system of fuzzy-logical regulation by temperature mode of a drum boiler // *IIUM Engineering Journal* 21(1):182-192. <https://doi.org/10.31436/iiumej v 2lil.1220>.

- 
- [9] Yunusova S.T. (2013) On the formalization of the optimization criterion of the cleaning process of raw cotton to Tashkent State Technical University. Bulletin. 3:35-40.
- [10] Sidikov I.H, Atajonov M.O, Yunusova S.T, Nashvandova. G.M. (2020) Adaptive analytical control of technological parameters based on the probability method of oil refining installations, European Science Review, Scientific Journal, 1(2):78-83 <https://doi.org/10.29013/ESR-20-1.2-78-83>.
- [11] Kholmatov D. A, Yunusova S. T. Setmetov N. U, Khuzhanazarov U. O. (2014) Information and algorithmic technological monitoring system algorithmic processes processing of raw cotton., WCIS-Eighth World Conference on Intelligent Systems for Industrial Automatic. Toshkent .261-264
- [12] Siddiqov IH, Yunusova ST, Izmailova NR. (2018) Algorithm for optimization of the membership function of the fuzzy control model on the basis of the probabilistic approach. WCIS – 2018, Tenth World Conference on Intelligent Systems for Industrial Automation October 25-26, Tashkent, Uzbekistan, 251-254
- [13] Yunusova ST. (2019) Fuzzy logic model of temperature control of a drying unit based on a probabilistic approach. Collection of reports of the Republican scientific and practical conference on "Innovations in the development of information and communication technologies" April 15-17.
- [14] Kholmatov DA, Yunusova ST, Setmetov NU, Khuzhanazarov UO. (2019) Software tool monitoring process of processing raw cotton. International Journal of Advanced Research in Science, Engineering and Technology, 6(2): 8140-8143.
- [15] Igamberdiyev H.Z, Yusupbekov A.N, Zaripov O.O,Sevinov J.U. (2017) Algorithms of adaptive identification of uncertain operated objects in dynamical models. Procedia Computer Science.120. 854-861. DOI: 10.1016/j.procs.2017.11.318.
- [16] Sidikov I.H, Atajonov M.O, Atajonova S.B. (2019) Fuzzy-Situational Diagnostics of Technological Safety of Petrochemical Plants, 4(7):182-186. DOI:10.33564/IJEAST.2019.v04i07.030

# CRACK INFLUENCE ON A PIPE WITH DOUBLE SLOPE UNDER INTERNAL PRESSURE: NUMERICAL SIMULATION WITH XFEM

SALMI HOUDA<sup>1\*</sup>, HACHIM ABDELILAH<sup>1,2</sup>, EL BHILAT HANAN<sup>1</sup>  
AND EL HAD KHALID<sup>1,2</sup>

<sup>1</sup>Hassan II University of Casablanca, National Higher School of Mechanics (ENSEM),  
Laboratory of Control and Mechanical Characterization of Materials and Structures,  
Casablanca, Morocco

<sup>2</sup>Institute of Maritime Studies, Laboratory of Materials and Structures  
Casablanca, Morocco

\*Corresponding author: [houda.salmi111@gmail.com](mailto:houda.salmi111@gmail.com)

(Received: 14<sup>th</sup> April 2020; Accepted: 9<sup>th</sup> May 2020; Published on-line: 4<sup>th</sup> July 2020)

**ABSTRACT:** This work analyses the effect of elliptical cracks on a pipe with double slope thickness transition, using the extended finite element method (XFEM), level sets were defined to describe the three-dimensional (3D) cracks. The Computation of the stress intensity factors (SIFs) of cracks is performed. The values of SIFs are compared between straight pipes and pipes with a double (single) slope thickness transition. The results show that the XFEM is an effective tool for modelling cracks in pipes. A pressurized pipe with double slope thickness transition is more sensitive to the defect in comparison with another type of pipe. Parameters of the transition zone have an effect on stress intensity factors, precisely, the parameters of the first thickness transition are more influential on the gravity of the defect compared to the second thickness transition.

**ABSTRAK:** Kajian ini menganalisa kesan retakan elips pada paip dengan peralihan ketebalan cerun berganda, menggunakan kaedah elemen terhingga dipanjangkan (XFEM), set tahap ditentukan bagi menentukan keretakan tiga dimensi (3D). Pengiraan faktor intensiti tekanan (SIF) retakan dilakukan. Nilai SIF dibandingkan antara paip lurus dan paip peralihan ketebalan cerun berganda (tunggal). Hasil kajian menunjukkan bahawa XFEM adalah alat yang berkesan bagi memodel keretakan paip. Paip bertekanan mengikut peralihan ketebalan cerun berganda, lebih sensitif terhadap kecacatan berbanding paip lain. Parameter zon peralihan mempunyai pengaruh terhadap faktor intensiti tegangan, tepatnya, parameter peralihan ketebalan pertama lebih mempengaruhi pada graviti kecacatan berbanding dengan peralihan ketebalan kedua.

**KEYWORDS:** *extended finite element method (XFEM); pipe with double slope thickness transition; stress intensity factors (SIFs); three-dimensional cracks*

## 1. INTRODUCTION

Presently, pressure equipment is used in various applications, such as energy production and chemical industry [1-4]. In the field of pressure equipment, cylindrical or spherical structures are often found, those shells can be affected by axi-symmetric or semi-elliptical internal or external cracks, it is then very important to evaluate the influence of these cracks on pressure equipment [5].

The French Alternative Energies and Atomic Energy Commission (CEA) [6] developed the finite element software (Castem) for structural and fluid mechanics [7]. CEA [6-8] used the finite element method (FEM) to investigate straight pipes with circumferential cracks. The field of pressure equipment also deals with the thickness of transition pipes, these pipes are classified into two types: transitions with a single slope and transitions with a double slope [3,4]. Those structures correspond to a connection between two cylinders of the same internal radius but with different thicknesses, those structures are subjected to circumferential cracks at the base of the thickness transition, those defects are modelled as cracks located in a pipe of uniform thickness  $t$  [1,3,4].

Using FEM, Rahman et al. [1] evaluated the effect of the thickness transition zone on the crack opening displacement (COD), [1] showed that the thickness transition produces a dissymmetric distribution of the COD on the crack lips. Hariri [3,4] used 3D finite element method (FEM) to study transition with a single slope containing elliptical crack subjected to tensile stress and bending moment, the result showed that for elastic plastic material, the thickness transition zone is the weakest position of the whole pipe.

The traditional finite element calculations have a cumbersome cost in the modelling of a crack. The accuracy of the results in the FEM depends on the mesh refinement, but a fine mesh implies a large number of nodes, so it requires a long calculation time [8]. Hence, XFEM is introduced to facilitate the solving of crack problems in complex geometries. In this work, the XFEM is used to analyse in 3D the external circumferential elliptical cracks in the thickness transition zone. In this method, the standard finite element approximation is locally enriched to discontinuities modelling [9,10]. For stationary cracks, the XFEM gives an accurate result, thanks to enrichment functions even with coarse meshes near the crack tip [9]. The XFEM was initiated by Belytschko and Black [11]. Stolarska et al. [12] coupled between the level set method (LSM) and XFEM to investigate the problem of cracks.

In the field of pressurized equipment, [13] used the XFEM to study the fracture behaviour of pipes under internal detonation loads. Sharma [14] performed a numerical investigation with XFEM to evaluate the stress intensity factor of a semi-elliptical crack in a pipe band.

Using the XFEM to investigate the effect of the crack on a thickness transition with two slopes besides evaluating the influence of transition zone on SIF were however not treated in [3], also, taking account of internal pressure was required to complete the work in [3]. The purpose of this work is the application of XFEM to evaluate the effect of a 3D external circumferential crack in thickness transition with a double slope in a pipe and investigate the effect of the parameters of the transition zone on SIF.

## 2. XFEM METHODOLOGY

### 2.1 XFEM Formulation

Using enrichment functions, the displacement approximation  $U$  is given by Eq. (1) [9]:

$$U(x) = \sum_{i \in N} N_i(x)u_i + \sum_{i \in N_d} N_i(x)(H(x) - H(x_i))a_i + \sum_{i \in N_f} [N_i(x)(\sum_{\alpha=1}^4 (\beta_{\alpha}(x) - \beta_{\alpha}(x_i))b_i^{\alpha})] \quad (1)$$

where  $N_i$  is the standard finite element (FE) function of node  $i$ .  $u_i$  is an unknown of the standard FE part at a node  $i$ .  $N$  is a set of all nodes in the domain.  $N_d \subset N$  is a nodal subset of the enrichment Heaviside function  $H(x)$ .

$$H(x) = \begin{cases} 1 & \text{if } \varphi(x) > 0 \\ -1 & \text{otherwise} \end{cases} \quad (2)$$

where  $\varphi(x)$  is the normal level set function.  $\alpha_i$  is an unknown of the enrichment  $H(x)$  at a node  $i$ , these nodes are surrounded by a square in Fig. 1.  $N_p \subset N$  is a nodal subset of the enrichment  $\beta_\alpha$ , the tip of the crack is described by four enrichment functions [9].

$$\{\beta_\alpha(r, \theta)\} = \{\beta_1, \beta_2, \beta_3, \beta_4\} = \left\{ \sqrt{r} \sin\left(\frac{\theta}{2}\right), \sqrt{r} \cos\left(\frac{\theta}{2}\right), \sqrt{r} \sin\left(\frac{\theta}{2}\right) \sin(\theta), \sqrt{r} \cos\left(\frac{\theta}{2}\right) \sin(\theta) \right\} \quad (3)$$

where  $r = \sqrt{(\varphi^2 + \psi^2)}$  and  $\theta = \tan^{-1}\left(\frac{\varphi}{\psi}\right)$  with  $\varphi$  and  $\psi$  are respectively normal and tangential level sets.

$b_i$  is an unknown of the enrichment  $\beta_\alpha$  at a node  $i$ , these nodes are surrounded by a circle in Fig. 1.

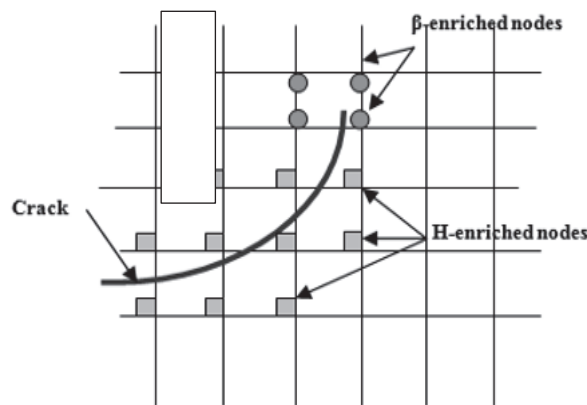


Fig. 1: The strategy of the enrichment in XFEM.

## 2.2 Calculation of SIF in XFEM

The energy release rate  $G$  is the energy released for a crack advance, the  $G$ -theta is a method that calculates the  $J$ -integral in elastic-plastic behaviour [16]. Rice [15] showed that the  $J$ -integral can be approached by the energy release rate  $G$  in the elastic range.

Let  $I$ , a point in crack front  $C$ ,  $\Gamma_c$  a crack surface that is composed with an outer surface  $\Gamma_c^+$  and an inner surface  $\Gamma_c^-$ . We consider  $V$  a volume containing the crack front  $C$  (red arc in Fig. 2a) with  $V = \Gamma_c^+ \cup \Gamma_c^- \cup \Gamma_0 \cup \Gamma_1 \cup \Gamma_2$ . For calculating the SIF in XFEM, the level sets are used as a local basis at the crack front.

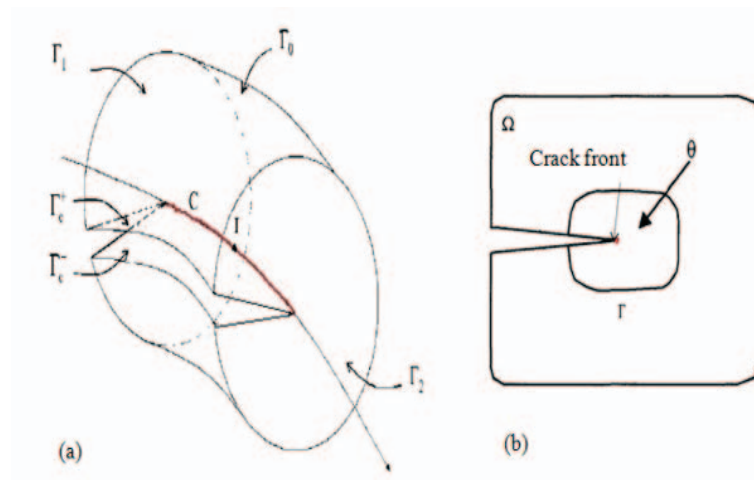


Fig. 2: (a) The domain  $V$  in integral  $J$  computation, a (b) example of  $\theta$  field in 2 dimensions.

Sukumar [17] has used the gradient of the level sets, [16] has defined this local basis (Fig. 3) by  $e_1 = \nabla \psi$ ,  $e_2 = \nabla \phi$  and  $e_3 = e_1 \wedge e_2$ .

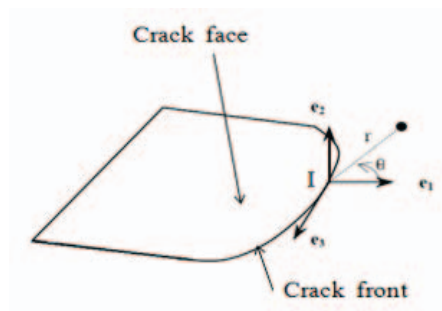


Fig. 3: The local basis on the crack front.

$J$  is expressed in a local basis (Fig. 6) formed of level set functions,  $J$  is given by Eq. (4) [16]:

$$J = \int_{\Gamma_c^+ \cup \Gamma_c^-} \theta_i P_{ij} n_j d\Gamma - \int_V \theta_i P_{ij} dV \quad (4)$$

where  $P_{ij}$  is the Eshelby tensor [17], it is given by Eq. (5):

$$P_{ij} = w\delta_{ij} - \sigma_{ij} \varepsilon_{ik} \quad (i, j, k) \in \{1, 2, 3\} \quad (5)$$

where  $w$  is the elastic energy density,  $\sigma$  and  $\varepsilon$  are respectively stress and strain expressed in the basis  $(e_1, e_2, e_3)$  (Fig.3).  $\theta$  is a field of displacement parallel to the plane of the crack and normal to the front (Fig. 2. b), it is defined by Eq. (6):

$$\theta = \mu e_1, \mu(I) = 1 \text{ and } \mu(x) = 0 \text{ for } x \in \Gamma_0 \cup \Gamma_1 \cup \Gamma_2 \quad (6)$$

For elastic behaviour of materials,  $G$  is deduced from the  $J$ -integral by Eq. (7) [9]:

$$G = \frac{E}{2(1-\mathcal{G}^2)} \times \frac{J}{\int_C \mu dC} \quad (7)$$

The SIF is deduced from G by Eq. (8) [9]:

$$G = \frac{K^2}{E'} \quad \text{with } E' = \frac{E}{(1-\nu^2)} \quad \text{in plane strain} \quad (8)$$

### 2.3 The Meshing of the Cracked Pipe

The cracked pipe is symmetrical, so we modelled only a half-pipe with thickness transition and an external elliptical crack (Fig. 4b), we used 3150 XFEM XC8R elements with 512 Gauss points in block crack. We used 18080 standard elements CUB8 for the rest of the mesh. The thickness transition with two slopes is generally located at the outlet of reservoirs (valves) [3], therefore in boundary conditions, we fixed the displacement of the end of the thicker part of the pipe, in addition, we blocked the translation and the rotation in  $u_y$  and  $u_z$  axes by applying symmetry boundary conditions (Fig. 4a). In this study, the crack is represented by level sets, we defined a normal level set from the crack front (red bow Fig. 4b) and tangential level function from the crack face.

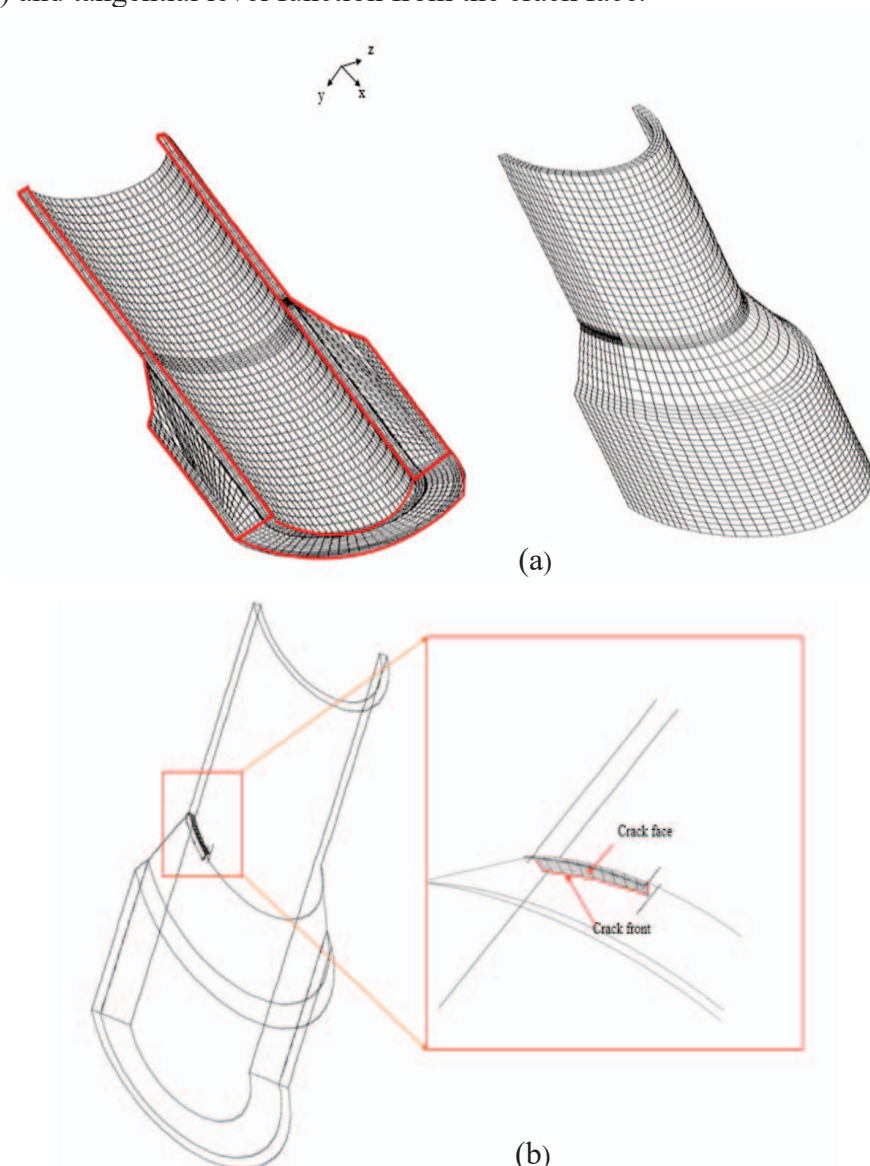


Fig. 4: (a) Cracked half-pipe with thickness transition with double slope, (b) meshing of the crack.

The normal level set  $\phi$  (PHI) gives the distance of a point  $x$  to the surface of the crack and the tangential level set  $\psi$  (PSI) gives the distance of a point  $x$  to the crack tip, these level functions define the crack as follows: for a point  $x$  of the solid (Fig. 5a):

$$x \in \text{crack} \Rightarrow \begin{cases} \phi(x)=0 \\ \psi(x) \leq 0 \end{cases} \text{ with } (|\nabla \psi| = |\nabla \phi| = 1) \quad (9)$$

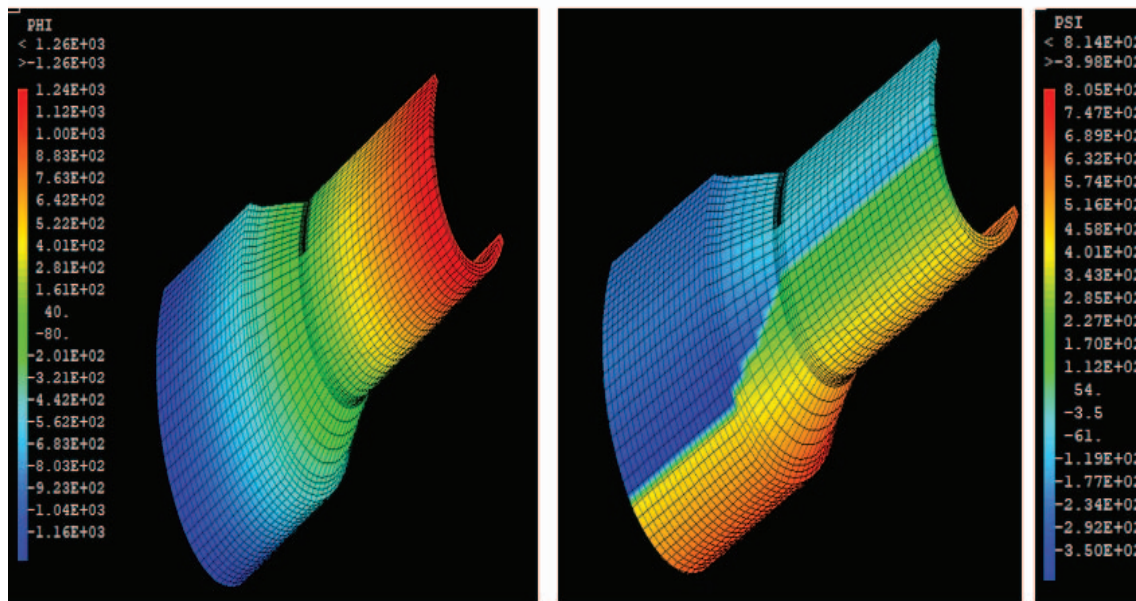
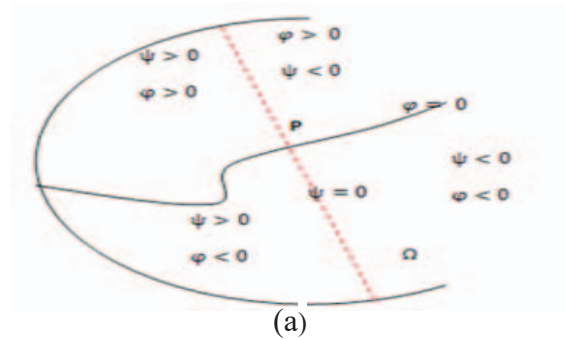


Fig. 5: (a) Representation of a crack with level sets, (b) normal level set, PHI, (c) tangential level set, PSI.

### 3. GEOMETRY AND LOADING

The study considered the elastic behaviour of the material in P265GH steel with the following properties. The geometries of the studied cracked pipes are defined by dimensionless parameters:

- A fraction of thickness  $t$  on the inner radius of the pipe:  $(t_1 / R_i)$ .
- Shape parameter defining elongation of the elliptical crack:  $(a/c)$ .
- The depth of the defect standardized by the thickness of the tube:  $(a / t_1)$ .

In the present work, we model a pipe of average thickness  $(t_1 / R_i = 0.1)$ , the parameter  $(a/c)$  takes values 1, 1/2, 1/4, and 1/8,  $(a / t_1)$  takes values 0.1, 0.2, 0.4, 0.6, 0.8. This gives a set of 20 geometries.

Table 1: Properties of P265GH steel

Young's modulus, $E$ , (MPa)	Yield stress, $\sigma$ , (MPa)	Poisson's ratio, $\nu$	Breaking stress, $\sigma_u$ , (MPa)	Nominal stress, $f$ , (MPa)
200000	320	0.3	470	148

Elliptical cracks are considered to be located at the base of the transition in the thin part of the pipe (Figs. 4 and 6).

The study considered pipe with thickness transition with a single slope ( $t_1, t_2, \alpha_1$ ) and thickness transition with double slopes ( $t_1, t_2, t_3, \alpha_1, \alpha_2$ ) (Fig. 6). Pressurized pipe with thickness transition is a connection between pipe of thickness  $t_1$  assembled to another pipe of a thickness  $t_2$  and  $t_3$  ( $t_3 > t_2 > t_1$ ).

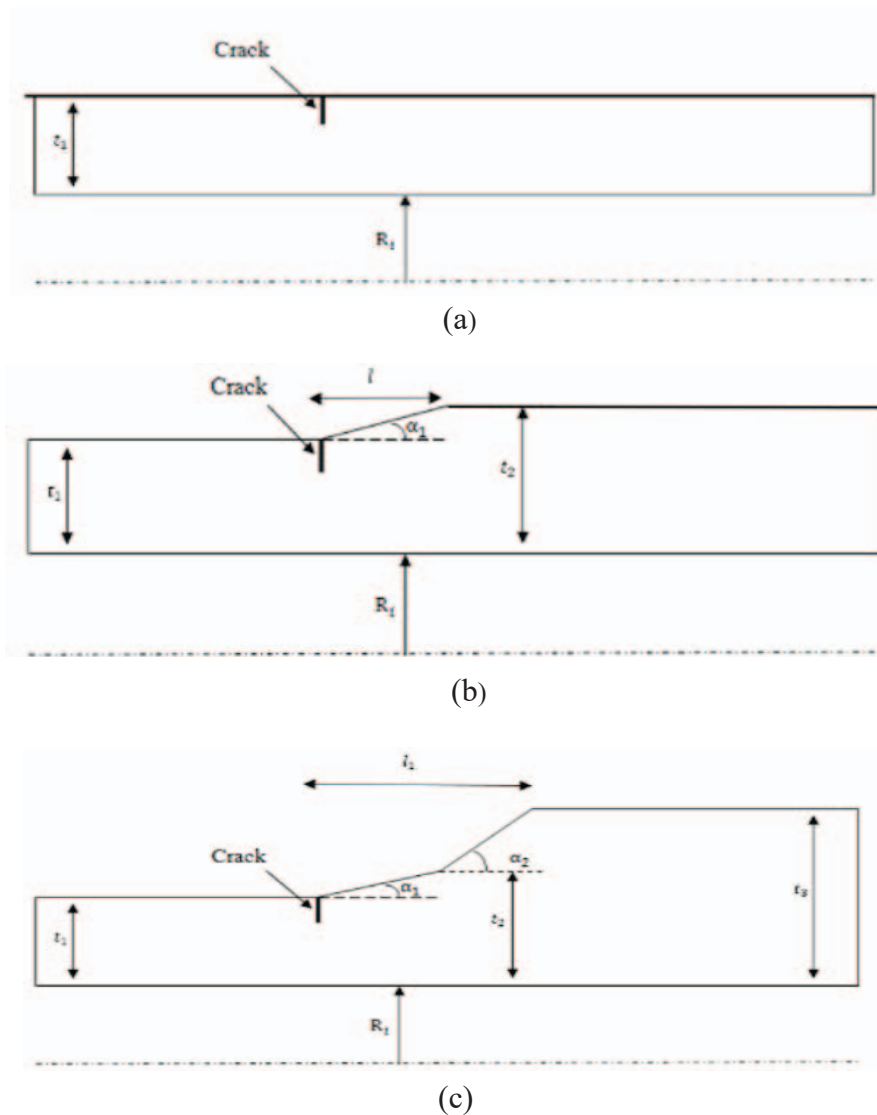


Fig. 6: Geometry of different types of pipes: (a) straight pipe, (b) pipe with thickness transition (single slope), (c) pipe with thickness transition (double slope).

$t_j$  is the thickness of the pipe, with  $j \in \{1, 2, 3\}$ . ( $\alpha_j$ ) is the slope of a thickness transition in a pipe with  $j \in \{1, 2\}$ . SIF, (K) is the stress intensity factor. The purpose of this study is

the investigation of the impact of  $t_j$  and  $(\alpha_j)$  on the stress intensity in a pipe with thickness transition. So, we consider  $t_j$  and  $(\alpha_j)$  as variable parameters, and analyse their effect on SIF.

Pipes are subjected to an internal pressure P (Fig. 7), for the purpose of comparison with the straight cylinder, the internal pressure is calculated in the thin part (thickness  $t_1$ ) of the pipe with thickness transition, P is calculated according to the CODAP (C2.1.4.2) instructions [18]:

$$P = \frac{2 \times f \times t_1 \times z}{D_m} \quad (10)$$

where z is the welding coefficient.  $D_m = R_e + R_i$  is the inner diameter of the pipe.  $R_i$  and  $R_e$  are respectively inner and outer radius of thin pipe where  $R_e = t_1 + R_i$ . So, Eq. (10) becomes:

$$P \left( \frac{R_i}{t_1} \right) = \frac{2f}{2 \left( \frac{R_i}{t_1} \right) + 1} \text{ with } \frac{R_i}{t_1} = 10 \quad (11)$$

The internal pressure is  $P = 14\text{MPa}$ , this pressure does not cause general plastic behaviour in the pipe of an average thickness ( $t_1/R_i = 0.1$ ).

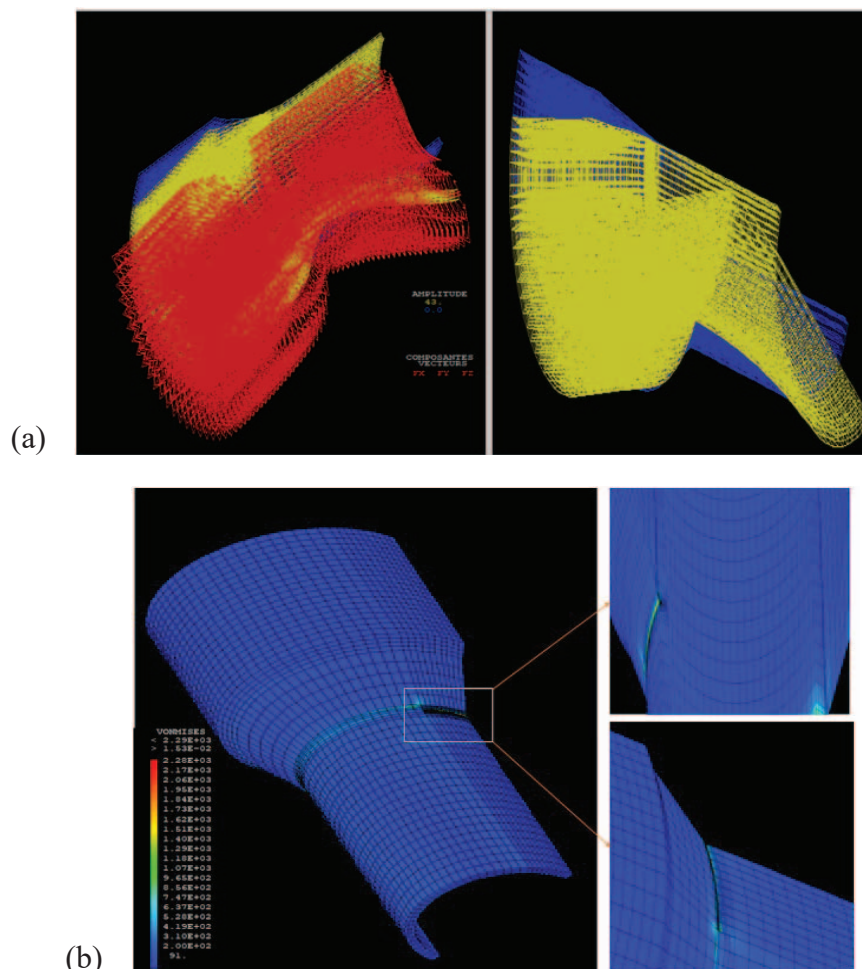


Fig. 7: Pipe with thickness transition: (a) subjected to internal pressure, (b) Von Mises stress.

## 4. RESULTS AND DISCUSSION

### 4.1 Verification of the XFEM model

The Castem 2016 software [7] was used for modelling and calculation; it has XFEM and G-Theta capabilities. The position of a point P on the crack front is defined by the angle  $\phi(^{\circ})$  (Fig. 8),  $\phi$  takes the value of  $90^{\circ}$  at the deepest point (**D point**) and  $0^{\circ}$  at the surface point (**S point**), those two points characterize the semi-elliptical crack. In general, the evaluation of SIF at those two points is enough to judge the severity of the defect. At those points, the average value of K is given by Eqs. (12) and (13) [8]:

$$K_{average} = \frac{1}{5}(4K_{point2} + K_{point3}) \quad \text{in D point} \quad (12)$$

$$K_{average} = \frac{1}{6}(K_{point4} + 4K_{point5} + K_{point6}) \quad \text{in S point} \quad (13)$$

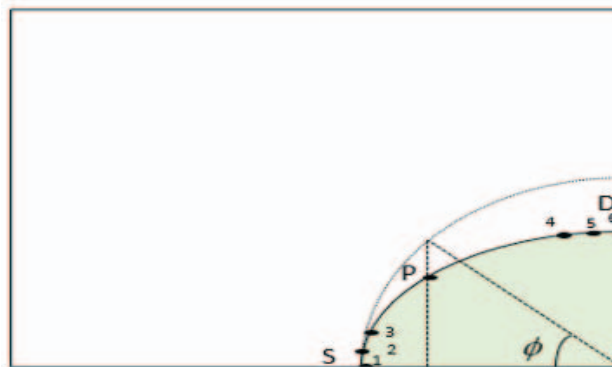


Fig. 8: Definition of average values on the element [8].

The French Alternative Energies and Atomic Energy (CEA) [6] studied straight pipes containing external circumferential cracks, CEA [8] calculated the influence factor ( $i_0$ ) using the finite element method (FEM).

$$i_0 = \frac{K}{\frac{PR_i^2}{(R_e^2 - R_i^2)} \sqrt{\pi a}} \quad \text{for an external circumferential crack} \quad (14)$$

where P is the pressure calculated in Eq. (10) and K is the SIF calculated by the G – Theta method in XFEM. The verification of the model was made by the comparison of the values  $i_0$  calculated by XFEM in the present paper and the results of CEA [8]. The relative error was calculated according to the Eq. (15):

$$e_1 = 100 \times \left| \frac{(i_{0_{CEA}} - i_{0_{XFEM}})}{i_{0_{CEA}}} \right| \quad (15)$$

$i_0$  is calculated at D and S points and along the crack front (Fig. 8) for all fractions ( $a/t_1$ ) and ( $a/c$ ), a sample of the results is presented in Figs. 9-11. The relative error between the XFEM results and literature [8] is between 0.09% and 0.7%. This gives confirmation to use numerical simulation based on XFEM to investigate the SIF at a thickness transition with one and two slopes in pressurized pipe.

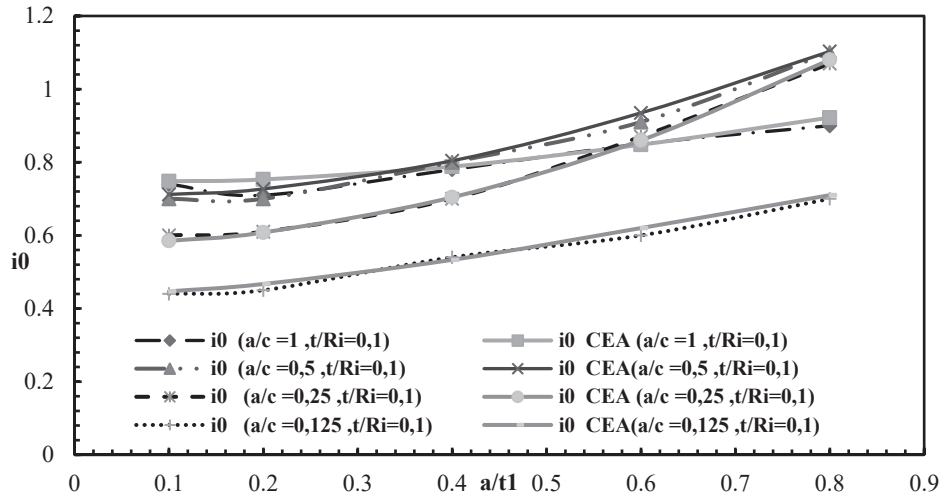


Fig. 9: Comparisons of  $i_0$  calculated by XFEM in the present study with the literature [8], at S point,  $t_1 / R_i = 0.1$ .

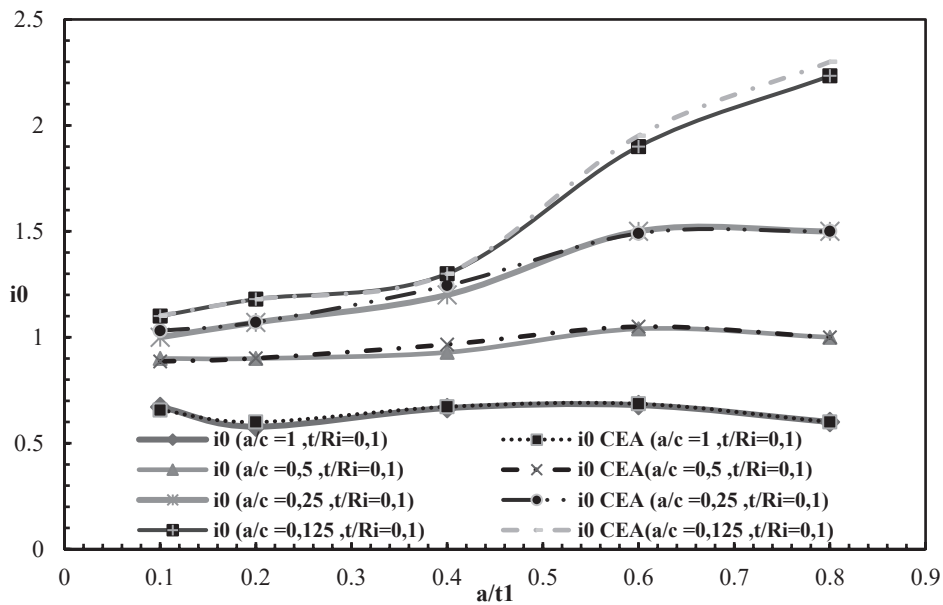


Fig. 10: Comparisons of  $i_0$  calculated by XFEM in the present study with the literature [8], at D point,  $t_1 / R_i = 0.1$ .

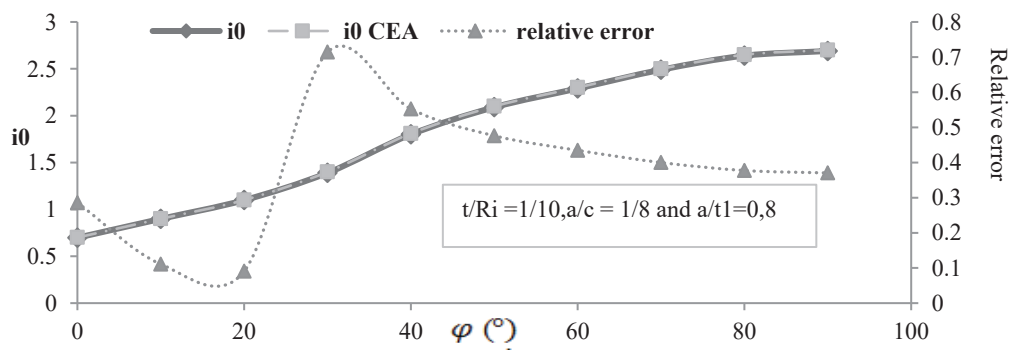


Fig. 11: Comparisons of  $i_0$  calculated by XFEM in the present study with the literature [8], along the crack front.

## 4.2 Comparison between K of the Pipe with Uniform Thickness and the Pipe with Thickness Transition

In a previous paper, we analysed the effect of cracks in the thickness transition zone of pressurized pipes using XFEM [19,20]. We have considered the elastic behaviour of the material and thickness transition with a single slope. The calculations of K for different geometries of the pipe subjected to internal pressure showed that cracks in the transition are the most severe. This result is in concordance with [3] which considered tensile stress and a bending moment. The present paper extends the previous work to the case of thickness transition with two slopes.

Figures 12 and 13 present the evolution of K value according to  $a/t_1$  in deepest and surface points in case of  $t_1 / R_i = 0.1$ , for three types of pipes: uniform thickness, thickness transition with one slope, thickness transition with two slopes.

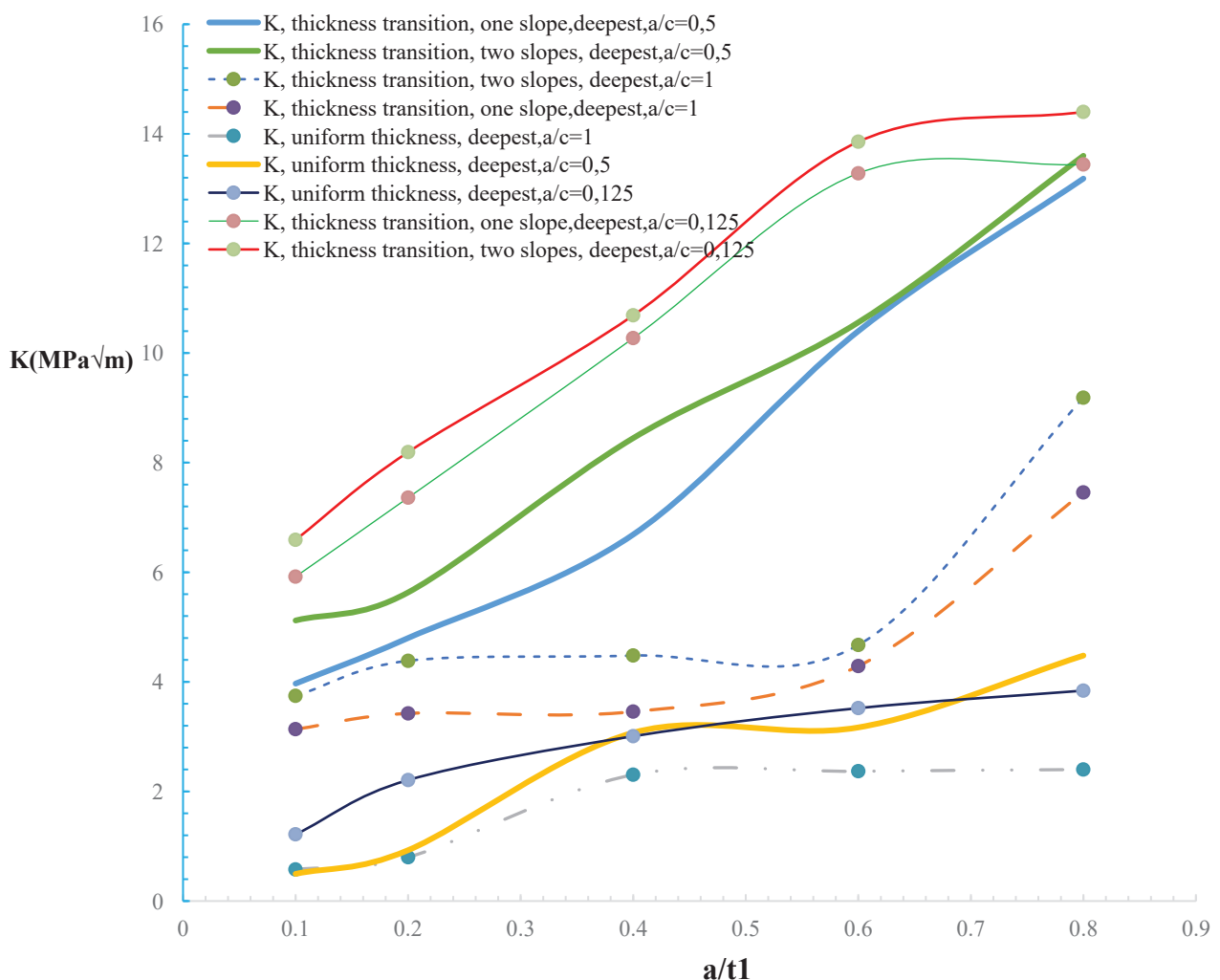


Fig. 12: Evolution of K value according to  $a/t$  for pipes: uniform thickness, transition thickness with one slope, transition thickness with one slope, D point,  $t_1 / R_i = 0.1$ , internal pressure.

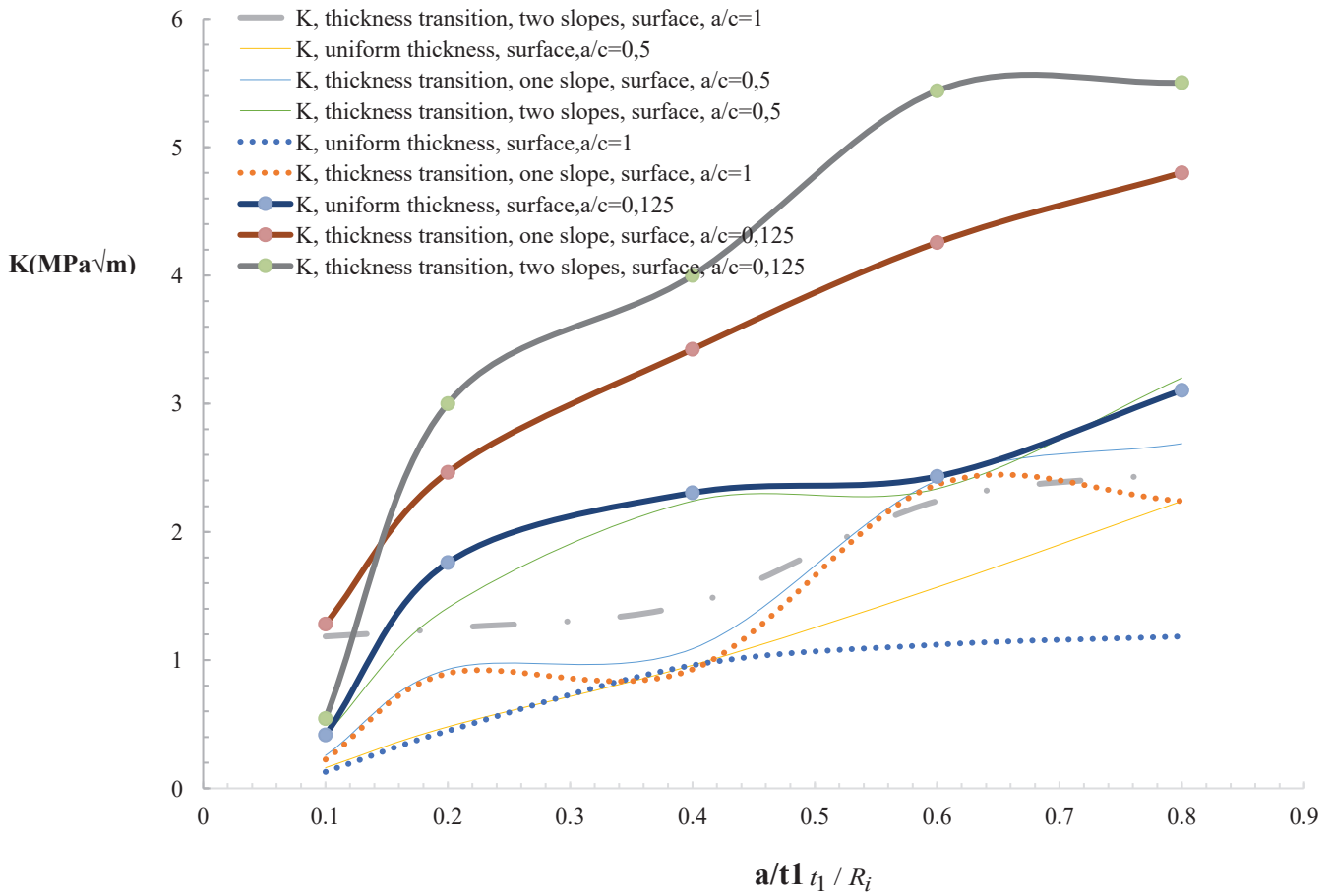


Fig. 13: Evolution of K value according to  $a/t_1$  for pipes: uniform thickness, transition thickness with one slope, transition thickness with one slope, S point,  $t_1/R_i=0.1$ , internal pressure.

The results show that for the deepest point we have:

- K increases when  $a/t_1$  increases for all types of pipe that to say K is higher for depth crack ( $a/t_1=0.8$ ) for all pipes with different thicknesses and slopes.
- K is sensitive to the parameter  $a/c$ , K increases when  $a/c$  decreases for all depths of the crack ( $a/t_1$ ), that's to say K is higher (14 MPa) for longer crack ( $a/c=0.125$ ).
- K is high for pipe with thickness transition, at the same time thickness transition with two slopes have the highest K for all forms of cracks.

The results show that for the surface point we have:

- K depends on the parameter  $a/t$  for different pipes
- K varies slightly when  $a/c$  decreases for all depths of the crack ( $a/t_1$ ), for  $a/c=0.125$  K attain only 5 MPa.

As a result, in the case of a pipe with an average thickness ( $t_1/R_i=0.1$ ), for a fixed angle  $\alpha_1 = 30^\circ$  and  $\alpha_2 = 45^\circ$ , we found that the thickness transition with two slopes has the greatest value of K, so it presents the greatest risk compared to the straight pipe and pipe with thickness transition and a single slope.

Do these values of  $\alpha_1 = 30^\circ$  and  $\alpha_2 = 45^\circ$ , lead to a greater value of K? How does the variation of the parameters  $\alpha_1$ ,  $\alpha_2$  and  $t_j$  ( $j \in \{1,2,3\}$ ) influence the variations of K for a pipe with average thickness?

### 4.3 Effect of the Transition Zone on the Variation of K

Based on the triangular relation, the length of the thickness transition is related to the angle of the slope by the following relation:

$$l = t_2 \left[ \frac{(1 - t_1/t_2)}{\tan(\alpha_1)} + \frac{(1 - t_3/t_2)}{\tan(\alpha_2)} \right] \quad \text{with} \quad 0 < \alpha_1 < \frac{\pi}{2} \quad \text{and} \quad 0 < \alpha_2 < \frac{\pi}{2} \quad \text{and} \quad t_1 < t_2 < t_3 \quad (16)$$

(l) mainly depends on  $(t_2/t_1)$ ,  $(t_3/t_2)$ ,  $\alpha_1$  and  $\alpha_2$ . We consider those parameters as variable and analyze their effect on the variation of K.

#### 4.3.1 Effect of the Slope in Thickness Transition on the Variation of K

In this study, we considered a pipe with an average thickness where  $(t_2/t_1) = (t_3/t_2) = 2.5$ , the pipe contained an elliptical crack defined by  $a/c = 0.125$  and  $a/t_1 = 0.8$ , the pipe is exposed to internal pressure. Figure 14 (a) presents the evolution of K according to  $\alpha_1$  for a fixed value of  $\alpha_2$  in a deepest and surface points.

The result shows that K increases when  $\alpha_1$  increases, K attains the maximum ( $K_{\text{deepest point}} = 55 \text{ MPa}\sqrt{\text{m}}$ ) for  $\alpha_1 = 30^\circ$ . For  $\alpha_1 > 30^\circ$ , K decreases and tends to stabilize to equal a great value compared with the value of K when  $\alpha_1 < 30^\circ$ .

K in deepest point is higher than K in surface point for  $20^\circ < \alpha_1 < 50^\circ$  but for  $\alpha_1 > 50^\circ$   $K_{\text{surface point}}$  exceeds  $K_{\text{deepest point}}$ . The transition reacts as an amplifier of stress, it magnifies the stress close to the surface, so the value of K is higher for the great value of  $\alpha_1$  ( $\alpha_1 > 50^\circ$ ) of the slope of the first transition ( $\alpha_2$  is fixed). When  $\alpha_1$  decreases ( $\alpha_1 < 50^\circ$ ), the concentration of the stress decreases at S point, because at S point, the thickness transition impact noticeably reduces in comparison with the effect of internal pressure which increases the concentration of stress in the deepest point. Therefore, the value of K at D point becomes higher compared to the value of K in the surface point for small values of  $\alpha_1$ .

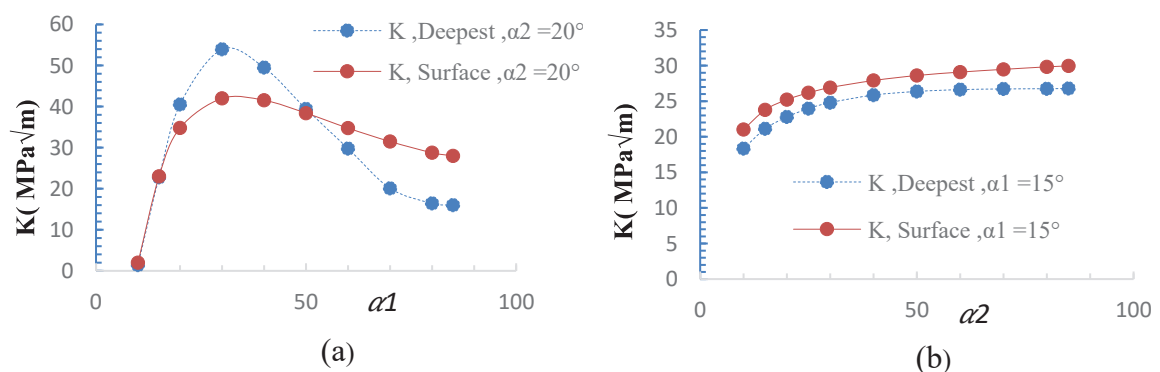


Fig. 14: Variation of K at deepest and surface points:  
 (a) According to  $\alpha_1$ , (b) According to  $\alpha_2$ .

Figure 14 (b) presents the evolution of K according to  $\alpha_2$  for a fixed value of  $\alpha_1$  in deepest and surface points. The result shows that K increases in a weak way, when  $\alpha_2$

increases and it attains the maximum ( $K_{surface\ point} = 29\ MPa$ ) for  $\alpha_2 = 45^\circ$ . For  $\alpha_2 > 45^\circ$ , K keeps a stable value, At the same time, the values of K at the deepest point are close to those of K at the surface point for all values of  $\alpha_2$ , that's to say the angle of the slope  $\alpha_2$  does not have a great effect on the variation of K.

As a result, the slopes  $\alpha_1 \geq 30^\circ$  and  $\alpha_2 \geq 45^\circ$  present a grave case for thickness transition with a double slope, also the angle of the first slope ( $\alpha_1$ ) in thickness transition has more impact on the variations of K than the angle of the second slope ( $\alpha_2$ ).

#### **4.3.2 Effect of Parameters ( $\alpha_1$ , ( $t_2/t_1$ )) and ( $\alpha_1$ , ( $t_3/t_2$ )) on the Variation of K in Thickness Transition with a Double Slope**

In the part (4.3.1), we supposed  $\alpha_1$  and  $\alpha_2$  as variables and analyzed their effect on the variation of K in thickness transition for fixed values of ( $t_2/t_1$ ) and ( $t_3/t_2$ ). In this part, firstly, we consider  $\alpha_1$  and ( $t_2/t_1$ ) as variables and we fix ( $t_3/t_2$ ) and  $\alpha_2$ , in this case, the parameter  $\alpha_1$  is varied within the range of  $5^\circ$  to  $50^\circ$  and the ratio ( $t_2/t_1$ ) is varied from 1.1 to 6, secondly, we vary  $\alpha_1$  and ( $t_3/t_2$ ) and fix other parameters, the ratio ( $t_3/t_2$ ) is varied from 1.1 to 4.

Figure 15a-b present the variations of K according to the parameters  $\alpha_1$  and ( $t_2/t_1$ ), for ( $t_3/t_2$ ) = 1.30 and  $\alpha_2 = 30^\circ$  at deepest and surface points. Figure 15a-b, show that for both D and S points, we have:

- For  $1.1 \leq (t_2/t_1) \leq 1.5$ , the value of K is high and exceeds the toughness of materials P265GH ( $K_C = 96\ MPa\sqrt{m}$ ).
- For all values of  $\alpha_1$ , in the case of  $1.5 < (t_2/t_1)$ , we note that K decreases when ( $t_2/t_1$ ) increases and stabilizes for ( $t_2/t_1$ ) greater than 4.5.
- For  $\alpha_1 \geq 30^\circ$ , K takes the greatest value for all ( $t_2/t_1$ ).

As a result, the great value of the angle of the first slope in a cracked pipe has an important effect on the variation of K, more precisely  $\alpha_1 \geq 30^\circ$  is a grave case for the construction of the pipe and increasing the ratio of thicknesses ( $t_2/t_1$ ), is an effective way to reduce the risk of the defect in a pipe.

Figure 15c-d present the variations of K according to the parameters  $\alpha_1$  and ( $t_3/t_2$ ), for ( $t_2/t_1$ ) = 1.40 and  $\alpha_2 = 30^\circ$  at deepest and surface points. The curves of stress intensity show that for D and S points, we have:

- In the case of  $\alpha_1 \geq 30^\circ$ ; K exceeds the toughness of materials ( $K_C$ ), K decreases when ( $t_3/t_2$ ) increases.
- In the case of  $\alpha_1 < 30^\circ$ ; K increases when ( $t_3/t_2$ ) increases but it but this evolution of K as a function of ratio ( $t_3/t_2$ ) is not remarkable.

As a result, the parameter ( $t_3/t_2$ ) does not have more impact on the variation of K in thickness transition with a double slope for a pressurized pipe.

#### **4.3.3 Effect of Parameters ( $\alpha_2$ , ( $t_2/t_1$ )) and ( $\alpha_2$ , ( $t_3/t_2$ )) on the Variation of K in Thickness Transition with a Double Slope**

Proceeding as before; we analysed the evolution of K in the thickness transition by fixing two parameters of the transition zone and varying the rest.

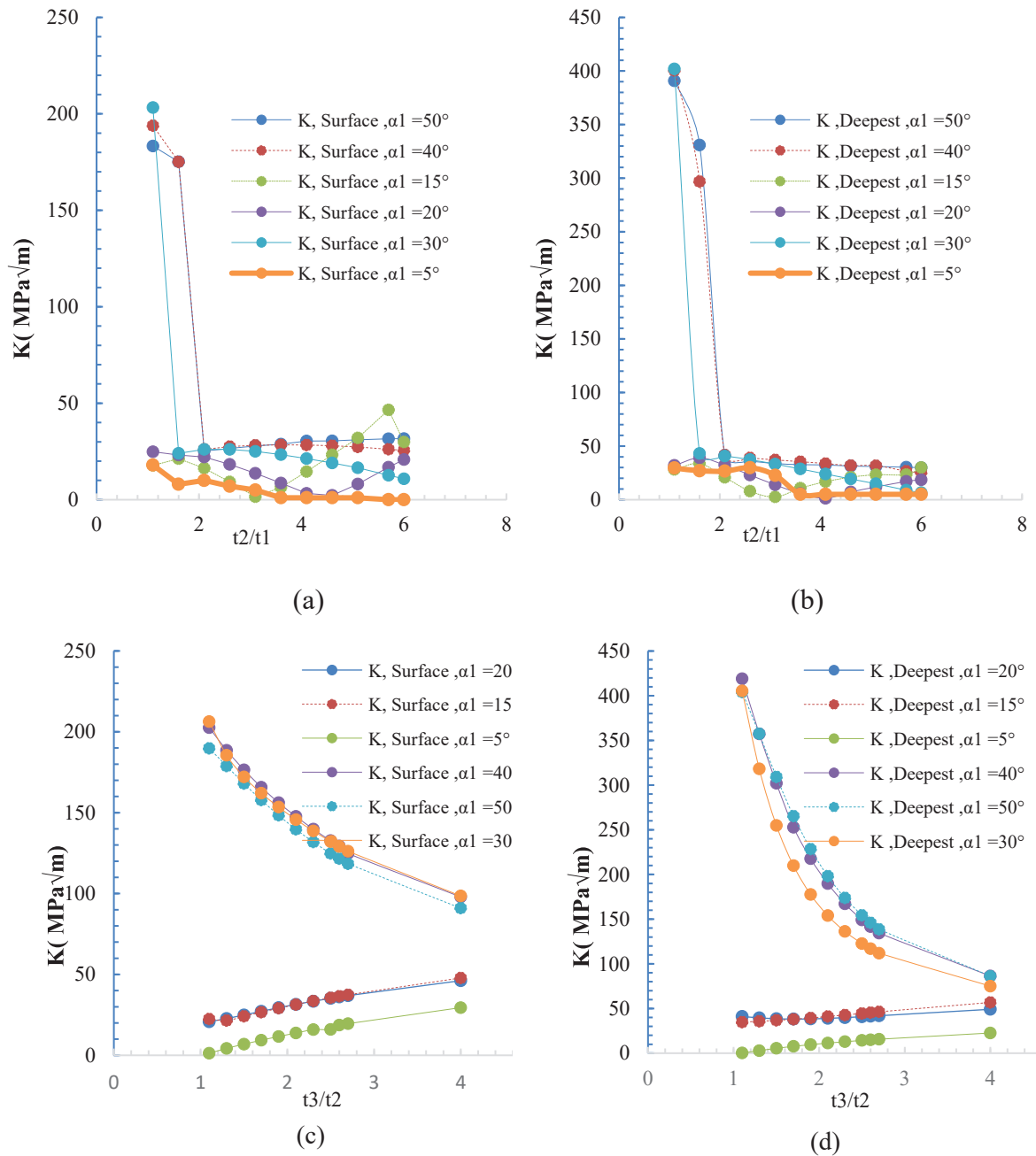


Fig. 15: Variation of  $K$  at deepest and surface points: (a-b), according to  $\alpha_1$  and  $(t_2/t_1)$ , (c-d), according to  $\alpha_1$  and  $(t_3/t_2)$ .

Figure 16a-b present the variations of  $K$  according to the parameters  $\alpha_2$  and  $(t_2/t_1)$ , for  $(t_3/t_2) = 1.30$  and  $\alpha_1 = 20^\circ$  at deepest and surface points. The parameter  $\alpha_2$  is varied within the range of  $10^\circ$  to  $50^\circ$  and the ratio  $(t_2/t_1)$  is varied from 1.1 to 6. The result shows that the stress intensity curves don't depend on the variation of  $\alpha_2$  for S and D points. The variation of  $K$  relates mostly on the parameter  $(t_2/t_1)$  of the first thickness transition, the range  $3.5 \leq (t_2/t_1) \leq 4$  allows small values of  $K$  ( $K < 9 \text{MPa}$ ).

Figure 16c-d present the variations of  $K$  according to the parameters  $\alpha_2$  and  $(t_3/t_2)$ , for  $(t_2/t_1) = 1.40$  and  $\alpha_1 = 20^\circ$  at deepest and surface points. The ratio  $(t_2/t_1)$  is varied

from 1.1 to 4.5. The results show again, that  $\alpha_2$  does not have enough effect on the variation of K, in addition, K increases when  $(t_2/t_1)$  increases but this variation of K is not very remarkable, the range  $1.5 \leq (t_3/t_2) \leq 2.5$  allows small values of K ( $K < 35$  MPa).

As a result, the parameters of the thickness transition in a pipe have an influence on the variations of K, precisely the parameters of the first thickness transition ( $\alpha_1, (t_2/t_1)$ ) are more influential on the gravity of defect compared to the second thickness transition ( $\alpha_2, (t_3/t_2)$ ).

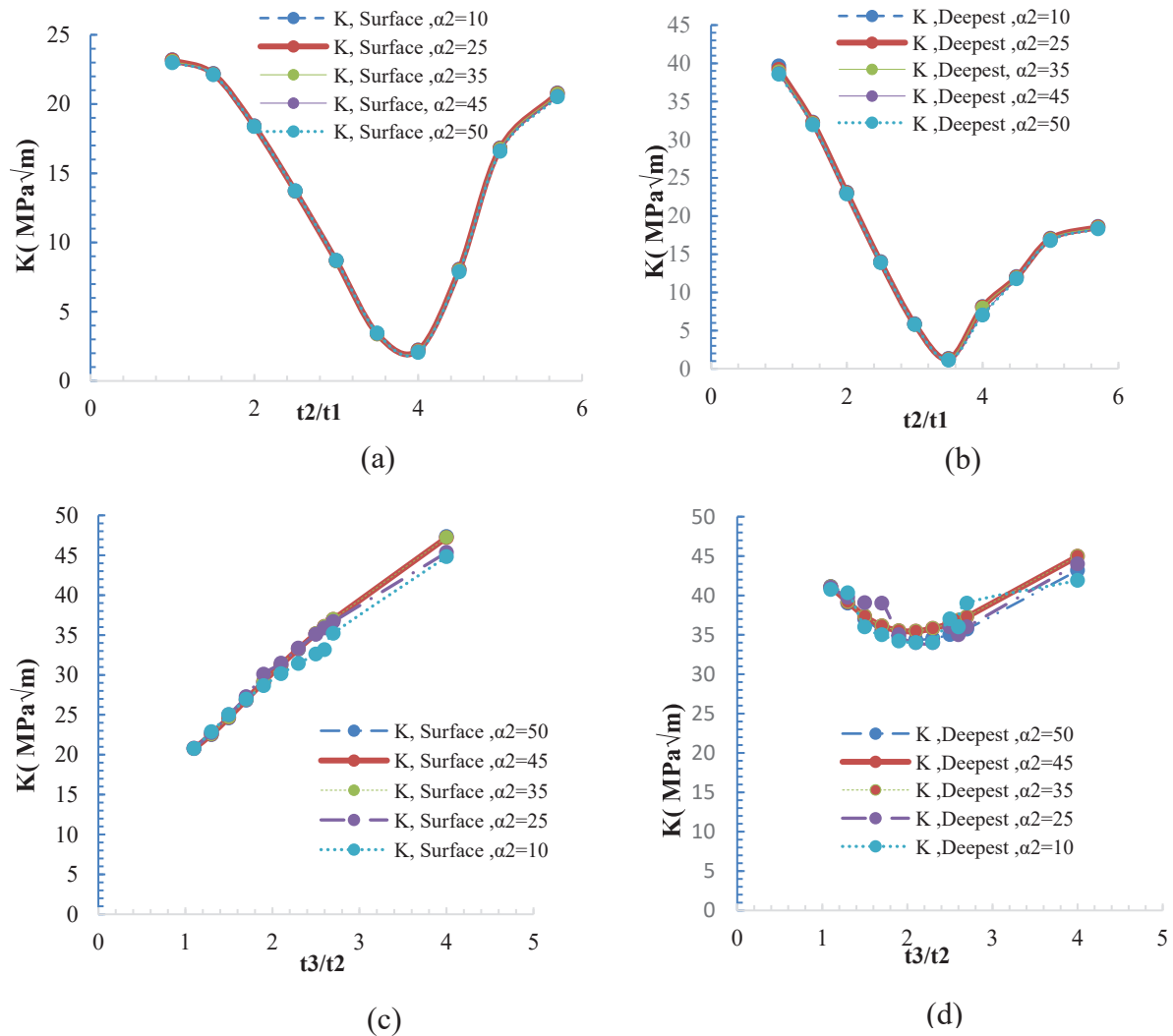


Fig. 16: Variation of K at deepest and surface points:  
 (a-b) According to  $\alpha_2$  and  $(t_2/t_1)$ , (c- d) According to  $\alpha_2$  and  $(t_3/t_2)$ .

## 5. CONCLUSION

In this paper, we analysed the effect of an external circumferential elliptical crack located at the thickness transition zone of a pipe with double slopes. The study showed that for the surface and the deepest points, the angle  $\alpha_1 = 30^\circ$  and  $1.1 \leq (t_2/t_1) \leq 1.5$  are grave cases of the first slope of the thickness transition. The angle  $\alpha_2 = 45^\circ$  and  $(t_2/t_1) = 3.5$  lead to an increase in the value of K but in general, the effect of the second slope

isn't remarkable, that is to say the parameters  $(\alpha_1, (t_2/t_1))$  are more influential than the parameters  $(\alpha_2, (t_3/t_2))$ .

Considering the internal pressure, this work highlighted the investigation of a 3D crack problem in a thickness transition pipe using XFEM. In XFEM, level sets and enrichment zone were defined. A crack is easily modelled by enrichment functions. The comparison between the stress intensity factors showed that the pipe containing a thickness transition with double slopes is more sensitive to the considered cracks. The decreasing of the angle of slopes and the increase of the ratio of thickness is one effective method of reducing the SIF.

## REFERENCES

- [1] Rahman S, Ghadiali N, Wilcowski GM, Moberg F, Brickstad B. (1998) Crack-opening-area analysis for circumferential trough-wall cracks restrain of bending thickness transition and weld residual stresses. *Int J Pres Ves Pip*, 75(6):397-415.
- [2] Hanan El Bhilat, Khalid El Had, Houda Salmi, Abdelilah Hachim. (In press). Thermo-mechanical characterization of post-consumer recycled high impact polystyrene from disposable cups: influence of the number of processing cycles. *Journal of Computational & Applied Research in Mechanical Engineering (JCARME)*. DOI [10.22061/JCARME.2019.5187.1643](https://doi.org/10.22061/JCARME.2019.5187.1643)
- [3] Abdelkader Saffih, Hariri S. (2006) Numerical study of elliptical cracks in cylinders with a thickness transition' *International Journal of Pressure Vessels and Piping*; 83(1):35-41. DOI: [10.1016/j.ijpvp.2005.10.002](https://doi.org/10.1016/j.ijpvp.2005.10.002)
- [4] Abdelkader Saffih, Hariri S. (2006) Comparison of semi-elliptical cracks in cylinders with a thickness transition and in a straight cylinder – Elastic-plastic behavior, *Engineering Fracture Mechanics*, 73(4):2685-2697
- [5] Hariri S, El Hakimi A, Azari Z. (2008) Etude numérique et expérimentale de la nocivité des défauts dans des coques cylindriques et sphériques: aide à la détermination des facteurs de contraintes, *Revue de Mécanique Appliquée et Théorique*, 1(10):791-804. <http://smsm.fsac.ac.ma/larevue/2008/art9vol1n10.pdf>
- [6] CEA; The French Alternative Energies and Atomic Energy Commission (CEA). 'Commissariat à L'Energie Atomique (France)' <http://www.cea.fr/>.
- [7] CASTEM; [<http://www-cast3m.cea.fr/>]
- [8] Chapuliot S, Lacire MH. (1999) Stress intensity factors for external circumferential cracks in tubes over a wide range of radius over thickness ratios. *American Society of Mechanical Engineers, Pressure Vessels and Piping Division*, 50(2):395-106. <https://inis.iaea.org/collection/NCLCollectionStore/Public/31/058/31058406.pdf>
- [9] Moës N, Gravouil A. Belytschko T. (2002) Non-planar 3D crack growth by the extended finite element and level sets; Part I: Mechanical model. *International Journal for Numerical Methods in Engineering*, 53(11):2549-2568. <https://doi.org/10.1002/nme.429>
- [10] Salmi H, El Had K, El Bhilat H, Hachim A. (2020) Numerical Study of SIF for a Crack in P265GH Steel by XFEM. In: Dos Santos S., Maslouhi M., Okoudjou K. (eds) *Recent Advances in Mathematics and Technology. Applied and Numerical Harmonic Analysis*. Birkhäuser, Cham. doi.org/10.1007/978-3-030-35202-8\_6
- [11] Belytschko T, Black T. (1999). Elastic crack growth in finite elements with minimal remeshing, *Int. J. Numer. Methods Eng*, 45(5):601–62.
- [12] Stolarska M, Chopp D, Moes N, Belytschko T. (2001) Modelling crack growth by level sets in the extended finite element method, *Int. J. Numer. Methods Eng*, 51(1):943–960.
- [13] Seyed Javid Zakavi, Behzad Shiralivand, Mohammad Nourbakhsh. (2017) Evaluation of combined hardening model in ratcheting behavior of pressurized piping elbows subjected to in-plane moments. *Journal of Computational & Applied Research in Mechanical Engineering (JCARME)*; 7(1): 57-71. DOI [10.22061/JCARME.2019.5187.1643](https://doi.org/10.22061/JCARME.2019.5187.1643)

- [14] Kamal Sharma IVS, Mishra BK, Bhasin V. (2014) Numerical Modeling of Part-Through Cracks in Pipe and Pipe Bend using XFEM, *Procedia Materials Science*, 6(2):72-79.
- [15] Rice JR. (1968) A Path Independent Integral and the Approximate Analysis of Strain Concentration by Notches and Cracks, *Journal of Applied Mechanics*, 35(1):379-386.
- [16] Sukumar N, Chopp DL, Moran B. (2003), Extended finite element method and fast marching method for three-dimensional fatigue crack propagation, *Engineering Fracture Mechanics*, 70(1): 29-48.
- [17] Eshelby JD. (1956) The Continuum Theory of Lattice Defects, *Solid State Physics*, 3(2):79-144.
- [18] CODAP (2005); French construction code. Construction des Appareils à Pression non soumis à l'action de la flamme, 'the Code for Construction of unfired Pressure Vessels, Division 1, part C – design and calculation, section C2 – rules for calculating cylindrical, spherical and conical shell subjected to internal pressure.
- [19] Houda Salmi, Khalid El Had, Hanan El Bhilat, Abdelilah Hachim. (2019). Numerical Analysis of the Effect of External Circumferential Elliptical Cracks in Transition Thickness Zone of Pressurized Pipes Using XFEM. *J. Appl. Comput. Mech.*, 5(5):861-874. DOI: 10.22055/JACM.2019.28043.1452.
- [20] Houda Salmi ; Khalid El Had; Hanan El Bhilat; Abdelilah Hachim (In press). Numerical modeling and comparison study of elliptical cracks effect on the pipes straight and with thickness transition exposed to internal pressure, using XFEM in elastic behavior. *Journal of Computational and Applied Research in Mechanical Engineering*. DOI: 10.22061/JCARME.2019.3597.1448.





# IIUM ENGINEERING JOURNAL

---

## CHIEF EDITOR

Ahmad Faris Ismail, IIUM, Malaysia

## EXECUTIVE EDITOR

AHM Zahirul Alam, IIUM, Malaysia

## ASSOCIATE EDITOR

Nor Farahidah Za'bah, IIUM, Malaysia

## LANGUAGE EDITOR

Lynn Mason, Malaysia

## COPY EDITOR

Hamzah Mohd. Salleh, IIUM, Malaysia

## EDITORIAL BOARD MEMBERS

Abdullah Al-Mamun, IIUM, Malaysia  
Abdumalik Rakhimov, IIUM, Malaysia  
Ali Sophian, IIUM, Malaysia  
Erry Yulian Triblas Adesta, IIUM, Malaysia  
Erwin Sulaeman, IIUM, Malaysia  
Hanafy Omar, Saudi Arabia  
Hazleen Anuar, IIUM, Malaysia  
Konstantin Khanin, University of Toronto, Canada  
Ma'an Al-Khatib, IIUM, Malaysia  
Md Zahangir Alam, IIUM, Malaysia  
Meftah Hrairi, IIUM, Malaysia  
Mohamed B. Trabia, United States  
Mohammad S. Alam, Texas A&M University-Kingsville, United States  
Mustafizur Rahman, National University Singapore, Singapore  
Ossama Abdulkhalik, Michigan Technological University, United States  
Razi Nalim, IUPUI, Indianapolis, Indiana, United States  
Rosminazuin AB. Rahim, IIUM, Malaysia  
Waqar Asrar, IIUM, Malaysia

## AIMS & SCOPE OF IIUMENGINEERING JOURNAL

The **IIUM Engineering Journal**, published biannually (January and July), is a carefully refereed international publication of International Islamic University Malaysia (IIUM). Contributions of high technical merit within the span of engineering disciplines; covering the main areas of engineering: Electrical and Computer Engineering; Mechanical and Manufacturing Engineering; Automation and Mechatronics Engineering; Material and Chemical Engineering; Environmental and Civil Engineering; Biotechnology and Bioengineering; Engineering Mathematics and Physics; and Computer Science and Information Technology are considered for publication in this journal. Contributions from other areas of Engineering and Applied Science are also welcomed. The IIUM Engineering Journal publishes contributions under *Regular papers and Invited review papers*. It also welcomes contributions that address solutions to the specific challenges of the developing world, and address science and technology issues from an Islamic and multidisciplinary perspective.

## REFEREES' NETWORK

All papers submitted to IIUM Engineering Journal will be subjected to a rigorous reviewing process through a worldwide network of specialized and competent referees. Each accepted paper should have at least two positive referees' assessments.

## SUBMISSION OF A MANUSCRIPT

A manuscript should be submitted online to the IIUM-Engineering Journal website at <http://journals.iium.edu.my/ejournal>. Further correspondence on the status of the paper could be done through the journal website.

---

ISSN 1511 - 788X



**IIUM Engineering Journal**

ISSN: 1511-788X E-ISSN: 2289-7860